

Society of Automotive Engineers
of China (SAE-China)
International Federation
of Automotive Engineering Societies (FISITA)
Editors

Proceedings of the FISITA 2012 World Automotive Congress

Volume 5: Advanced Transmission
System and Driveline



Lecture Notes in Electrical Engineering

Volume 193

For further volumes:
<http://www.springer.com/series/7818>

Society of Automotive Engineers of China
(SAE-China) · International Federation of
Automotive Engineering Societies (FISITA)
Editors

Proceedings of the FISITA 2012 World Automotive Congress

Volume 5: Advanced Transmission System
and Driveline



 Springer

The Springer logo, consisting of a stylized chess knight (horse) facing left, positioned to the left of the word 'Springer' in a serif font.

Editors
SAE-China
Beijing
People's Republic of China

FISITA
London
UK

ISSN 1876-1100
ISBN 978-3-642-33743-7
DOI 10.1007/978-3-642-33744-4
Springer Heidelberg New York Dordrecht London

ISSN 1876-1119 (electronic)
ISBN 978-3-642-33744-4 (eBook)

Library of Congress Control Number: 2012948289

© Springer-Verlag Berlin Heidelberg 2013

This work is subject to copyright. All rights are reserved by the Publisher, whether the whole or part of the material is concerned, specifically the rights of translation, reprinting, reuse of illustrations, recitation, broadcasting, reproduction on microfilms or in any other physical way, and transmission or information storage and retrieval, electronic adaptation, computer software, or by similar or dissimilar methodology now known or hereafter developed. Exempted from this legal reservation are brief excerpts in connection with reviews or scholarly analysis or material supplied specifically for the purpose of being entered and executed on a computer system, for exclusive use by the purchaser of the work. Duplication of this publication or parts thereof is permitted only under the provisions of the Copyright Law of the Publisher's location, in its current version, and permission for use must always be obtained from Springer. Permissions for use may be obtained through RightsLink at the Copyright Clearance Center. Violations are liable to prosecution under the respective Copyright Law. The use of general descriptive names, registered names, trademarks, service marks, etc. in this publication does not imply, even in the absence of a specific statement, that such names are exempt from the relevant protective laws and regulations and therefore free for general use.

While the advice and information in this book are believed to be true and accurate at the date of publication, neither the authors nor the editors nor the publisher can accept any legal responsibility for any errors or omissions that may be made. The publisher makes no warranty, express or implied, with respect to the material contained herein.

Printed on acid-free paper

Springer is part of Springer Science+Business Media (www.springer.com)

Contents

Part I Clutch System and Controls

Application of Overbend Blind Riveting in Designing and Manufacturing of Multiple-Plates Torque Converter	3
F2012-C01-001 Kunding Wang, Alfredo Jiminez Perez Mitre, Zhiru Shi and Ricardo Andreoli	
Analysis of the Influence of Clutch Pedal to Vehicle Comfort	15
F2012-C01-002 Jiangchuan Li, Feng Deng, Shaojin Liu and Hao Hu	
Modeling and Parametric Study on Drag Torque of Wet Clutch.	21
F2012-C01-003 Heyan Li, Qi Jing and Biao Ma	
Modeling and Simulation of an Electric Clutch Actuator	31
F2012-C01-004 Hanqi Yue, Bin Wang, Lijiao Yu, Bingzhao Gao and Hong Chen	
Methods for Clutch Dimensioning	39
F2012-C01-009 Albers Albert, Sascha Ott and Philipp Merkel	
Drive Train Vibrations: Solving the Conflict Between Efficiency and Drivability	49
F2012-C01-010 Ad Kooy and Jürgen Kroll	

Part II Gear Systems and Driveline

Definition of Slippage Parameters of Friction Clutches in Gearboxes with Fixed Shaft Axles	65
F2012-C02-001 Mikhail Dmitriev and Valery Sharipov	
The Influence of Torque and Speed Sensitive Differential Characteristics in a Front Wheel Drive Vehicle During On-Limit Manoeuvres	79
F2012-C02-003 Anthony Tremlett, David Purdy, Nick Vaughan, Francis Assadian, Adrian Moore and Martin Halley	
Design and Performance Prediction of a Tri-Mode Power-Split Transmission.	93
F2012-C02-004 Donghao Zhang, Changle Xiang and Lijin Han	
Transient EHL Gear Contact Simulation	107
F2012-C02-006 Peter Fietkau, Axel Baumann and Bernd Bertsche	
An Enhanced Finite Element Model for Determination of Load Capacity in Planetary Gear Trains	119
F2012-C02-008 Ignacio Gonzalez-Perez, Alfonso Fuentes and Kenichi Hayasaka	
Gear Oil Viscosity Modifiers and Their Impact on Efficiency	131
F2012-C02-009 William Barton, Elizabeth Schiferl, Mark Baker and Simon Chai	
On the Behaviour of Asymmetric Cylindrical Gears in Gear Transmissions.	143
F2012-C02-010 Alfonso Fuentes, Ignacio Gonzalez-Perez, Francisco T Sanchez-Marin and Kenichi Hayasaka	
Efficiency Optimization of Transmissions	151
F2012-C02-013 Kathrien Inderwisch, Rashad Mustafa and Ferit Küçükay	

Research on Safety Performance for Parking Mechanism on a 7-Speed Dual Clutch Transmission 163
 F2012-C02-015
 Lingling Fu, Zhiling Qiu, Yuxiang Chen, Dawei Luo, Yong Chen, Daguo Luo and Fuquan Zhao

Control Strategy and Function Design Based on Lever Analogy 175
 F2012-C02-019
 Hua Tian and Peng Chen

Research on Precision Forging Tooth Billet of Driven Bevel Gear. 183
 F2012-C02-021
 Baoyang Song, Chenglin Xu, Chenglin Fu, Zhuang Fu, Guansheng Wang, Shibao Liu, Zhaodan Yuan, Xiaohui Li and Xinghua Li

Schaeffler Lightweight Differentials 199
 F2012-C02-022
 Thorsten Biermann, Xiaogang Chang and Bernd Robert Höhn

Part III Advanced Transmission System

The Design Concept of Complete Traction Electric Equipment Sets for Hybrid Vehicles 217
 F2012-C03-002
 Stanislav Florentsev, Dmitry Izosimov and Ivan Ksenevich

The Design, Development and Industrialization of Shangri New Type of Automatic Transmission in China 229
 F2012-C03-003
 Jan Gang Lu and Xingwu Liu

The Double Roller Full Toroidal Variator: A Promising Solution for KERS Technology 241
 F2012-C03-006
 Giuseppe Carbone, Francesco Bottiglione, Leonardo De Novellis, Luigi Mangialardi and Giacomo Mantriota

CVT’s Evolution and Nissan’s Latest CVT Technologies. 251
 F2012-C03-009
 Yoshitaka Miura, Kiyonari Yamamoto and Tetsuro Ito

Development of a New 6-Speed Dual Clutch Transmission for the China Market	261
F2012-C03-018	
Chao Jiang, Mingli Huang, Gold Eckart and Xiaoning Xiang	
Development of New CVT for K-Car	271
F2012-C03-019	
Koichi Konishi	
Research on Development Process of 7 Speed Wet Dual Clutch Transmission	275
F2012-C03-022	
Yong Chen, Mike Turner, Michael Gilcrist, Wenjiang Zhao, Daguo Luo and Fuquan Zhao	
A Study on Performance Simulation and Optimization of an Automatic Transmission	283
F2012-C03-023	
Yong Chen, Daguo Lou, Hua Chen and Fuquan Zhao	
Development of the Electric Vehicle AMT Control Strategy	295
F2012-C03-025	
Zhangzhen Deng, Haiyun Gan, Pengyi Deng, Rongming Shan and Liangyi Yang	
Kinematic Study and Mode Analysis of a New 2-Mode Hybrid Transmission	309
F2012-C03-026	
Xuerui Ma, Yong Zhang and Chengliang Yin	
CVT Driving to a Green Future	319
F2012-C03-027	
Aaron Cai	
 Part IV Transmission Control System	
The Control Authority of Passive and Active Torque Vectoring Differentials for Motorsport Applications	335
F2012-C04-002	
Anthony Tremlett, Francis Assadian, David Purdy, Nick Vaughan, Adrian Moore and Martin Halley	

Modeling and Simulation of a New Type Hydraulic System on CVT 349
 F2012-C04-009
 Yanhui Lu, Mingshu Liu and Yang Liu

Research and Control of Shift Without the Disengagement of the Clutch for Automatic Mechanical Transmission in Hybrid Vehicle 361
 F2012-C04-010
 Shaohua Sun, Yulong Lei, Hongbo Liu, Yao Fu and Huabing Zeng

Analysis of Desert Adaptation on Shifting Strategy for Heavy Off-Road AMT Vehicle 373
 F2012-C04-011
 Yanghong Xue, Yuhui Hu and Huiyan Chen

Fuzzy Logic Controlled Electromagnetic Actuated Cvt System for Passenger Car 387
 F2012-C04-013
 Rahman Aatur and Sharif Sazzad Bin

Modelling and Simulation of DCT Gearshifting for Real-Time and High-Fidelity Analysis 399
 F2012-C04-014
 Lionel Belmon, Jun Yan and Andreas Abel

Optimized AMT Systems from ZF: A Choice for Comfort and Fuel Consumption Improvement in the Small Car Segment 413
 F2012-C04-015
 Benedikt Schauder and Joerg Buhl

Shifting Control Strategy Research in the Hard Accelerating Condition Based on the AMT Vehicle 423
 F2012-C04-016
 Yang Gao, Yong Chen, Daguo Luo, Wenzhong Liu, Mingqi Gu and Fuquan Zhao

Robust Design Method for Automatic Calibration of Automatic Transmission Shift Control System 433
 F2012-C04-020
 Ryoichi Hibino, Tomohiro Miyabe, Masataka Osawa and Hideaki Otsubo

Clutch Transmissible Torque Estimation for Dry Dual Clutch Transmission Control	449
F2012-C04-021 Kihoon Han and Yongsoon Yoon	
AMT Control for Parallel Hybrid Electric Vehicles	457
F2012-C04-022 Gianluca Zito	
Part V Other	
Numerical Sensitivity Analysis of the Effect of Pump Outlet Radius on the Performance of Torque Converter	471
F2012-C05-001 Qingdong Yan, Cheng Liu, Wei Wei and Boshen Liu	
Modelling of Oil Heating of Disengaged Lubricated Clutches in Hybrid Vehicles	479
F2012-C05-002 Friedrich Brezger and Albert Albers	
AWD Coupling Modeling and Contribution to Vehicle Dynamics	495
F2012-C05-005 Aris Maroonian, Tsutomu Tamura and Robert Fuchs	

Part I
Clutch System and Controls

Application of Overbend Blind Riveting in Designing and Manufacturing of Multiple-Plates Torque Converter

Kunding Wang, Alfredo Jiminez Perez Mitre, Zhiru Shi
and Ricardo Andreoli

Abstract Automotive torque converter clutch may require multiple friction plates to transmit engine torque. Engine torque flows from the cover to the piston plate through the friction plates. The piston plate cannot directly connect to the cover because of manufacturing difficulty. A drive plate is customarily used for connecting the piston plate to the cover. To eliminate the drive plate, overbend blind riveting technology is required to directly connect the piston plate to the cover. The overbend blind riveting technology faces challenges in terms of design optimization, and process robustness. Innovative solutions in design, process, and verification are examined. Integrated manufacturing simulations, measurements, experiments, and tests are discussed. Benefits of the application in terms of axial space saving, clutch weight reduction, production cost reduction, and fuel consumption improvement are discussed.

1 Introduction

For more than a century, the automotive torque converter has continually proven itself a remarkable launch device. The fundamental concept behind the success of the torque converter is that the torque converter prevents impact at launch for driver comfort and the torque converter clutch locks up at certain engine speed for better fuel economy while torsion damper isolates the drivetrain from the engine firing frequency. Depends on size and torque, some torque converter clutches require multiple friction plates to transmit engine torque. Torque flow establishes

F2012-C01-001

K. Wang (✉) · A. J. P. Mitre · Z. Shi · R. Andreoli
LuK USA LLC, Schaeffler Group, Herzogenaurach, Germany

from the cover to the piston plate through the friction plates. A drive plate is customarily used as an intermediate component between the cover and the piston plate to resolve the manufacturing difficulty in terms of assembly sequences [1]. The piston and the drive plate are previously assembled through the leaf springs riveting connections. The piston assembly then is riveted to the cover through the leaf springs. Additional manufacturing processes and components are required to complete the assembly. In summary, the custom TCC production method involves:

1. 1st set of leaf springs are riveted to the drive plate.
2. 2nd set of leaf springs are riveted to the drive plate at difference circumferential location.
3. The drive plate connects to the piston plate by riveting the 1st set of leaf springs to the drive plate.
4. The piston plate connects to the cover by riveting the 2nd set of leaf springs to the cover.

In process 3, the riveting punch accesses the rivet body through the piston bore and the riveting die provide the back support. Figure 1 shows the drive plate connecting to the piston plate and to the cover through the leaf springs. This process solves the riveting punch accessibility problems, however, it adds complexity to design and process. It is desirable to directly connecting the cover to the piston plate by riveting one end of the leaf springs to the cover and the other end of same leaf springs to the piston plate. The drive plate is eliminated. Figure 2 shows the direct connection method eliminating the drive plate, one set of leaf springs, and one set of rivet. However, the direct connection method faces challenges in terms of no direct back support. The riveting die cannot access the rivet head to provide direct support when riveting the piston plate to the leaf springs. Without the direct support, the rivet joint may not have proper expansion and the piston plate may have excessive permanent set. Overbend blind riveting technology is required to solve the problems.

1.1 Overbend Blind Riveting Technology

Overbend blind riveting technology is a “blind” riveting operation that connects the piston plate to the cover without using intermediate component between the cover and the piston plate. Figure 3 shows the overbend blind riveting system layout. The supporting die is activated to pull up the cover and the piston plate moves against the stripper until gap closes. The riveting punch deflects the piston plate and forms the rivet body to make a rivet joint until the punch reaches its predetermined limit. The friction paper inner edge becomes a pivot point when the stripper moves down to the piston plate to close the gap. During the operation, the stripper and the supporting die hold the piston plate and the cover in place.

Because no direct support can be provided for the rivet head when riveting the leaf springs to the piston plate:

Fig. 1 TCC with a drive plate

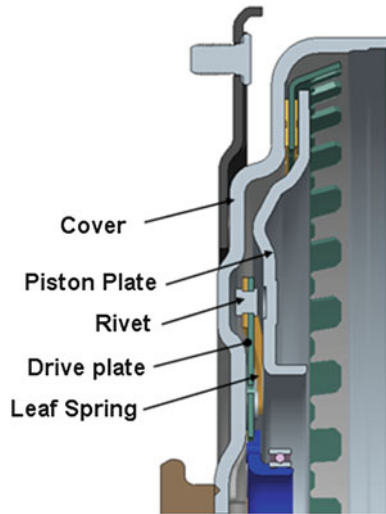
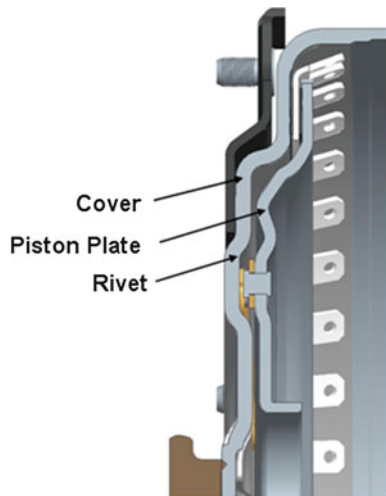


Fig. 2 TCC without a drive plate



1. The piston plate may be overbent until the head of the rivet is supported by the cover. Effects of the overbend may cause excess distortion and permanent set in the piston plate.
2. The piston plate releases and returns back into an elastically balanced position. Without a proper support, the rivet joint may not have proper expansion to ensure joint robustness.
3. The gap between rivet head and the cover may not meet requirement to provide adequate clutch controllability.
4. The friction paper may be severely compressed because of the overbend force and therefore cause durability problems.

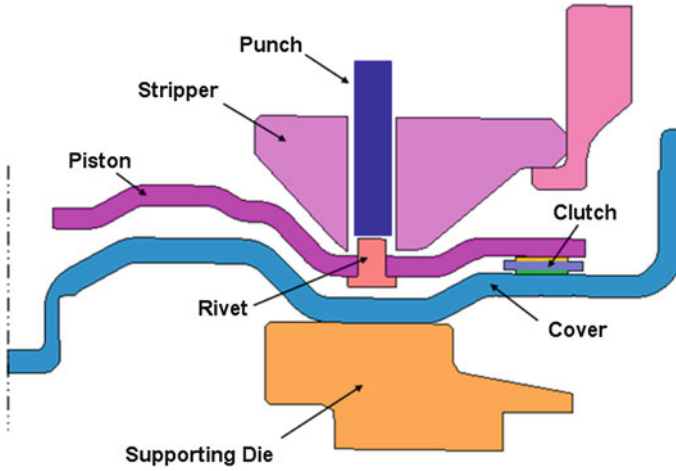


Fig. 3 The overbend blind riveting dies layout

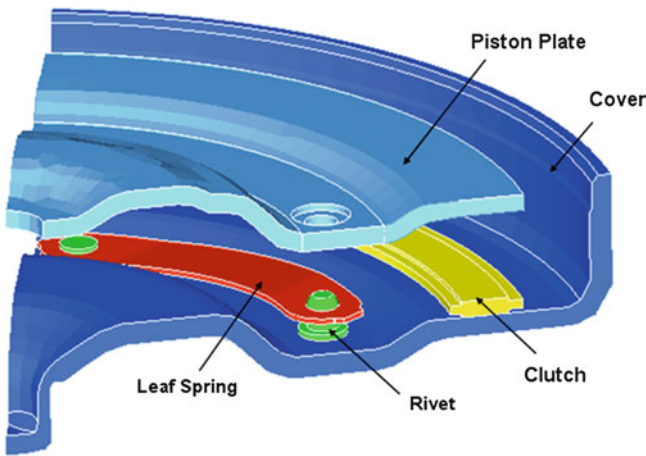


Fig. 4 The integrated simulation model

The critical factors that affect 1–3 include (but not limited to) rivet joint parameters, process parameters, riveting tooling parameters, and material properties cannot be quickly understood by time consuming tryouts. Integrated manufacturing simulation is used to find feasible solutions that will be expanded by technical ideas. Figure 4 shows the 60° axis-symmetry model with re-meshing capability setting on the rivet body when any element distortion becomes too large to accurately calculate progressive strain. The simulation predicts the piston plate deformation and stress, the rivet joint geometry and stress, the rivet head to the cover gap, and the friction paper compression and stress.

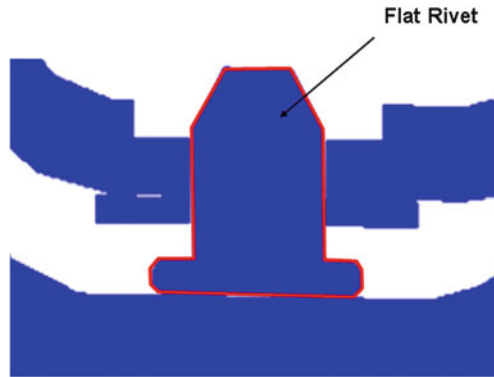


Fig. 5 The flat rivet geometry before operation

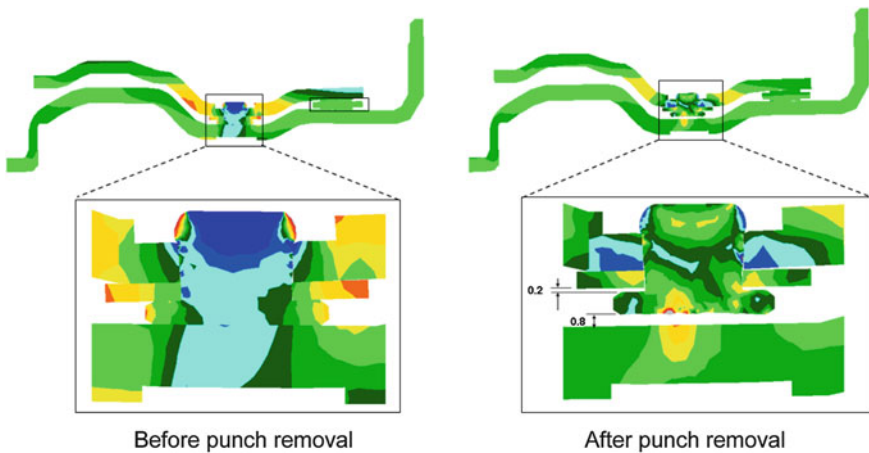


Fig. 6 The Flat rivet simulation results

2 Rivet Joint Optimization

Figure 5 shows the first rivet design using the regular flat rivet idea. Rivet geometry and rivet expansions must be analyzed to ensure proper rivet expansion.

Figure 6 shows no gap being found in the rivet joint just before removing the punch. Because the riveting punch bends the piston plate, it inclines an angle with the rivet head and the cover, an un-balanced internal force builds up in the piston plate and in the rivet joint. Upon removing the punch, the piston plate springs back to balance the internal force and causes a 0.8 mm gap between the piston plate and the cover. The upset rivet joint elastically relaxes to cause a maximum 0.2 mm gap between the leaf springs and the rivet formed head. Results of the fatigue analysis

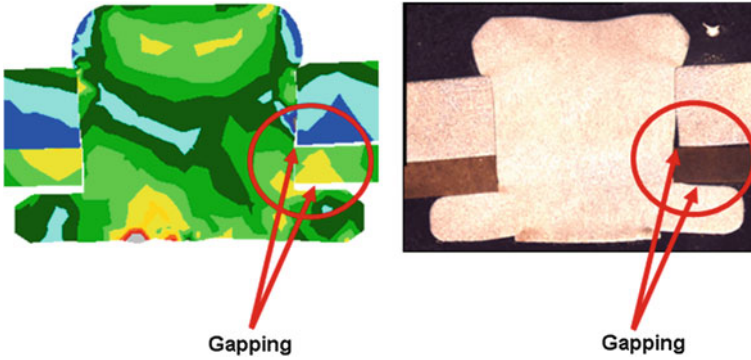
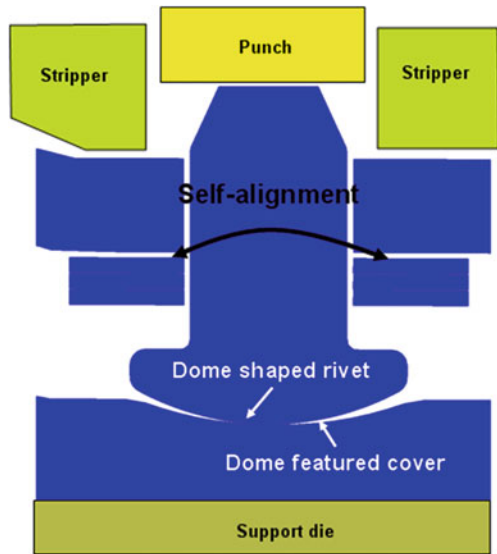


Fig. 7 Comparison between prediction and actual result

Fig. 8 The dome shaped rivet joint design



conclude that the 0.2 mm gap would increase the rivet failure potential. The flat rivet concept is not recommended for being used with the overbend blind riveting technology. Figure 7 shows the comparison between the prediction and the actual result.

2.1 Dome Rivet

Custom riveting method is very effective as long as the piston plate is maintained parallel to the cover during the riveting operation. However, when the piston plate

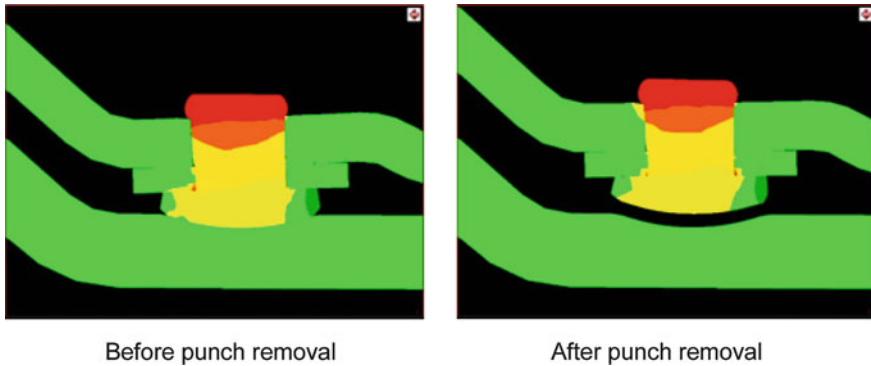


Fig. 9 Dome shaped rivet simulation results

is deflected in an angle, the rivet body can not be in line with the punch. To avoid the misalignment, the rivet head should be designed with a self-align mechanism. Many simulations are performed to understand the critical features of the mechanism within the design constraints. A dome shaped rivet head and a dome shaped feature in the cover appear to promise a certain degree of self-align mechanism as shown in Fig. 8. Several combinations of dome dimension are explored in depth through simulations to find the best solution.

The self-align rivet is used with the overbend blind riveting technology because of the back support surface are not parallel to the riveted plates. This is particularly useful for the piston plate. The self-align rivet consists on a rivet head with a convex dome and a cover with a concave dimple. The rivet pivots to match the angle of the piston and the cover during the riveting operation and the rivet head is fully supported by the dimpled cover such that rivet head distortion is minimized. Figure 9 shows no obvious gap being found in the rivet joint right before removing the punch. Also shown in Fig. 9, the piston plate springing back to cause a 1.8 mm clearance between the rivet head and the cover. Figure 10 shows the comparison between the prediction and the actual result. The prediction agrees well with the actual result.

Results of the simulations conclude that the dome shaped rivet joint design would meet the functionality and durability requirements. The dome shaped rivet and the dimple feature in cover must be developed for each application in terms of tolerances, diameters and force required to coin and ensure minimum rivet head distortion during riveting operation. To develop them, several simulations are performed and several different combinations are tested. Optimization between the maximum tolerance and minimum deformation is achieved by the simulations. Six sigma studies are conducted to ensure robust production in terms of piston plate permanent set and the clutch clearance.

Dome shaped rivet is successfully developed for the overbend blind riveting technology. The predictions agreed very well with the actual results. No gaps are found in the dome shaped rivet joint. Our experience suggests that no real concerns

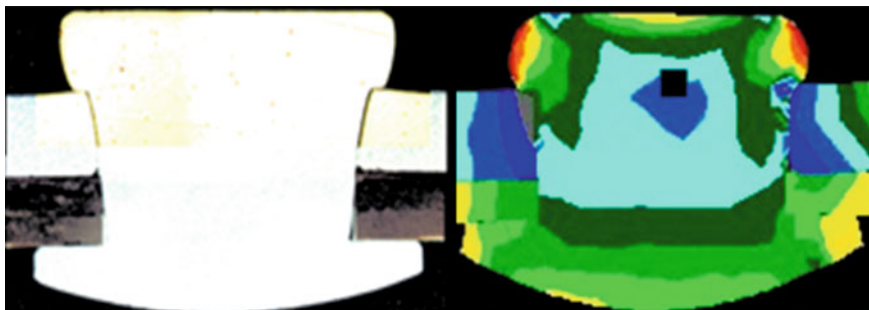


Fig. 10 Comparison between the prediction and the actual result

for the rivet durability. But with the flat rivet joint design, large gaps are found in the rivet joint which may increase the rivet failure potential.

3 Piston Plate Durability

Piston plate stiffness is the summation of material properties and geometry strength. The stiffness must be calculated for every design to make sure the piston does not exceed the elastic limit and minimize the desirable clearance. If the piston plate stiffness exceeds the elastic limit during the riveting process, it may cause excessive permanent set and therefore lead to capacity issues. The simulation is then used to assess the effects of the overbend blind riveting method on the piston plate permanent set and durability.

Figure 11 shows that under the riveting influence, the piston plate material goes beyond the yield point. As it is removed, it relaxes to a lower stress level. As the pressure is applied, it starts to strain the material from the initial stress to a higher stress level. Also shown in Fig. 11, without the riveting influence, the piston plate stress goes from the forming residual stress to a moderate stress level and then relaxes back to the initial stress level. Less damage is made to the piston plate with riveting force influence than that with no riveting force influence.

The residual stress and the application stress are transformed by the Goodman diagram [2] to fully reversed stress amplitude which is used to look up the S–N curve to determine durability. Figure 12 shows the S–N curve and resulting durability. The results conclude that the overbend piston plate would be durable for 4.9 million cycles while the current production piston plate would be durable for 2.2 million cycles. A later durability test proves that the overbend piston plate passes 4 million cycles. The overbend blind riveting technology significantly improves the piston plate durability.

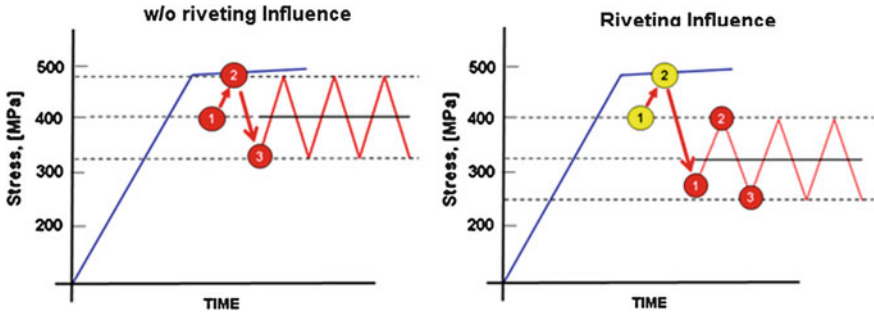


Fig. 11 Influences of overbend blind riveting method on piston plate stress

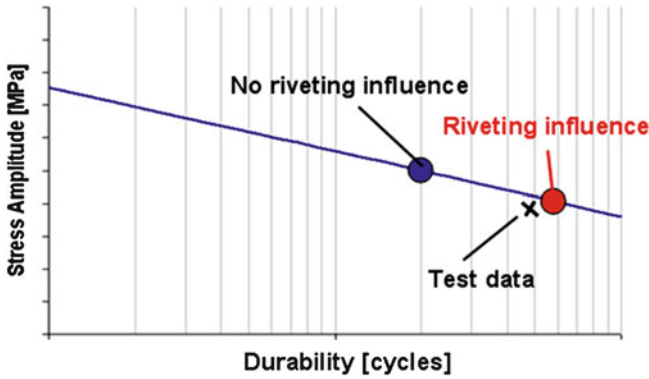


Fig. 12 The piston plate durability

4 Friction Paper Compression and Durability

The riveting force is transferred from the riveting dies to the friction papers and causes some level of compression and durability problems in terms of delaminating and thickness loss. Therefore, the puck tests [3] are performed to determine the effects of the riveting force on the axial compression and durability [4]. The critical thickness value (CTV) is determined in this study. The CTV expresses durability as a function of the paper’s thickness. The simulation is used in conjunction with the ductile fracture criteria to determine the durability. The damage is the cumulative measure of the compression. The fatigue fracture occurs when the minimum thickness value (MTV) of the friction paper reaches the CTV. It accounts for the geometry, the damage, and the strain in the paper.

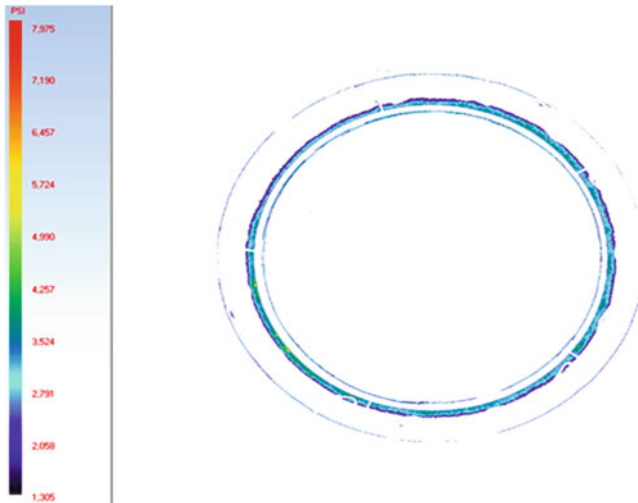


Fig. 13 The pressure mapping

4.1 The Puck Test

In the test, the standard unit loading calculation is done in order to evaluate the amount of load that the friction paper is receiving when riveting punch upsets the rivet. The puck test includes:

1. The friction paper thickness measured before assembly at three different radial locations,
2. Pressure mapping is made by placing one pressure sensitive film between the cover and the friction paper and the other one between the friction and the piston.

The test result indicates about 1 % friction paper thickness change and the high contact unit pressure in the inner side of the friction paper. Figure 13 shows the piston plate side pressure mapping results. The blue color indicates the friction paper facings are under maximum pressure and the violet color for the minimum pressure. This information is then used to determine the range of puck sample size to meeting unit loading requirements.

Various samples are prepared for all the potential unit loading applications. The friction paper thickness is frequently checked at a per-determined time interval. By monitoring the thickness change, the friction paper durability may be determined. Figure 14 shows the CTV value is determined to be about 8 % when the friction paper broke at about 850,000 cycles. The riveting force effect is predicted to reduce the paper durability by about 20 % to 680,000 cycles at a 8 % CTV.

Figure 15 shows the pressure cycling model. The Initial compression is assumed in the simulation for durability assessment. The MTV is calculated to be

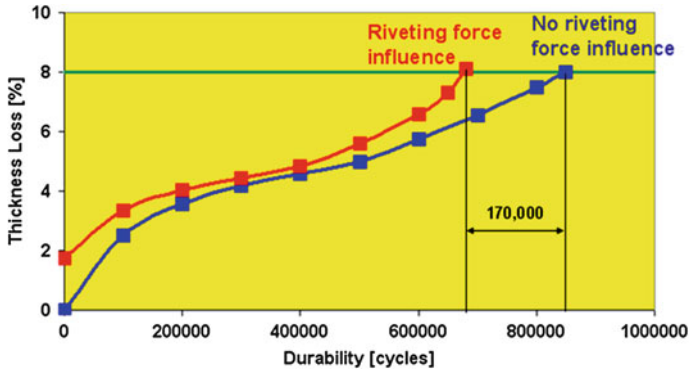


Fig. 14 The friction paper thickness-life curve

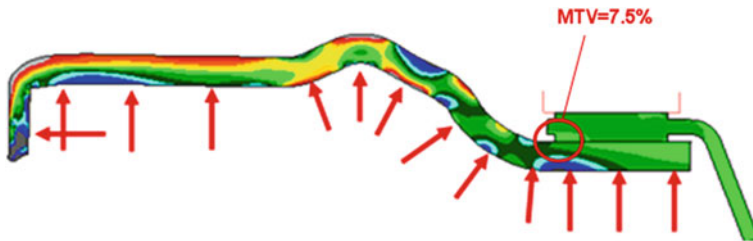


Fig. 15 The pressure cycling FEA result

about 7.5 % which is less than the 8 % CTV, so the friction paper durability is more than 650,000 cycles. Actual friction paper passes 600,000 cycles. The compression’s impact on paper durability is therefore confirmed.

5 Summary

Overbend blind riveting technology solves the more than 10 years of manufacturing difficulty. It eliminates the drive plate and associated manufacturing processes. The dome shaped rivet and the dimple feature in the cover, the piston plate, and the friction papers are optimized to meet the functionality and durability requirements. Desirable clutch clearance and minimum piston plate permanent set are proven to be robust through six sigma studies. Overbend blind riveting technology has been launched successfully into production. This technology saves the axial space, lowers the torque converter clutch weight, and reduces the production cost. In addition, the space saving allows the installation of a higher performance pendulum damper, enabling the torque converter clutch to lock up at much lower engine speed to significantly improve fuel economy.

References

1. Wang et al., US patents, #7,313,851, #7,024,746, #6,193,036, #5,826,690, #5,666,710, #5,666,710, #5,600,878, #5,027,631, #4,580,435, #4,353,444, #2,841,262
2. Markiewicz, Langrand E Analysis of riveting process forming mechanics. *Int j mater prod technol* 13(3–6):123–145
3. Firoz Ali Jafri, Martin Fuss, George Bailey Shudder durability if a wet launch clutch Part 1: Thermal study and development of durability test profile, SAE paper 2009-0103
4. Katsuhiro Ito, Keith A. Barker, Masamitsu Kubota and Shigekata Yoshida Designing paper type wet friction material for high strength and durability, SAE paper 992034

Analysis of the Influence of Clutch Pedal to Vehicle Comfort

Jiangchuan Li, Feng Deng, Shaojin Liu and Hao Hu

Abstract Driving comfort is one of the most important factors affecting automobile comfort, it also reflect the quality of automobile design. Clutch pedal force and pedal motion stroke mainly affect the driving comfort. Too light pedal force makes drivers feel the juncture not obviously, too heavy pedal force makes drivers fatigue; Separation would lead to clutch would release excessive if the separation distance was too short, there would be flameout problem if the combined distance is too long and this may also make drivers feel pedal engagement point is much more higher. This paper mainly analyzes the influence of clutch comfort to vehicle comfort according to theoretical calculation, objective test and subjective evaluation of the clutch system. The impact of clutch pedal to drive comfort can be analyzed mainly from pedal travel and pedal load. A multi-body vibration model with four degrees of freedom, including toe-in, camber angle, vertical jumping and self-vibration of tread in the lateral orientation, is set up. Parameters sensitivity, which would affect the vehicle bifurcation speed, are calculated by means of numerical simulation method in Matlab, and several control strategies which would suppress the tire self-excited vibration are proposed. This study mainly focuses on clutch pedal comfort analysis of economic car, the model in this research is the company's developing car, but the research method is applicable to any vehicles. A multi-body self-vibration model is established to predict the polygonal wear of tire and several suggestions are made to avoid the polygonal wear of tire. Conclusions: The result showed that separation distance of 100–125 mm and engagement point pedal force of 85–100 N can satisfy the requirements of vehicle driving comfort better.

F2012-C01-002

L. Jiangchuan (✉) · D. Feng · L. Shaojin · H. Hao
Changan Auto Global R&D Centre of Changan Automobile Co LTD, Chongqing, China
e-mail: sunqiemail@163.com

Keywords Clutch pedal · Comfort · Engagement point · Clutch · Vehicle performance

1 Introduction

Nowadays people have much more requirements in vehicle performance including power, economy and safety, especially the vehicle comfort. Ride comfort and driving comfort are the two aspects in research of automobile comfort [1]. The analysis of car operating comfort mainly focuses on the pedal, driving environment and the seat [2]. Among them, quality of clutch pedal is directly related to the safety performance of the vehicle, as it is a car security part which separate or combine clutch and engine by trampling clutch pedal. In order to provide a more comfortable and easier operating clutch, the first job is to analyse the main factors influencing the clutch.

2 Analysis Factors Influencing the Comfort of Clutch Pedal

Pedal force and pedal motion stroke are the main factors influencing clutch manipulation. Main factors effecting pedal force and pedal stroke are diameter of both clutch main cylinder and sub-cylinder, leverage ratio of clutch pedal and clutch parameters.

Pedal force is definitely the force acting on the pedal by feet; joint pedal force is the main characteristics evaluating pedal comfort. Pedal motion stroke contains separating stroke and combining stroke showed in Fig. 1. Separating stroke is the travel form top limiting position to clutch separating point, while combining stroke is the pedal travel form bottom limiting position to combing point.

2.1 Motion Stroke of Clutch Pedal

A certain clutch separating bearing demands the moving distance during separating should between 7.5–8.5 mm, but there is abnormal sound when the pedal is trampling to the bottom according to road trial feedback which influences the driving comfort seriously (Fig. 2).

Separating characteristics of this certain clutch show that total separating trip is 7.5 mm, separating point trip is about 2.4 mm, while combining point trip is not sure. Theoretical calculation is showed below in Table 1 case of separating point has the same position as combining point.

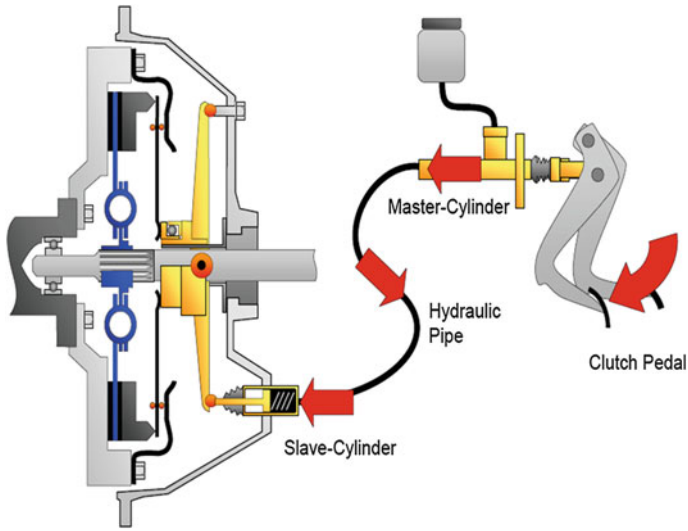
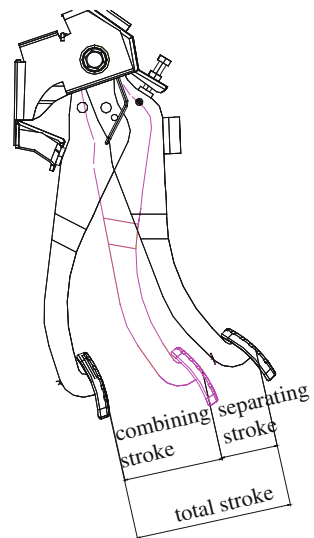


Fig. 1 Schematic diagram of clutch separating system

Fig. 2 Schematic diagram of clutch pedal motion stroke



Testing data of these above three schemes are showed in Figs. 3, 4, and 5. Scheme 1 show that 134 mm total travel is much better, but the combining position is a little bit higher; scheme 2 present a worse driving comfort evaluation with no combining point and 138 total travel; while scheme give a too long total trip and higher combining position, shifting motion can go smoothly even though the pedal is not trampled during the last 20 mm trip.

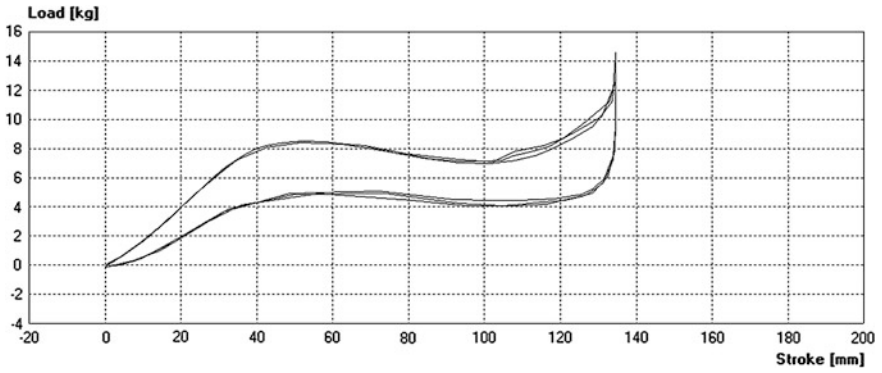


Fig. 3 Testing data of scheme 1

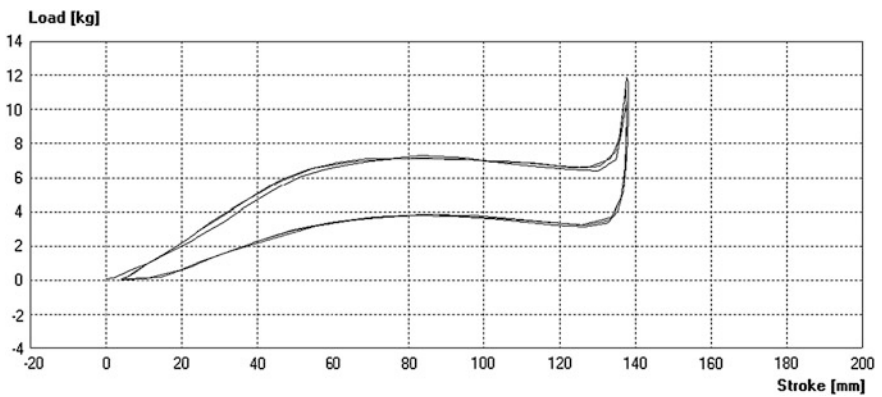


Fig. 4 Testing data of scheme 2

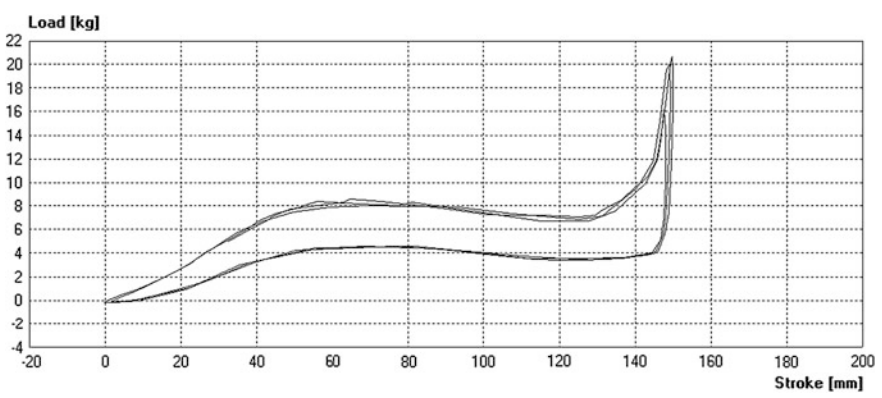


Fig. 5 Testing data of scheme 3

Table 1 System calculating

	Scheme1			Scheme2			Scheme3		
	1050	750	850	1050	750	850	1050	750	850
Clutch separating force N	1050	750	850	1050	750	850	1050	750	850
Sectional area of sub-cylinder mm ²	590	590	590	590	590	590	590	590	590
Clutch separating stroke mm	2.4	5.75	7.5	2.4	5.75	7.5	2.4	5.75	7.5
Separating pressure needed Mpa	1.78	1.27	1.44	1.78	1.27	1.44	1.78	1.27	1.44
Diameter of main cylinder mm	19.05	19.05	19.05	15.87	15.87	15.87	17.46	17.46	17.46
Sectional area of main cylinder mm ²	285.02	285.02	285.02	197.81	197.81	197.81	239.43	239.43	239.43
Total stroke of main cylinder mm	27.00	27.00	27.00	34.00	34.00	34.00	27.00	27.00	27.00
Thrust force of main cylinder needed N	507.24	362.32	410.63	352.03	251.45	284.98	426.10	304.36	344.94
Stroke loss	0.90	0.90	0.80	0.90	0.90	0.80	0.90	0.90	0.80
Main cylinder stroke needed mm	5.52	13.23	19.41	7.95	19.06	27.96	6.57	15.74	23.10
Pedal force lever ratio	6.50	6.50	6.50	6.50	6.50	6.50	6.50	6.50	6.50
Pedal force N(theoretic) N	78.04	55.74	63.17	54.16	38.68	43.84	65.55	46.82	53.07
Pedal force N + 25 N	103.04	80.74	88.17	79.16	63.68	68.84	90.55	71.82	78.07
Pedal stroke (theoretic) mm	48.88	98.96	126.14	64.70	136.86	181.76	55.71	115.33	150.16

2.2 Pedal Force

Combining point pedal force comfort need experienced drivers to evaluate subjectively as whether the pedal force is appropriate or not is related to drivers' subjective sensation based on operating all sorts of devices through acting force during driving process.

84.9 N combining pedal force is accepted in scheme 1, scheme 2 gives 72.9 N pedal force, scheme 3 shows that 82.6 N pedal force is more proper through the above testing results and experienced drivers' evaluation.

3 Conclusion

Above the theoretical calculation and practical test show that 100–125 mm separation trip is more appropriate. Clutch will separate excessively with a too short separating stroke which can lead friction between clutch diaphragm spring and clutch friction plate rivet. The proposal is presenting less than 50 mm combining stroke, too long combining stroke lead vehicles flameout easily because drivers feel the pedal combining position is too higher.

We can also conclude from the above analysis that 85–100 N combining pedal force is more suitable. The pedal can not provide enough support to feet if the pedal force is too light, while too heavy pedal force makes drivers tired easily.

Proper pedal feeling ensure driving safety, it is also the important factor influencing driving comfort that makes drivers keep steady mood and quick response to ensure driving safety and vehicle service life as well.

References

1. Jing Hu (2010) Measurement and Evaluation System of Vehicle Control Comfort Based on Correlation Analysis. *J Hefei Uni Technol* 33(12):1775–1778
2. Meng Aihua (2011) Study on Test Method of Clutch Comfort. *J Mech Electr Eng* 28(5):553–555

Modeling and Parametric Study on Drag Torque of Wet Clutch

Heyan Li, Qi Jing and Biao Ma

Abstract In order to analyze the power torque characteristics of wet clutch produced under the disengaging state and reduce the drag torque of wet clutch, a flow rate equation under full film state was deduced based on the Navier-Stokes equations and a new equation calculated oil film equivalent radius was derived according to the relationship of oil flow rate and volume between import and export, whereafter the drag torque model considering the friction gap non-uniform was established based on the Newton internal friction theorem with front formula. The performance of simulation shows that the drag torque increased monotonically with the rise of speed in low speed. But when the speed increased to a certain value, the drag torque began to decrease. Then, two evaluation indexes for drag torque were presented which were peak value of drag torque and the corresponding critical speed. Subsequently, the sensitivity for the effect of clutch parameters on drag torque was calculated. The conclusion of research have some reference value to the design of wet clutch.

Keywords Wet clutch · Drag torque · Parameter sensitivity · Friction pair · Non-uniform

F2012-C01-003

H. Li · B. Ma

Beijing Institute of Technology, Beijing, China

Q. Jing (✉)

The 206 Institute of the Second Academy of China Aerospace, Mainland, China

e-mail: 001jingqi@163.com

1 Introduction

Wet clutches are frequently used in the drive trains of many modern vehicles. The study of wet clutch drag characteristics have important meaning to improve the transmission efficiency. Therefore, it is necessary to develop an accurate mathematical model for the drag torque.

A large amount of work has been done in this area, however, none model can provide predictions of engineering-level accuracy. In 1974, Lloyd [1] studied the influence factor of drag torque by experiment, then Kato [2] utilized Hashimoto's [3] equations to derive drag torque model which considered the deficit of the oil film firstly. Whereafter, the study of drag torque was focused on the reason and model of oil film shrink. Yuan [4] and Paul [5] thinks the surface tension is the main reason to reduce oil film. Chinar [6] derived a mathematical model from Navier-Stokes equations with verification using FLUENT and experiments. Biao [7] derived the traditional drag torque equation, and studied the effect of oil flow rate on drag torque by experiment. Jibin [8] deduced the drag torque for laminar flow using an equivalent circumferential degree to calculate the integral area after aeration. Zhang Zhigang and Xiaojun [9] derived an oil film model considering the surface tension. Shihua [10] also derived an oil film equivalent radius model by the identity that the max value of oil radial speed appeared in oil film external border.

From the above review of the previous study, it is clear that the model of oil film equivalent radius considering shrink in high seed has not been to date. So this paper introduce a new way to calculate the shrinking oil film radius to establish drag torque model. And the mechanism of non-uniform distribution of the friction pair gap was considered.

2 Mathematical Model

The wet clutch disengagement is shown in Fig. 1. Under the actual conditions in disengaged wet clutch, we assume some conditions as follows.

(1) Oil is assumed to be incompressible and steady state, (2) Flow in the wet clutch clearance is laminar and symmetrical, (3) Gravity can be neglected, (4) Wet clutch plate was no-grooved, (5) Friction plate and counter plate have no glide with its surface layer oil.

According above presupposition, the boundary conditions can be written as follows:

$$\begin{cases} v_r(r, 0) = v_r(r, h_i) = 0 \\ v_\theta(r, 0) = 0, v_\theta(r, h_i) = \omega r \end{cases} \quad (1)$$

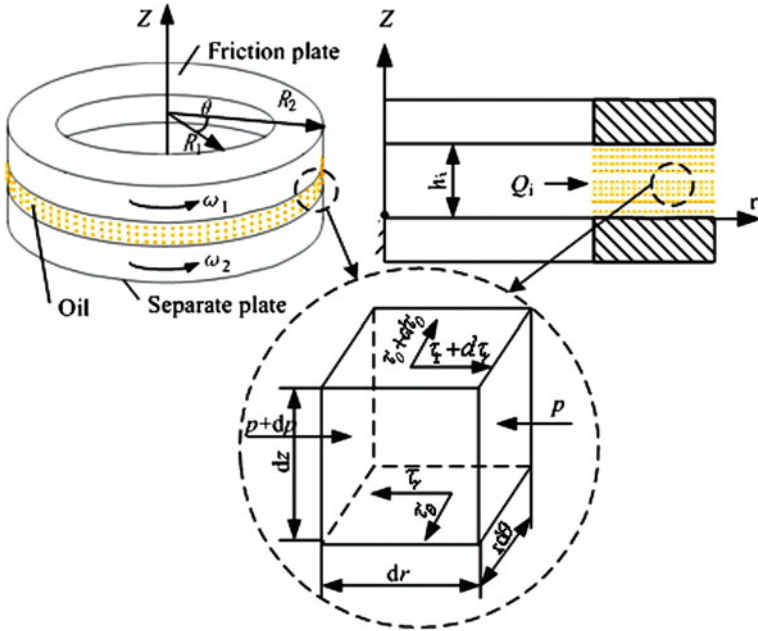


Fig. 1 Schematic diagram of wet clutch disengagement

where v_r is the oil speed in radial direction, v_θ is the oil speed in circumferential direction, h_i is axial clearance, ω is the rotating speed of friction plate relative to counter plate.

The oil motion in the radial direction between the plates is essentially driven by the centrifugal force, whereas the viscous tend to resist this motion. The relative rotating motion causes the drag torque due to the oil viscosity.

According to the assumptions, the Navier-Stokes equations in the viscous fluid [11] in cylindrical coordinates can be can be simplified to:

$$\begin{cases} -\frac{\partial p}{\partial r} + \mu \frac{\partial^2 v_r}{\partial z^2} = \rho(v_r \frac{\partial v_r}{\partial r} - \frac{v_\theta^2}{r}) \\ \mu \frac{\partial^2 v_\theta}{\partial z^2} = \rho(v_r \frac{\partial v_\theta}{\partial r} + \frac{v_\theta v_r}{r}) \\ \frac{\partial p}{\partial z} = 0 \end{cases} \quad (2)$$

The oil pressure gradient equation can be deduced by Eqs. (1) and (2), as follows:

$$\frac{dp}{dr} = \frac{27\rho Q^2}{70\pi^2 h_i^2 r^3} + \frac{3\rho\omega^2 r}{10} - \frac{6\mu Q}{\pi r h_i^3} \quad (3)$$

Table 1 Conditions of clutch simulation

R_1/mm	R_2/mm	h_i/mm	$Q_i/\text{L}\cdot\text{min}^{-1}$	$\mu/\text{Pa}\cdot\text{s}$	$\rho/\text{kg}\cdot\text{m}^{-3}$
86	125	0.6	1/1.5	0.086	875

Radial pressure distribution of oil in friction pair can be obtained from the integration of Eq. (3) along the radial direction with the boundary conditions:

$$p(r) = -\frac{27\rho Q^2}{140\pi^2 h_i^2} r^{-2} + \frac{3}{20} \rho \omega^2 r^2 - \frac{6\mu Q}{\pi h_i^3} \ln r + C \quad (4)$$

In the existing researches [8–10], the import pressure of friction pair is approximately the same as the export pressure of friction pair. But in the actual clutch, they are not equivalent. So in this paper, the pressure difference between import and export of friction pair was considered as follows:

$$p(R_1) - p(R_2) = \Delta p \quad (5)$$

Substituting Eqs. (4) into (5), so the flow rate equation under full film state can be deduced based on the Navier-Stokes equations considering the centrifugal effect, the result as follow:

$$Q = \frac{\frac{6\mu}{\pi h_i^3} \ln \frac{R_1}{R_2}}{\frac{27\rho}{70\pi^2 h_i^2} (R_2^{-2} - R_1^{-2})} + \frac{\sqrt{\left(\frac{6\mu}{\pi h_i^3} \ln \frac{R_1}{R_2}\right)^2 - \frac{81\rho^2 \omega^2 (R_2^{-2} - R_1^{-2}) (R_1^2 - R_2^2) - 540\rho (R_2^{-2} - R_1^{-2}) \Delta p}{700\pi^2 h_i^2}}}{\frac{27\rho}{70\pi^2 h_i^2} (R_2^{-2} - R_1^{-2})} \quad (6)$$

Equation (6) is the needing feed flow rate equation to maintain full oil in clearance between the plates. It is clear that the needing feed flow rate is relate to rotating speed. A trend chart of needing feed flow rate can be plot by simulation. The simulation conditions were summarized in Table 1.

The result of simulation as follows:

As shown in Fig. 2, the needing feed flow rate for full oil film increase with the rise of the rotating speed of friction plate, but the actual feed flow is constant regardless of the rising of rotating speed. So the oil film will shrink when the needing feed flow rate exceed the actual feed flow rate in high speed. Just like Fig. 3.

The principle for oil film shrinking can be explain as that the clutch clearance can not be full of oil when actual feed flow rate below the needing feed flow rate. Define R_s as the equivalent radius of oil film.

When $Q_i \geq Q$, $R_s = R_2$.

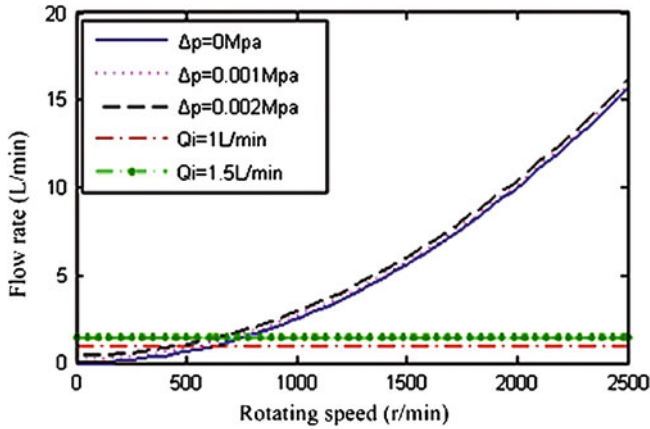


Fig. 2 Needing feed flow rate curve for full oil film

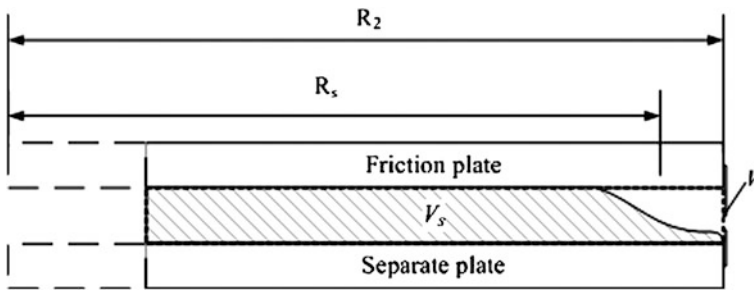


Fig. 3 Schematic diagram of partial oil filming the clearance

When $Q_i < Q$, according to the relationship of oil flow rate and volume between import and export, the equivalent radius of oil can be written as follows:

$$R_s = \sqrt{\frac{Q_i}{Q} R_2^2 + R_1^2 \left(1 - \frac{Q_i}{Q}\right)} \tag{7}$$

A trend chart of the equivalent radius can be plot by simulation. The simulation conditions as Table 1. The result of simulation as follows:

As shown in Fig. 4, the equivalent radius predicted by above model is a function of the clutch speed. When the speed was low, there is a full oil film and the equivalent radius equals the outer radius. When the speed was high, the equivalent radius starts to drop.

As shown in Fig. 5 shows, a tiny circle was taken in friction pair to analyze the shear stress.

The integral outer diameter of shear stress was the equivalent radius.

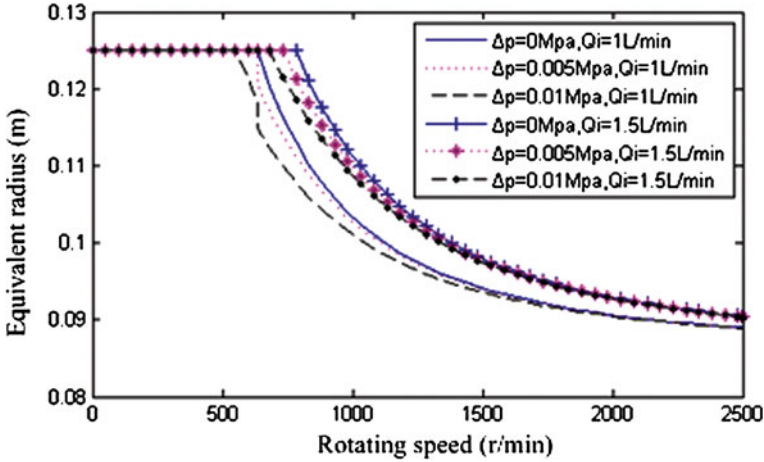
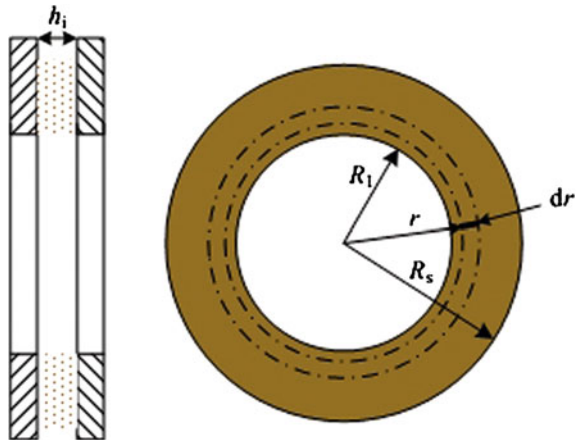


Fig. 4 Equivalent radius curve with speed

Fig. 5 Calculation principle of drag torque



According to the Newton internal friction theorem, the drag torque of each friction pair then can be expressed as follows:

$$T_i = \frac{\pi\mu\omega}{2h_i} (R_s^4 - R_1^4) \tag{8}$$

A trend chart of the drag torque can be plot by simulation. The simulation conditions as Table 1. The result of simulation as follows:

As shown in Fig. 6, the drag torque increased monotonically with the rise of speed in low speed. But when the speed increased to a certain value, the drag torque began to decrease. In high speed, the drag torque decreased with the rise of the pressure difference and increased with the rise of the oil flow rate.

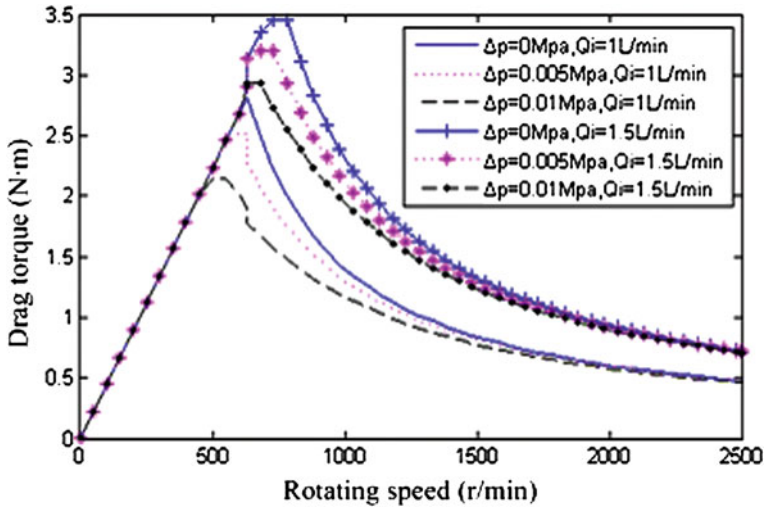


Fig. 6 Drag torque of single friction pair

In the existing researches of drag torque [8–10], the friction gap thickness of each friction pair in clutch was considered uniform. But it they were non-uniform in actual clutch. So there introduced a non-uniform coefficient to improve model. The results as follows:

$$T = \frac{Z\pi\mu\omega}{2h_0} (R_s^4 - R_1^4) \delta_T \quad (9)$$

Where h_0 is the average friction gap thickness, δ_T is the non-uniform coefficient.

3 Validation of the Model

In order to validate the mathematical model above, A special experimental rig which can eliminate the influence of bearing loss was set up to test the drag torque of wet clutch. The text bench as follows.

As shown in Fig. 7, a 200 kW inverter-type motor drives the test box of wet clutch. Transient sensor of rotational speed and torque were used to measure the needing date. The test conditions were summarized in Table 2.

When non-uniform coefficient δ_T was 1.6, the predicted drag torque from the model agree well with experimental data. The results as follows:

As shown in Fig. 8, the drag torque model considered friction gap non-uniform could better simulate the actual clutch compared with the uniform model.

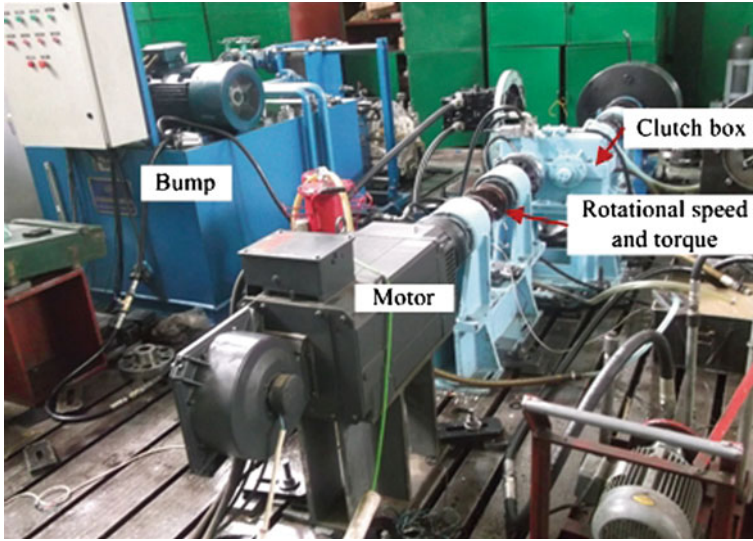


Fig. 7 Photograph of the test bench

Table 2 Conditions for clutch test

R_1/mm	R_2/mm	h_i/mm	$Q/L\dot{n}\text{min}^{-1}$	$\mu/\text{Pa}\cdot\text{s}$	$\rho/\text{kg}\dot{m}^{-3}$	Z
86	125	0.6	1.5	0.062	875	4

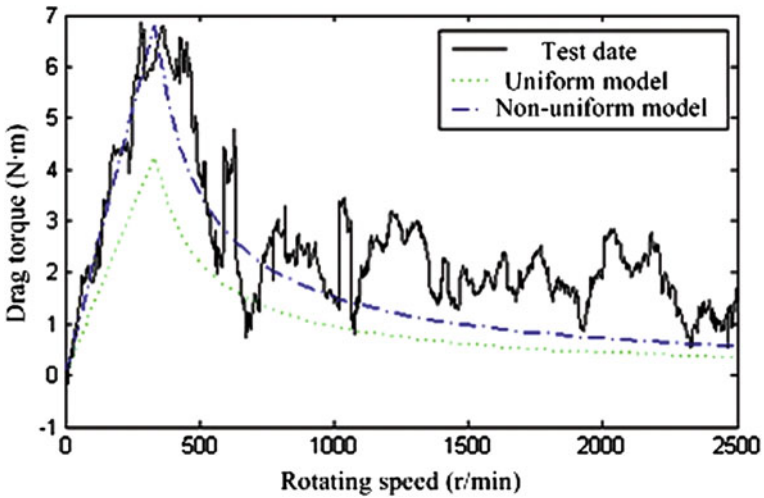


Fig. 8 Comparison of drag torque between model prediction and test result

Table 3 Input parameters of clutch

输入参数	Z	r_0/mm	h_f/mm	$\mu/\text{Pa}\cdot\text{s}$	$\rho/\text{kg}\cdot\text{m}^{-3}$	$Q_f/L\cdot\text{min}^{-1}$
x_0	5	102	0.5	0.05	850	6
x_{max}	10	170	0.3	0.09	890	12
x_{min}	1	68	1	0.03	800	3

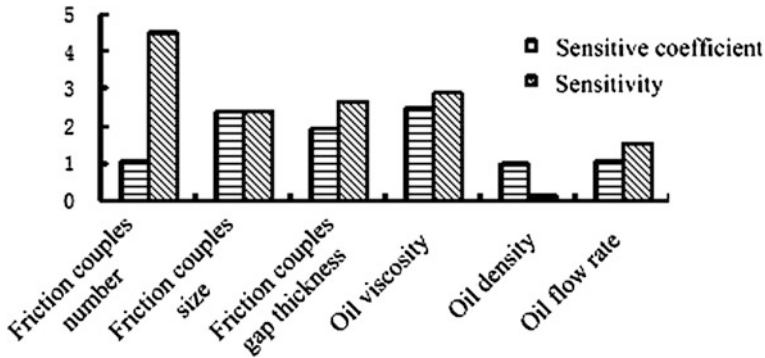


Fig. 9 The sensitive coefficient and sensitivity of clutch parameters

4 Sensitivity Analysis

According to the characteristic of drag torque, two evaluation indexes for drag torque were presented which is peak value of drag torque and the corresponding critical speed. When design the clutch system, there were many parameters need to consider. The drag torque was different with the select order of clutch parameters. So it is necessary to study the sensitivity that the clutch parameters influence the drag torque. This paper used the sensitivity analysis method [12].

Sensitive coefficient η_{SR} was defined as the ratio of the output rate percentage and the output rate percentage and input parameter percentage, just as follows:

$$\eta_{SR} = \frac{\left| \frac{f(x_0 + \Delta x) - f(x_0)}{f(x_0)} \right| \cdot 100 \%}{\left| \frac{\Delta x}{x_0} \right| \cdot 100 \%} \tag{10}$$

Where x_0 is input parameter, η_{SR} is sensitive coefficient.

The sensitivity of input parameter was obtained by the sensitive coefficient multiplying the weight of the input parameter, the results as follows:

$$\eta_{SS} = \eta_{SR} \cdot \frac{x_{\text{Max}} - x_{\text{Min}}}{x_0} \tag{11}$$

Where x_{max} is upper limit of input, x_{min} is lower limit of input, η_{SS} is sensitivity.

According to the above Eqs. (10) and (11), the sensitive coefficient and sensitivity could be calculated. The input parameters were summarized in Table 3.

As shown in Fig. 9, the sensitivity for the effect of clutch parameters on drag torque was calculated, the result was oil viscosity, friction couples size, gap thickness, friction couples number, oil flow rate, oil density according to the influence degree of design parameters on drag torque from high to low.

5 Conclusions

The drag torque model considered friction gap non-uniform could better simulate the actual clutch compared with the uniform model. The sensitive coefficient and sensitivity of clutch parameters was obtained, it would have some reference value to reduce drag torque when designing wet clutch.

References

1. Lloyd FA et al (1974) Parameters contributing to power loss in disengaged wet clutches. *SAE Trans* 83(9):1026–1032
2. Kato Y, Murasugi T, Hirano H et al (1993) Fuel economy improvement through tribological analysis of the wet clutches and brakes of an automatic transmission. *Soc Automot Eng Jpn* 16(12):57–60
3. Hashimoto H, Wada S et al (1984) The performance of a turbulent lubricated sliding bearing subject to centrifugal effect. *Trans Jpn Soc Mech Eng* 49:1753–1761
4. Yiqing Y, Liu Eysion A et al (2007) An improved hydrodynamic model for open wet transmission clutches. *J Fluids Eng* 129(3):333–337
5. Paul DW, None Z et al (2011) Simulations of drag torque affecting synchronisers in a dual clutch transmission. *Springer* 28(5):121–140
6. Chinar RA, Jinhyun C et al (2006) Modeling and parametric study of torque in open clutch plates. *J Tribol* 128(4):422–430
7. Biao M (1999) Dynamic characteristic simulation research for tracked vehicle power-shift steering transmission. Beijing Institute of Technology, Beijing
8. Jibin H, Zengxiong P et al (2009) Drag torque prediction model for the wet clutches. *Chinese J Mech Eng* 22(2):238–243
9. Zhigang Z, Xiaojun Z et al (2011) Drag torque prediction model of wet multi-disk shifting clutch. *J Zhejiang Univ* 45(4):708–713
10. Shihua Y, Zengxiong P et al (2011) Experimental research and mathematical model of drag torque in single-plate wet clutch. *Chinese J Mech Eng* 24(1):91–97
11. Chao Y, Yiji Q et al (2005) *Viscous fluid mechanics*. Beijing University Press, Beijing
12. Saltelli A, Chan K, Scott EM (eds) (2000) *Sensitivity analysis*. Wiley, New York

Modeling and Simulation of an Electric Clutch Actuator

Hanqi Yue, Bin Wang, Lijiao Yu, Bingzhao Gao and Hong Chen

Abstract For the development of an electric clutch actuator adopting DC motor and ball screw, a simulation model of the whole actuator system is set up using MATLAB/Simulink. At the same time, this chapter also gives a detailed introduction to the identification of the parameters. In the selection of motor parameters, the friction and spring parameters, lookup tables are used. By lookup tables, the model can get accurate data, and the simulation time can be reduced significantly.

Keywords Clutch actuator · DC motor · Ball screw · Modeling · Simulation

1 Introduction

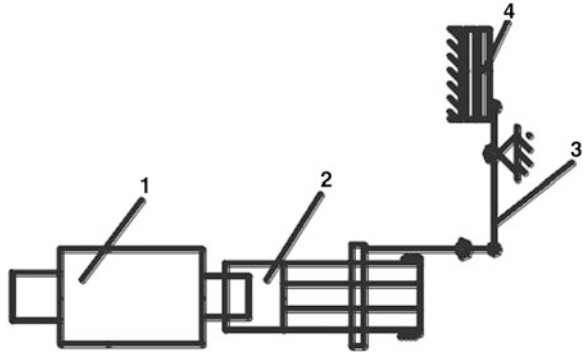
Automatic clutch system is not only an important part of AMT [1, 2] and DCT, it is also widely used in hybrid electric vehicles to implement the operations of gear shifting and mode-switching. Usually, automatic clutch is actuated by electro-hydraulic, electro-pneumatic, or electro-mechanical systems. The electro-hydraulic (pneumatic) actuator contains a relatively complex system, including pump, tank and valves, etc. References [3, 4] introduced the design and simulation of this kind of

F2012-C01-004

H. Yue · B. Wang · L. Yu · B. Gao · H. Chen
State Key Laboratory of Automotive Simulation and Control, Jilin University, Changchun, China

H. Chen (✉)
Department of Control Science and Engineering, Jilin University, Changchun, China
e-mail: chen@jlu.edu.cn

Fig. 1 Structure of automatic clutch actuator,
 1 DC motor 2 Ball screw 3 Release lever 4 Clutch plate



actuators. Electro-mechanical actuator always adopts DC motor as the power source and worm-wheel or screw-nut as the speed reduction mechanism [5]. However, the transmission efficiency of worm-wheel and screw-nut is low (maybe less than 50 %), which affects the response speed of the actuator and consequently the dynamic performance of the vehicle is limited. Our Electro-mechanical actuator adopts ball screw as the speed reduction mechanism. Although ball screw is more expensive than sliding screw, the characteristics of ball screw include high transmission efficiency, short response time, long service time.

This chapter first introduces the structure and working process of this automatic clutch. Part 2 describes the model establishment. In Part 3 we compare the simulation results and the actual operation of the automatic clutch actuator.

2 Structure and Working Process of Automatic Clutch Actuator

This automatic clutch actuator mainly consists of DC motor, ball screw, load. There is no other gear set. The rotational motion of the DC motor is transformed into linear motion by the ball screw, and then the clutch lever is pushed (clutch disengaged) or released (clutch engaged). A potential meter is installed on the nut to measure the position of the clutch lever. DC motor is driven by an H-bridge circuit, which consists of 4 MOSFETs, and PWM control is used to modulate the motor current (Fig. 1).

3 Mathematic Model of Automatic Clutch Actuator

3.1 DC Motor

In order to meet the demands of clutch, DC motor must have following characteristics

- Forward rotation and reverse rotation are realizable for this DC motor.
- The motor can stop when taking up load.
- Making sure the clutch can engage smoothly.
- Short response time.

Mathematical model for DC motor

Voltage balance equation:

$$v_a + L_a \frac{di_a}{dt} = v_m - v_b \quad (1)$$

$$v_b = k_v \frac{d\theta_m}{dt} \quad (2)$$

Torque balance equation:

$$T_m = k_t i_a \quad (3)$$

$$T'_m = T_m - T_{mf} - J_m \frac{d^2\theta_m}{dt^2} \quad (4)$$

where

v_a Voltage-reduction of motor resistance(V), motor resistance is not constant, it changes with voltage on it. Considering non-ideal switching characteristics of semiconductor components, when the frequency of PMW is fixed, electric resistance of armatures circuits will change with duty-ratio. We can measure the value of current and voltage, and then we can simulate the change of voltage with current by lookup tables, as shown in Fig. 2.

i_a Armature current (A)

L_a Total inductance of the armature circuit 5×10^{-4} H (inspecting device parameters)

v_m Armature voltage (V)

v_b Back-EMF (V)

k_v Back-EMF coefficient 40.5×10^{-3} V/rad/s (inspecting device parameters)

θ_m Motor rotary angle (rad)

T'_m Motor output torque (N.m)

T_{mf} Loss of motor torque due to friction 0.01 N.m (measuring)

J_m Motor inertia 1×10^{-4} kg m² (measuring)

Considering H—bridge driver links:

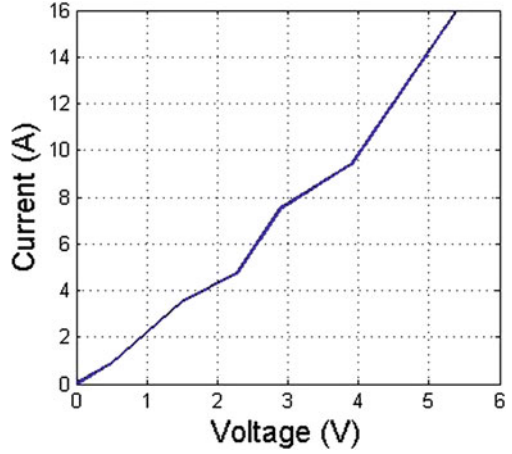
$$\bar{v}_m = v_{bat} u \quad (5)$$

\bar{v}_m The average value of v_m in a control cycle (V)

v_{bat} Car battery voltage (12 V)

u PWM duty-ratio

Fig. 2 Relationship between current and voltage of motor driving circuit



From equations (1.1) ~ (1.5)

$$T'_m = k_t i_a - T_{mf} - J_m \frac{d^2 \theta_m}{dt^2} \quad (6)$$

where

$$\frac{di_a}{dt} = \frac{\bar{v}_m - v_b - v_a}{L_a} \quad (7)$$

3.2 Ball Screw

Ball screw consists of two parts, nut and screw.

The requirements of ball screw.

- High transmission efficiency, smooth transmission, high sensitivity.
- Sufficient stiffness.
- Long service life.

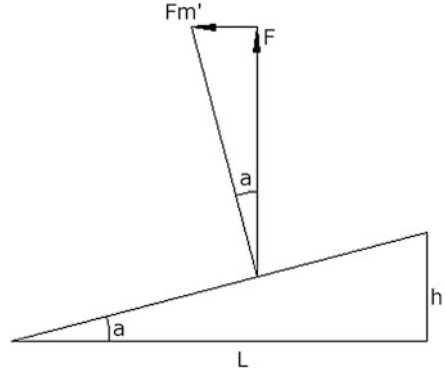
From Fig. 3, we have force balance equation of ball screw

$$\tan a = \frac{F'_m}{F_l} = \frac{h}{L} \quad (8)$$

$$L = D \pi \quad (9)$$

$$F'_m = \frac{T'_m}{\frac{D}{2}} \quad (10)$$

Fig. 3 Force analysis



We have

$$F_l = \frac{2\pi}{h} \cdot T'_m \tag{1.11}$$

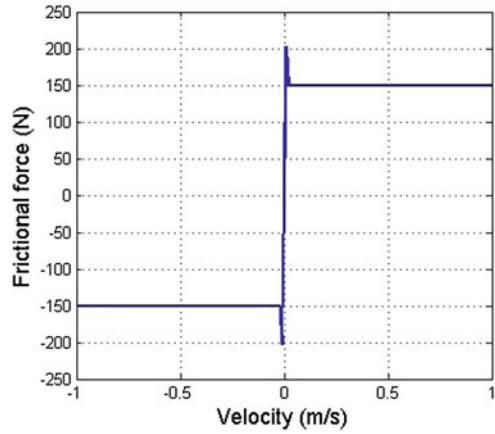
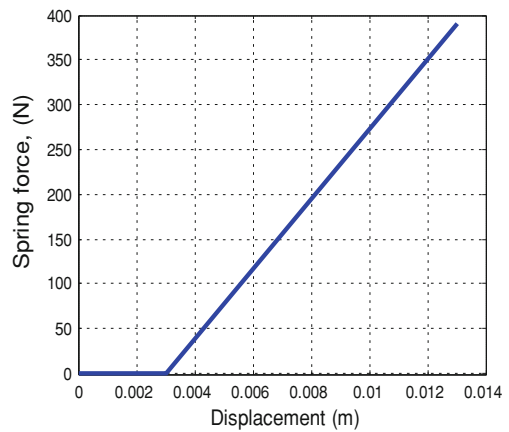
F_l	Force on nut (N)
L	Circumference of the screw (m)
D	Diameter of the screw 0.016 m (inspecting device parameters)
h	Screw lead 5×10^{-3} m(inspecting device parameters)
Model input	motor output torque T'_m (N.m)
Model output	displacement of rod x (m)

$$T'_m \frac{2\pi}{h} = m \frac{d^2x}{dt^2} + F + f \tag{12}$$

- m Mass of the nut and rod (0.75 kg)
- F Spring force (N)
- f Frictional force (N)

3.3 Modeling of Frictional Force

Friction is caused by rotation of ball screw and sliding of lead rail. Due to the direction of rod movement changes in a circle, the direction of friction force changes too. When the rod keeps motionless, friction is static friction and when the rod moves forward or moves backward, the friction is sliding friction. The maximum static friction is a little bigger than sliding friction. Figure 4 shows the changes of frictional force with velocity.

Fig. 4 Friction force**Fig. 5** Spring force

3.4 Modeling of Spring Force

We use a spring to simulate the resistance force that the clutch needs to overcome in real separation, giving no consideration to the mass of the spring. Because of the clearance of the clutch, the rod will move first to cross the clearance and promote the spring, overcoming the pressure of the spring and pressing the clutch plate of the clutch tightly. Given that the clearance is 3 mm, the change of the spring force F with the change of rod displacement is shown in Fig. 5.

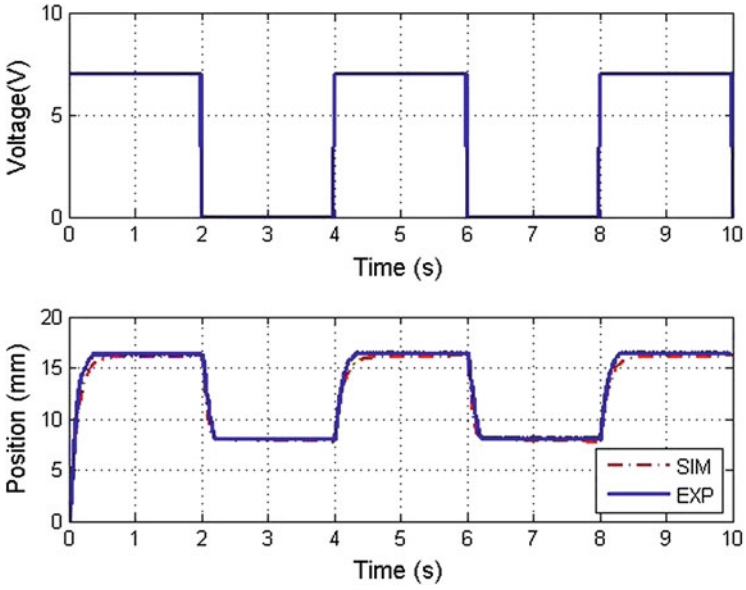


Fig. 6 Comparison between simulation and experiment, voltage of 7v

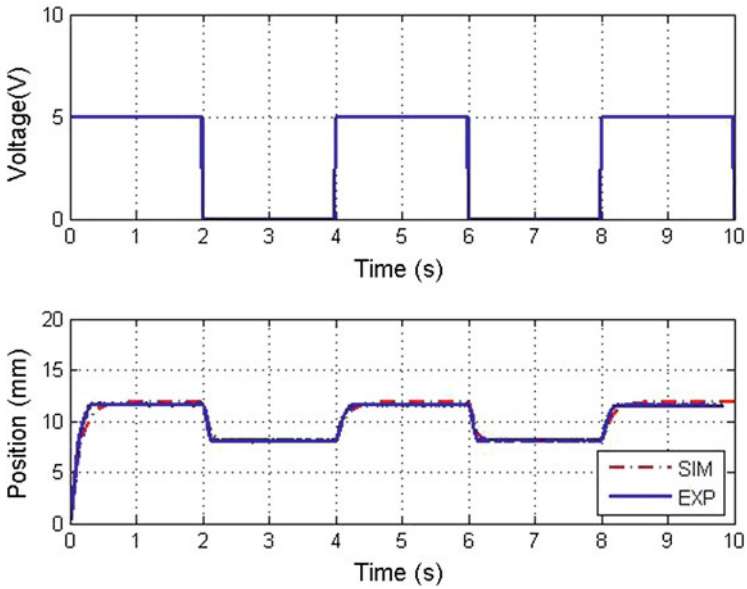


Fig. 7 Comparison between simulation and experiment, voltage of 5v

4 Simulation

We set input signal as square-wave, with period of 4 s. By changing the amplitude of duty-ratio, different v_{bat} can be simulated. The actual operation and simulation results are given in Figs. 6 and 7.

Through the figures we can see that the simulation model has good enough performance. When voltage is applied to the motor, the clutch responses quickly. In 0.4 s, the rod reaches its maximum displacement and remains motionless. When voltage becomes zero, the rod returns because of spring force. But it can not go back to the original position under the impact of friction force. In general there is no large difference between simulation results and the actual operation of the automatic clutch actuator. Comparing with actual movement distance of the rod, the simulation results only have error of about 4 %.

5 Conclusion

By using ball screw, we designed simpler automatic clutch actuator with higher efficiency. The simulation model is constructed. The simulation model has accurate enough precision, and it can be used for model-based control development.

At the stage of product development, modeling and simulation by MATLAB/simulink help a lot shorten product development cycles, reduce development costs. We can design our product flexibly and get optimization design easily.

Acknowledgments This work is supported by the National Nature Science Foundation of China (61034001, 51005093) and the Program for Changjiang Scholars and Innovative Research Team in University (No. IRT1017) and the Jilin Provincial Science & Technology Department (No. 20116010).

References

1. Gao L (2011) Design of automatic clutch system and simulation of engagement process for amt. *Appl Mech Mater* 69:67–72
2. Braun ER, Oak R, Michigan (1985) Autom clutch control
3. Langjord H, Johansen TA (2010) Dual-mode switched control of an electro pneumatic clutch actuator. *IEEE/ASME Trans Mechatron* 15(6):969–981
4. Kasai H, Ogawa N, Hattori T, Ishihara M, Uriuhara M (1986) Autom clutch control syst
5. Moon SE, Kim MS, Yeo H, Kim HS, Hwang SH, Song HL, Han KS (2004) Design and implementation of clutch-by-wire system for automated manual transmissions. *Int J Veh Des* 36(1):83–100

Methods for Clutch Dimensioning

Albers Albert, Sascha Ott and Philipp Merkel

Abstract In early phases of the product development of clutch or brake systems not every component, especially the facing is not available in its finish shape. Therefore the friction behavior is investigated by using a generic shape of the desired facing material. In order to predict the behavior of the friction material in full ring form for the future application simulative and experimental methods are needed. This chapter presents a method to describe the dynamic behavior of a drivetrain with a dry running clutch, whose facing is not available in a full ring form, but in segment or pellet form. The chapter deals on the one hand with the opportunities of the transfer of the tribology behavior from low test level (segment or pellet shape) to high test level on the example of a dry running clutch and on the other hand it is also an objective to connect the results (behavior of the friction coefficient) of the experimental investigations with the simulation model of the future drivetrain to predict the dynamic behavior. In order to achieve the research objective the first step is to identify the influence of the facing shape on the friction coefficient. In several experimental investigations on a clutch test bench, which represents the drive train stiffness and inertia, the influence of the shape form on the friction coefficient was identified. In addition to that the influences on the tribological behavior of the test bench (rotational stiffness, thermal mass, providing of the axial force) are also important and need to be known. Furthermore the mounting of the friction pairs on the test bench has a huge influence on the temperatures during the synchronizations, the wear and the friction coefficient and is also analyzed. Beside the experimental investigations a detailed simulation

F2012-C01-009

A. Albert · S. Ott · P. Merkel (✉)
IPEK—Institute of Product Engineering, Karlsruhe Institute of Technology (KIT), Kaiserstr.
10, 76131, Karlsruhe, Germany
e-mail: philipp.merkel@kit.edu

model of the test bench was build up, which considers the mechanical (stiffness, inertia, damping) characteristics and the electric engines of test bench. After having identified the influence of the shape form of the facing on its tribological behavior it is possible to predict the dynamic behavior of a full ring facing on the test bench by using the results of a e.g. segmented facing, the transfer function and the simulation model.

Keywords Dry running clutch · Simulation · Validation

Nomenclature

ω	Angular speed output machine (rad/s)
r_m	Calculated friction radius (mm)
q_A	Specific friction work (J/mm^2)
q	Specific friction power (W/mm^2)
p	Contact pressure (Mpa)
v_0	Sliding speed at the beginning (m/s)
μ	Coefficient of friction
T_{surface}	Temperature 0.2 mm under the friction surface ($^{\circ}C$)
μ_{mean}	Mean friction coefficient out of 100 cycles

1 Introduction

The dimensioning and calculation of dry and wet clutch systems is still one of the biggest challenges of a power train development. The main function of the clutch system is to transmit the torque of the engine to the powertrain and to interrupt the power flow to enable shifting. Beside that the comfort is also very important. Self-excited or forced-excited shudder causes rotational vibrations in the drive train, which are percept as longitudinal oscillations by the driver. The effect of self-excited shudder on the drive train is especially hard to predict, because there are a lot of interactions and typically the specific components are not available at a certain time in necessary maturity. Due to this the system borders or clutch dimension and investigations are difficult to define. Depending on the system borders a lot of experimental investigations with huge parameter field are necessary to make sure that the clutch is working in the intended drive train. A further challenge is to validate such subsystems or components adequately. In order to achieve this goal new suitable methods must be applied. Actual dimensioning don't take all of these aspect in account, e.g. VDI 2241 [1]. The XiL (see Fig. 1) allows developing and validating virtual and real systems in consideration of the systems driver and environment. This allows taking all relevant aspects for the considered phenomena or maneuvering into account.

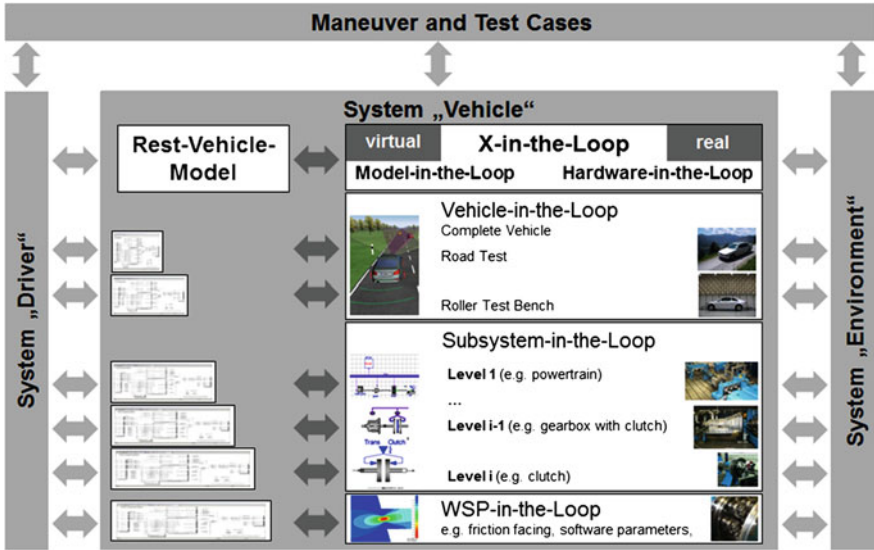


Fig. 1 X-in-the-loop-validation environment [2, 3]

The XiL takes the complete system as well as the environment and the driver into account. “X” represent the unit under test. The unit under test can be a single component, a vehicle or software code. For each unit under test the systems driver an environment will be simulated (e.g. torque oscillations by a dynamic electric engine): During product development usually no complete products but only partitions are available at a certain time. Therefore the validation must be feasible on a partitioned level as well. In the XiL approach this is realized by simulating the required remaining system virtually or physically. At the same time the unit under test might also be only available as a virtual model.

This chapter shows an approach for a clutch dimension method for dry running clutch systems. Experimental and simulation investigations are conducted and connected in appropriate method. The chapter starts with an extract of experimental investigations regarding the geometry (variation of inner and outer diameter) of the friction lining. Beside the experimental methods also simulative test environments were developed. The multi-body simulation model of the intended is used to calculate the dynamic effect of the coefficient of friction (cof) on the drive train. The model represents in addition to the stiffness, the damping, and the inertias also the dynamic of the clutch actuation system. A finite-element model was built up to calculate the temperature and the deformation during a coupling procedure.

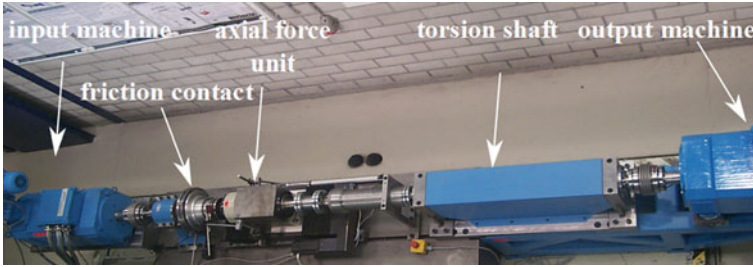


Fig. 2 Dry running clutch test bench of the IPEK

2 Experimental Investigation Methods

The experimental investigations are conducted on the dry running clutch test bench of the IPEK. The test bench consists of two high dynamical electric engines, a torsion shaft and an axial force unit to apply the force on the friction pairings. The input engine represents the power machine. The output machine is the work machine, which simulates the rest system (vehicle). Hence test under realistic conditions are possible. In addition the friction pairing is imbedded in a climate chamber, which defines the ambient temperature and humidity (Figs. 2, 3).

The axial force unit actuates the clutch and applies the contact pressure on the friction contact. During the test the speed of the engines, the friction torque and axial force close to the test probe are measured. In addition the speed of the test probe is measured by a laser, to identify and evaluate the torsional oscillations caused by a negative friction gradient (Fig. 4).

In order to identify the geometric influence three pairings (A, B, C) were investigated. Table 1 shows the geometric dimensions. Pairing A has the largest friction surface and ratio of the inner and outer diameter as opposed to pairing C. The specific values pressure, friction work, friction energy are constant for all variants. The calculated friction radius r_m is also constant. Figure 5 shows the schematic test procedure. The input machine is mechanical blocked. At the beginning of one cycle the test probe is open and the output machine is accelerated to specific speed (blue dashed line). After the speed is reached, the axial force unit applies the contact pressure (red line). The green dotted line shows the temperature behavior close to the friction surface. There are five temperature positions overall which are distributed in radial direction. All temperatures are measured 0.2 mm under the surface.

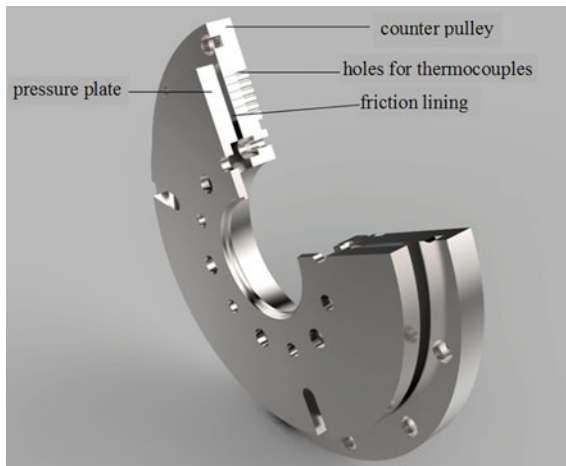
Figure 6 shows the influence of the contact pressure ($p = 0,35$ and $0,7$ Mpa) and the sliding speed v_0 . The temperature of the surface at the beginning of each cycle was $T_{\text{surface}} = 75$ °C. The friction work was the same for all variants and test programs. The sliding speed v_0 was 7 and 14 m/s (in relation to r_m). The friction coefficient is the mean value (μ_{mean}) out of 100 measured cycles.

With the objective to minimize the experimental volume procedure a multiple regression model is built up. The multiple regression analysis allows predicting a

Fig. 3 Test bench with climate chamber



Fig. 4 Test probe with friction lining [4, 5]



target variable y_i in dependence of several variables x_i , which correlates with the target variable. The variables x_i are weighted with the regression coefficients β_i . The regression coefficients are calculated by using the criteria of the robust least square method. Within this method there is an iterative procedure to minimize the effect of outlier on the target variable β_i .

$$y_i = \beta_o + \beta_1 \cdot x_{1i}^n + \beta_2 \cdot x_{2i}^n + \dots \tag{1}$$

Equation 1: Basic equation for multiple regression [6]

The variables x_i in Eq. 1 are in this chapter the pressure p , the initial velocity v_0 and the product of them (see Eq. 2). In order to consider the non-linear influence an exponent n is introduced for all variables. The equation was modified for this chapter to the following form:

Table 1 Investigated friction pairings (r_m is constant)




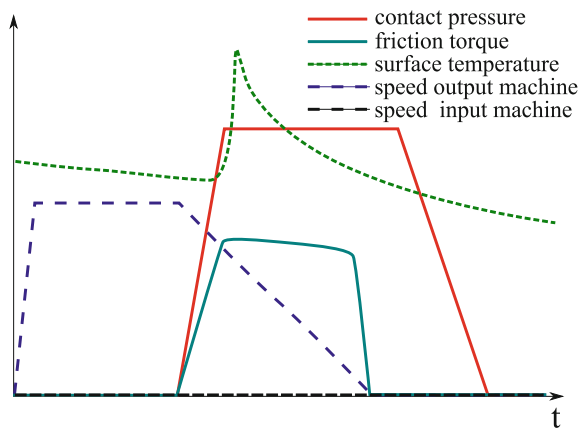
Pairing	Shape	Friction surface (mm ²)	da/di (mm)
A		12475,07	188/139,5
B		10304,42	184/144
C		8010,28	180/149

Fig. 5 Schematic progress a cycle (braking operation)



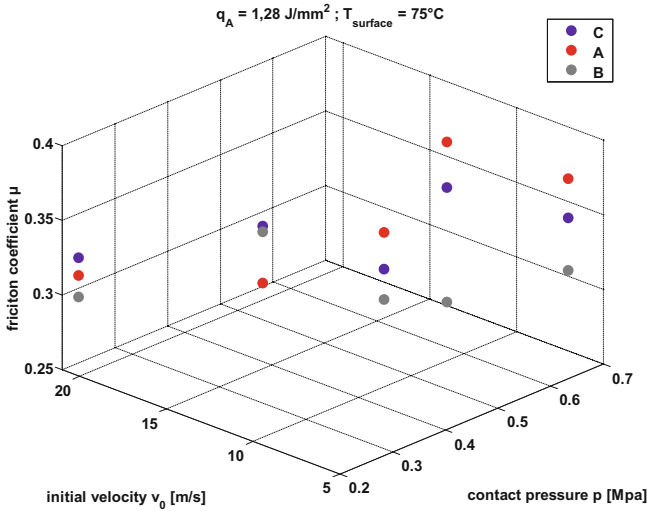


Fig. 6 Experimental results of different friction pairings (μ_{mean} out of 100 cycles)

Table 2 Calculated parameters for each friction pairing

	β_0	β_1	β_2	β_3	n	R^2
A	3.65	-3.04	-2.63	2.43	0.1	0.87226
B	-1.41	-1.4085	-3.0e-015	-6.2e-012	10	0.97949
C	0.36	-0.21	-2.0e-011	-9.3e-010	7	0.99998

$$\mu_i = \beta_0 + \beta_1 \cdot p_{1i}^n + \beta_2 \cdot v_{2i}^n + \beta_3 \cdot (p \cdot v)_{3i}^n \tag{2}$$

Equation 2: Approach for multiple regression analysis

After the experimental investigations the regression coefficients and the exponent n for every friction pairing were calculated. Equation 2 shows the parameters β_i , the optimized exponent n and the coefficient of determination (R^2). The closer the coefficient of determination is to the value 1 the better fits the model the measured data. The influence of the pressure p is dominating in all models (high β_1), in contrary to the parameter v_0 (low β_2). The initial speed has only a significant influence in pairing A. It is observable that there is a low influence of v_0 on the pairings B and C. The regression model of pairing C shows the best coefficient of determination (Table 2).

Figure 7 illustrates the regression model for pairing C. The measured and calculated friction coefficients are very similar. Furthermore the model gives an approximation about the level of the friction coefficient. At higher v_0 and contact pressure p the model predicts a significant declining of the friction level. This behaviour can be explained thus the specific friction work increases, which leads usually to a collapse of the friction coefficient of organic linings.

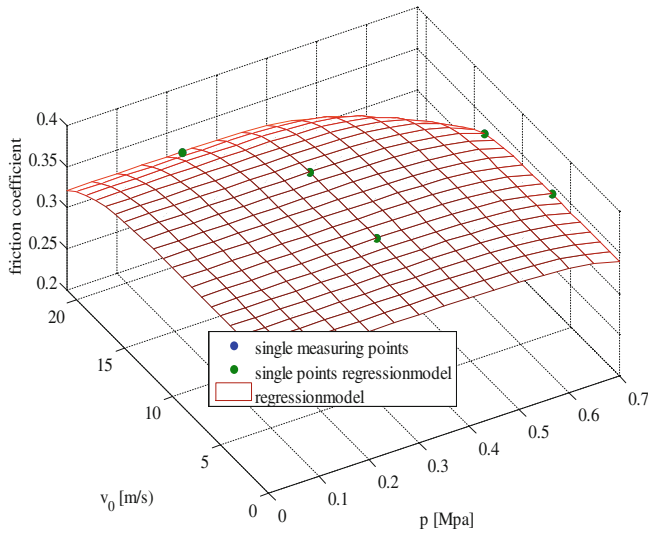


Fig. 7 Measured and calculated friction coefficient of pairing C

The light declining of the cof at higher v_0 and pressure is represented by the model. In the range of $v_0 = 0$ to 15 m/s and $p < 0.6$ Mpa a nearly constant cof is predicted. This means for the possible application that in this range a stable behaviour of the system is probable. It is not only a stable or in certain ranges predictable friction coefficient important for the future application, but also the dynamic behavior of the whole powertrain.

3 Simulative Investigation

The simulative investigation methods have the target to one the one hand to reduce the experimental effort and on the other hand to conduct simulation on a complete powertrain with experimental results (e.g. friction coefficient, friction gradient).

The powertrain is represented by the dry running test bench. Figure 8 shows the developed simulation model. During the model buildup the focus was not only on the inertia, stiffness and damping, but also on the dynamic (transfer function) of the axial force unit and the electric inertia simulation.

The control structure and the controller itself are considered as well. This makes it possible to carry out detailed simulations and to investigate influences on the dynamic of the drive train.

The simulation model in Fig. 8 does not take the temperature development into account. One solution is a FE-Simulation to calculate the temperature on the surface. The comparison of the simulated and measured temperature shows Fig. 9. The high temperatures are simulated at the inner radius (~ 75 mm); this fact is

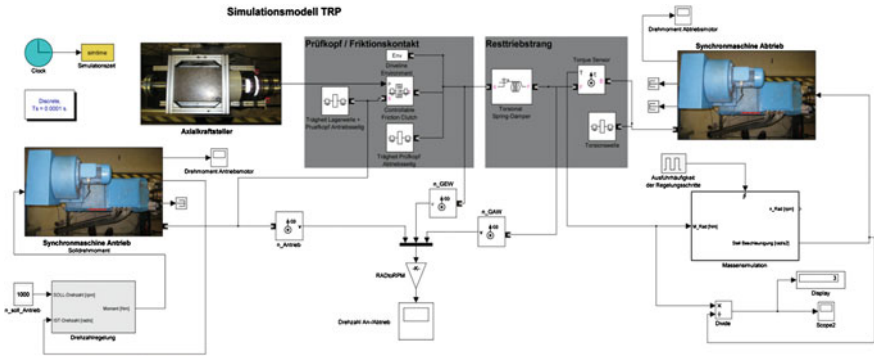


Fig. 8 Simulation model of the dry running test bench

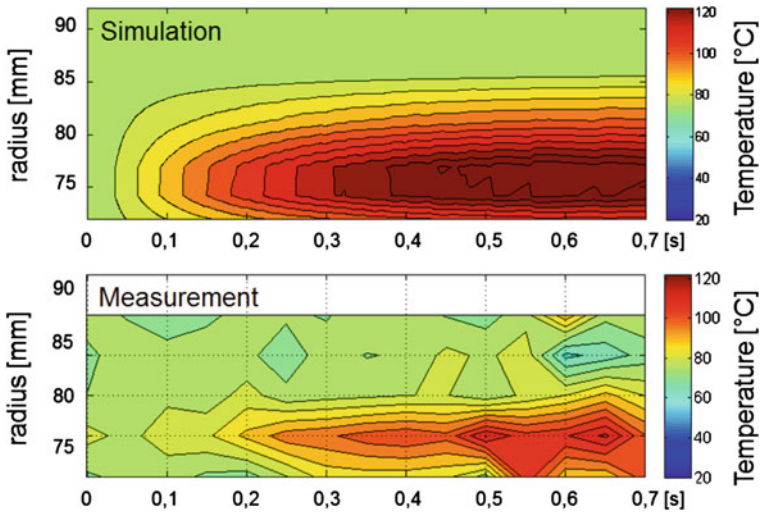


Fig. 9 Simulated and measured temperature distribution during one cycle (see Fig. 5)

confirmed by the measurements (Fig. 9, top). This makes it possible to determine also the local pressure, which is important for the local friction coefficient. Future research works will deal with the task how the procedures and the results of these different domains can be connected in an appropriate way.

4 Summary and Outlook

The present chapter gives a short view on the opportunity's to integrate experimental results in a simulative environment. At first the shape geometry of the friction pairing on the friction coefficient was investigated and a mathematical

model was created by using the multiple regression analysis. A detailed simulation model of the dry running test bench (represents the power train), which was used to conduct the experimental test, was built up. Now the experimental results, the regression analyses and the simulative model can be used to make simulation to investigate the dynamic behavior of the future powertrain.

In prospective research work the temperature development during the synchronization needs to be considered and to be implemented into the simulation environment. In addition the local contact pressure is unequally distributed over the friction lining, which results in different local friction coefficients.

References

1. Verein deutscher Ingenieure (1984) Schaltbare fremdbetätigte Reibkupplungen und –bremsen—Blatt 2, Bd. VDI 2241
2. Düser T, Albers A (2010) X-in-the-Loop—ein durchgängiges Validierungsframework für die Fahrzeugentwicklung am Beispiel von Antriebsstrangfunktionen und Fahrerassistenzsystemen, Karlsruhe
3. Albers A, Merkel P, Geier M, Ott S (2009) Validation of powertrain systems on the example of real and virtual investigations of a dual mass flywheel in the X-in-the-Loop (XiL) environment. In: Internationales CTI Symposium Innovative Fahrzeug-Getriebe, Berlin
4. Albers A, Ott S, Späth C (2010) Zwischenbericht FVA Forschungsvorhaben 607: Kupplungsmodell zur Beschreibung der Übertragbarkeit tribologischer Prüfergebnisse von Teilbelag- auf Bauteiluntersuchungen. In: FVA Informationstagung 2010
5. Albers A, Ott S, Merkel P (2011) Zwischenbericht: Kupplungsmodell zur Beschreibung der Übertragbarkeit tribologischer Prüfergebnisse von Teilbelag auf Bauteiluntersuchungen. In: FVA Informationstagung 2011
6. Chatterjee S, Price B (1995) Praxis der Regressionsanalyse, 2. Aufl. R. Oldenbourg, Wien

Drive Train Vibrations: Solving the Conflict Between Efficiency and Drivability

Ad Kooy and Jürgen Kroll

Abstract The current status of the conflict between drivability and efficiency will be shown here. Future legal regulations will require even higher fuel efficiency from tomorrow's vehicles. A major source of potential for enabling this fuel efficiency to be achieved is the operation of the internal combustion engine at lower speeds (rpm). For years, progress in this field has been hampered by the lack of suitable damper technology that would allow engines to be operated in this way while ensuring an acceptable level of comfort for the driver. The introduction of the CPA (Centrifugal Pendulum-Type Absorber) technology by LuK could provide the solution to this conflict. Various applications and design variants of this technology for manual transmissions and double clutch transmissions are available. The connection between the achievable isolation in the drive train with the influencing parameters is shown using a simplified energy-based approach. It is of great importance to include this technology at a very early stage of the development in order to achieve an optimum solution for the complete drive train. Through the integration of a CPA into a DMF, driving comfort can be improved considerably while allowing concepts such as downspeeding (to improve fuel efficiency by an additional 10 %) to be adopted. The CPA can also be integrated into a torsional clutch disk, which provides a cost-effective alternative to a plain DMF.

F2012-C01-010

A. Kooy (✉) · J. Kroll
LuK GmbH & Co. KG, Bühl, Germany
e-mail: hui.su@schaeffler.com

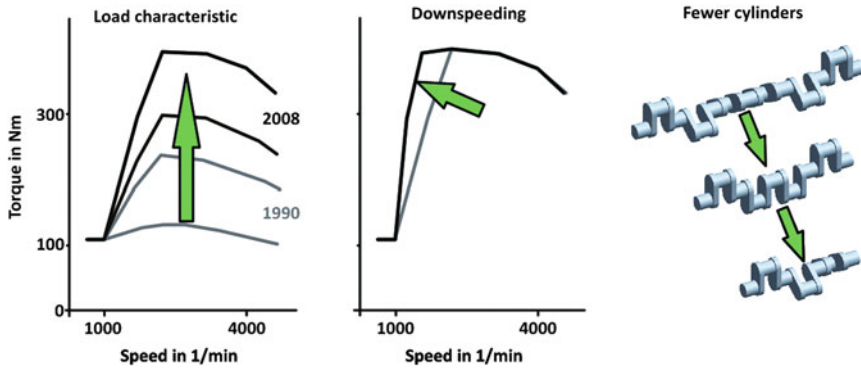


Fig. 1 Development trends in engines

1 Necessity of the CPA

Worldwide efforts in the automotive industry to reduce fuel consumption are leading to complex hybridization-based approaches that, when looked at in terms of overall energy usage, are questionable and thus are still the subject of controversial discussions. Approaches based on reducing the number of cylinders and on downspeeding (Fig. 1) are simpler and their effectiveness is undisputed.

In addition, the maximum engine torque is being shifted to increasingly low speeds in order for the vehicle to retain good driving dynamics despite these low speeds. These measures mean significantly increased requirements for drive train damping systems, because customers will not accept a loss of comfort due to the inevitable higher level of engine excitations. Reducing the number of cylinders and downspeeding reduces the excitation frequency, which leads to a significant increase in speed fluctuations (Fig. 2). The increased torques at low speeds also make a considerable contribution.

Despite the continuous optimization of dual mass flywheels (DMFs), standard measures are often no longer sufficient to meet requirements that have increased to such an extent. The earlier introduction of high-performance diesel engines led to an increase in the use of the DMF. A new and comparable evolutionary stage is now needed, which will be achieved by combining the DMF with a centrifugal pendulum-type absorber (CPA).

2 Functional Principle of the CPA

The functional principle and the fundamental physics behind the CPA have already been explained in earlier publications [1–7]. The basic idea is to use an absorber whose “spring rate” is dependent on the speed (in reality a centrifugal force that acts in a similar way). This constantly changes the natural frequency of the CPA in

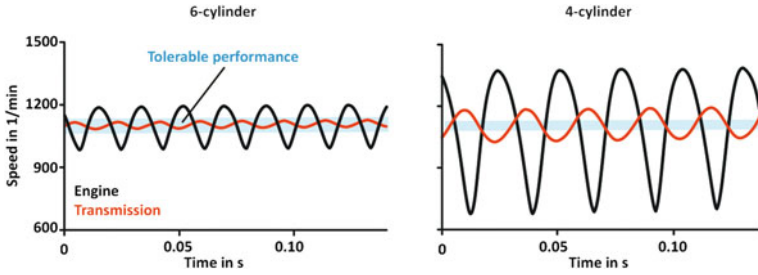


Fig. 2 Rising demand for vibration isolation with downsizing

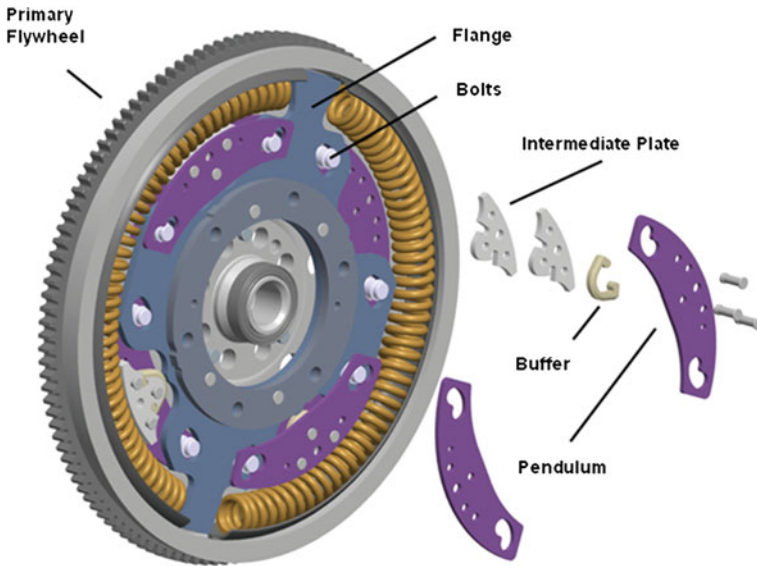


Fig. 3 CPA design in DMF

such a way that the main engine vibration order is canceled out in the optimum manner. A bifilar pendulum, i.e. a pendulum with two suspension points, is used in this application (Fig. 3).

Parallelogram-type motion of the pendulum mass is thus achieved, which prevents disruptive rotary motion in relation to the flange. All points on the pendulum describe the same trajectory curve, and the pendulum is largely the same as a mathematical pendulum with lumped mass. The pendulums are suspended by bolts that move in kidney-shaped tracks in the pendulum masses and in the DMF flange. The absorber order is determined by the shape of these tracks and of the bolts. This type of CPA, which is arranged on the secondary side, is particularly

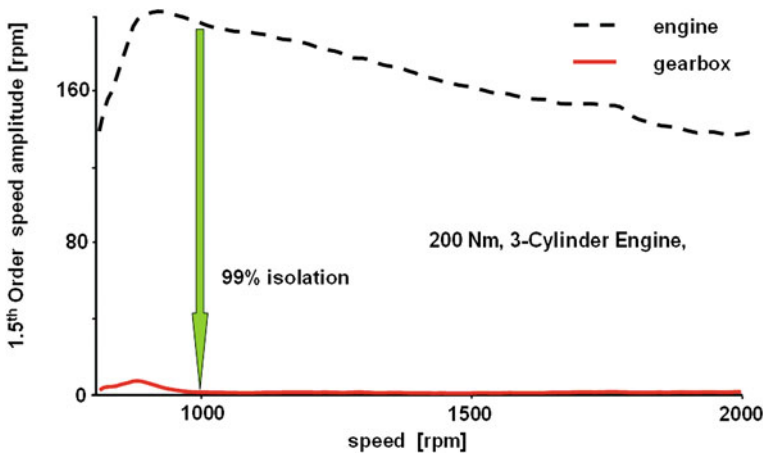


Fig. 4 DMF with internal damper and external CPA (see Fig. 9)

effective in isolating vibrations and typically improves NVH results by two ratings. Up to 99 % decoupling was achieved in tests by combining the CPA with a DMF equipped with an internal damper (Fig. 4).

3 Simplified Energy-Based Analysis

A simplified energy model can be used to provide a good description of the relatively complex interactions between the drive train and pendulum and thus give a comprehensible representation of the key influencing factors. The simplified model works on the assumption that the pendulum is supported without friction and the natural frequency is precisely matched to the relevant primary order of excitation (the 2nd order in the case of a 4-cylinder engine). In terms of excitation, only the primary order of excitation is taken into consideration, as higher orders generally have lower amplitudes and, due to the higher frequency, are less likely to cause boom or chatter. For greater ease of understanding, the rotating drive train has been changed to a linear vibration model, which makes further simplifications necessary (Fig. 5).

The CPA becomes a linear absorber whose natural frequency automatically adjusts itself to match the excitation frequency. The absorber's function means that its amplitude increases until the countereffect of the damper has completely damped the secondary flywheel. This means that, in this condition, all the energy that is applied to the secondary flywheel via the damper is stored by the absorber.

Energy losses are prevented, as the energy is stored rather than converted into a form that cannot be reused by the engine. It is interesting that the ideal isolation can initially be achieved without the inert mass of the secondary flywheel being taken into consideration. The pendulum only needs to be capable of storing all the

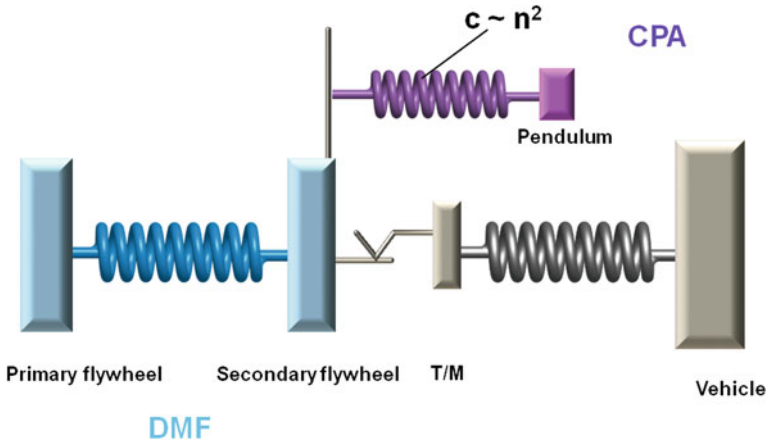


Fig. 5 Linear vibration mode

vibration energy. Simulations can be used to show that a reduced mass moment of inertia of the secondary flywheel does not pose any direct disadvantage for the vibration isolation when the aforementioned condition is met.

The system’s inherent regulation also leads to automatic adaptation to different excitations such as partial load/full load and represents one of the particular advantages of this principle. If the degree of excitation is low, the CPA reacts with a smaller vibration angle and thus prevents “overcompensation”. It automatically sets a new, optimum equilibrium for itself without requiring any additional regulation.

4 The Influence of Friction

Friction in the CPA would reduce the amount of stored energy and disturb the equilibrium, and the secondary flywheel would then begin to vibrate again. The largely frictionless pendulum support that is required is achieved through the use of ribs on the bolts (Fig. 6).

These prevent contact between the pendulums and the flange and produce only minimal friction, as the relative speed in the contact area between the two is minimal.

5 The Influence of the Vibration Angle

The design envelope and the centrifugal force loads limit the maximum possible vibration angle of the pendulum, taking the issue of pendulum strength into consideration. This, together with the pendulum masses, defines the amount of

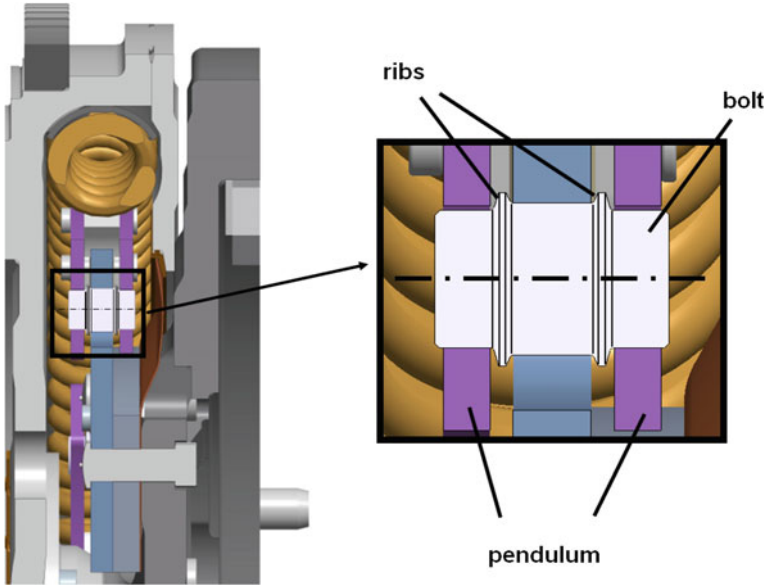
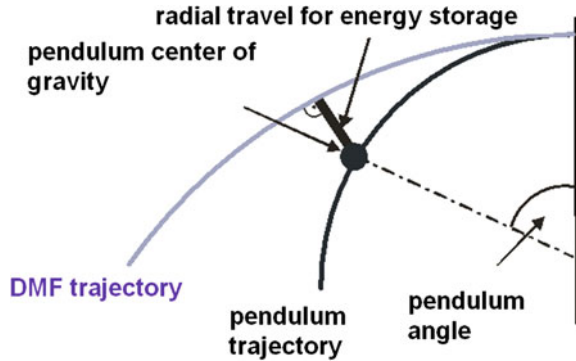


Fig. 6 Pendulum bearing

Fig. 7 Radial movement of the pendulum's center of gravity



vibration energy that can be stored. At the end of the trajectory, the vibration energy is essentially stored as a type of potential energy, and the pendulums' centers of mass have shifted inwards in a radial direction (Fig. 7). A wider vibration angle increases this radial travel, and thus the amount of energy from the pendulum that can be stored, even more as a proportional increase in mass. The new generation of centrifugal pendulum-type absorbers (Fig. 8) allows wider vibration angles to be achieved by placing the joining rivets together in one central area and replacing the 3 end stop buffers that were previously used with 1 central end stop buffer. The main task of the end stop buffers is to prevent impact noise when stopping, as the acceleration due to gravity is greater than the centrifugal

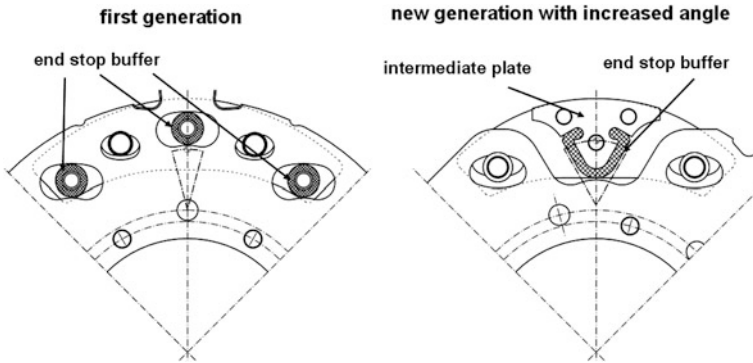


Fig. 8 New generation of CPAs with wider vibration angle

force at very low speeds, which means that the pendulums leave their regular trajectories. The mass can also be increased by adding an intermediate plate into the pendulum.

6 Influence of the Pendulum’s Mass Inertia

It goes without saying that not only the mass but also the radial position of the center of mass is decisive in determining the energy absorption capacity.

Because the radial distance increases by a quadratic factor the mass inertia and additionally it is also possible to accommodate more mass externally at a tangent, external pendulums (Fig. 9) are superior especially at very low speeds.

The DMF with an internal CPA combines the advantages of a long arc spring damper with a CPA that often does not affect space requirements. It achieves very good isolation of vibrations across a wide speed range while constantly maintaining good starting performance. Cost optimization of the internal arc spring damper is possible in the case of the DMF with external CPA, but this results in a smaller arc spring damper. The shorter characteristic curves that this produces are a disadvantage when starting, but they can be partially compensated by the automatic starts that are becoming increasingly widespread through the introduction of start-stop systems. The external pendulums allow the very good insulating effect of the pendulum to be achieved even at low speeds, however, the good basic isolation of the DMF then deteriorates. Up to 99 % isolation can be achieved, depending on the design envelope and the vehicle parameters.

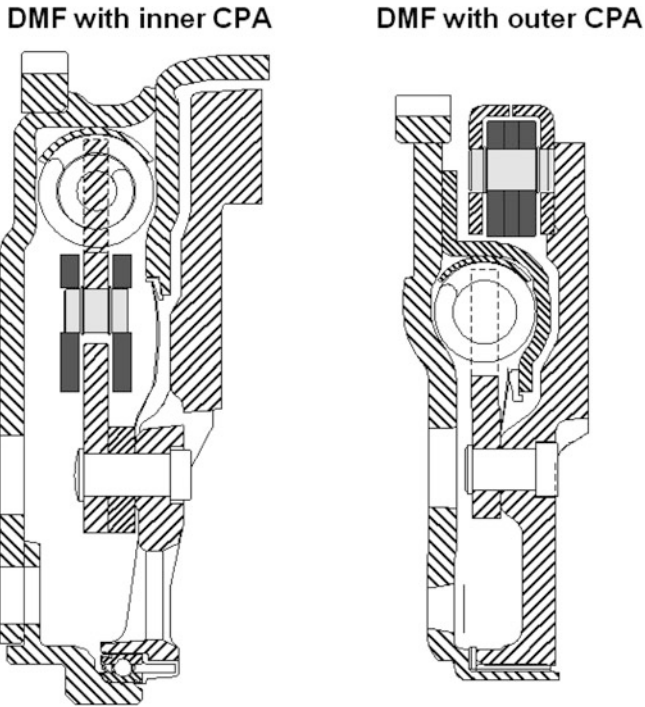


Fig. 9 Integration of CPA into DMF

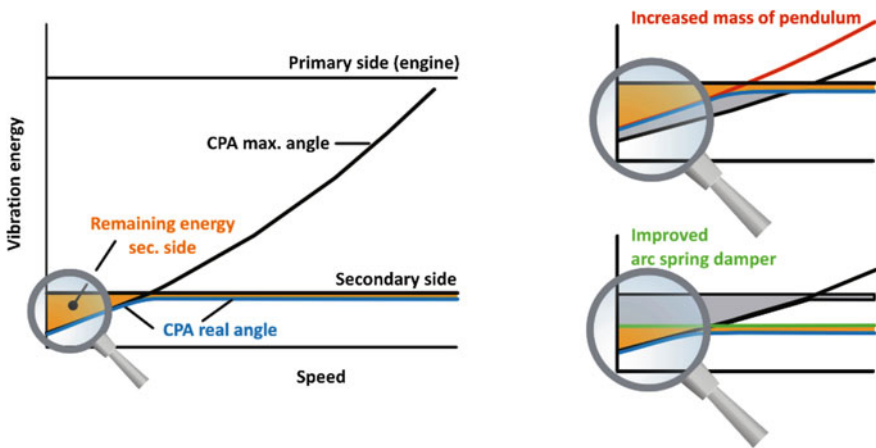


Fig. 10 Improving the isolation of the DMF with CPA by optimizing the arc spring damper

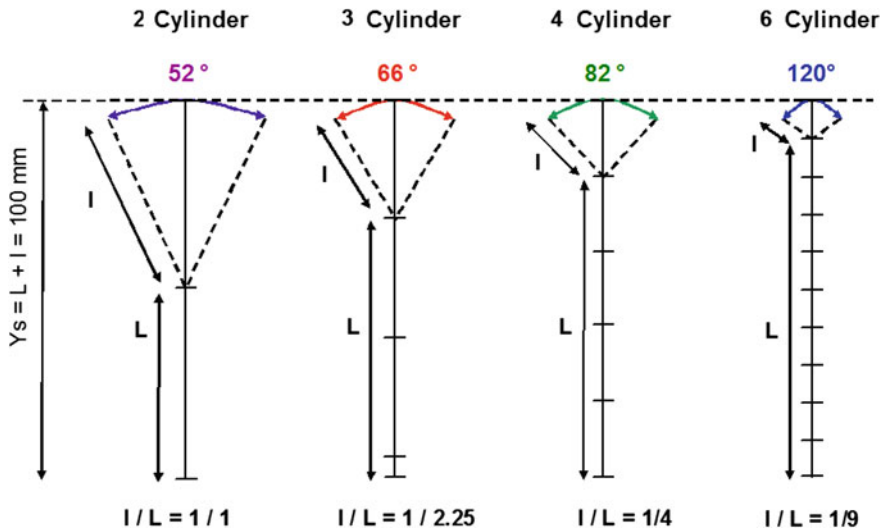


Fig. 11 Pendulum’s trajectory for the same energy storage capacity

7 The Influence of Speed and Downsizing

The CPA allows downsizing with no loss of comfort. The relationship between the achievable isolation with the speed is explained in Fig. 10.

The maximum amount of energy in the pendulum that can be stored is limited by the maximum vibration angle and increases quadratically as the speed increases. A range in which the centrifugal pendulum-type absorber cannot store all of the residual energy from the secondary flywheel is created in the low speed range (close to idle). The basic isolation of the damper becomes particularly important here, and arc spring dampers are particularly suitable in this context due to their long springs. If the full engine torque is not yet applied at speeds approaching idling speed, further improvements can still be achieved through the specific use of a 2-stage system.

Above this speed range, the pendulums are capable of storing so much energy that the maximum possible vibration angle is not utilized.

All analyses made thus far have been of the qualitative type. However, detailed individual simulations of the CPA for the respective vehicle, with its particular sensitivities to boom and chatter etc., are indispensable if an absolute evaluation of the designs being presented is to be made. Complex interactions with the drive train and essential operating modes can thus be analyzed and used for further optimization of the CPA.

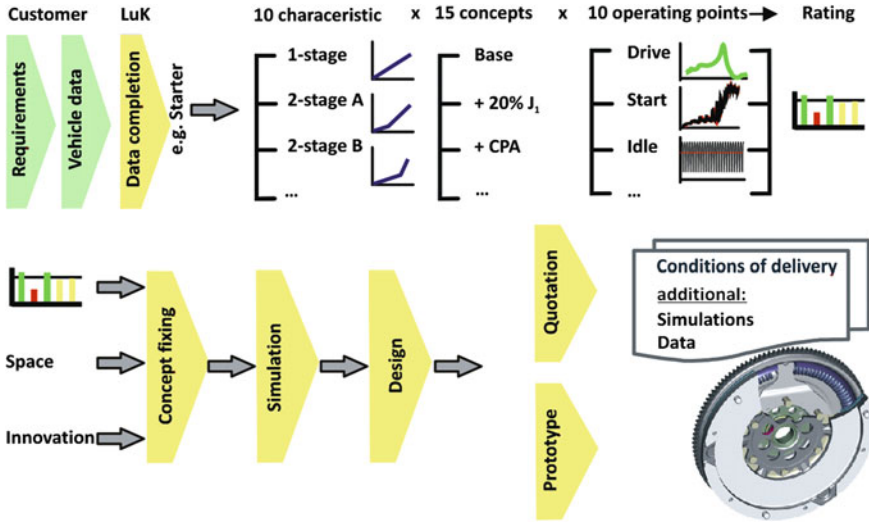


Fig. 12 Simulation variations for DMF design

8 Reducing the Number of Cylinders

In addition to downspeeding, reducing the number of cylinders is a method of reducing fuel consumption that has already seen widespread use. This not only means that the damper has to deliver a significantly higher degree of isolation, the trajectory of the CPA is also significantly widened due to the change in the order of excitation (Fig. 11).

An identical energy storage capacity can be achieved with the same mass inertia by maintaining the same radial travel (Fig. 7). This means that the trajectory becomes wider as the number of cylinders decreases, and thus becomes increasingly difficult to combine with existing design envelopes. New pendulum systems are now available that can be used even with 2-cylinder engines.

9 Optimization of Damper and Centrifugal Pendulum-Type Absorber Systems

In order to minimize development times and risks when designing damping systems, the basic design and parameters should ideally be defined in the early stages of development, qualified by extensive system simulations using one-dimensional vibration models within the time range.

Based on 20 years of experience, all significant operating points, such as start and drive, can be fully simulated with all relevant drive train parameters, such as the starter characteristic and the arc spring characteristics. Multiple design parameters

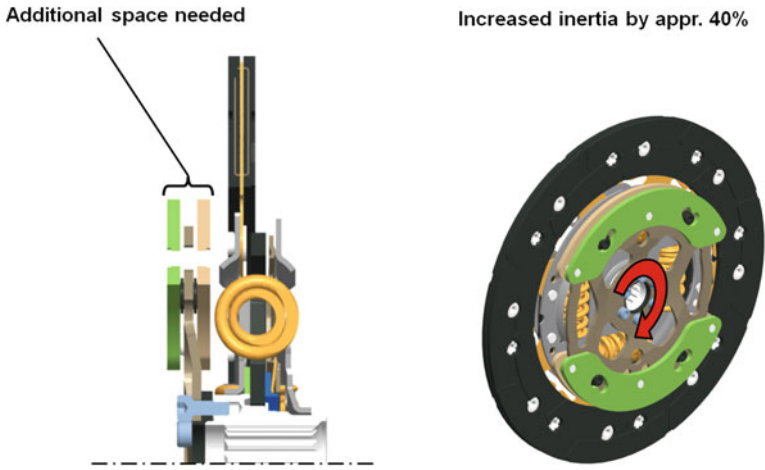


Fig. 13 Clutch disk with CPA

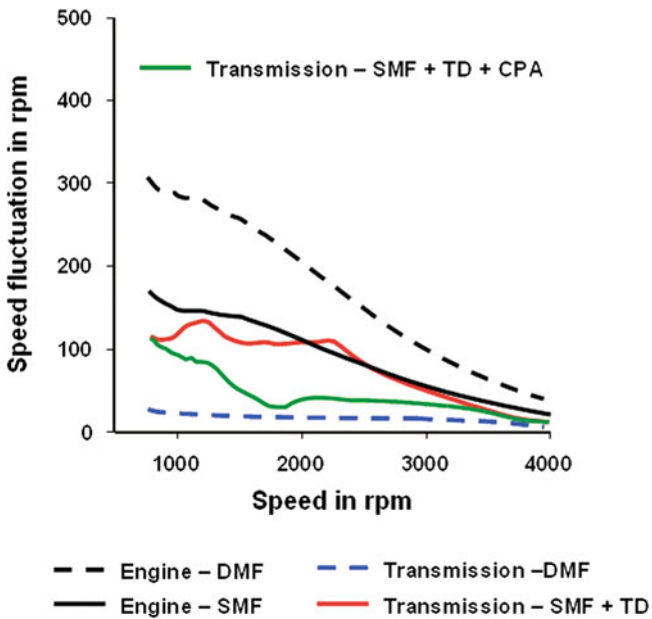


Fig. 14 Isolation in drive mode for the clutch disk with centrifugal pendulum-type absorber

can be evaluated practically over night (Fig. 12). This makes it possible to evaluate a vibration-optimized complete drive train concept through simulation.

While extensive automation means that running the programs themselves presents no major problems, the drive train parameters, engine regulation data, and vehicle sensitivities necessary for the data input are often of insufficient quality during the

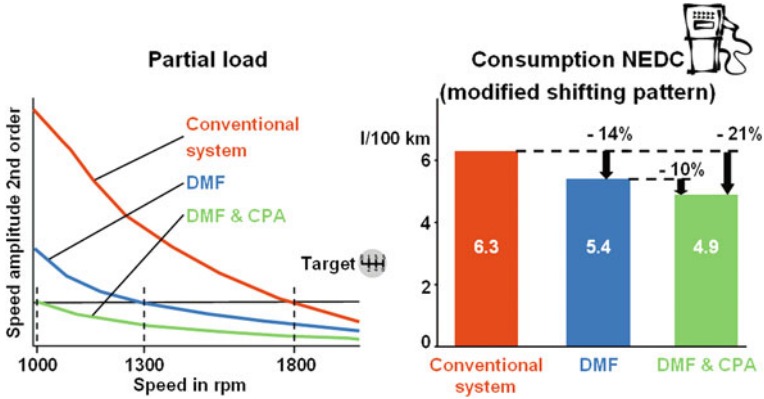


Fig. 15 Fuel savings by DMF and DMF with CPA

design phase. In some cases, up to 90 % of the simulation-relevant parameters must be estimated. Of course, the great wealth of experience built up at LuK over many years helps in such estimations, but close cooperation between customer and supplier is required in order to optimize function and —very importantly—costs.

10 Centrifugal Pendulum-Type Absorber on the Clutch Disk

A cost-effective option is to place the centrifugal pendulum-type absorber downstream from the clutch disk (Fig. 13).

This combination significantly improves the isolation in the lower speed range and is functionally positioned between a single mass flywheel and a dual mass flywheel without a CPA (Fig. 14). This is a possible alternative when the required design envelope is available and the increase in the mass moment of inertia does not lead to shifting problems.

11 Market Acceptance and Outlook

The DMF with CPA changes the driving behavior of the driver, as he/she can now drive comfortably even when the engine is close to idling speed. The engine's power can now be utilized even at low speeds and fuel consumption can be significantly lowered by downspeeding and reducing the number of cylinders. Even the use of a normal DMF allows fuel consumption to be reduced by 14 % compared to a single mass flywheel. This can be reduced by a further 10 % when the DMF is combined with a CPA (Fig. 15).

It is therefore not surprising that this system has awakened a great deal of interest on the part of automobile manufacturers. The old conflict between NVH and reducing fuel consumption at low engine speeds has been resolved.

References

1. Jürgen Kroll, Ad Kooy, Roland Seebacher (2010) Land in Sicht? 9th Schaeffler Symposium, April 2010
2. Ad Kooy, Uwe Grahl, Mikhail Gvozdev Prinzipielle Betrachtungen und Optimierungen zum Fliehkraftpendel, VDI Report 2139
3. Matthias Zink, Markus Hausner, Das Fliehkraftpendel-Anwendung, Leistung und Grenzen (2009) drehzahladaptiver Tilger ATZ. Vol. 111, July 2009
4. Wolfgang Reik, Alexander Fidlin, Roland Seebacher, Gute Schwingungen-Böse Schwingungen (2009) VDI Conference, Vibrations in Drives
5. Wolfgang Reik, Bertrand Pennec (2008) The centrifugal pendulum absorber calming down the drive train, 7th international CTI symposium innovative automotive transmissions, Berlin, Germany, December 2008
6. Dmitry Balashov, Lidia Burkovski, Frank Ferderer, Alexander Fidlin, Maria Kremer, Bertrand Pennec, Roland Seebacher (2006) Simulation bei Drehschwingungsdämpfern ATZ. Vol. 108, December 2006
7. Roland Seebacher, Alexander Fidlin (2006) Simulationstechnik am beispiel des ZMS 8th LuK Symposium

Part II
Gear Systems and Driveline

Definition of Slippage Parameters of Friction Clutches in Gearboxes with Fixed Shaft Axles

Mikhail Dmitriev and Valery Sharipov

Abstract The paper is about a calculation method for slipping parameters of friction clutches (of the slipping work and time) in tractor gearboxes at various gear overlaps and at bench tests of full-sized prototypes.

Keywords Gearbox · Slippage · Clutch · Friction · Fixed shaft axles

Modern wheeled and track vehicles broadly use the gearboxes, where gearing is made both with and without interruption of power flow from the engine by means of friction clutches (FCs) with hydraulic constriction and different gear overlapping. However, until today, the gear shifting process executed inside the gearbox by means of FCs has not been completely studied.

As an example, let us consider the gear shifting process in a tractor gearbox. The gear shifting under load can be made both with and without a short-term interruption of power flow from the engine. The continuous (non-break) gearing ensured by simultaneous operation of two gears within a short period of time t_p (gear overlap time) has some peculiarities. The process of continuous gear shifting depends on the parameters of the FCs, which ensure shifting, the overlap duration, specifications of the tractor unit (or machine-tractor unit–MTU) and its operation conditions.

F2012-C02-001

M. Dmitriev (✉) · V. Sharipov
Moscow State University of Mechanical Engineering (MAMI), Russian Federation,
Moscow, Russia
e-mail: ostashkov@bk.ru

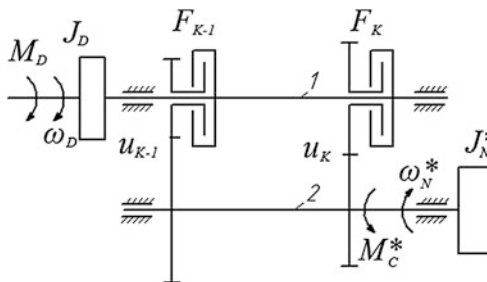


Fig. 1 Double-mass vehicle dynamic system with elementary gearbox. 1—driving shaft, 2—driven shaft; F_{K-1} and F_K —FCs of the $K - 1$ and K gears respectively; M_D —torque on the engine shaft, brought to the shaft of the engaged FC, ω_D —angular velocity of the engine shaft, brought to the shaft of the engaged FC; J_D —the inertia moment of moving parts of the engine and parts connected thereto, brought to the shaft of the engaged FC; M_C^* —the resistance moment to motion, of the tractor unit brought to the driven shaft of the gearbox, J_N^* —the inertia moment of the tractor unit brought to the driven shaft of the gearbox, ω_N^* —the angular velocity of the driven shaft of the gearbox; and u_{K-1} and u_K —the transmission ratios of the gearbox at the $K - 1$ and K gears respectively

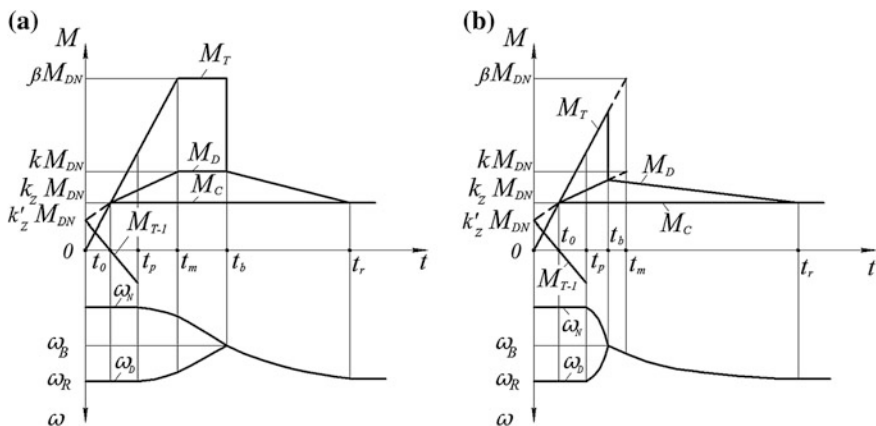


Fig. 2 Acceleration diagram of the tractor unit at gear shifting without interruption of the power flow from the engine. **a** with a flat section ($t_b > t_m$), **b** shape of “triangle” ($t_b \leq t_m$)

Let us consider the gear shifting process with overlap at shifting from lower to higher gear on the example of an elementary gearbox with two parallel shafts (Fig. 1).

The basic parameters defining the gear shifting process are the work L and the time t_b of FC slippage F_K when shifting to higher gear. To define these parameters, let us make use of a theoretical diagram for acceleration of the tractor unit (Fig. 2), which assumes that the friction torque M_T of the engaged FC changes linearly. This assumption was confirmed by experimental acceleration studies of various tractor units, which established that at the regular rate of FC engagement F_K (see

Fig. 1), the friction torque M_T phases up under the law, which is close to linear [1–6].

When defining the law of changing the engine torque M_D , when the tractor unit is accelerating (see Fig. 2), let us assume that within the time interval (from 0 to t_0), it varies in proportion to the current time t of slippage from the value of $k'_z M_{DN}$ to the value of $k_z M_{DN}$. Here, k'_z and k_z are the load factors of the engine at the low and high gears, respectively; M_{DN} is the nominal torque of the engine reduced to the shaft of the engaged FC. We also assume that at the time point t_0 we have $M_D = M_T = M_C$. We further assume that within the time interval ($t_0 - t_m$), by the end of which the FC engagement is over, that M_D also varies in proportion to the current time t of slippage and reaches the value of $k M_{DN}$, where k is the engine adjustability factor; and t_m is the FC engagement time. Within the time interval ($t_m - t_b$), by the end of which the FC slippage is over (Fig. 2a), we assume that $M_D = k M_{DN} = \text{const}$. The torque of resistance to the tractor unit motion, which is brought to the FC shaft, is $M_C = \text{const}$ [1–6]. When drafting our calculation formulas, we neglect the yield effect and damping in the tractor transmission elements, the tangential yield and the slippage of the mover, and the gaps in toothed gears of the transmission and in the towing unit [1–6].

Based on the aforesaid, when a vehicle accelerates from rest, we assume for our calculations that it is to be a double-mass dynamic system of the tractor unit with one frictional bond. A similar dynamic system is used for calculating the slippage of automobile FCs [7].

In our case, the double-mass dynamic system of the tractor unit with two frictional bonds (see Fig. 1) is adopted for calculations, since at gear shifting such operation mode is possible, when the engine power is delivered at the same time by two FCs in the gearbox. The difference of our assumptions from those presented in the works [3–6] lies in the fact that we accelerate the driven parts of the engaged FC F_K not from the rest but starting from the angular velocity ω_N , which corresponds to the end of the acceleration of the tractor unit at the previous gear.

Let us conventionally split the gear shifting process into two phases: overlap and acceleration. We can split the overlap phase into two periods: optimal and excessive overlaps. The period of the optimal overlap corresponds to the period of time from 0 to t_0 , where t_0 is the time, when the friction torque M_T of the engaged FC F_K reaches the value of the resistance moment to motion M_C of the tractor unit, brought to the shaft of the engaged FC at the higher gear (see Fig. 2). We assume that at the initial time ($t = 0$) the FC F_{K-1} is engaged, and the power flow from the engine is delivered only through the gear $K - 1$ (Fig. 3a).

The gear shifting process starts with the engagement of the FC F_K and simultaneous disengagement of the FC F_{K-1} . We assume in this case that the FC F_{K-1} does not slip; therefore, the angular velocity of the driven shaft 2 does not change and corresponds to the gear $K - 1$, i.e. $\omega_2 = \omega_N^* = \omega_D / u_{k-1}$ (Fig. 3b). This is because the friction torque of the FC F_{K-1} is defined by the value of the static friction coefficient in contact of fixed plates, which is by its value significantly higher than the dynamic friction coefficient of the moving plates of the FC

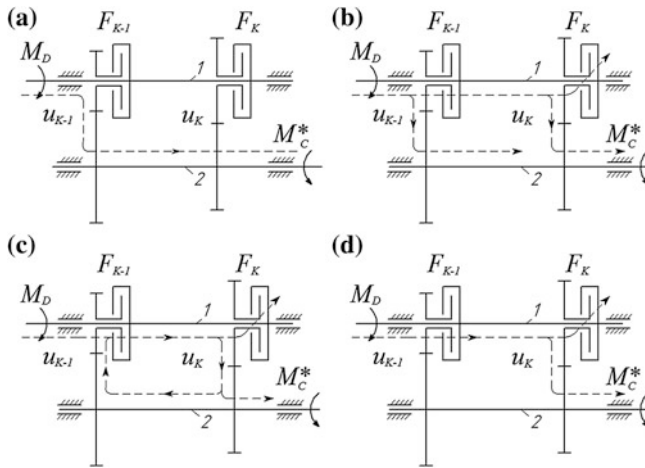


Fig. 3 Power flows in the gearbox. **a** at the engaged $K - 1$ gear, **b** at the optimal gear overlap, **c** at the excessive gear overlap, **d** at acceleration of the tractor unit at the K gear after the end of gear overlap

F_K . The angular velocity ω_N of the driven parts of the FC F_K is $\omega_N = \omega_D u_k / u_{k-1}$, and $u_k / u_{k-1} < 1$. Therefore, at the start of the gear shifting process, the driving plates of the FC F_K rotate faster than the driven ones. Consequently, the engaged FC F_K starts, while sliding, delivering the power from the driving shaft 1 to the driven shaft 2 of the gearbox. However, the value of the friction torque M_T of the FC F_K at the start of shifting (at $t < t_0$) is not enough to overcome the resistance moment to motion M_C of the tractor unit brought to the shaft of the engaged FC. Therefore, to overcome the resistance moment M_C , the FC F_{K-1} is also delivering the torque M_{T-1} , which value, at other equal conditions, depends on the value of friction torque M_T of the engaged FC F_K at the gear K . Thus, at this phase of gear shifting, the power is delivered from shaft 1 to shaft 2 by two parallel flows through the gears $K - 1$ and K (Fig. 3b).

As we show below, with increase of the torque M_T , the power flow delivered through the gear K increases, while the one delivered through the gear $K - 1$ decreases. The phase of the continuous gear shifting at the optimal overlap is over, when the power flow through the gear $K - 1$ becomes zero, although the FC F_{K-1} , and, therefore, the gear $K - 1$ may still be engaged. This happens at the time t_0 .

The dynamic equations for the driving and driven parts of the engaged FC F_K look as follows (see Fig. 1):

$$M_D - M_T - M_{T-1} = J_D \frac{d\omega_D}{dt}; \quad (1)$$

$$M_{T-1} \frac{u_{k-1}}{u_k} + M_T - M_C = J_N \frac{d\omega_N}{dt}, \quad (2)$$

Where J_D is the inertia moment of the engine rotating elements and other parts linked thereto, brought to the shaft of the FC F_K ; and J_N is the inertia moment of the tractor unit brought to the shaft of the FC F_K . It follows from Eq. (2) that at the first phase of gear shifting, the torque M_D is delivered from shaft 1–2 of the gearbox via both FCs at the same time by two parallel flows. In this case, each of the gears transforms the part of the torque M_D delivered to it according to its transmission ratio.

Let us assume that there is no change in angular velocity ω_D of the engine shaft during the overlap, i.e., $d\omega_D/dt = 0$.

Therefore, Eqs. (1 and 2) take the following forms:

$$M_D - M_T - M_{T-1} = 0; \quad (3)$$

$$M_{T-1} \frac{u_{k-1}}{u_k} + M_T - M_C = 0. \quad (4)$$

At the phase of optimal overlap in the time interval from 0 to t_0 (see Fig. 2), we have:

$$M_T = M_{DN} \frac{k_z t}{t_0}, \quad (5)$$

Where $t_0 = t_m k_z / \beta$.

Then, from Eqs. (3 and 4), with account of (5), we have:

$$M_D = M_C \frac{u_k}{u_{k-1}} + M_T \left(1 - \frac{u_k}{u_{k-1}} \right). \quad (6)$$

Since resistance moment to motion M_C of the tractor unit at gear K brought to the shaft FC F_K is $M_C = k_z M_{DN}$, and $u_k/u_{k-1} = k'_z/k_z$,

then, Eq. (6) takes the following form:

$$M_D = k'_z M_{DN} + M_T \left(1 - \frac{u_k}{u_{k-1}} \right) = k'_z M_{DN} + M_{DN} \frac{k_z t}{t_0} \left(1 - \frac{u_k}{u_{k-1}} \right). \quad (7)$$

From Eq. (3) with account of (7) we have:

$$M_{T-1} = k'_z M_{DN} - M_T \frac{u_k}{u_{k-1}} = k'_z M_{DN} - M_{DN} \frac{k_z t}{t_0} \times \frac{u_k}{u_{k-1}}. \quad (8)$$

The work of the slippage of the FC F_K within the time interval $(0 - t_0)$ is defined by the following expression (see Fig. 2):

$$L_0 = \int_0^{t_0} M_T (\omega_D - \omega_N) dt.$$

By replacing the values of M_T , ω_D and ω_N by their values for the first phase, we have:

$$L_0 = \frac{M_{DN} \omega_R k_z^2 t_m}{2\beta} \left(1 - \frac{u_k}{u_{k-1}} \right),$$

where $\omega_R = \omega_{DH} - k'_z(\omega_{DH} - \omega_{DN})$. Here, ω_R and ω_{DH} are the angular velocities of the engine shaft respectively at operating load at gear $K - 1$ and at idle speed brought to the shaft of the engaged FC.

If upon the end of the first phase, the FC F_{K-1} is not disengaged, then the second phase of gear shifting (with the excessive overlap) starts. It starts at the moment of time t_0 , when the torque M_{T-1} delivered by the FC F_{K-1} becomes equal to zero (see Fig. 2). We should note here that at the moment of time $t = t_0$, the torque M_{T-1} on the shaft of the FC F_{K-1} becomes equal to zero even at the completely disengaged FC. This is because at the moment of time $t = t_0$, the value of friction torque M_T on the shaft of the FC F_K becomes sufficient for overcoming the resistance to motion of the tractor unit, and the FC F_{K-1} does not slip.

At $t > t_0$, the friction torque M_T at the engaged FC F_K keeps going up. As a result, the gear to be engaged starts delivering to the driven shaft greater power than it is necessary to ensure the motion of the tractor unit at the speed V_{K-1} , which corresponds to gear $K - 1$; this is supposed to cause acceleration of the tractor unit from speed V_{K-1} up to V_K . However, if the friction torque M_{T-1} of the FC F_{K-1} of the gear to be disengaged is still high enough, then, the gear $K - 1$ prevents acceleration of the tractor unit by putting out the excessive power, which is delivered by gear K , back from driven shaft 2 to driving shaft 1 of the gearbox (Fig. 3c). This results in circulation of power in the circuit of the unit of the gearbox formed by shafts 1 and 2, gears, $K - 1$, and K . Therefore, at the first phase, the possibility of accelerating the tractor unit at slippage of the FC F_K with a constant angular velocity is excluded (see Fig. 2). However, the circulation causes no interruption of the power flow from the engine to the driving wheels of the tractor, since only an excessive part of the power delivered to the driven shaft by gear K is circulating. At the full disengagement of the FC F_{K-1} , the phase of excessive overlap is over.

The dynamic equations for the driving and driven parts of the engaged FC F_K for the time interval $(t_0 - t_p)$ differ from Eqs. (1 and 2) by the sign at torque M_{T-1} :

$$M_D - M_T + M_{T-1} = J_D \frac{d\omega_D}{dt}; \quad (9)$$

$$M_T - M_{T-1} \frac{u_{k-1}}{u_k} - M_C = J_N \frac{d\omega_N}{dt}. \quad (10)$$

Here, the behavior of the friction torque M_T of the engaged FC F_K is defined similarly to the previous phase (see Fig. 2) by expression (5). The overcoming of load of M_C , which is accompanied by circulation of power and slippage of the FC F_K , can result in overload of the engine. To define the dependence of the angular velocity of the engine shaft ω_D on the duration of power circulation (the time of

the excessive overlap) and other parameters, let us make use of equations of the torques (9 and 10), as well as of the connection equation for driving and driven plates of the FC F_K :

$$\omega_N = \omega_D \frac{u_k}{u_{k-1}}. \quad (11)$$

As a result, we have that:

$$\omega_D = \omega_R + \frac{M_{DN}\beta(t_p - t_0)^2}{2t_m \left[J_D + J_N \left(\frac{u_k}{u_{k-1}} \right)^2 \right] (\beta - k_z)} \cdot \left[k - \beta \left(1 - \frac{u_k}{u_{k-1}} \right) - k'_z \right]. \quad (12)$$

It follows from the analysis of expression (12) that the decrease of angular velocity ω_D of the engine shaft at gear shifting with excessive overlap becomes more significant with the increase of the load factor k'_z of the engine at gear $K - 1$, safety factor β of the FC F_K , and value u_{k-1}/u_k . In this case, the higher is the adjustability factor k of the engine the smaller is the decrease of the angular velocity ω_D of its shaft. However, the practice shows that the angular velocity ω_D of the engine shaft at the phase of excessive overlap has little changes. Therefore, to schematize the law of ω_D change, in order to simplify the mathematical manipulations, let us assume that at the phase of excessive overlap, as well as at the phase of optimal overlap, the angular velocity of the engine shaft, and, therefore, of the driven parts of the transmission do not change.

In time interval $(t_0 - t_p)$ of gear shifting (see Fig. 2), the work of the slippage of the FC F_K is:

$$L_1 = \int_{t_0}^{t_p} M_T(\omega_D - \omega_N) dt.$$

Then, with account of expressions (5, 11) and at the condition that $d\omega_D/dt = 0$, we have:

$$L_1 = \frac{M_{DN}\omega_R k_z (t_p - t_0)^2}{2t_0} \left(1 - \frac{u_k}{u_{k-1}} \right).$$

Further, let us consider the phase of acceleration of the driven parts of the tractor unit, which starts after disengaging the FC F_{K-1} . At the start of this phase, the angular velocity of the driven plates of the FC $F_K \omega_N = \omega_D u_k / u_{k-1}$. Therefore, the driven plates of the FC F_K rotate at smaller angular velocity than the driving ones; the FC slips and the power from shaft 1-2 is delivered through gear K (Fig. 3d). As a consequence, the torque M_T causes an acceleration of the tractor unit and at the same time a decrease of the angular velocity of the engine shaft (see Fig. 2). We should note here that only at this phase, the speed ratio $u = \omega_D / \omega_N$ of the unit of the gearbox changes from u_{k-1} to u_k . Then, after the end of the slippage

of the FC F_K , the tractor unit accelerates at gear K up to speed V_K of the steady motion. Here, the gear shifting process and the acceleration of the tractor unit is over.

This phase of shifting differs from the process of starting the tractor unit from rest by means of the main FC basically only in their initial conditions.

At the start of this phase of gear shifting, the relative angular velocity ω_{rel} of the driven and driving plates of the FC F_K is defined from the following expression:

$$\omega_{rel} = \omega_D - \omega_N = \omega_R \left(1 - \frac{u_k}{u_{k-1}} \right).$$

The work of the slippage of the FC F_K for the case of accelerating the tractor unit according to the diagram with a flat section (see Fig. 2a) within the time interval $(t_p - t_m)$ is:

$$L_2 = \int_{t_p}^{t_m} M_T (\omega_D - \omega_N) dt. \quad (13)$$

Within the preset time interval $(t_p - t_m)$, according to the above assumptions, the torques M_T and M_D are defined from the following expressions:

$$M_T = \frac{M_{DN}(\beta - k_z)(t - t_0)}{(t_m - t_0)} + M_C; \quad (14)$$

$$M_D = \frac{M_{DN}(k - k_z)(t - t_0)}{(t_m - t_0)} + M_C, \quad (15)$$

and the changes of the angular velocities ω_D and ω_N —from the following expressions:

$$\omega_D = \omega_R - \frac{M_{DN}(\beta - k)(t - t_0)^2}{2J_D(t_m - t_0)}; \quad (16)$$

$$\omega_N = \omega_R \frac{u_k}{u_{k-1}} + \frac{M_{DN}(\beta - k_z)(t - t_0)^2}{2J_N(t_m - t_0)}. \quad (17)$$

By using dependences (14, 15, 16, and 17), after respective transformations, the integral of expression (13), which presents the work of the slippage within the time interval $(t_p - t_m)$, is written as follows:

$$L_2 = \frac{M_{DN}\beta}{t_m} \left[\frac{\omega_R}{2} \left(1 - \frac{u_k}{u_{k-1}} \right) (t_m^2 - t_p^2) - \frac{M_{DN}}{24} (t_m - t_p)^2 \left(\frac{\beta - k}{J_D} + \frac{\beta - k_z}{J_N} \right) \times \left((3t_m + t_p) - \frac{(t_p - t_0)(3t_p + t_m)}{t_m - t_0} \right) \right]. \quad (18)$$

For the case of accelerating the tractor unit according to the “triangular” diagram (see Fig. 2b), within the time interval $(t_p - t_b)$, the work of the slippage will be:

$$L_2 = \int_{t_p}^{t_b} M_T(\omega_D - \omega_N) dt. \quad (19)$$

Then, with account of expressions (14, 15, 16, and 17), the integral of expression (19), which presents the work of the slippage within the time interval $(t_p - t_m)$, is written as follows:

$$L_2 = \frac{M_{DN}\beta}{t_m} \left[\frac{\omega_R}{2} \left(1 - \frac{u_k}{u_{k-1}} \right) (t_b^2 - t_p^2) - \frac{M_{DN}}{24(t_m - t_p)} \left(\frac{\beta - k}{J_D} + \frac{\beta - k_z}{J_N} \right) \times \left((t_b - t_p)^3(3t_b + t_p) - \frac{(t_p - t_0)}{(t_m - t_0)} \left\{ (t_b - t_m)^3(3t_b + t_m) + (t_m - t_p)^3(3t_p + t_m) \right\} \right) \right]. \quad (20)$$

Here, the time of slippage t_b is defined from (16, 17) from condition $t = t_b$ and $\omega_D = \omega_N$:

$$t_b = \sqrt{(t_m - t_0) \left(t_p - t_0 + \frac{2\omega_R \left(1 - \frac{u_k}{u_{k-1}} \right)}{M_{DN} \left(\frac{\beta - k}{J_D} + \frac{\beta - k_z}{J_N} \right)} \right)} + \frac{t_m k_z}{\beta}. \quad (21)$$

The work of the slippage L_3 for the case of the final phase of accelerating of the tractor unit under the diagram with the a flat section (see Fig. 2a) within the time interval $(t_m - t_b)$ is calculated by the following formula:

$$L_3 = \int_{t_m}^{t_b} M_T(\omega_D - \omega_N) dt. \quad (22)$$

When defining L_3 within the time interval $(t_m - t_b)$, by assuming that the friction torque of the engaged FC $M_T = M_{Tmax} = \beta M_{DN} = \text{const}$, $M_D = k M_{DN} = \text{const}$, from Eqs. (1 and 2), we find:

$$\omega_D = \omega_R - \frac{M_{DN}(\beta - k)}{J_D} \left[\frac{(\beta - k_z) t_m}{2\beta} + (t - t_m) \right]. \quad (23)$$

$$\omega_N = \omega_R \frac{u_k}{u_{k-1}} + \frac{M_{DN}(\beta - k_z)}{J_N} \left[\frac{(\beta - k_z) t_m}{2\beta} + (t - t_m) \right]. \quad (24)$$

By using expressions (23, 24) and values of the torques M_T and M_D for intervals $(t_m - t_b)$, we reduce the work of the slippage presented by the integral of dependence (22) to the following form:

$$L_3 = \frac{M_{DN}\beta(t_b - t_m)}{2} \left\{ 2\omega_R \left(1 - \frac{u_k}{u_{k-1}} \right) - M_{DN} [t_b - t_p] \left(\frac{\beta - k}{J_D} + \frac{\beta - k_z}{J_N} \right) \right\}.$$

Here, time of slippage t_b is defined from (23, 24) at the condition that $t = t_b$ and $\omega_D = \omega_N$.

Then:

$$t_b = \frac{\omega_R \left(1 - \frac{u_k}{u_{k-1}} \right)}{M_{DN} \left(\frac{\beta - k}{J_D} + \frac{\beta - k_z}{J_N} \right)} + \frac{t_m + t_p}{2}. \quad (25)$$

The total work of the slippage for the acceleration diagram of the tractor unit with a flat section (Fig. 2a) is defined from the following expression:

$$L = L_0 + L_1 + L_2 + L_3, \quad (26)$$

Where L_2 is defined from expression (18), and time t_b of the slippage—from expression (25).

For the case with the “triangular” acceleration diagram (Fig. 2b), the total work of the slippage will be:

$$L = L_0 + L_1 + L_2, \quad (27)$$

where L_2 is defined from expression (20), and time t_b of the slippage—from expression (21).

To calculate the work of the slippage L of the FC, we need to know, which of the cases the acceleration of the tractor unit should be referred to (see Fig. 2). With this aim, from expression (21 or 25), let us define time t'_m of engagement of the FC for a particular case of accelerating the tractor unit, at which $t_m = t_b$:

$$t'_m = \frac{2\omega_R \left(1 - \frac{u_k}{u_{k-1}} \right)}{M_{DN} \left(\frac{\beta - k}{J_D} + \frac{\beta - k_z}{J_N} \right)} + t_p. \quad (28)$$

If $t'_m > t_m$, then $t_b > t_m$ (Fig. 2a). Then work L and time t_b of the slippage of the FC of the gear to be engaged are defined respectively from expressions (26 and 25).

If $t'_m \leq t_m$, then $t_b \leq t_m$ (Fig. 2b). Then work L and time t_b of the slippage of the FC are defined respectively from expressions (27 and 21).

One of the most important parameters of the accelerating process of the MTU (machine-tractor unit) is a minimum angular velocity ω_b of the engine shaft at the end of the slippage of the FC. To define ω_b , we need to substitute $t = t_b$ for the case when $t_b > t_m$ (Fig. 2a) into expression (23 or 24), and for the case when $t_b \leq t_m$ (Fig. 2b)—into expression (16 or 17). As a result, we have the general dependence, according to which:

$$\omega_b = \omega_R \frac{1 + \frac{u_k}{u_{k-1}} \frac{J_N(\beta-k)}{J_D(\beta-k_z)}}{1 + \frac{J_N(\beta-k)}{J_D(\beta-k_z)}}. \quad (29)$$

When defining the acceleration time of the MTU t_r at the gear to be engaged, let us consider the time interval $(t_b - t_r)$, when the acceleration is ensured by the torque backup of the engine. Let us write down the equation of the torques based on double-mass dynamic model relating to the elementary unit of the gearbox (Fig. 1) with the condition that the FC in this time interval has already no slippage:

$$M_D - M_C = (J_D + J_N) \frac{d\omega_D}{dt}. \quad (30)$$

At other conditions being equal, the acceleration time t_r of the MTU depends on the type of the acceleration diagram (Fig. 2). Therefore, let us consider both cases of accelerating the MTU at the preset gear.

By solving Eq. (30) for the case of accelerating the MTU under the diagram with a flat section (Fig. 2a) at $t = t_r$ и $\omega_D = \omega_R$ we find the acceleration time of the MTU at the engaged gear:

$$t_r = t_b + \frac{2(\omega_r - \omega_b)(J_D + J_N)}{M_{DN}(k - k_z)}. \quad (31)$$

By solving Eq. (30) for the case of accelerating MTU according to the “triangular” diagram (Fig. 2b) at $t = t_r$ and $\omega_D = \omega_R$, we find the acceleration time of the MTU at the gear to be engaged:

$$t_r = t_b + \frac{2(\omega_r - \omega_b)(J_D + J_N)}{M_{DN}(k - k_z)} \sqrt{\frac{t_m}{t'_m}}. \quad (32)$$

The obtained expressions for calculating the work and the time of FC slippage at gear shifting in the gearbox with different overlap degrees are universal, since they allow calculating the work and the time of the FC slippage and acceleration of the MTU both at gear shifting with various overlap degrees, and at tractor's acceleration and start from the rest. When the tractor starts from the rest and accelerates at the preset gear, we assume the overlap time $t_p = 0$, and the ratio $u_k/u_{k-1} = 0$.

Table 1 Comparison of experimental and calculated values of FC slippage at gear shifting in the gearbox

Source of information	Work type	t_m, s	t_p, s	β	J_b	J_N	$M_{DN}, N \cdot m$	$\omega_{DH}, rad/s$	k	k_z	$\frac{u_k}{u_{k-1}}$	Experiment		Error, %
												L, J	Calculation	
[2]	Tillage	1.5	0.71	2.0	1.67	2.8	195.2	201	1.10	0.88	0.85	3300	3704	+10.9
		1.5	0.78	2.0	1.67	2.8	195.2	201	1.10	0.88	0.85	3500	3800	+7.9
		1.5	0.84	2.0	1.67	2.8	195.2	201	1.10	0.88	0.85	3700	3857	+4.1
		1.5	0.59	2.0	1.67	2.3	195.2	201	1.10	0.72	0.68	8500	8850	+4.0
		1.5	0.66	2.0	1.67	2.3	195.2	201	1.10	0.72	0.68	8700	8910	+2.4
[5]	Tillage	1.5	0.72	2.0	1.67	2.3	195.2	201	1.10	0.72	0.68	8850	8986	+1.5
		1.2	0.54	1.9	2.55	1.03	274.4	220	1.05	0.85	0.90	8624	9648	+10.6
	Sowing	1.0	0.37	1.9	2.55	1.16	274.4	220	1.05	0.70	0.90	7742	7727	-0.2

To verify the reliability of the mathematical model of the FC slippage process in the gearbox, and the calculation methods of the slippage work at gearing under various overlaps, we made a comparison of the calculated and experimental values of the work L of the slippage. The experimental data for the case of the optimal overlap were taken from the work of Ananyin [5], where the optimal overlap at gear shifting at tillage and sowing was ensured by installing a free-travel clutch into the gearbox. The results of the experimental studies at gear shifting without interruption the power flow for various overlaps were borrowed by us from the work of Lvovskiy [2].

The comparison of calculated and experimental data is presented in Table 1.

It follows from the analysis of the results that the divergence of calculated and experimental results of the work of the FC slippage in the gearbox with various degrees of the overlap does not exceed 10.9 %.

References

1. Ananyin AD (1972) Study of energy load of the clutch coupling of a wheeled tractor at acceleration of a speedy machine-tractor unit. Dissertation of a Doctor of Philosophy in Technical Sciences, Moscow
2. Lvovskiy K Ya (1970) Study of processes of gear shifting under load in tractor transmissions. Dissertation of a Doctor of Philosophy in Technical Sciences, Moscow
3. Sharipov VM (2009) Design and calculation of tractors. Mashinostroenie, Moscow
4. Chunikhin VI (1977) Study of durability of friction pairs of tractor coupling clutches, and certain ways to improve it. Dissertation of a Doctor of Philosophy in Technical Sciences, Moscow
5. Barskiy IB, Eglit IM, Sharipov VM (1977) Engineering calculations of the full slippage work of a tractor friction coupling clutch. Tractors Agric Veh 9:16–17
6. Zakharov VE (1981) Study of loads, part wear, and update of methods of bench trials of tractor coupling clutches. Dissertation of a Doctor of Philosophy in Technical Sciences, Moscow
7. Scherenkov GM (1976) Friction pairs of automobile clutches (theory, experimental and calculated data). Dissertation of a Doctor of Philosophy in Technical Sciences, Yaroslavl

The Influence of Torque and Speed Sensitive Differential Characteristics in a Front Wheel Drive Vehicle During On-Limit Manoeuvres

Anthony Tremlett, David Purdy, Nick Vaughan, Francis Assadian, Adrian Moore and Martin Halley

Abstract Passive Limited Slip Differentials (PLSD) are a well-established means of improving the traction limitation imposed by the open differential, and achieve this by transmitting a bias torque from the faster to slower rotating driven wheel. This torque bias is typically proportional to the differential input torque (torque sensing) or the speed difference between driven wheels (speed sensing). In the motorsport environment however, there exist devices which are able to bias torque through both methods simultaneously, but to date, remain unexplored with respect to their influence on handling and the differential models required to study them. Plate (Salisbury) type and Viscous Coupling (VC) differential models are formulated, then combined into a Viscous Combined Plate (VCP) model and used as a basis for handling characterisations through typical cornering scenarios. An 8 degree of freedom (DOF) vehicle model created in the MATLAB/Simulink environment is parameterised around a front wheel drive (FWD) saloon racing vehicle. Path preview steering control is used to give a robust means of comparing the necessary driver inputs to maintain a particular racing line, whilst reaching the lateral acceleration limit of the vehicle. At low lateral accelerations ($<5 \text{ m/s}^2$) VC, VCP and locked differentials were shown to increase levels of understeer most, as the torque bias of a plate differential is proportionally less due to the minimal throttle input required to maintain vehicle speed. At these low speeds, any torque bias acts to reduce initial turn-in yaw rate response. At higher lateral accelerations ($>5 \text{ m/s}^2$), inner wheel tyre saturation ultimately limits the maximum speed through a corner. The degree of

F2012-C02-003

A. Tremlett (✉) · D. Purdy · N. Vaughan · F. Assadian
Cranfield University, Cranfield, Bedfordshire, UK
e-mail: a.j.tremlett@cranfield.ac.uk

A. Tremlett · A. Moore · M. Halley
Xtrac Limited, Thatcham, Berkshire, UK

torque bias that a PLSD can provide to the outer wheel will delay the onset of inner tyre saturation, and increase the maximum lateral acceleration limit. In raw performance terms, this means a locked differential is up to 0.05 s quicker through a constant 50 m radius corner when compared to an open differential equivalent.

Keywords Vehicle dynamics · Limited slip differential · Viscous coupling · Torque sensitive · Speed sensitive

Nomenclature

A_p	Empirical differential friction constant
$C_{\mu 1,2,3}$	Empirical friction surface constant
F_p	Differential preload force (N)
K_g	VC disc geometry correction factor
R_r	Mean contact radius between ramp and crosspin (m)
$R_{o,i}$	Outer and inner clutch surface/shear surface radius (m)
s	Distance between VC shear surfaces (m)
T_d	Differential input torque (Nm)
$T_{dd,dc}$	Drive and coast critical input torque (Nm)
$T_{p,vc,vcp}$	Plate, VC and VCP differential locking torque (Nm)
T_{max}	Normalisation locking torque (Nm)
Z_f	Number of friction/shear faces
θ_r	Drive/coast ramp angle (degrees)
$\mu_{p,r}$	Clutch plate and ramp-crosspin surface friction coefficient
μ_{max}	Normalisation friction coefficient
ν	VC fluid kinematic viscosity (mm^2/s)
ρ	VC fluid density (kg/m^3)
ω_d	Driven wheel speed difference (rpm)

1 Introduction

Automotive differentials are well-established as a means of transferring torque to wheels rotating at different speeds. Provided there is a sufficient level of grip at each wheel, the open differential is a perfectly satisfactory device. However, in extreme instances where traction at one wheel is compromised, Limited Slip Differentials (LSD) have been shown to offer distinct improvements in traction and vehicle stability [1–3]. LSDs achieve these performance benefits through the transfer of torque from the faster to slower driving wheel. In the majority of racing formulae, regulations dictate that this torque bias is controlled passively, either through differential input torque (torque sensing) or driven wheel speed difference (speed sensing) [4]. However, there exist devices which are able to bias torque

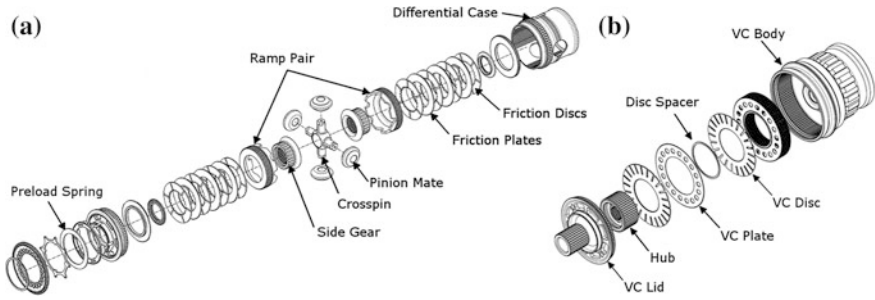


Fig. 1 a Exploded view of Xtrac [4] plate differential and b viscous coupling

through both methods simultaneously, but to date, remain unexplored with respect to their influence on handling and the differential models required to study them.

This paper aims to formulate a more comprehensive plate differential model and combine with a Viscous Coupling (VC) unit to produce a Viscous Combined Plate (VCP) simulation model. This is primarily to allow the influence of its locking characteristics on vehicle handling to be studied, but also for future optimisation of the torque bias itself. Figure 1a shows an exploded view of an Xtrac [5] plate type, or ‘Salisbury’ differential [3], in which a torque bias is generated through the thrust loads of a ramp pair acting against two wet clutch packs. Conversely, the speed sensitive VC (see Fig. 1b) relies on the torque generated from a number of plates shearing through a viscous silicon fluid to generate its torque bias [3].

2 Differential Simulation Models

2.1 Torque Sensitive: Plate Type

The most basic method to calculate the locking torque generated by a clutch plate assembly uses uniform pressure clutch theory [6]. This analysis can be extended and applied to the particular case of a plate differential, by incorporating the effects of ramp angle (θ_r) and the number of friction faces (Z_f) [7]. Furthermore, it is common to allow a residual clamp force (F_p) or ‘preload’ to clamp the plate pack. This is both to improve lockup response and to allow a degree of torque bias to take place when little differential input torque (T_d) can be distributed to each driven wheel (e.g. when a wheel is in mid-air due to a curb strike). The resulting locking torque (T_p) can be defined for both on-throttle (drive) and off-throttle (coast) conditions. Below critical drive and coast input torques (T_{dd} , T_{dc}), T_p is equal to a preload locking torque (T_{lp}). Above these critical input torques, T_p is governed by a more significant ramp locking torque (T_{lr}). These regions are defined in Eqs. 1 and 2 and typical locking characteristics are shown in Fig. 2a.

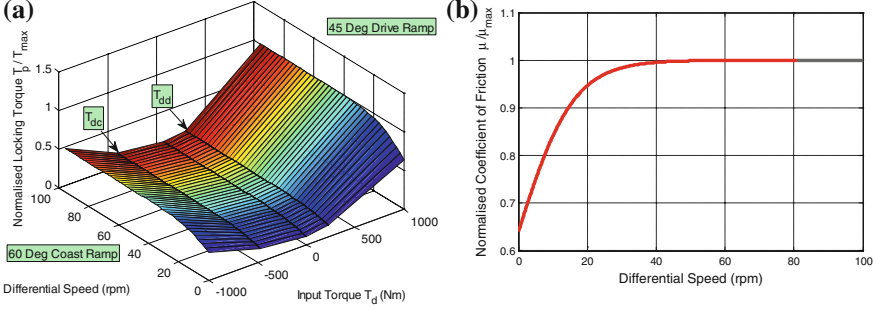


Fig. 2 **a** Normalised locking characteristics of an Xtrac [4] plate differential, **b** normalised coefficient of friction approximation with differential speed

$$\text{Ramp Locking Torque } (T_r) \frac{2}{3} \left[\frac{T_d}{R_r} \left(\frac{\cos\theta_r - \mu_r \sin\theta_r}{\sin\theta_r + \mu_r \cos\theta_r} \right) \right] \mu_p Z_f \left(\frac{R_o^3 - R_i^3}{R_o^2 - R_i^2} \right) \quad (1)$$

$$\text{Preload Locking Torque } (T_p) \frac{2}{3} \left(\frac{R_o^3 - R_i^3}{R_o^2 - R_i^2} \right) \mu_p F_p Z_f + A_p T_d \quad (2)$$

Where Z_f is the number of friction faces, μ_p the coefficient of friction between friction faces and A_p an empirical constant representing the inherent friction of rotating elements within the differential housing (bearings, side gear, pinion mates). Crucial to the accuracy of this model, is the calculation of plate friction. The friction coefficient changes with many factors including clamp load, oil temperature, differential speed and friction material [8, 9]. One of the most relevant of these factors is sensitivity of the friction coefficient with differential speed. Most simply, this can be represented by an approximation of empirical data defined in Eq. 3 and depicted in Fig. 2b.

$$\mu_p = C_{\mu 1} \tanh(C_{\mu 2} \omega_d) + C_{\mu 3} \quad (3)$$

where $C_{\mu 1}$, $C_{\mu 2}$, $C_{\mu 3}$ are empirically determined constants and ω_d is the difference in rotational speed of the friction faces. The resulting locking torque gradient shown in Fig. 2a is governed mainly by input torque but also relative wheel speed at lower speeds. The locking torque gradient is an important aspect, since it will control the rate of differential torque bias and the resulting yaw moment imparted to the vehicle through longitudinal tyre forces. As the input torque and therefore torque bias varies substantially during typical driving conditions, this has the potential to influence vehicle stability.

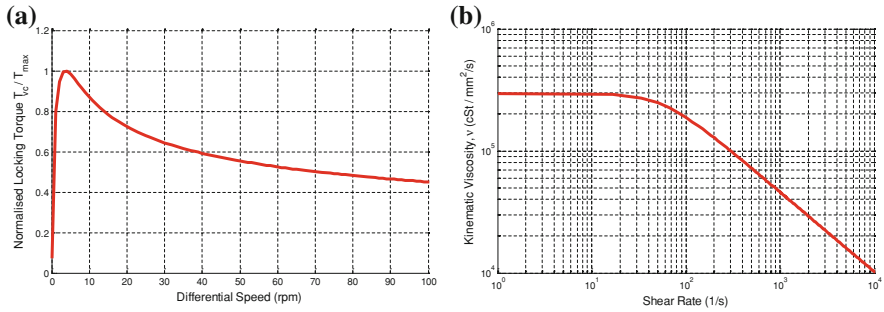


Fig. 3 **a** Normalised VC locking characteristics and **b** variation of fluid viscosity with shear rate

2.2 Speed Sensitive: Viscous Coupling

In contrast to torque sensing differentials, speed sensing differentials are not reliant on an input torque to generate locking. Of the current types in use, VCs used in conjunction with a conventional bevel gear open differential have proved popular since they provide a reliable, cost efficient solution, which can be easily tuned to give a range of locking characteristics. Of crucial importance is the fluid viscosity relationship with temperature and shear rate [10, 11]. Assuming the device is maintained at a constant operating temperature an isothermal representation can be used to calculate the locking torque generated from viscous shearing of the silicon fluid. This is defined in Eq. 4 [10] where, ρ and ν are the density and kinematic viscosity of the fluid, s the distance between shear plates, and K_g a correction factor used to account for the reduction in shear area due to plate geometry (e.g. slots and perforations).

$$VC \text{ Locking Torque } (T_{vc}) = Z_f \frac{K_g \rho \nu \omega_d}{2s} (R_o^4 - R_i^4) \quad (4)$$

Typical locking torque characteristics and the variation of fluid viscosity with shear rate are shown in Figs. 3a and b, at a nominal fluid temperature of 25 °C.

2.3 Viscous Combined Plate

The characteristics of both differentials can be utilised by coupling the VC unit between the outputs of a conventional plate differential, as shown in the schematic in Fig. 4a. This yields what is termed a VCP Differential. Consequently, locking torque is now governed both by input torque (T_d) and the difference in driven wheel speed (ω_d). Total locking torque (T_{vcp}) can be described by Eqs. 5 and 6 and is depicted in Fig. 4b.

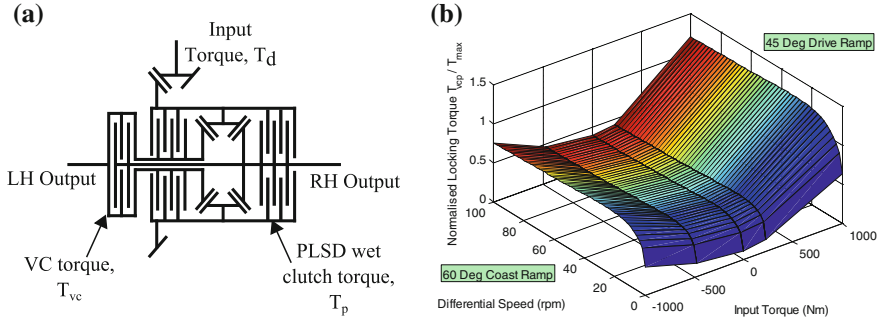


Fig. 4 a VCP schematic and b normalised locking characteristics of VCP differential

$$VCP \text{ Locking Torque } (T_{rvcp}) = T_{lr} + T_{vc} \text{ (ramp region)} \quad (5)$$

$$VCP \text{ Locking Torque } (T_{pvcp}) = T_{lp} + T_{vc} \text{ (preload region)} \quad (6)$$

3 Vehicle Model

To evaluate the influence of plate, VC and VCP locking characteristics on vehicle handling, an 8 degree of freedom (DOF) model constructed in the Matlab/Simulink environment was used (see Fig. 5). The equations of motion for the system describe longitudinal, lateral, yaw and roll vehicle motions in addition to four wheel rotations [12]. This was combined with a non-linear Pacejka tyre model [13] and vehicle parameters from a FWD saloon racing vehicle. To replicate a degree of driver realism, a preview steer driver model was employed [14] which uses a pre-defined path to generate steering corrections based on vehicle position and yaw angle. Longitudinal velocity is controlled with a Proportional Integral (PI) throttle parameter (ranging from 0 to 1), used in conjunction with saturation functions generated from each tyre. This effectively limits the control input under conditions in which the tyres have exceeded their optimum longitudinal slip ratio (i.e. slip at which peak longitudinal force is generated). The differential models were included as look-up tables and considered perfect actuators, which did not account for any dynamic clutch engagement effects.

4 Simulation Results

4.1 Constant Radius Acceleration

To evaluate the performance of each differential at the traction limit, a 30 m radius skid pan test was conducted. The vehicle was first held at a steady state speed to provide initial starting conditions and then requested to accelerate at 0.2 g until the

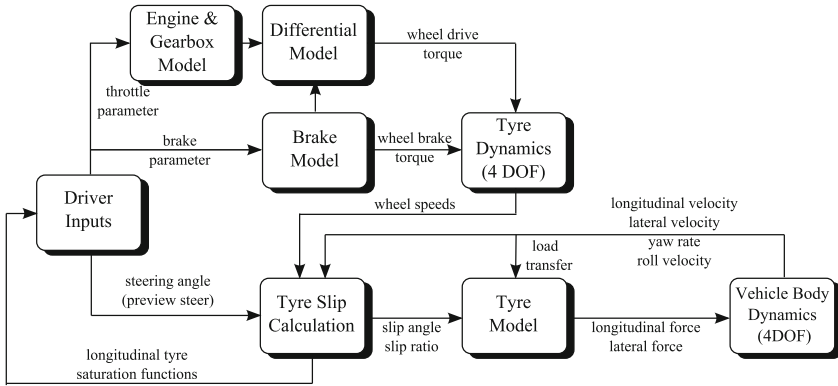


Fig. 5 8 DOF Vehicle Model Structure

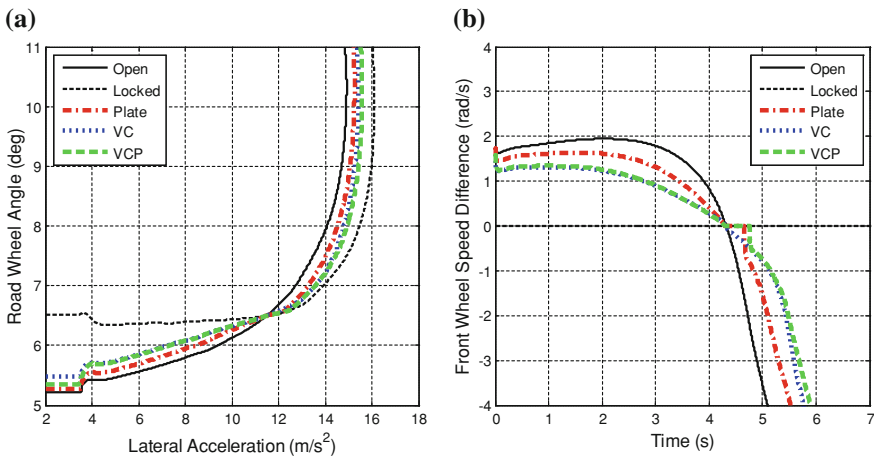


Fig. 6 a Understeer gradient comparison of plate, VC and VCP differentials, b front wheel speed difference, (30 m Skid pan radius, 0.2 g longitudinal acceleration)

lateral acceleration limit of the vehicle had been reached. Figure 6 shows the steering angle and resulting driven wheel speed difference required to maintain the 30 m radius. A maximum path error of ± 0.2 m was permitted throughout the manoeuvre.

Figure 6a shows that at low lateral accelerations ($< 5 \text{ m/s}^2$), VC, VCP, plate and locked differentials increase the steering required to keep the vehicle on the 30 m radius. This steering increase is proportional to the torque bias generated by each device. As lateral acceleration increases to 12 m/s^2 the plate and VCP differentials force driven wheel speeds to synchronise and ‘lock’ (see Figs. 6b, 7b). This occurs when the differential can support a sufficient bias torque to overcome the difference in longitudinal tyre forces. Both differential types remain locked until

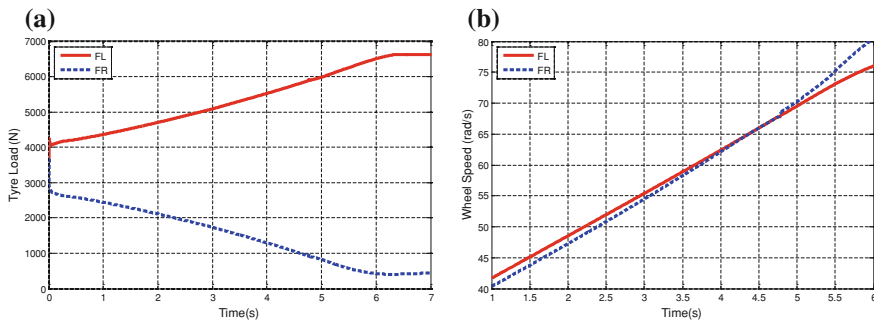


Fig. 7 **a** Front left (*FL*) and front right (*FR*) tyre loads, **b** Front wheel speeds, (VCP differential)

the difference in longitudinal tyre forces becomes more significant. In this case, this has occurred due to lateral load transfer (see Fig. 7a) compromising inner (front right) wheel traction. The locked differential is shown to increase the lateral acceleration limit from that of an open differential (14.9 m/s^2) up to 16.1 m/s^2 .

4.2 Constant Velocity Corner

A further series of simulated test manoeuvres were conducted through a sequence of straight—constant radius bend (50 m)—straight, negotiated at three constant speeds (15, 27.5 and 28.0 m/s). These speeds were intended to start well below the vehicle lateral acceleration limit and to increase up to and beyond the lateral acceleration that the tyres could support. At the lowest speed of 15 m/s the road wheel angle trace (Fig. 8a) shows that the locked differential requires the highest steering angle, with the VC, VCP and plate all falling in between the locked and open differential steering traces. Figure 8c shows the yaw moment generated by each differential which is directly related to the magnitude of the differential locking torque. The locked differential yaw moment dominates due to the higher longitudinal slip induced at each driven wheel. However, due to the relatively low throttle input (Fig. 8b) required to maintain vehicle speed, the plate yaw moment is proportionally small. Importantly, the direction of the torque bias gives a negative moment, i.e. the differential acts to reduce the initial turn-in yaw moment and effectively increases the yaw damping of the car. In raw performance terms however, the manoeuvre time of each differential type is identical (see Table 1). The longitudinal and lateral tyre force saturation plots shown in Fig. 9 also confirm that the tyres are well below their adhesion limit.

When the vehicle speed is increased to 27.5 m/s both the steering angle and throttle required to maintain the manoeuvre speed increase dramatically (see Fig. 10a, b). Due to lateral load transfer, an open differential promotes inner wheel saturation, and road wheel angle increases to almost 10° to allow the vehicle to negotiate the corner. The remaining devices which support a torque bias (plate,

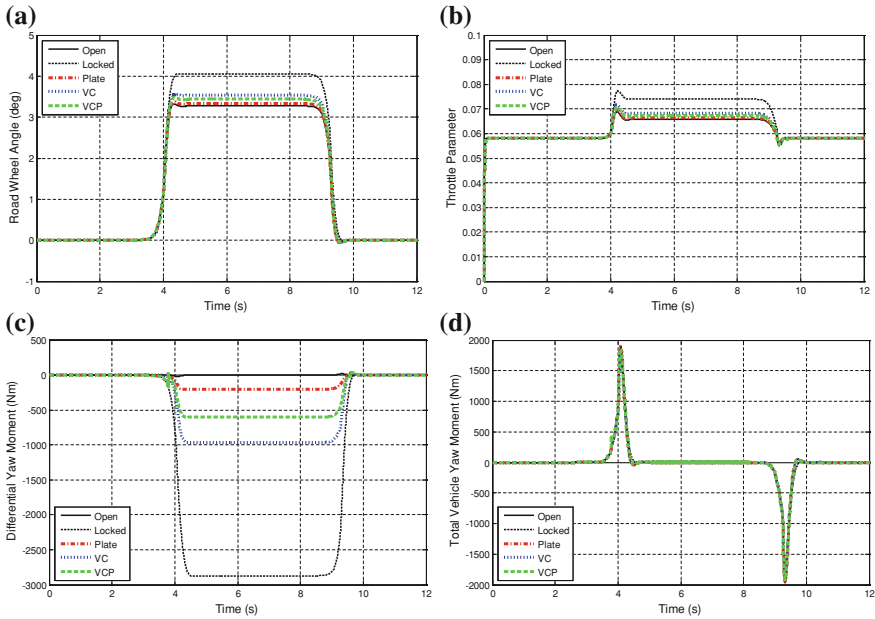


Fig. 8 a Road wheel angle, b throttle parameter, c differential yaw moment and d total vehicle yaw moment (sub-limit, constant vehicle speed 15 m/s, 50 m radius turn)

Table 1 Constant velocity corner manoeuvre time(s) and maximum lateral acceleration (m/s^2)

	Open	Locked	Plate	VC	VCP
Manoeuvre time (15.0 m/s)	13.240	13.240	13.240	13.240	13.240
Peak lateral acceleration	4.55	4.56	4.55	4.56	4.55
Manoeuvre time (27.5 m/s)	7.254	7.226	7.226	7.226	7.226
Peak lateral acceleration	15.29	15.78	15.62	15.73	15.70
Manoeuvre time (28.0 m/s)	7.169	7.097	7.111	7.109	7.103
Peak lateral acceleration	15.26	15.87	15.64	15.75	15.72

VC, VCP) show reduced levels of steering, but importantly the differential yaw moment now reverses its direction from being negative (understeer) to a positive, oversteer moment at 2.5 s (see Fig. 10c).

The magnitude of the moment generated by plate and VCP differentials has also increased due to the higher throttle and therefore higher differential input torque. However, at this higher lateral acceleration, all differential yaw moments are now much smaller than those generated by lateral tyre forces. This can be seen in Fig. 10d, where the total turn-in yaw moment has increased to over 4kNm, with the differential yaw moment only starting to approach—1kNm before switching directions at 2.5 s. This means that the closer the vehicle is to its lateral acceleration limit, the less dominant differential yaw moments become in influencing

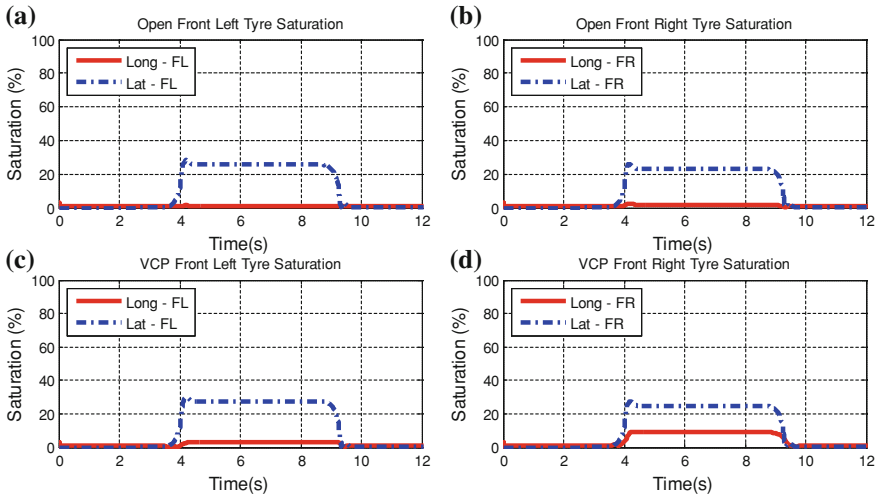


Fig. 9 a Front left and b front right tyre saturation for an open differential, c front left and d front right tyre saturation for a VCP differential

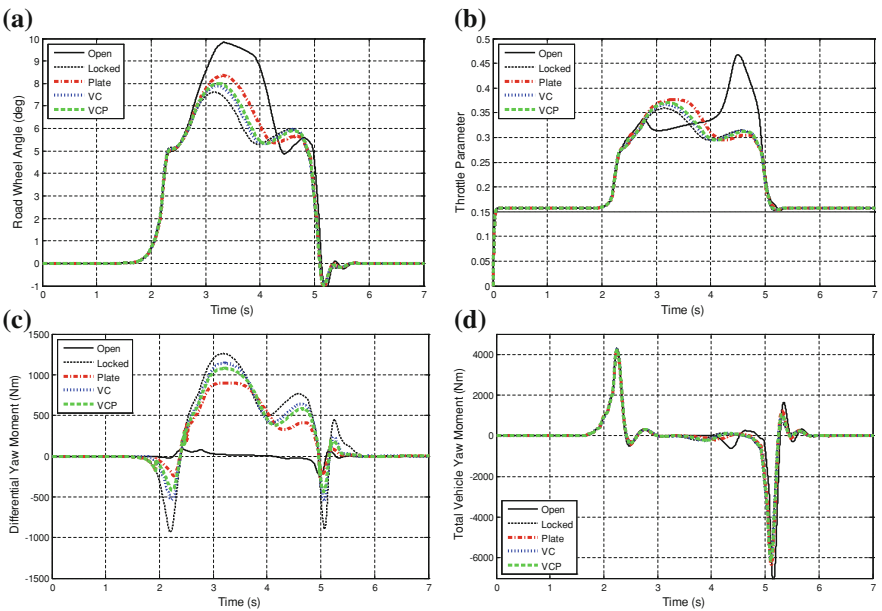


Fig. 10 a Road wheel angle, b throttle parameter, c differential yaw moment, d total vehicle yaw moment (on-limit, constant vehicle speed = 27.5 m/s, 50 m radius turn)

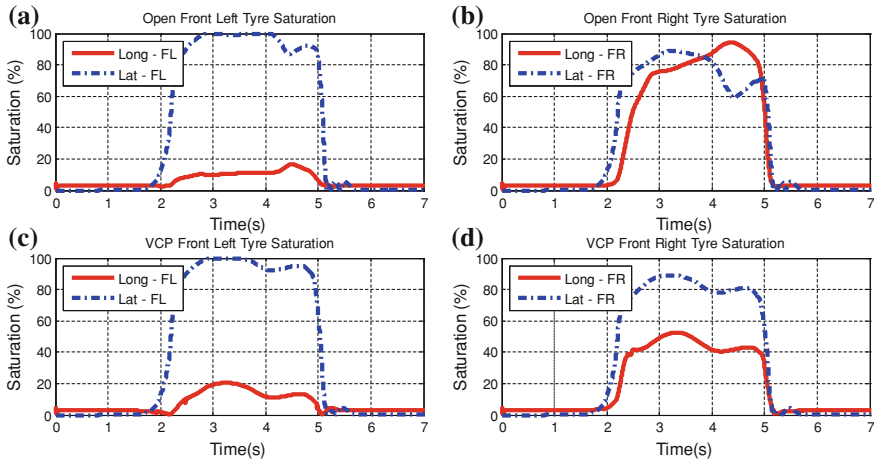


Fig. 11 **a** Front left and **b** front right tyre saturation for an open differential, **c** front left and **d** front right tyre saturation for a VCP differential

the fundamental understeer/oversteer balance of the car. Nevertheless, any differential torque bias helps to limit the longitudinal slip of the inside tyre and maintain a greater lateral tyre force utilisation. This is shown on the lateral force saturation curve of the inner tyre of the VCP (see Fig. 11d). Furthermore, this is reflected in the peak lateral acceleration and manoeuvre time (Table 1) which now shows a more marked performance improvement for locking differentials, both at 27.5 and 28 m/s. It must be borne in mind however, that although offering the largest performance benefit, a locked differential will also dramatically increase tyre wear.

5 Conclusions

This paper has described a plate differential model that is able to show the effect of ramp angle, friction faces and preload on locking characteristics. This is combined with a VC model to produce a novel VCP differential, capable of biasing torque through torque sensing and speed sensing means. An 8 DOF vehicle model was used to show how each device influences handling during on-limit manoeuvres. It is apparent that there are two modes of operation:

Low speed, low lateral accelerations ($<5 \text{ m/s}^2$):

- VC and VCP differentials give higher levels of understeer than plate types, since torque bias is speed and therefore manoeuvre radius dependant. The relatively small throttle input required to maintain vehicle speed means the plate differential generates a proportionally smaller bias torque. However, this also depends

on the particular plate differential configuration (ramp angle, friction faces and preload).

- All differential types, (excluding open) will generate an understeer moment during turn-in. This reduces vehicle agility but may also be used to help stability under heavy braking.

High speed, high lateral accelerations ($>5 \text{ m/s}^2$):

- Greater amounts of differential locking increase the vehicle lateral acceleration limit by delaying the onset of inner tyre saturation. This limit was shown to increase from 14.9 m/s^2 for an open differential to 16.1 m/s^2 for a locked differential (8 % increase).
- At high lateral accelerations, due to lateral load transfer, the inner tyre becomes unladen and allows the direction of torque transfer to reverse for all but open differentials. This generates an oversteer yaw moment, but is small when compared to the yaw moment generated by lateral tyre forces.
- VC, VCP and plate locking differentials can be tuned to give equivalent levels of locking which will all approach the maximum lateral performance of a locked differential. The point at which this will occur depends on corner radius and throttle application.
- A locked differential was shown to be up to 0.05 s quicker through a constant 50 m radius corner when compared to an open differential.

References

1. Kopf P, Escher M, Gazyakan U, Oberhauser M (1990) Optimization of traction and driving stability in 2-wheel drive cars by means of electro-hydraulic limited-slip differentials, SAE paper 905108
2. Morselli R, Zanasi R, Sandoni G (2006) Detailed and reduced dynamic models of passive and active limited-slip car differentials. *Math Comput Modell Dyn Syst* 12(4):347–362
3. Milliken WF, Milliken DL (1995) Race car vehicle dynamics, SAE
4. FIA technical regulations,—<http://www.fia.com/sport/regulations>. Accessed 9 July 2012
5. Xtrac, Xtrac Limited, Kennet Park, Gables Way, Thatcham, Berkshire, RG19 4ZA
6. Rothbart HA, Brown TH (Jr.) (2006) Mechanical design handbook: measurement, analysis, and control of dynamic systems. McGraw Hill, New York
7. Dickason I (2008) Development of a theoretical locking model for a motorsport mechanical plate differential, Master's thesis, School of engineering. Cranfield University
8. Maki R (2005) Wet clutch tribology, Doctoral thesis, Lulea University of technology, Department of applied physics and mechanical engineering
9. Ivanovic V, Deur J, Herold Z, Hancock M, Assadian F (2008) Experimental setups for active limited slip differential dynamics research, SAE world congress and exhibition. April 2008, (2008-01-0302)
10. Mohan SK, Ramarao BV (2003) A comprehensive study of self-induced torque amplification in rotary viscous couplings. *J Tribol* 125(1):110–120
11. Peschke W (1986) A viscous coupling in the drive train of an all-wheel-drive vehicle, SAE technical paper series 860386

12. Genta G (1997) Motor vehicle dynamics: modeling and simulation (series on advances in mathematics for applied sciences—vol. 43), World Scientific Publishing Co. Pte. Ltd
13. Pacejka HB, Besselink IJM (1997) Magic formula tyre model with transient properties. Veh Syst Dyn Suppl 27:234–249
14. Sharp RS, Casanova D, Symonds P (2000) Mathematical model for driver steering control, with design, tuning and performance results. Veh Syst Dyn 33(5):289–326

Design and Performance Prediction of a Tri-Mode Power-Split Transmission

Donghao Zhang, Changle Xiang and Lijin Han

Abstract The tri-mode power-split transmissions, compared with the single-mode and dual-mode ones, can further optimize the operating point of the engine, make full use of the characteristics of the motor/generator and improve the driving performance and the fuel economy of the vehicles. As the structure of tri-mode systems is more complex, it is difficult to apply the design method of single-mode or dual-mode systems in the tri-mode ones. Therefore, it is quite necessary to further study the method of design and performance prediction of tri-mode power-split transmissions. The design method of power-split transmissions based on ideal driving performance and the operating characteristics of the components was put forward, and a tri-mode power-split transmission was designed. The optimal parameter matching method was developed by taking the driving performance, fuel economy and cost as optimization objective, the feasible schemes as research object and the system parameters and control parameters as optimized variables. Then, based on MATLAB and Simulink, a performance prediction method was provided and the steady-state performance and dynamic performance of the power-split transmission was predicted.

Keywords Tri-mode · Power-split · Design · Parameter · Prediction

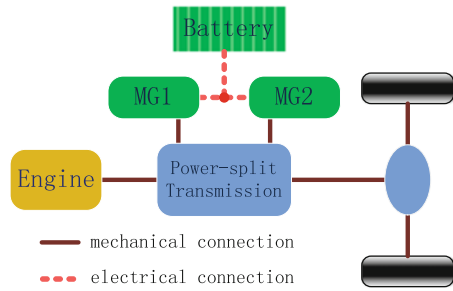
The rapid development of automobile industry has not only given great convenience to people's life, but also brought up with serious energy and environment

F2012-C02-004

D. Zhang (✉) · L. Han
Beijing Institute of Technology, Beijing, China
e-mail: zhdonghao@163.com

C. Xiang
National Key Lab of Vehicular Transmission, Beijing, China

Fig. 1 Structure of power-split hybrid vehicle



problems. Due to the shortage of oil resources, the oil price is increasingly rising; at the same time, the emission standard for automobiles is becoming more and more stringent. In order to solve these problems, almost all the leading automobile companies are developing new energy vehicles. As Toyota's single-mode Prius and GM's dual-mode SUV comes into the market, the power-split hybrid vehicle based on planetary gears becomes a research focus [1]. The characteristics of single-mode, dual-mode and tri-mode power-split transmissions were analysed, and a tri-mode power-split transmission was designed in the paper. On this basis, the parameter matching and the performance prediction was done for the feasible schemes. It would be helpful for the design and performance prediction of various types of transmissions, especially the multi-mode power-split ones.

1 Design of Power-Split Transmission

1.1 Compare of Different Power-Split Transmissions

The power-split hybrid vehicle is the current research focus. Its basic structure is shown in Fig. 1. It is consisted with one engine, two motors/generators (MGs), one power battery pack and one power-split transmission. MGs can be used as both motor and generator. The operating principle is as follows: firstly the engine's power is split by the power-split transmission, and then one part of it drives the generator to generate electricity, which could be used to charge the battery or supply power to the motor; the other part is transmitted as the form of mechanical energy, which will be output after converged with the motor's power.

A power-split transmission is generally consisted with several planetary and clutches/brakes. Its performance will vary if the connecting form of the components is different. According to the number of its speed ranges, the power-split transmission can be divided into single-mode (Fig. 2), dual-mode (Fig. 3) and multi-mode (Fig. 4) power-split transmission.

The single-mode power-split transmission, which has only one speed range, has become the research focus for a long time because of its simple structure. However,

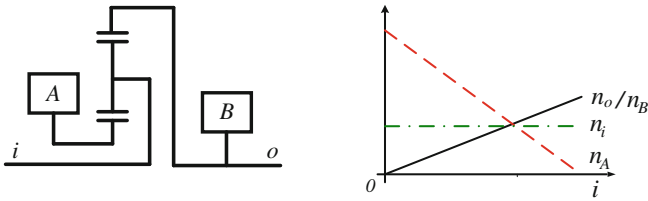


Fig. 2 Single-mode power-split transmission of PRIUS and its speed characteristic

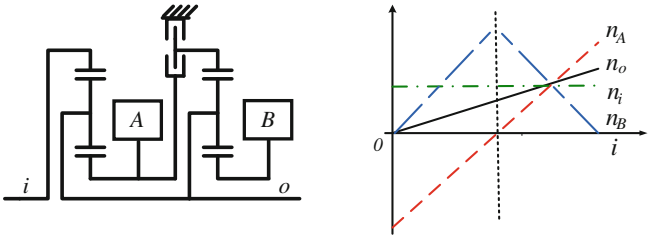


Fig. 3 Dual-mode power-split transmission of GM and its speed characteristic

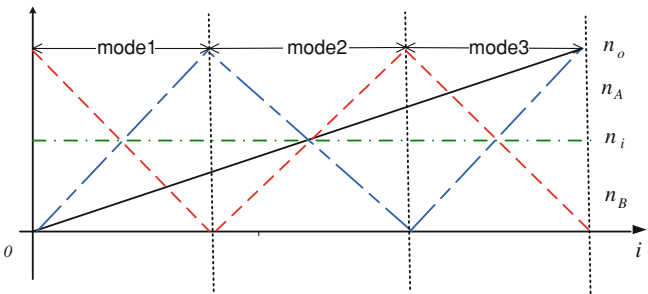


Fig. 4 Multi-mode power-split transmission's speed characteristic

with a narrow speed range, it has a high demand to the speed and power of the MGs. At present, this system is mainly applied in small vehicles on city roads.

With two speed ranges, the dual-mode power-split transmission has a more complex structure. As it can expand the speed range and reduce the power demand of the MGs and the power storage, this structure was applied in SUVs which have a high demand to driving performances.

The multi-mode (including tri-mode) power-split transmission, consisted with three or more planetary and several clutches/brakes, has various connecting forms and performances. With a contrast with the single-mode, dual-mode and tri-mode power-split transmission, it can tell that on the condition of a constant speed range, the increase of modes can reduce the power demand of the MGs and the batteries. Thus, with the current limited condition of MGs and batteries, the performance demand of the hybrid transmission can be satisfied by increasing the modes.

1.2 Design Method of Power-Split Transmission

With only one planetary, the single-mode power-split transmission can be connected with other components through the sun, ring and carrier in six ways. Besides, by increasing the clutches/brakes, the performance of the system can be improved further. Due to the simple structure of the system, all the possible design schemes can be listed manually, and the optimal one can be got by analysis of each scheme's characteristics.

However, the dual-mode power-split transmission generally has several planetary and clutches/brakes, as well as tens of thousands connecting ways. Thus, it is very hard to find the optimal scheme in a manual way. The scheme design work has to be completed with computer. Different design methods of the hybrid system were adopted in references [2, 3]. Based on the ideal driving performance and the characteristics of the power components, a design method of the multi-mode power-split transmission was put forward and a tri-mode power-split transmission was designed in the paper. The design procedure is shown as follows (Fig. 5):

1.2.1 Ideal Driving Performance

The Ideal Driving Performance, including the vehicle speed range, the maximum driving torque and power, are the optimal driving performances of the vehicle. Therefore, the demand of characteristics of the power-split transmission, including the output speed range, the maximum driving torque and power, can be calculated through the ideal driving performance.

As shown in Fig. 6, the vehicle's ideal driving performance can be divided into two ranges: the output torque is constant in the low-speed stage, while the output power is constant in the high-speed stage. The maximum output speed of the power-split transmission can be calculated through the maximum vehicle speed,

$$n_{\text{Max}} = f_1(v_{\text{Max}}) \quad (1)$$

where, f_1 is related to the wheels' effective radius and the rear gear ratio. The maximum output speed determines the power-split transmission's output speed range. As it is easy to analyze the transmission speed, the output speed calculation should be firstly taken into consideration in the process of scheme design. If it does not match the speed condition, the scheme should be directly given up, so that much time will be saved in the later calculation.

$$T_{\text{Max}} = f_2(D) \quad (2)$$

where, D represents the dynamic factor. The system's maximum value of torque can be calculated through the vehicle's dynamic factor D . Function f_2 is related to the weight of the vehicle, the effective radius of the wheels and the rear gear ratio. The maximum output torque determines the power-split transmission's output

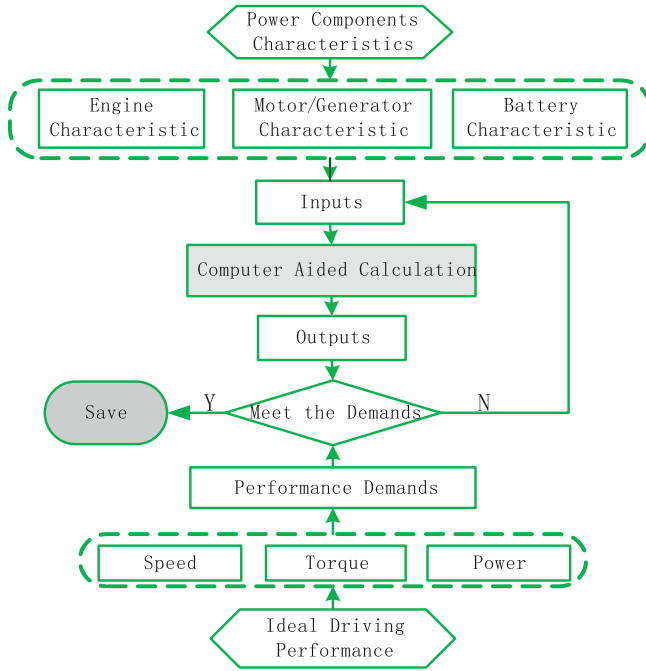
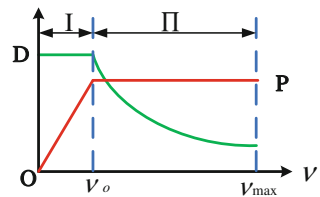


Fig. 5 Design procedure of power-split transmission

Fig. 6 Ideal driving performance



torque range. Therefore, in the process of scheme design, in order to satisfy the demand of the vehicle’s driving performance, the maximum torque of the designed scheme should not lower than that.

$$P = f_3(v,D) \tag{3}$$

where, P stands for the vehicle’s power requirement, and it is the function of the vehicle speed and the dynamic factor. Function f_3 is a binary function, which is only determined by the vehicle’s weight. Generally, the main power source of hybrid vehicle is the engine. Thus, in order to meet the vehicle’s driving power demand, the power-split transmission should be able to transmit the engine’s power at any speed ratio.

Fig. 7 Engine characteristics

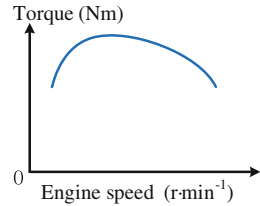
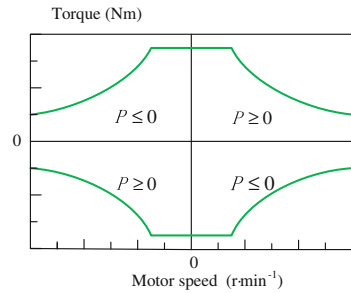


Fig. 8 MG characteristics



1.2.2 Characteristics of the Power Components

Here power components include the engine, MGs and power battery. For power-split transmission, its inputs are determined by the characteristics of the power components. Therefore, for different power components, the best scheme of the system is also different. As the technical level of the power components is gradually improved, the current bad or even infeasible scheme may become the optimum one someday in future (Figs. 7 and 8).

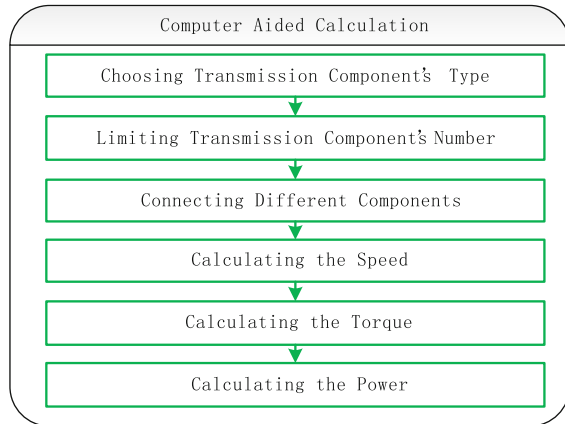
It has been mentioned above that the characteristics of the power components have a great influence in the power-split transmission design. At the early stage of the scheme design, the characteristics of the power components should be determined according to the technical level of the current and near future, as well as some comprehensive factors, such as the space design inside the vehicle and the cost. The inputs of the power-split transmission designed should not go beyond the given characteristic range. In this way, the inputs condition of the power-split transmission could be determined.

1.2.3 Computer Aided Calculation

After the input and output conditions of the power-split transmission are got from the ideal driving performance and the characteristics of the power components, the structure scheme which satisfies the condition can be searched automatically by computer program calculation. The computer aided calculation process mainly includes the following parts (Fig. 9):

Firstly, choose the components’ model from the Model Library, which includes ordinary gear, planetary, clutch and brake at present, and some new transmission

Fig. 9 Computer aided calculation process



structures may be added in future. The current power-split transmissions are mostly using ordinary planetary, so the possible connecting ways are extremely limited. We add up the double and duplex planet multi-member planetary into the Model Library. It is useful for us to find the suitable scheme.

Secondly, make limitation to the number of the components according to the space inside the vehicle, size of the components and cost of the system. Later, list all the connecting schemes with computer program, and generate the constraint equation automatically. The reference [4] completed the choosing process by matrix analysis and calculation. Here we use the method of graph theory, the specific introduction of which can be found in reference [5].

Lastly, based on the characteristics of the power components, analyze the speed, torque and power of all the possible schemes, so as to judge that whether they meet the demands generated from the ideal driving performance. Only all the performance demands are satisfied, the corresponding connecting scheme can be saved and further analyzed.

1.3 A Tri-mode Power-split Transmission

By using the method mentioned above, a tri-mode power-split transmission was designed in this paper. Its structure is shown as the following Fig. 10:

The tri-mode power-split transmission is consisted with three planetary, two clutches, two brakes, and two MGs. Here 'i' stands for the input shaft which is connected with the engine, and 'o' represents the output shaft which is connected with the driving shaft. Remarkably, there is a dual-planet planetary in the transmission, the speed and torque characteristics of which are different from that of an ordinary planetary. It is particularly suitable to be used here, as it can make the power-split transmission meet the input and output performance demands well.

Fig. 10 A tri-mode power-split transmission

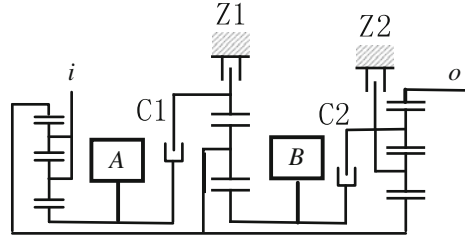


Table 1 Operating mode and clutches/brakes' condition

	C1	C2	Z1	Z2
EVT1			✓	✓
FG1	✓		✓	✓
EVT2	✓			✓
FG2	✓	✓		✓
EVT3	✓	✓		
FG3	✓	✓	✓	

The tri-mode power-split transmission has three EVT modes and three fixed gear ratio (FG). The relationship between the modes and the state of clutches and brakes is shown in Table 1. Methods of parameter matching and performance prediction of the power-split transmission will be introduced in detail by taking this structure as an example in the following parts.

2 Parameter Matching

There are many references introducing parameter matching [6–8], and the related technics have already been mature. The optimization based parameter matching method was adopted here. The optimal parameter matching method was developed by taking the driving performance, fuel economy and cost as optimization objective, the feasible schemes as research object and the system parameters and control parameters as optimized variables.

Most of the existing parameter matching methods all took driving performance, fuel economy and emission as optimization objectives. The tri-mode power-split transmission, applied in heavy off-road vehicles, emphasizes on the cost rather than the emission performance, so the comprehensive cost of the power-split transmission was taken as an optimization objective,

$$J = \text{Min}[-f_1(x), f_2(x), f_3(x)] \tag{4}$$

where, $f_1(x)$ is the function of the driving performance. The better the driving performance is, the larger $f_1(x)$ is. Thus, its opposing value was taken as one of the

optimization objectives. $f_2(x)$ is the function of fuel consumption and $f_3(x)$ is the function of cost. Both of them are the smaller the better, so they are taken as another two optimization objectives.

The constraint conditions contained the operating range of power components, the speed, torque and power equations of the system and other performance constraints,

$$\begin{cases} g(x) \leq 0 \\ h(x) = 0 \end{cases} \quad (5)$$

With the optimization objectives and constraint conditions, the optimization model could be built by utilizing computer programming. Here the optimizing variables mainly conclude the characteristic parameters such as the power of the engine, electric motor, and battery. As it is related with the dynamic programming algorithm, the control variable needs to be chosen as the optimizing variables, which will be specifically introduced in the following part.

3 Performance Predictions

For the power-split transmission is a multiple-degree-of-freedom system, the components can work in different operating states, although the demands are the same. Thus the performance of the system largely depends on the quality of the control strategy. It can be known from the control theory that strategies based on optimization are better than those based on rules, and the performance of global optimization is better than that of instantaneous optimization [9]. The dynamic programming algorithm is a kind of global optimization algorithm which can achieve the optimum comprehensive performance of the system. As the calculated amount of dynamic programming algorithm is huge, it would be difficult to implement if the dynamic model is directly used. Therefore, the steady-state model was adopted at first, and the optimal scheme and system parameter was found through steady-state optimization by MATLAB. Then the dynamic model was built with Simulink, and the dynamic performance of the system was predicted through dynamic simulation.

3.1 Dynamic Programming Algorithm

The dynamic programming algorithm is a kind of multiple procedure decision optimization algorithm. According to the demands of control accuracy and calculating time, the driving circle needs to be divided into several segments. The calculation is made from back to front, and the optimum performance of the system can be realized within the whole time range.

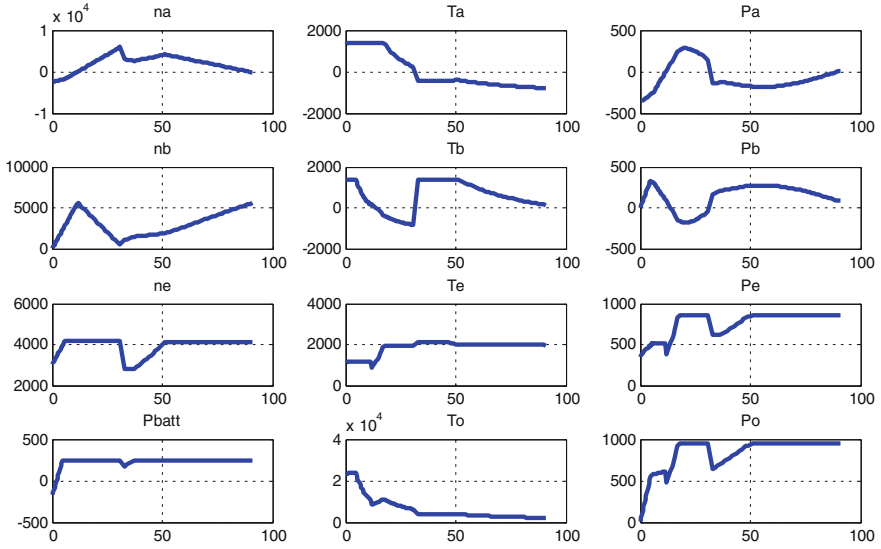


Fig. 11 Operating states of components of the tri-mode power-split transmission

The inherent resistance model of the battery was adopted, the power of which is shown as follows,

$$P_{batt} = V_{oc}I_{batt} - I_{batt}^2 R_{batt} \quad (6)$$

where, V_{oc} is the open-circuit voltage, I_{batt} is the charge or discharge current and R_{batt} is the inherent resistance. SOC can be got through the following expression,

$$\frac{d}{dt}(SOC) = \frac{-I_{batt}}{3600C_{batt}} \quad (7)$$

where, C_{batt} is the capacity of the power battery. Then the following result can be derived through the express (6) and (7):

$$\frac{d}{dt}(SOC) = -\frac{V_{oc} - \sqrt{V_{oc}^2 - 4P_{batt}R_{batt}}}{7200C_{batt}R_{batt}} \quad (8)$$

3.2 Steady-State Performance Prediction

The optimal structure scheme, system parameters and control parameters were obtained by solving the steady-state optimization model. Then the operating state of each component, and the output speed and torque of the power-split transmission was calculated, which was shown in Figs. 11 and 12.

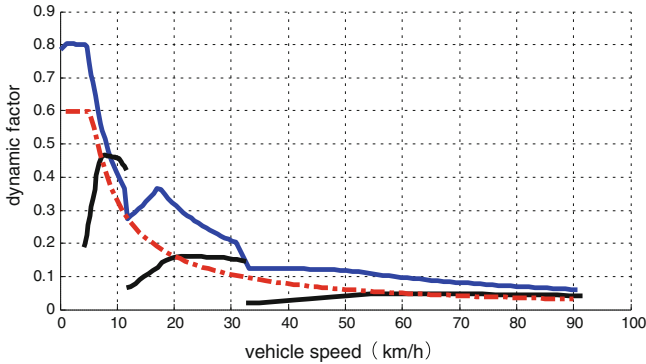


Fig. 12 Driving performance of the tri-mode power-split transmission

The abscissa and the ordinate respectively stand for the vehicle speed and the operating condition of the components. The operating condition of the components at different vehicle speed is obtained through steady-state calculation, so that it can provide necessary condition for the prediction of the system's steady-state performance.

The abscissa stands for vehicle speed, the blue lines stand for the dynamic factors of three EVT modes, the red stands for the ideal dynamics factors and the black lines stand for the dynamic factors of three FG modes. The value of the vehicle's maximum dynamic factor is larger than that of the ideal dynamics characteristic at each speed. Therefore, this tri-mode power-split transmission is able to meet the vehicle's driving performance demand.

3.3 Dynamic Performance Prediction

After the scheme design, parameter matching and steady-state performance prediction of the power-split transmission had been made through steady-state calculation, the dynamics model of the chosen scheme would be built, and its dynamic performance would be predicted through dynamic simulation. The dynamic model of a complete vehicle was built by using the common models in Simulink, Simdriveline and SimpowerSystem. The control system model was built by using Stateflow and some common models. There are many references introducing the model building method of the hybrid system. Hence, the simulation result of the dynamic performance prediction is directly given in the paper, which is shown in Figs. 13 and 14.

In Fig. 13, the abscissa and the ordinate respectively represent the simulation time and the operating condition of the components. Due to the usage of the dynamic model, the operating condition of the components has a slight fluctuation with the time. But the fluctuation range is relatively small. The operating condition

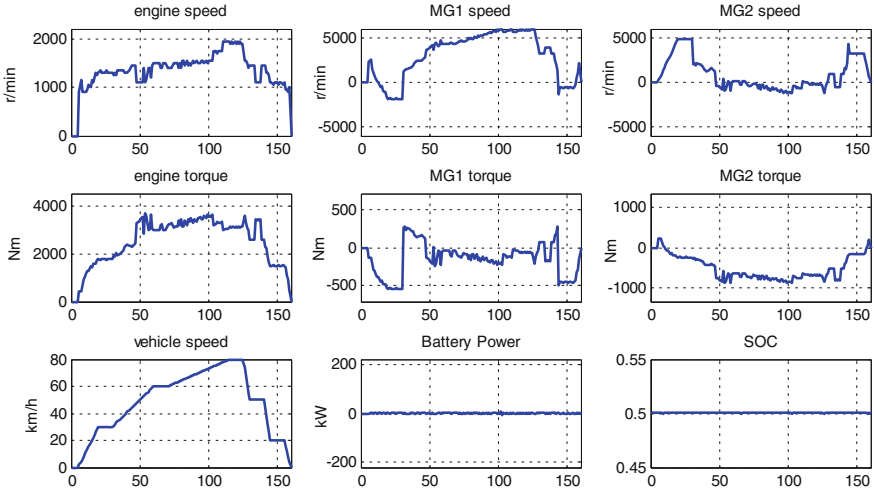


Fig. 13 Operating states of power components in dynamic simulation process

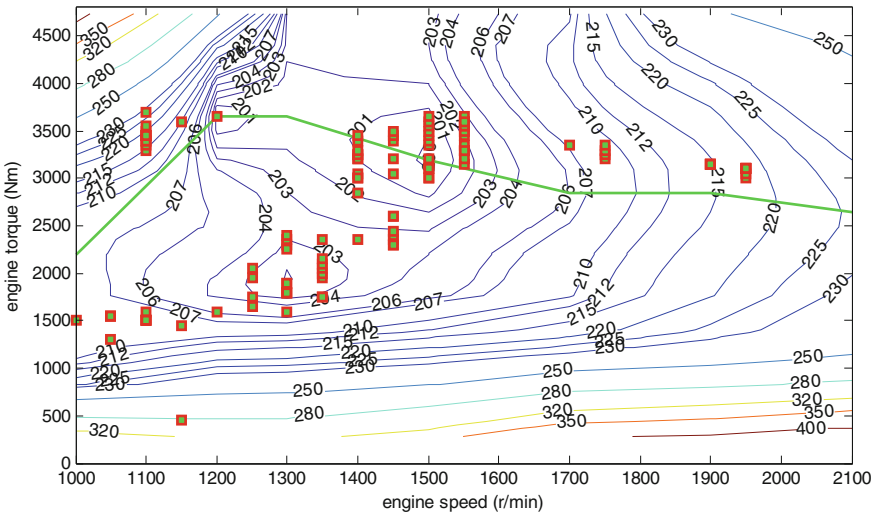


Fig. 14 Engine's operating points distribution in process of dynamic simulation

of the components obtained through dynamic simulation will provide references for system's dynamic performance prediction.

It can be seen from Fig. 14 that most of the engine's operating points are near the lowest fuel consumption rate, so the whole vehicle's fuel economic performance is guaranteed. It can be known from the dynamic simulation result that the tri-mode power-split transmission designed in this paper can not only adapt the change of vehicle speed rapidly, but also optimize the operating zone of the

engine, so that the system has good driving performance and fuel economic. Therefore, the method of combining the scheme design, parameter matching and performance prediction is effective and successful.

4 Conclusions

After comparing the current structures of power-split transmission, a design method of the power-split transmission based on ideal driving characteristic and component's output characteristic was put forward. An optimal parameter matching method was developed by taking the driving performance, fuel economy and cost as optimization objective, the feasible schemes as research object and the system parameters and control parameters as optimized variables. Besides, a performance prediction method based on MATLAB and Simulink was provided. The scheme design, parameter matching and performance prediction, respectively as the foundation, necessary condition and evaluation criterion, were inseparable. It can be known from the steady-state calculation and dynamic simulation results that the designed power-split transmission could achieve good driving performance and fuel economic, which proved that the research method in this paper was feasible.

References

1. Han L (2010) A Study on performance matching and control strategy for power-split hybrid electric vehicles. Beijing Institute of Technology, Beijing
2. Salgado DR, Del Castillo JM (2005) Selection and design of planetary gear trains based on power flow maps. *J Mech Des* 127(1):120–134
3. Delagrammatikas GJ (2001) A design optimization methodology for advanced and hybrid, diesel-based, automotive powertrains. The University of Michigan, Michigan
4. Lei T, Lu L-Q (1997) Matrix system for the analysis of planetary transmissions. *J Mech Des* 119(1):333–337
5. Shai O, Pennock GR (2006) Extension of graph theory to the duality between static systems and mechanisms. *J Mech Des* 128(1):179–181
6. Kukhyun A, Sungtae C, Wonsik L, Yeong-il P, Jang LM (2006). performance analysis and parametric design of the dual-mode planetary gear hybrid powertrain. *Automob Eng* 334(1):1601–1614
7. Yimin G, Mehrdad E (2006) Parametric design of the traction motor and energy storage for series hybrid off-road and military vehicles. *IEEE Trans Power Electron* 21(3):749–755
8. Xing J (2007) Parameter matching and simulation of the mechanical-electric power combined device on hybrid electric vehicle. Beijing Institute of Technology, Beijing
9. Weimin L, Guoqing X, Zhancheng W, Yangsheng X (2008) Dynamic energy management for hybrid electric vehicle based on approximate dynamic programming. In: Proceedings of the 7th world congress on intelligent control and automation on June 25–27, Chongqing, China, pp 7864–7869

Transient EHL Gear Contact Simulation

Peter Fietkau, Axel Baumann and Bernd Bertsche

Abstract The aim of this work is to simulate the contact of gear tooth flanks under realistic operating conditions. This implies the calculation of film heights, the hydrodynamic as well as the dry pressure distribution and the resulting forces on the gearwheels. Especially the dynamic behavior of gearwheels during tooth impacts is of great interest, because preliminary investigations showed that the lubricant has an extensive wide range of influence in such situations. These impacts are critical for automotive gear-rattle noises (noises caused by loose parts movement under engine excitation). Nevertheless, with the presented model highly-loaded power-transmitting gear contacts may also be investigated in order to determine vibration under load or lubrication conditions. To simulate the contacts two different solutions of the Reynolds equation were developed: A simplified analytical and a numerical one. Both consider the wedge and the squeeze term of the Reynolds equation to allow for a full transient analysis. The analytical solution is accomplished using assumptions for the gap shape and the pressure in the middle of the gap. The numerical problem is solved using fast multilevel multi-integration algorithms. The method is implemented as a force element in the multi-body simulation environment SIMPACK. Therefore it is easy to transfer the developed element to other models and use it for a multitude of different engineering problems. After implementation of the model several simulations have been done with gearbox models. The pressure distributions, gap heights, type of friction (hydrodynamic/mixed/dry) and resulting forces of all flanks in contact can be determined. Furthermore, with the use of a very detailed elastic multi-body model of the transmission, direct determination of housing vibrations is possible. The results are validated with measurements on a special test bench.

F2012-C02-006

P. Fietkau (✉) · A. Baumann · B. Bertsche
Institute of Machine Components, University of Stuttgart, Stuttgart, Germany
e-mail: peter.fietkau@ima.uni-stuttgart.de

Keywords Gear contact · Elastohydrodynamic lubrication · Oil film · Transmission noise · Gear rattle

1 Introduction

Due to rapid development in automotive engineering, the simulation of powertrains at an early development stage is becoming increasingly important. Problems in the field of noise, vibration and harshness usually arise in the testing or validation phase of a product. Hence corrective actions are cost-intensive and should be avoided. For this reason it is useful to investigate dynamics of powertrains with simulation models at an early product development stage.

NVH issues and durability of gears are of special interest in the field of automotive transmissions. Engine's ignition-induced rotational speed irregularity causes torsional vibrations in the vehicle powertrain. These vibrations may lead to vibrations of loose parts in automotive transmissions (i.e. idler gears, synchronizer rings) and can cause so called rattle noises. Furthermore vibrations of loaded gearwheels may cause whining noises. Other aspects of interest are the lubrication conditions such as minimum film height or type of friction which are important to ensure sufficient transmission lifetime [1].

Current multi-body simulation models for gear rattle simulation are based on impact laws [2] or simple spring-damper models [3]. Similar approaches are used for loaded gear contacts [4]. Oil films and flank deformations are neglected or just implemented indirectly [5–7], i.e. the gear force is given a priori or determined using the energy equation. This chapter describes a novel transient EHL gear contact simulation model which implements oil films and elastic deformations directly in the multi-body simulation. Complete transmissions can be modeled which allows direct determination of the vibration behavior and of structure-borne noise. It is possible to investigate gear rattle, vibrations of loaded gears as well as lubrication conditions with just one model.

2 Contact Modeling

In the following section, the developed contact model of gearwheels will be presented. First an overview of the general approach is given. Afterwards an analytical and a numerical way of teeth force calculation will be presented.

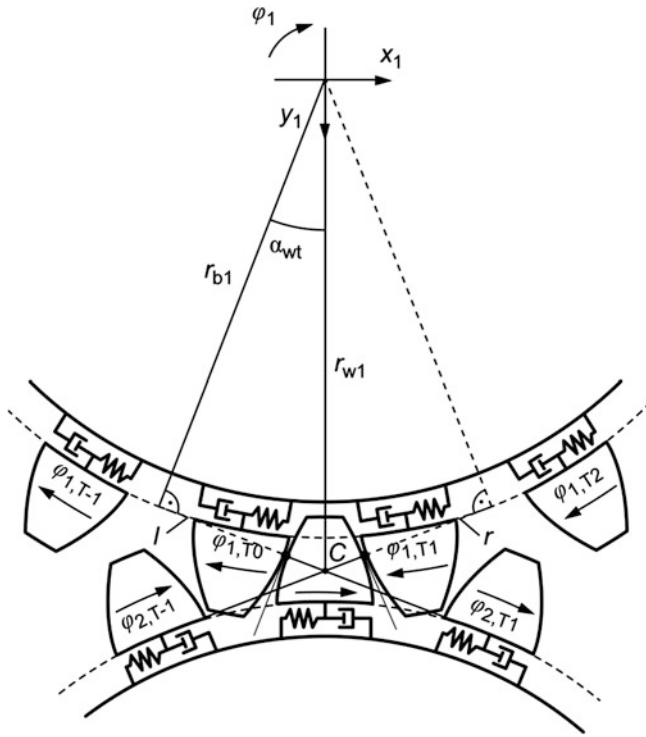


Fig. 1 Gearwheel model with circumferentially moveable teeth

2.1 Gearwheel Modeling

The aim of the model is to describe the dynamic behavior of gearwheels including effects of the oil film at flank contacts. For that purpose every tooth and respective flanks are treated separately. Basis of the development was the force element “Gear Pair” [8] of the multi-body simulation software SIMPACK [9]. The existing force element was extended by a new contact geometry calculation, flexible teeth and elastohydrodynamic lubrication at tooth flanks. The new force element was written in the programming language FORTRAN 90 and compiled for SIMPACK.

The forces at tooth flanks resulting from lubricated contacts and tooth flexibility are mechanically connected in series. Therefore it is necessary to introduce state variables for teeth deflection. An approach according to Ebrahimi [10] was chosen with circumferentially movable teeth. Figure 1 shows a gear pair as well as important geometrical parameters of the gear mesh. Each tooth has one degree of freedom: the rotation about the wheel center with the angle φ_{Ti} . The stiffness of the springs between teeth and wheel body is determined according to standard ISO 6336 [11]. For a tooth pair at the pitch point the stiffness related to face width is 14N/(mm μ m).

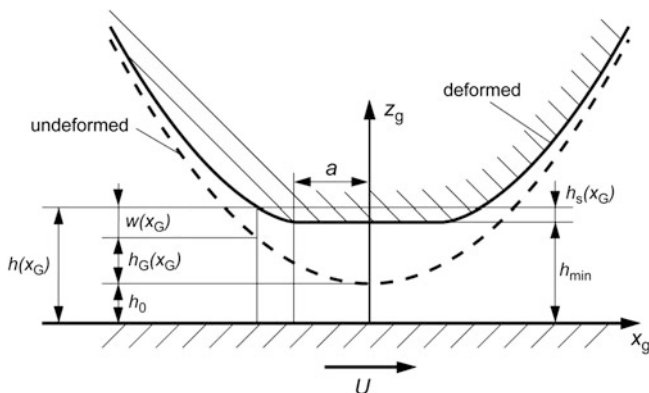


Fig. 2 Dimensions of fluid gap between meshing teeth

During time integration the force element obtains at each time step the actual positions and velocities of the teeth and of the two wheel bodies from the integrator of the multi-body environment. Further state variables are the minimal distances h_{\min} between corresponding flanks which describe elastic flank deformation, see Fig. 2. These are also given to the force element by the integrator. Because each tooth has just one rotational degree of freedom and the undeformed flank geometries are known, the lines of flank contact can be determined analytically. As a result, the distance h_0 between the theoretical undeformed flanks can be calculated. It can be positive or negative depending on whether the flanks are in contact or not, cf. Fig. 2.

In the next step the flank forces are calculated. Generally three forces act on each tooth flank, one normal and two tangential ones. All flanks are assumed to be lubricated with oil and to be elastically deformable. Furthermore, the oil viscosity rise with pressure is incorporated. Therefore the lubrication regime is elastohydrodynamic piezoviscous. Two different solutions for this problem were developed, an efficient analytical and a more detailed numerical one. These are presented in the following sections. With known flank forces the derivatives of the state variables $\dot{\varphi}_{Ti}$, $\ddot{\varphi}_{Ti}$ and \dot{h}_{\min} , can be determined. These are given back to the integrator together with the resulting forces and moments on the wheels. It calculates the state variables for the next time step and the process starts all over again.

2.2 Analytical Gear Force Calculation

The basis for the analytical approach is the one-dimensional Reynolds equation for thin fluid films [12] including wedge and squeeze terms

$$\frac{\partial}{\partial x_g} \left[\frac{\rho h^3}{\eta} \frac{\partial p}{\partial x_g} \right] = 6 \left(\frac{\partial}{\partial x_g} (\rho h U) + 2 \frac{\partial (\rho h)}{\partial t} \right) \quad (1)$$

with the coordinates according to Fig. 2, the fluid pressure p , the oil density ρ , the oil viscosity η , the gap height h , the time t and the sum velocity in x_g -direction U . The pressure gradient in y_g -direction as well as the velocity in y_g -direction may be neglected, because the dimension of the flanks in y_g -direction is much longer than in x_g -direction and the velocities are fairly small. The undeformed gap height is assumed to be parabolic and one gets (cf. Fig. 2)

$$h = h_{\min} + h_s(x_g) = h_0 + h_g(x_g) + w(x_g) = h_0 + \frac{x_g^2}{2R} + w(x_g) \quad (2)$$

with the elastic deformation w and the combined flank radius of curvature R . Depending on load the Reynolds equation (1) is solved differently. For small forces the elastic flank deformation w can be neglected and the fluid may be treated as iso viscous. In this case the Reynolds equation can be integrated directly. For high forces the contact is deformable and the lubrication is piezoviscous. The gap shape is assumed to be like the gap shape for a dry contact and Equation (1) is solved using limit values. During integration the force element decides on the basis of actual gap height and load which solution is applicable.

2.2.1 Hydrodynamic Solution for Small Flank Forces

For this solution the elastic flank deformation w is neglected and therefore the shape of the fluid gap is known a priori. The Reynolds equation (1) is integrated directly with the boundary conditions $p(-x_{\text{in}}) = 0$ and $p(x_{\text{in}}) = 0$ for a given x_{in} . Furthermore, Half-Sommerfeld boundary conditions are used, which means that all negative pressures are set to zero because fluids are not able to transmit tensile stresses. A further integration of the pressure yields the normal flank force. The tangential forces are obtained by the integration of the surface shear stresses. This problem can be solved completely analytically but the resulting equations are quite long and therefore not given here. The solution is valid for small forces and big gap heights. Therefore dry and mixed friction may be neglected at this point.

2.2.2 Elastohydrodynamic Solution for High Flank Forces

At high forces the viscosity depends on pressure and the tooth flanks are deformed. To solve the problem, the shape of the gap is assumed to be equal to a dry Hertzian contact. That means that there is a constant gap height in the middle of contact (parallel gap), cf. Fig. 2. The relationship between pressure and viscosity of the lubricant is given by Barus law

$$\eta = \eta_0 e^{\alpha p} \quad (3)$$

with the viscosity at ambient pressure η_0 and the pressure-viscosity coefficient α [13]. Furthermore a reduced pressure q is employed with $\alpha q = 1 - e^{-\alpha p}$ [12] and the Reynolds equation (1) becomes

$$\frac{\partial}{\partial x_g} \left[h^3 \frac{\partial q}{\partial x_g} \right] = 6\eta_0 \left(\frac{\partial}{\partial x_g} (hU) + 2 \frac{\partial h}{\partial t} \right). \quad (4)$$

The density is assumed to be constant because the change with pressure is small when using oil as lubricant [14]. This problem can be solved for high pressures in the parallel gap and therefore $e^{-\alpha p} \ll 1$ or $q \approx 1/\alpha..$ It is assumed, that for the squeeze term $\partial h/\partial t$ only the minimum gap height h_{\min} is relevant and not $h_s(x_g)$, i.e. $\dot{h}_s \approx 0$, cf. Eq. (2). Vichard [15] solved this problem and one obtains a differential equation for the minimum gap height

$$\dot{h}_{\min} = \frac{3\alpha\eta_0 U G_p \sqrt{\left(\frac{F_n}{2\pi b E'}\right) R - \left(\frac{F_n}{2\pi b E'}\right)^2}}{6\alpha\eta_0 R \left(G_s h_{\min}^3 + 4 \left(\frac{F_n}{2\pi b E'}\right)^3 \right)} h_{\min}^3 \quad (5)$$

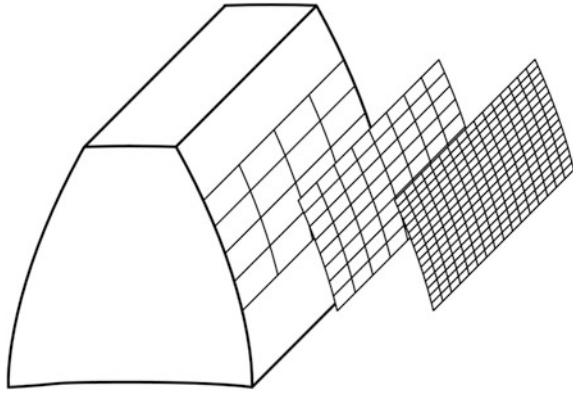
with

$$G_p = \begin{cases} 0.394 \left(\frac{F_n}{2\pi b E' h_{\min}}\right)^{1.387} & \text{for } \left(\frac{F_n}{b E' h_{\min}}\right) < 41.85 \\ 0.4747 \left(\frac{F_n}{2\pi b E' h_{\min}}\right)^{1.476} & \text{otherwise} \end{cases} \quad (6)$$

$$G_s = \begin{cases} 2.0965 \left(\frac{F_n}{2\pi b E' h_{\min}}\right)^{2.247} & \text{for } \left(\frac{F_n}{b E' h_{\min}}\right) < 41.85 \\ 1.378 \left(\frac{F_n}{2\pi b E' h_{\min}}\right)^{2.0496} & \text{otherwise.} \end{cases} \quad (7)$$

The value h_{\min} is given by the integrator. With h_{\min} the normal force F_n can be calculated according to Hertz. Together with the reduced Young's modulus E' and the face width b the derivative \dot{h}_{\min} is calculated with Eq. (5) and given back to the integrator. So a time integration of h_{\min} and therefore of F_n is possible. Tangential forces resulting from the fluid are calculated by integrating shear stresses at surfaces and using an Eyring model for the non-linear stress—shear rate relationship [16]. Additionally for small gap heights dry contact is considered according to Greenwood and Tripp using Gaussian-distributed asperity heights and purely elastic deformation [17, 18]. Dry tangential forces are calculated with Coulomb friction. The dry contact forces are added to the before mentioned hydrodynamic forces.

Fig. 3 Different grids used by the multi-grid method for pressure and deformation calculation



2.3 Numerical Gear Force Calculation

For the numerical gear force calculation a two-dimensional Reynolds equation is used which includes pressure gradients in the x_g - and y_g -direction. The influence of surface roughness is regarded by using pressure and shear flow factors [19]. For the description of the elastic deformation of the tooth flanks an approximation of the bodies by semi-infinite half spaces is applied. The flanks are discretized and the gradients in the Reynolds equation are approximated by finite differences. Reynolds conditions (also known as Swift Steiber conditions) are used as boundary conditions which means that $p = 0$ and $\partial p / \partial x_a = 0$ respectively $\partial p / \partial y_a = 0$ at the edges of the pressure field [12]. The problem is solved using a Multilevel Multi-Integration method according to [14].

Multiple grids with different sizes are used to accelerate the solution process of the Reynolds equation, see Fig. 3. The calculation of elastic deformations is also done on different grid levels. The results are hydrodynamic pressure as well as dry pressure, deformed gap heights and tangential stresses at grid points. The flank forces and derivatives of state variables can be calculated here from. Theoretically, the effort for solving this problem is of order $O(N \ln N)$ with the number of grid points in the finest level N [14].

3 Simulation Model

Two different multi-body simulation models were used to validate the described approach. First, simulations with just a single gear pair under different operating conditions were carried out. In this model, the two wheels are just able to rotate around their axis (2° of freedom) and the only force element is the described gear force element. The forces are calculated using geometrical tooth data, material data, oil data and calculation parameters such as calculation mode (analytical/

numerical) as inputs. The force element calculates resulting forces and torques on the gearwheels every time step for a given relative position and velocity of the wheels and furthermore integrates the state variables such as tooth positions and elastic deformations.

In a second step, the gear pair model was mounted in a complete experimental transmission, which was also available as hardware so that validation measurements could be done [20]. The transmission consists of two shafts and one gear pair. Each gearwheel is fixed to a shaft. All parts are enclosed by an aluminum housing which contains oil to lubricate and cool the transmission. The aim of this three-dimensional elastic multi-body model was to predict the movement of all parts as well as the structure-borne noise of the transmission for frequencies up to 10 kHz. The two shafts as well as the gearbox housing are treated as elastic bodies using modal reduction. This is done using component mode synthesis and super elements [21, 22]. For the shafts, all modes up to 20 kHz and for the housing up to 11 kHz are regarded. Comparisons with full transient FE calculations showed that these reduced models are capable of representing the elastic behavior of the housing and shafts completely for frequencies up to 10 kHz. Therefore the typical subsequent FE calculation to determine housing accelerations may be omitted for further computations.

The rolling bearings are modeled by non-linear characteristic maps [23] and the axial plain bearings as hydrodynamic bearings [20]. The drag torques of the gearwheels, rotary shaft seals and bearings are calculated as a function of relative speed, as well as oil viscosity, type, and level. The total system has 353° of freedom.

4 Results

First simulations with the single gear pair were done with the fixed input wheel driven at a mean speed of 900 rpm. Figure 4 shows the relative motion between the wheels. On the left-hand side, the input gear is driven with a constant speed and the output gear is loaded with a torque of 150 Nm. The meshing frequency can clearly be seen.

For the other two conditions, sinusoidal speed oscillations were superimposed to the input speed to achieve rattle conditions in which the idler gear moves within gear backlash. In the middle diagram, the angular acceleration amplitude is 200 rad/s^2 . The brake torque of 0.5 Nm simulates drag torque. There are single-sided rattle impacts which mean that the drive flanks lift off and hit each other again. On the right-hand side the amplitude is 2000 rad/s^2 and there are double-sided impacts, i.e. there are alternating impacts on drive and thrust flanks.

Figure 5 shows the force on a single tooth flank for the three above-mentioned load conditions. The load peak in the left diagram results from the single tooth pair mesh. Before and after the load peak, there are two pairs of teeth in mesh. The other two diagrams show flank impacts during rattling, which means short contact

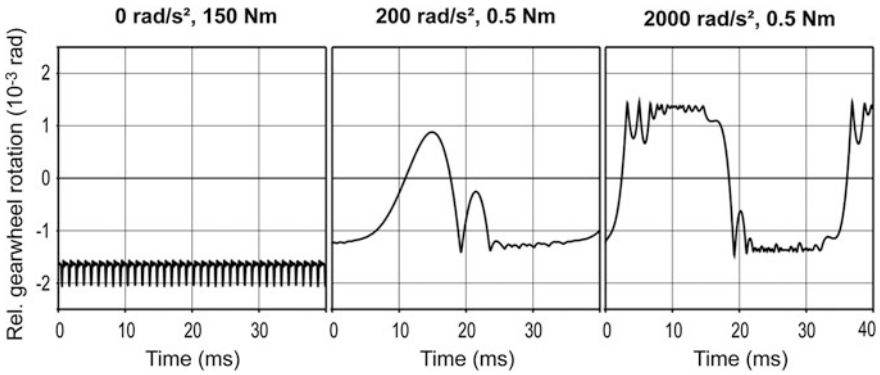


Fig. 4 Relative gear rotation for different loads and excitations

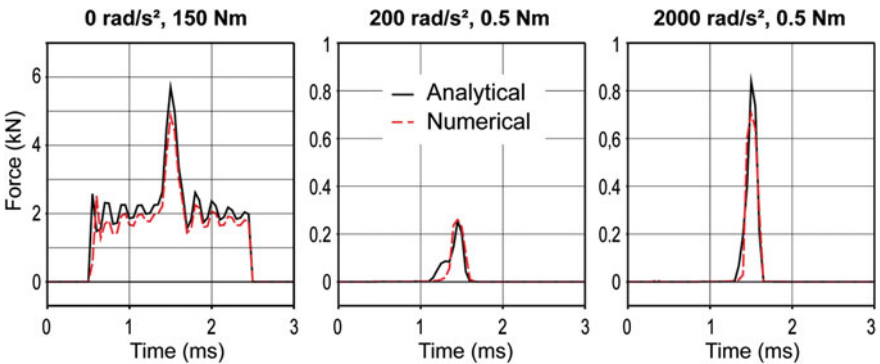


Fig. 5 Force on a single tooth for different loads, excitations and solution types

times and relatively high forces. The consistency of the analytical and numerical solution is fairly good. One can state, that if just the movement of the wheels and the gear forces are of interest, the analytical solution is sufficient. The corresponding gap heights in the middle of the flank for points of maximum loads are shown in Fig. 6. For a load of 150 Nm there is a clear deformation of flanks with a parallel gap and a typical narrowing at the downstream end. Despite the simplicity of the analytical solution the analytically and the numerically determined gap forms are quite similar. In the other two cases on the right there are some deviations at the beginning of the parallel gap but they are still small. The minimum gap height falls and the flank deformation rises with rising load.

Figure 7 shows the hydrodynamic and the dry contact pressure distribution on a tooth flank for the same conditions as on the leftmost graph of Fig. 6. For this result the numerical solution is necessary. The hydrodynamic pressure reaches a maximum of about 11 000 bar and is zero at the flank edges, which was a

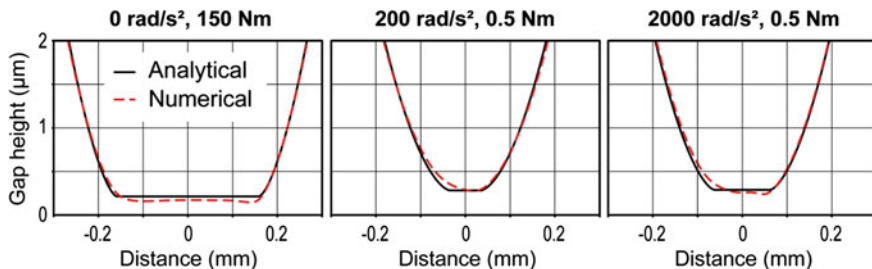


Fig. 6 Gap height for different loads, excitations and solution types

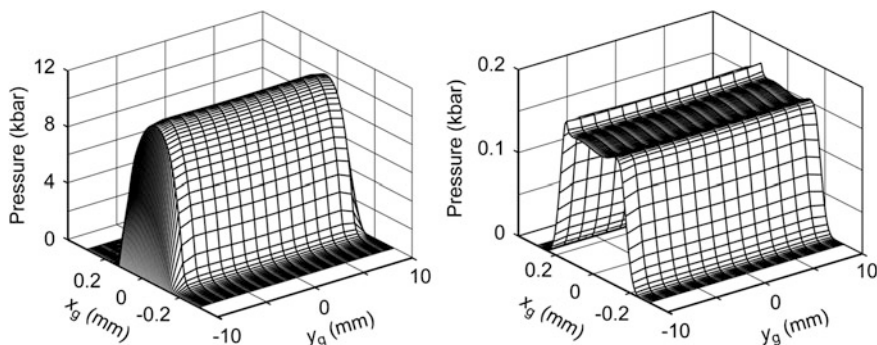


Fig. 7 Hydrodynamic (left) and dry contact pressure (right) on a tooth flank for 150 Nm load at the point of maximum force

boundary condition. The dry contact pressure is shown on the right-hand side. There is a peak at the downstream end of the parallel gap because this is where the smallest gap heights are. The dry contact pressure level is about a factor of 100 smaller than the hydrodynamic pressure, which means there is a nearly pure hydrodynamic friction at the flank contacts.

Next the simulation model for the complete experimental transmission was used to validate the simulation results. The model was excited with different sinusoidal excitations with amplitudes between 0 and 1,000 rad/s^2 . The mean speed was still 900 rpm. The simulated housing acceleration at a reference point was compared with the one measured at the real transmission on a test bench. The result is shown in Fig. 8. The deviations at small excitations result from vibrations of the test bench itself, which cannot be taken into account in the simulations. For amplitudes between 200 and 1,000 rad/s^2 , which is the most relevant range for passenger car transmissions, the results are fairly good. This means that the model is capable of predicting the transient gear dynamics of automotive transmissions.

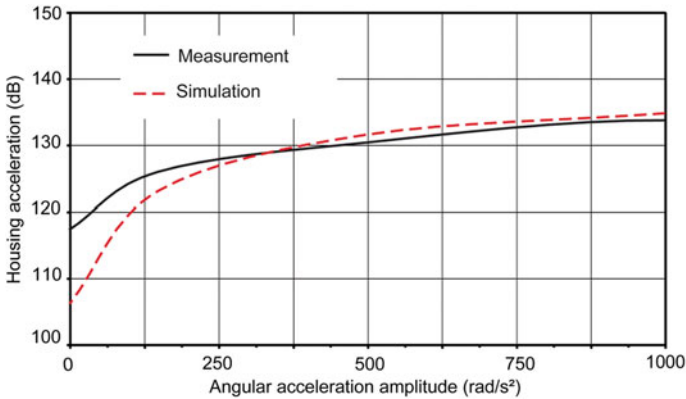


Fig. 8 Measured and simulated housing acceleration of an experimental transmission

5 Conclusion

A transient EHL gear contact model was developed and integrated into the multi-body simulation software SIMPACK. The gear contact model is based on the Reynolds equation and an analytical and a numerical solution were derived. The model is suitable for calculating the dynamic behavior of gear wheels under different operating conditions such as rattling or load vibrations as well as of predicting lubrication conditions. Two multi-body models, one consisting of a single gear pair and one of a complete transmission were used to study the behavior of the developed approach. Gearwheel movements, gear forces, film heights and pressure distributions were calculated for loaded as well as for unloaded and rattling conditions. Finally the simulation approach was validated with a measurement on an experimental transmission and showed good consistency. For this reason the simulation model is capable of predicting transient gear contact behavior at an early product development stage.

Acknowledgments The authors would like to thank C.H. Venner of the University of Twente for his help with the numerical multilevel algorithm. The authors also wish to acknowledge SIMPACK AG and especially Dr. L. Mauer for providing the source code of the original gear pair force element.

References

1. Naunheimer H, Bertsche B, Ryborz J, Novak W (2011) Automotive transmissions—fundamentals, selection, design and application 2nd edn. Springer Berlin
2. Lang C-H (1997) Losteilschwingungen in Fahrzeuggetrieben. Dissertation. University of Stuttgart. Institute of Machine Components

3. Wang MY, Zhao W, Manoj R (2002) Numerical modelling and analysis of automotive transmission rattle. *J Vibr Control* 8(7):921–943
4. Gerber H (1984) *Innere Dynamische Zusatzkräfte bei Stirnradgetrieben. Modellbildung, innere Anregung und Dämpfung.* TU München
5. De la Cruz M, Theodossiades S, Rahnejat H (2009) An investigation of manual transmission drive rattle. In: *Proceedings of the institution of mechanical engineers, Part K* (ed) J Multi-Body Dyn 224:167–181
6. Bartel D, Bobach L, Beilicke R, Deters L (2010) 3D-TEHD-Simulation von mischreibungsbeanspruchten Tribosystemen—Anwendungsbeispiele Wälzlager und Zahnrad. *GETLUB Tribologie- und Schmierstoffkongress, Würzburg*
7. Stringer DB, Younan A, Sheth PN, Allaire PE (2007) Generalized stiffness gear-mesh matrix including ehd stiffness. In: *Proceedings of ASME/STLE international joint tribology conference IJTC 2007, Oct 22–24, San Diego*
8. Mauer L (2004) Gearwheels in SIMPACK. *SIMPACT News* 8(1):10–11
9. Simpack AG (2012) *SIMPACT Documentation, Version 9.1.* Gilching
10. Ebrahimi SA (2007) *Contribution to computational contact procedures in flexible multibody systems.* Dissertation. University of Stuttgart, Institute of engineering and computational mechanics
11. International Organization for Standardization ISO 6336-1 (1996) *Calculation of load capacity of spur and helical gears—Part 1: Basic principles, introduction and general influence factors.* Genf
12. Gohar R (2001) *Elastohydrodynamics*, 2nd edn. Imperial College Press, London
13. Bartel D (2010) *Simulation von Tribosystemen: Grundlagen und Anwendungen.* Vieweg + Teubner Verlag/GWV Fachverlage GmbH Wiesbaden
14. Venner CH, Lubrecht AA (2000) *Multilevel methods in lubrication.* Elsevier Science Amsterdam
15. Vichard JP (1971) Transient effects in the lubrication of hertzian contacts. In: *Proceedings of the institution of mechanical engineers, Part C, J Mech Eng Sci* 13(3):173–189
16. Eyring H (1936) Viscosity, plasticity, and diffusion as examples of absolute reaction rates. *J Chem Phys* 4(4):283
17. Greenwood JA, Tripp JH (1970) The contact of two nominally flat rough surfaces. In: *Proceedings of the institution of mechanical engineers* 185(48):625–633
18. Lagemann V (2000) *Numerische Verfahren zur tribologischen Charakterisierung bearbeitungsbedingter rauher Oberflächen bei Mikrohydrodynamik und Mischreibung.* Dissertation. University of Kassel. Institut für Maschinenelemente und Konstruktionstechnik
19. Patir N, Cheng HS (1978) An average flow model for determining effects of three-dimensional roughness on partial hydrodynamic lubrication. *TransASME, Series F: J Lubr Technol* 100:12–17
20. Fietkau P, Baumann A, Bertsche B (2012) Simulation of passenger car synchronizer ring movement during rattling. In: *Proceedings of the institution of mechanical engineers, Part K* (ed), *J Multi-body Dyn* 226(1):3–16
21. Craig RR Jr, Bampton MCC (1968) Coupling of substructures for dynamic analyses. *AIAA J* 6(7):1313–1319
22. Sellgren U (2003) *Component mode synthesis. A method for efficient dynamic simulation of complex technical systems.* Technical Report 2003. Department of machine design. The Royal Institute of Technology (KTH), Stockholm, Sweden
23. Vesselinov V, Weber J, Hahn T (2007) *Wälzlagerkennfelder für MKS-Programme.* In: *Proceedings of the ATK 2007 (Gold PW ed), 8–9 May 2007, Aachen, 213–223*

An Enhanced Finite Element Model for Determination of Load Capacity in Planetary Gear Trains

Ignacio Gonzalez-Perez, Alfonso Fuentes and Kenichi Hayasaka

Abstract Planetary gear trains are being intensively applied in automobile drivelines during recent years due to its high load capacity, compact size, high gear ratio, and axial direction of power path. Determination of the load capacity in the design stage requires the calculation of contact pressures and bending stresses at the ring, sun, and planet gears. The knowledge of the load sharing between the planet gears and how it is affected by any assembly error or by the deflection of supporting shafts and carrier is needed for the determination of tolerances before manufacturing and assembly stages are accomplished. An enhanced finite element model is presented in this paper for the purpose of determination of the load capacity in planetary gear trains and investigation of the load sharing between the planet gears. A numerical example is presented.

Keywords Planetary gear trains · Stress analysis · Finite element method

1 Introduction

Planetary gear trains are being intensively applied in automobile drivelines during recent years and have been an object of intensive research [1–4]. The knowledge of the load sharing between the planet gears and how it is affected by any assembly

F2012-C02-008

I. Gonzalez-Perez (✉) · A. Fuentes
Polytechnic University of Cartagena (UPCT), Cartagena, Spain
e-mail: ignacio.gonzalez@upct.es

K. Hayasaka
Space Creation Co. Ltd, Hamamatsu, Japan

error or by the deflection of supporting shafts and carrier is needed for the determination of the actual load capacity.

An enhanced finite element model is presented in this paper for the purpose of determination of the load capacity in planetary gear trains and investigation of the load sharing between the planet gears. The finite element model is built from the designed bodies of the sun, the ring, and the planet gears. Besides the gear bodies, the carrier body and the supporting shafts are included into the model.

The presented research work has been performed through the following steps:

- (1) Computerized generation of the gear geometry corresponding to the sun gear, the ring gear, and the planet gears. Involute tooth surface equations and portions of the corresponding rims are considered in the determination of the designed bodies.
- (2) Assembly of the sun gear, the ring gear, and the planet gear bodies for different contact positions.
- (3) Determination of the designed bodies of the carrier and the supporting shafts.
- (4) Automatic generation of the finite element model for the planetary gear train.
- (5) Determination of contact and bending stresses at the gear teeth.
- (6) Determination of stresses and deformations in the carrier and supporting shafts.

The presented enhanced finite element model constitutes a step forward in the design of planetary gear trains since: (1) the mesh of the gear bodies is automatically generated for any design data, (2) the modelling of the gear shafts and the carrier is included, (3) the boundary and load conditions can be easily adapted to the working conditions of this type of gear drives, and (4) a different design of the carrier can be easily integrated into the model.

2 Computerized Generation of Gear Geometry and Assembly

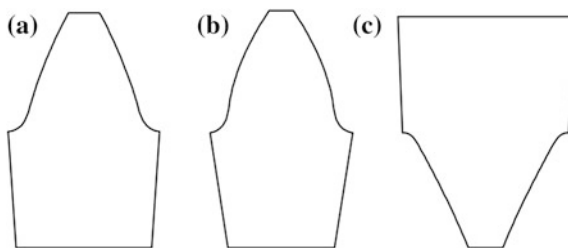
Generation of gear tooth surfaces is a well-known topic in theory of gearing [5]. For the determination of the geometry of each gear of the planetary gear train, involute profiles are considered for the active parts of the gear tooth surfaces.

The geometry of the gear tooth surfaces for gears 1 (the sun gear), 2 (the planet gear), and 3 (the ring gear) are obtained computationally. Figure 1 shows the normal sections of three teeth, each one corresponding to the sun gear, the planet gear, and the ring gear, respectively.

The assembly of the planetary gear train requires the determination of the phase angles $\mu_2^{(k)}$ of the planet gears (see Fig. 2). Here, the index 2 refers to any planet gear and the index k , $k = \{1, \dots, n\}$, refers to a specific planet gear, where n is the number of planet gears. The phase angles are determined as [5]

$$\mu_2^{(k)} = -\delta_1^{(k)} \cdot \frac{N_1}{N_2}$$

Fig. 1 Illustration of the normal sections of **a** a sun gear, **b** a planet gear, and **c** a ring gear tooth



or

$$\mu_2^{(k)} = \delta_3^{(k)} \cdot \frac{N_3}{N_2}$$

Here, N_1 , N_2 , and N_3 are the tooth number of the sun, the planet, and the ring gears, respectively. Angles $\delta_1^{(k)}$ and $\delta_2^{(k)}$ are determined as

$$\delta_1^{(k)} = m_1^{(k)} \cdot \frac{2\pi}{N_1} - \frac{2\pi}{n} (k-1)$$

$$\delta_3^{(k)} = m_3^{(k)} \cdot \frac{2\pi}{N_3} - \frac{2\pi}{n} (k-1)$$

where $m_1^{(k)}$ and $m_2^{(k)}$ are obtained as

$$m_1^{(k)} = NINT \left[(k-1) \cdot \frac{N_1}{n} \right]$$

$$m_3^{(k)} = NINT \left[(k-1) \cdot \frac{N_3}{n} \right]$$

Here, the function $NINT$ provides the nearest integer value of the argument. A positive sign of the phase angles means a counter-clockwise rotation of the reference axis of the planet gear respect to its initial position.

Figure 2 shows the assembly of the planetary gear train where three-tooth designed bodies are identified by means of dark lines. Such designed bodies are considered later in the finite element model generation of the planetary gear train.

3 Finite Element Model Generation

The finite element model is built with the designed bodies represented in Fig. 3 and considering the assembly shown in Fig. 2.

The meshing of the designed bodies is performed automatically [5] as a function of the number of nodes in profile and longitudinal directions. Figure 4 shows the mesh of a three-tooth sun gear designed body. In the case of the sun gear

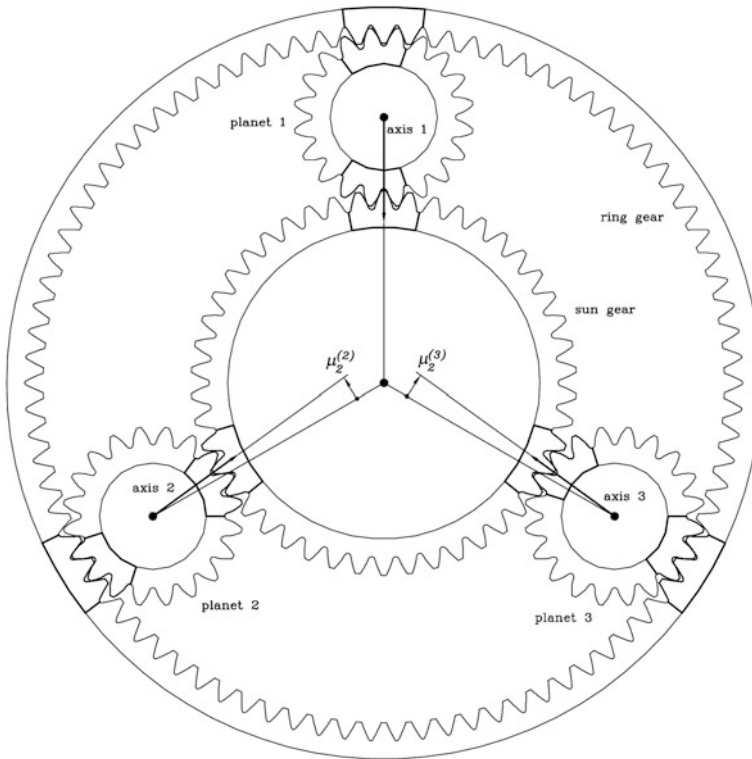


Fig. 2 Assembly of the planet gears in the planetary gear train

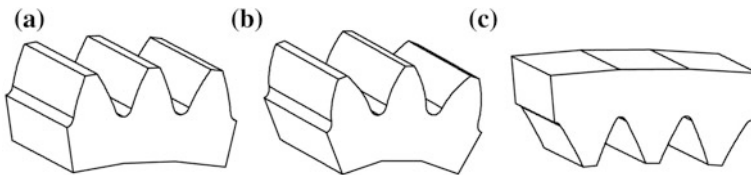


Fig. 3 The designed bodies for: **a** the sun gear, **b** the planet gear, and **c** the ring gear

or the ring gear, a total of n three-tooth designed bodies are considered, where n is the number of planet gears. In the case of the planet gears, two three-tooth designed bodies are considered for each planet gear, one in contact with the sun gear model and the other one in contact with the ring gear model.

Two configurations of the finite element model have been considered for the planetary gear train. The first configuration named as *rigid* configuration assumes an infinite value of the coefficient of rigidity for the carrier and supporting shafts of the planets. The second configuration named as *flexible* configuration assumes a coefficient of rigidity according to the modelled carrier and supporting shafts of the planets.

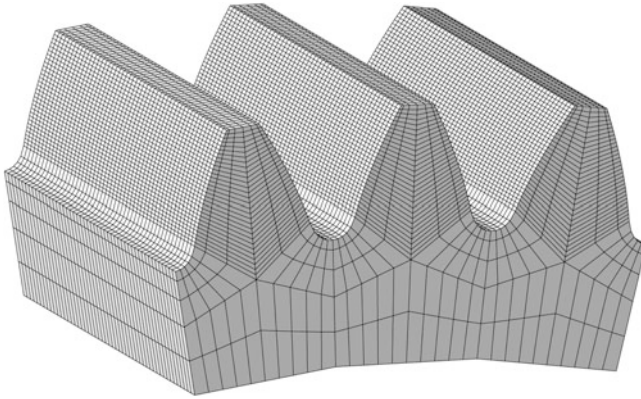


Fig. 4 The finite element meshing of a three-tooth designed body for the sun gear model

In the case of the *rigid* configuration, the boundary conditions are applied as follows (see Fig. 5):

- (1) Nodes on the two sides and the bottom part of the sun gear rims, the planet gear rims, and the ring gear rims, form rigid surfaces S_{1i} , S_{2ia} , S_{2ib} , and S_{3i} , where $i = \{1, \dots, n\}$.
- (2) Reference nodes N_{1i} , N_{2ia} and N_{2ib} , and N_{3i} , located on the axes of the sun gear, the planet gear, and the ring gear, respectively, are used as the reference points of the previously defined rigid surfaces.
- (3) Rigid surfaces S_{2ia} and S_{2ib} are rigidly connected to reference nodes N_{2ia} and N_{2ib} , respectively. Each node N_{2ib} is connected to a node N_{2ia} for each planet gear through a *weld* connection [6]. The whole set constitutes one rigid body for each planet gear and its boundary conditions are defined at each node N_{2ia} , $i = \{1, \dots, n\}$.
- (4) Rigid surfaces S_{1i} are rigidly connected to reference nodes N_{1i} , $i = \{1, \dots, n\}$, that are connected each other through a *weld* connection [6]. The n three-tooth designed bodies of the sun gear constitute one rigid body where the boundary and load conditions are defined at node N_{11} .
- (5) Rigid surfaces S_{3i} are rigidly connected to reference nodes N_{3i} , $i = \{1, \dots, n\}$, that are connected each other through a *weld* connection [6]. The n three-tooth designed bodies of the ring gear constitute one rigid body where the boundary and load conditions are defined at node N_{31} .
- (6) Boundary conditions for the stress analysis of the planetary gear train are applied to the inverted mechanism of the planetary gear train where the carrier is fixed and the ring gear is free to rotate.
- (7) At each contact position, sun, planet and ring gear models are installed in a fixed reference system considering their angular positions, which are obtained from the gear ratios and the phase angles.

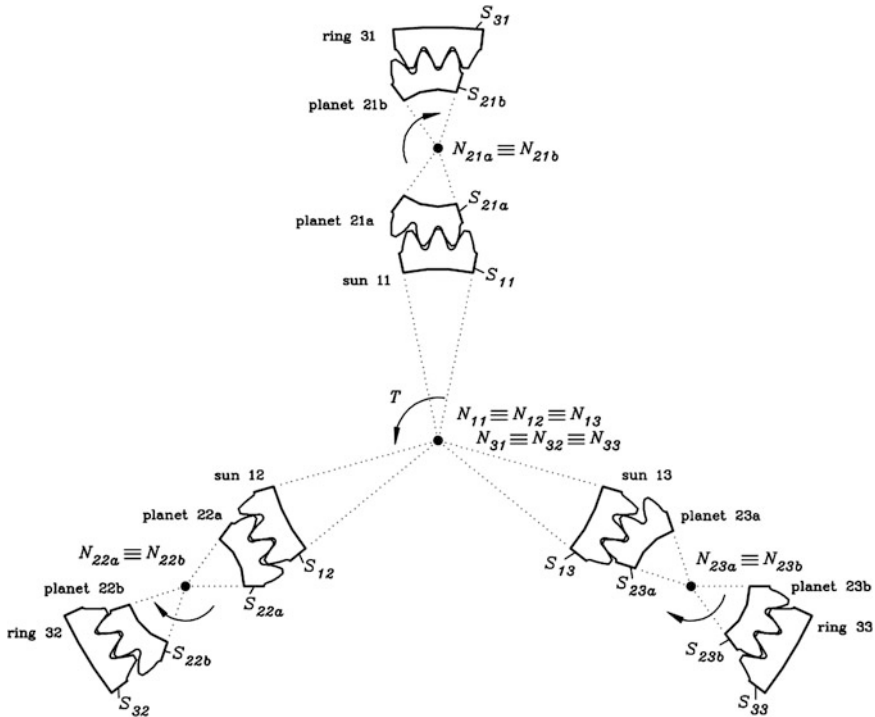


Fig. 5 For application of the boundary conditions at the *rigid* configuration of the planetary gear train

- (8) For the stress analysis at a given contact position, all the degrees of freedom of reference node N_{31} are restricted, whereas nodes N_{11} and N_{2ia} , $i = \{1, \dots, n\}$, are just free to rotate about the sun and the planet axes, respectively.
- (9) A torque T is applied at the free rotational motion of reference node N_{11} and this allows the load to be transmitted to the sun gear model through the rigid surfaces S_{1i} , $i = \{1, \dots, n\}$.
- (10) Each planet gear model, which can rotate freely around its planet axis, is loaded by the push of the sun gear model and by the blocked ring gear model.

In the case of a *flexible* configuration, some differences are incorporated to the finite element model respect to the *rigid* configuration (see Figs. 6 and 7):

- (1) The planet gear models are provided with their corresponding shafts, which are modelled by beam elements. Nodes N_{2ia} , $i = \{1, \dots, n\}$, are connected to a node of the corresponding planet shaft by means of a *hinge* connection [6]. This means that the designed bodies of the planet gears can freely rotate around their axes.

Fig. 6 A flexible configuration for the planetary gear train

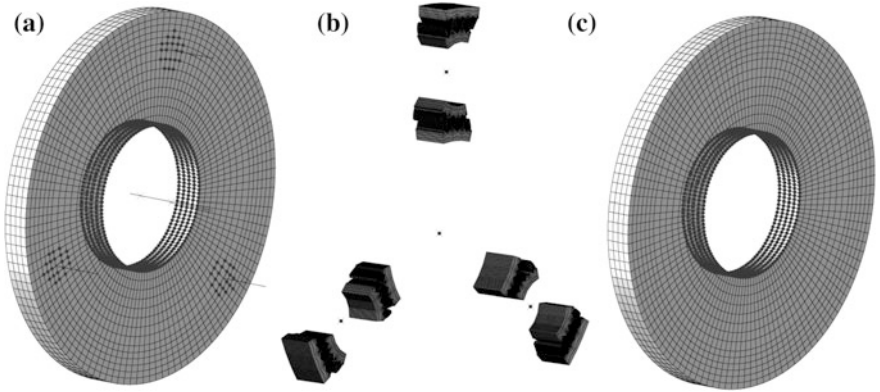
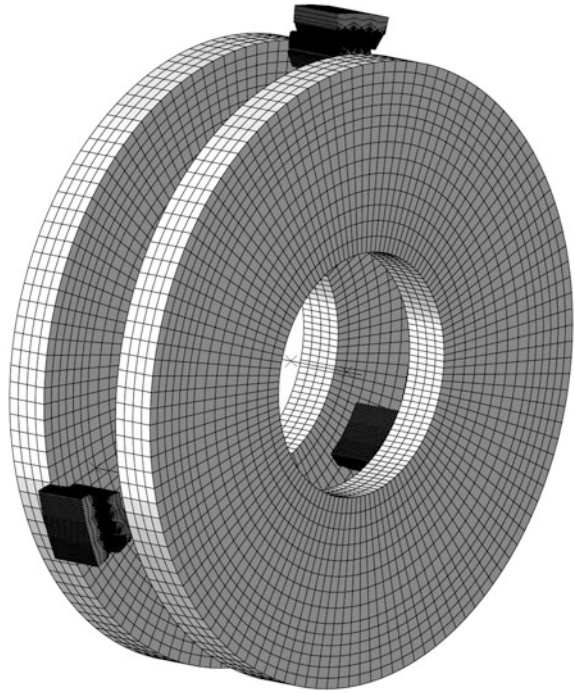


Fig. 7 Flexible configuration parts of a planetary gear train: **a** disk 1 of the carrier, planet shafts and carrier shaft, **b** gears, and **c** disk 2 of the carrier

(2) The carrier is incorporated to the finite element model by means of two disk-shape bodies and one shaft. A set of nodes on the inner surfaces of both disks are rigidly connected to two nodes on the carrier shaft.

Table 1 Basic design data of the planetary gear train

	Sun gear	Planet gear	Ring gear
Number of teeth	46	20	86
Module [mm]		2.0	
Pressure angle [degrees]		25.0	
Profile shift coefficient	-0.2408	+0.1052	+0.03
Face width [mm]		15.0	
Centre distance [mm]		65.7873	
Input torque [Nm]	200.0		

- (3) Each planet shaft is rigidly connected to the carrier through both end nodes using a *weld* connection [6] between each end-node and a predefined set of nodes on the face of the carrier disks.
- (4) The rotation of the carrier shaft is blocked while a torque T is applied to the sun gear reference node N_{11} .

Figure 6 shows the finite element model of a *flexible* configuration for the planetary gear train. Figure 7 shows the *flexible* configuration parts based on the two disk-shape bodies of the carrier, the planet and carrier shafts, and the gears.

4 Numerical Example

A planetary gear train based on $n = 3$ planet gears is considered for stress analysis. The main design data for such a train is shown in Table 1. The required phase angles for the assembly of the planetary gear train (see Fig. 2) are shown in Table 2.

A total of four configurations of the planetary gear train are considered for stress analysis. The main data for such configurations are shown in Table 3. The *rigid* configuration has a total of 414007 elements and 504912 nodes. The *flexible* configuration has a total of 427576 elements and 523036 nodes. A Young's module is 207 GPa and a Poisson's ratio of 0.29 are considered.

Two types of assembly errors of the planet gears on the carrier are considered for stress analysis. Figure 8 shows a possible tangential assembly error Δt and a possible radial assembly error Δr of planet gear 1. The considered values of assembly errors for stress analysis are $\{0, 2, 4, 6, 8, 10\}$ μm .

For each analysis, the maximum contact pressure is determined at each planet gear. Figure 9 shows a maximum contact pressure of 525.7 MPa in planet gear 1 for the case of the *rigid* configuration when no assembly errors are considered.

Figure 10 shows the evolution of maximum contact pressure at the three planet gears for different values of the tangential assembly error Δt of planet gear 1. In the case of the *rigid* configuration (Fig. 10(a)), the tangential assembly error Δt causes larger differences of contact pressures between the planet gears than in the case of a *flexible* configuration (Fig. 10(b)). Therefore, the maximum contact pressure in

Table 2 Phase angles for the assembly of planet gears in the planetary gear train

	Planet 1	Planet 2	Planet 3
$m_1^{(k)}$	0	15	31
$m_3^{(k)}$	0	29	57
$\delta_1^{(k)}$ [rad]	0	-0.045530	+0.045530
$\delta_3^{(k)}$ [rad]	0	+0.024353	-0.024353
$\mu_2^{(k)}$ [rad]	0	+0.104720	-0.104720
$\mu_2^{(k)}$ [degrees]	0	+6.0	-6.0

Table 3 Rigid and flexible configurations of the planetary gear train

	Rigid	Flexible 1	Flexible 2	Flexible 3
Planet shaft radius [mm]	∞	9.0	11.0	9.0
Disk thickness [mm]	∞	12.0	12.0	8.0

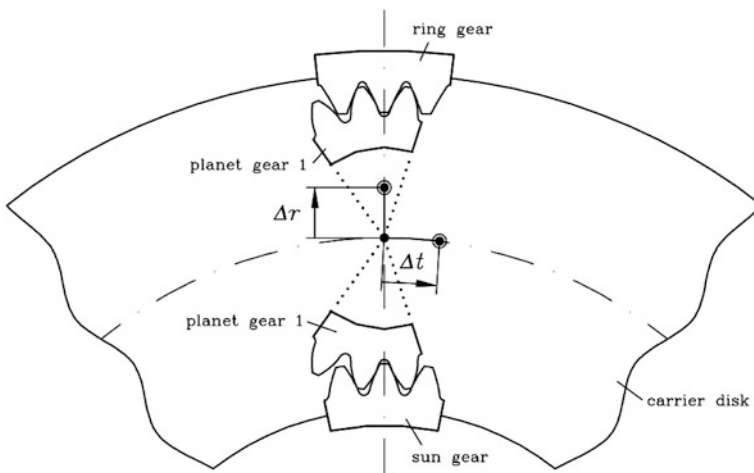


Fig. 8 Assembly errors Δt and Δr of planet gear 1 on the carrier

the planetary gear train is larger in the *rigid* configuration than in any *flexible* configuration as a consequence of a larger uneven distribution of the load between the planet gears.

Figure 11 shows the evolution of the maximum contact pressure at different configurations of the planetary gear train considering several values of the tangential assembly error Δt and the radial assembly error Δr (see Fig. 8). Figure 11a shows that the radial assembly error Δr does not cause an increment of the maximum contact pressure in the planetary gear train and therefore this type of error does not contribute to an uneven distribution of load between the planet gears. Figure 11b shows some differences between the three *flexible* configurations (see Table 3) when a tangential assembly error Δt is considered.

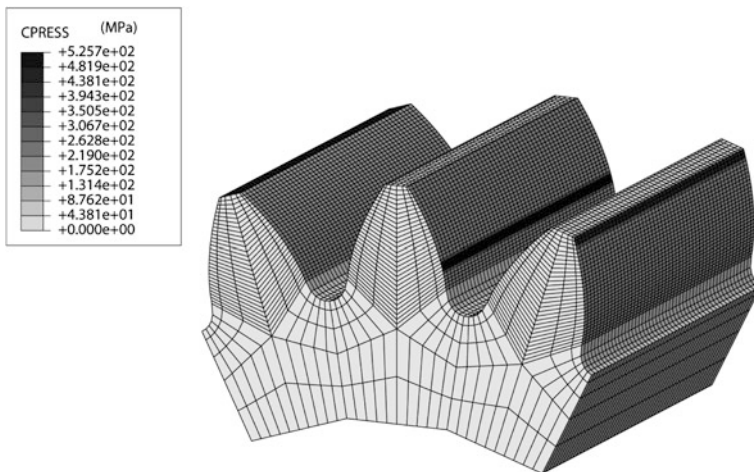


Fig. 9 Contact pressure in planet gear 1 when the *rigid* configuration and no assembly errors are considered

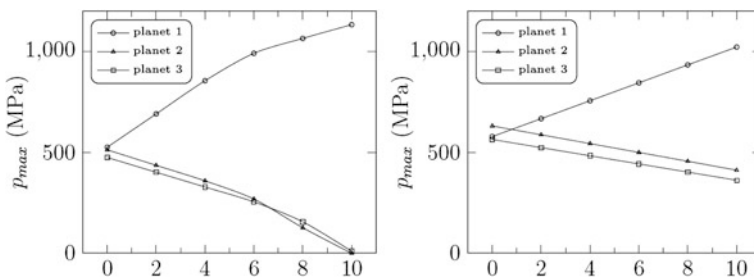


Fig. 10 Evolution of maximum contact pressure at the three planet gears for several values of Δt error in the assembly of planet gear 1 in case of **a** the rigid configuration and **b** the flexible configuration number 1

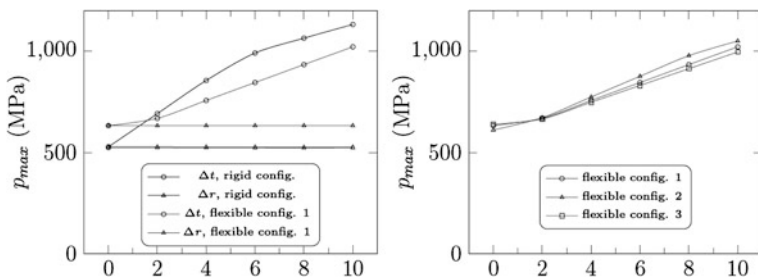


Fig. 11 Evolution of maximum contact pressure at the planetary gear train for several values of assembly errors Δt and Δr of planet gear 1 on the carrier

5 Conclusions

The developed research allows the following conclusions to be drawn:

- (1) An enhanced finite element model for determination of the load capacity in planetary gear trains has been proposed.
- (2) The designed bodies of the sun gear, the ring gear, the planet gears, the carrier and the supporting shafts have been included into the model.
- (3) Stress analysis can be performed considering different types of assembly error of the planet gears on the carrier and different design parameters of the planetary gear train.
- (4) A different design of the carrier can be easily integrated into the model.

Acknowledgments The authors express their deep gratitude to the Spanish Ministry of Economy and Competitiveness—MINECO (formerly Ministry of Science and Innovation) for the financial support of research project Ref. DPI2010-20388-C02-01 (financed jointly by *FEDER*).

References

1. Bodas A, Kahraman A (2001) Influence of manufacturing errors and design parameters on the static planet load sharing behavior of planetary gear sets. International motion and power transmission conference, Fukuoka, Japan
2. Kahraman A, Kharazi AA, Umrani M (2003) A Deformable Body Dynamic Analysis of Planetary Gears with Thin Rims. *J Sound Vib* 262:752–768
3. Mundo D (2006) Geometric design of a planetary gear train with non-circular gears. *Mech Mach Theory* 41:456–472
4. Vecchiato D (2006) Tooth contact analysis of a misaligned isostatic planetary gear train. *Mech Mach Theory* 41:617–631
5. Litvin F, Fuentes A (2004) *Gear geometry and applied theory*. Cambridge University Press, New York
6. Abaqus 6.11 user documentation, Simulia, Dassault Systèmes

Gear Oil Viscosity Modifiers and Their Impact on Efficiency

William Barton, Elizabeth Schiferl, Mark Baker and Simon Chai

Abstract The essential functions of an automotive gear lubricant viscosity modifier (VM) are to maintain fluid film protection of gears and bearings as the lubricant warms to operating temperature, to improve cold temperature flow for efficient lubrication in winter and to minimise viscosity loss in a high shear, high load environment. Although a number of different VM technologies can be considered appropriately resistant to permanent shear for automotive gear oils use, their effect on fluid efficiency can vary widely. This paper outlines the study of a series of different VM technologies assessing relationship of operating temperature, operating viscosity and axle efficiency under different load and speed regimes. The fluids presented were formulated to equal kinematic viscosity at 100 °C but vary widely in viscosity index (VI), elastohydrodynamic (EHD) traction and EHD film thickness. The differences observed during efficiency testing were qualitatively related to the rheological properties of the VM technology present and further related to the operating temperature and operating viscosity.

Keywords Gear oil · Viscosity modifier · Efficiency · Operating temperature

F2012-C02-009

W. Barton (✉)
Lubrizol Limited, Derby, UK
e-mail: wlba@lubrizol.com

E. Schiferl · M. Baker
Lubrizol Corporation, Ohio, USA

S. Chai
Lubrizol China, Beijing, Peoples Republic of China

1 Introduction

The first paper in this series on the impact of viscosity modifiers (VM) on automotive gear oil (AGO) efficiency described the shear stability, cold flow, spur gear efficiency and rheological traits of a series of SAE 75W90 VM based fluids compared to a Newtonian SAE 80W90 brightstock fluid [1]. The evaluations showed significant differences could be achieved in EHD film support, EHD traction, VI and cold flow among other traits by simply changing VM type at equal kinematic viscosity at 100 °C (17.5 cSt). Spur gear efficiency testing was also conducted under controlled temperature, load and speed conditions and differences in efficiency were correlated to lower traction and higher VI. The same fluids are the subject of this comparison in which the sump fluid temperature is not controlled in a hypoid gear efficiency test to evaluate their impact on operating temperature and efficiency by VM type.

$$\text{SSI} = \frac{(\text{initial blend viscosity} - \text{after shear blend viscosity})}{(\text{Initial blend viscosity} - \text{viscosity of Newtonian components})} \times 100 \quad (1)$$

For AGO applications it is preferable to have a low shear stability index (SSI, Eq. 1), i.e. a highly shear stable VM, in the order of 0–10 as determined by 20 h KRL, CEC L-45 for consistent fluid film support and minimal viscosity loss in operation. The fluids were prepared using shear stable VM technologies only according to the details below for comparison.

- *Additive performance package (10 wt % treat):* A Total Driveline Lubricant (TDL) suitable for transmission and axle applications
- *Base stock:* PAO-4 for VM containing fluids, Group II for brightstock

For improved efficiency it is preferable to have a high viscosity index (VI) [2], the fluid viscosity data is summarised in Table 1 below. The fluids are ranked by VI as the first measure of operational efficiency. High VI fluids (such as new VM, DPMA) have lower viscosity at ambient temperature and higher viscosity at extreme high temperature operation providing a more consistent fluid response across temperature extremes. Additionally, pour point and Brookfield low temperature viscosity (BV40) and cold flow are improved by the use of high performance VMs.

Previous studies have shown that VM and base stock can significantly impact operating temperature [3] and this can be modelled to some extent [4]. The interplay of VM, viscosity and base oil was shown to lead to varied temperature and end of test viscosity in ARKL testing. Additionally, axle operating temperature under different operating conditions has been evaluated with fluids having different viscosity, EHD film formation and frictional properties [5]. The work determined torque transfer efficiency could be correlated to operating temperature at high torque, low speed. Specifically, the authors identified robust EHD film

Table 1 Viscosity modifier chemistries used in comparison

	KV100 ^a	KV40 ^a	VI	BV40 ^b	Pour point ^c	HTHS ^d	SSI ^e	VM description
	(cSt)	(cSt)		(cP)	(°C)	(cP)		(dispersant Y/N)
New VM	17.58	102.5	189	41,500	−57	6.02	3	Complex ester (Y)
DPMA	17.21	106.7	177	49,000	−51	5.85	8	Poly(alkyl methacrylate) (Y)
PAO100	16.92	112.8	164	57,000	−48	5.36	1	Poly(<i>alpha</i> -olefin)
PIB	17.63	127.2	153	88,000	−54	5.56	6	Poly(<i>isobutylene</i>)
Brightstock	17.52	174.7	103	TVTM	−27	5.05	1	Complex hydrocarbon

^a Kinematic viscosity at 40 °C (KV40) and 100 °C (KV100), ASTM D2270-10

^b Brookfield viscosity at −40 °C (BV40), ASTM D2983

^c Pour point (°C), ASTM D5950

^d High temperature, high shear at 150 °C (HTHS), CEC L-36-90

^e SSI (shear stability index) determined by 20 h KRL, CEC L-45

formation and low EHD traction as being essential to operational efficiency. The contributions of additive chemistry on efficiency and break in temperature can also be pronounced [2] but does not form part of this study.

Thus, EHD traction, EHD film formation and viscosity index are established contributors to the improvement of efficiency across broad viscosity ranges. However, at equal viscosity and within the same shear stability (0–10 SSI) range it can be a challenge to show operational efficiency benefits. The findings of our study are presented herein on the contribution of VM to operating temperature and what impact this has on efficiency and viscosity.

2 Experimental

EHD Traction measurements: The fluids were evaluated using a mini traction machine (MTM) commercially available from PCS instruments UK. A concentrated contact forms between a steel ball and polished steel disc allowing one to measure the traction of a given fluid. A series of discrete measurements were made at a speed of 2.5 m/s and a Hertz pressure of 1 GPa between 40 and 120 °C in 20 °C temperature increments and slide to roll ratio (SRR) of 0–50 %.

EHD film thickness measurements: EHD film thickness measurements were carried out using a commercially available ultra-thin EHD film thickness tester manufactured by PCS Instruments. An optical interferometry technique is used to measure fluid film thickness under rolling conditions in highly concentrated contact formed between a steel ball and a coated sapphire disc. The films were measured at a Hertz pressure of 0.5 GPa at 20 °C temperature increments between 40 and 120 °C.

Hypoid gear efficiency measurements: Hypoid gear efficiency was evaluated with a 7.4 l V8 engine and automatic transmission equipped with data acquisition

Table 2 Hypoid gear efficiency test conditions

Stage	Pinion speed	Pinion load	Pinion power (kW)
1	Low	Moderate	4.7
2	Low	Moderate-high	11.9
3	Low	Moderate-high	18.1
4	Low	Moderate-high	22.2
5	Low-moderate	Low	3.8
6	Low-moderate	Moderate	10.6
7	Low-moderate	Moderate-high	17.5
8	Low-moderate	Moderate-high	25.2
9	Moderate	Low	3.5
10	Moderate	Low	10.7
11	Moderate	Moderate	19.7
12	Moderate	Moderate-high	26.7
13	High	Low	4.7
14	High	Low	11.2
15	High	Moderate	18.2
16	High	Moderate	24.9

and control (DAC) to a light duty truck axle as per published procedure by [_Akucewich et al. \[2\]](#) and summarised below in [Table 2](#). The rig is arranged in an L-configuration with power transferred to one dynamometer. Relative efficiency evaluated by torque transfer with single in-line torque meter on the input shaft and on the output shaft (between differential and dynamometer). The torque meters are appropriately sized for use and maximum torque is 90 % of rated capacity.

The light duty axle procedure was developed to simulate Federal Test Procedure 75 (FTP-75) under a series of steady state conditions. Axle lubricant temperature is measured via a thermocouple directly next to the ring gear and the lubricant can be cooled between phases through auxiliary cooling loop fitted with a heat exchange employing chilled glycol. Ambient temperature and humidity is controlled by flooding a box shroud covering the axle.

3 Results and Discussion

[Table 2](#) shows the load and speed conditions of each stage in the hypoid gear test procedure. Since these are discreet, steady state conditions comparisons can be made between test lubricants for each speed-torque stage or a weighted average of the stages can be used to provide an estimate of known driving cycles or service conditions [\[6\]](#). However, the following discussion is concerned more with the ability to differentiate fluids with different VM chemistry at a common kinematic viscosity at 100 °C. The impact of the VM chemistry on efficiency and operating temperature may then be determined as speed and load are varied.

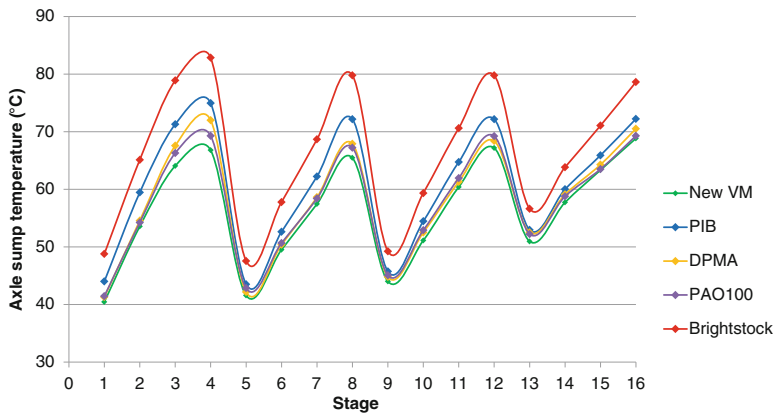


Fig. 1 Plot of steady state operating temperature by test stage

Figure 1 shows the steady state operating temperature of each fluid evaluated over the 16 stages. As pinion load is increased within a given speed profile (Table 2) a requisite increase in temperature is observed as energy transfer is lost through the generation of heat through a combination of churning and frictional losses. The new VM distinguishes itself as running cooler across a broad range of speeds and loads. At low loads, heat generated in the system is largely due to churning (stages 1, 5, 9, 10, 13, 14), and the new VM, DPMA and PAO100 run cooler due to their lower viscosity. The high VI of these fluids, e.g. new VM, results in lower viscosity during start up and can account for some of the reduced energy losses in this case.

The range of differences in temperature is between 5 and 15 °C when comparing the most consistent fluid (new VM) to the fluid experiencing the greatest increases in temperature (brightstock) in a given stage. The most significant increases and improvements in temperature are observed under high load (stages 4, 8 and 12, 16) and most telling is the difference in operating temperature under low speed, high load (stage 4) where frictional losses will begin to dominate efficiency. In all instances the operating temperature trend in consideration of relative VI suggests heat generated by viscous dissipation may be a factor in all stages. However, severe high load conditions or cycling conditions were not evaluated; this may increase operating temperatures differences.

The proportionately greater temperature differences under low speed and higher load conditions is suggestive that EHD, mixed and possibly boundary efficiency impact of the fluids are also significantly different. By keeping the additive package the same and the base oil consistent in each VM fluid the comparisons by VM type are then exemplified. Under mixed and EHD conditions the traction coefficient can have a pronounced effect on operational efficiency and can vary by VM type. Figure 2 shows the traction coefficient of the fluids at 20 % SRR, 1 GPa at 2.5 m/s at 5 different temperatures. The benefits of the lower traction from the new VM and DPMA and to a lesser extent PAO100 are good indicators of

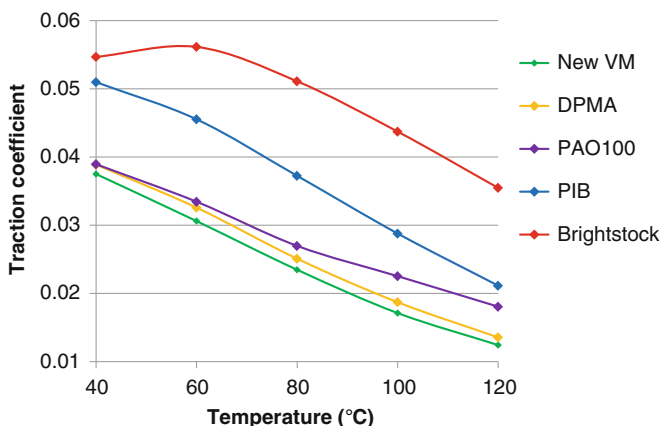


Fig. 2 EHD traction coefficient at 20 % SRR

improved operational efficiency under EHD conditions. This generalised observation can be related to the operating efficiency under speeds, loads and operating temperatures where fluid film is compromised (moderate to high loads, low to moderate speeds, high operating temperatures).

Figure 3 shows the EHD film forming properties of the test fluids at 40, 80 and 120 °C. At 40 °C the film thickness of the brightstock fluid stands out as substantially higher than its VM peers and the ranking is in line with kinematic viscosity at this temperature. However, as temperature increases, and EHD film protection becomes more important, the low speed film in particular begins to rapidly become compromised. PAO100 and PIB provide consistently high EHD fluid support. The new VM stands out as providing proportionately improved EHD film thickness at low speed as temperature increases and EHD support becomes more significant for efficiency and durability.

For the purpose of the following discussion the data are going to be considered not only by stage, but also by the trends observed between different stages at increasing pinion power. The 16 stages have been split into 3 load regimes in which pinion power is progressively increased between these phases. Higher stage number indicates higher speed as summarised in Table 2.

The axle efficiency dataset in Figs. 4, 5 and 6 is limited to the 5 test fluids previously described, however, a line of best fit has been applied to show the overall trend of viscosity and operating temperature to efficiency as load is increased. Relative efficiency is at its lowest in this test at high speed, lowest load (Fig. 4, Stage 9 and 13) and the fluctuation in relative torque loss is most varied under low load conditions. This is largely because absolute torque loss is relatively low and so churning losses have a proportionately larger reduction in efficiency.

Figure 4a below shows the correlation of viscosity to axle efficiency at low load stages (speed increasing at higher stage number) the data suggests that lower viscosity improves torque loss efficiency under all speed conditions. The effect is

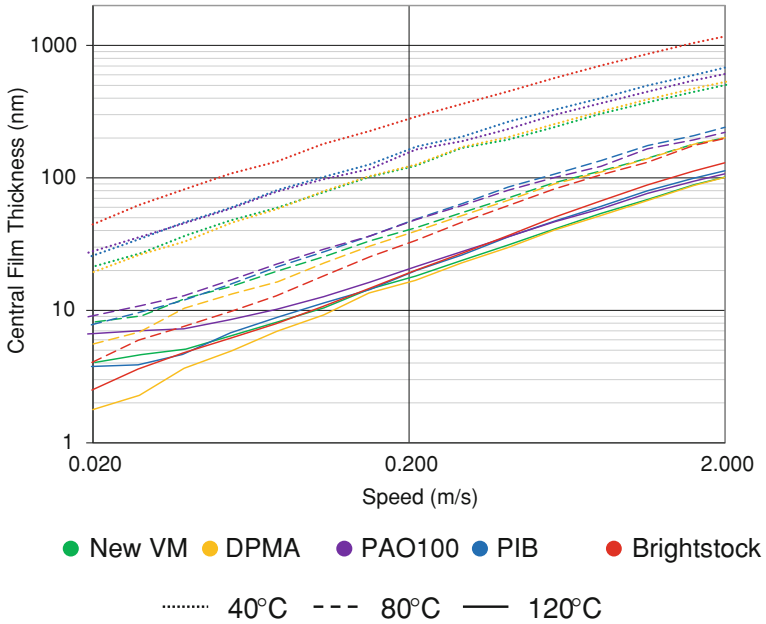


Fig. 3 EHD film thickness at three temperatures

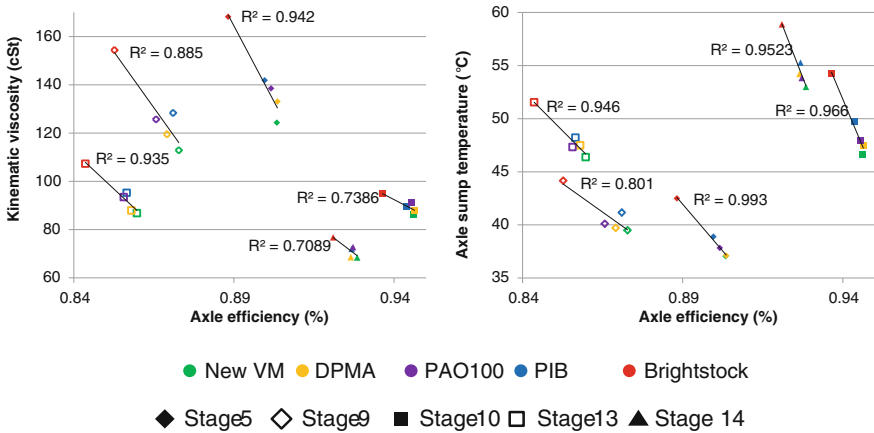


Fig. 4 Efficiency at low load and increasing speed, (a) efficiency versus kinematic viscosity and (b) efficiency versus sump temperature

less pronounced in stages 10 and 14 where pinion load and speed is highest. The steady state operating temperature under low load at all speeds shown in Fig. 4b suggests that a positive correlation between operating temperature and efficiency can be established.

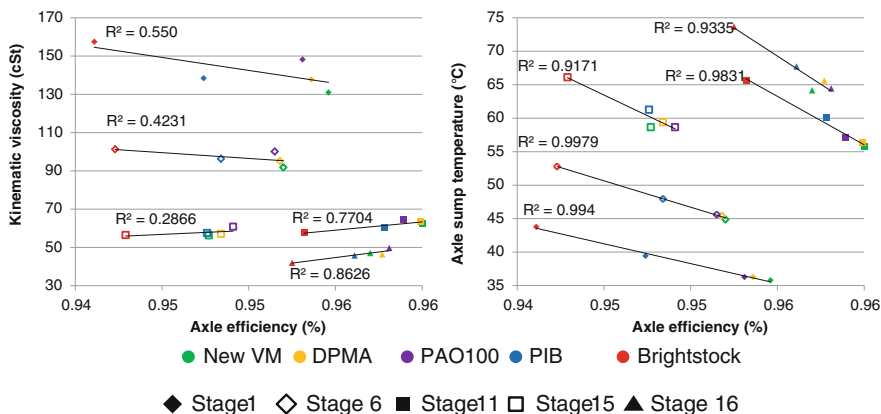


Fig. 5 Efficiency at moderate load and increasing speed, (a) efficiency versus kinematic viscosity and (b) efficiency versus sump temperature

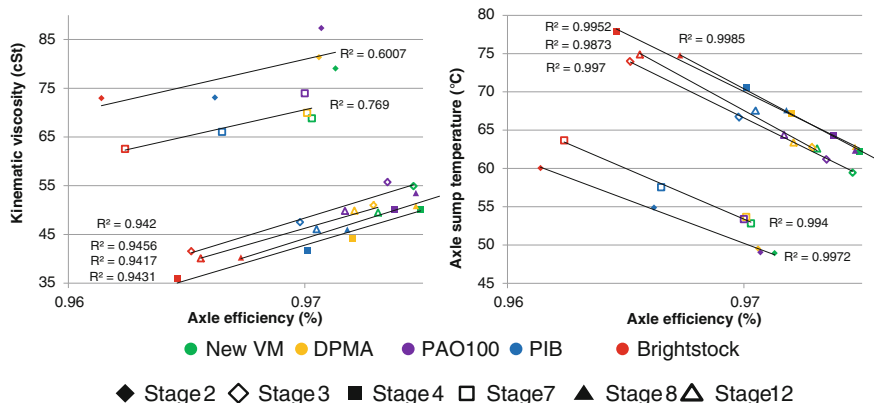


Fig. 6 Efficiency versus kinematic viscosity at moderate-high load stages and increasing speed (higher stage, faster pinion speed)

At low load (churning losses dominating), the impact of viscosity and viscous dissipation is apparent with low VI fluids operating at higher temperatures with lower efficiency. Under these conditions improved torque transfer efficiency favours low viscosity, high VI and low traction fluids such as the new VM and DPMA. Efficiency gains are relatively subtle between the best performing fluids, however, the trends are consistent and benefits typically average 2 % improvement in axle efficiency at a given load stage between the new VM fluid and the brightstock fluid.

Figure 5a shows that under moderate loads the correlation of viscosity to efficiency is less pronounced with no common trend. In fact at low speed, moderate load (e.g., stage 6) there is essentially no correlation between operating viscosity and efficiency. However, in this dataset under these conditions lower axle

fluid operating temperature can be correlated to improved torque transfer efficiency in much the same manner as at lower loads (Figs. 4b and 5b). This relationship is in contrast to the broader study cited earlier [5] although in this instance all fluids are isoviscous at 100 °C and the fluids are operating below this temperature at all speeds and loads. The referenced material operating temperatures were considerably higher overall and the range of fluid viscosities also broader.

The fluid consistently operating at lower temperature and with most favourable torque loss is the new VM fluid followed by DPMA and PAO100. The favourable churning losses previously described is augmented by lower traction and improved film thickness to provide efficiency gains.

Overall, at moderate load the friction losses from EHD film efficiency are beginning to increase in significance in the overall torque loss, hence poor correlation of viscosity and operating efficiency is observed in Fig. 5a as neither churning or frictional losses are dominant. The churning losses are consistent though and so overall losses can be minimised through improved separation of moving parts minimising surface–surface contact and minimal internal fluid resistance or traction; the VM can impact each of these parameters.

Under moderate-high load in Fig. 6a the trends indicate improved efficiency is favoured under higher viscosity conditions at all speeds. Correlation improves at lower viscosity/higher operating temperature as film support is reduced. Frictional losses are now dominating total torque losses and the impact of EHD film and traction is more significant in addition to boundary losses.

The high performance VMs (new VM, DPMA, PAO100) operate at higher viscosity at all speeds despite having higher VI due to lower operating temperatures. The lower operating temperatures result from elements of lower fluid frictional losses, lower viscous dissipation, lower churning losses and reduced boundary contact through high temperature, low speed EHD film support.

Comparison of Figs. 4b, 5b and 6b show that lower operating temperature can be related to improved operating efficiency under all speed and load conditions in this evaluation. The fluid rheology driven by the different VM chemistries is markedly different in terms of EHD traction, EHD film thickness, VI, low temperature flow and the relative contribution can be related to operational efficiency improvements observed. The new VM is consistently capable of operating as the most efficient fluid at lower operating temperature due to the excellent VI, EHD traction and film thickness. The VMs PAO100, PIB and DPMA are capable of either good EHD film thickness or low traction respectively. All three high performance VMs are capable of significant efficiency gains compared to a conventional 80W90 brightstock fluid.

Figure 7 is a summary of the impact of load on relative efficiency for a larger dataset. Relative efficiency is shown in this instance and is the comparison of the efficiency measurement to a baseline fluid to give a relative value. The baseline fluid is a 75W90 gear lubricant and is regularly run to remove rig drift. A comparison of the plots highlights that as load increases, the impact of lowering viscosity can be detrimental to relative efficiency. Factors other than viscosity are governing efficiency at moderate and moderate-high load.

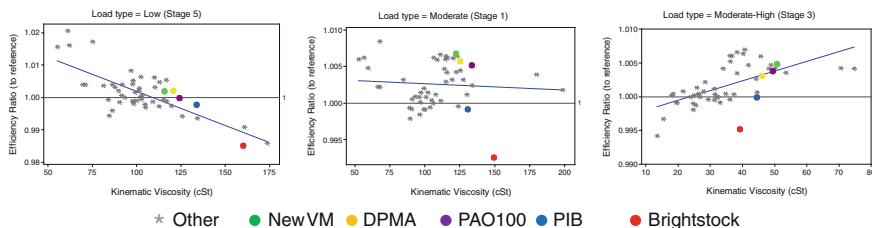


Fig. 7 Impact of load on viscosity-efficiency relationship

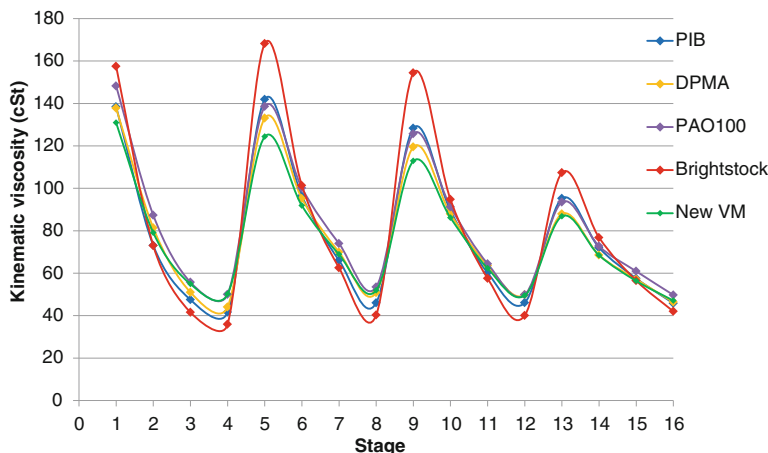


Fig. 8 Plot of kinematic viscosity by stage

Figure 8 summarises the operating viscosity data for the fluids over all stages. The wide variation in operating temperatures and VI between the fluids has a significant impact on the operating viscosity, however, the impact of viscosity on efficiency depends on the load and speed regime. Worthy of note is that the steady state axle sump temperature does not reach or exceed 100 °C (point at which they would be isoviscous) and the fluids with high VI also have the lowest traction. Therefore, the benefits of film support of high VI above 100 °C cannot be presented and the relative benefit of VI and traction is harder to deconvolute. The new VM in particular is capable of operating at a consistent viscosity.

4 Summary/Conclusions

Under steady state axle efficiency testing under varied load and speed conditions the comparison of 5 isoviscous fluids (at 100 °C) with different VM technologies shows the following

- Lower operating temperature correlates to improved axle efficiency as determined by torque transfer under all speeds and load conditions but operating viscosity varies depending on the load regime.
- Low operating viscosity can be related to improved efficiency at low load, all speeds.
 - VM systems such as the new VM or DPMA lose less energy through viscous drag or viscous dissipation and low viscosity (high VI) is a benefit
- High operating viscosity can be related to improved efficiency at high loads, all speeds but traction and film thickness play a role in overall efficiency.
 - Low traction and low speed EHD film support of VMs such as new VM and PAO100 in conjunction with the lower energy lost fluid churn result in lower operating temperatures and higher viscosity (film support at high load)
- At moderate load the effect of churning losses and frictional losses become difficult to separate and operating viscosity cannot be linked to efficiency directly.

The high performance VM systems consistently operate at lower temperatures than 80W90 brightstock based fluid. The new VM in particular exemplifies the benefits of a good VM: at low load, where operating temperatures are lower, the high VI and low EHD traction minimise churning losses and differentiate it as a more efficient fluid. Under high load and low speed the good low speed EHD film protection and low traction coefficient of the new VM fluid enable the fluid to run cooler and provide a more robust and efficient fluid film support.

References

1. Barton W, Payne J, Baker M, O'Connor B, Qureshi F, Huston M, Knapton D (2012) Impact of viscosity modifiers on gear oil efficiency and durability. *SAE Int J Fuels Lubr* 5(1):470–479
2. Wincierz C, Hedrich K, Müller M (2002) Formulation of multigrade gear oils for high efficiency and low operating temperature. 2002-01-2822
3. Devlin MT, Senn J, Sturtz M, Milner J, Jao T, Bala V (2003) Improved understanding of axle oil rheology effects on torque transfer efficiency and axle oil operating temperature. SAE, 2003-01-1972
4. Bala V, Rollin AJ, Brandt G (2000) Rheological properties affecting the fuel economy of multigrade automotive gear lubricants. SAE Technical Paper, 2000-01-2051
5. Akucewich E, O'Connor B, Vinci J, Schenkenburger C (2003) SAE technical paper, 2003-01-3235
6. Wincierz C, Schweder R, Kreutzer I, Neveu C (2000) Influence of VI improvers on the operating temperature of multi-grade gear oils. SAE technical paper, 2000-01-2029

On the Behaviour of Asymmetric Cylindrical Gears in Gear Transmissions

**Alfonso Fuentes, Ignacio Gonzalez-Perez,
Francisco T. Sanchez-Marin and Kenichi Hayasaka**

Abstract Asymmetric gears have been proposed more than twenty years ago as the ultimate solution to increase the load capacity of gear drives while reducing their weight and dimensions. However, there are apparently contradictive statements in the literature regarding whether the higher pressure angle should be applied to the driving or coast side of the gear tooth surfaces. In this work, modern technologies of design and analysis of enhanced gear drives will be applied in order to validate the advantages of application of asymmetric gears and to determine what the right configuration of the asymmetric gear drive should be in terms of application of the higher pressure angle to the driving or coast side of the gear teeth. The evolution of contact and bending stresses as well as contact pressure for the whole cycle of meshing is investigated and compared for symmetric and asymmetric gears. Two configurations of asymmetric gears will be considered, taking into account both, the higher and the lower pressure angle for the driving side. In this way, the advantages of application of asymmetric cylindrical gears as well as the right configuration to get them are established.

Keywords Gear transmissions · Asymmetric gears · Finite element analysis · Stress analysis

F2012-C02-010

A. Fuentes (✉) · I. Gonzalez-Perez
Polytechnic University of Cartagena (UPCT), Cartagena, Spain
e-mail: alfonso.fuentes@upct.es

F. T. Sanchez-Marin
Universitat Jaume I, Castellón de la Plana, Spain

K. Hayasaka
Space Creation Co. Ltd, Wan Chai, Japan

1 Introduction

Asymmetric gears have been proposed more than twenty years ago as the ultimate solution to increase the load capacity of gear drives while reducing their weight and dimensions [1]. The term asymmetric means application of different pressure angles for both sides of gear tooth surfaces. Detailed procedures of design and computation of asymmetric spur gear geometry can be found in [1, 2]. Other works [6–12] are focused in different aspects of design, analysis and optimization of asymmetric gear drives.

A common subject of investigation regarding applicability of asymmetric gears has been the determination whether the higher pressure angle should be applied for the driving or coast sides. One of the first works referring to the application of asymmetric gears and proposing using higher pressure angles for the coast side of the gear tooth surfaces in order to achieve the advantages enumerated above according to [2] was [3]. However, shortly after, many works applied the higher pressure angle for the driving side of the gear tooth surfaces in order to get an increased load capacity or reduced weight and dimensions of the gear set. Recently, in [4] the application of higher pressure angles for the coast side of the gear tooth surfaces is again proposed, showing the advantages by numerical and experimental tests of prototypes. These apparently contradictory statements have motivated this work, with the main goal of validation whether application of asymmetric gears yield indeed advantages and if so, determine what the right configuration should be in terms of application of the higher pressure angle to the driving or coast side of the gear teeth.

2 Methodology

In this work, modern technologies of design and analysis of enhanced gear drives will be applied based on the computerized generation of gears, application of tooth contact analysis and application of FEA enhanced models for stress analysis [5]. Application of modern gear technologies of design and analysis allows the time of development of new gear drives to be drastically reduced, lowering production costs and offering high quality final products wherein gears are applied. In this case, those modern gear technologies will be applied by using the Integrated Gear Design (IGD) software developed by the Enhanced Gear Drives Research Group (GITAE) in order to investigate the advantages of application of asymmetric cylindrical gears with respect to traditional symmetric cylindrical gears.

The bending stresses as well as contact stresses and contact pressure will be determined by using enhanced finite element models that allows investigation of the formation of the contact patterns on the gear drive along the whole cycle of meshing. We will be considering 21 different positions of meshing along a cycle of meshing. The evolution of contact and bending stresses as well as contact

Table 1 Common basic design data of all cases of design of a symmetric and asymmetric spur gear drive

	Pinion	Wheel
Number of teeth	24	34
Module [mm]	2.0	
Addendum coefficient	1.0	
Dedendum coefficient	1.25	
Face width [mm]	20	
Input torque [Nm]	210.0	

pressure will be compared for symmetric and asymmetric gears in order to find and quantify the real advantages of application of asymmetric gears. Two configurations of asymmetric gears will be considered, taking into account both, the higher and the lower pressure angle for the driving side. In this way, this paper will definitely establish what the advantages of application of asymmetric cylindrical gears are and what configuration has to be used in order to get those advantages.

3 Numerical Example and Discussions of Results

In order to establish the baseline design, a spur gear transmission 20×20 (symmetric gear set with 20° for the pressure angle of the driving side and 20° for the coast side) has to be optimized. The common basic design data for the baseline design is shown in Table 1.

A torque of 210.0 N·m will be applied to the pinion for all cases of design. When investigating the evolution of maximum contact and bending stress, and contact pressure for the baseline design with no surface modifications, high contact stresses and contact pressures are obtained for the pinion and wheel tooth surfaces contacting on the top-edge. In order to get an optimized design, a top relief have been provided to the pinion and wheel members of the gear set, by application of a rack-cutter with modified generating profile as shown in Fig. 1.

As shown in Fig. 1, a top-relief height h_{tr} of 0.7 mm has been used for the baseline design, in order to provide gear tooth surface modifications outside of the single tooth contact area, and not introduce, in this way, transmission errors into the gear drive design. Figure 2 shows the modified top-edge area with a maximum profile modification at the top edge of 14.3 μm for the pinion and 9.1 μm for the gear.

Figure 3 shows the evolution of contact and bending stresses (Figs. 3a, b) as well as contact pressure (Fig. 3c) for the pinion, along 21 contact points of a cycle of meshing. Several cases of design, obtained by application of gradually increased value of parabola coefficient of top-relief area of the generating rack-cutter profile (see Fig. 1), have been investigated in order to establish the optimum value of top relief. The values in parenthesis in the legends of Fig. 3 represent the maximum top relieves applied to the pinion. As represented in Fig. 3, a value of 14.3 μm of

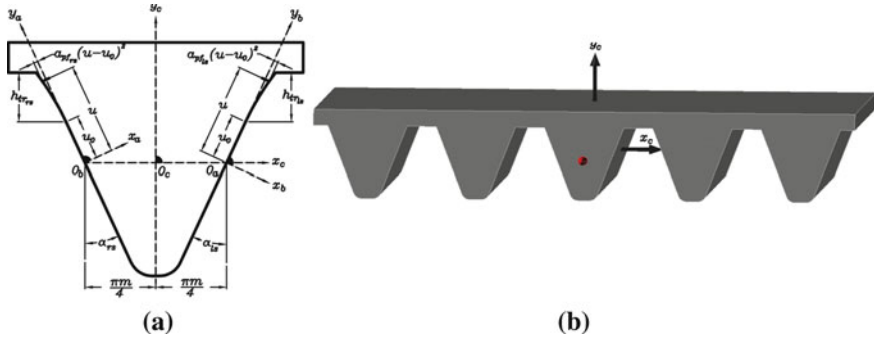


Fig. 1 a Rack cutter with modified generating profile for top-relief generation. b Three-dimensional model of the generating rack-cutter

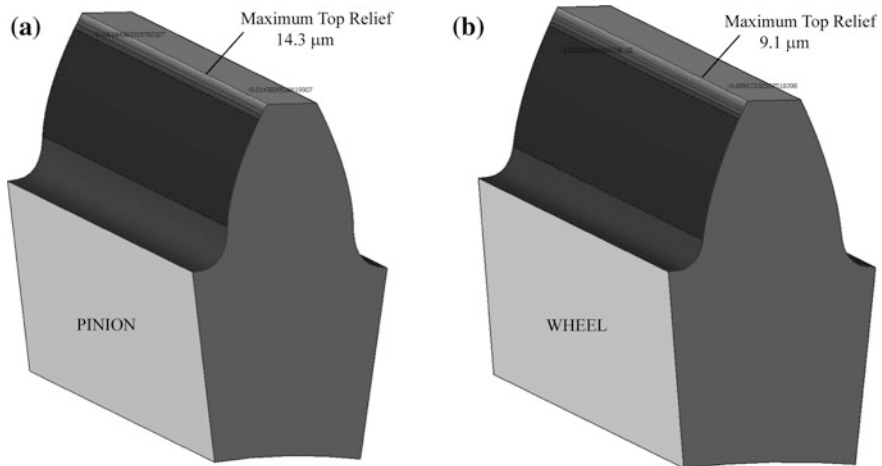


Fig. 2 Comparison of top-reliefs modifications for optimized design of a pinion and b wheel members of the baseline design of the gear set

top relief yields a smooth evolution of contact stresses and contact pressure, and can be considered the optimum value of the top-relief for the base-line design. It has to be mentioned that higher or lower values than the optimal ones of top-relief yield high contact stresses and contact pressure, so that optimization of the top-relief is very important in order to get a smooth evolution of contact stress and contact pressure all over the cycle of meshing.

Figure 4a shows the contact stresses for the pinion at contact point number 7. As shown in Fig. 4a, an area of high contact stresses appears all over the top edge of the pinion tooth surfaces. In Fig. 4b, contact stresses for the optimized design with top-relief modification of $14.3 \mu\text{m}$ are represented, reducing in this way substantially the maximum contact stress at the pinion tooth surfaces, allowing a smooth load transfer between consecutive gear teeth.

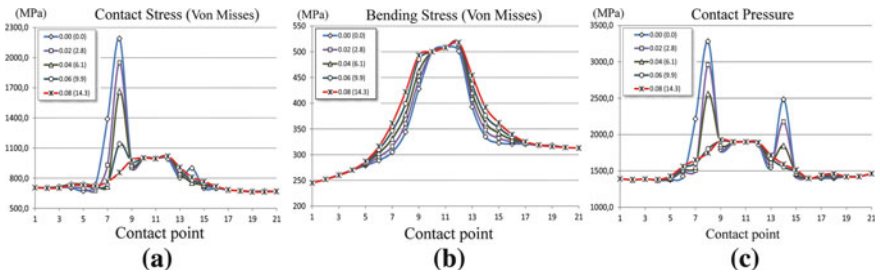


Fig. 3 Evolution of **a** contact stress, **b** bending stress, and **c** contact pressure for several cases of design

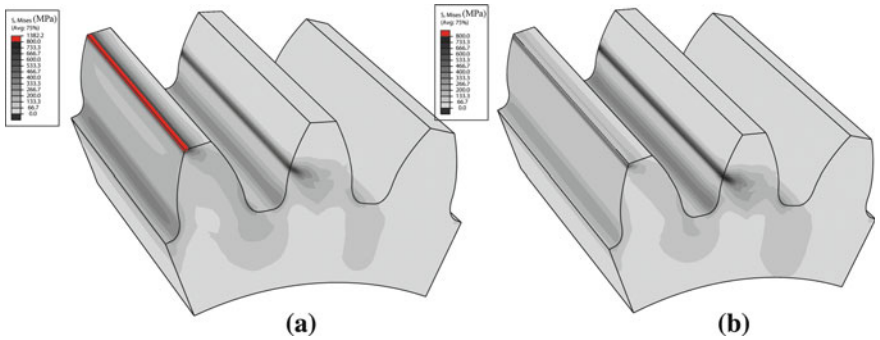


Fig. 4 Contact stresses for the pinion with **a** no top-relief, and **b** an optimized top-relief of 14.3 um

Figure 5 shows three cases of design to be investigated and compared. A rotation counter clockwise will be considered to determine the driving side of the gear tooth surfaces. In Figure 5a, a symmetric gear drive with 20° of pressure angle for both the driving and coast sides is shown. In Fig. 5b an asymmetric gear drive with pressure angle of 30° for the driving side and 20° for the coast side is represented, and finally in Fig. 5c an asymmetric gear drive with pressure angle of 20° for the driving side and 30° for the coast side is represented.

Figure 6 shows the evolution of contact stress (Fig. 6a), bending stress (Fig. 6b), and contact pressure (Fig. 6c) for the pinion of cases of design obtained by considering increased pressure angle for the coast side with respect of baseline design. The legend in Fig. 6 is self-explanatory. As shown in Fig. 6a, maximum contact stress on the pinion only depends on the pressure angle of the driving side. No reduction of contact stresses or contact pressure is obtained by considering different pressure angles for the coast side. In the same way, Fig. 6c shows that maximum contact pressure only depends as well on the pressure angle of the driving side. On the contrary, a reduction of bending stresses is obtained for higher pressure angles on the coast side. This result is in total agreement with statements in [3, 4] and according to experimental tests presented in [4].

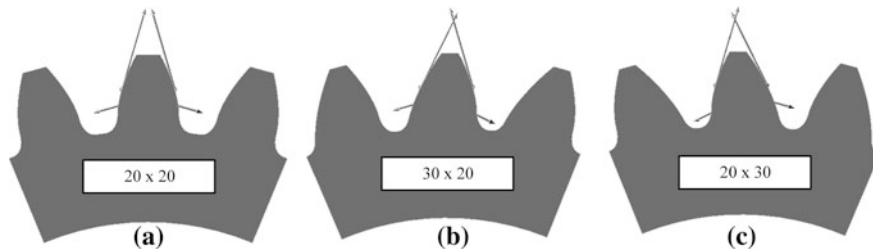


Fig. 5 Cases of design of **a** symmetrical gear drive; **b** asymmetric gear drive with higher pressure angle for the driving side; and **c** asymmetric gear drive with higher pressure angle for the coast side

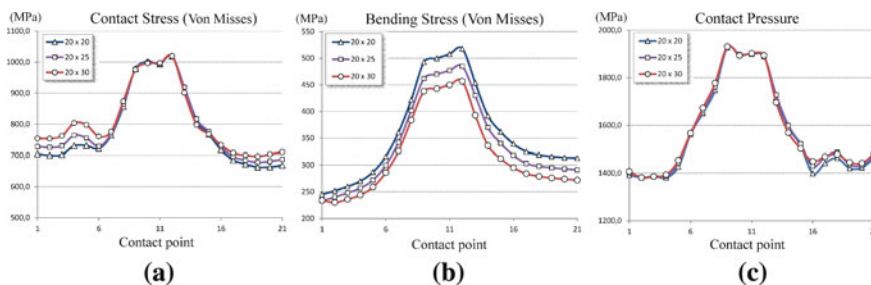


Fig. 6 Evolution of **a** contact stress, **b** bending stress, and **c** contact pressure for the pinion of symmetric and asymmetric gear drives for increasing angle of pressure angle for the coast side

Figure 7 shows the evolution of contact stress (Fig. 7a), bending stress (Fig. 7b), and contact pressure (Fig. 7c) for the pinion of cases of design obtained by considering increased pressure angle for the driving side with respect of baseline design. As shown in Fig. 7a, the minimum contact stress is obtained for the case of design with higher pressure angle for the driving side. Figure 7b shows also that bending stresses are reduced for case of design with higher pressure angle for the driving side. Same results are obtained when considering contact pressure. By observing Fig. 7, we can conclude that application of higher pressure angle for the driving side, not only a reduction of bending stresses is obtained but also reduction of contact stresses and contact pressure is expected, increasing in this way life and endurance of the gear drive.

Finally, in order to evaluate what design is more favourable, the baseline design is compared with asymmetric designs considering the same increased angle of pressure angle for the coast and driving sides of the pinion and wheel tooth surfaces. Figure 8a shows that reduction of contact stresses is only achieved for design 30×20 , wherein higher pressure angle is applied for the driving sides. Regarding bending stresses, Fig. 8b shows that reduction is achieved in almost similar values for both asymmetric designs, being this result in agreement with previously published works with apparently contradictory statements. Contact pressure is reduced significantly for the case of design 30×20 .

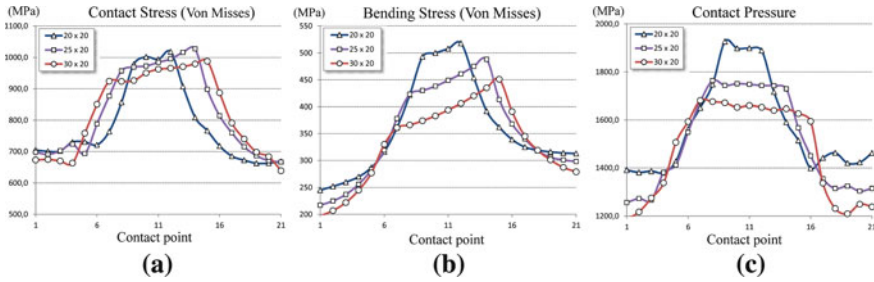


Fig. 7 Evolution of **a** contact stress, **b** bending stress, and **c** contact pressure for the pinion of symmetric and asymmetric gear drives for increasing angle of pressure angle for the driving side

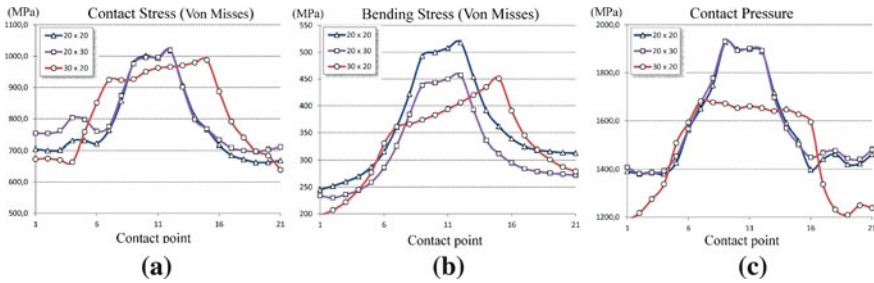


Fig. 8 Comparison of evolution of **a** contact stress, **b** bending stress, and **c** contact pressure for base line design and asymmetric gear drives for higher pressure angle applied to the driving side (case 30×20) and to the coast side (20×30)

4 Conclusions

The developed research allows the following conclusions to be drawn:

1. The application of asymmetric gears is directed indeed to the reduction of contact and bending stresses, and therefore contributes to the increase of the endurance and life of the gear drive.
2. Maximum contact stresses and contact pressure on the gear teeth depends only on the pressure angle of the contacting side (driving side) of the gear drive, no matter what the pressure angle of the coast side is.
3. Bending stresses are reduced when higher pressure angles are used, not only for the coast side as stated in [3, 4] but also for the driving side.
4. The driving side of the gear drive should have the highest pressure angle, when the goal is to reduce contact stresses and contact pressures, and not only reduce bending stresses.

Acknowledgments The authors express their deep gratitude to the Spanish Ministry of Economy and Competitiveness—MINECO (formerly Ministry of Science and Innovation) for the financial support of research projects ref. DPI2010-20388-C02-01 (financed jointly by FEDER) and DPI2010-20388-C02-02.

References

1. Kapelevich AL (2000) Geometry and design of involute spur gears with asymmetric teeth. *Mech Mach Theor* 35(117-130): 2000
2. Litvin FL, Lian Q, Kapelevich AL (2000) Asymmetric modified spur gear drives: reduction of noise, localization of contact, simulation of meshing and stress analysis. *Comput Methods Appl Mech Eng* 188(1–3):363–390
3. Hayer L (1986) Advanced transmission components investigation. Sikorski Aircraft Division, USAAVRADCOM TR-82-D-11
4. Sanders A, Houser DR, Kahraman A, Harianto J, Shon S (2011) An experimental investigation of the effect of tooth asymmetry and tooth root shape on root stresses and single tooth bending fatigue life of gear teeth. In: Proceedings of the ASME 2011 international design engineering technical conferences, IDETC/CIE 2011, Washington DC, USA
5. Litvin F, Fuentes A (2004) *Gear geometry and applied theory*. Cambridge University Press, New York
6. DiFrancesco G, Marini S (1997) Structural analysis of asymmetrical teeth: reduction of size and weight. *Gear Technol* 14(5):47–51
7. Karpat F, Cavdar K, Babalik FC (2005) Computer aided analysis of involute spur gear with asymmetric teeth. *VDI Berichte* 1904(I):145–163
8. Kapelevich AL (2009) Direct design of asymmetric gears: approach and application. In: International conference on motion and power transmissions
9. Kapelevich AL (2010) Measurement of directly designed gears with symmetric and asymmetric teeth. In: International conference on gears
10. Kapelevich AL (2011) Asymmetric gears: parameter selection approach. In: International conference on power transmissions of Xian
11. Kapelevich AL, Shekhtman YV (2009) Tooth fillet profile optimization for gears with symmetric and asymmetric teeth. *Gear Technology*, pp 73–79
12. Yang SC (2005) Mathematical model of a helical gear with asymmetric involute teeth and its analysis. *International Journal of Advanced Manufacturing Technology* 26(5):448–456

Efficiency Optimization of Transmissions

Kathrien Inderwisch, Rashad Mustafa and Ferit Küçükay

Abstract Nowadays, the automotive industry have been received more attention to improve the transmission efficiency. Most of the researches have been concentrated on development and optimization on transmission actuators, shifting elements, bearings, lubricants or lightweight constructions. Due to the low load requirements and associated low efficiencies for transmissions in driving cycles the transmissions cause energy losses which cannot be neglected. Two main strategies can be followed up for the optimization of transmission efficiency. At first the efficiency benefit of transmissions through optimization of hardware components will be presented. The second possibility is the representation of an optimal thermal management especially at low temperatures. Warming-up the transmission oil or transmission components can increase the efficiency of transmissions significantly. Techniques like this become more important in the course of electrification of drivetrains and therefore decreased availability of heat. A simulation tool for calculation and minimization of power loss for manual and dual-clutch transmissions was developed at the Institute of Automotive Engineering and verified by measurements. The simulation tool calculates the total transmission efficiency as well as the losses of individual transmission components depending on various environmental conditions. In this chapter, the results in terms of increasing the efficiency of transmissions by optimization of hardware components will be presented. Furthermore, the effects of temperature distribution in the transmission as well as the potential of minimizing loss at low temperatures through thermal management will be illustrated. These considerations take

F2012-C02-013

K. Inderwisch (✉) · R. Mustafa · F. Küçükay
Institute of Automotive Engineering, TU Braunschweig, Braunschweig, Germany
e-mail: k.inderwisch@tu-bs.de

different cycles, including representative customer use into account, based on experience with the so-called 3D method.

Keywords Efficiency · Transmission · Thermal management · 3D-method · Customer operation

1 Introduction

The energy consumption of vehicles results from energy required for driving resistances, energy due to losses in drivetrain components and energy needed by auxiliaries devices such as air conditioning, control systems and much more.

The driving resistances have the highest influence on full vehicle energy consumption. The energy required from the auxiliary devices is relatively small, however, within the electrification of the power train important. Even small improvements have therefore of great importance and have a positive effect on vehicle range. The increasing restrictions on fuel consumption and CO₂-emissions, but also the increasing electrification of the drivetrain require a significant increase in efficiency of drivetrain components (Fig. 1).

In a combustion engine driven vehicle, the largest part of loss come from the conversion of chemical energy in fuel into mechanical energy within the internal combustion engine. It can be assumed for example that only 23 % of the initial energy in fuel can be used after combustion engine.

The transmission as converter in the drivetrain, cause power losses, which have to be minimized. These power losses are influenced by load point (speeds, torque, engaged gear and temperature). In the example in Fig. 1 the transmission efficiency is assumed with 85 %. The drivetrain efficiency in this example is only 20 % for the combustion driven vehicle. In case the vehicle is electrical driven, due to higher efficiency of e-machine (80 %), the drivetrain efficiency is 70 %.

Automatically shifting transmissions have a key position in this regard: the shift strategy determines the operating point of the engine and therefore the overall efficiency of the drivetrain on the one hand. As converters in the drivetrain, they also cause power loss on the other.

2 Transmission Model

The transmission model consists of two simulation models. First, the model for transmission loss calculation, provides the efficiency and energy consumption of each transmission component for desired load point. Furthermore, this loss of

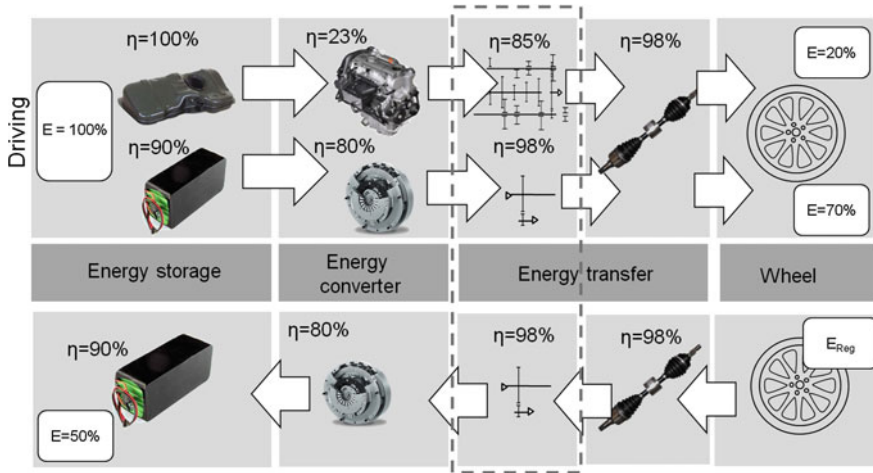


Fig. 1 Drivetrain efficiency

energy is used as input for the evaluation of thermal management in the thermal transmission model.

2.1 Transmission Power Loss Calculation

Power loss of transmissions are caused by bearings, gearings, seals, synchronization devices, clutches and hydraulic loss of the gearing, independent of load [1–3]. The overall efficiency as well as the loss of the individual transmission components, depending on transmission input speed and torque, engaged gear and transmission oil temperature are calculated with one model.

$$\begin{aligned}
 P_{loss} = & \sum_i P_{loss,bearing} + \sum_j P_{loss,gearing} + \sum_k P_{loss,sealing} + \sum_l P_{loss,synchronization\ devices} \\
 & + \sum_m P_{loss,clutches} + \sum_o P_{loss,hydraulic}
 \end{aligned}
 \tag{1}$$

Relevant characters, like geometrical values (e.g. pitch circles), design related characteristics of components (e.g. gearing surfaces) as well as transmission oil properties (e.g. dynamic viscosity) of transmission and its components are stored in a database. All necessary speeds and torques are allocated by a kinematical model (Fig. 2).

The transmission loss model determines the energy dissipation of each transmission component from physical connections and empirical assumptions.

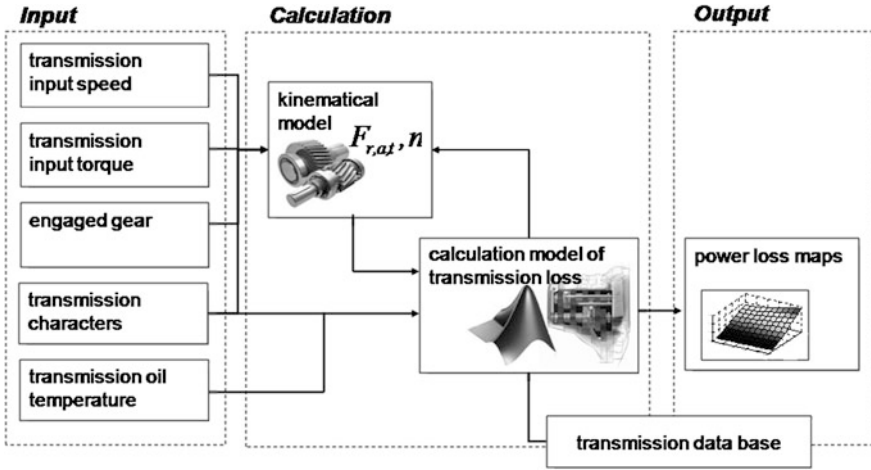


Fig. 2 Model of transmission loss calculation

2.2 Thermal Management

A thermal co-simulation model includes engine and transmission friction models as well as cooling cycles. The engine cooling cycle is divided into water cycle, which exchanges heat with the environment, the engine's thermal mass and the oil cycle. The engine's oil cycle exchanges heat with the water cycle, the engine's thermal mass and the transmission oil cycle via the transmission oil heat exchanger. The heat flow generated by combustion and friction is modeled as a heat input into the engine's thermal mass. Heat is transferred between engine thermal mass and transmission case. The engine's cooling system is simplified to the water cycle, to model heat flow from the engine block mass into the cooling system which then enters different heat exchangers [4].

The applied thermal transmission model is more complex. It regards several thermal masses: Transmission inside components like gears and shafts, case, shift elements and pump. Oil temperatures are calculated at sump, inflow and outflow to shift elements and pump and heat exchanger. An additional cycle for using energy from the other heat sources (for example exhaust gas) can be switched on and off. A valve switches the water flow between exhaust gas heat exchanger (for heating) and the cooler.

There are heat flows between thermal masses and between thermal masses and oil, as well as between transmission case and engine mass and outside air. Heat sources are friction losses in the transmission's load bearing elements, the pump and friction in shift elements and launch device. Figure 3 shows a scheme of the thermal system. In this chapter the influences of different load spectra at transmission oil temperature and the effect on transmission efficiency are studied.

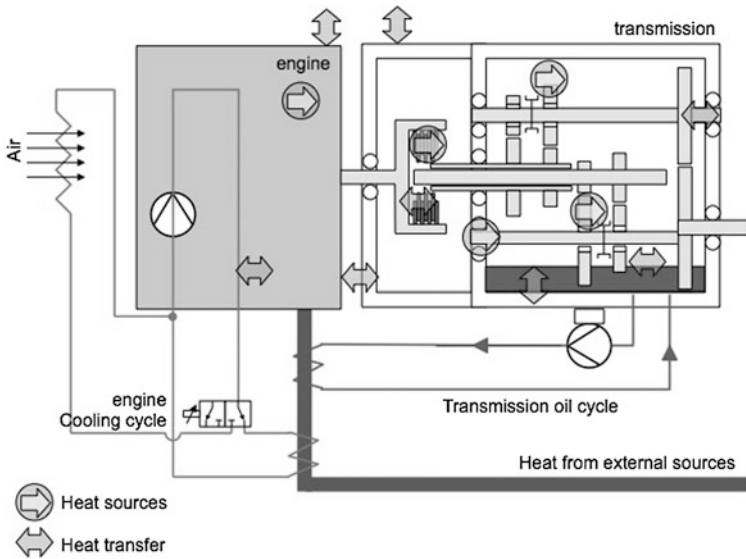


Fig. 3 Model of the thermal system

3 Customer Use

The 3D-method is an efficient tool for analyzing the field of customer use. The key element of the method is the so-called 3D parameter space, which was derived from extensive measurements and is represented in the simulation.

The axes of the 3D parameter space represent three variables: driver, driven vehicle, and driving environs (Fig. 4). “Driver” is characterized by driving style, divided into mild, average and sporty. “Driven vehicle” is defined by the four load conditions light, average and full as well as fully loaded with trailer. “Driving environs” is influenced by the type of road the customer chooses, which means that customer use is fully covered by taking urban, extra urban, mountain and highway roads into account. This results in 48 different customer types that have to be considered [5–9].

3.1 Determination of the 3D Parameter Space

The determination of the requirements resulting from customer use is based on the identification of the driver behavior of all 48 customer types. This has been done in extensive measurements at the Institute of Automotive Engineering (IAE), TU Braunschweig, for several years. Based on objective criteria, the test persons are divided into three driving style groups for this purpose and their driving behavior with different loads is recorded on different representative roads. In these

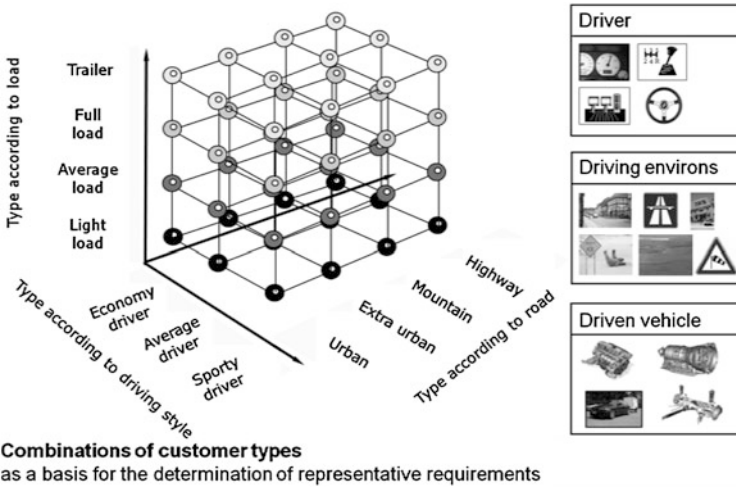


Fig. 4 3D parameters of drivetrain load

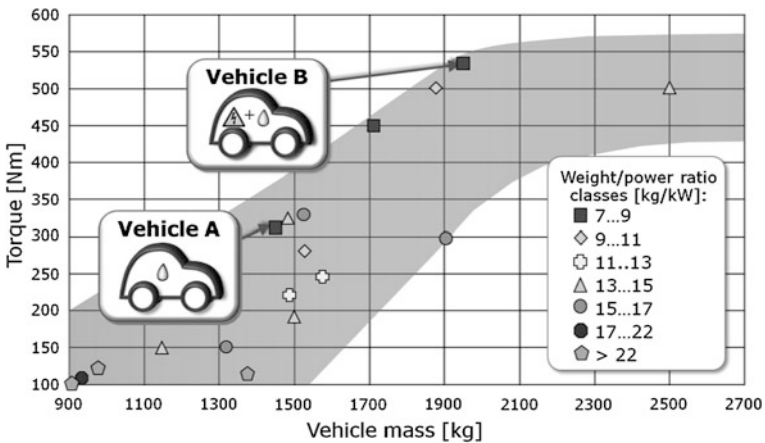


Fig. 5 Database of the vehicles measured in the 3D parameter space. Classification of the vehicles according to weight/power ratio (kg/kW)

measurement studies, covering the 3D parameter space for the drivetrain completely with approx. 60,000 km for each measured vehicle, time data on driver, vehicle and driving environs is recorded from various measuring channels, comprising all operating conditions of the drivetrain. The database for determining the characteristics of and requirements in customer use represented in Fig. 5 is based on these measurements.

The database is continuously extended by taking further vehicle classes and types into account. These data give information for example about speed distribution and drive train loads of the examined vehicle.

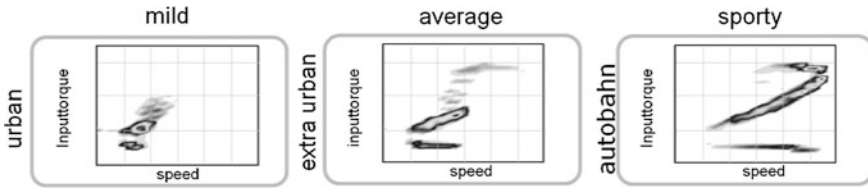


Fig. 6 Speed/Torque distribution for different customer types

While the 3D parameter space acquired by measurements is analysed, driver and road information is additionally evaluated statistically and used as input parameters for the driver and road model of a statistical simulation environment. It reproduces the 3D parameter space and thus the complete customer operation virtually, so customer-related load and operation profiles of different vehicle components are already available at an early development stage. The calculated cycles are basis for a representative evaluation of CO₂-potential of thermal management systems.

3.2 Customer Load Spectra for Transmission

The effects of component improvement as well as thermal influences on transmission losses will be examined using customer relevant duty cycles for all customer types regarded in the 3D-method. Each customer type is simulated once, generating information on torque and speed for engine and transmission input, used gear as well as for the vehicle speed. In a co-simulation model, the torque and speed profiles are used for calculating temperature curves of the transmission oil, beside others. Information on oil temperature, gear signal, transmission input speed and torque is then used to determine cumulated friction and drag losses in the transmission, based on loss-maps.

The co-simulations are performed for a variety of structures of the cooling systems for example exhaust gas heat exchanger) and for different performances of the heat exchangers as well as different heat flows from engine to. A further possible variation factor is the outside temperature at cold starting conditions.

In this chapter, a mid-size car with gas engine and automatically shifting 6-speed transmission is regarded. The simulation uses a static engine torque map and a transmission model. The shifts are commanded via a shift map. In the simulation environment (MOVE3D), the driver model operates accelerator and brake pedal according to the statistic databases for a similar vehicle. Outputs from these simulations are time data for vehicle speed as well as speed and torque at transmission input and engine. Figure 6 shows the torque speed profile for different customers.

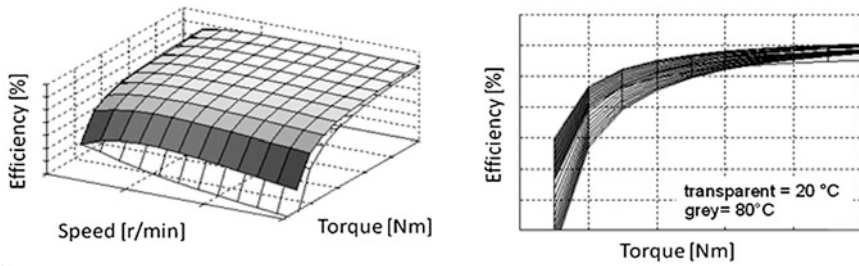


Fig. 7 Transmission efficiency for different oil temperatures

4 Efficiency and Thermal Management

The identified load profiles are used as input for the co-simulation model to calculate various temperatures (transmission oil sump) based on the loss from the transmission power loss calculation routine. These are implemented as power loss maps.

4.1 Transmission Oil Temperatures for Different Customer Types

Figure 7 shows the efficiency of the regarded transmission for outside temperature as well as for operating temperature. It is clearly visible that to low loads and temperatures the efficiency drops significantly.

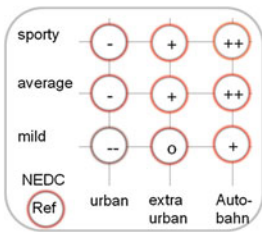
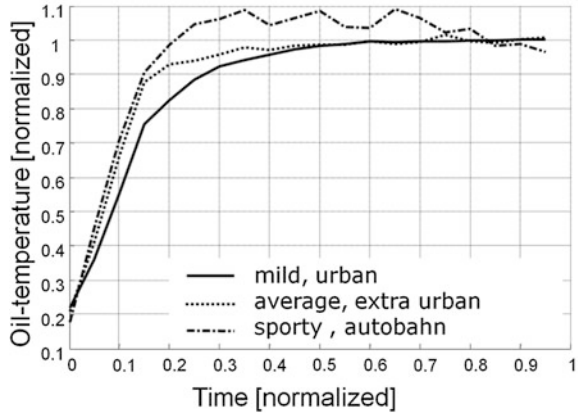
For comparison a time window from cold start until the latest time of reaching steady-state temperature of the transmission oil sump is regarded. Comparative value is the cumulated transmission loss (energy) which can be transformed into CO₂-equivalent using average engine efficiency and standard fuel transformation factors. Figure 8 shows different time curves of the transmission oil temperature for three customer types in comparison. Outside temperature is 20 °C in each case.

It is evident, that the temperature curves look different for different customer types dependent on the average engine load and resulting transmission friction losses. Clearly visible is that, the higher the average load, the higher the losses, the faster the temperature rises. The faster increase in temperature lead to lower friction losses of the transmission during warm up. The simulations cover only the warm up phase time, until steady state conditions are reached.

4.2 Optimisation and Transmission Losses for Different Customer Types

The following analysis show, how transmissions efficiency is influenced by customer and road type. The differences between the customer types result from

Fig. 8 Comparison of temperature curves of transmission oil for 3 different customer types (normalized)



System: Reduced oil level

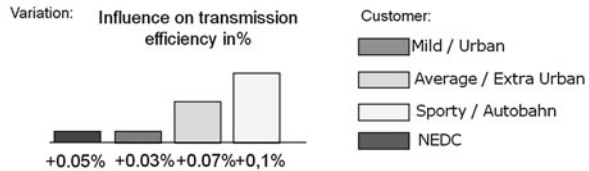


Fig. 9 Transmission efficiency in customer operation (left); Results for reduced oil level by collector (right)

varying load spectra. The transmission efficiency is best for sporty customers. This customer type has highest average torque and engine speed for all road types. In Fig. 9 (left side) the influence of different customer types is shown. Reference is the NEDC cycle.

First regarded measurement is the reduced oil level for lower splashing losses. Plashing losses result from immersion of gearings in oil sump. They are mainly influenced by geometric parameters of gearings, oil viscosity and transmission speeds.

An oil collector realizes an oil level depending oil sump temperature. At low temperatures the high viscosity oil will not fit through the grid of this collector, the oil level is constant. The higher the oil temperature the lower the oil viscosity. The oil level drops because up to 20 % of the oil accumulates in the collector. The immersion depth of gearings is reduced, the efficiency of the transmissions is optimized.

For the NEDC there are nearly no potentials for this measurement (Fig. 9 right side). Reason for this are low speeds so the splashing losses has low influences on transmission efficiency. Due to low temperatures within the cycle, the oil level will be nearly constant. In customer operation, the reduced oil level shows best results for sporty autobahn driver.

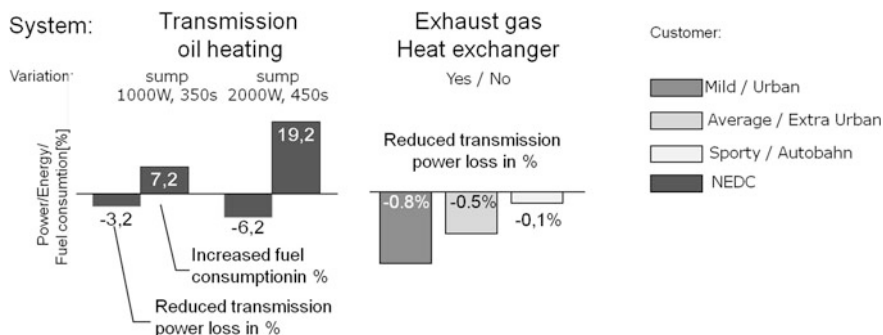


Fig. 10 Energy consumption in customer operation for exhaust gas heat exchanger

Now effects of active oil heating on transmission losses are shown (Fig. 10). The heater was placed at oil sump. The heating power of the electrical heater varies between 1,000 and 2,000 W, the heating time between 300 and 400 s. Although transmission power loss in NEDC could be minimized up to 7.5 % the full vehicle fuel consumption increase to compensate the required power of the heating system.

If the power for transmission oil heating comes from other systems like exhaust gas heat exchanger the heat exchanger between transmission oil and exhaust gas can be used, to shorten the warm up of the transmission oil and thus reduce transmission losses and CO₂-emissions. A basic layout of this heat exchanger, transferring an average of 400 W from exhaust gas to 90 °C warm transmission oil is used as basis. Figure 10 shows this performance compared to no heat exchanger. Outside temperature is 20 °C in customer operation.

The results will of course be relativized by increased weight and flow losses in the cooling circle and, depending on the design, in the exhaust system.

5 Summary

The 3D-method, especially in combination with simulation, is an efficient tool for determining how customer operation and synthetic operations influences the component loads already at an early development stage. The simulation of the customer operation is based on the database researchers at the Institute of Automotive Engineering have set up from extensive measurements. In this chapter was shown, how the 3D-method can be used to quantify effects of optimization and thermal management measures on transmission losses in customer operation. Simplified models and co-simulations have been used in this case; more complex models can of course be attached to the described statistical driver model. The integration of complex control strategies and the use of optimization routines are possible.

References

1. Mauz W (1987) Hydraulische Verluste von Stirnradgetrieben bei Umfangsgeschwindigkeiten bis 60 m/s; IMK Bericht Nr. 159; 1987; Dissertation Universität Stuttgart
2. Berthold S (2009) Maschinenelemente: Getriebe, Verzahnungen, Lagerungen, Pearson Deutschland GmbH, Germany
3. Felix F (2011) Modellierung von Wälzlagern als generische Maschinenelemente einer Mehrkörpersimulation. KIT Scientific Publishing, Germany
4. Mustafa R, Schulze M, Küçükay F, Eilts P (2012) Improved energy management using engine compartment isolation and grille shutter control. SAE 2012, Detroit
5. Eghtessad M, Meier T (2012) Identifikation optimaler Antriebsstrang Konfigurationen für Elektrofahrzeuge. FVA-Bericht 641
6. Fugel M, Kassel T, Küçükay F (2008) Simulation eines parallelen hybridantriebs im kundeneinsatz. Tagung: innovative fahrzeugantriebe 2008, VDI-Berichte 2030. VDI Verlag S, pp 125–150
7. Fugel M (2009) Parallele Hybridantriebe im Kundenbetrieb, Dissertation, TU Braunschweig, Institut für Fahrzeugtechnik
8. Müller-Kose J-P (2002) Repräsentative Lastkollektive für Fahrzeuggetriebe, Dissertation, TU Braunschweig, Institut für Fahrzeugtechnik
9. Kollmer H, Küçükay F, Pötter K (2011) Measurement and fatigue damage evaluation of road profiles in customer operation. Int J Veh Des 56:106–124

Research on Safety Performance for Parking Mechanism on a 7-Speed Dual Clutch Transmission

Lingling Fu, Zhiling Qiu, Yuxiang Chen, Dawei Luo, Yong Chen,
Daguo Luo and Fuquan Zhao

Abstract Parking mechanism is a critical safety device in automatic vehicle transmission. Its safety features give a good indication of safety performance of AT vehicle. This chapter takes the parking mechanism on 7-speed dual clutch transmission as an example, uses kinematics theory to analyze difference of travel times between parking pawl and parking gear. In order to verify the safety performance at high speed parking, a rigid-flexible coupling multi-body dynamic model is established with ADAMS software, based on which the non-linear analysis is conducted to key components of the parking mechanism with peak impact load at high speed parking as input. In addition, through combining mechanics theory and kinematics simulation, the critical friction coefficient is estimated from the aspect of self-locking performance, which serves as references for future design of parking mechanism.

Keywords Parking mechanism · Difference of movement time · Self-locking performance · Impact load · ADMAS · Parking at high speed · Critical friction coefficient

F2012-C02-015

L. Fu (✉) · D. Luo · Y. Chen · D. Luo · F. Zhao
Zhejiang Geely Automobile Research Institute Co., Ltd, Hangzhou, China
e-mail: full@rd.geely.com

Z. Qiu
DSI Holdings Pty Limited, Springvale, Melbourne, VIC, Australia

Y. Chen
South China University of Technology, Guangzhou, China

1 Introduction

Parking mechanism is a critical safety system in automatic transmission. It is designed to break the vehicle reliably on a specific position or even on slope, and its safety performance is one of vehicle evaluation indicators. With the rapid development of the automotive industry, the method to combine theoretical analysis and computer simulation [1, 2], has been widely used on vehicle transmission research. However, due to lacking of auto transmission research in China, the research on Auto transmission parking mechanism is also conducted much less.

Using the parking mechanism of 7-speed dual clutch transmission as an example, this chapter analyzed the movement time difference between the parking pawl and the parking gear based on the kinematics theory. In addition, the rigid-flexible coupling multi-body dynamic model is established with ADAMS and Pro/e software and the peak impact load under high speed ratcheting was found by simulation. This load is taken as the input condition to conduct nonlinear finite element analysis on key components of parking mechanism with considering of material nonlinearity and contact nonlinearity, to verify the strength of parking mechanism components under high speed ratcheting. Through a combination of mechanics theory and kinematics simulation, the critical friction coefficient of key components is analyzed. Consequently, the self-locking safety performance of parking mechanism is validated, which can serve as a reference for the design of future parking mechanism.

2 Safety Performance Analyses for High Speed Parking Condition

The structural layout of the parking mechanism of a 7-speed dual clutch transmission is shown in Fig. 1. If the vehicle is traveling at high speed, the gear shift bar is placed in P position unintentionally the parking mechanism shall not engage with the vehicle drive system to prevent vehicle braking suddenly. There are two requirements for the parking mechanism: first, in the condition of high speed (normally above 8 km/h), the parking pawl and parking gear will not engage even the gear shift bar is placed in parking position [3, 4] and parking pawl will be flicked; second, when the parking pawl is flicked by the parking gear, the parking mechanism should withstand the impact load. The strength of parking mechanism components must be ensured.

2.1 Kinematics Theory Analysis of High Speed Parking Performance

During the shift process of the parking mechanism, the parking pawl rotates around the pivot shaft whilst the parking gear rotates differential shaft. The movement diagram of the parking pawl and the parking gear is shown in Fig. 2. The travel of

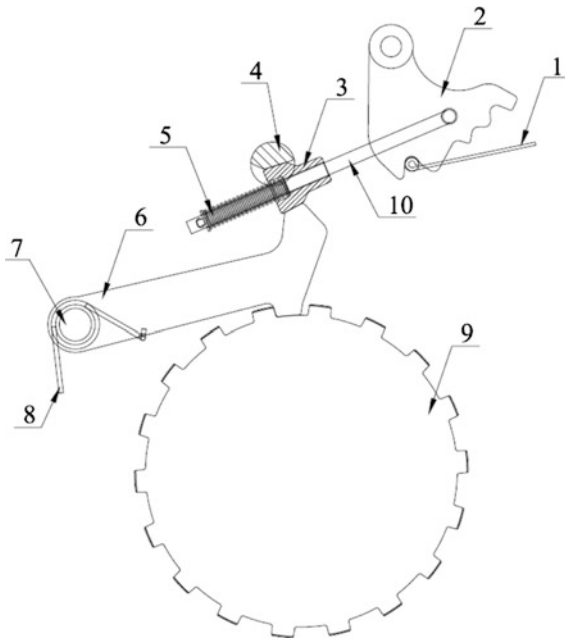


Fig. 1 Sketch layout of parking mechanism of 7-speed dual clutch transmission. 1 Detent spring, 2 Detent lever, 3 Cam collar, 4 Support pin, 5 Ratcheting spring, 6 Parking pawl, 7 Pivot shaft, 8 Torsion spring, 9 Parking gear

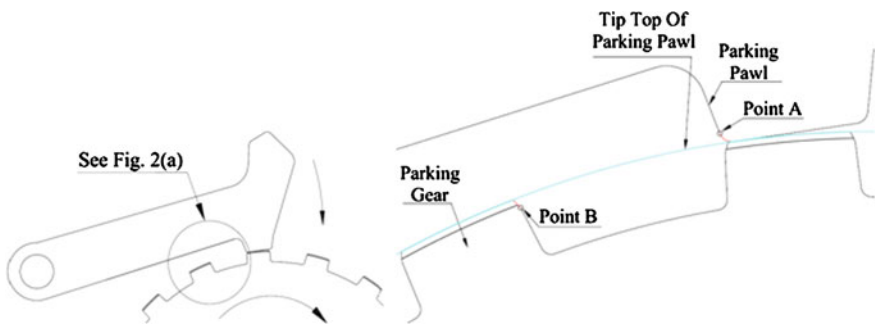
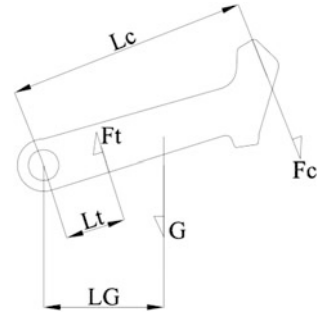


Fig. 2 Movement process of parking pawl and parking gear

parking pawl from top face of parking gear to the chamfer corner of parking gear is considered as the effective engagement of parking pawl and parking gear. As shown in Fig. 2a, i.e. if Point A of parking pawl moves to below Point B of parking gear, parking pawl and parking gear is engaged and vehicle is brake.

When the gear box T bar is shifted from R to P position, the forces acted on the parking pawl is as shown Fig. 3. Due to force F_c (from cam collar to parking pawl), the parking pawl has angle acceleration ε . The force balance equation is:

Fig. 3 Force analysis of parking pawl



$$F_c L_c + G L_G - F_t L_t = J \varepsilon \tag{1}$$

If the rotating angle of parking pawl is φ for it to engage with the parking gear, and the travel time of parking pawl is T_1 . Then,

$$T_1 = \sqrt{2\varphi/\zeta} \tag{2}$$

As the parking gear is connected to the differential shaft in the transmission, so the rotating speed of parking gear is the same as vehicle wheel speed. If the space of parking gear teeth is S_2 and vehicle speed is V_2 , and then it takes time T_2 to pass one space of parking gear. Thus,

$$T_2 = \frac{S_2}{V_2} \tag{3}$$

$\Delta = T_1 - T_2$. Δ is the difference of travel time between parking pawl and parking gear. When $\Delta > 0$, the parking pawl and parking gear could not engage effectively and the parking function could not be achieved by parking mechanism; when $\Delta < 0$, the parking pawl and parking gear could engage effectively and the parking function could be achieved.

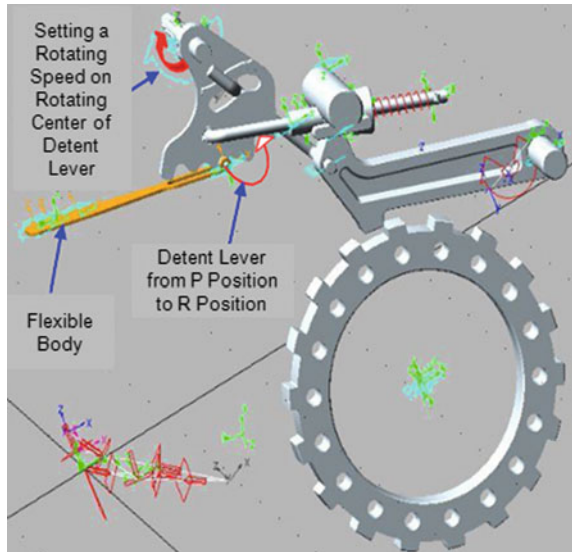
According to the analysis above, if vehicle runs fast with high speed of parking gear rotation, parking pawl would hit and slide on the top surface of parking gear and then the parking brake function cannot be realized. According to the calculation, the critical parking speed is 4 km/h. It means if vehicle runs at speed of over 4 km/h, then parking mechanism of 7-speed dual clutch transmission should not achieve the parking function. And in theory, this structure design of parking mechanism can satisfy the requirement of high speed parking performance.

2.2 Simulation Analysis of High Speed Parking Performance

2.2.1 Establishment of Dynamic Model

Rigid-flexible coupling multi-body dynamic model is established with software of ADAMS, Pro/e and HyperWorks [5, 6], in order to conduct kinematics simulation

Fig. 4 Dynamic model of parking mechanism



of impact load of parking mechanism in the condition of high speed. Taking R Position of parking mechanism as the initial position, a rotating speed on detent lever rotating center is set, the shift process is simulated, shift time is 0.5 s and the time of totally simulation is 20 s. According to the principle of kinetic energy conservation, the vehicle mass can be converted into equivalent moment of inertia on parking gear as shown at formula (4),

$$\frac{1}{2} J_e \omega^2 = \sum_{t=1}^n (m_t v_{st}^2 + j_{st} \omega_t^2) \tag{4}$$

where, ω is the angle speed of parking gear, n is the number of components, v_{st} is the velocity at the mass center, and the estimated equivalent moment of vehicle mass is 262.735 kg*m². And the dynamic model of parking mechanism is shown as Fig. 4.

2.2.2 Impact Load Analysis in High Vehicle Speed

A vehicle has two driving directions: reverse and forward. The impact load is analyzed for critical components, with vehicle speeds of 7, 10 km/h in reverse direction and speed of 7, 10, 15, 30, 60, and 100 km/h in forward direction. According to kinematics simulation, the peak impact load among key components (parking pawl, parking gear, cam collar and support pin) increases gradually with the increase of vehicle speed. The relationship between vehicle speed and peak impact load is shown as Fig. 5.

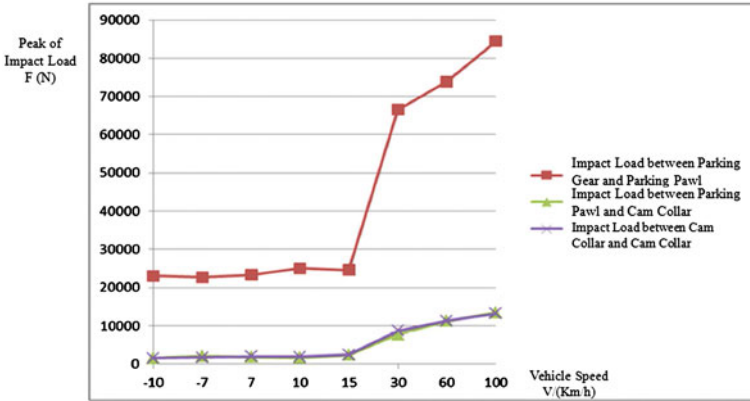


Fig. 5 Peak impact load among key components of parking mechanism

Table 1 Peak impact load among key components of parking mechanism

Vehicle speed (km/h)	Parking gear speed (rad/s)	Peak impact load (N)			
		Load between Parking pawl and parking gear	Load between parking gear and cam collar	Load between cam collar and support pin	
Reverse	-10	8.875	22697.78	2095.26	1549.73
	-7	6.212	23079.51	1539.48	1728.15
Forward	7	6.212	23372.51	1829.77	1982.65
	10	8.875	25051.25	2275.69	2088.49
	15	13.312	24597.03	2351.45	2394.65
	30	26.624	66520.65	7675.89	8720.60
	60	53.248	73866.31	11253.71	11262.17
	100	88.747	84442.43	13485.21	13221.56

In different vehicle speeds, the peak impact load of key components of parking mechanism is listed in Table 1.

2.3 Strength Check of Key Components in High Speed Condition

2.3.1 Method of Finite Element Contact Analysis

Working process of parking mechanism is one of contact issues. In order to solve this contact issue, the contact algorithm of enhancement Lagrange based on constraint is used to find out exact Lagrange multipliers, namely contact force. Enhancement Lagrange algorithm is a prolongation of penalty function [7], which

combines the advantages of Lagrange multiplier algorithm and penalty function algorithms. Penalty function algorithm is brought into Lagrange multiplier, thus, enhancement Lagrange algorithm can accurately meet constraint condition and ensure coefficient matrix of equation to be positive and definite. As a result, it can not only improve constringency of contact issue, but also can improve precision of penalty function [8].

2.3.2 Simulation of Parking Mechanism in High Speed Situation

For FEA (Finite Element Analysis), the worst peak impact load at 100 km/h vehicle speed is used as input. FEA is conducted for important component of parking mechanism. Heat treatment of all key components is tempered and carburized, with surface hardness approximately 60HRC and the core hardness 35HRC–45HRC. Thereby, combining the material non-linear, contact analysis is done on parking pawl, parking gear, cam collar and support pin. The detailed FEA results of these key components were shown in the Fig. 6.

The strength of contact surface will not be considered for distortion of contact load on contact surface. Compared the design strength with FEA result of parking mechanism components and it is shown in Table 2. At speed 100 km/h of impact loading condition, all key components of parking mechanism can meet the strength requirement.

3 Analysis of Self-Locking Performance of Parking Mechanism

3.1 Theoretical Analysis of Self-Locking Performance of Parking Mechanism

Assume the pulling out force from P position to R position with vehicle on slope is zero, self-locking performance of parking mechanism can be estimated. And the pulling out force of P position is decided by the forces between cam collar and support pin and parking pawl. In the condition of 30 % grade, force analysis of cam collar is shown in the Fig. 7 and calculation for the force is shown as formula (5):

$$TGS = \frac{1}{2} (2F_f \cos\theta - 2F_C \sin\theta) \quad (5)$$

Where, TGS is the pulling out force from P position to R position on the vehicle gears selector, F_c is the force between parking pawl and cam collar, F_f is the friction force, $F_f = \mu F_c$, μ is the coefficient of kinetic friction between these two components, θ is the design geometric angle and it is 5.4° .

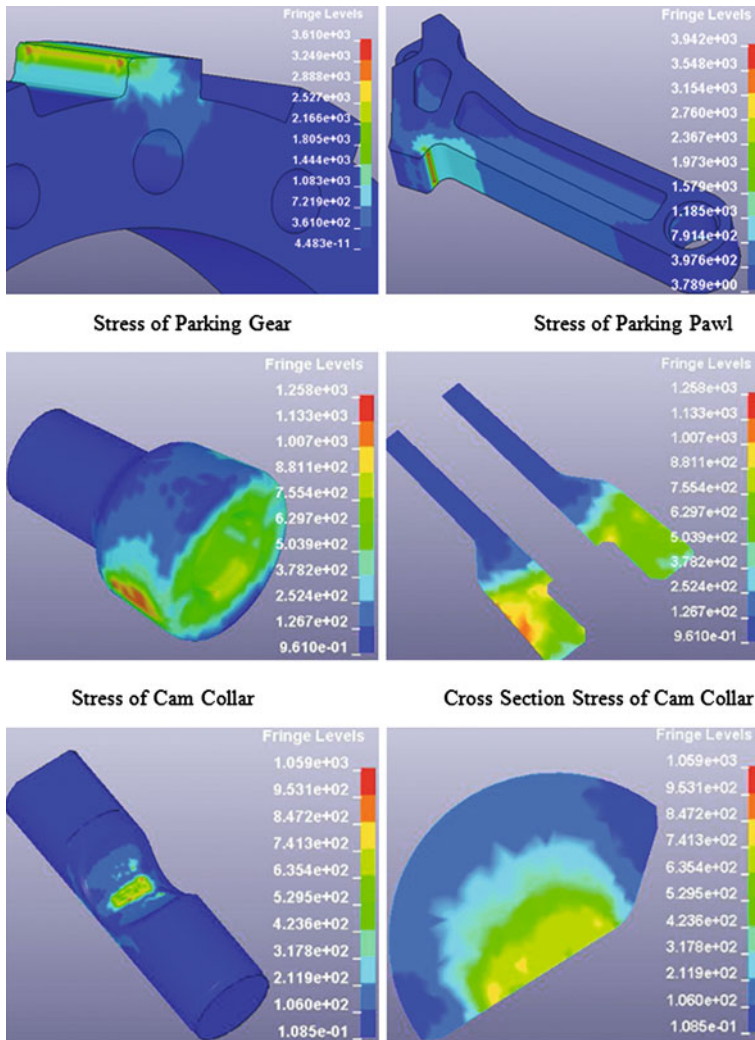


Fig. 6 FEA result of key components in parking mechanism

Table 2 Compare design strength with FEA results of key components in parking mechanism

Components	Design strength		FEA stress
	Design hardness of surface	Corresponding stress	
Parking gear	58 ~ 62HRC	2,400 MPa	2,200 MPa
Parking pawl			1,600 MPa
Cam collar			880 MPa
Support pin			635 a

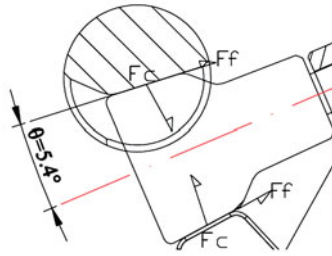


Fig. 7 Forces analysis of cam collar

Therefore, in order to achieve self-locking performance, the design coefficient of kinetic friction of parking mechanism in this 7-Speed dual clutch transmission should meet the requirement in formula (6),

$$\mu \geq \tan\theta \approx 0.1 \tag{6}$$

3.2 Self-Locking Performance Simulation Analysis

With P Position set as the initial position for parking mechanism of auto transmission, the similar rigid-flexible coupling multi-body dynamic model is established with ADAMS and Pro/e software, and the equivalent torque as vehicle mass is imposed on parking gear. During dynamical analysis, friction coefficient between cam collar and support pin and Parking Gear is reduced gradually, until cam collar moves, and then it can be considered the parking mechanism losing its self-locking function. Through simulating analysis, when static friction coefficient is set as 0.13 and 0.14 respectively, the relationship between displacement of cam collar L (mm) and simulation time t (s) is shown in Fig. 8.

From the result of simulation analysis, the critical static friction coefficient of self-locking performance is 0.14. Generally, kinetic friction coefficient is about 0.03–0.06 smaller than static friction coefficient, so the critical coefficient of kinetic friction is about 0.09, which complies with the result obtained by kinematics simulation and theoretical analysis.

According the above analysis, kinetic friction coefficient of this parking mechanism should be designed to 0.1. Thus, the surface roughness Ra between cam collar and parking pawl and support pin is all designed to 1.6, and then the self-locking safety performance of parking mechanism can be ensured.

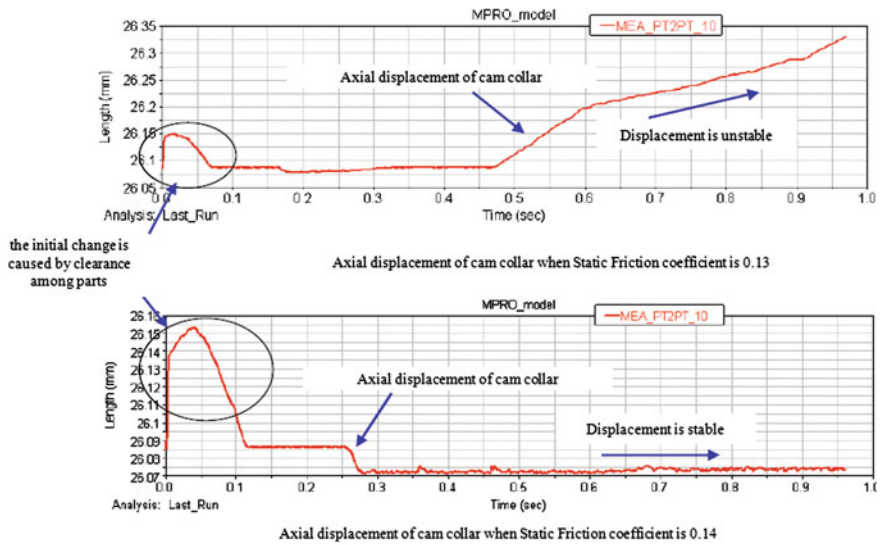


Fig. 8 Relationship between displacement of cam collar and simulation time

4 Conclusions

Firstly, according to the structural design of parking mechanism structure, the maximum parking speed is 4 km/h. Basing on the travel time difference between parking pawl and gear, a rigid-flexible coupling multi-body dynamic model is established with ADAMS software. The peaking impact loads among key components under different abuse R to P test speeds were obtained.

Secondly, the parking mechanism can satisfy safety requirement under worst abuse test speed of 100 km/h based on the FEA results of critical components under the peak impact load.

Thirdly, the critical kinetic friction coefficient of parking mechanism is analyzed by the two aspects of structure design and simulation of ADAMS software. The value of kinetic friction coefficient is approx. 0.1. According to these analysis results, the roughness of cam collar, parking pawl, support pin is designed to meet to insure self-locking safety performance of parking mechanism about 7-speed dual clutch transmission.

References

1. Salam Akanda MA, Reaz Ahmed S (2002) Stress analysis of gear teeth using displacement potential function and finite differences. *Int J Numer Meth Eng* 53:1629–1640
2. Kleemola J, Lehtovaara A (2007) Experimental evaluation of friction between contacting discs for the simulation of gear contact. *Tribotest* 13(1):13–20

3. Gabriel MG (1994) SAE transmission/axle/driveline forum committee. Design practices: passenger car automatic transmissions. Soc Automot Eng Inc 3:15–17
4. Lechner Gisbert, Naunheimer Harald (1999) Automotive transmissions [M]. Springer, New York, p 2
5. Guoqiang W, Jinping Z, Ruoding M (2002) Dummy sample technology and its application on ADAMS[M].Xi'an. Publishing Company Of Northwest Industry University, pp 10–14
6. Chen L, Ren W, Zhang Y (2005) Dynamic analysis of mechanical system and application tutorial of ADAMS [M]. Publishing Company of Qinghua University, Beijing, pp 52–62
7. Wangji C, Guoqing C (2007) Nonlinear complementarity model and nonsmooth algorithm about frictional contact problem. Scientific Annals
8. Bazaraa MS, Sherali HD, Shetty CM (1993) Nonlinear programming: theory and algorithms [M]. Wiley, New York

Control Strategy and Function Design Based on Lever Analogy

Hua Tian and Peng Chen

Abstract Lever analogy is very useful in analyzing gear-train including more than one planetary gear sets. The lever analogy is a translational-system representation of the rotating parts for the planetary gear. Applying lever analogy to GM 6T40E transmission, kinematic and dynamic analysis is shown in this paper. Model based shift control strategy is based on dynamic lever analogy. By setting target output torque and desired turbine speed profile, the clutch pressure and torque request to engine can be commanded. With more investigation on lever analogy, enhanced control strategy and new function are already invented.

Keywords Lever analogy · Planetary gear · Steady state analysis · Dynamic analysis · Shift control strategy

1 Introduction

For AT, planetary gear-set is always a complicated mechanism to analysis. Even we can build the right equation from the basic math model, the analysis is not flexible especially with different connection mechanism or working condition. With lever analogy, the planetary mechanism can be simplified. Steady state analysis is the primary usage of this method. Besides that, the control strategy can be designed based on lever analogy too. And with deeper understanding on lever structure, new function can be invented.

F2012-C02-019

H. Tian (✉) · P. Chen

Powertrain Department, Pan Asia Technical Automotive Center, Shanghai, China
e-mail: hua_tian@patac.com.cn

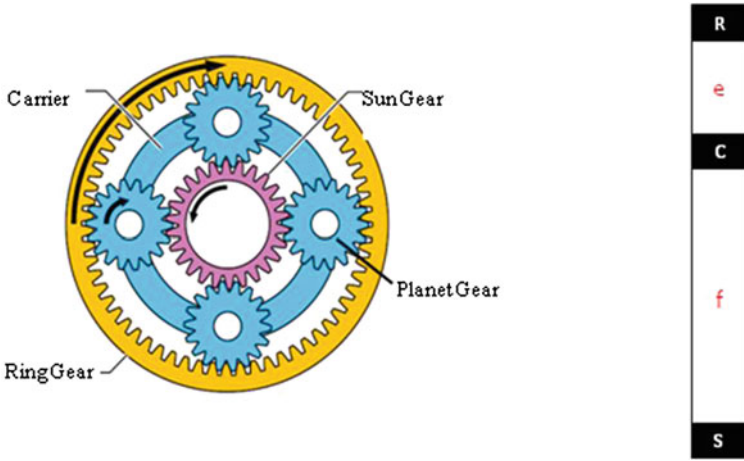


Fig. 1 Lever analogy of simple planetary gear set

2 Lever Analogy

Lever analogy is a translational-system representation of the rotating parts for the planetary gear. In the lever analogy, an entire simple or compound planetary gear train can be usually represented by a single vertical lever. The input, output and reaction torques are represented by horizontal forces on the lever. The lever motion, relative to the reaction point, represents rotational velocities.

A simple planetary gear set consists of sun gear, planet gear, ring gear and carrier. As shown in Fig. 1, it can be represented as a lever, which has 3 nodes. 3 nodes are sun gear (S), carrier (C), and ring gear (R). The distance between sun gear node and carrier node (f) represents the number of teeth on ring gear, and distance between ring gear node and carrier node (e) represents the number teeth on sun gear. The lever can be rescaled in the architecture with more than one simple planetary gear set.

With the lever, torques of rotating parts is analogous to force on nodes. Angular velocities of parts are analogous to linear velocities on nodes. Angular accelerations are analogous to linear accelerations on nodes. For each lever, it needs to be at balanced state with summary of force and torque to be zero.

3 Steady State Analysis

GM 6T40E is a six-speed clutch-to-clutch automatic transmission. It consists of 3 sets of simple planetary gear architecture [1]. Figure 2 shows the cross section. For multiple planetary gear sets, the lever can be rescaled based on some basic rules. The relative relationship between each node of one lever should not be changed

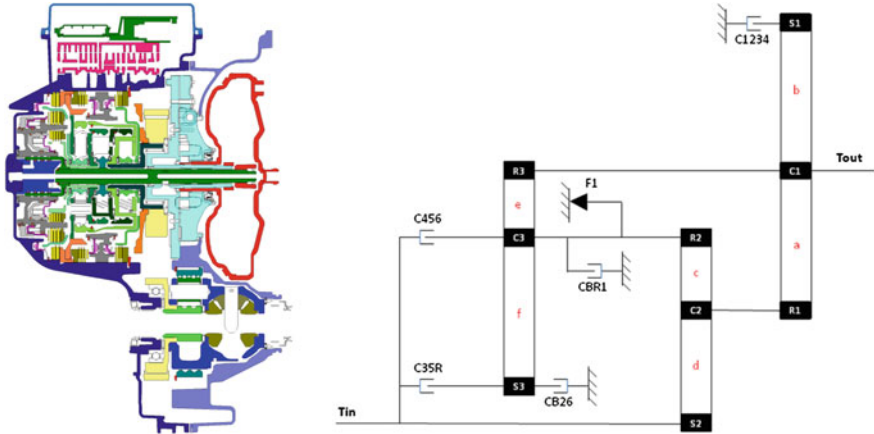


Fig. 2 Cross section and lever analogy of 6T40E

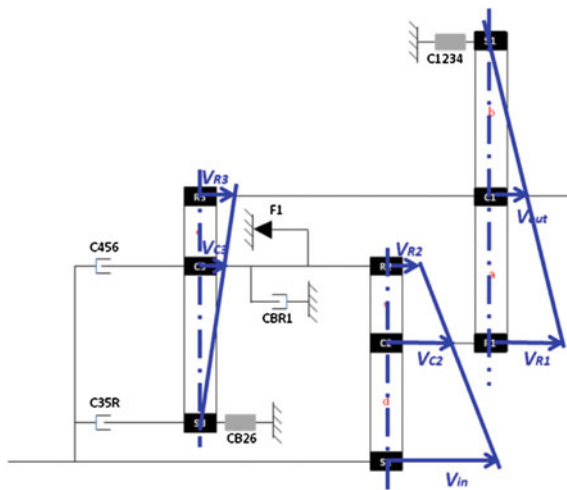


Fig. 3 Rotating speed analogy

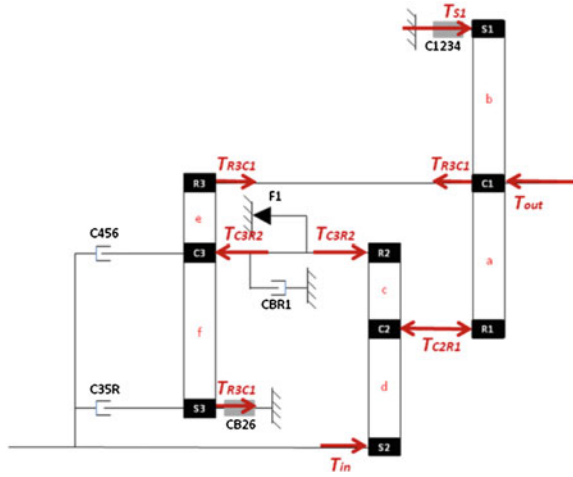
although the length can be rescaled. Also, the distance between same parts should be same at different lever. Based on these rules, the lever analogy is built as shown in Fig. 2.

Taking second gear as example, Figs. 3 and 4 show the kinematic and dynamic status for each node and lever. Figure 3 is used to calculate the rotating speed. Figure 4 is used to calculate torque.

Based on Fig. 3, equations can be built as below:

$$V_{out} = V_{R3}$$

Fig. 4 Torque analogy



$$V_{out}/V_{R1} = b/(a + b)$$

$$V_{C3}/V_{R3} = f/(e + f)$$

$$(V_{C2} - V_{R2})/(V_{in} - V_{R2}) = c/(c + d)$$

$$V_{C3} = V_{R2}$$

$$V_{C2} = V_{R1}$$

Then, gear ratio of second gear is calculated as:

$$\frac{V_{in}}{V_{out}} = \left(1 + \frac{d}{c}\right) \left(\frac{a+b}{b} - \frac{f}{e+f}\right) + \frac{f}{e+f} = 2.964$$

Based on Fig. 4, equations can be built as below:

$$(T_{out} + T_{R3C1}) \times b = T_{C2R1} \times (a + b)$$

$$T_{C2R1} \times c = T_{in} \times (c + d)$$

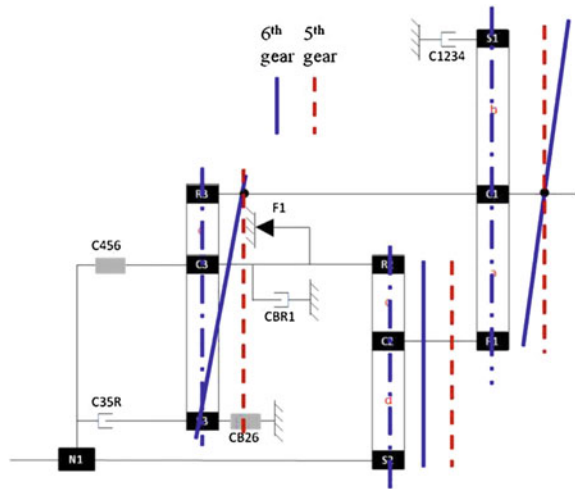
$$T_{R3C1} \times (e + f) = T_{C3R2} \times f$$

$$T_{C3R2} \times c = T_{in} \times d$$

Then, torque ratio of second gear is calculated as:

$$\frac{T_{out}}{T_{in}} = \frac{(a + b) \times \frac{c+d}{c} - \frac{d}{c} \times b \times \frac{f}{e+f}}{b} = 2.964$$

Fig. 5 Rotating speed analogy



4 Dynamic Analysis and Shift Control Strategy

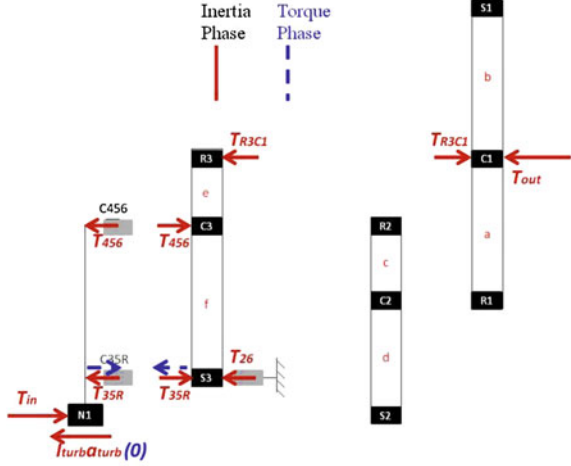
During shift, some clutches are controlled to have slip. The torque it carries is decided by the pressure on clutch plates, relative rotating speed, and the power flow status of whole system. At the same time, rotating speed makes inertia have impact on the shift process. So, dynamic analysis is more complicated. This paper will take power on downshift from 6th gear to 5th gear as example. Compared to other rotating parts, input shaft related inertia is much bigger. To simplify the calculation, only the input shaft related inertia is taken into consideration.

An idea shift process is separated into inertia phase and torque phase. During inertia phase, clutch is controlled to slip and achieve the target speed ratio. Torque transfer between different clutches is accomplished in torque phase. Figures 5 and 6 show the lever analogy during shift.

4.1 Inertia Phase

During inertia phase, one clutch named as offgoing clutch is controlled to slip. Turbine speed is increasing with the clutch slip. In this phase, inertia torque needs to be considered.

Fig. 6 Torque analogy



$$\begin{aligned} \sum F_1 = 0 &\Rightarrow T_{R3C1} - T_{out} = 0 \Rightarrow T_{out} = T_{R3C1} \\ \sum M_{C3} = 0 &\Rightarrow T_{R3C1} \times e - T_{26} \times f + T_{35R} \times f = 0 \Rightarrow T_{R3C1} = (T_{26} - T_{35R}) \times \frac{f}{e} \\ \sum M_{R3} = 0 &\Rightarrow T_{456} \times e + (T_{35R} - T_{26}) \times (e + f) = 0 \Rightarrow T_{456} = (T_{26} - T_{35R}) \times \frac{e+f}{e} \\ \sum F_{N1} = 0 &\Rightarrow T_{in} - I_{turb} \times a_{turb} - T_{456} - T_{35R} = 0 \Rightarrow a_{turb} = \frac{T_{in} - T_{456} - T_{35R}}{I_{turb}} \end{aligned}$$

Then we have:

$$T_{out} = (T_{26} - T_{35R}) \times \frac{f}{e} \quad a_{turb} = \frac{T_{in} - \frac{e+f}{e} \times T_{26} + \frac{f}{e} \times T_{35R}}{I_{turb}}$$

4.2 Torque Phase

When it goes into torque phase, clutch C35R changed the relative rotating speed. As a result, the direction of torque will change. In torque phase, the speed ratio of target gear has been achieved. Within the short time of shift, we can deem vehicle speed as constant. Equations are built as:

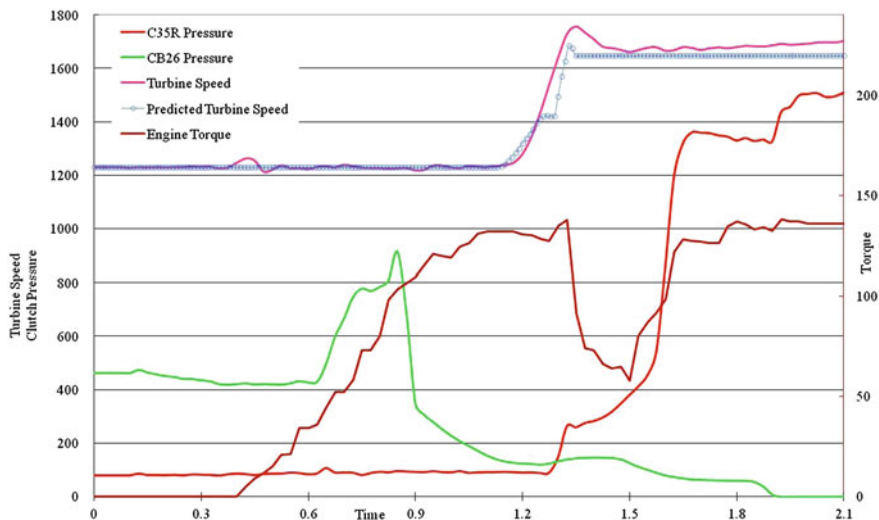


Fig. 7 Predicted turbine speed by lever analogy

$$\sum M_{R3} = 0 \Rightarrow T_{456} \times e - (T_{35R} + T_{26}) \times (e + f) = 0 \Rightarrow T_{456} = (T_{26} + T_{35R}) \times \frac{e+f}{e}$$

$$\sum F_{N1} = 0 \Rightarrow T_{in} - T_{456} + T_{35R} = 0 \Rightarrow T_{in} = T_{456} - T_{35R}$$

$$\sum F_1 = 0 \Rightarrow T_{R3C1} - T_{out} = 0 \Rightarrow T_{out} = T_{R3C1}$$

$$\sum F_3 = 0 \Rightarrow T_{456} - T_{35R} - T_{26} - T_{R3C1} = 0 \Rightarrow T_{456} = T_{35R} + T_{26} + T_{R3C1}$$

Then we can get:

$$T_{in} = \frac{e+f}{e} \times T_{26} + \frac{f}{e} \times T_{35R}$$

$$T_{out} = \frac{f}{e} \times T_{26} + \frac{f}{e} \times T_{35R}$$

Model based control strategy is based on those equations [2]. By setting the target output torque and desired turbine speed profile, the expected clutch torque and input torque can be calculated. Then clutch pressure and torque request to engine is commanded.

To check how accurate the model strategy is, we did some tests in the car. An imperfect shift is picked to be investigated. For this shift, the lever analogy would be more complicated because speed change is not finished by the end of inertia phase, which means inertia torque needs to be considered in torque phase. And the torque would change based on relative rotating speed. Using collected clutch real pressure and engine torque, turbine speed can be calculated by the lever analogy. Figure 7 shows the trace. We can see the flare exist in torque phase. And the predicted turbine speed by lever analogy model is very sensitive to show that.

5 Conclusion

Lever analogy is very useful for gear-train analysis especially more than one planetary gear sets. It is a good tool for analysis and design. As shown in this paper, it can be used for steady state and dynamic analysis. It is also used in control strategy design like model based control strategy in 6T40E. With more investigation with this method, an enhanced control strategy on power on down-shift is developed by GM and started to be implemented. Based on the lever analogy, a hill-hold function is proposed by author and in the patent process.

References

1. Lewis C, Bollwahn B (2007) General motors hydra-matic & ford new FWD six-speed automatic transmission family. SAE, 2007-01-1095
2. Marano JE, Moorman SP, Whitton MD, Williams RL (2007) Clutch-to-clutch transmission control strategy. SAE, 2007-01-1313

Research on Precision Forging Tooth Billet of Driven Bevel Gear

Baoyang Song, Chenglin Xu, Chenglin Fu, Zhuang Fu, Guansheng Wang, Shibao Liu, Zhaodan Yuan, Xiaohui Li and Xinghua Li

Abstract This paper researched on the driven bevel gear 344. We used the precision forging process instead the traditional tooth processing of rough milling, studied the truck driven bevel gear tooth precision forging process and the precision forging die structure, developed the driven bevel gear tooth electrode shaping and the electrode tooth mold manufacturing methods.

Keywords Driven bevel gear · Tooth billet · Precision forging technical · Tooling

1 Introduction

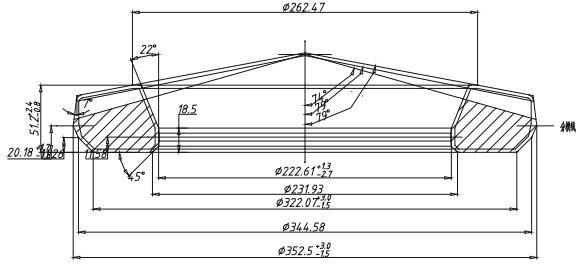
In recent years, the precision forging technology was more and more widely used in the automotive industry because of its own characteristics. It especially played an important role in lowering production costs and improving product quality. The tooth surface of driven bevel gear for heavy trucks is now commonly produced by rough milling after making ordinary forging blank and then fine milling (or pull teeth), with low productivity and high material consumption. Because of the stress during the machine grinding of teeth-shaped and notching, the deformation during

F2012-C02-021

B. Song (✉) · C. Xu · C. Fu · Z. Fu · G. Wang · S. Liu · Z. Yuan
FAW R&D Center, Changchun, China
e-mail: songbaoyang@rdc.faw.com.cn

X. Li · X. Li
FAW JIEFANG Automotive Company, LTD, Changchun, China

Fig. 1 Figure of the rough of precision forging gear blank



heat treatment is difficult to control, which affects the gear tooth accuracy after the heat treatment. In addition, a large amount of metal flow lines of parts is cut off during the machine cutting tooth. It leads to the lower part strength. Processing methods using precision forging tooth to replace the rough milling alveolar can improve production efficiency and part quality, while also reducing the cost of parts manufacturing.

2 The Design of Process

The project uses a combination technology program of experiment and numerical simulation analysis. Process: Cutting—heating—upsetting—punching—reaming—precision forging on friction press—normalizing—machining—carburizing—machining after heat treatment.

2.1 Design of Forgings Figure

According to GB12361-2003 and GB12362-2003, we determine the parting surface and the machining allowances and tolerances of precision forging rough.

Considering the factors of subsequent fine milling, the uneven shrinkage after forging and normalizing deformation, etc., the tooth side margin was decided for 0.5 mm (unilateral), and the others was 1.5 mm. Forging diagram as shown in Fig. 1.

2.2 Calculation of Open Forging Crack Force

Theoretical formula [1]

$$P = \alpha(2 + 0.1 \frac{F\sqrt{F}}{V_F})\sigma_b F = 2907 \text{ ton}$$

Fig. 2 Tooth surface points cloud data of the driven bevel gear 344



In the formula:

- P nominal pressure;
- α related to the coefficient and forging, $\alpha = 4$ at open die forging and $\alpha = 5$ at closed die forging;
- F the projected area of the forging in the plane;
- VF forging volume;
- σ_b tensile strength of the metal at final forging

Approximate formula: [2]

$$P = (9.5 \sim 10) \sigma_b F_F = 2275 \text{ ton}$$

In the formula:

- P the pressure of the screw press;
- σ_b tensile strength of the metal at final forging;
- FF the projected area on the horizontal die surface of the forging.

Through the above calculation, forging tonnage of 1600 tons friction press (available with borrowed equipment) was insufficient. So we needed to form reaming blank. The under voltage calculation should be fully considered when design forging die cavity.

2.3 Design of Tooth Profile

The tooth surface data “point cloud” generated by Kimos was the basic to form the electrode. The accuracy of the gear tooth shape electrode was ensured when processing it by the machining center. They were shown in Figs. 2, 3 and 4.

Fig. 3 NURB tooth surfaces of the driven bevel gear 344

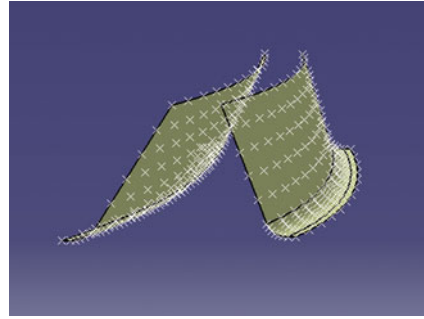


Fig. 4 Gear model of the driven bevel gear 344

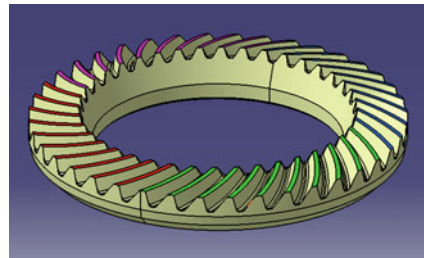


Fig. 5 The upper forming die

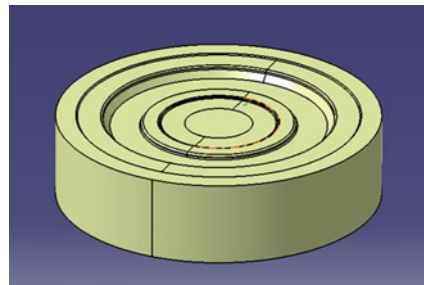
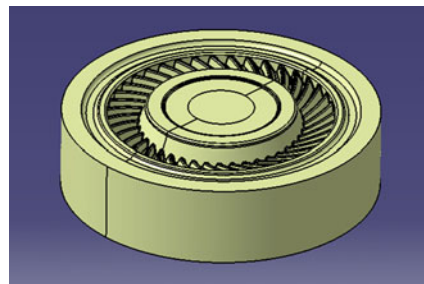


Fig. 6 The lower forming die



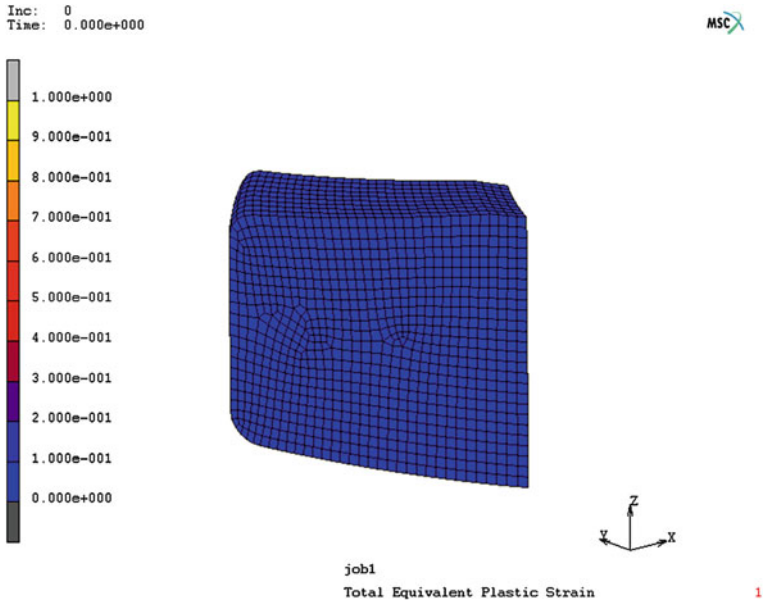


Fig. 7 Total equivalent plastic strain of billet state

3 Finite Element Analysis

3.1 Model of Finite Element Analysis

Figs. 5 and 6

3.2 Quantitative Analysis of the Forming Process

As shown in Figs. 7 and 8, we made quantitative analysis of the forming process of the driven bevel gear 344 with MSC.Marc. We only did process analysis calculation of one tooth because of its rotation cycle structure.

Analysis of simulation results:

Through the forming simulation, we knew that the effect of tooth filling was good. The forming load was about 3048t. The rolling ring billet size and the die structure were optimized according to the simulation.

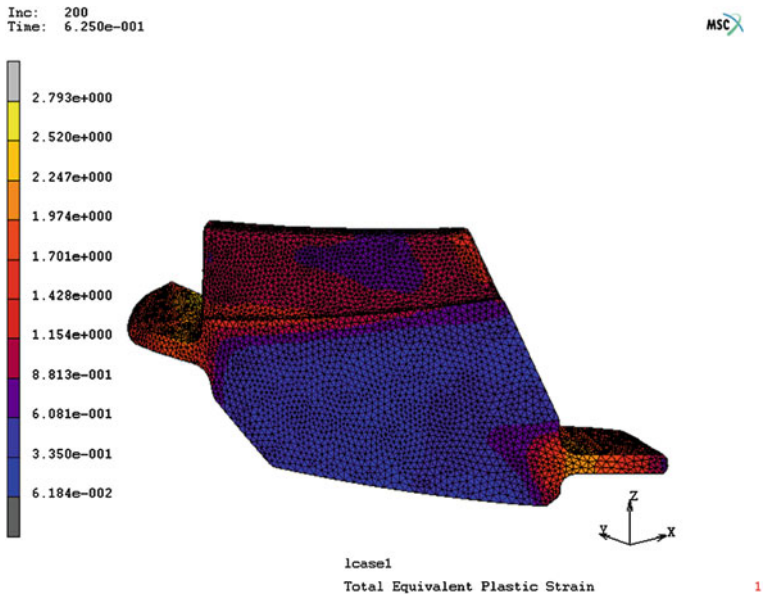


Fig. 8 Total equivalent plastic strain after forming

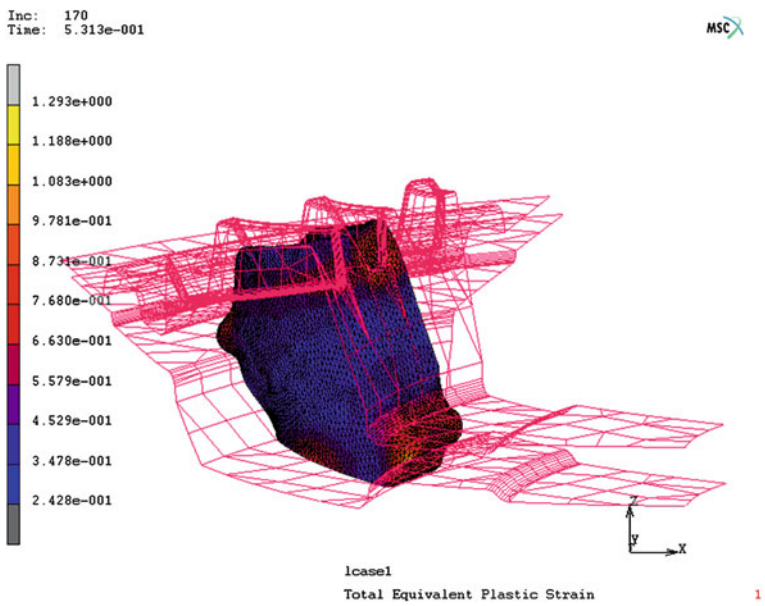


Fig. 9 Total equivalent plastic strain of intermediate state

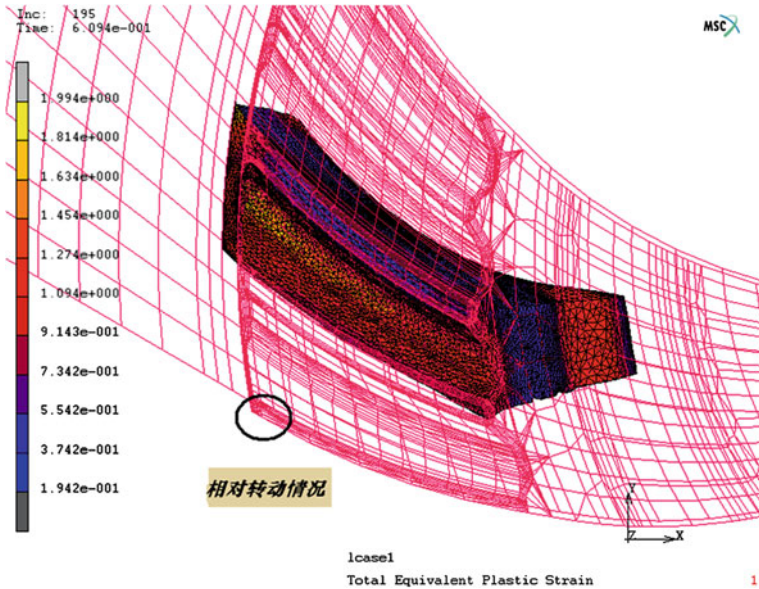


Fig. 10 Rotation of the mold in the molding process

3.3 Simulation of the Tooth Die with the Circumferential Direction Free

During the forming process, there was circumferential current trend about the metal because of the presence of the tooth helix angle. There must be circumferential thrust on the tooth mold must be the role of weeks to, which will affect the mold strength, life, and even part accuracy. The simulations were shown in Figs. 9 and 10.

The above analysis showed that using the floating punch could reduce the forming load to a certain extent. It could be seen that we could design a punch with free circumferential spin, which was beneficial for improving the life of the die and reducing the forming force. The technology had been patented.

4 Mold Design and Manufacturing

4.1 Design of Mold Structure

Because the tonnage of forming equipment was less than that used in the experiment, we considered a 1 mm undervoltage during the design of the final forging die bore. Due to the presence of the driven bevel gear arc tooth helix angle, there

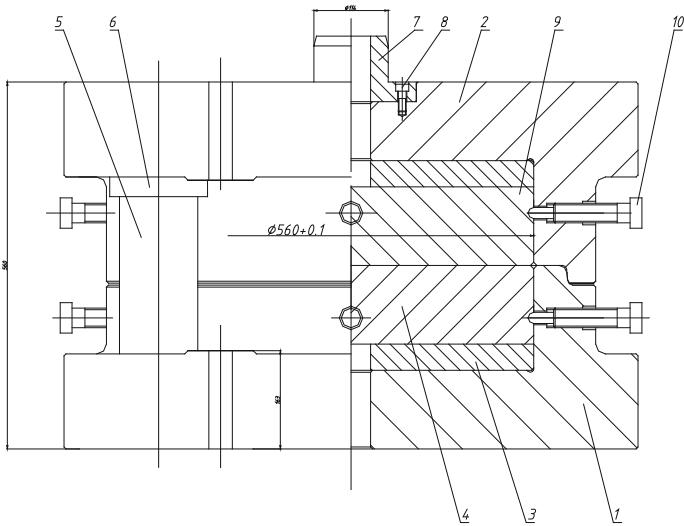


Fig. 11 Mold structure diagram

Fig. 12 Mold electrode processed by the machining center

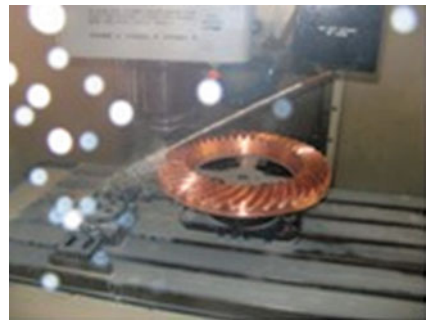


Fig. 13 Tooth cavity processed by EDM



Fig. 14 Precision forging



Fig. 15 Appearance of cold forging



was larger tangential force on the mold tooth site. So we designed the institutions of the tooth mold rotation in order to ensure the strength of the mold tooth parts. The mold was shown in Fig. 11.

4.2 Processing of Tooth Mold

We processed the mold electrode using the machining center. The technical characteristics of it was that we could modified the root of the tooth, which could ensure that the tooth root of the gear blank after the precision forging was no longer processing in the subsequent fine milling process. In addition, the tooth part could be modified according to the need.

First, we processed tooth electrodes using a machining center as shown in Fig. 12. The accuracy of the tooth electrode was grade 7 (DIN3965). Then the tooth cavity was processed by EDM. The tooth mold after processing was shown in Fig. 13.

Table 1 Machining accuracy of face bore (mm)

Gear	1#	2#	3#	4#	5#
Face flatness	0.037	0.032	0.023	0.047	0.042
Internal roundness	0.011	0.008	0.013	0.008	0.01

Fig. 16 Precision of forging gear billets (positioning surface after processing)

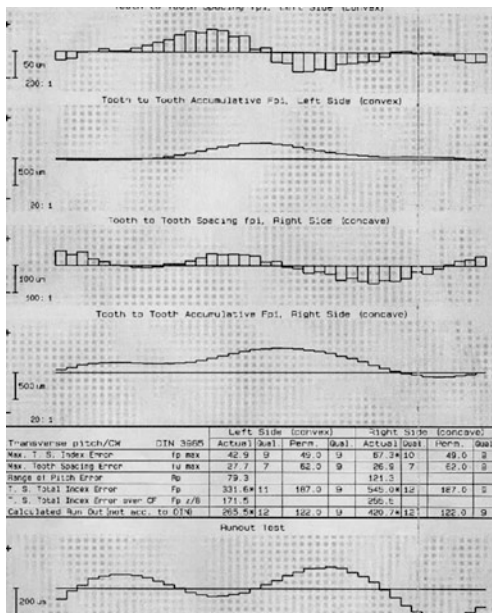


Fig. 17 Tooth appearance of forged gear billet

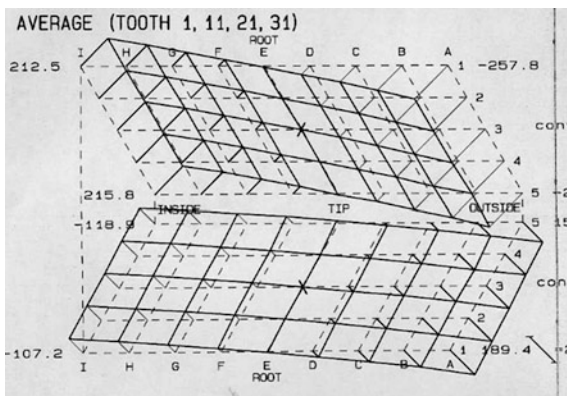


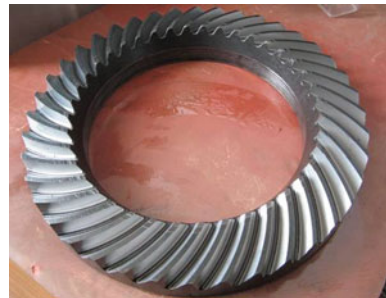
Table 2 Precision of precision forging gear billets (μm) DIN3965

Part number	Convex		Concave				
	fp	fu	Fp	fp	fu	Fp	Fr
1#	119.6	186.1	381.9	34.1	25.9	200.1	365.8
2#	60.3	63.4	385.8	44.8	30.4	294.4	254.6
3#	93.1	122.3	554.1	69.7	46.8	374.9	224.9
4#	94.1	128.1	616.2	39.8	43.4	262.7	375.9
5#	78.3	55.3	522.3	36.1	37.8	244.1	309.4
Corresponding accuracy of grade 11	126	159	478	126	159	478	240

Table 3 Error of helix angle and pressure angle (deg)

Part number		Pressure angle	Helix angle
		1#	Convex
	Concave	0.207	0.34
2#	Convex	0.026	0.500
	Concave	0.195	0.421
3#	Convex	-0.064	0.584
	Concave	0.308	0.37
4#	Convex	-0.086	0.534
	Concave	0.443	0.361
5#	Convex	0.041	0.523
	Concave	0.253	0.315

Fig. 18 The driven bevel gear 344 in the fine milling before heat treatment



5 Forging Process

Experimental equipment: Furnaces—750 kg air hammers—400 reaming machine—1600-ton friction press

Experimental material: 20CrMnTiH

Billet Size: $\Phi 130 \times 180$: 18.75 kg

Heating temperature: 1200 ± 50 °C

Forming process: heating—upsetting—punching—(heating)—reaming—forging. The test processes were shown in Figs. 14 and 15.

Fig. 19 Precision after the fine grinding of teeth

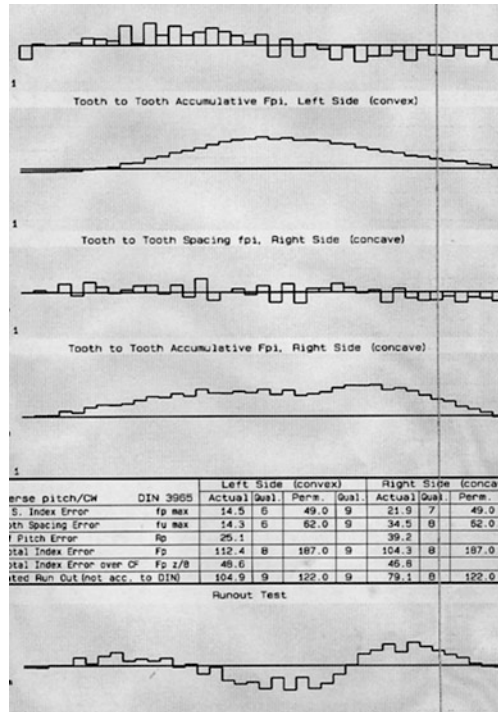
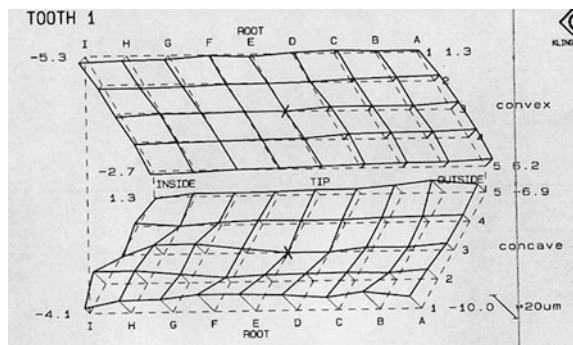


Fig. 20 Tooth appearance after grinding of teeth



Test results and analysis of the forging: As a result of three strikes forged and the mold release and cleaning up the oxide after one hit, the tooth surface of the gear billets and the situation of filled with were good. The forging structural dimensions were satisfactory addition to the thickness, which was ultra-poor about 2.5 mm because the devices forming pressure was insufficient.

Table 4 Accuracy of precision forging gear after finishing before heat treatment (μm) DIN3965

		2#	6#	Corresponding accuracy of grade 7
Maximum error of single pitch (μm)	Convex	16.3	17.1	22
	Concave	33	27.3	
Adjacent pitch error (μm)	Convex	22	29.9	28
	Concave	52.8	38.9	
Accumulated pitch (μm)	Convex	44.9	43.4	83
	Concave	95.4	68	
Ring gear beat (μm)		78.3	78.5	62
Internal roundness		0.01	0.009	
The flatness of the back		0.043	0.041	

Fig. 21 The driven bevel gear 344 after carburizing



6 Subsequent Machining and Detection of Precision

6.1 Processing Reference Plane and the Hole in Tooth Positioning

The testing situation was shown in Table 1.

6.2 Accuracy Assessment of Precision Forging Gear Billets

Upon completion of the positioning face and hole processing, measurement and evaluation data of the forging gear billets were shown in Figs. 16, 17, Tables 2 and 3.

Analysis of test data:

Precision was assessed in accordance with DIN3965. The accuracy of single pitch was grade 7 while the cumulative accuracy was about grade 11 and the diameter jump accuracy of ring gear was grade 12. Margin detection of tooth thickness was in parts of the midpoint of the tooth surface. The test results showed that the control of each gear margin was basically the same, was about 1.1 mm (both sides).

Table 5 Accuracy of precision forging gear after heat treatment (μm)DIN3965

		2#	6#	Corresponding accuracy of grade 8
Maximum error of single pitch (μm)	Convex	19.5	22.8	31
	Concave	37.7	35.5	
Adjacent pitch error (μm)	Convex	22.3	28.9	39
	Concave	43.8	65.3	
Accumulated pitch (μm)	Convex	109.2	103.5	117
	Concave	168.6	131.1	
Ring gear beat (μm)		172.9	112.1	87
Internal roundness		0.039	0.044	
The flatness of the back		0.238	0.081	

6.3 Fine Milling the Tooth

We processed the teeth with the Gleason 600 HC gear cutting machine pole forming method. Hardness after normalizing of the gear billet was 156-176HB.

Gear after fine milling was shown in Figs. 18, 19, 20 and Table 4.

6.4 Change of Gears Precision Before and After the Heat Treatment

Precision: Without preparing the corresponding fixture, there was no pressure quenching during the heat treatment process, which resulted in different degrees of loss of accuracy about roundness of the positioning surface and flatness of the end face. As a result, the tooth pitch cumulative precision and ring gear diameter jump accuracy had decreased, the general precision was about grade 9 after heat treatment, with an average accuracy loss of 2 grade. The single pitch accuracy changed little. We could see them in Fig. 21 and Table 5.

Tooth appearance: Tooth appearance after heat treatment changed little. The helix angle decreased about 0.01° , while the pressure angle had an increase of 0.05° .

7 Conclusion

1. The test proved that the modeling of the hot precision forging driven bevel gear tooth billet was accurate, the mold method is feasible and the margin of tooth side was reasonable. The technology was: efficient with material savings, the metal flow line of the driven gear was reasonable, the heat deformation was small, and the intensity was high. Compared with the ordinary forging process,

precision forging process of the driven bevel gear could save 13 min/piece, and 3.6 kg materials/piece.

2. According to DIN3956, the accuracy of the tooth electrode processed by the machining center was 7 grade. In addition to the ring gear beating was 12 grade, the other accuracies of tooth precision forging billet were all less than 10 grade.
3. The accuracy loss of the tooth precision forging billet after fine milling that was heat treated deformation under the pressure quenching conditions was quite with the full-cut gear under pressure quenching.
4. Through the experiment, we knew that the tooth surface of the precision forging driven bevel gear tooth billet had a hard layer, which influenced the life of the fine milling cutters.

References

1. Juzhan X, Fenglin H, Yiping Z (2003) China mold design ceremony. Nanchang: Jiangxi Science and Technology Press
2. Chenggong L (1989) Forging technology handbook. Beijing: National Defense Industry Press

Schaeffler Lightweight Differentials

A Family of Differentials Reduced in Space and Weight

Thorsten Biermann, Xiaogang Chang and Bernd Robert Höhn

1 Preface

In addition to improving the efficiency of individual drive train components and making energy conversion more efficient, reducing the weight of a transmission is essential for saving fuel while improving driving dynamics. Considerable success in weight reduction has been achieved in the past by using more efficient materials, but no major improvements have been made in differential technology. The most common axle differential design continues to be a bevel gear differential. Due to the high component loads, this design does not allow weight reductions by replacing materials.

Schaeffler's lightweight differential offers a solution that combines low weight and cost efficiency with remarkable design space reduction. This move away from conventional bevel gear differential designs toward spur gear differentials provides opportunities for integrating innovative design ideas and state-of-the-art manufacturing technology.

This paper discusses of the possibilities of lightweight differentials, beginning with a description of the design and the function of these differentials. This is followed by a comparison with conventional bevel gear differentials, specifically with regard to weight and space reduction for various torque classes.

F2012-C02-022

T. Biermann (✉)

Schaeffler Technologies AG & Co. KG, Herzogenaurach, Germany
e-mail: hui.su@schaeffler.com

X. Chang

Schaeffler Trading (Shanghai) Co., Ltd, Shanghai, China

B. R. Höhn

FZG München, München, Germany

Fig. 1 Spur gear differential
by FZG Munich



2 Introduction

2.1 History

The present developments are based on a research project that was initiated by the FZG Munich in 2002. The purpose of the research project was to develop a spur gear differential that is more compact and lighter than conventional bevel gear differentials (see Fig. 1).

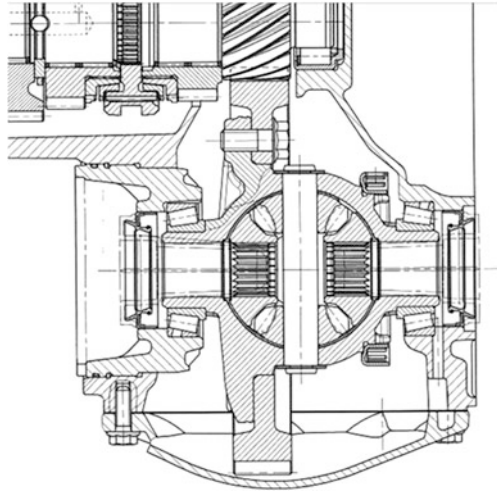
Industry partners in the project were General Motors Powertrain -Germany GmbH in Rüsselsheim and Schaeffler KG in Herzogenaurach. During the project, Prof. Dr.-Ing. Bernd-Robert Höhn of FZG Munich supervised the setup and testing of prototypes on test stands and in vehicles [1].

Successful vehicle tests with this first spur gear differential led Schaeffler to continue its development work with the goal of offering a solution for large-volume production.

In this new differential design, the main focus was initially on manufacturing aspects and on the optimization of production costs while allowing for greater design space requirements compared to the spur gear differential developed by FZG. However, now that some development cycles have been completed, this differential designed for large-volume production is on a par with FZG's original design.

Besides new gear teeth designs that were developed in cooperation with FZG, the consistent use of Schaeffler's core expertise for cold-forming sheet steel played a major role because its design and structure ensures a high level of rigidity for the differential housing. The housing design was developed based on current planet carriers in conventional automatic transmissions that use similar technologies.

Fig. 2 Standard final drive with bevel gear differential



Their design was optimized in the past to further increase the power density of the relevant transmissions.

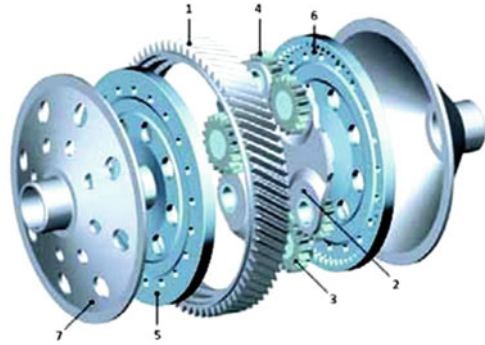
2.2 State of the Art

As mentioned at the start, bevel gear differentials are used in most final drive units in motor vehicles (see Fig. 2). The design of the bevel gear differential offers flexibility and the opportunity of combining different drive gears.

On a front-wheel drive vehicle with an engine mounted transversely at the front, the drive is introduced via a spur gear, which transfers the torque to the differential cage. On rear-wheel drive vehicles or vehicles with front-wheel drive and an engine mounted longitudinally at the front, a hypoid gear is usually used instead of a spur gear. The differential cage transmits the torque to a pinion shaft on which the differential pinions are mounted. These differential pinions, together with the axle drive bevel gears, form the gear teeth of the differential. There are two gear teeth contacts in the flow of force from axle to axle with a stationary gear ratio of $i_0 = -1$.

Torque is distributed via the differential pinions to both axle drive bevel gears. Two differential pinions are normally used. The differential cage is usually a single-piece, solid cast design. Openings in the differential cage enable the differential pinions and the axle drive bevel gears to be assembled from the side. It is possible to increase the number of differential pinions in order to enable the transmission of higher axle torques. The loads in the individual tooth contacts are reduced by these measures. The differential pinions and axle drive bevel gears are arranged spatially in a spherical housing. The contact surfaces between the

Fig. 3 Exploded view of the spur gear differential by FZG



bevel gears and the housing are also usually spherical. In most applications, the axle drive bevel gears and differential pinions are manufactured as forgings in a tolerance range of IT9 to 11.

3 Spur Gear Differential by FZG

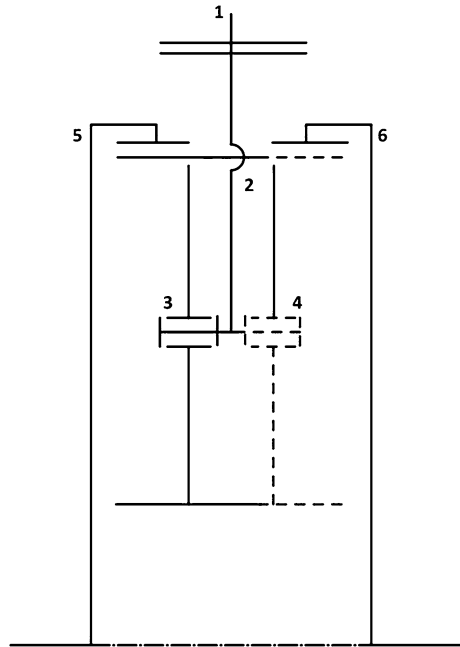
3.1 Concept

The spur gear differential concept is at least as old as the bevel gear differential. The author has, amongst other things, an extract from a specialist American book with the title “Self-Propelled Vehicles” from 1911, which contains a detailed report about spur gear differentials [2] Fig. 3.

According to Müller [3], the spur gear differential concept by FZG is a reversing transmission with a stationary gear ratio $i_0 = -1$. The torque is introduced via the drive gear (1) and a center bar (2) on which pinions or planet gears (3, 4) are arranged in pairs Fig. 4.

The pinions (3, 4) of a pair mesh with each other across part of their gear tooth width. One pinion (3, 4) of each pair is also geared with the left, internal-gear output wheel (5); the other is geared with the right, internal-gear output wheel (6). The objective of this arrangement is to minimize the loads in the gear teeth contact, especially the tooth flank pressures between the pinion and the internal-gear wheel, by a suitable pairing of the internal and external gear teeth. Furthermore, the point of contact between internal-gear wheels (5, 6) and planets (3, 4) is on a larger pitch circle compared to other differential designs, which leads to lower circumferential forces in the differential gear teeth [4] for the same total wheel torque.

Fig. 4 Transmission diagram of FZG spur gear differential



3.2 Advantages of the Compact Differential Design

The lower gear teeth forces compared to a bevel gear differential enable an extremely narrow gear teeth contact, which allows the design space and weight to be reduced compared with a bevel gear differential. According to Heizenröther [4], the reduction in weight is approximately 17 % compared with a conventional bevel gear differential. The possibilities resulting from the reduction in the spacing between the semi-locating bearings are also of interest. Normally, the design space of the differential infringes the clutch housing space. The radial dimensions of the clutch are only limited by the differential housing. This leads to problems especially with two-shaft transmissions if additional design space is required for the clutch. An increase in the length of the transmission is then often unavoidable.

Double clutch transmissions are currently presenting engineers with new challenges. The design space required by the clutch system is also making engineers rack their brains here, too. Particularly as the performance capability of these new transmissions depends significantly on the clutch.

Further areas of application can be developed from integrating additional functions in the spur gear differential, for example, switchable accessory drives or also center differentials. In this way, standard transmissions can be equipped with additional functions relatively cost effectively and contribute to more efficient design of the drive train.

Ultimately, at least part of the gained design space can be used for optimizing the bearing positions. The reduced bearing spacing has not proven to be a disadvantage here. On the contrary, the thermal influence on the bearing position is reduced because thermal expansion of the transmission housing has a correspondingly reduced effect on the bearing position. In addition, the decisive portion of the radial force is transferred in almost equal parts to the main bearings. This fact enables a reduction of the preload and replacement of the tapered roller bearings previously used by more efficient ball bearings which have lower friction.

4 Schaeffler Lightweight Differential

4.1 Concept

The prototype of the FZG differential is certainly a milestone with regard to its design space requirements and weight. It does have a design disadvantage that can only be compensated by an extremely narrow gear teeth width. Employing internal-gear wheels on the axle drive makes it impossible to mount the differential planets in the housing. An additional center bar must be inserted that serves as the planet carrier. The sheet steel housing is only needed to support the final drive gear (1). Torques are not transmitted.

The idea behind the lightweight differential developed by Schaeffler here is to eliminate the center bar and mount the pinions (3, 4) in the housing (2). This only works if the design does not include an output with internal-gear wheels and uses classic suns (5, 6) instead Fig. 5.

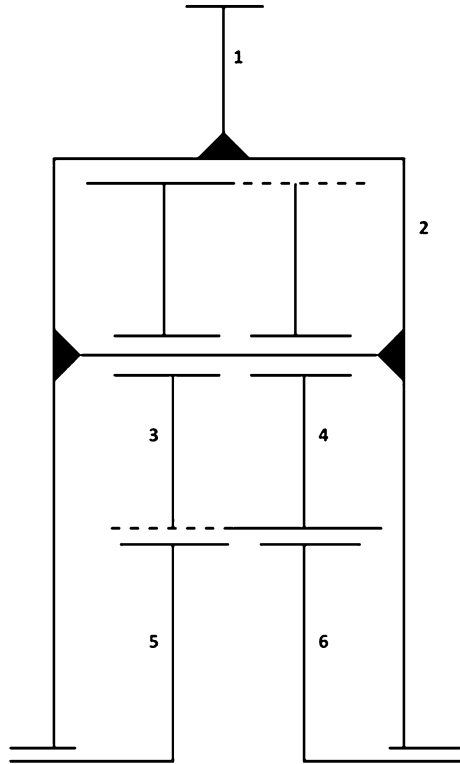
From a manufacturing technology standpoint, this can lead to cost savings over the original FZG design since one less component is required and the low weight of the suns (5, 6) makes them less expensive to produce than the internal-gear wheels.

In terms of the design, the differential planets (3, 4) can be arranged on a relatively large pitch circle diameter, which reduces the forces in the gear teeth contact between the differential planets. However, the actual innovation of this Schaeffler design is not in the concept shown here, but rather in the various gear teeth variants that have been developed since.

4.2 Gear Teeth Design in Schaeffler's Lightweight Differentials

Schaeffler selected a Volkswagen transmission as the test carrier in the lightweight differential advance development project. A manual six-speed transmission with the designation MQ350 was selected for the first prototype.

Fig. 5 Transmission diagram of Schaeffler spur gear differential



The transmission architecture consists of a triple-shaft transmission with a front transverse design. This unit was designed for input torques of up to 350 Nm and is typically used in vehicles with more powerful engines produced by the Volkswagen Group.

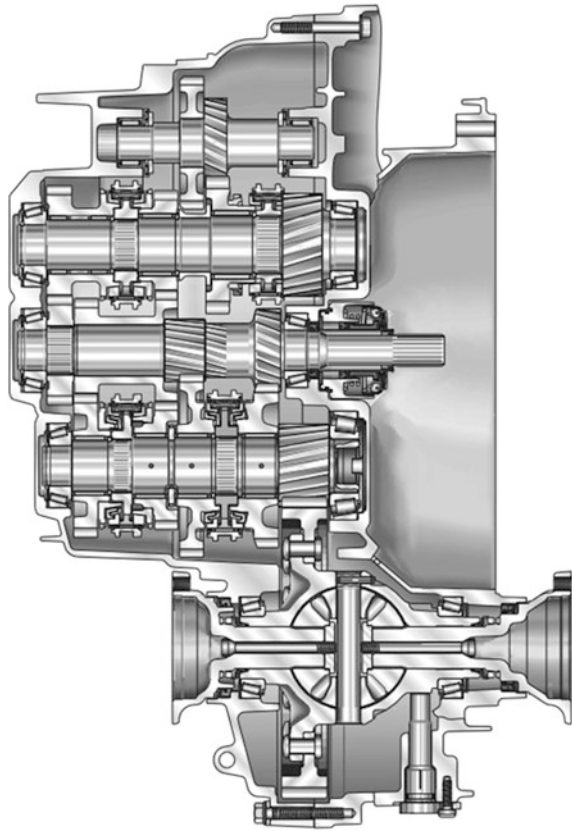
For the transmission of first gear, an axle torque of up to 5500 Nm is theoretically possible for a maximum transmission input torque. This torque was used as the basis for designing the gear teeth even though the slip limit is much lower and was assumed to be in a range of approximately 3000 Nm.

Figure 6 shows a cross-section of the MQ350. In triple-shaft transmissions, the clutch design space is not limited as much by the differential as in twin-shaft transmissions. The standard installation is a final drive with a bevel gear differential, and the differential cage is riveted to the final drive gear.

Our lightweight differential also eliminated a bolted connection using rivets instead. The weight of the bevel gear differential, including the final drive gear, is around 9 kg. During development, our goal was to reduce this weight by at least 15 % and to reduce the design space so much that the differential bearing seat is on a plane with the main bearings of the output shaft.

On the following pages, a distinction is made between type 1 and type 2 differentials. Figure 7 shows type 1 differential gear teeth. Three planet differential

Fig. 6 VW MQ350



pairs are arranged on the circumference of the planetary gear. The number of planet pairs is irrelevant. Four or five planet pairs could be used if the surrounding structure permits, although according to Müller [3] the following condition for the number of teeth should be observed:

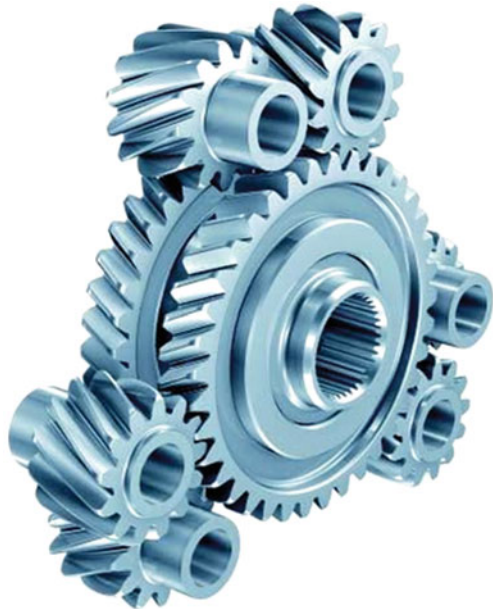
$$\frac{Z_{SO1} + Z_{SO2}}{Z_{PP}} = \text{whole number}$$

Z_{SO1} and Z_{SO2} are the number of teeth for the output suns, Z_{PP} is the number of planet pairs on the circumference. Failure to follow this rule leads to an uneven distribution of the planet pairs on the circumference. The number of teeth of suns Z_{SO1} and Z_{SO2} are identical for axle differentials with the same torque distribution.

What is typical for type 1 gear teeth are three gear teeth areas that are arranged coaxially and contiguously. In the left and right areas, one planet of the respective planet pairs meshes with the relevant output sun. In the center, the planets mesh with each other. The gear teeth of the suns have been recessed here.

The drawing also shows that the sun gears and the planet gears on the left and right of the variant with helical gear teeth have a mirror-symmetrical structure, the

Fig. 7 Type 1 gear teeth with helix angle $>0^\circ$



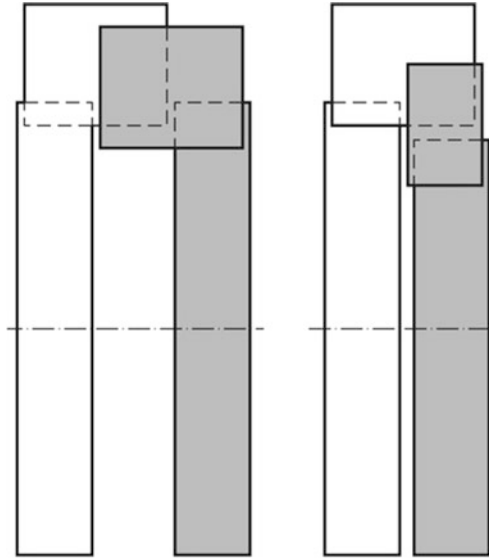
only distinction being their spiral direction. The helix angle serves to increase the differential lock value. In traction mode, the sun gears contact the housing wall. If a friction disk is inserted between the sun gears and the housing wall, the increased friction in this contact generates the desired locking effect. The differential behaves similar to a torque-sensor locking differential in which the differential lock value for the series is affected by the helix angle and the friction disk. Resin-bonded friction linings made by Luk Friction are currently being tested as material for the friction disk in some prototypes.

Supporting the suns through the housing has another function-relevant effect. In traction mode, the differential builds up internal counter pressure which increases bearing preload. As a result, the rigidity of the bearing system varies depending on the torque. This ensures optimum support of the final drive's gear teeth even for high torques. This design reduces the probability of noise generation.

For all spur gear differentials, the gear teeth of the existing bevel gear differential were first analyzed. The maximum tooth root loads and tooth flank pressures of the differential pinions and axle drive bevel gears in first gear served as a reference for designing the gear teeth of the spur gear differential.

The design of the spur gear differential was not solely based on loads. Component strength was also analyzed. However, since both differential types use comparable, case hardened steel and the relatively small component sizes are also similar; many influencing factors that increase or reduce material rigidity are assumed to be identical. Other differences in tooth root load capacity, due to various roughness values, for instance, were initially neglected because the focus was on static loads.

Fig. 8 Diagram of gear teeth (type 1 *left* and type 2 *right*)



Proof of strength for high static loads is provided on the assumption that they severely damage the differential components. The calculated loads are correspondingly high for the tooth root and the flank. Since the exact load spectrum is not known and thus cannot be converted to the load conditions in the spur gear differential with changed load cycles, a worst case scenario was assumed. This scenario provides for the bevel gear differential to be designed exactly on the border of static strength and fatigue strength, which would mean that both an increase in loads and an increase in load cycles would cause the gear teeth to fail.

The basic idea behind type 2 differentials is to utilize the axial design space between the suns of the type 1 differentials, resulting in an additional narrowing and weight reduction. This is made possible by moving a sun-planet tooth contact into the same tooth contact plane with the planet-planet tooth contact. Type 1 with three axially arranged tooth contact planes is thus translated into type 2 differentials with only two tooth contact planes (Fig. 8).

The diagram shows that type 2 differentials can only be designed asymmetrically. In this design, one of the suns is smaller than the other sun by negative profile displacement, which also reduces the wheel distances of this stage with the sun. The gear teeth profile of the second sun is subject to a strong positive displacement, which results in a large wheel distance. As a consequence, it is possible to move a sun-planet tooth contact under the planet-planet tooth contact. Both gear teeth contacts are thus in one gear teeth contact plane. All gear wheels continue to have the same gear teeth module. To ensure that the torque is distributed evenly over the two sun gears, both have an identical number of teeth despite their size difference (see Fig. 9).

An even torque distribution could also be achieved using a different number of sun teeth and gear teeth module. In this case, at least one of the planets would have

Fig. 9 Type 2 spur gear differential with straight-cut design



to have a stepped design with two different sets of gear teeth, which has significant production disadvantages compared to the suggested design. However, in order to ensure that the differential functions smoothly, the distance a between the tip circles of sun 2 and planet 1 would have to be sufficiently large to prevent these gear teeth from meshing. This would entail relatively large profile displacements on the suns.

The size difference between the two sun gears also leads to a difference in their circumferential forces, which at first glance contradicts an even torque distribution. If the rolling circle diameters of the planets are also considered, as in Fig. 10, the connection becomes clear. As a result of the different gear teeth parameters of each gear teeth contact, the planet gears have two clearly dissimilar rolling circle diameters. Because of this, the circumferential forces between the planets and the suns are transmitted according to the ratio of these two rolling circle diameters. As a result, the higher circumferential force impacts the smaller sun gear in comparison to the larger sun gear, which ultimately allows an even torque distribution.

The challenge with regard to the gear teeth design is in the load capacity of sun gear 2. Due to the negative profile displacement of these gear teeth and the resulting narrow tooth roots, the load capacity of the tooth root is reduced significantly. As a consequence, the gear teeth contact must be designed to be wider than that between sun 1 and planet 1. This partially compensates the advantage of utilizing the design space between the planets. However, in sum this enables a

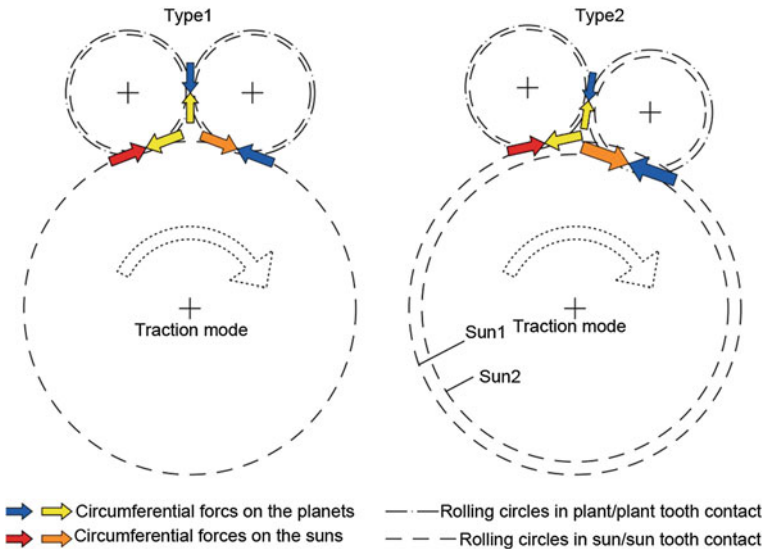


Fig. 10 Comparison of circumferential forces on the gear teeth of differentials type 1 and 2

significant narrowing of the gear teeth contacts by approximately 30 %, both for straight-cut variants and variants with helical gear teeth.

4.3 Housing Design

Figure 11 shows an assembled final drive manufactured by Schaeffler. Cold-formed sheet steel forms the housing of the differential and also supports the final drive gear. The planet pairs are arranged on a pitch circle diameter that is as large as possible to minimize the gear teeth forces. For this reason, the final drive gear is not fully connected to the differential housing on the circumference but only via three flanges that remained as material between the planet pairs. When the rivet connection was designed, current riveted final drives were used as a reference.

The differential housing consists of two sheet steel half cups which can be designed differently from each other depending on the gear teeth design. For differential type 1, the two half cups are designed to be completely identical. For type 2 differentials, the base carriers are identical, but the hole pattern of the planet bearings is arranged in a mirror-inverted fashion because of the different pitch circle diameters of the planets. Straight-cut type 1 differentials have the largest number of similar parts. Here, besides the housing half cups, all differential planets and the suns are made from similar components.

Fig. 11 Schaeffler lightweight differential with housing



4.4 Advantages of the Schaeffler Lightweight Differential

Figure 12 shows the various gear teeth designs for type 1 and 2 differentials. The comparison shows that the axial design space can be reduced further by type 2 gear teeth.

Generally this means a further reduction in axial design space of approx. 17 % between the straight-cut type 1 differential and the type 2 differential with helical gear teeth. The width of the gear teeth was reduced by 30 %.

4.5 Comparison Between the Bevel Gear Differential and the Schaeffler Lightweight Differential

The goal of the project was to develop a differential whose support bearings are on a plane with the main bearing of the output shaft, and this goal has been achieved. The type 2 differential even remains completely within the design space width of the final drive gear so that collisions with gear wheels are prevented. Compared to the bevel gear differential, the savings shown in Fig. 13 are achieved for the higher torque class.

Based on the insights gained, developments for other differentials in various torque classes have already been initiated. The tendency in these developments is basically comparable. Even for transmissions with lower torque capacity, benefits of a similar magnitude are achieved. Among other things, a design for a transmission with maximum axle torque of 2,100 Nm has been prepared to evaluate the efficiency of the Schaeffler design. Figure 14 shows a compilation of the results.

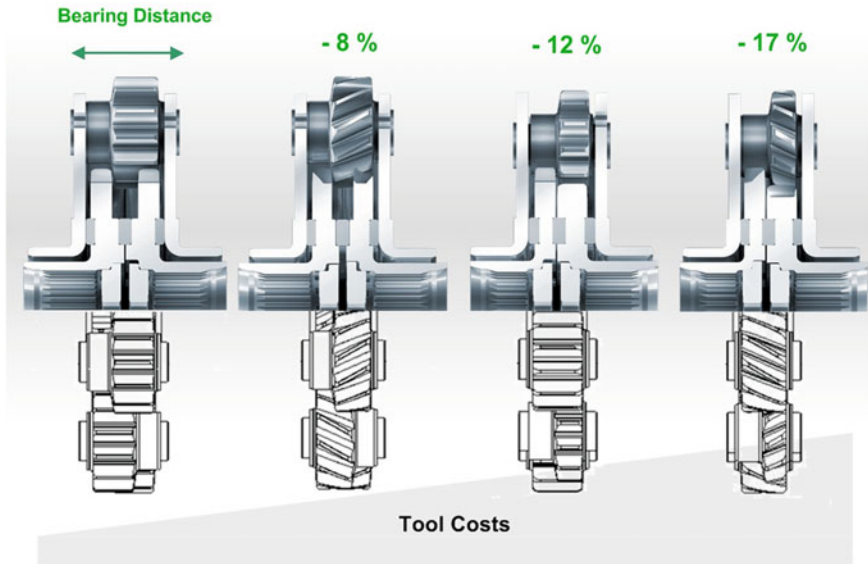


Fig. 12 Comparison of gear teeth and axial design space of type 1 and 2 differentials with straight-cut and helical gear teeth

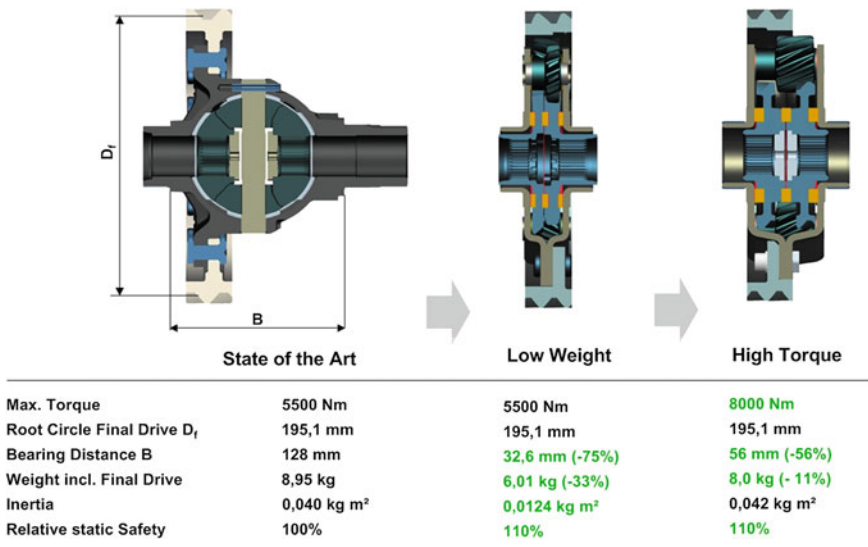
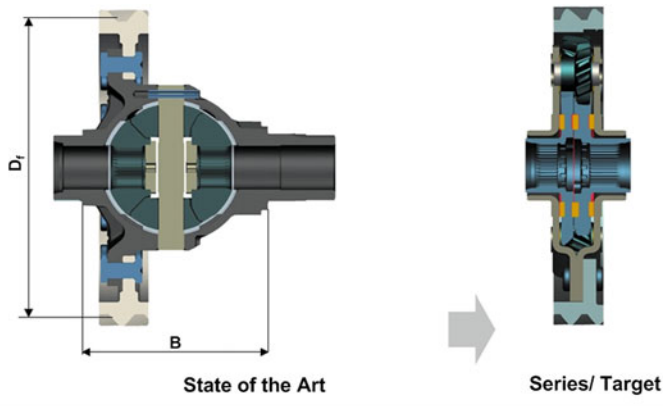


Fig. 13 Weight and design space savings for 5,500 Nm axle torque



	State of the Art	Series/ Target
Max. Torque	2100 Nm	2100 Nm
Root Circle Final Drive D_f	171,5 mm	171,5 mm
Bearing Distance B	96 mm	26,3 mm (-73%)
Weight incl. Final Drive	5,5 kg	3.6 kg (-34%)
Relative static Safety	100%	110%

Fig. 14 Weight and design space savings for 2,100 Nm axle torque

5 Summary

The successful development of the Schaeffler lightweight differential, is a development which many experts had not expected for a 100 year old product. The actual basic idea of locating the planets as far outboard as possible, and thereby accepting a weakening of the final drive gear in the process, borders on negligence. Alongside the predicted problems relating to manufacturing and function, excessive noise emissions from the final drive gear were also expected.

The results that are now available are all the more pleasing. The lightweight differential by Schaeffler has shown that it is extremely robust and quiet, both during the acoustic test and also during the rating life tests.

The current level of development indicates that despite inferior manufacturing tolerances and greater out of roundness of the final drive gear, the noise level of the spur gear differential is as much as 10 dB under the noise level of a comparable bevel gear differential. The acoustic test was carried out at AFT in Werdohl (Germany).

These findings indicate that the spur gear differential in its current development level not only has an enormous potential compared with the bevel gear differential, but also compared with different Torsen concepts. Due to the large number of similar parts, straight-cut type 1 differentials are intended for production in smaller quantities and to cover the range of functions of bevel gear differentials.

Type 2 differentials with helical gear teeth necessitate large production quantities due to the different planets, suns and housing halves, and the design which is

based on manufacturing technology using forming methods. The differential lock value, which is increased by suitable helix angles and friction disks, also offers an alternative to different, mechanical Torsen differentials.

The design space, which is significantly reduced compared with a bevel gear differential, also enables the integration of additional functions, which could not be previously provided in transmissions mounted in a front transverse arrangement. Schaeffler has already initiated development for a switchable rear axle output or also integrated center differentials. Type 2 differentials are also an essential component of an electric axle described in a further presentation [5].

All in all, the presence of the lightweight differential on the market can only increase in view of increasing energy and raw material prices or procurement problems and based purely on cost considerations.

References

1. Höhn B-R, Michaelis K, Heizenröther M (2006) Kompaktes achsgetriebe für Fahrzeuge mit frontantrieb und quer eingebautem motor, ATZ 1/2006
2. Homans JE (1911) Self-propelled vehicles. Theo Audel Company, New York
3. Müller HW (1998) Die Umlaufgetriebe (Auslegung und vielseitige Anwendungen), 2nd edn. Springer, Berlin Heidelberg
4. Heizenröther M (2005) Entwicklung eines Stirnraddifferenzials mit Innenverzahnung in Blechbauweise, Abschlussbericht zum Forschungsvorhaben P546 der Forschungsvereinigung Stahlanwendung e.V. (FOSTA)
5. Smetana T, Biermann T, Höhn B-R, Kurth F (2010) Schaeffler active differential—the active differential for future drivetrains: 9. Schaeffler, Symposium, 2010

Part III
Advanced Transmission System

The Design Concept of Complete Traction Electric Equipment Sets for Hybrid Vehicles

Stanislav Florentsev, Dmitry Izosimov and Ivan Ksenevich

Keywords Hybrid vehicles · Kinematical configurations traction drive · Gearbox · Control strategy

Principals of electromechanical devices are not yet stable concerning the specific of their application, and there is necessary reconsideration of many principal subjects. Transfer from the input data to the parameters of the specific devices now is based on the experience of development of these devices for other applications and appears to be more an art of designers. There are no standard and proven choosing procedures of the basic parameters of electromechanical devices for hybrid automotive machinery: reduction ratios, number of gears, rotation frequencies, electric machines power source frequencies, number of pole pairs, etc. The cases of correct comparison of the developed configurations are rare as there are no criteria of quality of their design work. All this largely constrains the development of the perspective samples of hybrid machinery, complicates mutual understanding of experts—designers of electric machines, electric drives, mechanical devices and transport experts.

The chapter considers kinematical configurations of hybrid vehicles, specific requirements to traction drives and motor-generators, perspective types of electric machines and power converters, characteristic features of the systems “ICE-generator”, “buffer power storage”, “power converter—electric motor”, “reduction gear and gearbox”. Problems of synthesis of the control strategy for electric drive and the complete set of traction and power equipment are discussed.

F2012-C03-002

S. Florentsev (✉) · D. Izosimov
RUSELPROM-ElectricDrive Ltd., Moscow, Russia
e-mail: florentsev@ruselprom.ru

I. Ksenevich
Russian Engineering Academy, Moscow, Russia

1 Introduction

Hybrid vehicles or—as sometimes is preferred to call them—vehicles with the combined powertrain (CPT) are something average between a traditional vehicle (i.e. a vehicle driven by a thermal engine) and electric vehicle (i.e. a vehicle driven by an electric motor supplied from on-board electric power source). CPT consists of two or more energy sources: internal combustion engine (ICE), generator, accumulator, buffer storage, fuel cell battery and etc. Thus, there happens a process of “genetical mutation” of vehicles, qualitative transformation of their structure and structure of the basic power devices.

Minimally [1, 2] the electric drive may be used as a motor-generator (MG), mounted directly on the ICE shaft and allowing to stop the ICE at any vehicle stop with a following fast start of the ICE according to the driver’s command to begin the movement of the vehicle. The better results and flexibility of control are provided by the configuration with an additional traction electric motor (TEM) having inverter, reduction gear and mechanical clutch allowing realizing the transfer of a tractive force from the TEM to the driving wheels commonly with the tractive force from the ICE. This is a “classical” parallel kinematical configuration. Also, there are applied combined kinematical configurations where ICE and MG “work” for a two-entry planetary gear (“SPLIT” system). The further development of the abovementioned kinematical configurations is a series one where kinematical coupling of ICE and driving wheels is excluded principally. Series configuration allows variety of new designs, new arrangements. Series configuration makes it possible to exclude a gearbox, clutches, driveshaft which lowers the total weight of the power equipment significantly; there appears possibility to exclude the “last” mechanical transfer—differential which in principal significantly complicates building of a high-quality motion control system, degrades the controllability and maneuverability of the vehicle.

It is appropriate to consider separately the problems of ecological pureness (more correctly, the grade of environmental-friendliness), fuel efficiency and commercial attractiveness of vehicles which apply electric drive, with various types of on-board energy sources and applied technologies. Firstly it should be noted that there is no a common decision of these problems; for correct comparison it is necessary to differ:

- emission levels in the places of vehicle’s use and in places of generation of the primary energy;
- degree of emissions toxicity;
- levels of the fuel consumption—also in the places of vehicle’s use and in places of fuel extraction;
- damage caused to the environment during the use (excluding emissions);
- damage caused to the environment during fuel extraction;
- total ecological damage, cost and charge analysis, life-cycle analysis, including extraction and processing of the raw materials, production, use, maintenance and recycling of the vehicle and wastes.

It is obvious, that the structure of criteria is wide enough, thus “stressing” of advantages only according to one criterion frequently leads to incorrect comparison of different types of vehicles and technologies. For example, let us consider the following.

1. Battery electric vehicles (BEV or EV). Their 100 % ecological purity is mentioned especially frequently. Really, while riding such an electric vehicle has no harmful exhaust into atmosphere. However, accumulator battery (AB) is characterized by significantly (in two to three times) higher weight compared to the ICE with a fuel tank in a traditional vehicle (with comparable cruising range). Hence, energy consumption for motion of the BEV (per distance unit or per ton-kilometer) is higher by approximately 20 % (dependent on type). And besides, efficiency of the charge discharge process of the accumulator is 0.6–0.8 (dependent on the accumulator type). This means further rise of the relative energy consumption to the level of approximately 1.5–2 times the consumption of the traditional vehicle. Because the electric energy for charging is produced by the combustion of the fossil fuel at power stations (it is not worth mentioning another—e.g. renewable—sources, their volume is not enough even to cover 10 % of the total consumption), BEV by consumption of the primary fuel and by total exhaust is as much more “dirty” than a traditional vehicle. Its advantage, or more correctly, specific is separation of the place of exhausts emitting (power station) and the place of use (which in some applications is a necessary condition), but with higher total ecological impact. Actually, serious ecological analysis should be based on methods of the lifecycle analysis (LCA). It is abundantly clear that conclusion of the LCA of BEVs will be even more severe, considering factors of:

- relatively short operation life of the battery,
- high expenses (including cost and energy supply) for production of accumulators,
- difficulty of recycling, especially of high volumes of used accumulators.

All the mentioned allows to conclude that niche of application of BEVs is where the critical factor is absence of exhausts during use (closed rooms, stadiums, green zones etc.), at undoubted estimation of effects of the total damage to the environment.

2. Also, vehicles with fuel cells (FCV) are frequently mentioned (mostly with fuel cell system type “hydrogen-air”), whose exhaust during use is a pure water. Efficiency of systems of hydrogen generation and its cold combustion in the fuel cells is even lower (not more than 0.5–0.7), than the efficiency of the AB charge/discharge. Their cost is out-of-limit. An infrastructure of refueling does not exist (it viably will not be created in the near future). Hence, it will be right to give even more severe deductions than the given above for BEVs. It is especially necessary to note the so-called ecological friendliness of FCVs. Their emission is pure water, no doubt, but what is their “absorption”? Why it is forgot that there is consumed the oxygen from the ambient air? It is not

allowed to use such vehicles in closed rooms (while sometimes we can hear about metro and similar places of use). Really, taking into account oxygen emissions during water electrolysis, there is no total ecological impact concerning the oxygen (from the fuel cells themselves; ecological damage of FCVs due to the higher energy consumption is about twice as high as that of traditional vehicles). However, here the situation is the opposite to the situation with the exhausts of BEVs: oxygen generation takes place where the fuel (hydrogen) is generated, and oxygen consumption takes place where the vehicle is used.

The viable application niche of FCVs for now (until significant technological breakthrough will appear) first of all is special machinery where the price is not the key factor.

3. Numerous mentions of demonstration projects in transport, in households (“hydrogen” and “solar” houses, “green villages”, wind, tide, biofuel, etc.) need comments. A real conclusion of demonstration projects actually is that after removal of the state grants all these projects die. It indicates their artificiality and lifelessness: cost (hence, ecological damage produced by them, anyway not an advantage) is excessively high. It is necessary a serious, not a populist analysis of all approaches, including applications of alternative and renewable fuels. Unfortunately, alternative energy sources for a while bring “totally” more damage, than advantage. If it would be otherwise, industry players would grasp the new technology long time ago.
4. The only approach allowing real decrease of environmental impact both in the place of use and in the place of fuel production now is orientation on hybrid vehicles with ICE and electric traction. Economy of fuel in these vehicles appears mainly because ICE is “uncoupled” with wheels. This allows operating it in the optimal (in terms of fuel efficiency and emissions toxicity) quasi-steady state mode. Economy of up to 30 % of fuel means the proportional reduction of energy consumption (and emissions) in the place of fuel production. In the place of use of the hybrid emissions reduction is even higher due to the operation of the ICE in quasi-steady state, emission-optimal mode. Practically, emissions are reduced ten-fold. Taking into account that costs of traditional and hybrid vehicles are comparable and use and maintenance spends for the last mentioned are certainly lower, it is possible to say surely, that LCA results will be in favor for hybrids. While there will be not created principally new power engineering technology, it’s impossible to discuss other alternatives. At application of the hybrid vehicular technology with ICE creation of a new refueling infrastructure is not necessary; however it is necessary to create new services for maintenance of devices of the electric traction.

Hybrids can not be a “universal panacea” for emission reduction, their most effective application field is limited to the transport intended for traffic with frequent accelerations brakes (for example, route city bus) and also to the cases when designing of the traditional mechanical transmission is complicated and

electromechanical drivetrain is preferred (e.g. powerful tractors, heavy-duty trucks [3]). In other cases emissions reduction for transport is provided by traditional methods: improvement of ICE, vehicle design, modification of fuel etc.

It should be noted that for use of the electric traction important factors are improvement of the controllability, maneuverability, simplification of control.

2 Specifics of the Electric Drive Application in the Vehicular Technology

2.1 Traction Drive

In the traction drive maximum torque and power on the drive shaft are restricted. Restriction of the maximum torque is related first of all with the requirements, determined by the power electronics (maximum current of the power converter); restriction to the “power hyperbole” is determined by the power rating of the on-board power source (ICE, buffer storage).

In the basic power range 20...200 kW most widespread are asynchronous electric motor/drive (AM/AED) and synchronous electric motor/drive with permanent magnets (SMPM/SEDPM). There are (not very successful) examples of application of switch-reluctance motor/drive. Also, a synchronous-reluctance motor should be noted as promising. It should be stressed that now there is no correct method of comparison of the different type motors [4]. AED is characterized by the best cost/quality ratio. SEDPM has some advantage in efficiency but cost is higher. In the AED operation with power limitation is provided with limitation of the source voltage of the motor by means of the relevant field weakening. In SEDPM the field is practically uncontrollable which leads to a need to uprate the converter rated power in 3–10 times. It is acceptable for drives of the light-duty vehicles; for medium- and heavy-duty vehicles it leads to non-allowable rise of the drive system cost.

2.2 Motor-Generator

Typical range of frequencies and torques of MGs functioning commonly with ICEs in the range of their operating fuel economy-optimal and emissions-optimal modes is characterized by the fact that maximum torque is achieved at maximum rotation frequency.

It is hard to recognize the optimal type of electric motor for MG. Maybe it is also AM with squirrel-cage type rotor or SMPM, or synchronous-reluctance motor.

Thus, operating modes of electric motors in traction drive and in generators are much different which requires the respective difference in techniques of their development [5].

2.3 System “*Electric Machine: Mechanical Reduction Gear*”

Usually powers, torques and rotation frequencies of output (for TEM) and input (for MG) shafts are pre-set; as a rule, demands for efficiency, dimensions and the maximum weight limitations of the system “electric machine—reduction gear” are known. Specific characteristics of electric motors and reduction gears defined by the parameters of the applied materials and production technologies differ substantially. Reduction gears, as a rule, are characterized by higher values of the “specific weight—transferred torque” relation, as compared to electric machines. It seems that for optimization of the total parameters it is reasonable maximal use of the advantages of reduction gears. Widespread is the opinion that selection of the reductor with maximum reduction ratio and, respectively, application of the electric machine with maximum rotation frequency provides lowering the weight of the system “electric machine—reduction gear”. For traditional TAMs it is generally true: decreasing the torque at the fixed number of pole pairs allows to apply of the motor of lower weight. But for optimized motor it isn’t so. Weight of the optimized motor is determined by its power and insignificantly depends on its rotation frequency. The conclusion is that it is reasonable to exclude the mechanical reduction gear which only pays for increase of the weight and cost of the system. If dimensional limitations are overcome it is reasonable to use a reductor.

Application of the reduction gear doesn’t change the equivalent inertia moment of rotating weights of the electric motor.

2.4 System “*Electric Machine: Gearbox*”

Firstly, let us consider the simplest case of the two-step gearbox. Let reduction ratios at the high and low steps be differ in two times. It is expectable that it will allow applying TEM with electromagnetic torque of the half value. Reduction of the electromagnetic torque of the TEM in two times will provide two-fold decrease of its weight. Respectively, its cost will be reduced, but thus cost of mechanical devices will be increased.

An efficiency of application of the gearbox is the higher, the higher is “maximum electromagnetic torque—maximum rotation frequency torque” ratio. Maximum specific decrease of the motor weight due to the application of the gearbox can be estimated by a value of $M_{\max} \cdot N_{\max} / 2P_{\max}$. The respective minimum number of the gearing steps is estimated by a value equal to the $\log_2(M_{\max} \cdot N_{\max} / P_{\max})$ with rounding up to the nearest higher integer. Real efficiency of application of the simplest gearbox is somewhat lower.

Hence, application of the gearbox provides to decrease of both the weight and the dimensions of the TEM. It should be noted that it is worth taking into account total cumulative parameters of the electromechanical system “electric machine—

gearbox” from the point of view of their common weight and dimensions and also cost, operation life and other factors.

Application of the gearbox in the traction drive increases the inertia moment of rotating weights at lower gear steps and decreases the inertia moment at higher steps.

2.5 System “Electric Machine: Power Converter”

The most promising industrial type of power converter for TEM power supply in vehicles is an autonomous voltage-source inverter (VSI) functioning in a mode of the high-frequency pulse-width modulation (PWM). Vector PWM algorithms [6] allow to: reduce switching energy losses (up to 2.25 times); improve usefulness of the DC bus voltage (approximately in 1.15 times); lower the number of commutations (in 1.5 times); increase maximum duration of the control pulses.

In the traction drive reduction of cost of the complete set of equipment while providing the required traction parameters is important. Cost of the power converter which forms the basic part of cost of the traction drive is determined by the price of the power devices which in its turn is proportional to the converter installed capacity. TEM installed capacity is equal to the product of maximum electromagnetic torque and maximum rotation frequency. The value of a power hyperbola, limiting the field of achievable torques and frequently treated as the TEM power, is usually significantly smaller than the value of the electric motor installed capacity. There arises a question, to which of these two values should the power converter installed capacity correspond? At application of the AED the second statement is closer to the true which allows significant decrease of the power converter cost.

In generators maximum torque is achieved at maximum rotation frequency and the generator installed capacity is the same with the power converter installed capacity. This once more demonstrates the difference in the design process of electric drives and generators.

2.6 Modes of Operation of the ICE in Hybrid System

The majority of autonomous sources of electric energy (on-board, mobile and stationary) are rotating electromachine-type generators driven by the ICEs. From the point of view of raising the fuel efficiency it is desirable that operating modes will be within the field of the multi-parametric characteristic of the ICE with minimal specific fuel consumption. The multi-parametric characteristic allows defining fuel efficiency-optimal values of the rotation frequency and torque dependent on the power and afterwards using these dependences for control of ICE rotation speed and loading mode. It should be reminded that ICE in a series hybrid configuration is not connected with wheels by a kinematical coupling; vehicle’s

motion speed is determined by the TEM and can be selected with any value within the available resource of the ICE power. Reduction of the fuel consumption with application of the fuel efficiency-optimal mode may be significant, at the maximum power it may reach 30 % and even more in comparison with the traditionally used ICE rotation frequency.

The demand for more perfect energy sources may be covered rather fast by radical improvement of the engine-generators by means of transfer to the shaftless linear free-piston design (FPEG) [7]. Volumetric power, specific weight and metal consumption of FPEG are lower in 2.5–3 times than that of traditional type engine-generators. The main operational advantage of the FPEG is reduced by approximately 30 % fuel consumption.

2.7 Buffer Storages

The requirements to the storages differ more from particular applications. For instance, in some cases the critical parameter is power and stored energy does not matter; in other applications the stored energy is a critical parameter. There present differences in the cycle number during the powertrain operating time; requirements to reliability, overload ruggedness etc. differ too which causes reasonable choose of this or that type of a storage for the specific application.

Alternatives of buffer storages are:

- super flywheel;
- accumulator battery (buffer);
- ultracapacitor.

Combination of separate types of storages is also possible (hybrid storage). Among hybrid storages, common application of accumulator batteries and ultracapacitors must be noted, which allows to increase both their specific energy and power rating of such a system.

It should be noted that choice of buffer storage in a series configuration does not influence the parameters of electromechanical devices which allows to design and test it separately according to criteria of an additional cost of the ICE and buffer power source, required peak power of the traction drive and acceptable level of exhaust.

2.8 Synthesis Methods of the Asynchronous Electric Drive Control

For operation of the drive system, application of high-quality control system—such as frequency or vector control—is necessary [8, 9]. Such a system should provide loss-optimal motor modes in all ranges of rotation frequencies, electromagnetic

torques, slip frequencies, inductances etc. However, for traction drives it is also necessary to consider criterion of maximum use of available resources, firstly the source voltage and current which are limited by the rated power capacity of the power converter.

The standard description which adequately reflects steady-state and transient modes of asynchronous motor (AM) is Park's AM model [10] based on the generalized electric machine equations. In the Park's equations there present values of stator and rotor resistances, stator, rotor and mutual inductances. However motor designers do not present such data. Designers of the adjustable drives, who need the information concerning the AM as an object of control, can do nothing except creating methods of experimental parameters identification based on measurements of voltage, current, electromagnetic torque and rotor rotation frequency.

The task of identification was traditionally understood as determination of parameters of the equivalent circuit according to the results of measurements. However it have been shown [11] that this approach is untenable: the same measured values of voltages, currents, torques and rotation frequencies are matched not by the only one AM (in sense of specific values of equivalent circuit parameters), but by plurality of motors with different values of leakage and mutual inductances (saving the value of the generalized leakage), and with different values of rotor resistance (saving the value of the rotor time constant). Probably, this circumstance explains the lack of the commonly accepted technique of an experimental AM parameter identification.

Principles of synthesis of the digital (processor) control of the traction drive are:

- (a) use of an incremental model of the processes;
- (b) estimation of variables which are not measured directly, with respective filtering;
- (c) asymptotic regulation for decrease of influence of noises in measurements;
- (d) application of predictors of variables for compensation of delay of calculations in the microprocessor controller due to its limited speed of calculation;
- (e) identification of motor parameters.

Sensitivity of the drive systems to the parameters variations, definition of the required accuracy are not yet investigated enough. The experiments allow making the following conclusion: it have been discovered that parameters of traction AM vary significantly. The influencing factors are:

- steel saturation (changes parameters by up to 50 % as a function of the field value);
- steel losses, especially frequency-dependent (change parameters by up to 20 % as a function of speed (frequency of the source voltage) and current values, including active current);
- temperature (operating temperature range of electric machines $-40^{\circ}\dots+150^{\circ}$ corresponds to approximately 50 % change of parameters).

2.9 Synthesis of the TEES Control

A set of electric drives, ICE, buffer storage, drivetrain as an object of control represents a complex mutually connected nonlinear dynamic system [12, 13]. In such a system there must be executed a number of restrictions of control inputs and state variables: restrictions of the motors supply voltages, currents, torques, rotation frequencies and variation ranges of the DC bus voltage. Obviously, for TEES control it is necessary to develop special algorithms providing autonomous operation of separate devices and stable coordinated control of all the TEES devices including ICE. A significant factor is uncertainty of initial parameters of the motion: the required traction power is not known in advance, it is determined by the instantaneous conditions of motion and driver's demands; the available power reserve is also unknown in advance or is known insufficiently exactly (maximum ICE power depends on multiple factors such as a fuel quality, ambient air pressure and humidity, temperature, at least condition (wearout) of the ICE and etc.). In these conditions it is necessary to provide power balance automatically without request of the exact data on the condition and operating mode of devices.

Power flows control is fulfilled by the high level controller (HLC).

2.10 Multimotor TAM Control in Hybrid Vehicles

Development logic of vehicles with electromechanical drivetrain (hybrids) will inevitably lead to exclusion of differential and traditional kinematical transmission characteristic for applications with gearboxes. Exchange of a mechanical differential by an electric one allows realizing any required torque distribution either among wheels of different boards, or among driving axles, any required difference among their rotation speeds, including consideration the driving wheel function at vehicle turns, and also among speeds of the driving and driven wheels (controlled slipping). Thus the mechanical transfer is simplified significantly and is reduced, as a rule, to a planetary (possibly, multistage) final drive.

In vehicles with individual wheel drive (with configuration "motor-wheel" or "motor-axle") it is desirable to have sensors of the driven wheels speed or a sensor of the vehicle's speed, which will allow the controlled slipping.

3 Conclusions

Traction electric drive is one of the basic units of electric vehicles; its features define parameters of the total vehicle in many respects. Development of the traction electric drive takes place on base of extremely high technical and economical requirement. It can be claimed absolutely reasonably that nowadays in the

traction electric drive there is realized a set of modern, advanced achievements in the field of electro mechanics, power and control electronics and control techniques.

Reasonable relation of powers of the main sources of the tractive force: ICE and TEM, as well as stored energy and power rating of the buffer storage depend on traffic modes in which vehicle will be used. The highest effect from application of the CPT is achieved in application of vehicles in the city traffic: according to the available experimental data fuel consumption may be reduced by 25–30 %, and sometimes it is twice lower.

Electromechanical devices are relatively new in vehicle technology, their design principals concerning the specific of their application are not yet stable, and there is necessary reconsideration of many principal subjects. Transfer from the input data to parameters of the specific devices now is based on the experience of development of these devices for other applications and appears to be more an art of designers. Really, there are no standards and proven choosing procedures of the basic parameters of electromechanical devices for hybrid automotive machinery: reduction ratios, number of gears, rotation frequencies, electric machines power source frequencies, number of pole pairs etc., not to say about choosing the type of the electric motor. Very rare are the cases of correct comparison of the developed configurations, as there are no criteria of quality of their design work. All this largely constrains the development of perspective samples of hybrid machinery, complicates mutual understanding of experts—designers of electric machines, electric drives, mechanical devices and transport experts.

References

1. Florentsev S (2008) Cost-effective, ecology-friendly city hybrid bus. *Electron Compon* 12:1–9
2. Zlatin PA, Kemenov VA, Ksenevitch IP (2004) Electric vehicles and hybrid vehicles. Agroconsult, Moscow
3. Belousov BN, Popov SD (2006) Wheeled vehicles of very high load capacity. Design. Theory. Calculation. Moscow State Technical University named by N.E. Baumann Publisher House, Moscow
4. Winter U (1998) Siemens automobiltechnik. Comparison of different drive system technologies for electric vehicles. In: Proceedings on EVS-15 CD-ROM, Paper No. 294, Brussels
5. Ksenevitch IP, Izosimov DB (2007) Design philosophy of electromechanical systems for hybrid mobile machinery. *Tract Agric Mach* 1, 2
6. Izosimov DB, Bayda SV (2004) Algorithms of vector pulse-width modulation of the three-phase autonomous voltage inverter. *Electrotechnica* 4:16–21
7. Pinsky FI (2004) Power systems with free-piston engine-generators. *Mobile Tech* 2:12–17
8. Izosimov DB (2004) Issues of design of a perspective asynchronous traction drive. *Mobile Tech* 1, 2, 3, 4
9. Izosimov DB (1997) New approaches to synthesis of the digital control of AC electric drive. *Drive Tech* 4:8–14
10. Park R, Robertson B (1928) The reactances of synchronous machines. *Trans AIEE* 31

11. Izosimov DB, Abolemov EN (2008) Features of equations of the generalized asynchronous electric motor with a squirrel-cage rotor. *Electricity* 4:35–40
12. Florentsev SN (2009) Traction electric equipment set for AC electric transmission various vehicles. In: *Proceedings of international exhibition & conference power electronics, intelligent motion. Power quality (PCIM-2009)*, pp 625–627
13. Ksenevitch IP, Ipatov AA, Izosimov DB (2003) Technologies of hybrid vehicles: state and ways of development of the domestic vehicle technology with combined powertrains. *Mobile Tech* 2–3:4–9

The Design, Development and Industrialization of Shangri New Type of Automatic Transmission in China

Jan Gang Lu and Xingwu Liu

Abstract Shengrui Transmission Limited Corporate (Shengrui) has developed a new 8 speed automatic transmission (SR 8AT) for front wheel drive (FWD) vehicle. The concept of SR 8AT is unique and different from the conventional automatic transmission. The design of the SR 8AT system and components are new and compact. By combining an innovative gear train which is similar with the conventional manual transmission and the simple planetary gear structure, SR 8AT achieved 8 speed with the shortest length of the FWD transmission, the competitive fuel economy and the smooth shift performance among comparable automatic transmissions.

Keywords 8AT · Transmission · Shengrui · Industrialization · China

1 Introduction

In the last decade, the energy resources and the environmental issues such as the auto emissions have become increasingly important to the automotive industry and even to the economy of the World. The emission regulation and the energy policy from the governments in different Countries have forced the automakers to produce the vehicles with superior fuel efficiency and cleaner exhaust gases while improving basic performance characteristics like acceleration time and NVH. As a

F2012-C03-003

J. G. Lu (✉) · X. Liu
Shengrui Transmission Limited Corporate, Weifang, China
e-mail: lujg@shengrui.cn

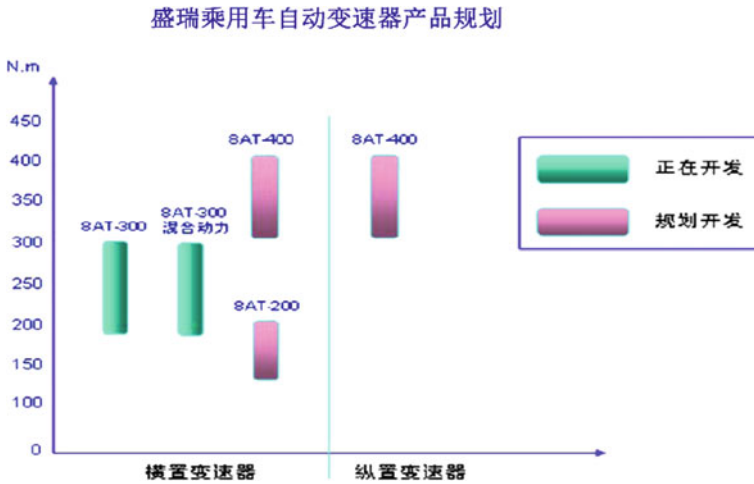


Fig. 1 Shengrui automatic transmission product line

solution to meet these requirements, Shengrui has designed and developed the new SR 8AT with the new technology for the usage of SUVs and sedans in China.

Figure 1 shows Shengrui automatic transmission product line with the torque range of the engines. Shengrui has developed and is developing the automatic transmissions not only to adapt to the engine torques, but also appeal to more customers and obtain better fuel economy by expanding the product line from the SR 8AT 300 nm up to SR 8AT 300 nm hybrid, SR 8AT 400 nm and down to SR 8AT 200 nm. These transmissions are capable of handling the torque between 100 and 400 nm and offering greater satisfactions in powertrain match and vehicle performance.

As shown in Fig. 2, SR 8AT adopts a compact and efficient gear train which was conceived by Dr. Peter Tenberge and awarded to Shengrui as Outstanding Patented Invention by Chinese State Intellectual Property Office and World Intellectual Property Organization in 2011. The gear train structure consists of 5 shifting elements, 3 sets of spur gears and 3 sets of simple planetary gears for 8 well stepped forward gears and 1 reverse gear. By combining the gear train with the precise controls of the clutch to clutch and the lower drag friction discs, SR 8AT achieves an outstanding fuel economy among the comparable automatic transmissions. The fuel economy of the vehicle equipped with SR 8AT is improved by 6 % or more comparing to conventional 4 and 6 speed transaxles [1, 2].

2 Overall Design

The arrangement of the gear train with both spur gear sets and simple planetary gear sets allows the compact design of SR 8AT with 365 mm in length and the lower weight with 5 kg less than the comparable 6 speed transmission. The conventional

Fig. 2 SR 8AT concept schematic

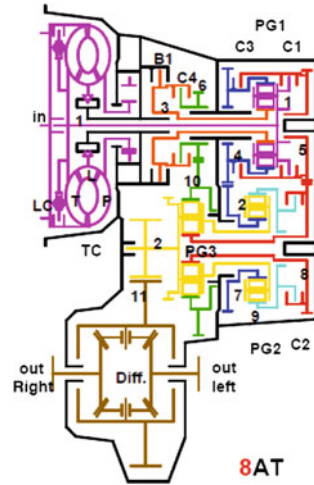
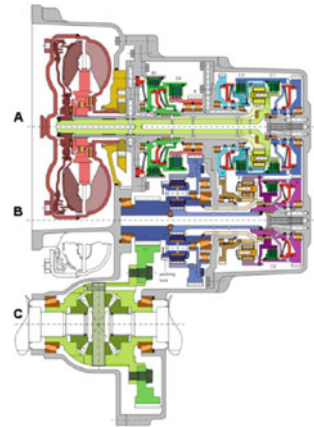


Fig. 3 SR 8AT cross section



one way clutch (OWC) is not used in the design and the spur gear set takes place as the role of OWC along with the control of clutch to clutch. The differential gears and the set of primary speed reduction gear are packaged well with the suitable ratio of the differential in the overall design.

The cross section of SR 8AT is shown in Fig. 3. The transmission oil pump is connected directly to the engine. Engine power is directed through a torque converter to the transmission input. The valve body and controls are packaged in the transmission sump. SR 8AT offers a wide range of features which are summarized as following: All wheel drive availability, TCC availability 1st–8th gears, Skip shifting, Reverse lock-out, Transmission Abuse protection, Dual gear limp home strategy, Driver shift control, Internal transmission electro-hydraulic control module, Winter mode, Manual Mode, Sporty Mode, Performance algorithm shifting, Automatic grade braking, etc.

Table 1 Gear ratio data

Gear	Ratio	Total ratio	Ratio steps
1st	3.85	14.79	
2nd	2.453	9.424	1.57
3rd	1.631	6.266	1.5
4th	1.343	5.16	1.21
5th	1.068	4.103	1.26
6th	0.854	3.281	1.25
7th	0.701	2.693	1.22
8th	0.544	2.09	1.29
Reverse	2.434	9.351	
Overall ratio spread	7.076		

Table 2 Operation chart of shift control elements

Limp H	Gear	B1	C1	C2	C3	C4
X	R					
	NR					
	N1					
	N2					
	1					
	2					
	3					
	4					
X	5					
	6					
	7					
	8					

Fig. 4 Shift control logic

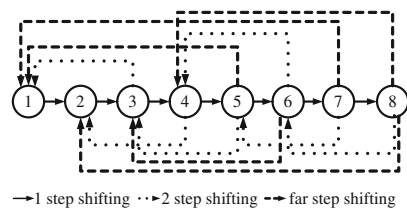
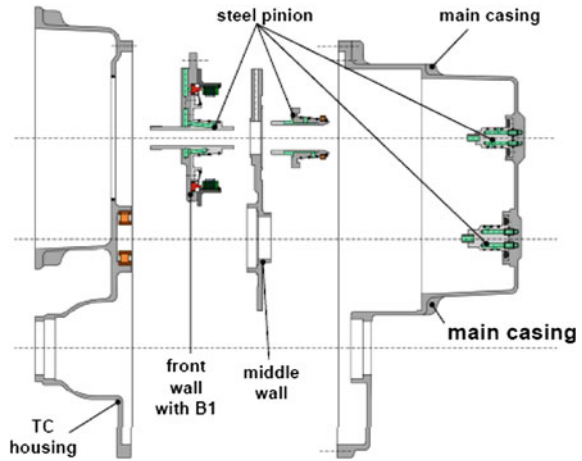


Table 1 shows the gear ratio data of SR 8AT. The speed gear ratio is well spreaded for 8 speeds based on the optimization of the calculation for the traction efforts of the vehicle launch and the vehicle performance.

Fig. 5 Casing and supporting structure



The gear ratio arrangement is optimized to match the characteristics of the vehicle and the engine. It contributes to a spectacular advance in the acceleration performance. SR 8AT used the fully developed linear solenoid and low friction clutch design which provides a precise and quick response in the electro-hydraulic pressure control meanwhile maintaining good shift feeling.

Table 2 shows the operation of the shift control elements in SR 8AT. Limp home features are achieved at both reverse gear and 5th gear in drive. Total 5 shift elements which include 1 brake and 4 clutches, are used to achieve 8 forward gears and 1 reverse gear. SR 8AT gear structure is a unique set up with four degree of freedom. Three shifting elements are used to fulfil the engagement of each gear.

As shown in Fig. 4, 1 step and 2 step shifting and multi step shifting all are “simple shift”. All the shifts are executed with single transition ratio changes. It is achieved by disengaging off-going clutch (current gear) and engaging on-coming clutch (target gear). The selected gear ratios provide small step sizes between 3rd, 4, 5, 6, 7 and 8th gears that enable optimum ratios for a majority of vehicle operating conditions. Large step sizes between 1st and 2nd gears allow for a large overall ratio spread 7.076 which in turn delivers high torque multiplication during vehicle launch for the improved performance while simultaneously delivering high fuel economy. Especially the down shift from the higher gears to the lower gears for the more frequent stop go in city traffic is a truly advantage for the further improvement of the fuel economy.

3 Transmission Casing

Figures 5 and 6 show Casing and Supporting Structure and Transmission Casing. The Casing is designed by making full use of a 3-dimensional model. The main target in this design process is to improve poor quality such as casting porosity.

Fig. 6 Casing

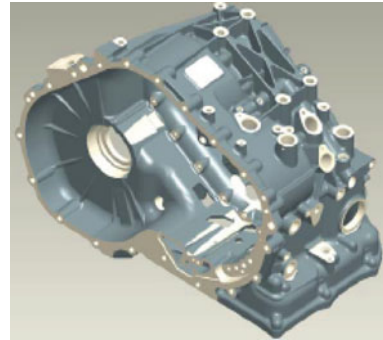
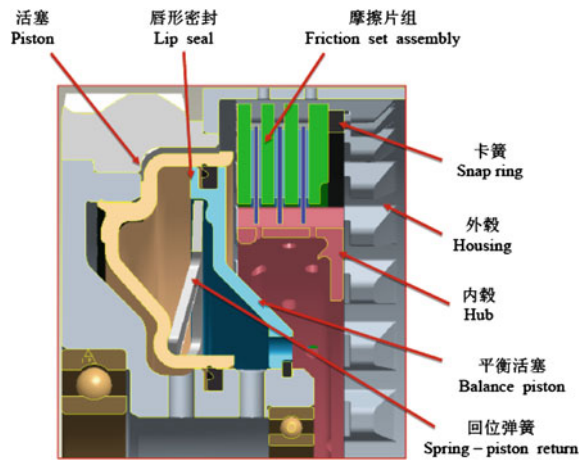


Fig. 7 Clutch pack



The Casing shape is designed while estimating and minimizing poor quality by utilizing computer simulation from the beginning. This activity contributes to reducing the number of prototypes needed. Another goal is to ensure better performance in NVH and strength by elaborating a computer simulation. Thickness and Casing ribs are designed to have optimum rigidity.

4 Clutch

B1, C1, C3 and C4 are located at the main input shaft and C2 is located at the counter shaft. The rotational drag torque affects the transmission efficiency. The groove shape of the friction discs used in SR 8AT is optimized to reduce drag torque. The groove of the friction discs are easily affected by the amount of lubrication oil. Torque formed by oil around the rotating friction discs causes a sudden rise in drag torque. To reduce drag torque, the inner friction material of clutch discs is bounded on the core plate with a “Y” shape in both the inner side

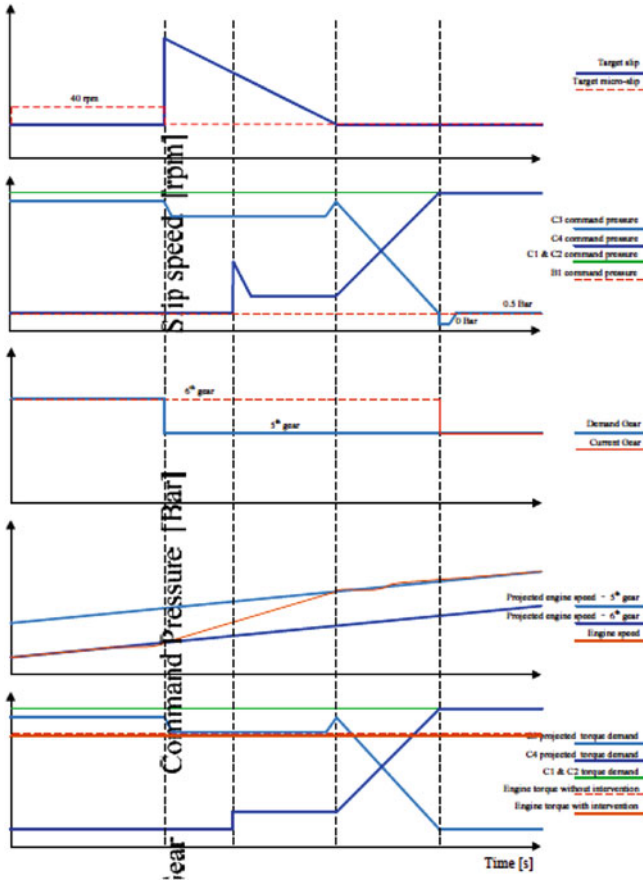
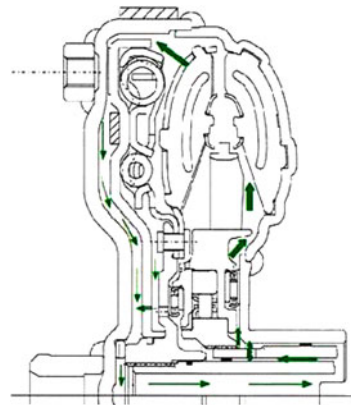


Fig. 8 Clutch control schematics

Fig. 9 Cross section of torque converter



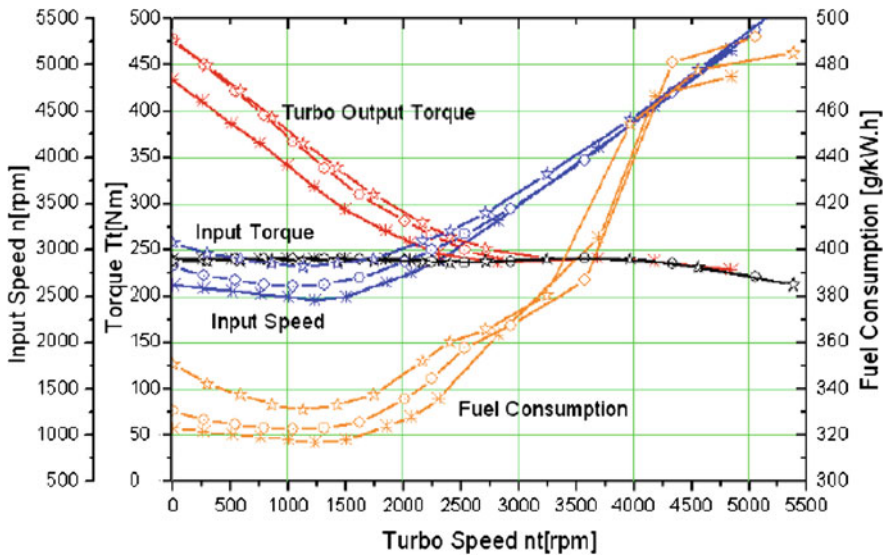


Fig. 10 Torque converter performance curve

and the outer side of the discs. Friction discs can rotate properly with mating plates by adjusting a balance in oil flow between drain in radial direction and supply in rotational direction at this “Y” shape. Reduction in drag torque is a significant amount more than the existing disc (Fig. 7).

5 Electrical Hydraulic Control

Individual hydraulic control with pilot valve is used in order to gain the quick, reliable and smooth shift change. The focus on the precise design of the hydraulic system, and the engine torque demand system, the down shift logic and the multiple shift logic is conducted in both hardware and the software for better shift quality. For further improvement in fuel economy, the multi step down shifting from higher gear to lower gear along with the precise control of engine fuel cut provides a better method for the fuel saving especially in city traffic operation of vehicle. Figure 8 shows the well defined control points for the simultaneous alignment of the pressure, the speed, the clutch engagement during and the clutch disengagement during the up-shift and down shift of the transmission.

6 Torque Converter

A well designed existing torque converter is used for SR 8AT. Figure 9 shows the cross section of the torque converter. The high torque capacity and a maximum efficiency of 92 % leads to a damper design with low torsional rigidity and low



Fig. 11 SR 8AT goal and requirement

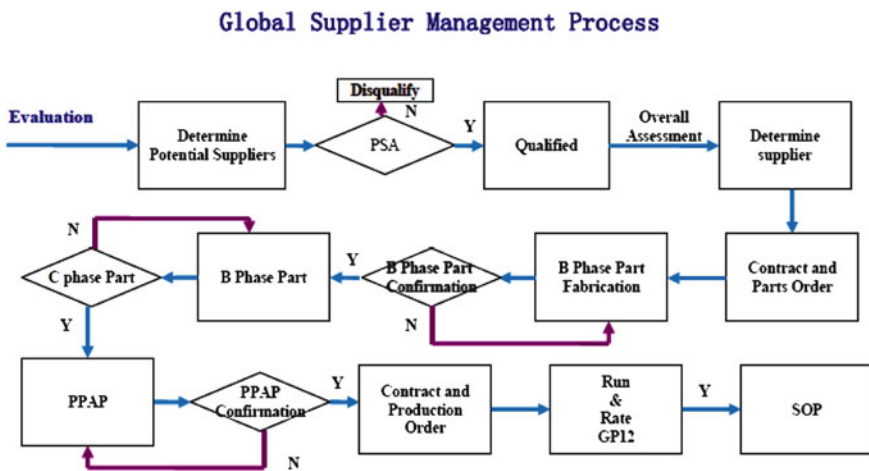


Fig. 12 Global supplier management process

hysteresis torque. By optimizing inertia distribution and balance of stiffness in the damper, lock-up is able to be operated at higher engine speed. The torque converter clutch (TCC) lock-up at lower engine speed further increases the fuel economy. The torque converter Casing and its sensitivity to NVH in a vehicle are also adjusted to ensure a good quietness when TCC lock-up is operated. Figure 10 shows the performance curve of the selected torque converter. It is obvious the selected torque converter delivers the best fuel consumption and the adequate torque capacity.

Shengrui Manufacturing Quality Processes

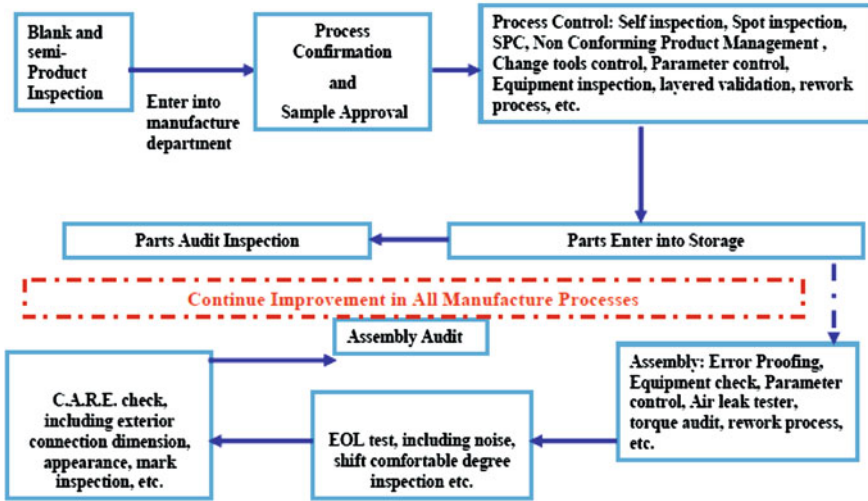


Fig. 13 Shengrui manufacturing quality processes

7 Quality Control and Endurance

The sense of quality and the process of quality control for automotive manufacturers are not developed in proportion to the rapid expansion of automotive industry in China. The manufacturing of engine and manual transmission has been done well over the decades, but not the manufacturing of automatic transmission. Infrastructure of manufacturing of the major components of automatic transmission in China is still under development in a long run. This becomes a great challenge to manufacturers of automatic transmission. The approach for Shengrui to produce SR 8AT in high quality is to set up a clear goal (Fig. 11 SR 8AT Goal and Requirement) in quality and establish a global process of the supplier management process and (Fig. 12 Global Supplier Management Process) a manufacturing quality management process (Fig. 13 Shengrui Manufacturing Quality Processes) along with the required quality control process of TS16949 and ISO such as APQP and PPAP.

8 Conclusion

The SR 8AT is the first model of new, three variant, FWD 8 speed automatic transaxle family. The performance of this newly developed SR 8AT has demonstrated significant advantages in the areas of fuel economy, compactness, weight,

drive performance, NVH and shift quality comparing with 6 or more speed transaxles of AT and DCT in China market. The higher goal and the higher requirements of Shengrui 8AT is processed through the design, the development, the manufacturing and the assembly. The short length, lower weight, better fuel economy and smooth shift have been the keys for the customer satisfaction of vehicle OEMs in the present time and foreseeably in the future.

References

1. Lu J, Xu X, Tenberge P (2012) Shengrui automatic transmission design, development and manufacturing. Transmission symposium of China SAE, Apr 2012
2. Lu J (2011) Industrialization of automotive transmission. Annual technical symposium of Chinese gear manufacture association, Sept 2011

The Double Roller Full Toroidal Variator: A Promising Solution for KERS Technology

Giuseppe Carbone, Francesco Bottiglione, Leonardo De Novellis,
Luigi Mangialardi and Giacomo Mantriota

Abstract We have analyzed in terms of efficiency and traction capabilities a recently patented toroidal traction drive variator: the so-called double roller full toroidal variator (DFTV). We compare its performance with the single roller full-toroidal variator (SFTV) and the single roller half-toroidal variator (SHTV). Interestingly, the DFTV shows an improvement of the mechanical efficiency over a wide range of transmission ratios, and in particular at the unit speed ratio as in such conditions the DFTV allows for zero-spin, thus strongly enhancing its traction capabilities. The very high mechanical efficiency and superlative traction performance of the DFTV have been exploited to investigate the performance of a flywheel based Kinetic Energy Recovery Systems (KERS) where the efficiency of the variator plays an important role in determining the overall energy recovery performance. The energy boost capabilities and the overall round trip efficiency have been calculated for every type of mechanical drive and a comparison has been discussed. The results suggest that SHTV and DFTV are the best choices to improve the energy recovery potential of the mechanical KERS.

Keywords Continuously variable transmissions · Toroidal traction drives · Kinetic energy recovery systems

F2012-C03-006

G. Carbone (✉) · F. Bottiglione · L. Mangialardi · G. Mantriota
Dipartimento di Meccanica Matematica e Management, Politecnico di Bari, Bari, Italy
e-mail: carbone@poliba.it

G. Carbone
Center of Excellence in Computational Mechanics, Politecnico di Bari, Bari, Italy

L. De Novellis
Faculty of Engineering and Physical Sciences, University of Surrey, Guildford, UK

1 Introduction

Present developments in the automotive field are related to the design of drive-trains with the aim of improving the exploitation of the thermal engine, according to the requirements of reduction of fuel consumption and polluting emissions [1–3].

To achieve these targets, the hybrid power trains are being studied and developed. Among all possibilities, some research works claim that mechanical hybrids are more efficient and give the greatest advantages in terms of reduction of fuel consumption and polluting emissions. Several investigations have been made to estimate the effective benefits that such systems can give in mainstream cars and trucks at the present state-of-the-art. Computational results demonstrate that a fuel economy improvement up to 25 % can be obtained in mainstream passenger cars and trucks, which can also be improved further with engine downsizing [4–7].

Continuously variable drives are the core of mechanical hybrids. Chain/belt Continuously Variable Transmissions (CVTs) have been widely studied either theoretically either experimentally [8–10]; however, limitations of the maximum transmittable torque and of control possibilities made the toroidal traction variators a valid alternative for the development of CVT drive trains [11]. A toroidal traction drive is made of input and output disks, which are coupled, respectively, with drive and driven shafts and shaped in such a way to realize a toroidal cavity. A power roller, rotating inside the toroidal cavity, is employed to transfer torque from the drive disk to the driven one, by means of shearing action of elasto-hydrodynamic oil film; furthermore, the tilting of the power roller allows shifting maneuvers.

Referring to the toroidal variators which are actually on the market for automotive applications, the basic geometric distinction is on the position of the roller tilting center (point O in Fig. 1), if it coincides or not with the center of the toroidal cavity. Indeed, we use to refer to the full-toroidal variator [see Fig. 1b] in the first case, and to the half-toroidal variator in the second case [see Fig. 1a]. In Fig. 1c a new patented toroidal geometry [12], the so-called Double roller Full Toroidal Variator (or DFTV), is depicted: two counter-rotating rollers are arranged inside the full-toroidal cavity, with the aim of reducing the spin losses at the roller-disk contact; also, the roller conical shape allows to balance the normal forces, thus making unnecessary the employment of a thrust roller-bearing. In this way, the main advantages of the single-roller toroidal geometries can be combined with consistent improvements of the overall transmission efficiency [13].

The ratio spread and the efficiency of the variable drive are its key feature for application to mechanical hybrid systems. A compromise between a large ratio spread and a good efficiency in both forward and reverse operation must be found to optimize the operating conditions of the KERS. It has been shown (see [14]) that shunted CVT architectures ([15, 16]) which enlarge the ratio spread of the variable drive, can not improve the performance of the KERS as a consequence of a loss of efficiency, in particular in reverse operation (see also [17]).

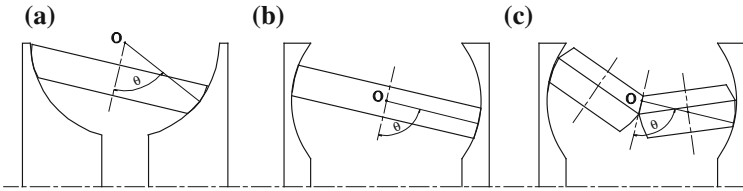


Fig. 1 The toroid geometries: SHTV (a), SFTV (b), and DFTV (c)

For these reasons, in this chapter, the focus is on the performance of toroidal traction drive units. A recently patented toroidal traction drive variator (the DFTV) is analyzed in terms of efficiency and traction capabilities and its performance are compared with the single roller full-toroidal variator (SFTV) and the single roller half-toroidal variator (SHTV). The results are used to investigate the performance of a flywheel based Kinetic Energy Recovery Systems (KERS) where the efficiency of the variator plays an important role in determining the overall energy recovery performance.

2 Traction Efficiency of the Toroidal Drive

In this section we define the main geometric and kinematic characteristics of the Double roller Full Toroidal Variator. Looking at Fig. fig toroideometry, r_0 is the first principal radius of the input and output disc, whereas r_{11} and r_{33} are the second principal radii respectively of the input and output discs. Each power roller has a conical part and a toroidal part: the rollers are in contact along the conical part, whilst the toroidal part is shaped as a typical half-toroidal roller and it is in contact with the input or output disk. Therefore, we call r_2 the curvature radius of a section perpendicular to the roller axis and r_{22} is the second principal radius. For practical aspects, it is useful to define the conformity ratio $CR = r_{22}/r_0$ and the aspect ratio $k = e/r_0$, where e is the eccentricity.

An important control parameter is the tilting angle γ , therefore we can express the dimensionless discs curvature radii formulation as a function of the cone angle θ and of the tilting angle γ (see Fig. fig toroideometry) as $r_{11} = r_1 / \cos(\theta + \gamma)$ and $r_{33} = r_3 / \cos(\theta - \gamma)$ where $r_1 = r_0(1 + k - \cos(\theta + \gamma))$ and $r_3 = r_0(1 + k - \cos(\theta - \gamma))$. From geometric relations we also obtain $r_2 = (r_0 + e) \sin(\alpha/2)$. For studying the kinematics of the DFTV variator, we define the geometric speed ratio $s_{r_{TD}}$ as the ratio of the radial coordinates r_1 and r_2 , namely $s_{r_{TD}} = r_1/r_3$. Said ω_1 the input angular velocity and ω_3 the rotational speed of the output disk, we define the speed ratio s_r as $s_r = |\omega_3|/|\omega_1|$. Percentage differences of the velocities of the sliding contact pairs are taken into account by defining input and output creep coefficients, respectively $C_{r_{in}}$ and $C_{r_{out}}$, as $C_{r_{in}} = (|\omega_1| r_1 - |\omega_2| r_2) / |\omega_1| r_1$ and $C_{r_{out}} = (|\omega'_2| r_2 - |\omega_3| r_3) / |\omega'_2| r_2$ and the slip coefficient $s_c = |\omega'_2|/|\omega_2|$ where ω_2 and ω'_2 are the angular

velocities of the two counter-rotating rollers. The transmission ratio can be expressed as a function of the overall creep coefficient C_r

$$s_r = (1 - C_r)s_c s_{r_{ID}} \quad (1)$$

with $(1 - C_r) = (1 - C_{r_{in}})(1 - C_{r_{out}})$. For each roller i of the roller pair we can define points Θ_i , which represents the point of intersection of the tangents to the toroidal cavity at the roller-disc contact points, and Ω_i , defined as the intersection point of the roller and disk rotation absolute axes. The angular velocities of the roller relative to the input and output disks, $\omega_{21} = \omega_2 - \omega_1$ and $\omega_{23} = \omega'_2 - \omega_3$ have spin velocity components, ω_{21spin} and ω_{23spin} , which can be directed inwards or outwards. By choosing a proper value of the cone incidence angle α , it is possible to have zero spin velocities at $s_{r_{ID}} = 1$ and the spin coefficients can be expressed as:

$$\begin{aligned} \sigma_{21} &= \frac{\omega_{21spin}}{\omega_1} = \sin(\theta + \gamma) - (1 - C_{r_{in}}) \frac{1 + k - \cos(\theta + \gamma)}{1 + k} \\ \sigma_{23} &= \frac{\omega_{23spin}}{\omega_3} = \sin(\theta - \gamma) - \frac{1}{(1 - C_{r_{out}})} \frac{1 + k - \cos(\theta - \gamma)}{1 + k} \end{aligned} \quad (2)$$

Following the same approach proposed in [13, 18], let us define the traction coefficient $\mu = F_T/F_N$ as the ratio between the tangential force at the roller-disc interface F_T and the normal load F_N and the spin momentum coefficient $\chi = M_S/F_N r$, where M_S is the spin momentum and r the disk radial coordinate of the contact point. From the momentum equation applied to the counter-rotating rollers about each roller axis, the parameters μ and χ have been calculated according to [13, 18] considering that the angle $\theta_{DT} = (\pi - \alpha)/2$ (see Fig. 2) and the radial coordinates in dimensionless form, namely $\tilde{r}_1 = r_1/r_0$ and $\tilde{r}_3 = r_3/r_0$. The term t_B represents the dimensionless torque losses due to roller bearings on the variator roller axes, which has been evaluated according to the SKF technical documentation. From the equilibrium equations of the disks we can evaluate the effective torque coefficients at the input and output variator side:

$$\begin{aligned} t_{in} &= \mu_{in} + \chi_{in} \sin(\theta + \gamma) \\ t_{out} &= \mu_{out} - \chi_{out} \sin(\theta - \gamma) \end{aligned} \quad (3)$$

with $t_{in} = T_{in}/mnF_N r_1$, $t_{out} = T_{out}/mnF_N r_3$ can be interpreted as effective torque coefficients at the input and output variator side. In the previous relations we have considered the possibility to arrange n set of rollers inside m toroidal cavities. Moreover, we can express the thrust force acting in the disk axial direction F_D as a function of the normal load F_N and of the tilting angle γ

$$\begin{aligned} F_{D_{in}} &= nF_N \sin(\theta + \gamma) \\ F_{D_{out}} &= nF_N \sin(\theta - \gamma) \end{aligned} \quad (4)$$

With these positions, a straightforward expression of the overall mechanical efficiency $\nu = P_{out}/P_{in}$ can be obtained:

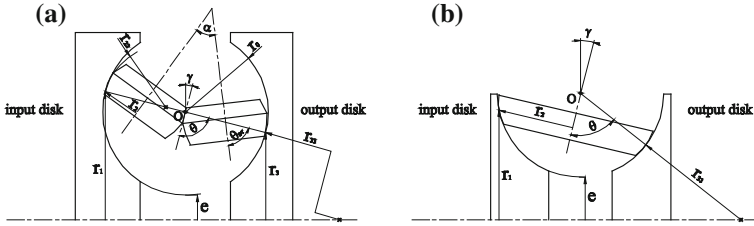


Fig. 2 The double roller full toroidal (DFTV) geometric quantities

$$v = s_c(1 - C_r) \frac{\mu_{out} - \lambda_{out} \sin(\theta - \gamma)}{\mu_{in} + \lambda_{in} \sin(\theta + \gamma)} \tag{5}$$

A fully flooded isothermal contact model [13, 18] has been utilized to calculate the shear stresses at the interface of the elements in contact, and thus, the traction and spin coefficients.

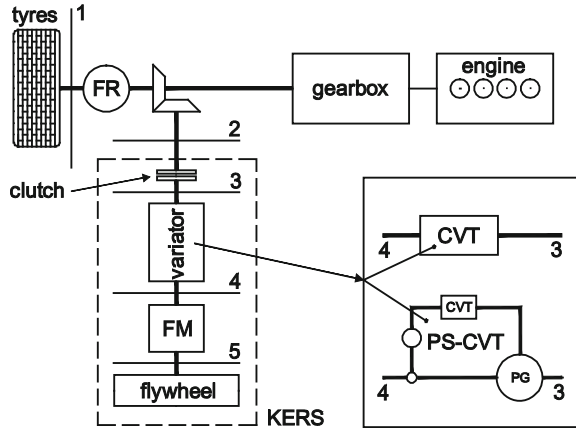
3 Simulation of KERS Performance References

Among all the possible configurations of mechanical hybrid power trains [7] a flywheel KERS connected into the vehicle prop shaft through a friction clutch (see Fig. 3) is considered. This configuration gives larger fuel economy improvements than others when it works in synergy with stop and re-start system [7].

The simulation has been performed via inverse dynamic simulator of the vehicle power train. The driving cycle is given as a velocity pattern and the driveline parameters are calculated backwards with kinetic, kinematic and efficiency models. In this chapter the focus is on the energy recovery potential of the KERS and the gearbox and the engine included in the model. Further investigation is needed to get the fuel economy and CO₂ emissions reduction potential of the KERS. The driveline with KERS which has been considered is made of wheels, differential and final drive (FR), KERS driving clutch, toroidal CVT, final step-up drive and high-speed rotating flywheel. We define two KERS performance indexes: the KERS boost and the Round Trip efficiency. In the Sect. 2 of the driveline (see Fig. 3), the torque which is necessary to drive the vehicle following the driving schedule is called T_2^{nec} , which can be positive or negative. The quantity $T_2^{'nec}$ is defined, which is equal to T_2^{nec} only when $T_2^{nec} \geq 0$, zero otherwise. The torque that is actually given by the KERS in the Sect. 2 is T_2 , and it can be positive (re-use mode) or negative (recovery mode). Moreover, we define: T_2' which is equal to T_2 if $T_2 \geq 0$, zero otherwise; T_2'' which is equal to T_2 if $T_2 < 0$, and zero otherwise. The KERS boost is defined as:

$$\text{KERS boost} = \frac{\int_0^{t_{cycle}} T_2' \omega_2 dt}{\int_0^{t_{cycle}} T_2' nec \omega_2 dt} \tag{6}$$

Fig. 3 Schematic picture of the driveline of the mechanical hybrid vehicle. Sections of the driveline are tagged with numbers. FR is the final drive of the vehicle driveline, FM is the final multiplier. The KERS is plugged in the vehicle propshaft through a friction clutch. A second clutch (not shown in the figure) can disconnect the FM from the variable drive when the flywheel is in idle rotation



where t_{cycle} is the time duration of one driving cycle and ω_2 is the angular velocity of shaft 2. The KERS boost is the energy given by the KERS to the vehicle prop shaft per cycle, divided by the energy that is needed to follow the driving schedule per cycle and calculated in the Sect. 2 of the driveline. The Round-Trip efficiency is calculated as:

$$\text{RoundTripEfficiency} = \frac{\int_0^{t_{cycle}} T'_2 \omega_2 dt}{-\int_0^{t_{cycle}} T''_2 \omega_2 dt} \quad (7)$$

The Round Trip Efficiency is the energy actually given by the KERS into the vehicle prop shaft per cycle divided by the energy actually given by the prop shaft to the KERS per cycle.

4 Results

Figure 4 compares quantitatively the different toroidal variators in terms of traction capabilities and efficiency. Calculations have been carried out at given constant values of the primary speed $\omega_1 = 2000$ RPM and of the normal load $F_N = 20$ kN, with the geometric features reported in Ref. [13, 18]. The dimensionless output torque t_{out} is plotted against the overall creep coefficient C_r , whereas the efficiency ν is represented as a function of the input dimensionless torque t_{in} . In all cases we observe, as expected, an almost linear increase of t_{out} as C_r is increased from zero. However, as the creep increases the curve starts to deviate from the linear trend and reach a saturation values in correspondence of the maximum transmissible torque. Interestingly the slope of the linear part of the three traction curves is different for the three different variators and also changes as the geometric speed ratio s_{rD} is changed. In all cases the SFTV shows a significantly worse behavior if compared to the other two typologies. More interesting is to

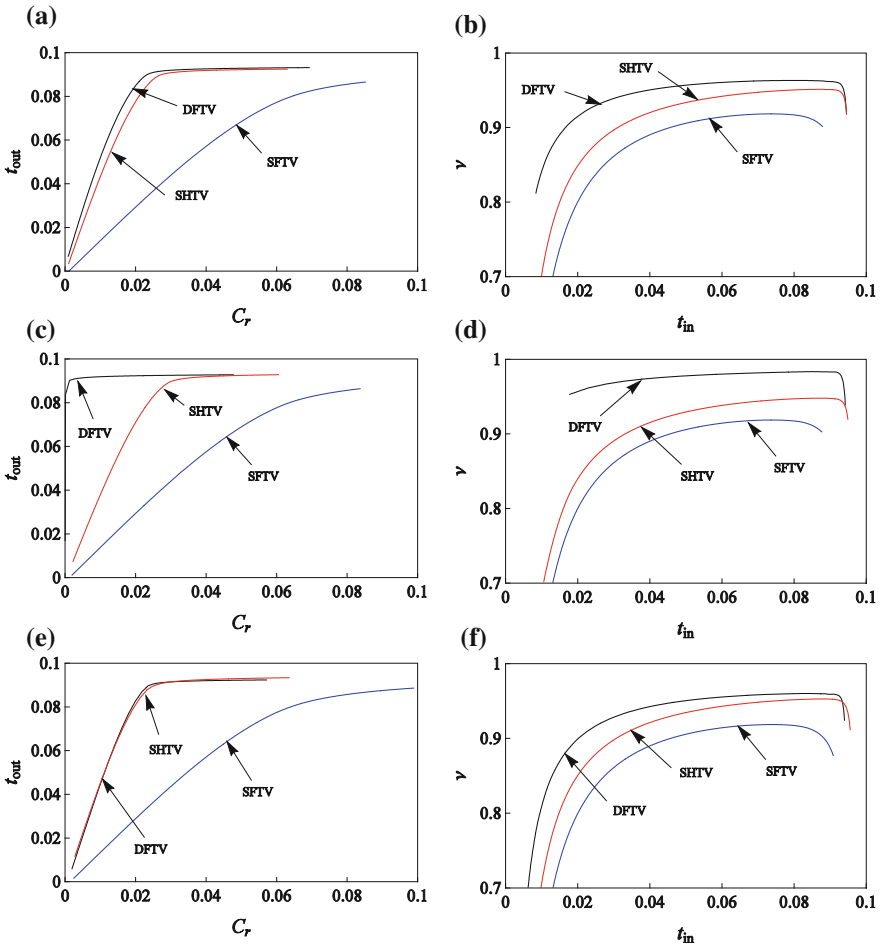
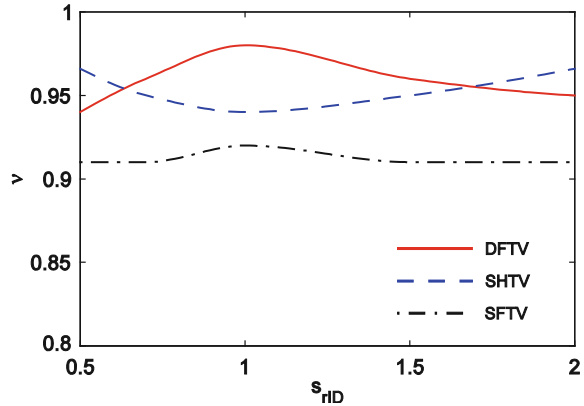


Fig. 4 The dimensionless output torque as a function of the creep coefficient (*left side*), and the efficiency as a function of the dimensionless input torque (*right side*) for the three variators—DFTV, SHTV, SFTV. Results are present for three values of the geometric speed ratio and for a normal contact force of 20 kN

compare the SHTV and the DFTV. At ratios $s_{rID} = 0.7$ and $s_{rID} = 1.5$ the two variators show almost the traction capabilities however, the DFTV performs significantly better than the SHTV in terms of mechanical efficiency. We also observe that DFTV strongly outperforms both variators in terms of traction and mechanical efficiency the SHTV at geometric speed ratio $s_{rID} = 1$, as a consequence of the very limited amount of spin motion and spin momentum.

The simulations of KERS performance have been done with the data of a typical city car (more details are in [14]). The main features of the KERS device follow. We have considered a CVT KERS mass equal to about 25 kg. The

Fig. 5 The optimal efficiency of the three toroidal CVTs as a function of the geometric speed ratio



simulations have been performed considering a flywheel with the following characteristics: flywheel inertia $J_f = 0.0562 \text{ kgm}^2$, flywheel minimum velocity $\omega_{f_{\min}} = 12 \text{ kRPM}$, flywheel maximum velocity $\omega_{f_{\max}} = 24 \text{ kRPM}$ (upper and lower bounds have been chosen according to Ref. [16]). The mechanical hybrid under analysis can be exploited for urban driving application. With the given inertia and upper angular velocity of the flywheel the maximum energy which can be stored is about 178 kJ that corresponds to the kinetic energy of the vehicle at 60 kph. The simulations have been performed following the urban FTP-75 driving schedule. The driving schedule has been considered as a periodic function which must be followed by the vehicle. The state of charge of the flywheel is the same at the beginning and at the end of the cycle [4]. In order to compare the performances which can be achieved with different variators, for any given toroidal traction drive under investigation the τ_{FM} has been optimized and the optimal value has been used in the simulation.

To simulate the performance of KERS equipped with three different types of toroidal variators, the efficiency of DFTV, SHTV and SFTV have been calculated by means of the analytical models (see also [13, 18]). We assume that the clamping system allows to control the clamping force F_N in order to optimize the efficiency of the toroidal traction drive for any given speed ratio and the input torque. In order to perform simulations under these working conditions, the efficiency has been calculated with the optimal value of the normalized input torque t_{in} with different speed ratios and the results are shown in the Fig. 5. The ratio spread of the three variators is equal to 4, with the speed ratio ranging from $s_{rIF} = 0.5$ to $s_{rIF} = 2.0$. It is shown that the efficiency of the SFTV is smaller than the efficiency of the DFTV and the SHTV with every value of the speed ratio, whereas the DFTV efficiency is larger than SHTV's with intermediate values of the speed ratio and it is smaller close to the extremities of the speed ratio range.

The results of our simulations are shown in the Fig. 6. The KERS boost (see Fig. 6a) in the FTP-75 driving schedule is equal to 20.4 % with DFTV and 20.2 % with SHTV (the difference is negligible) whereas it is about equal to 18.4 % with

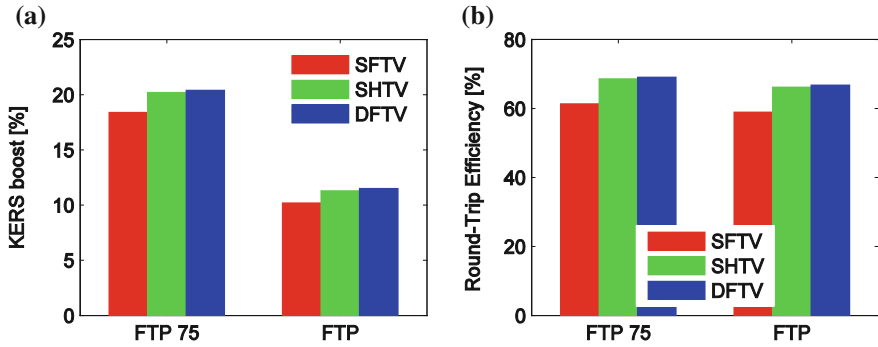


Fig. 6 The KERS boosts (a), and the KERS round trip efficiency (b). Results are shown for the FTP 75 (*urban*) and FTP (*mixed*) driving schedules

SFTV. Because SFTV is the one which is presently used in mechanical hybrid systems (Torotrak toroidal traction drive is SFTV), it is here shown how a correct choice of the variator leads to improve the KERS boost of about 10 %. Similar results are shown in FTP driving schedule, in which the KERS boost is about 10.2 % with SFTV, 11.3 % with SHTV and 11.5 % with DFTV. As expected, the best performances are given in urban drive. Figure 6b shows the overall round-trip efficiency of the KERS in FTP-75 and FTP driving schedules and a comparison of the results achieved with SFTV, SHTV and DFTV. The round-trip efficiency is not much affected by the driving style, whereas the SFTV efficiency is about 7 % smaller than the DFTV's and SHTV's. A lower efficiency gives drawbacks on the KERS boost but also on the heat generation inside the KERS device (variator and clutch in particular). Finally, we have performed the calculations with a given ratio spread for all the toroidal traction drives under analysis. It is known [14] that a variable drive with a larger ratio spread and a good efficiency performs better in terms of KERS boost. Therefore, the optimal design of the DFTV should be sought in order to increase the ratio spread without affecting the (very high) efficiency of the DFTV itself, and let the DFTV strongly outperform the SHTV in KERS applications.

5 Conclusions

We have presented a traction/efficiency analysis of a recently patented geometry of a toroidal traction drive: the Double roller Full Toroidal Variator, which has been designed in such a way to combine the advantages of existing toroidal geometries in order to enhance the efficiency of the variator. In particular, the DFTV variator consists of a set of counter-rotating conical rollers which are placed into a toroidal cavity: the geometric characteristics of the power rollers allow to reduce the spin losses in a wide range of speed ratios and to get rid of the thrust ball-bearing,

which contributes to the torque losses of the half-toroidal type geometry. In order to evaluate the performance of the toroidal traction drive, we have developed a fully-flooded contact model, based on the results of EHL lubrication theory. Our calculations have shown the effectiveness of the DFTV geometric characteristics in terms of reduction of spin losses and improvement of the overall efficiency. The very high mechanical efficiency and superlative traction performance of the DFTV have then been exploited to investigate the performance of a mechanical Kinetic Energy Recovery Systems (KERS). The energy boost capabilities and the overall round trip efficiency have been calculated for DFTV, SHTV and SFTV and a comparison has been discussed. The results have shown that the choice of DFTV and SHTV leads to a KERS boost capability in urban drive that is of about 10 % larger than the result achieved with SFTV, which is the traction drive of the Torotrak Mechanical Hybrid Systems.

References

1. Mantriota G (2005) *Int J Veh Des* 37:327–342
2. Brace C et al (1999) In proceedings of the international congress on continuously variable power transmission CVT'99, Eindhoven, The Netherlands, September 16–17 1999:pp 27–33
3. Carbone G, Mangialardi L, Mantriota G (2002) *SAE J Engines* 110(3):2474–2483
4. Cross D, Brockbank C (2009) SAE Technical paper 2009-01-1312
5. Brockbank C (2010) CVT 2010 CVT hybrid international conference, Maastricht, The Netherlands November 2010 pp 163–169
6. Barr A, Veshnagh A (2008) SAE Technical Paper 2208-01-0083
7. Brockbank C, Body W (2010) Proceedings of the ASME 2010 International Design Engineering Technical Conferences & Computers and Information in Engineering Conference IDETC/CIE 2010. August 15–18, Montreal, Quebec, Canada
8. Carbone G, De Novellis L, Commissaris G, Steinbuch M (2010) *ASME J Mech Des* 132(2):1–8
9. De Novellis L, Carbone G (2010) *ASME J Mech Des* 132(12):121004
10. Carbone G, Mangialardi L, Mantriota G (2002) *ASME J Mech Des* 124(3):543–557
11. Imanishi T, Machida H (2001) *Motion & Control* No. 10:2–10
12. Durack M (2011) World intellectual property organization, International publication number: WO 2011/041851 A1
13. Carbone G, Mangialardi L, Mantriota G (2004) *Mech Mach Theory* 39:921–942
14. Bottiglione F, Mantriota G (2012) Submitted to *ASME J Mech Des*
15. Mangialardi L, Mantriota G (1999) *Mech Mach Theory* 34(7):973–994
16. Greenwood CJ (2009) International Patent, WO 2009/141646A1
17. Bottiglione F, Mantriota G (2011) *ASME J Mech Des* 133:084503
18. De Novellis L, Carbone G, Mangialardi L (2012) *ASME J Mech Des* 134(7):071005

CVT's Evolution and Nissan's Latest CVT Technologies

Yoshitaka Miura, Kiyonari Yamamoto and Tetsuro Ito

Abstract A continuously variable transmission (CVT) is an excellent system for achieving high levels of well-balanced performance in terms of fuel economy, acceleration, vehicle mountability and smoothness. It can be regarded as the optimum transmission solution for passenger vehicles at the present time. This paper describes the evolution of CVTs with regard to technical aspects. It first reviews the evolution of torque capacity and ratio coverage, which are the major specifications providing diverse CVT performance attributes. It then surveys the evolution of technology for improving fuel economy, which has been a key issue in recent years. Finally, the technologies incorporated in the latest CVT are described to illustrate the present level of achievement

Keywords CVT · Evolution · Torque capacity · Ratio coverage · Fuel economy

1 Diverse Transmission Requirements

Automotive transmissions have diverse requirements. Suitable ratio coverage and torque capacity are required to deliver the desired acceleration performance. Size and weight are critical requirements with respect to vehicle mountability. Fuel economy, smoothness, noise, vibration and reliability are still other performance

F2012- C03-009.

Y. Miura (✉) · K. Yamamoto
Nissan Motor Co., Ltd, Yokohama, Japan
e-mail: yoshi-miura@mail.nissan.co.jp

T. Ito
JATCO Co., Ltd, Fuji, Japan

Fig. 1 External appearance of CVT



requirements. It is also necessary to satisfy simultaneously diverse production requirements with regard to reducing investment costs, manufacturing costs, and the number of model types.

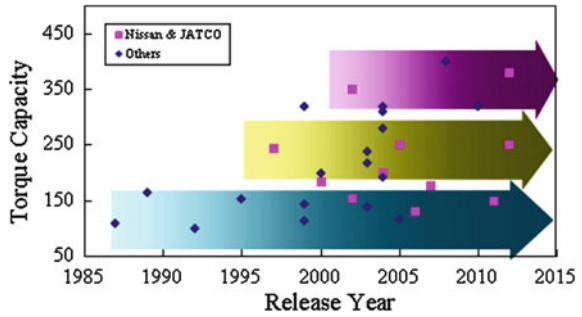
Moreover, the balance of these performance requirements for continuously variable transmissions (CVTs) differs depending on the performance required by the character of the vehicle. For example, sport utility vehicles (SUVs) have severe requirements for torque capacity and ratio coverage because such vehicles emphasize acceleration performance, though the requirements for transmission size and weight are moderate. In contrast, compact cars have rigorous requirements for size and weight, though the requirement for torque capacity is moderate. These examples illustrate that the balance of performance required of a CVT varies greatly depending on the character of the vehicle (Fig. 1).

CVTs represent an excellent transmission system for achieving high-levels of all-around performance with respect to fuel economy, acceleration, mountability and smoothness. At present, CVTs appear to be the optimum transmission solution for passenger vehicles.

2 Diverse Evolution of CVTs

CVTs have continued to evolve at a fast pace. Besides progressing rapidly, CVTs have also evolved to satisfy diverse requirements. The evolution of CVTs can be seen as the accumulation of wide-ranging improvements. Therefore, tracing the history of each performance requirement is an effective way of describing their evolution. This paper begins with a discussion of torque capacity and ratio

Fig. 2 Evolution of torque capacity



coverage, which are among the major specifications of CVTs, and also describes the technologies adopted to improve fuel economy that has been one focus of attention in recent years.

2.1 Evolution of Torque Capacity

Automotive CVTs have a long history, and diverse variator systems have been developed from the early 1900s. However, the first successful example of a mass-produced automotive CVT was installed on a Subaru car by Fuji Heavy Industries in 1987. Nissan adopted a similar CVT in 1992, and since then Nissan has been developing its own original CVTs [1] (Fig. 2).

Because a CVT transmits power by the frictional force of the pulleys and belt, it had a disadvantage in transmitting large torque compared with a geared transmission. For that reason, CVTs were initially paired with small engines having low torque ratings. Later, this problem was solved by increasing the belt size. CVTs have evolved at a fast pace to achieve a torque capacity at present of 380 Nm with a torque converter and can also handle 400 Nm without a torque converter [2].

2.2 Evolution of Ratio Coverage

Lower gear ratios are required for acceleration performance, but higher gear ratios are also needed to obtain better fuel economy in high-speed driving. We define ratio coverage as the spread between the largest and the smallest gear ratio (Fig. 3).

The evolution of CVT ratio coverage has matched the pace seen for automatic transmissions (ATs). The earliest CVTs had ratio coverage around 5.0, but ratio coverage has progressed rapidly over the years. CVT models with ratio coverage greater than 7.0 have appeared in recent years.

In the case of stepped ATs, improvement of ratio coverage means adding more gear speeds. However, because that presents size and mountability issues, ATs with more gear ranges have mainly been used on rear-drive vehicles where more space is allowed.

Fig. 3 Definition of ratio coverage

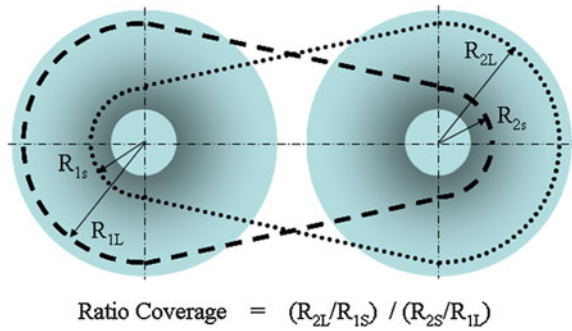
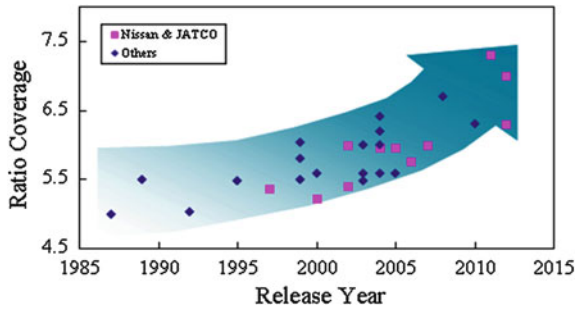


Fig. 4 Evolution on ratio coverage



The ratio coverage extension of CVTs depends on the running diameter of the belt. To obtain larger ratio coverage in a compact size, it is necessary to have a smaller minimum running diameter. A CVT that achieves large ratio coverage with the addition of an auxiliary transmission has also been put on the market [3] (Fig. 4).

2.3 Analysis of Evolution of Torque Capacity and Ratio Coverage

This section presents an analysis of the combined evolution of torque capacity and ratio coverage. These two major CVT specifications are closely related as key parameters for balancing fuel economy with acceleration performance. Both torque capacity and ratio coverage are constrained by the belt strength at its minimum running diameter. There is a trade-off between torque capacity and ratio coverage, resulting in smaller ratio coverage in order to ease the belt strength requirement.

Figure 5 shows the evolution of CVTs in terms of torque capacity and ratio coverage. In the first generation of CVTs, torque capacity and ratio coverage were both small. The second generation showed an expansion of ratio coverage. Improvements made to the third generation expanded torque capacity and also widened ratio coverage at the same time.

Fig. 5 CVT evolution in terms of torque capacity and ratio coverage

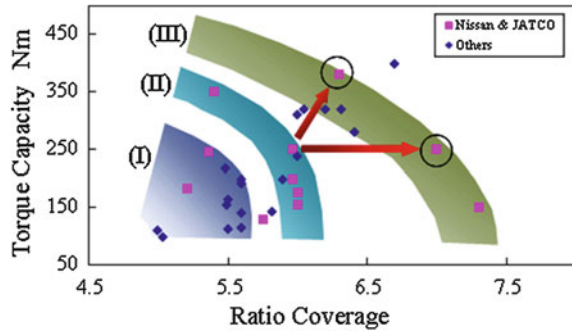


Figure 6 lists examples of the constraints, namely, belt strength, mountability, noise and vibration, which had to be overcome to achieve the evolution shown in Fig. 5. Belt strength and mountability have a strong relation to ratio coverage, and auxiliary transmission space relates to torque capacity, the chain noise connects with vehicle size respectively. In this way, the evolution of CVTs progressed through a balanced resolution of these constraints.

2.4 Evolution of Fuel Economy

Among diverse CVT performance attributes, evolution with respect to fuel economy has attracted attention in recent years because of heightened market needs in this regard, and rapid progress has been made. The path of CVT evolution in the area of fuel economy cannot be discussed sufficiently only in terms of mechanical efficiency, as Hiraku [4] has noted. Ensuring the desired fuel economy also requires a good match with engine efficiency. It is important for the CVT to enable the engine to operate in the region of good fuel economy while satisfying the driver's demand for power. We refer to this capability as flexibility. It is necessary to discuss the two parameters of flexibility and efficiency that contribute to fuel economy (Fig. 7). The dashed line indicates equivalent US combined highway/city fuel economy.

The first generation of CVTs had limited flexibility because their ratio coverage was small and mechanical efficiency was also low. Subsequently, fuel economy followed an upward path, as indicated by (A) in Fig. 8, due to ratio coverage extension and improved shift control. Currently, the fuel economy path is headed in a lateral direction as shown by (B) in the figure. This indicates a shift toward mechanical efficiency improvement.

Fuel economy has already reached a high level. Flexibility has also attained a high level, and the margin ΔA for further improvement appears limited. In contrast, the mechanical efficiency has some margin ΔB for improving of the variator and oil pump. Therefore, activities to improve fuel economy further in the future will likely focus on enhancing mechanical efficiency.

Fig. 6 Constrains of torque capacity and ratio coverage

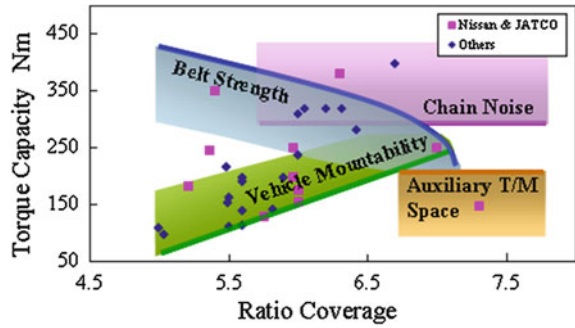


Fig. 7 Evolution on fuel economy

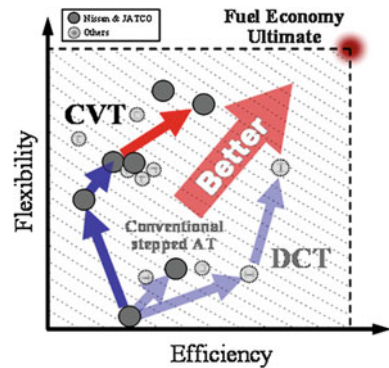
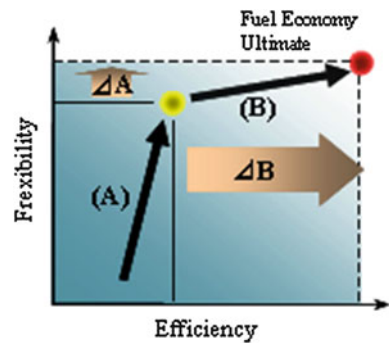


Fig. 8 Path of evolution for fuel economy



3 Technologies Supporting CVT Evolution

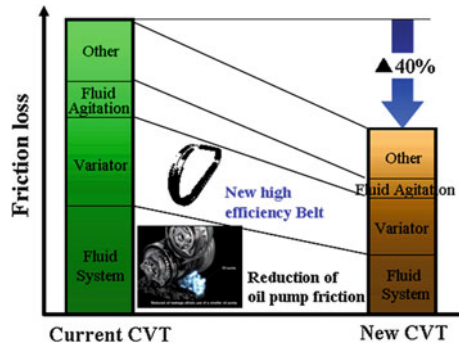
As examples of technologies supporting the evolution of CVTs, this section describes some of the technical features of a new Nissan/JATCO CVT has been started providing in 2012. The basic specifications are shown in Fig. 9 [5].

This new CVT has the large evolution step on torque capacity and ratio coverage, as it is shown the red line on Fig. 5. Though the center distance is identical,

Fig. 9 New Nissan/JATCO CVT Specification

Item		2.0L-class FWD-vehicles		3.5L-class FWD-vehicles	
		Current	New	Current	New
Torque Capacity (Nm)		250	250	350	380
Gear Ratio	Ratio Coverage	6.0	7.0	5.4	6.3
	Pulley Ratio	2.35-0.39	2.64-0.38	2.37-0.44	2.43-0.38
	Final gear ratio	5.1-6.4	4.8-6.4	4.8-6.3	4.7-5.8
Though Low Ratio		12.0-15.2	12.7-16.8	11.6-15.0	11.3-14.1
Weight		91.5	91.5	103.5	98.5
Overall Length		340	345	372.6	356
Distance between pulley Shafts		171	173	178	173
Distance between 1 st and 2 nd Shafts		197	197	205	205

Fig. 10 Friction breakdown for new CVT



there are two models; base model has ratio coverage 7.0 at torque capacity 250 Nm, and high torque model becomes ratio coverage 6.3 at torque capacity 380 Nm.

Dramatic progress has also been made in improving fuel economy as a result of markedly reducing mechanical friction by 40 % compared with an existing CVT (Fig. 10), as indicated by the red line in Fig. 7. This section describes the variator and oil pump, which are two key technologies that have especially contributed substantially to this progress.

3.1 Variator Technology

One remarkable improvement in the evolution of the variator is the marked expansion of ratio coverage by 17 %. The minimum running diameter had to be reduced to accomplish this. It involved reducing the shaft diameter while maintaining sufficient shaft strength. Additionally, large improvements were made to the belt, including changing the flank angle and relaxing the belt tension in the 250 Nm model [6]. Variator friction consists of internal belt friction and friction

Fig. 11 Variator efficiency

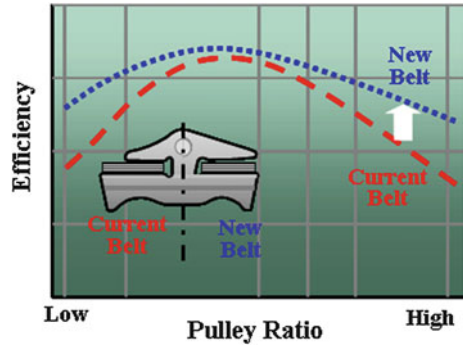
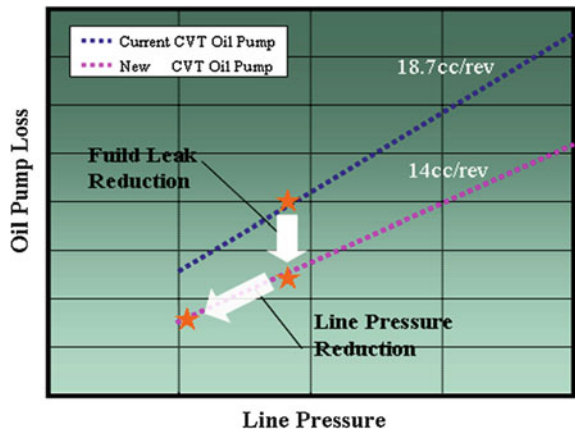


Fig. 12 Friction of oil pump



between the belt and pulleys. The friction reduction this time mainly involved reducing internal belt friction (Fig. 11). For the 380 Nm model, a new chain was adopted. It was previously reported that the chain friction was reduced. However, greater chain noise due to the longer pitch between the pins is a major issue. Increased efforts to reduce the pitch are expected in the future [7].

Variator friction accounts for a large proportion of overall CVT friction, so there is still considerable room for further improvement. The focus of future improvements will likely shift from internal friction to friction between the belt/chain and pulleys.

3.2 Oil Pump Technology

Improvements were made not only to the body of the oil pump of the new CVT but also to the hydraulic system, resulting in a significant improvement of mechanical efficiency. The discharge rate was reduced by simplifying the control valve so as to

reduce fluid leakage. The required hydraulic pressure was reduced by lowering the line pressure as a result of reducing the variator clamping force and expanding the pulley pressure area. These measures worked to improve efficiency substantially (Fig. 12).

4 Summary

In illustrating the evolution of CVTs, this paper has described the progress made in improving torque capacity, ratio coverage, and fuel economy. The technologies supporting this evaluation were then discussed, taking the latest CVT as an example. The main points presented are summarized below.

- (1) Torque capacity and ratio coverage have evolved to notably high levels. This evolution was accomplished by resolving the constraints posed by diverse vehicle requirements.
- (2) Advances in fuel economy were achieved through progress toward greater flexibility and mechanical efficiency. Future evolution will be focused mainly on improvement of mechanical efficiency.
- (3) Many new technologies have been incorporated in the variator and oil pump of the latest CVT and evolution toward higher levels of performance will continue in the future.

References

1. Hayasaki K (2004) Development of high torque capacity belt CVT. J JSAE 58(9):29–34
2. Schiberna P (2007) The newly developed second generation audi multitronic CTI, 6th international CTI symposium vol 2, 383–398
3. Nakano H (2011) The world's first new type CVT with auxiliary transmission that achieved downsizing, weight reduction and good fuel economy. Journal of JSAE 65(9):88–91
4. Hiraku R (2008) Strategic development target of transmission CTI, 7th international CTI symposium, vol 1, 133–150
5. Okakara F (2012) Next generation eco-friendly CVT for 2.0–3.5-class FWD-vehicle JSAE spring congress, 26–12, 5–8
6. van der Sluis F (2012) The success of the push belt CVT JSAE spring congress, 26–12 9–16
7. Englisch A, Teubert A (2010) The high value CVT CVT-hybrid international conference 4–9

Development of a New 6-Speed Dual Clutch Transmission for the China Market

Chao Jiang, Mingli Huang, Gold Eckart and Xiaoning Xiang

Abstract Shanghai Automotive Industries and its affiliate, Shanghai Automotive Gear Works present the DCT 360, the first dual clutch transmission developed specifically for the China automotive market. This transmission was jointly developed by SAIC with support from core cooperators and manufactured by SAGW. The first vehicle application of this 6-speed dual-clutch transmission is new generation of Roewe 550, produced by SAIC Motor Passenger Vehicle. The 6-speed dual-clutch transmission features BorgWarner DualTronic[®] technology, in the form of dual clutch and electro-hydraulic control modules, both produced by BorgWarner United Transmission Systems in Dalian, China. This paper will provide a design overview of the transmission architecture, main characteristics and key subsystems. The paper will also provide an overview of the development process, and the fuel economy benefit to the vehicle.

Keywords New Dual Clutch Transmission

F2012-C03-018

C. Jiang

SAIC Motor Passenger Vehicle Co, Shanghai, China

M. Huang

Shanghai Automotive Gear Works, Changchun, China

G. Eckart

BorgWarner United Transmission Systems Co., Ltd, Dalian, China

X. Xiang (✉)

BorgWarner Transmission Systems, Auburn Hills, USA

e-mail: xxiang@borgwarner.com

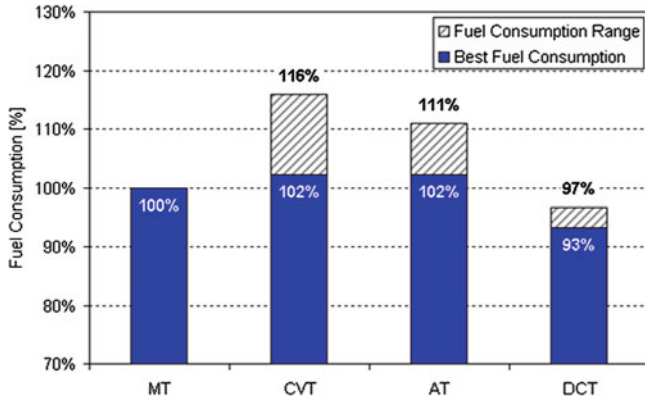


Fig. 1 Fuel efficiency comparison of small car with different transmissions in New European Drive Cycle (NEDC) [1]

1 Introduction:

1.1 Market Drivers for DCT:

- Fuel efficiency and CO₂ reduction—DCT is the efficiency benchmark—superior to Step AT, CVT and M/T.
- Performance and driving comfort—wet DCT offers the launch and shift quality of step AT with tuneable characteristics, with superior responsiveness and acceleration
- Flexibility—DCT offers a large variety of available gear ratios and ratio spread
- Compatibility—DCT is compatible with all new propulsion trends; high torque diesel, high speed gas, stop-start, hybrid, etc (Fig. 1).

1.2 Automatic Transmission and DCT Growth in China:

As they become increasingly popular with consumers, the growth rate of automatic transmissions in China is faster than it is globally. As this trend continues, production of automatic transmissions in China is expected to grow rapidly over the next 5–10 years. A significant portion of the locally produced AT population in China is expected to be DCTs (Fig. 2).

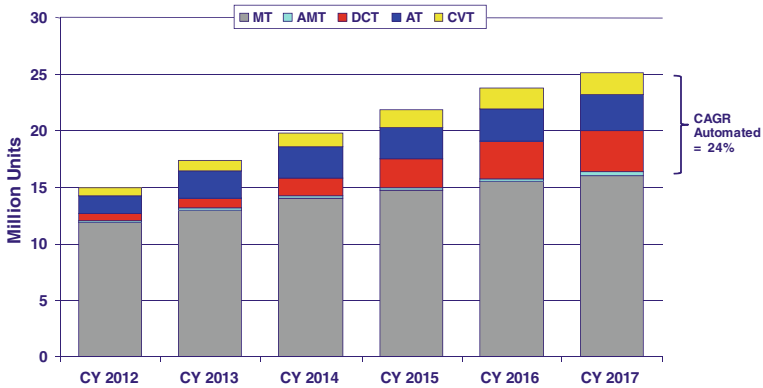


Fig. 2 Projected Transmission production in China by type

1.3 SAIC Drivers to Invest in Developing DCT:

- Improved vehicle performance and fuel economy as compared to base 5-speed AT
- Market differentiator for domestic brand, premium, high volume vehicles
- Reduces dependency on purchased transmissions
- Enables more control over brand improve image/brand ‘DNA’
- Significantly increased local content per vehicle
- Leverages SAGW core competency in manual transmissions
- Government regulations to reduce fuel consumption and emissions, and encouragement and support to develop new technology to achieve those goals (Figs. 3 and 4).

2 Program Targets

In addition to the strategic and market drivers, the wet DCT architecture was the best solution to meet key program targets, as listed in the table below (Table 1).

3 Dual-Clutch Technology Partner

Two enabling technologies for the commercialization of Dual Clutch transmissions have been electro-hydraulic controls and advanced wet friction materials and friction systems. BorgWarner United Transmission Systems Co. (BWUTS) is a joint venture between BorgWarner and the China Automotive Development



Fig. 3 SAGW Transmission product portfolio

SAIC Passenger Car Company Transmission Development Plan

Products: Wet Dual Clutch Transmission, Dry Dual Clutch Transmission; Electronic Drive Transmission; Automatic Mechanical Transmission(AMT); 6 Speed and 5 Speed Manual Transmission

Vehicle Model	Catalog	Ferrari	MG	Development Status			
				In Developing	In Production		
SEDAN	C	[Car icons]		DCT360	DCT360B	SCM360	
	B/B+	[Car icons]		DCT250	SCM250	SH78Z	EDU
	A+	[Car icons]		AMT	SH63Z		
	A	[Car icons]					
	A0	[Car icons]					
SUV	Medium	[Car icons]					
	Small	[Car icons]					

Fig. 4 SAIC transmission vehicle applications

United Investment Co. Ltd. (CDUI), which represents 12 leading China OEMs. The joint venture was formed specifically to bring DCT technology to the China market. The BWUTS operation is located in Dalian, China, and produces

Table 1 Transmission program targets

Program Target	Design Direction
Automatic transmission with best-in-class shift comfort	<ul style="list-style-type: none"> • Wet DCT for superior controllability over wide operating range
Improved fuel efficiency compared to Planetary AT	<ul style="list-style-type: none"> • DCT is best-in-class for fuel efficiency • Dual clutch module with waved friction plates to minimize open-pack drag
Stop-start compatibility	<ul style="list-style-type: none"> • DCT is compatible with stop-start without auxiliary electric pumps or charging devices
Overall length <350 mm	<ul style="list-style-type: none"> • Innovative gearbox layout with maximum gear sharing • Concentric dual-clutch module design
Multiple engine and vehicle applications	<ul style="list-style-type: none"> • Layout design for maximum ratio flexibility • Wet DCT for thermal robustness and low inertia
Minimum Weight	<ul style="list-style-type: none"> • DCT has high specific torque capacity

DualTronic[®] dual clutch modules and electro-hydraulic control modules for Dual Clutch transmissions. The value proposition of BWUTS is:

- The latest proven DCT technology from BorgWarner
- Shared investment through common module family design approach

4 Global Development Team

The DCT 360 is a product of a truly global development effort, with a team of experts from around the world collaborating daily. Some of the key development partners are listed in the table below: (Table 2).

5 Transmission Overview

The DCT 360 is a 6-speed transverse dual-clutch transmission for front-wheel-drive passenger vehicle applications.

6 Key Features

- Wet dual clutch module with integrated torsional damper
- Electro-hydraulic control system with integrated shift actuation
- 3-shaft layout with concentric inputs and multiple gear sharing
- Off-axis, gear driven pump
- Single, double and triple cone synchronizers
- Passenger compartment mounted TCU (Fig. 5 Table 3)

Table 2 Global transmission development team

Role	Partner	Location(s)
Overall project management, transmission design, TCU high level Software, system integration, manufacturing and vehicle integration.	SAIC Motor Technical Center (SMTC)	Shanghai, China
Engineering consulting	Shanghai Automotive Gear Works (SAGW)	
<ul style="list-style-type: none"> • Gearbox design and development • Controls and system integration 	Gesellschaft für Industrieforschung (GIF)	Allsdorf, Germany
DualTronic® DCT module technology	BorgWarner United Transmission Systems	Dalian, China
<ul style="list-style-type: none"> • Dual clutch module • Hydraulic control module 	BorgWarner	Shanghai, China
		Ketsch, Germany
		Auburn Hills, USA
		Tulle, France
TCU Hardware and low level software	BOSCH/United Automotive Electronic System Co. Ltd (UAES)	Stuttgart, Germany
		Shanghai, China

Fig. 5 DCT360 transmission

7 Dual Clutch Module

The DualTronic® dual clutch module is a concentric design with an integrated torsional vibration damper. This configuration represents best-in-class torque density and package efficiency (Fig. 6).

While this clutch module design is unique to the DCT360, it shares many components and features with the BWUTS family concept. The Common Clutch Family (CCF) represents a range of products with maximum sharing of

Table 3 Transmission specifications

Overall length (mm)	<360 (DQ250 = 408)
Total mass (kg)	<95 (including TVD and oil)
Maximum torque (Nm)	360
Forward speeds	6
Shafts	3 + R idler
Center distance (mm)	197
Maximum input speed (rpm)	6800
Maximum efficiency	>93 %

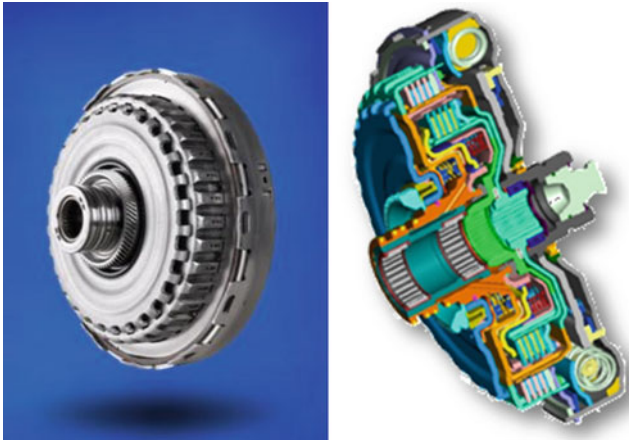


Fig. 6 DCT 360 dual clutch module

components to minimize development and tooling investment. Key Features of the CCF include:

- Compact design/high torque density
- Modular family design
- Scalable from 180 to 350 N-m
- Maximum number of common components
- Optional torsional vibration damper—tuneable for wide range of engines (Fig. 7).

8 Hydraulic Control Module

The DualTronic™ electro-hydraulic control module is a compact, self-contained control body with integrated gear actuation (Fig. 8).

This also represents a family approach, with FWD and RWD variants, and optional features that can be added or omitted while preserving the common architecture (Fig. 9).

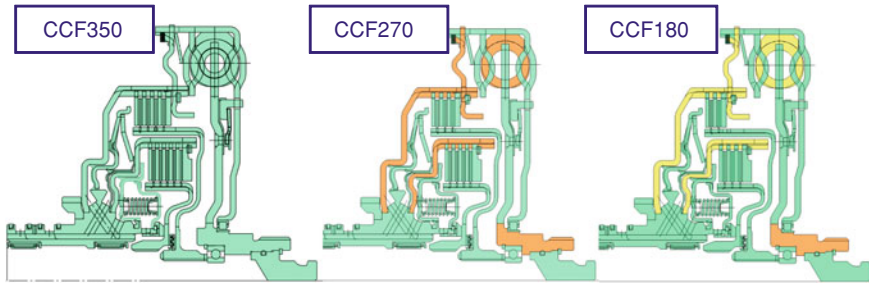


Fig. 7 BWUTS dual clutch module family

Fig. 8 DCT 360 hydraulic control module



9 Development Process

A comprehensive development program was planned using the latest processes and tools, which be grouped into four main categories; requirements development, mechanical system design, electronic controls development, and design verification and validation. The table below lists some of the key processes employed by the team in the development process (Table 4).

This approach leveraged the expertise of the global development team. At the same time, leading this program represented a significant investment in the local product development capability of SAIC, both in knowledge and infrastructure.

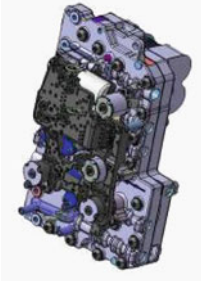
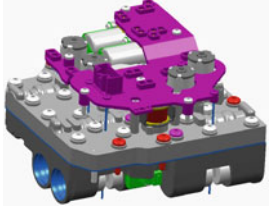
<i>Application</i>	<i>HCM-4110F</i>	<i>HCM-4110R</i>
Transmission type <ul style="list-style-type: none"> ▪ 6 or 7 speed Wet DCT 	Transverse (Front Drive)	Longitudinal (Rear drive)
Key Features <ul style="list-style-type: none"> ▪ Common Schematic ▪ Integrated Gear Actuation ▪ Proportional Actuation Control ▪ Proportional Clutch Control ▪ Lube Flow Control ▪ Line Pressure Control ▪ Cooler Pressure Protection 		

Fig. 9 BWUTS DCT hydraulic control module family

Table 4 Transmission development techniques

Requirements development	<ul style="list-style-type: none"> • In vehicle data acquisition • Benchmark data, to set performance, durability and fuel economy targets • Optimize gear ratios and shift patterns • Achieve the correct balance of performance and fuel consumption • Speed ratio N/V analysis • Dynamics analysis • Fuel economy simulation
Mechanical system design	<ul style="list-style-type: none"> • Layout analysis • Design model build up • Gear shaft system analysis • Hydraulic system analysis • Housing FEA analysis
Electronic control system development	Mature software development process <ul style="list-style-type: none"> • Graphical modeling and simulation of function module • Rapid prototyping strategy design capability code integration and code test • Complete diagnosis development and testing process • Hardware in loop testing capability
Design verification and validation	Comprehensive ADV Plan <ul style="list-style-type: none"> • Component characteristic test • Sub-system bench test • Transmission system bench test • Transmission test in vehicle

Table 5 Performance comparison in vehicle

Engine	Attribute	5AT	DCT360	chg	% chg
1.8 VCT	Average FC (l/100 km)	9.4	8.5	-0.9	-9.6
1.8 T		9.2	8.4	-0.8	-8.7
	Acceleration 0-100 km/h	10.8	10	-0.8	-7.4

10 Result: Vehicle Performance

The table below shows preliminary measured results first vehicle application, comparing both acceleration and fuel consumption of the DCT and 5AT equipped vehicles (Table 5).

These initial results show the program targets of increased performance and driving comfort, while also delivering significant gains fuel economy, have been achieved.

11 Conclusion

This new 6-speed dual-clutch transmission represents a significant milestone for leading-edge automotive technology developed and produced by a domestic OEM in China. The DCT360 utilizes the latest wet DCT technology to provide automatic transmission shifting comfort with world-class performance, efficiency and packaging.

Reference

1. Alexander M, Viren S, Paul M (2008) BorgWarner dual tronic[®] transmission concepts for efficiency, cost and robustness, cti symposium automotive transmissions, Berlin

Development of New CVT for K-Car

Koichi Konishi

Abstract A continuously variable transmission (CVT) adopting a parallel-shaft, helical gear primary reduction mechanism for greater transmission efficiency was developed for K-car use. The distance between the input shaft and output shaft in the front-to-back direction was reduced and the hydraulic control system was positioned all together below the transmission. This supported the reduction of engine compartment size and, by extension, contributed to the extended length of the K-car cabin interior. Two types of 0.66-L engine, naturally aspirated (NA) and turbocharged (TC), are supported, as well as two-wheel drive (2WD) and four-wheel drive (4WD) systems, with a minimum configuration of special parts. Idle stop was also supported with just the addition of an electric oil pump.

Keywords Power transmission · Continuously variable transmission · Mechanism · Efficiency · Structure

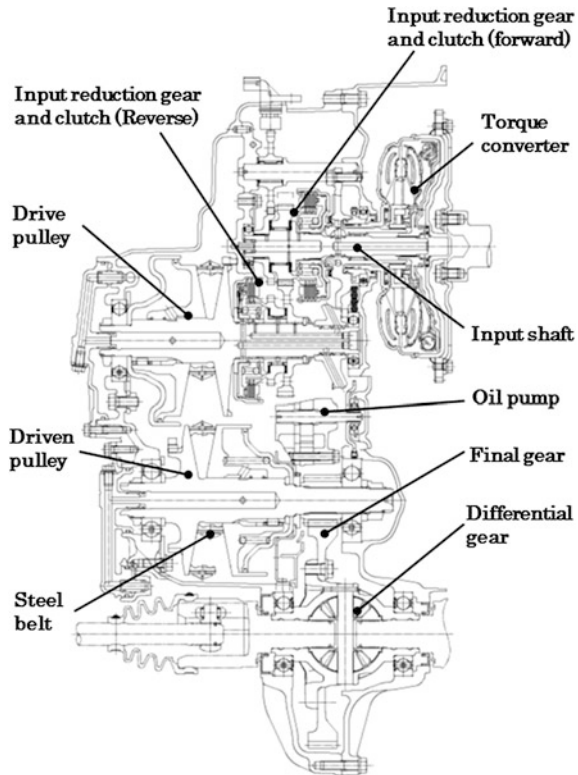
K-car fuel-saving performance has become a major focus of attention in recent years. An enhanced level of fuel consumption is also being demanded of Honda K-cars, and a new model continuously variable transmission (CVT) was developed for the K-car.

This CVT is to replace the lightweight, reasonably priced four-speed automatic transmission (AT) being used in Honda K-cars, and so a lightweight, compact structure was adopted. The previous CVT had the drive pulley positioned coaxially with the input shaft, so the separation between the input shaft and the output shaft

F2012-C03-019.

K. Konishi (✉)
Honda R&D Co., Ltd. Automobile R&D Center, Wakō, Japan
e-mail: koichi_konishi@n.t.rd.honda.co.jp

Fig. 1 Main section of development CVT



where the differential assembly is located could not be reduced. A main section view is shown in Fig. 1.

A parallel-shaft, helical gear primary reduction mechanism was adopted for this CVT, and the drive pulley was located above the input shaft. This allowed the distance between the input shaft and output shaft to be reduced. With this, the front-to-back length of the transmission could be shortened, and the result contributed to enlargement of the cabin space. A side view of the present CVT is shown in Fig. 2.

The adoption of a primary reduction mechanism lowers the rotational speed of the CVT's metal V-belt and increases the metal V-belt input torque. The metal V-belt has the greatest transmission efficiency when operated close to the belt's allowable input torque, so that setting an optimal primary reduction ratio enhanced the transmission efficiency of the CVT.

The previous CVT had a high secondary reduction gear-meshing frequency, and therefore required high machining accuracy for the gears as well as careful attention to the shaft supports. However, the present CVT has adopted a primary reduction mechanism with parallel-shaft helical gears, which allows a lower gear-meshing frequency than other mechanisms. This structure was therefore considered advantageous in terms of the quietness of the cabin.

Fig. 2 Side view of developed CVT

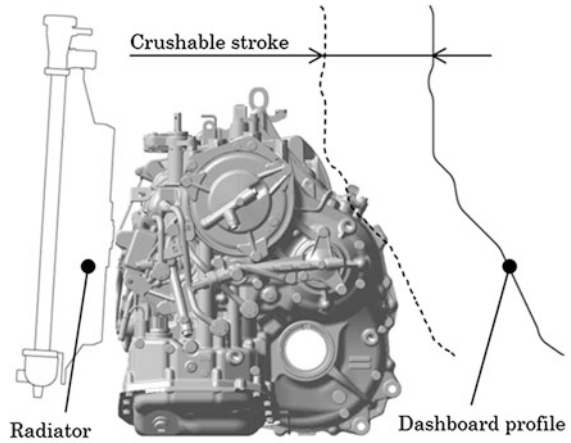
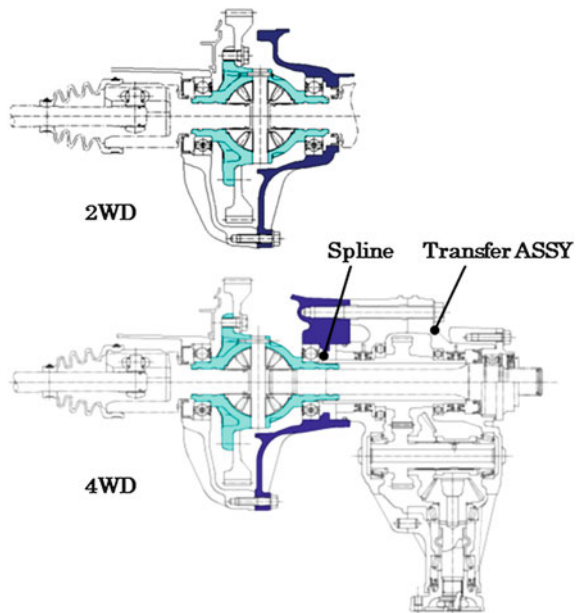
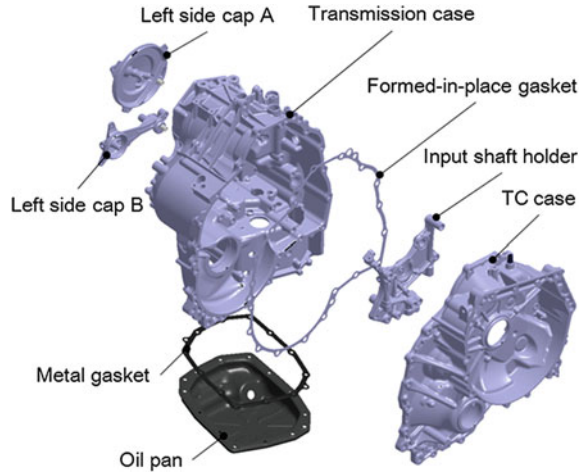


Fig. 3 Configuration of transfer coaxial with differential



The NA and TC engine types could be supported by differentiating specifications for torque converter and primary reduction gear, the 2 and 4WD drive system types by differentiating specifications for the torque converter case and the differential case. This enabled a higher common use ratio for parts. The 2 and 4WD drive system configuration is shown in Fig. 3.

The casing was given a two-piece structure in order to reduce weight and lower costs. A formed-in-place gasket (FIPG) and metal gasket were adopted. The case construction is shown in Fig. 4.

Fig. 4 Case construction

A reasonably priced hydraulic system structure with a smaller number of solenoids was adopted for the hydraulic control system. A new control that uses the forward gear clutch to cut off sudden excessive input torque was also adopted. An electric oil pump was also added and configured to support idle-stop.

In addition to optimization of the primary reduction ratio, measures to increase efficiency included re-examination of the arrangement of shafts. This resulted in the drive pulley being located above the oil level and reduced the agitation resistance from rotation of the pulley. This was combined with adoption of a baffle plate to reduce the agitation resistance of the large-diameter final driven gear. The result was an increase of about 2 % in the cruising efficiency of the CVT at vehicle speeds from 40 to 100 km/h.

Research on Development Process of 7 Speed Wet Dual Clutch Transmission

Yong Chen, Mike Turner, Michael Gilcrist, Wenjiang Zhao,
Daguo Luo and Fuquan Zhao

Abstract Seven speed wet dual clutch automatic transmission is a product characterized by an integration of electrics, mechanics and hydraulics. The optimized efficiency, good NVH performance and durability low cost are considered during the development. In order to save time and optimize design, process development research method based on simulation model is applied. Meanwhile, basic test is combined to guarantee validity of simulation model. Therefore, design process is optimized.

Keywords Dual clutch transmission (DCT) · Dual clutch · DCTF · NVH analysis · Basic test

1 Introduction

Dual clutch automatic transmission (DCT) technology is an advanced automatic transmission technology in recent 10 years. The DCT is consisted of two separate gear train controlled by electric hydraulic system, which can simultaneously control two sets of clutch engagement and disengagement. During the transmission is operating, one of the gear train is engaged. If the transmission tries to shift gear, the next set of relevant gears has been preselected, but still is in disengaged state; when shifting gear, the preselected target gear will be used. The shift strategy can

F2012-C03-022

Y. Chen · W. Zhao (✉) · D. Luo
Zhejiang Geely Automobile Research Institute CO., LTD, Hangzhou, China
e-mail: zhaowj@rd.geely.com

M. Turner · M. Gilcrist · F. Zhao
DSI Holdings Pty Limited, Springvale, Victoria, Australia

ensure that at least one group of gears on the output power, thereby avoids power interruption and improves power transmission efficiency and ensures the driving comfort.

In order to meet stringent requirements of the automobile market like reduces fuel consumption and carbon dioxide emissions, the GEELY Automobile Research Institute develops a 7 speed wet dual clutch automatic transmission with wholly-owned subsidiary Australian DSIH together. GEELY's 7DCT project adapts to the increasingly competitive market requirements, promotes GEELY Automobile Powertrain Product competitiveness [1].

2 7DCT Design Specification

GEELY 7DCT has to meet equal or preponderant performance requirements compared with similar products have in global market. The 7DCT design focuses on the following performance requirements:

- High performance efficiency and low emission designing principle;
- Precision electronic hydraulic control system;
- Higher lifetime and low cost development module;
- Light weight optimize;
- Excellent NVH performance and durability;
- Materials environmental protection recycling [2];

The performance of the product has been basically established during the design phase. Various influence factors must be taken into account in each component system design via simulation and basic testing. Therefore it can ensure the 7DCT performance requirements in limited time.

3 7DCT Transmission Design

In 7DCT drive system design and development concepts, there are a few certain degrees of repeatability of manual transmission could be used for reference. But the DCT integrates automatic-related functional system components, including dual clutch assembly system, electronic hydraulic control system and special transmission oil (DCTF) etc. (Fig. 1).

3.1 Gear train

Gear train is the basic part of 7DCT which is mainly composed of gear, synchronizer, bearing. During the gear layout design, the application of common drive

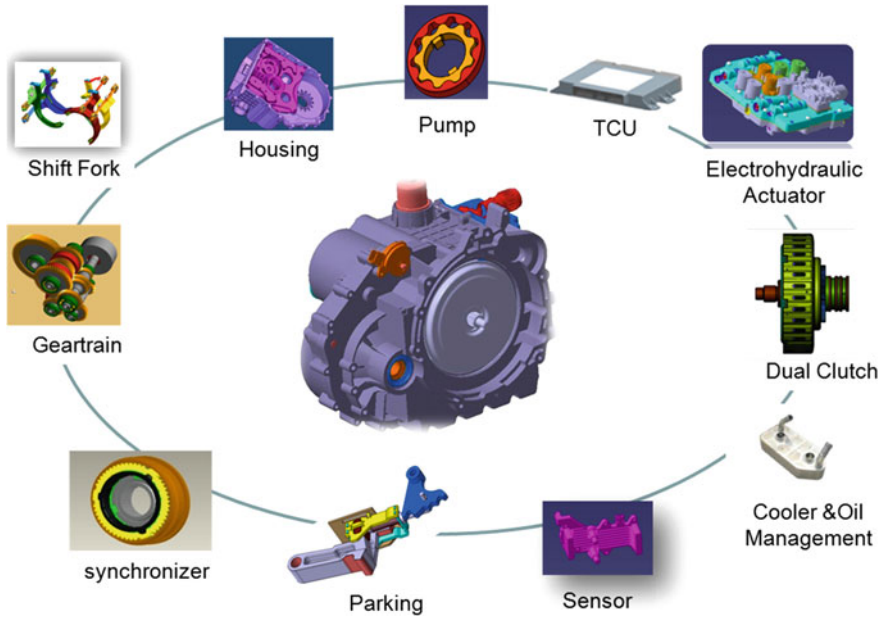


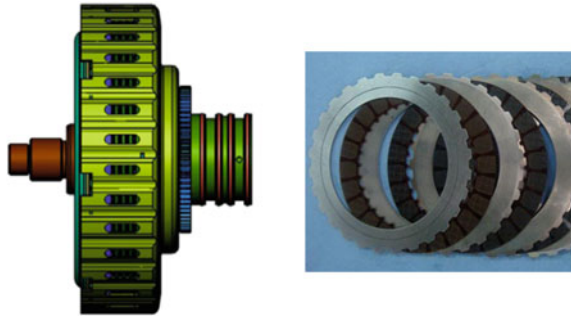
Fig. 1 Composing of 7DCT

gear design improves the overall transmission compact and helps for vehicle installation. On the other side, high performance bearing improves the vehicle efficiency. A synchronizer system requires wearable materials such as Carbon and other materials, to meet the DCT multiple frequency shift condition requirements.

3.2 Dual Clutch

7DCT applies wet multi-plate clutch form (show in Fig. 2), its main function includes launch and power on/off shifting function. Dual clutch transmission adds more continuous slipping properties function in comparison with clutch controlling in traditional AT. This dual clutch design not only meets the maximum torque capacity requirements, but also the heat capacity requirements. In order to meets the above requirements, friction plate selection is critical. At first, friction plate needs to select suitable DCTF oil which is well compatible (detail in 2.4), to ensure excellent friction torque and durability. On the other side, the compact system structure meets the transmission limited space requirements.

Fig. 2 Dual clutch & friction plate



3.3 Electronic Hydraulic Control System

Electronic hydraulic control part is the core in the 7DCT application system including sensors, TCU, hydraulic actuator system. As shown in the figure, the sensors in system get information about gear position, oil pressure, speed, temperature and send them to TCU in real time. The TCU calculates execution outputs to the hydraulic, synchronization and clutch controlling system according to the sensor information, vehicle signals and strategic algorithms (Fig. 3).

3.4 DCT Fluid

Wet DCTFs are different from MTFs and conventional ATF. Wet DCTFs must provide sufficient wear protection for the helical gears, and good friction characteristics and wear protection for the synchronizers which are not required by ATFs. Different to MTFs, Wet DCTF must provide good wet clutch friction characteristics and durability. For good fuel efficiency, wet DCTF must be sufficiently low in viscosity with wear protection. Wet DCTF therefore must have the functions including controlling dual clutch friction performance, controlling synchronizer friction performance, lubrication gears bearings, and shafts, hydraulically actuating clutches and synchronizers, minimizing component wear and corrosion, cooling or thermally controlling the system, and protecting other parts like seals (Fig. 4) [3].

4 Simulation Analysis

During the beginning of 7DCT system design, most key questions of design can be answered by system simulation calculation. Through the simulation like components analysis, whole transmission NVH simulation as well as lubrication distribution, most of design failure risk can be solved in advance.

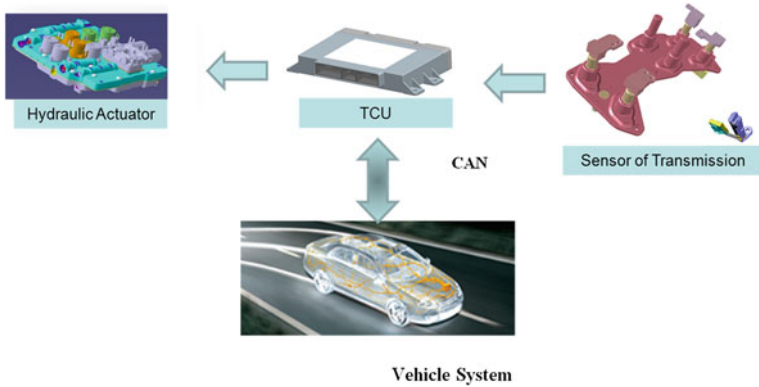


Fig. 3 Overview of electronic hydraulic control system

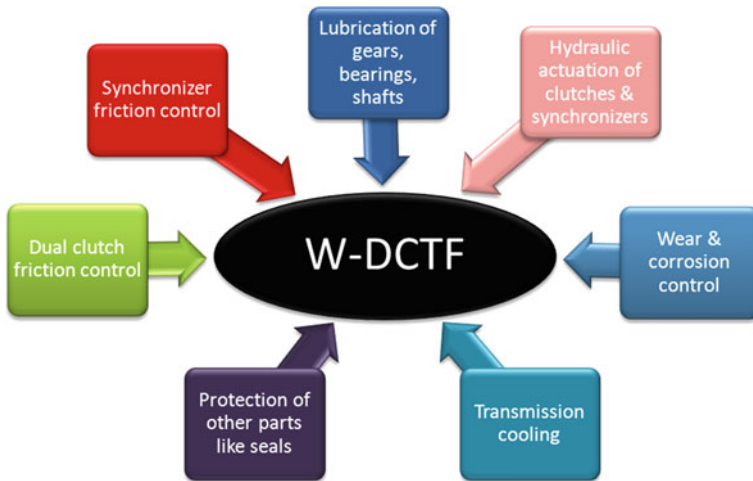


Fig. 4 Function of W-DCTF

FEA simulation analysis was applied for Dual clutch drum design. In order to have a lightweight design, the dual clutch drum, the carrier of plats and disc is manufactured by steel plate stamp. The spline of drum is integrated by Grob process. Regarding such structure, there is broken risk caused by high centrifugal force during high spin. But the accurate strength simulation can answer his broken risk and optimize the design. And the real testing experience done before can also promote the exactitude of simulation calculation (Fig. 5).

The simulation benefits a lot for 7DCT project development. The real similar testing experience done before can also modify the simulation module, which can help the simulation calculation result close to real happen. At the same time, the

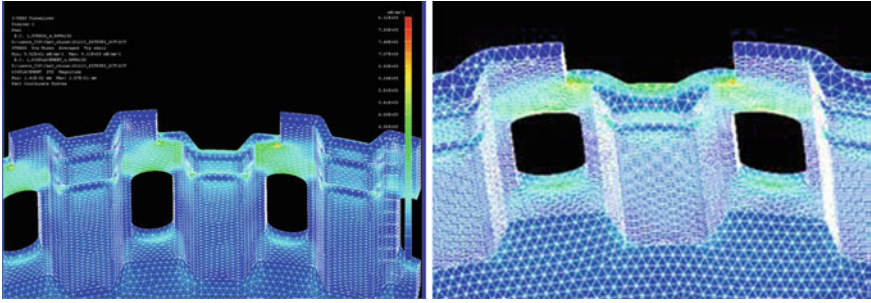


Fig. 5 FEA of clutch drum

simulation can also be applied for more complex system, like lubrication simulation, whole transmission NVH simulation as well as parking design optimization via multi-body dynamics simulation.

5 Basic Testing to Optimize the Design

During simulation, the basic test is also helpful to design optimization. Especially some basic testing can be done before finalizing the design. This can increase the reliability of design, reduce the fail risk during transmission validation testing, and control the design change. Therefore the project time is guaranteed.

5.1 Fluid Testing

As discussed above, the fluid selection is significant relating to the performance of transmission. At the beginning of concept design, the fluid needs to be selected. Most characteristic like viscosity, foaming, scuffing, shear stability, copper corrosion & rust can be obtain by rig testing. Compare with the current DCTF, 7DCT chooses an optimized fluid. The viscosity of DCTF of 7DCT is lower and more stable at different temperature for higher efficiency and better performance.

Except for the basic characteristic testing, the dual clutch friction performance with DCTF is also critical. The friction of performance will have a direct impact on the transmission shift performance and durability. Regarding this requirement, Positive μ -V characteristic, Anti Shudder Life, and Heat resistance are to be considered and evaluated. SAE2# LVFA and GK testing are the usual and effective way to evaluate this performance. As shown in Fig. 6, there was no shudder during continuous slip sequence after 300s, equal to 10,000 shifts.

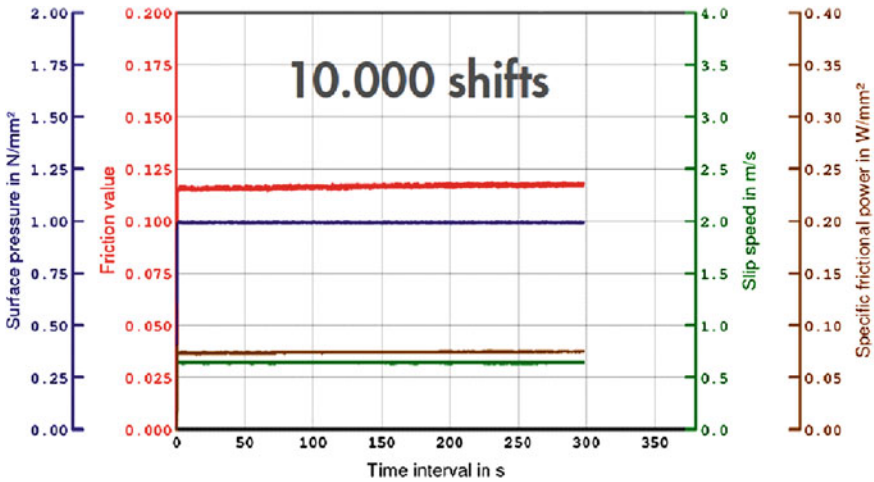


Fig. 6 GK friction continuous slip durability testing

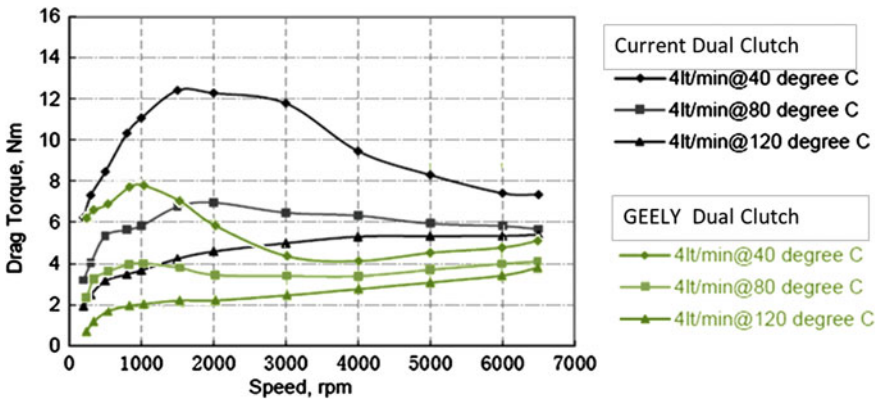


Fig. 7 Dual clutch drag testing

6 Dual Clutch Testing

As the key subsystem, dual clutch testing is necessary. The testing includes Torque Capacity, Clutch Drag Torque, mechanical torsion fatigue etc. As shown in the testing result of drag torque, 7DCT have better performance compared with the current wet DCT on the market, which will contribute the overall transmission efficiency promotion (Fig. 7).

7 Conclusion

In order to adapt to the increasingly competitive market requirements, GEELY chooses developing 7DCT to promote its product competitiveness. The optimized efficiency, good NVH performance and durability low cost are considered during the development. The most of transmission performance is determined as soon as the design is finalized. So the application of appropriate simulation and basic testing are significant before the design was finalized, thereby ensuring the reliability of design. Based on this, the next step of transmission testing can be more confident and the project time can be ensured.

References

1. Yong C (2011) Independent research and development of transmission in Geely technology 2011 TM Symposium China
2. Wagner G, Scherre H (2006) ZF 6-Speed automatic transmission fuel efficiency and contribution to environmental protection. Drive system technique 2006: 02-03-01
3. Hong Zhi Tang (2012) Development additive technology for wet dual clutch transmission. Lubricating Oil

A Study on Performance Simulation and Optimization of an Automatic Transmission

Yong Chen, Daguo Lou, Hua Chen and Fuquan Zhao

Abstract To shorten the AT development cycle and verify the design solution beforehand, the simulation analysis based modular development methods, including the NVH design and lubricating system CFD analysis of AT, are utilized to develop a hydraulic valve body with AMESIM and develop an oil pump with FLUENT, and carry out safety reliable design of transmission system with an advanced multi-body dynamic analysis method to optimize key component structure and effectively improve the AT performance. Meanwhile, the application of simulation drive design technology, in which CAE integrated technology is regarded as a key one, can significantly shorten the development cycle of new products and quantify the empirical knowledge and test data in the past development with higher development efficiency. In addition, the application of CAE engineering analysis and prediction technology helps the engineers with simulation analysis and prediction; therefore the product performance and quality can be significantly improved before obtaining type approval and putting into production, thereby reducing design cost and test frequency, as well as shortening the time for products to be put on the market.

Keywords Automatic transmission · Simulation analysis · NVH analysis · CFD analysis · Multi-body dynamics analysis

F2012-C03-023

Y. Chen · D. Lou · H. Chen (✉) · F. Zhao
Zhejiang Geely Automobile Research Institute Co., Ltd, Hangzhou, China
e-mail: chenhua@rd.geely.com

1 Introduction

The simulation technology with CAE as the core is the organic integration of finite element technology and virtual prototype of sports/dynamics technology. CAE simulation analysis functions are mainly for the following aspects [1]:

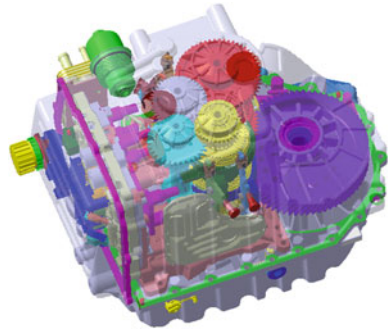
1. Realize structure analysis from linear and static calculation to nonlinear and dynamic calculation;
2. Make prediction and assessment for structure safety, reliability, service life;
3. Achieve the value and the change rule for the velocity, acceleration, force and the trajectory of mechanism or machine.

For the important components for powertrain-transmission, develop various computer models in use of different CAE analysis tools on the basis of fully study for the transmission theory, which greatly promotes the development for transmission research based on the virtual prototype technology. Especially in automatic transmission system development research, it needs more advanced test and simulation technology support. Test and simulation analysis is the essential link in the product development process. Carry on effective and accurate simulation research through the system modeling and analysis, which is a powerful tool to shorten the development cycle and reduce the cost of development [2].

2 Automatic Transmission Simulation Analysis Means Application Situation

Numerous domestic and international scholars also carried out the simulation analysis on automatic transmission in use of different modeling tools and methods. Zhao [3, 4] used Matlab/Simulink tool to establish a mathematical model for automatic clutch system based on DC electrical motor driver and real-time controlled the automatic clutch by means of enhanced fuzzy sliding mode controller and adaptive fuzzy sliding dynamic mode controller. Batans [5] used AMESim power transmission system model library to establish AT, AMT and DCT (Dual Clutch Transmission) model, and the compared the fuel economy on various structure form of transmission system. Zhao [6] carried on modeling and simulation for an AMT clutch control system by SimulationX, and obtained a good consistency compared with test results. Based on Dymola software platform, Otter [7] built certain AT system model in use of Modelica, but ignored the synchronizer combining process and clutch actuators in order to carry out the real-time simulation. The United States Meritor Automotive company [8] classified the simulation analysis models for the transmission system, and studied out six power transmission system performance prediction computer model (gears-shaft-bearing the dynamic model, vehicle performance prediction model,

Fig. 1 Particular DCT model

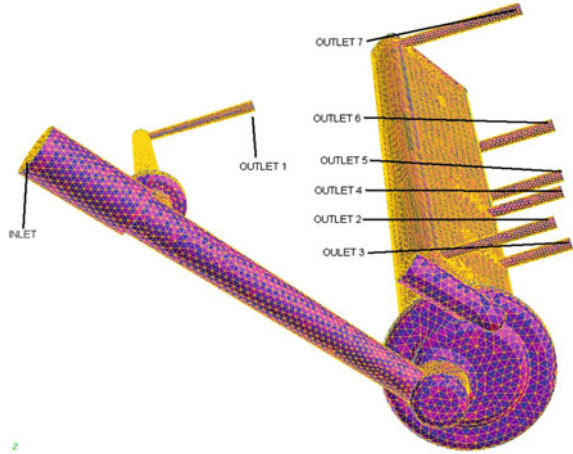


transmission parts of torsional vibration model, the fatigue life model of the parts, transmission suspension integration model, the gearing mesh dynamics model) in use of different types of modeling tools and methods (ADAMS, ANSYS, MATLAB, C/Fortran language).

At present, companies such as Geely Automobile, FAW, Shandong Shengrui, Hunan Rongda and the scientific research universities have carried on independent study for automatic transmission interiorly, especially carried out a great deal of work for automatic transmission key parts of AT, DCT, CVT, etc. [9]. The national science and technology department has also included the research and development of domestic automatic transmission into the key development projects of the national “863” plan during the period “11th Five-Year Plan” and “12th Five-Year Plan” and encouraged the cooperation of universities and enterprises. Zhejiang Geely holding group Co., LTD has undertook the research and development tasks for automatic transmission, and gradually mastered the development process of the key technology.

Taking the simulation analysis method application for development process of particular Geely automobile double clutch automatic transmission for example, the following illustrate the actual development and application of the simulation analysis method. Dual clutch automatic transmission (referred to as DCT hereinafter) is different from the common automatic transmission system in markets. It is based on manual transmission and different from traditional automatic transmission integrated the advantages of them. In addition to owing high efficiency of manual transmission and the comfort of automatic transmission, it still can provide uninterrupted power output and has greatly improved the fuel consumption. To ensure that DCT can reach the desired effect in the development stages, have carried on a large number of simulation analyses and achieved good effect in the virtual prototype stage (Fig. 1).

Fig. 2 Computational models for the oil rail



3 The Simulation Analysis Method and Effect for Lubricating System

The lubrication for each shift gears in DCT mainly depends on the forced lubrication, and the oil rail is the main component. The lubrication effect for the oil rail has a direct effect on the lubrication effect for each shift gears. In the virtual prototype stage, the research for it mainly adopted the multiphase transient calculation method, generally the PISO algorithm, Fig. 2 for oil rail computational models.

Figure 3 is the oil rail working situation at one point. From oil distribution in the graph, we can see that the injection oil from rail has smoothly reached the gear and rotated together with the gear, and the mixing oil of the gear would not affect its work. So it has achieved the expected effect.

Figure 4 shows the monomer test for the oil rail, in the condition of the inlet with the pressure 2 Bar, jet reflect effect from the monomer test shows it can meet the design requirements. As shown in figure, jet direction for each of the nozzle can fully reach the designated lubrication object.

4 The Simulation Analysis Method and Effect for NVH Design

Transmission error of gear is the excitation source of noise in the transmission. Controlling the gear accuracy and optimizing gear meshing effect, reducing load fluctuation between the gears, reducing error wave amplitude of static transmission, smoothing the static transmission error curve, mentioned above are beneficial to reduce the frequency excitation of meshing gears and low power frequency

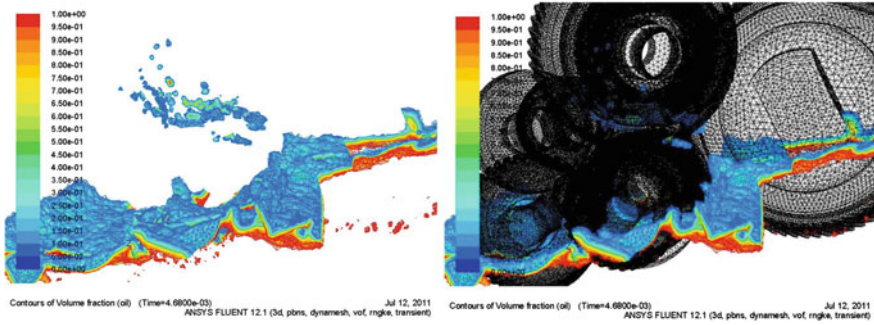


Fig. 3 Working situation for the oil rail ($t = 4.68e-3$ s)

Fig. 4 Monomer test for oil rail

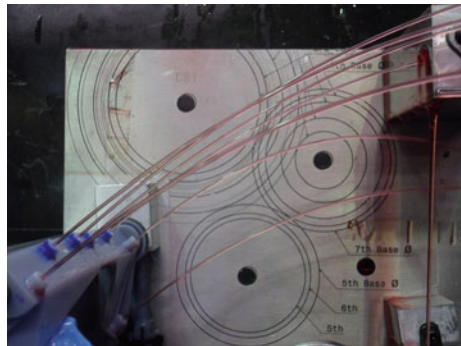
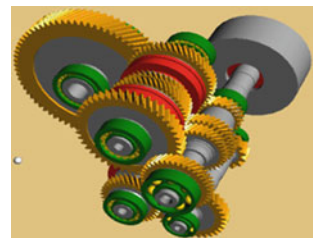


Fig. 5 Analysis model for the transmission system



excitation of meshing. Transmission structure is the spread way of the vibration noise. By means of the simulation method, modal analyze the shaft gear and shell and then optimize inherent frequency. Analyze the radiation noise of transmission, looking for the weak link of the transmission and strengthen the structure.

Simulate the transmission error in use of MASTA software in the project, take the assembly error of gear, flexibility of gear shaft and transmission shell into consideration in the simulation fully and optimize the design of the micro shape parameters with the purpose to minimize the static transmission error. Figure 5 for the analysis model for the transmission system, Fig. 6 for transmission error,

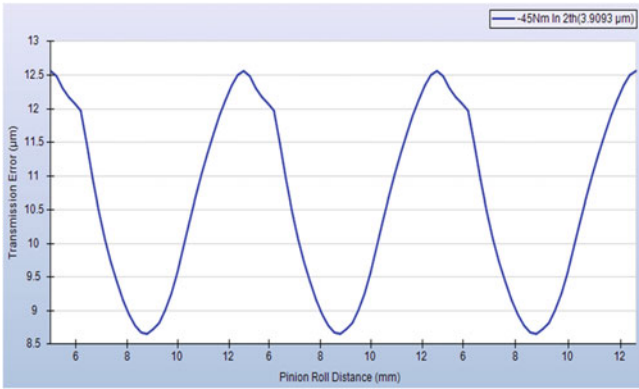


Fig. 6 Transmission error

Fig. 7 Gear micro repair form

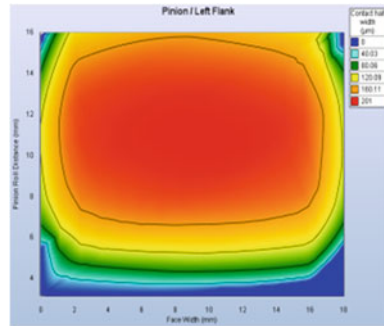


Fig. 8 Effect after the gear parameters optimization

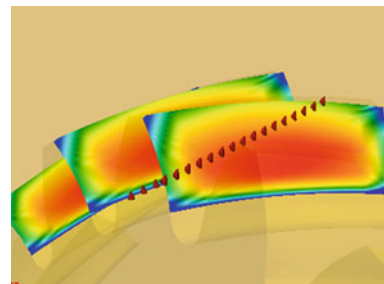


Fig. 7 for gear micro repair form, Fig. 8 for the effect after the gear parameters optimization.

In order to understand the influence on the noise of the transmission for structure, mainly use the simulation software such as HYPERWORKS, ANSYS and VIRTUALLAB to analyze the dynamic characteristics of transmission structure and simulate transmission screaming noise in order to verify the improvement effect on noise for the structure changes. In the transmission NVH test stage, according to the shape of the gear micro simulation results, and

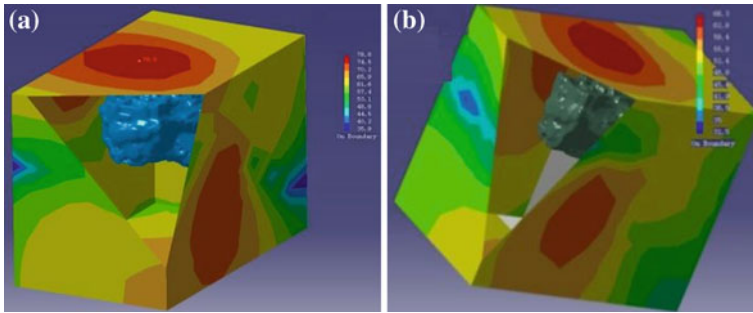


Fig. 9 Noise response result **a** Original noise response result, **b** Noise response result after improvement

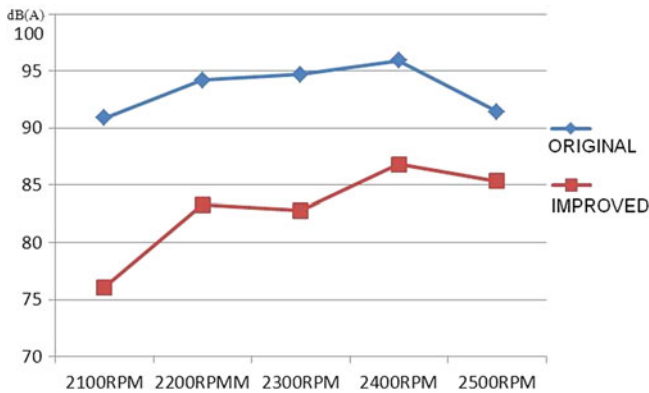


Fig. 10 Gear screaming noise effect after improvement

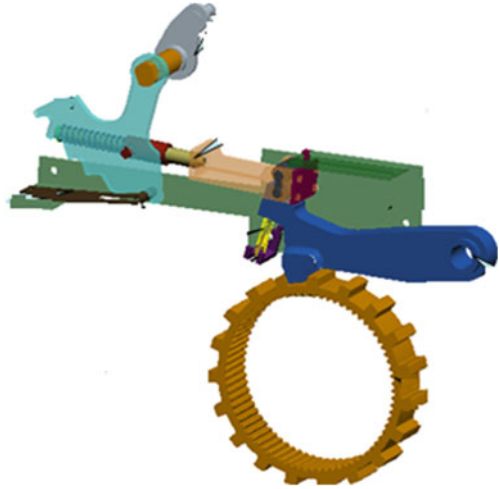
combining with actual processing ability, design and machine batch gears with different micro shape parameters. Determine the optimal shape parameters of the micro interval through the analysis of the experiment. Figure 9 for noise response result, Fig. 10 for the gear screaming noise effect after improvement.

Test location: 2nd gear from the drag, noise value above 300 mm from transmission.

5 Multibody Dynamics Simulation Analysis Method and Effect for Parking System Design

Parking mechanism is the key components involved in the safety performance for DCT. The structure of a particular parking mechanism is as shown in Fig. 11. Parking mechanism has more components and the structure is complex. According

Fig. 11 Parking mechanism models



to the working condition, it is studied by dynamics analysis mainly aimed at the shift torque from pawl leverage in the working process. Other support and connecting parts of transmission system, such as bearings, bolts and pins etc. as for the ratchet wheel, because they are not the active force object, their effect are small, which can be to simplify or omit the geometry model.

Build the rigid flexible coupling multi-body dynamics model for parking mechanism mainly in use of Pro/E software, Hyper Works software and ADAMS software.

According to the established parking mechanism simulation model, achieve shift torque simulation value after solving the problem. Figure 12 shows the contrast between simulation curve and experiment curve for shift torque and shift angle. From Fig. 12, we can see that simulation curve is consistent with that of experiment, which proves the accuracy for multi-body dynamics analysis method based on the rigid flexible coupling and the feasibility of the parking mechanism performance evaluation by means of this method. Therefore it can be used to forecast and evaluate shift feel for parking mechanism in order to improve the parts design efficiency and performance in the design stage.

6 Amesim Simulation Analysis Method and Effect for Hydraulic System

By means of AMESim simulation software, build the transmission hydraulic system simulation model. Simulate rotary piston characteristics using hydraulic components design library and then optimize and improve the design of each component in use of batch function. The simulation analysis mainly includes: analyze the influence on the hydraulic characteristics and leakage for rotary

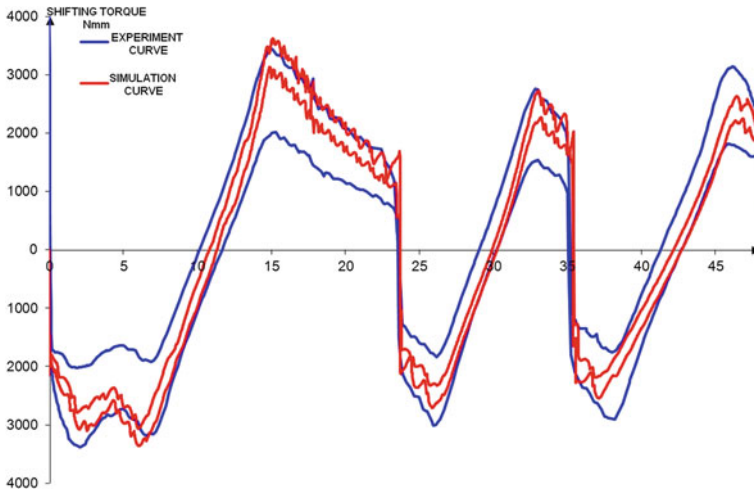


Fig. 12 Contrast between simulation curve and experiment curve

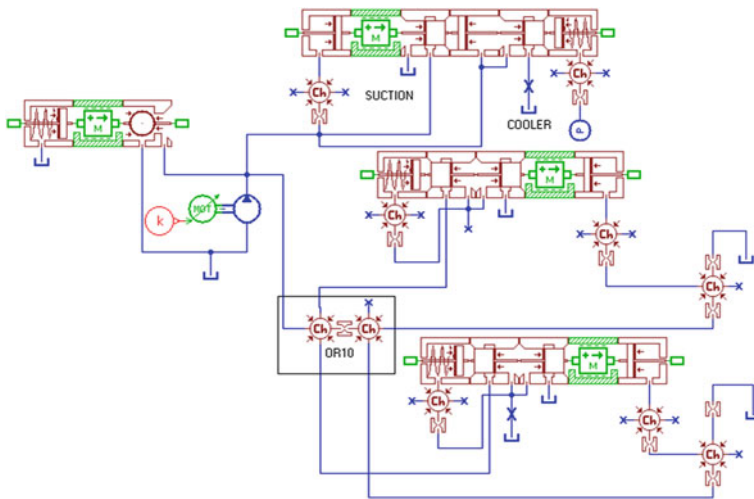


Fig. 13 Mechanism liquid dynamic models for hydraulic shift control system

parameters, such as the structure, clearance, spring force, spring stiffness, etc.; analyze the influence on system stability, responsiveness and the flow for orifice diameter. Reduce leakage and pressure loss and improve the efficiency of the hydraulic system by means of optimizing parameters. Forecast the hydraulic system performance and reduce design cycle through the AMESim simulation. It can also put on the overall analysis and evaluation for the system, so as to achieve the optimal system, shorten the design cycle and improve the stability of the

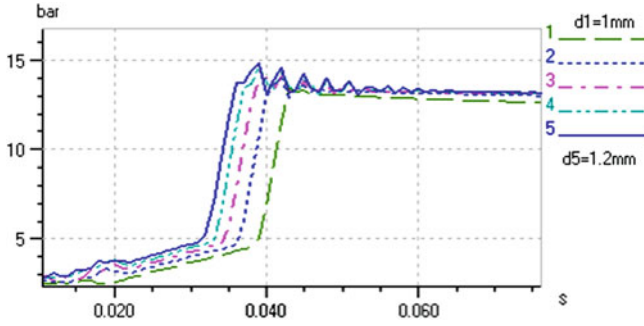


Fig. 14 Orifice (OR10) batch simulation results

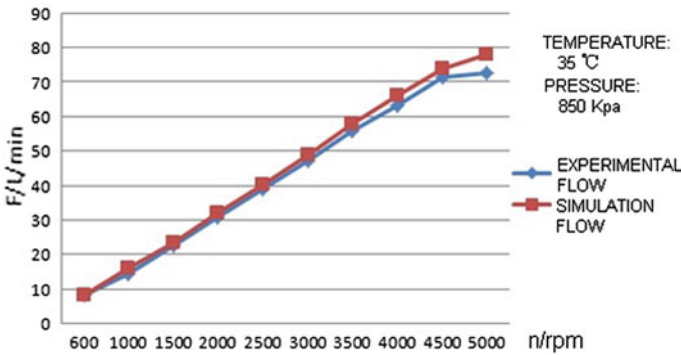


Fig. 15 Comparisons in condition of low temperature and pressure

system. Figure 13 shows the simulation for shift regulating system in the hydraulic system, Fig. 14 shows the batch simulation results of throttle orifice (The pilot pressure of the shift regulator is more than 13 bar and meet the design requirements, the diameter of orifice is small, and the system leakage is less.), Fig. 14 shows that pilot pressure is more than 13 bar when orifice is 1.1 mm (with consideration the diameter tolerance ± 0.05 mm of orifice).

7 Fluent Analysis Methods and Effect for Oil Pump Design

Simulate the oil pump mainly by means of the CFD technology. It can not only comprehensively analyze the effect on the performance of the pump for different factors, but also can fast get performance parameters of the pump.

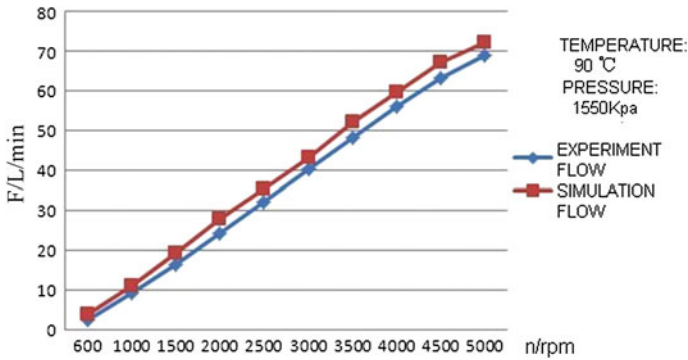


Fig. 16 Comparisons in condition of *high* temperature and pressure

For most of the oil pumps of DCT are rotor pump, and its structure is more complex, so build geometric model in use of UG software and simulate the internal flow field in use of FLUENT software. The import and export runners of oil pump use unstructured tetrahedron tri-prism grids, and the rotation of the area use the structured grids. By means of the unstructured grid SIMPLEC algorithm, simulate the internal flow field to realize pressure speed coupling. After simulation analysis, we can get a series of oil pump performance data of the pump in different conditions, such as the internal stress distribution and the oil output flow velocity vector. In comparison with the experimental data of DCT oil pump and FLUENT software simulation results, we can know that the two test methods of flow curve results are basically consistent with each other under the oil pump in the low temperature and low pressure condition, as shown in Fig. 15; In high temperature and high pressure condition, the flow of FLUENT software simulation is little larger than that of the test, but just with little deviation, as shown in Fig. 16. By comparison, we can come to a conclusion that FLUENT software simulation analysis for pump is reliable, which will provide effective support for the development of the late new pumps.

8 Conclusions

In this paper, by taking a particular type of Geely's DCT as research object, the transmission lubrication system analysis, NVH analysis, parking system performance analysis, hydraulic system analysis and oil pump performance analysis are introduced based on the virtual prototype validation method. The system structure is sufficiently optimized to ensure that the various transmission performances reach the standards. Some analysis results, including lubricating system analysis, NVH analysis, parking system performance analysis, oil pump performance analysis are compared with experimental results. It is concluded that the virtual

prototype test method described in this paper has already reached the expected goal. This method can be used as validation means of the future transmission development in virtual stage, thus shortening the development cycle and reducing development cost.

References

1. Ma Wenbo (2009) CAE analysis and research for new type of six speed automatic transmission [D]. Hefei University of Technology, Anhui
2. Jianzhen Z (2007) Shifting regulation research and control simulation for vehicle automatic transmission [D]. Wuhan University of Technology, Wuhan
3. Zhao Y, Chen L, Zhang Y, Yang J (2006) Enhanced fuzzy sliding mode controller for automated clutch of AMT vehicle. SAE Technical Paper Series (01): 1488
4. Zhao Y, Chen L, Zhang Y, Yang J (2007) Enhanced fuzzy sliding mode controller for launch control of AMT vehicle using a brushless DC motor drive. *Int J Automobile Technol* 8(3):383–394
5. Bataus M, Dragne F, Maciac A, Oprean M, Vasiliu N (2007) Models of Automotive Transmissions for Fuel Consumption Studies. IFP-Drive Library, AMESim Library Manual for Rev 9, LMS Imagine
6. Zhao L, Zhou Y, Zheng L (2009) Modeling and simulation of AMT clutch actuator based on simulationX. *Comput Intell Softw Eng* 2009:1–5
7. Otter M, Schiegel C, Elmqvist H (1997) Modeling and real-time simulation of an automatic gearbox using Modelica. European simulation symposium, Passau, pp 115–121, 19–22 Oct 1997
8. Hongwen Ma (2003) Dynamic simulation research for vehicle comprehensive transmission device in condition of straight running [D]. Beijing Institute of Technology, Beijing
9. Chen Yong (2011) Independent research and development of transmission in Geely. In 2011 TM Symposium China, Shanghai, pp 319–329, 19–21 Apr 2011

Development of the Electric Vehicle AMT Control Strategy

Zhangzhen Deng, Haiyun Gan, Pengyi Deng, Rongming Shan
and Liangyi Yang

Abstract Automatic mechanical transmission (AMT) is now widely used in electric vehicle (EV) to improve its performance. In this chapter different control strategies are proposed to deal with the characteristics of electric vehicle AMT system and its different working condition. And then the control strategy including shift schedule, driver's intention interpretation, driving cycle recognition and frequent gearshift suppression was systematically researched and modeled with SIMULINK. After verified by Model-In-Loop (MIL) and Hardware-In-Loop (HIL) tests, the control strategy model was interpreted to C codes and used in real control unit, verified in vehicle test. Test results show that this control strategy's performance can meet with the requirements of the AMT control system.

Keywords Automatic mechanical transmission · Control strategy · Shift schedule · Simulation mode · Electric vehicle

1 Introduction

With the upcoming petroleum shortage and greenhouse gas emission restrict, EVs become an inevitable solution. Variable transmission enables EVs with both rapid acceleration and high speed and is helpful for cycle life improvement of motor and inverter. Comparing to Automatic Transmission (AT), Continuously Variable

F2012-C03-025.

Z. Deng (✉) · H. Gan · P. Deng · R. Shan · L. Yang
Electric Vehicle Engineering Technology Research and Development Centre,
China Automotive Engineering Research Institute, Chongqing, China
e-mail: dengzhangzhen@evchina.org

Transmission (CVT), Automatic Mechanical Transmission (AMT) is of high efficiency, low cost and manufacturing convenience. So equipment of AMT with battery EVs has been a noticeable research focus.

Except the advantages and convenience mentioned above, there are emerging challenges with AMT control for EVs. Good control strategy should be designed to take comprehensive consideration of acceleration performance, energy efficiency and ride comfort. Control strategy development challenges are focused on gear shifting, driver intention recognition, driving cycle identification and frequent gearshift suppression. They are worthy of studying.

In this chapter, V-Mode of automotive controller development method is used. Firstly, the topology structure of EV was analyzed, and then the control strategy including shift schedule, driver's intention interpretation, driving cycle recognition and frequent gearshift suppression was systematically researched and modeled with SIMULINK. After testing with Model-In-Loop (MIL) and Hardware-In-Loop (HIL), the control strategy model was interpreted to C codes by means of automatic generating of code download into real control unit and verified in vehicle test.

2 The Constitution of Pure EV AMT Transmission System

Pure EV is one kind of new energy vehicle. In this chapter, the transmission system comprises of driving motor, power battery, battery charger and AMT gearbox. The clutch was taken away for the high performance of motor speed. The output characteristics are completely different between engine and motor. Motor could output a constant torque at low speed and constant power at high speed, and has a wider range for driving, so the gears are reduced from six files to three files in the AMT transmission. The power train is detailed in Fig. 1. The key parameters are shown in Table 1.

3 Establishment of AMT Control Strategy

The research on AMT control strategy is the key technology in AMT development. A good control strategy can imitate car driving by a skillful driver. In this case, the car could be more efficient, comfortable and safety. The development of AMT control strategy includes shift schedules, driver intention recognition, road identification, frequency shift suppression and so on [1].

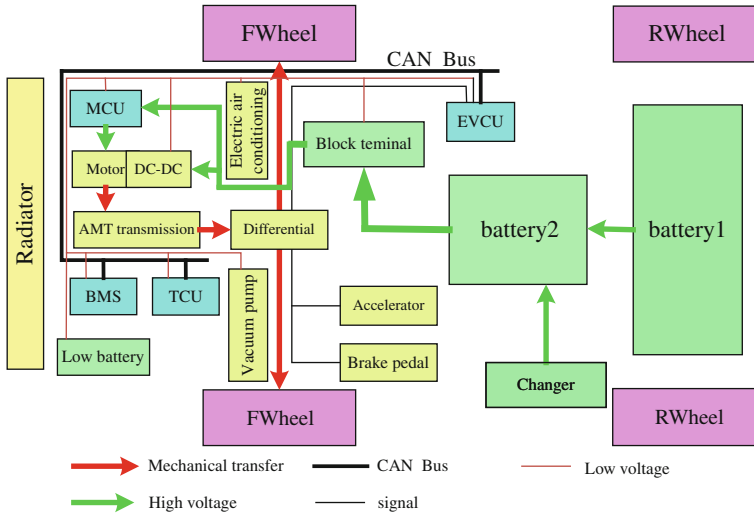


Fig. 1 The power-train system in pure EV

Table 1 Vehicle-related parameters

Curb weight (kg)	1,520	Full loaded weight(kg)	1,845
Rolling radius (mm)	308@195/ 65R15	Factor of vehicle rotation quality	1.1
Frontal area (m ²)	2.3		
Transmission type	Automatic mechanical transmission (AMT)		
Gear ratio	I	II	III
			Speed ratio range
	2.043	1.412	1.105
Efficiency	0.95	0.95	0.96
Differential mechanism ratio	4.25		
Structure	Pure electric vehicle		
Motor parameters	Rated power: 20 kw	Peak power: 50 kw	Speed: 6,500/ 2,650 rpm
Battery parameters	Voltage: 388 v	Current: 0-180 A	Torque(Nm): 72/180

3.1 Shift Schedule

Shift schedule interprets when the gear shifting will be executed based on different control parameters. Shift schedule directly influences the performance of AMT and is the key technology in the control strategy development.

The traditional shift schedule can be divided into single parameter, the two-parameter and three-parameter shift schedule, based on the different control

parameters. The single-parameter shift schedule takes the vehicle speed as the only control parameter with no consideration to both the energy efficiency and power performance. Two-parameter shift schedule is based on accelerator pedal opening and vehicle speed, takes consideration to both the energy efficiency and power performance and is widely used currently. Three-parameter shift schedule is based on speed, acceleration and accelerate pedal opening, well reflects, but it is too complicated to use. The two-parameter shift schedule is currently used in AMT control strategy development for EVs. The shift schedule can be divided into dynamic shift schedule and fuel economy shift schedule.

3.1.1 Dynamic Shift Schedule

The shift points based on dynamic shift schedule are the intersections of the profiles, which represent the driving torques of the motor with different gears, as shown in Fig. 2. The optimum shift point can be calculated using the vehicle's dynamic equation.

$$F_t = F_R + F_i + F_j \quad (1)$$

$$F_t = \frac{T_e i_f i_g n_T}{r} \quad (2)$$

Where,

T_e is the motor output torque

i_f is differential mechanism transmission ratio

i_g is the gearbox transmission ratio

n_T is the transmission efficiency

r is the radius of driving wheel

F_R is the rolling resistance, which can be calculated as (3)

$$F_R = mgf \cos \alpha \quad (3)$$

Where,

m is the curb weight

f is the rolling resistance coefficient

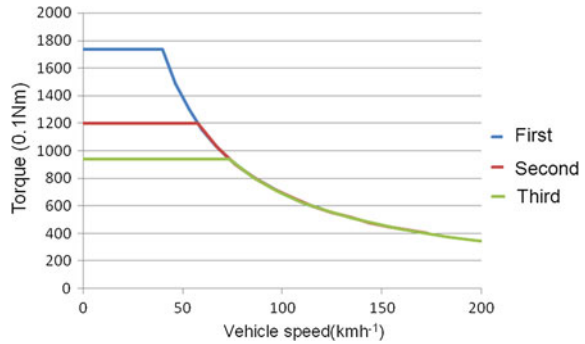
F_i is the hill climbing resistance, which can be calculated as (4)

$$F_i = mg \sin \alpha \quad (4)$$

F_j is the acceleration resistance, which can be calculated as (5)

$$F_j = \delta m \dot{v} \quad (5)$$

Fig. 2 The motor driving force curve in different gears



Where,

δ is increase coefficient of vehicle rotating mass

Combining with (2)–(5), (1) will be described as (6)

$$\frac{T_e i_f i_g \eta_T}{r} = mgf \cos \alpha + mg \sin \alpha + \delta_m \dot{v} \tag{6}$$

With air resistance being taken into account, F_w should be added onto the right in Eq. (6). F_w can be calculated as the following

$$F_w = C_D A \rho v^2 / 2 \tag{7}$$

Where,

F_w is air resistance

C_D is the coefficient of air resistance

A is the vehicle front area

ρ is the air density

v is the vehicle speed

Motor driving characteristics with different accelerator pedal opening is related to motor control strategies and the driver request. In this chapter, the driver request is interpreted as a power curve linear with the accelerator opening. So if the air resistance and ground resistance are ignored, the two-parameter power shift schedule can be simplified as that shown in Fig. 3.

3.1.2 Fuel Economy Shift Schedule

The principles of the dynamic and fuel economy shift schedule are similar. Theoretically motor has a broad driving range, which can meet the vehicle requests at different speed. Figure 4 illustrates the motor efficiency distribution. Each accelerator opening relates to a driving efficiency curve. The shift points based on fuel economy shift schedule are the intersections of the profiles, which represent the energy efficiency of the motor with different gears.

Fig. 3 Two-parameter power shift rule

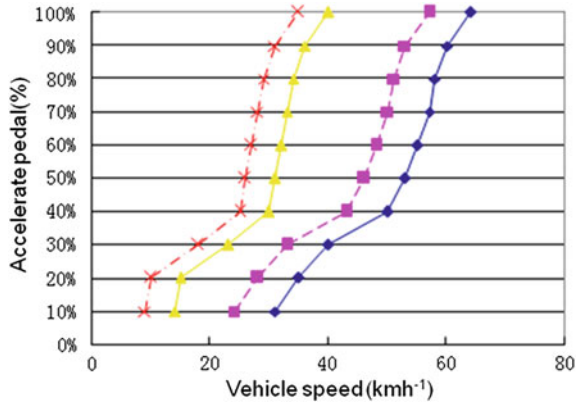
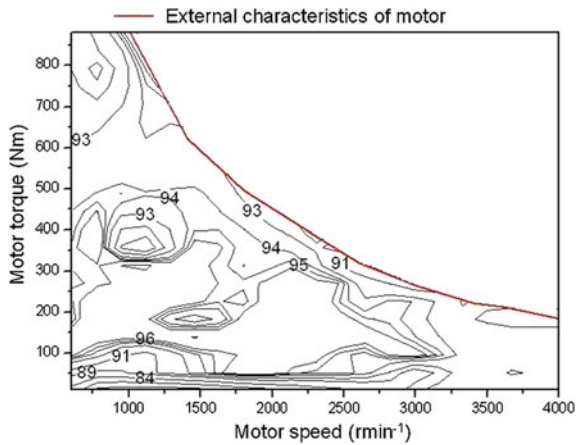


Fig. 4 Driving efficiency curve



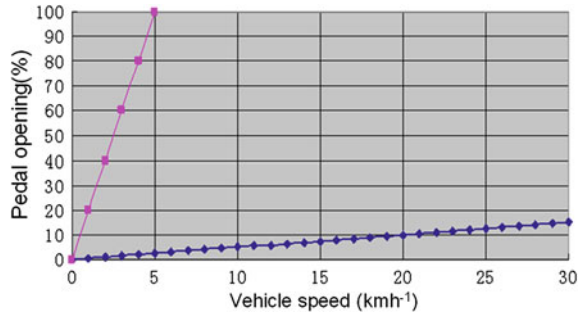
3.2 Identification of the Driver Intention

Identification of the driver request is key for a good control strategy. The driver intentions of starting, accelerating, decelerating, braking, stopping are distinguished through accelerator pedal, vehicle speed, brake pedal, cruising handle position and key signals.

Equipped with AMT, EVs could start with gear meshing because the motor performance is much better than the engine at low speed. The identification of vehicle starting is mainly concentrated on accelerator opening and the rate of pedal change. The start is divided into fast start, normal start and slow start. The key point is that how to calculate the torque request for the motor.

The process of acceleration and deceleration is identified by the opening and the changing rate of the accelerator pedal, which includes rapid accelerating, slow accelerating, rapid decelerating, and slow decelerating. The control strategy is related to the motor torque management and AMT gear shift control.

Fig. 5 Driving conditions partition



The process of braking is identified by the opening and the changing rate of brake pedal. The control strategy is also related to the motor torque management and AMT gear change control [2, 3].

3.3 Identification and Control of the Vehicle Driving Conditions

Vehicle driving conditions can be divided into downhill, uphill and normal driving. It could be identified by the speed and the accelerator opening though fuzzy reasoning as shown in Fig. 5.

In Fig. 5, there are three parts, respectively representing uphill, downhill and flat road driving. The distinction boundary between these three parts is influenced by many factors. E.g. the distinction line between uphill and flat road driving is influenced by resistance of the road, acceleration, brake pedal opening, and the throttle delay. So it needs to be calibrated. Figure 6 shows the recognition logic of these three parts.

Battery SOC low condition: The judgment of these conditions is relatively simple, mainly decided by the battery SOC. When the SOC is less than a certain threshold value, the vehicle works in the battery protecting mode, the judge logic and control strategy shown in Fig. 7.

Brake condition: Braking condition is recognized by the brake pedal; it is divided into ordinary brake and emergency brake. It is recognized by the changing rate and the opening of the brake pedal. Here is called emergency brake if brake pedal opening $>C1$ and the brake pedal changing rate $>C2$. Only if the brake pedal opening becomes zero, the emergency brake can be cancelled. $C1$, $C2$ are the constants to be calibrated. Normal brake condition is judged by the brake opening, zero or not.

Fault conditions: Fault condition is divided into sensor's failure and actuator's failure. And these faults are divided into five levels for the different effects; different control strategies are developed for different fault levels. E.g. when the car is in fifth fault level, it must be powered down quickly.

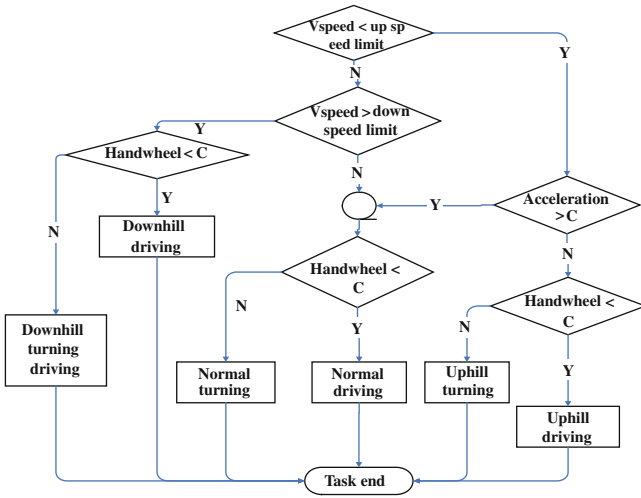


Fig. 6 Judgment process

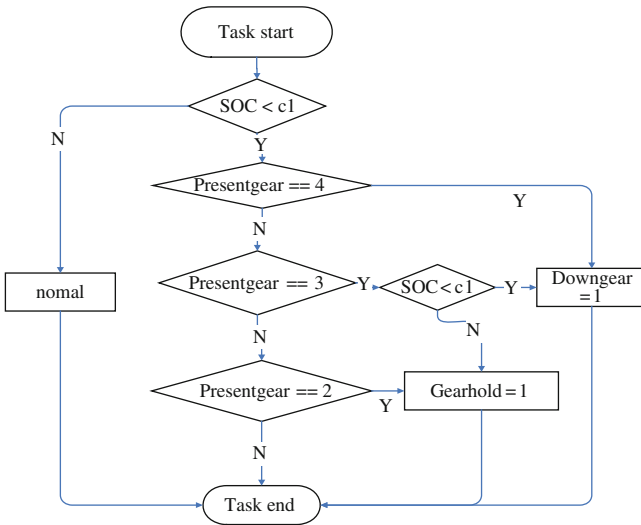


Fig. 7 Battery SOC low condition judge logic

Cruise condition: The judgments of the cruise condition are present gear, vehicle speed and the driver’s intentions-cruising key. When the vehicle is running at the speed designed for cruise condition, and if the present gear is the highest gear and the driver has pressed down the cruise key, then the vehicle is driven into cruise condition. The judge strategy is shown in Fig. 8.

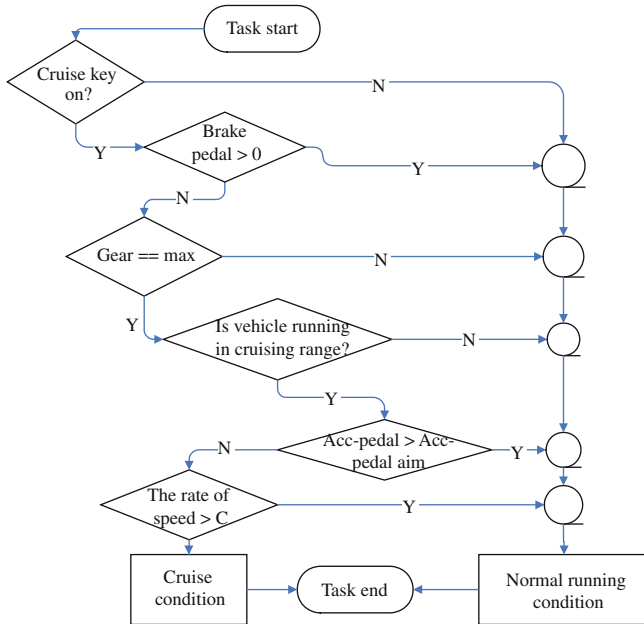


Fig. 8 Cruise condition judgment

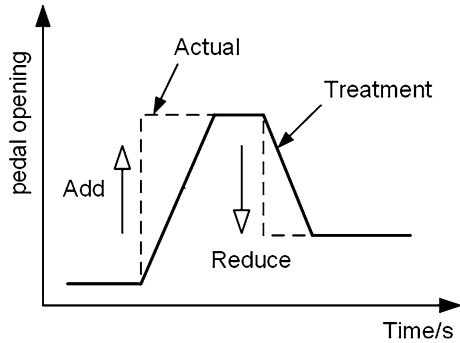
Energy regenerative condition: Energy regenerative condition has two trigger conditions: one is the driver depresses the brake pedal which belongs to be an ordinary brake and the other is the vehicle speed is too high;

3.4 Frequent Shift Suppression

Vehicle running environment is complex, and the drivers have different driving skills. Shift schedule with two parameters is determined by the accelerator and vehicle speed. So when the accelerator changes frequently or the vehicle speed changes fast, it may lead to the gear up and down frequently, which is an abnormal shifting and harmful to the vehicle to be avoided.

There are several control strategies for frequent shifting inhibition. In this chapter, the accelerator pedal deactivation and shift-delay strategy is proposed, according to abnormal shifting frequency caused by driver request and the road environment [4].

Fig. 9 Accelerator pedal passive strategy



3.4.1 Accelerator Pedal Deactivation Strategy

Accelerator pedal deactivation strategy is to turn the abrupt changes of accelerator pedal opening into gentle changes, to make it “bluntness”. The accelerator pedal signal will be amended to change slowly and smoothly with the strategy. And the frequent shifting could be avoided based on the “passive” accelerator pedal opening signal, as shown in Fig. 9.

3.4.2 The Strategy of Shift Delay and Shift Holding

There will be abnormal frequent shifting if the vehicle is on crooked roads or uphill with normal shift schedule.

In that case, it may be so dangerous that the vehicle loss driving power to slide down.

In this chapter, shift delay and shift holding strategies are used to avoid frequent shifting.

4 Modelling and Simulation

4.1 Building MATLAB/SIMULINK Simulation Model

In order to check the developed control strategies, the simulation model is built based on matlab/Simulink, which can be divided into three parts: input signal simulation, control strategy part and vehicle dynamic model. Figure 10 shows the control strategy part, it contains condition judging and control strategy.

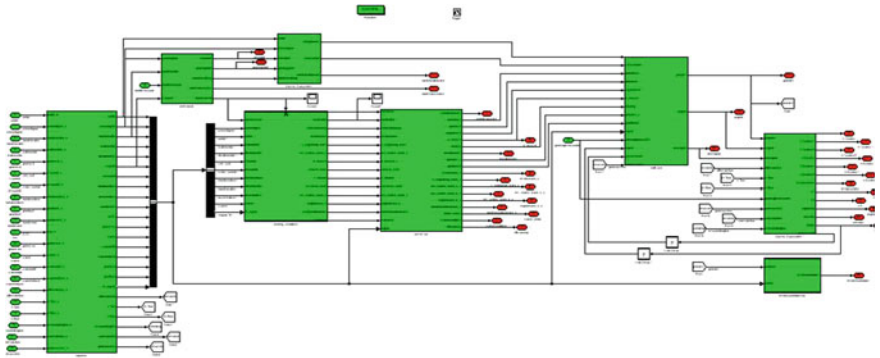


Fig. 10 MATLAB/Simulink simulation model

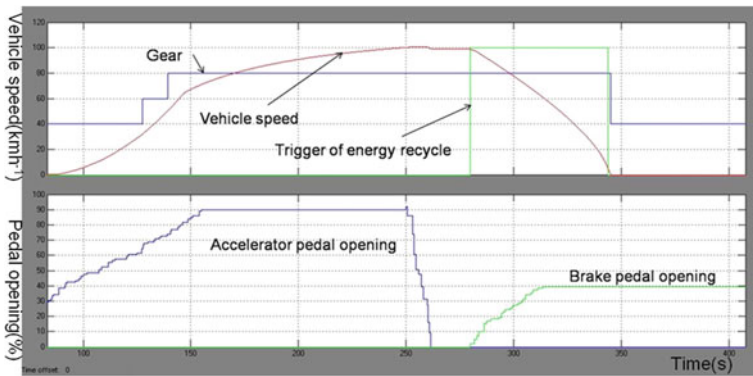


Fig. 11 Simulation of normal brake condition strategy

4.2 Simulation

Simulation tests include starting strategy, gearing process control strategy, automatic shift logic, driver intention identification and so on. In this chapter, the simulation results of AMT control and motor control on braking condition are illustrated. The brake condition can be divided into two parts: normal brake with energy recovery and hard brake without energy recovery.

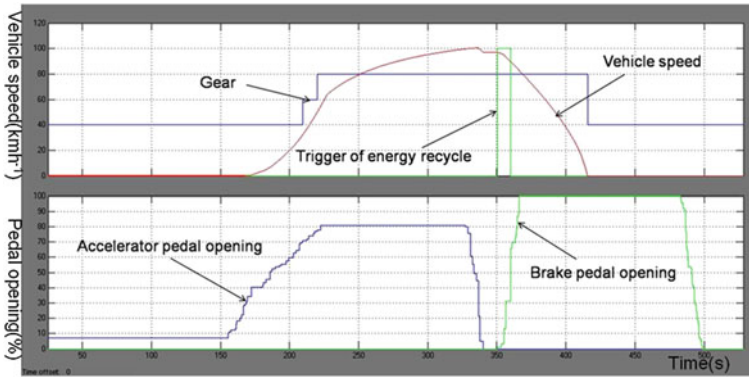


Fig. 12 Simulation of hard brake condition strategy

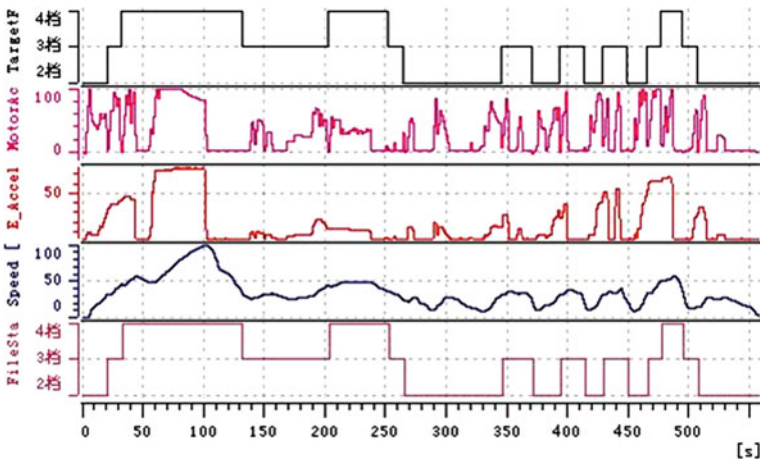


Fig. 13 The result of the automatic gearing strategy

4.2.1 Normal Brake with Energy Recuperated

The braking energy recycle strategy is used to control that when energy is recuperated and how much energy is to be recuperated Fig. 11 shows the simulation result. The first chart shows the changing of the vehicle speed, gear and trigger of the energy recycle. The second chart shows the change of the accelerator and the brake pedal. Within the first 300 s, the gear is shifted from the first file up to the third file, and the energy recycle is triggered when the brake pedal is pressed and the vehicle decelerates. When the speed drops to some value, the energy recycle ends and the gear shifts from the third file down to the first file.

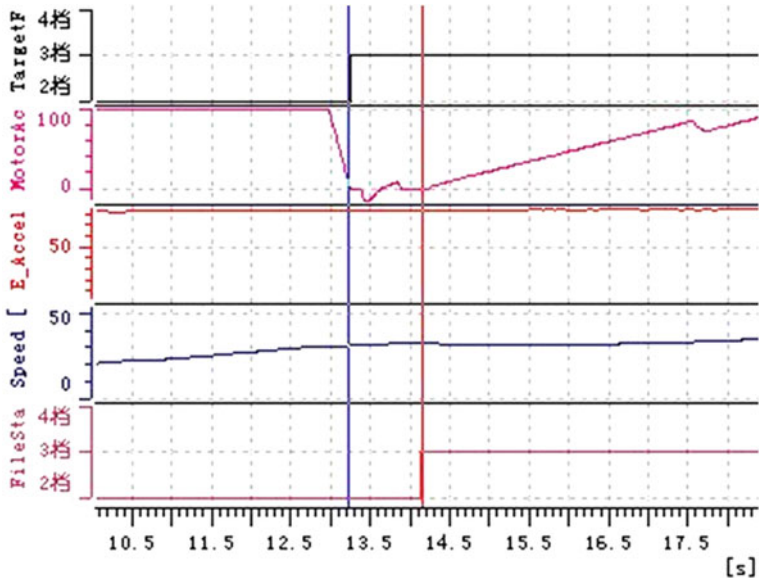


Fig. 14 Gearing process control from second to third file

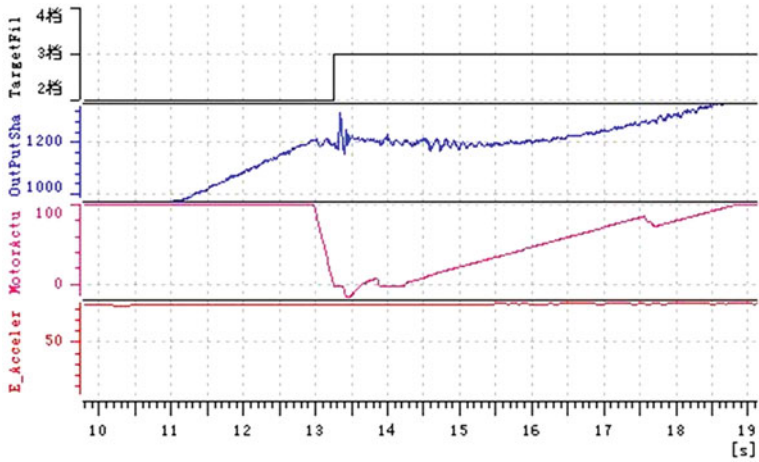


Fig. 15 Gearing process control from second to third file

4.2.2 Hard Brake Condition

The strategy of the hard brake condition is mainly about gear decision-making. The simulation result of the strategy is shown in the Fig. 12. The first chart shows the changing of the vehicle speed, gear and trigger of the energy recycle signal. The second chart shows the change of the accelerator pedal and the brake pedal.

At the beginning of the brake pedal depression, it's recognized as a normal brake condition with energy recycle. With the increasing of brake pedal opening, it is recognized as hard brake condition with energy recycle cancelled and gear preserved. Only if the vehicle decelerates to a low speed, the gear will be shifted down to the first file with the braking cancelled.

5 Vehicle Test Results

Figure 13 shows the test result of the AMT control strategy on actual vehicles.

The first chart shows the aim gear, the second chart shows motor torque (Nm), the third chart shows the opening of the accelerate pedal (%), the fourth chart shows vehicle speed (km/h), the last shows the present gear. The graphs show that the vehicle can shift automatically.

Figures 14 and 15 show the result of the control strategy of shift process.

The time between the two vertical lines is shift time, which is less than one second as shown.

The second chart shows the output shaft speed (r/min), whose change is no more than 50 r/min, as shown in Fig. 15.

6 Conclusions

Driver intention recognition method proposed in the article can identify the driver intentions effectively, fuzzy reasoning method, which is used to recognize vehicle running environment, can identify some specific road information, frequency gearshift suppression control strategy can reduce the unnecessary gearshift effectively when running.

References

1. Huifang K (2008) Study on AMT Fuzzy Shifting Strategy and Realization. Proceedings of the IEEE international conference on automation and logistics Qingdao, China Sept 2008
2. Yuhai W, Jian S, Xingkun L (2004) Simulation of AMT autoshift process based on Matlab/Simulink/Stateflow. SAE TECHNICAL PAPER SERIES 2004-01-2055
3. Saeks R, Cox C (1999) Design of an adaptive control system for a hybrid electric vehicle. IEEE SMC '99 conference proceedings. 1999 IEEE international, pp 1000–1005
4. Xi J, Ding H, Chen H (2009) Strategy of deactivated shift. Acta Armamentarii (3):257–261

Kinematic Study and Mode Analysis of a New 2-Mode Hybrid Transmission

Xuerui Ma, Yong Zhang and Chengliang Yin

Abstract A new 2-mode hybrid transmission for FWD mid-size passenger car integrated two electro-mechanical power-split operating modes. This new transmission includes two simple planetary sets with two transfer clutches and two braking clutches. With different activation of the four clutches, different modes can be obtained. In this chapter, firstly we analyze all modes and screen available ones respectively for pure electric propelling, engine-only propelling, hybrid propelling, engine-start, power generating, brake regenerating. The kinematic analysis based on the lever method researches both the speed and torque equation of available modes. Then we calculate and compare the max-torque capability of the propulsion modes to define the proper applications. Finally a numerical simulation of acceleration in the input-split mode runs in SimulationX.

Keywords Power-split · 2-Mode hybrid transmission · Kinematic analysis · Operating mode · Simulation

1 Introduction

Nowadays the power-split hybrid powertrain has become the main stream of hybrid electric vehicles. It absorbs both the advantages of the series and parallel hybrid architectures. And since the world most successful hybrid sedan Toyota

F2012-C03-026

X. Ma · Y. Zhang · C. Yin (✉)
National Engineering Laboratory for Automotive Electronic Control Technology,
Shanghai Jiao Tong University, Shanghai, China
e-mail: mayipian@sina.com

Prius hit the market, power-split architecture has drawn more and more attention and research interest.

The single mode power-split system consists of three different types, which are input-split, output-split and compound split according to the position where power-split happens. Summarized in [1] in general only the input split configuration is feasible as a full-range single mode hybrid system but requires high power, high output motor torque capability and high input motor speed capability. Output split systems are not feasible as single mode systems due to limits on achievable ratio coverage; however, they are useful as a sub-mode, especially at low gear ratio and engine start. The compound split mode is useful as a high range but not for launching due to poor efficiency and power circulating issues.

The combined of the input split and compound split is capable of providing full ratio coverage with moderate component speeds and torques and electrical path power less than 50 % of the engine peak. The compound split mode can work with low electrical losses during cruise conditions.

Among numerous power-split transmission designs two configuration, single-mode and 2-mode power-split transmissions, have big success in market. The most successful single-mode system is Toyota hybrid cars such as Prius and Lexus hybrid models.

GM has registered some 17 patents with different designs for 2-mode power-train, which contain a planetary architecture, two planetary gears and three planetary gears. The most popular configuration can be found in the 2008 GMC Yukon SUV and the 2008 Chevrolet Tahoe SUV. The configuration is a hybrid transmission with two EVT modes and four fixed gears [2].

There are also many designs from the researchers of some primary manufacturers like Renault IVT and Timken [3].

In this chapter a new 2-mode hybrid transmission with 2 planetary gears and 4 clutches/brakes has been studied via kinematic analysis and its characteristics like operating modes, transmission efficiency and maximum output torque has been provided here. Then a simulation of acceleration in input-split mode is implemented in SimualtionX and has indicated the hybrid transmission architecture can provide enough acceleration in this mode for a mid-size sedan.

2 2-Mode Hybrid Transmission Characteristics

2.1 Operation Modes

A new 2-mode hybrid transmission which shown in Fig. 1 has two planetary gear sets, two clutches and two brakes denoted by PG1, PG2, C0, C1, B0 and B1.

Compared with the no clutch design like THS, the new hybrid transmission combines two kinds of Electric Variable Transmission (EVT) modes which are input-split and compound-split respectively through different clutches action. With

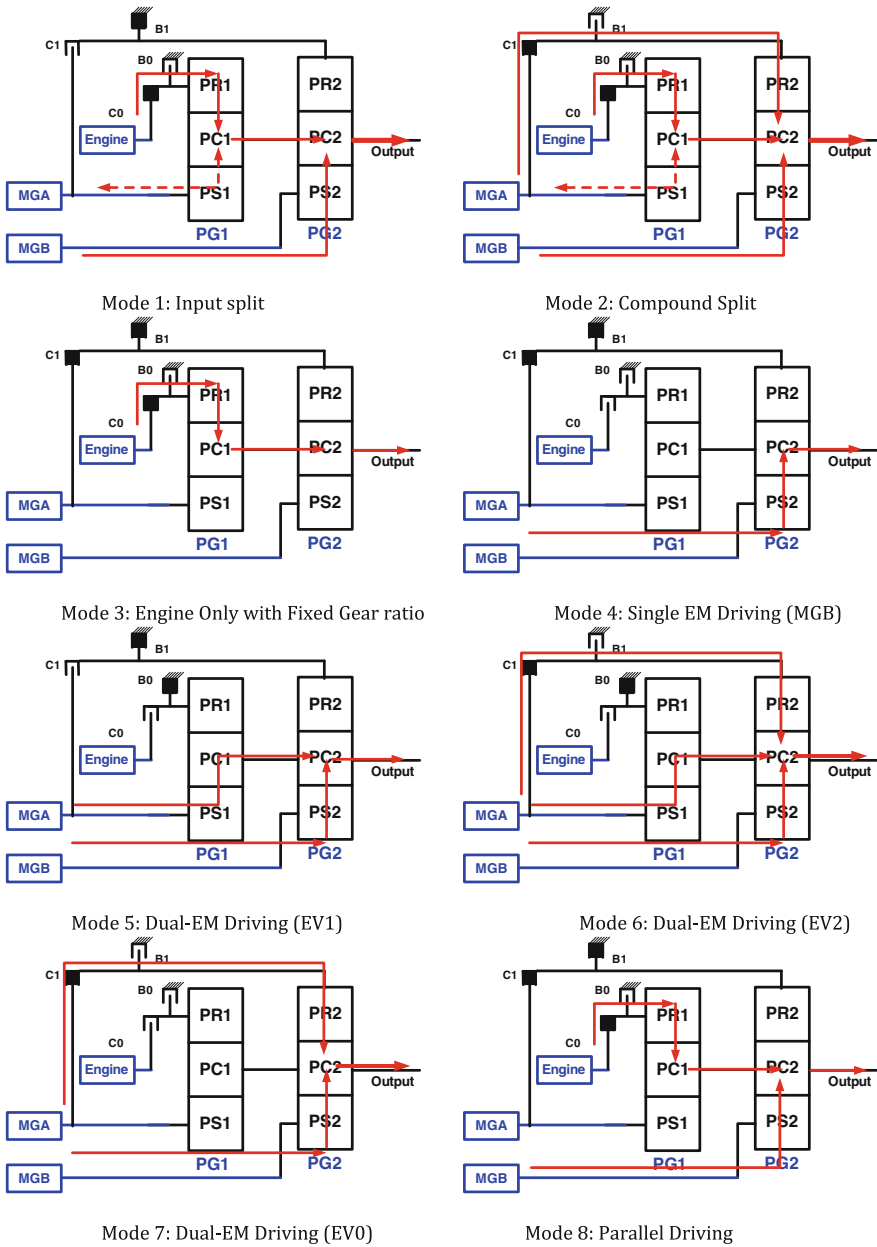


Fig. 2 Operation modes of the powertrain with this new 2-mode hybrid transmission.

gear of the first planetary gear and the ring gear of the second planetary gear simultaneously. With two connected ports $PC1(PC2)$ and $PS1(PR2)$ between the two planetary gear sets a combined lever analogy can be simplified from the

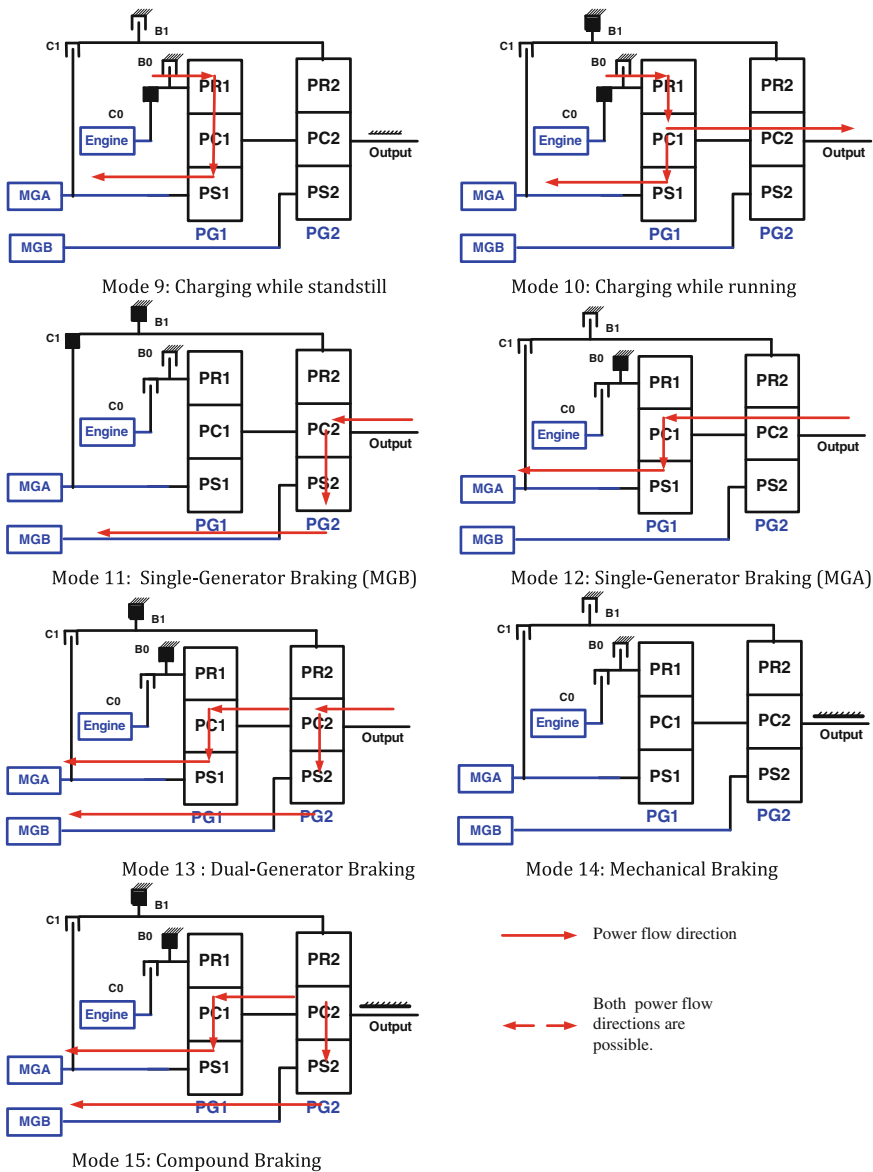


Fig. 2 continued

schematic as shown in Fig. 3c. The combined analogy is more forthright without interactional torque denoted as T_1 in Fig. 3b.

The rotational speed is denoted as ω_i and i represents the corresponding ports or components. The lever length ρ_1 and ρ_2 are equal to the teeth number ratio between the ring gear and sun gear of the two planetary gear sets respectively.

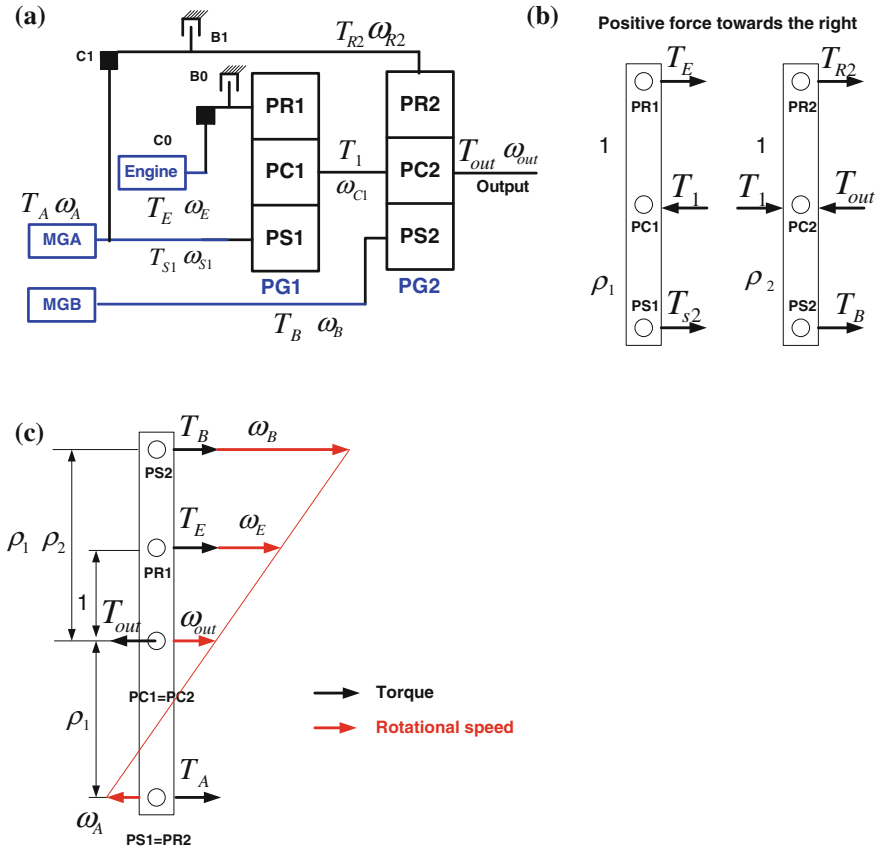


Fig. 3 Schematic and lever analogy of the compound split mode **a** Schematic of compound split mode, **b** Separate lever analogy, **c** Combined lever analogy

The equilibrium equations of static state can be presented as follows:

$$\omega_{out} = \frac{1}{1 + \rho_1} \omega_A + \frac{\rho_1}{1 + \rho_1} \omega_E \tag{1}$$

$$\omega_{out} = \frac{\rho_2}{1 + \rho_2} \omega_A + \frac{1}{1 + \rho_2} \omega_B \tag{2}$$

$$T_{out} = (1 + \frac{1}{\rho_1})T_A + (1 - \frac{1}{\rho_1\rho_2})T_E \tag{3}$$

$$T_{out} = (1 + \frac{1}{\rho_1})T_E + (1 + \rho_2)T_B \tag{4}$$

Table 1 Static equations of rotational speed and torque

Operation mode	Rotational speed equations	Torque equations
Input split	$\omega_{out} = \frac{1}{1 + \rho_2} \omega_B$	$T_{out} = (1 + \rho_2)T_B + (1 + \frac{1}{\rho_1})T_E$
	$\omega_{out} = \frac{1}{1 + \rho_1} \omega_A + \frac{\rho_1}{1 + \rho_1} \omega_E$	$T_A = \frac{1}{\rho_1} T_E$
Engine only	$\omega_{out} = \frac{\rho_1}{1 + \rho_1} \omega_E$	$T_{out} = \frac{1 + \rho_1}{\rho_1} T_E$
EV 0	$\omega_{out} = \frac{1}{1 + \rho_2} \omega_B + \frac{\rho_2}{1 + \rho_2} \omega_A$	$T_{out} = (1 + \rho_2)T_B = (1 + \frac{1}{\rho_2})T_A$

When the road condition and driver demand are known as ω_{out} and T_{out} , the system has one rotational DOF and one torque DOF.

The EV 1 and EV 2 modes are the special cases of EVT modes when engine speed is zero. The equations of input split mode, engine only mode and EV 0 mode are shown in the Table 1.

3 Transmission Efficiency

Using the torque and speed relationships derived in previous kinematics analysis, the transmission efficiency and power characteristic for two EVT modes are then calculated [5]. In the efficiency analysis it is assumed that the efficiency of the mechanical path is 100 % and that of the motor/generator is 85 %. In order to calculate the transmission efficiency it is also assumed no power from battery was used which means the electric power between generator and motor is balanced and only engine power is delivered to the output shaft.

Table 2 shows the powertrain parameters that were used in transmission efficiency calculation and later maximum propelling torque calculation.

Speed ratio is defined as engine speed compared to output shaft speed. Power split ratio represents the electric power from the engine output [6]. The transmission efficiency and power split ratio versus speed ratio is shown in Fig. 4. The points of 100 % efficiency means there is no electric conversion loss and the engine output has been completely delivered to the output shaft. The points are known as mechanical points where the power split ratio is zero. The map of transmission efficiency can also be applied to define the operation range of the EVT mode as a limit.

For this 2-mode hybrid transmission the input split mode and compound split mode has a common point which is also the mechanical point. According to the kinematic analysis we know at this point the speed ratio is exactly equal to that of the engine only mode, which is also as a fixed gear. It is remarkable that this point is not only the transition between the two EVT modes but also a standalone mode when the engine can run under efficient area.

Table 2 Powertrain parameters

Parameters		
Planetary gear ratio ρ	PG1	PG2
	2.17	2.242
Final reduction gear ratio	2.87	
Tire radius	0.308 m	
Engine	57 kW, 115 Nm max. torque, 4,700 rpm max. speed	
MGA	15 kW, 55 Nm max. torque, 6,000 rpm max. speed	
MGB	30 kW, 305 Nm max. torque, 6,000 rpm max. speed	
Vehicle mass	1,413 kg	

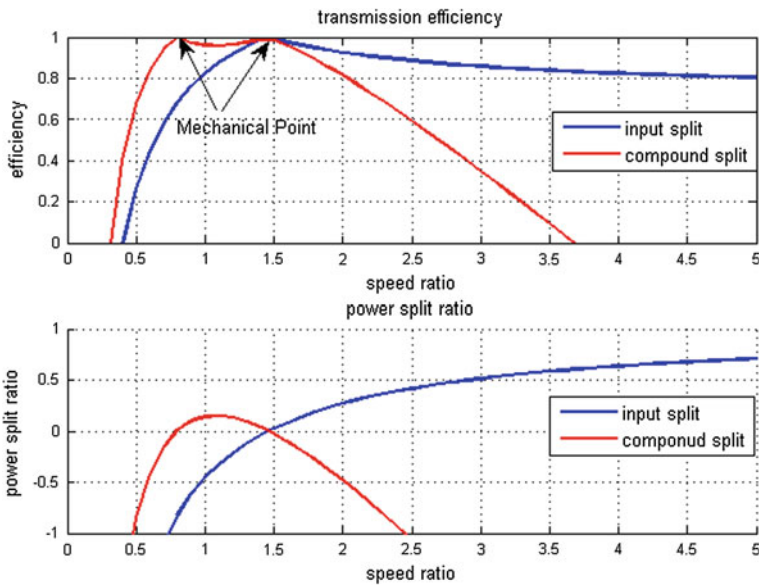


Fig. 4 Transmission efficiency and power split ratio

4 Maximum Propelling Torque Capability

Input-split, compound-split and engine only are the basic propelling modes. From the kinematic Eqs. (1)–(4) and Table 1, the maximum output torque can be calculated in iterative process [7]. The maximum output torque is shown in Fig. 5.

For the input split mode, it has a relatively higher torque capability for $V = 0\text{--}74$ km/h because the second planetary gear set with the ring gear locked acts as a reduction gear. But it is also limited when MGB reaches its maximum speed of 6,000 rpm from where the output torque is zero. The input split mode is quite suitable for low speed with high torque demand.

For the engine only mode, the maximum torque is lower because only the engine’s torque used to propel the vehicle. And the engine works with a fixed gear

Fig. 5 Maximum output torque of three propelling modes

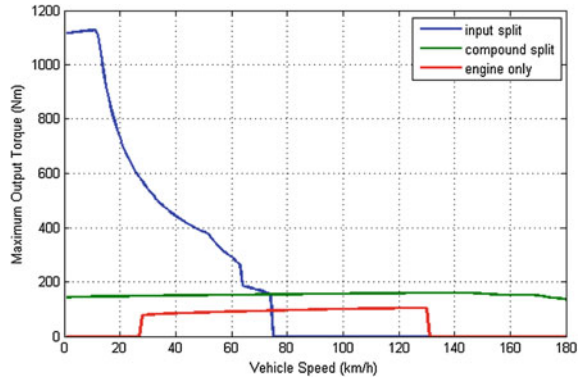
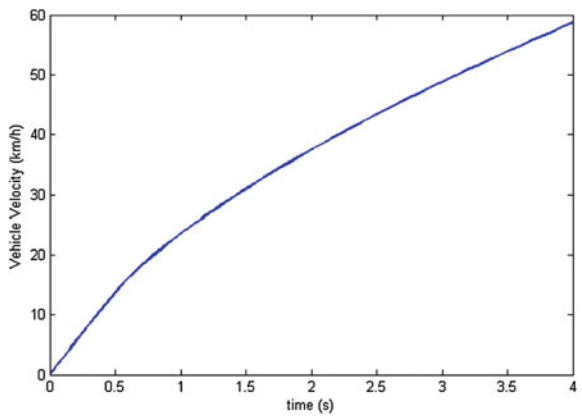


Fig. 6 Acceleration in the input split mode



ratio, so the effective velocity range is from 28 to 130 km/h limited by the engine idle speed and maximum speed. This mode is suitable for high speed cruise when engine works with high thermal efficiency. In addition with MGB is involved we can get the parallel mode.

For the compound-split mode, the maximum torque is steady for most of the velocity range. So this mode can supplement the output torque range besides the first two.

5 Simulation

The calculation in Part 3 gave out the maximum capability of the powertrain, but the actual performance is decided by the cooperation of all the power components. The input split mode has indicated high torque capability while low velocity. Therefore the simulation of the acceleration performance in such mode is implemented using SimulationX, which is a CAE software for physical system

simulation. Because of the input-split kinematic characteristic the engine can work decoupled from the wheel speed. During the acceleration the engine is working under a constant speed 2,000 rpm with high efficiency. The final velocity is then limited by MGB maximum speed. The acceleration curve is shown in Fig. 6. The acceleration time from 0 to 50 km/h is 3.14 s.

6 Conclusion

In this chapter, a systematic analysis of a new 2-mode hybrid transmission was implemented. The mode screening indicated that the transmission had various segmentations considering the driver demand. The efficiency analysis demonstrated the advantage of 2-mode hybrid which combined the input and compound split modes. And the engine only mode was the transition between input split and compound split modes, which had a fixed gear ratio that was equal to the mechanical point of input split mode. The maximum output torque calculation showed the capability of different propelling modes and provided the foundation for mode selection [7]. The simulation result showed the powertrain with this new 2-mode transmission had remarkable acceleration ability in the input-split mode which was adequate for mid-sized hybrid electric vehicles. Furthermore we will research on the transition between two EVT modes and the EV modes which are potential for Plug-in HEV.

References

1. Conlon B (2005) Comparative analysis of single and combined hybrid electrically variable transmission operating modes. SAE paper, no. 2005-01-1162
2. Grewe TM, Conlon BM, Holmes AG (2007) Defining the general motors 2-mode hybrid transmission. SAE Paper, 2007, no. 2007-01-0273
3. Miller JM (2006) Hybrid electric vehicle propulsion system architectures of the e-CVT Type. IEEE Trans Power Electron 21(3):759–767
4. Benford H, Leising M (1981) The lever analogy: a new tool in transmission analysis. SAE Paper, 1981, no. 810102
5. Jaeyoung K, Woulsun C, Sunghwa H, Jeongman P, Hyunsoo K (2011) Control strategy for dual-mode power split HEV considering transmission efficiency. IEEE Vehicle Power and Propulsion Conference (VPPC), 2011, Conference Publication, art. no. 6043008
6. Kukhyun A, Suk WC (2008) Developing mode shift strategies for a two-mode hybrid powertrain with fixed gears. SAE paper, 2008, no.2008-01-0307
7. Jeongmin K, Talchol K, Byungsoon M, Sungho H, Hyunsoo K (2011) Mode control strategy for two-mode hybrid electric vehicle using electrically-variable transmission (EVT) and fixed gear mode. IEEE Trans Veh Technol 60(3):793–803

CVT Driving to a Green Future

A. Cai

1 CVT Background

Since pushbelt CVT was invented in 1970s, it's already 40 years. There were over 25 million CVTs in the field, its annual volume has reached 5.9 million in 2011. Thus Continuously Variable Transmission (CVT) is mature and one of mainstream Automatic Transmission now. According to Bosch's analysis, in year 2019, global CVT volume can reach 14 million/year. The biggest portion will be Japanese market, but the main increase will be in Chinese, American and Rest of Asia. In China, the CVT volume will increase from 0.4 million (2011) to 3.0 million (2019).

What drivers make CVT popular? The markets in all regions are similar, most customers are expecting their car to be cheap, fuel economy, comfort but still be sportive. And the government regulation of fuel consumption and emission are more and more strict. The state-of-art CVTs can meet these requirements well:

1.1 Fuel Efficiency

The state of art CVT can achieve a state of art low fuel consumption which is lower than manual transmission's already. The most important 2 factors which influence F.C. are variability and efficiency. The efficiency means how much amount of internal loss. It can be split into 3 parts: friction loss, hydraulic system

F2012-C03-027

A. Cai (✉)
Bosch Trading (Shanghai) Co., Ltd., Shanghai, China
e-mail: Yanqing.Du@cn.bosch.com

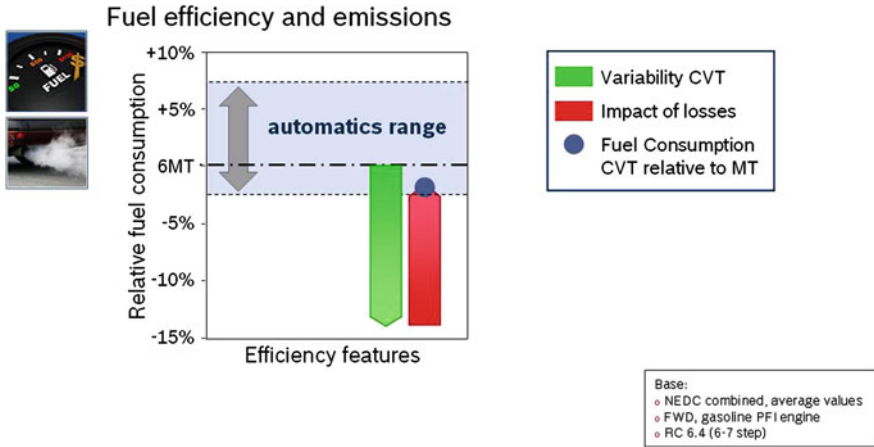


Fig. 1 Fuel efficiency and emissions

loss and transmit parts loss. The variability means the potential of increasing engine efficiency by optimizing the ratios. Thus we would find for the automatic transmissions with stepped ratios once the number of ratios is fixed, the potential of optimizing the ratios controls is fixed too. The only differences in Fuel consumption are the differences of internal loss. In transmission with gears, a large ratio range can be achieved with extending the ratios of first and last gears. By extending the ratio range, it's possible to provide a proper ratio for engine efficiency. However, when the ratio range extended, it needs more gears to reduce the gap between gears, to improve drivability, fuel economy and make gear shift softly. By doing so, it will increase the size and complexity of a transmission. For the stepless transmission—CVT, there are theoretically infinite ratios between LOW and OverDrive ratio, thus the ability to optimize the engine efficiency is the best. But due to still high loss of internal parts like friction and hydraulic system, the advantage of infinite ratios is withdrawn. Currently the average fuel consumption level of state of art CVT is less than MT's, a rather low F.C. of vehicles. Meanwhile, this high internal loss also offers the opportunity to improve the CVT's behavior, that if internal loss can be managed well, the CVT has the biggest potential to improve the fuel efficiency [1] (see Fig. 1).

1.2 Price

According to the 'Consumer add-on transmission prices study', which was done in Europe, the add-on price is calculated as in the same model, A.T. version price minus MT version's. AMT is the lowest, then 4AT and CVT. Due to simple structure and less parts, CVT's add-on price is lower than other transmission types.

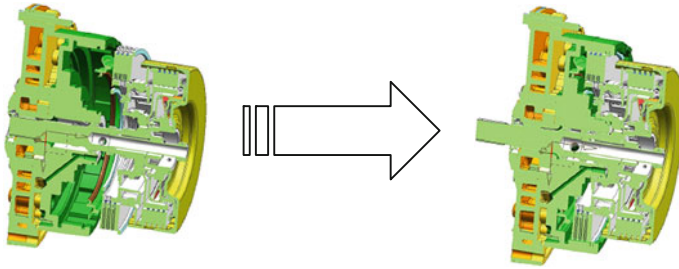


Fig. 2 Modify to a compact DNR

1.3 Comfort

Based on the J.D.Power Initial Quality Study (IQS) data 2011, the customer satisfaction of pushbelt CVT remains highest level (34 % higher than the average), followed by 4AT (28 % higher than the average). In this study, CVT (pushbelt and chain) are all above the average, all step ATs except 7-8AT are above the average as well, it has a good acceptance in US.

Aiming future market drivers from customers: operation cost, purchase cost, environment legislation, small & light car, prepare for electrification (hybrid) and so on, we can conclude 4 development criterias for development of next generation CVT. They are *low cost design*, *fuel efficient*, *compact & light design*, *adaptable* of upgrading to hybrid. Bosch has performed a series of innovations and solutions to meet these criterias.

2 CVT Innovations and Solutions

2.1 Concept Choice Enables Compact Design and Cost Reductions

The needs of acceleration and comfort in low segment are not sensitive but cost, so wet plate starting clutch can replace the launch function of torque convertor, and the design can be cheaper and more compact.

By optimizing the internal parts like oil pump, PRND (shift mechanism) and so on, CVT can be more compact. In the past, the DNR (drive-neutral-reverse gear) and oil pump are designed separately to meet its function. However, it is possible to design a more compact by sharing part of pump housing and inner space. (see Fig. 2).

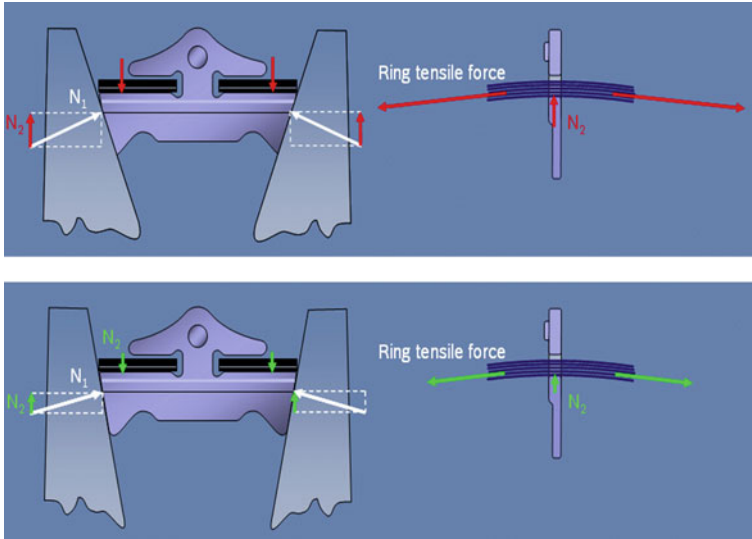


Fig. 3 Ring tensile force reduction in relation to clamping angle

2.2 High Power Density Variator

In CVT, torque is transferred by belt-pulley (so called variator). The variator's power density is limited by the ring tensile forces in the belt: in state-of-art CVTs, contact surface between belt and pulley is straight surface with a cone angle of 11° . In order to transfer a certain torque, belt must be clamped by pulleys on both sides to provide minimum normal force (N_1 in Fig. 3), from which a radial rising force (N_2) is derived. In order to keep the belt in a fixed ratio (no movements in radial direction), this radial force (N_2) must be balanced. In pushbelt system, balance force is provided by very large tensile forces in ring set (ring tensile force is the largest force in belt system, power density can be counted as this force). If the cone angle is changed to a smaller angle, the clamping force, which is needed to transfer the same torque, can be smaller as well. Thus it will reduce the ring tensile force a lot. So the transmitted torque can be enlarged by reducing the cone angle. Thus it's possible to design a more compact system for the same torque level.

Variator ratio is determined by belt working radius. Ratio change is performed by changing axle position of moveable pulley to change belt radius. Certain ratio range needs certain axle stroke of pulley to realize. Once the cone angle changed to smaller, the needed pulley stroke will be smaller too. Then the variator could be more compact as well. And, if the pulley stroke is less, the volume of cylinder (behind moveable pulley) can be smaller as well. Thus the flow needs for hydraulic system is less. This will result in a more efficient hydraulic system. According to the calculation, if the cone angle reduces every 1° , the pulley stroke can be 3 mm

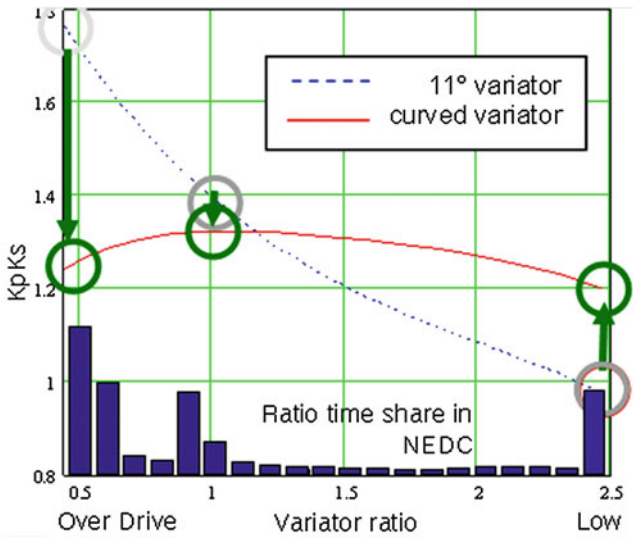


Fig. 4 KpKs optimization

less, the fuel consumption can be reduced by 0.75 %. So smaller cone angle can improve the fuel efficiency and make system more compact.

In reality, the cone angle is not simply reduced by 1–2° as a straight pulley, it’s realized by curved pulley, which has an optimized curve on running surface. The curve has optimized angles in different position, self-lock can be prevented. And another advantage is, it’s possible to optimize the clamping characteristics. In order to stabilize ratio in a fixed value, both primary clamping force ($F_{primary}$) and secondary clamping force ($F_{secondary}$) have to remain at a balanceable ratio, which is called KpKs:

$$K_p K_s = \frac{F_{primary}}{F_{secondary}}$$

This KpKs varies as a function of ratio (see blue dashed curve in Fig. 4), its value is less than 1 at Low ratio but more than 1.7 at OD ratio. If KpKs is less than 1, it means clamping safety applied on primary pulley is less than which is applied on secondary, risk of belt slip will increase at extreme working conditions. If KpKs is more than one, that is clamping safety is higher than needed (secondary safety), which will lead to over clamping and increase loss. With straight pulley, this characteristic is always the case. But in curved pulley design, it’s possible to optimize it. The red solid line in Fig. 4 shows one optimized KpKs curve, in which the value at LOW ratio is increased to 1.2 and value at OD ratio is lowered to a bit more than 1.2. With new KpKs characteristics, both over clamping at OD and lack clamping at LOW can be avoided, belt is clamped more safely and efficiently. And since the maximum clamping force level at primary is reduced, the pulley itself

can be designed smaller and lighter, because only a smaller cylinder is needed. Moreover, smaller cylinder will reduce the hydraulic flow needs, hydraulic loss can be further reduced as well.

So, a curved pulley can increase the power density of variator, reduce the CVT size and hydraulic loss, improve pulley variator's robustness.

2.3 Selection of Ratio Coverage

As we know the bigger ratio coverage can provide engine more chances to work at most efficient working conditions, thus the fuel economics can be better. In CVT design, the bigger ratio coverage will come to a larger pulley design, increase the CVT size and weight, increase the hydraulic loss etc. These will consume up the benefits of ratio extension. According to current study, the optimal ratio range is 6.0.

2.4 Control Strategy

Bosch has developed a brand new control strategy compared to the conventional control, which called clamping force control. In conventional control, clamping force is calculated and used as control base of both torque transfer and ratio control. The clamping force (F_{clamping}) is calculated as below formula:

$$F_{\text{clamping}} = \frac{\text{Torque} * \cos \lambda}{2 * \text{Radius} * \mu} * S_f$$

In this formula:

- Torque stands for input torque from engine. In reality, engine torque is not measured, but calculated/estimated by EMS (engine management system). Either model based calculation or data based estimation, the torque value will contain some error.
- λ stands for the pulley angle (normally 11°).
- Radius stands for belt running radius. This radius is calculated as function of speed ratio (primary speed divided by secondary speed). There is some error between dynamic radius (from calculation) and real radius (clamping position).
- μ stands for belt-pulley friction coefficient. μ is measured value from bench test. Considering there's some deviation among individual transmissions and the oil characteristics may variate over the years, it's not always the accurate value.
- S_f stands for safety factor.

Belt application should always secure the belt's safety, which means providing enough clamping force to prevent belt slip. Frequent belt slip will damage the belt-

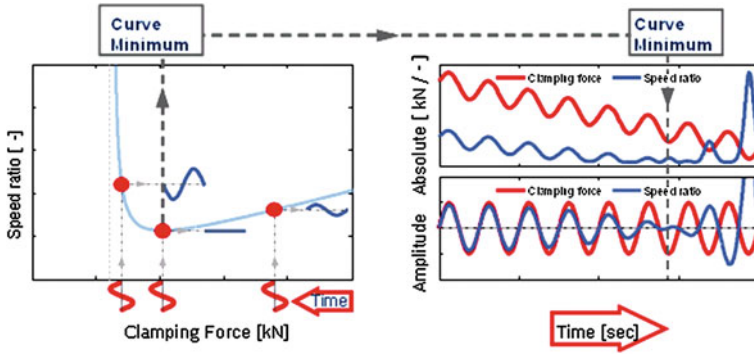


Fig. 5 Ratio-clamping force characteristics

pulley system, and finally lead to belt breakage. So in clamping force strategy, belt is always over clamped by using a safety factor >1 . When taking inaccuracy into account, the safety factor should be bigger. Moreover, there are torque peaks from driveline will finally react on belt-pulley, thus safety factor should be increased again. Typical safety factor is 1.3, which mean 30 % overclamping. Overclamping not only increase the loss in belt-pulley system, but also increase the pressure level and flow needs in hydraulic system. System efficiency is lowered.

Slip control: the purpose of belt control is to prevent belt slip at any torque level, so if the belt slip if detectable, it's possible to lower the clamping force to a just sufficient force.

There's a unique characteristics in belt-pulley system. The light blue curve (Oblique asymptotes) in left graph of Fig. 5 shows the relation between speed ratio and clamping force, we can call it belt-pulley characteristics. As we know the stiffness of pulley is not infinite. The pulley bending under clamping force will lead to belt radius sag towards center in radial direction. This reaction acts as proportional function in relation to clamping force, which is shown as right part of belt-pulley characteristics in this graph. If the clamping force reduces to a certain level, close to safety factor 1, the belt will likely to slip while the effect by pulley bending being small. Thus in the left part of belt-pulley characteristics shows the relation between speed ratio and clamping force will act as inverse proportional function. This characteristics is the base of slip control. The minimum point of belt-pulley characteristics is the optimize target (set-point) of slip control.

If applying different clamping forces (from high to low) and add a small vibration, the clamping force signal is shown in red in right graph of Fig. 5. Response to clamping force vibration will be speed ratio vibration due to belt-pulley characteristics. When clamping force is high, the speed ratio will response in same phase as force vibration. When clamping force is low, the speed ratio will response in opposite phase. If clamping force is around the optimize point, speed ratio response will be zero. This response is drawn in dark blue in the right graph of Fig. 5. If we filter both clamping force and speed ratio with band-pass filter, we

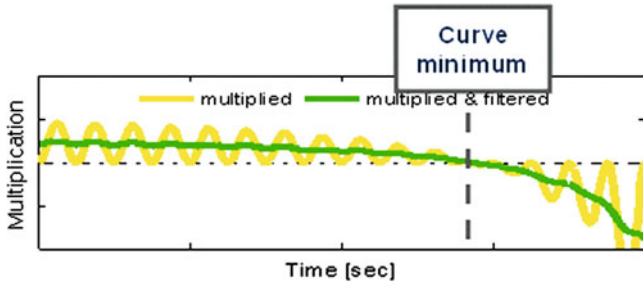


Fig. 6 Filtered control signal

will have the pure vibration and its response, shown in the right and bottom graph in Fig. 5, its x-axis is clamping force (from high-> low).

Multiply clamping force and speed ratio, result is shown in yellow curve in Fig. 6. Then filter this product with low-pass filter, filtered signal is plotted in green in Fig. 6, and this multiplied and filtered signal will show the belt slip status in relation with clamping force. If its value is positive, the clamping force and speed ratio response are in the same phase, which can be detected as over clamping. If its value is negative, the clamping force and speed ratio response are in the opposite phase, which can be detected as insufficient clamping. The zero value is the slip control target. Thus we can use the sign of green signal as control parameter for close loop control of clamping force.

In control diagram, add blocks in Fig. 7 can simply realize above control methods. In this diagram, ‘speed ratio’ and ‘clamping force’ are from existing sensors and calculation. Both signals are filtered with band-pass filter and multiplied, then filtered with low-pass filter, the result is control signal. Clamping force can be close-loop controlled around optimize point (control signal = 0). Thus the clamping force can be reduced and Fuel economics can be improved. Moreover, In order to apply slip control strategy, there’s no need to add new sensors or solenoids compared to conventional control.

Slip control strategy test in vehicle level:

1. The validation of control set-point is shown in Fig. 8. Test start with open loop control, clamping force is increased from safety <1.0 , then to increase to over clamping point (shown in gray point), the measured speed ratio and efficiency are shown in relation to clamping force in the graph. Then start close loop control of slip control, the dark blue plots track the clamping force controlled by slip control. In these graphs we can see, that the control signal value (dark blue curve in middle graph) finally stabilized around zero, corresponding speed ratio is controlled at target setpoint (red point in graph). In the efficiency curve (bottom graph in Fig. 8), we can see the target setpoint of slip control is almost the highest efficiency point of pulley. So we can conclude that, the slip control can keep belt-pulley system at high efficiency.

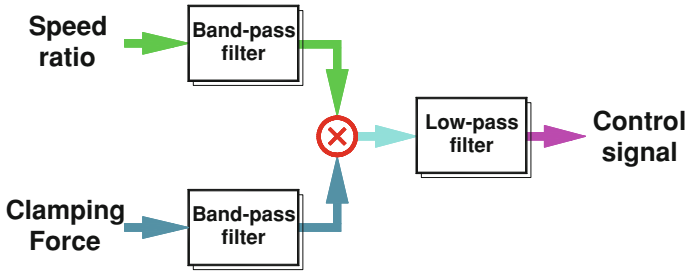
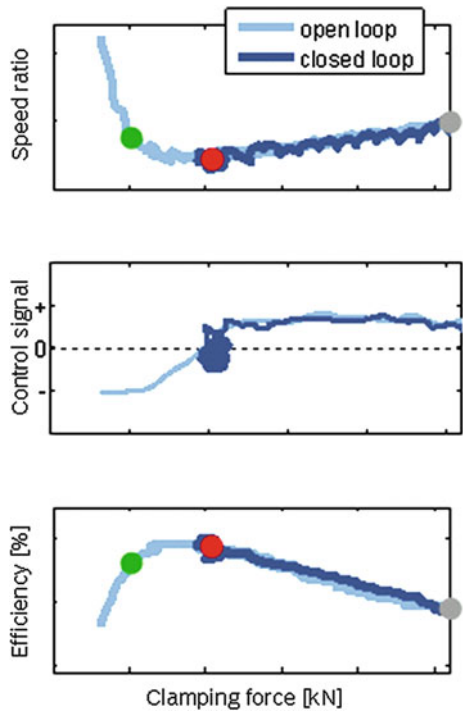


Fig. 7 Slip control diagram

Fig. 8 Test result of slip control



2. The fuel consumption measure in vehicle is shown in Fig. 9. Fuel consumption is evaluated as comparison between activating and deactivating slip control, tests were performed under European, American and Japanese vehicle cycles, while measuring activate rate of slip control as reference. Test result shows, when slip control is activated most of time (>90 %), the fuel consumption of vehicle level can be reduced a lot (3.7–4.5 %).

However, Slip control is now performing well in functional level and ready for A-sample. In order to put into series production, more development and validation are still needed.

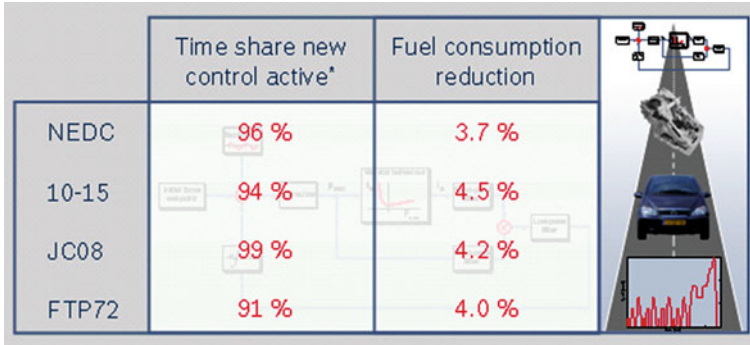
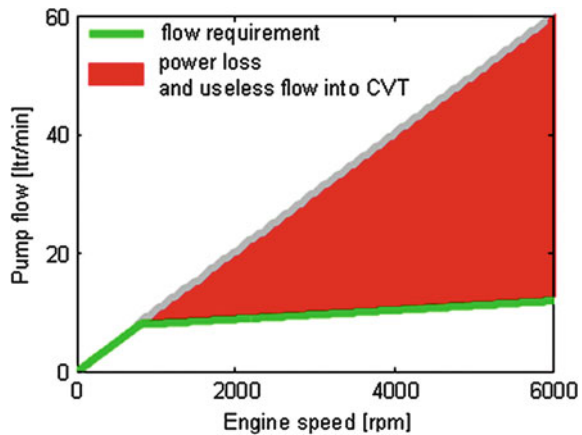


Fig. 9 Fuel consumption improvement of slip control

Fig. 10 Pump flow of single-stage pump



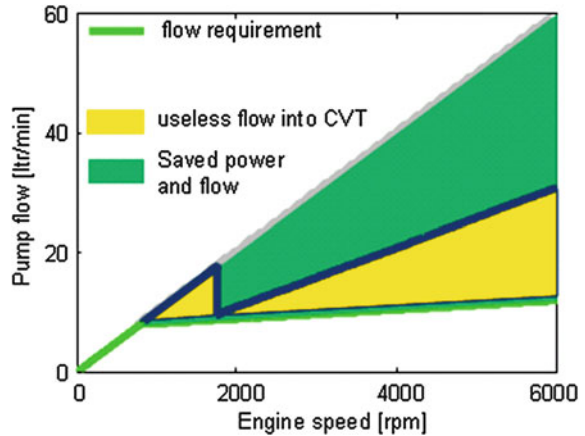
2.5 Passive Flow Control

Hydraulic system consumes a lot of energy in CVT system. Especially in conventional CVT, a single-stage mechanical pump is used. As shown in Fig. 10, the need flow for CVT operation is shown in green curve. But a mechanical pump whose displacement is design for the most severe situation, will produce a large portion of surplus flow when driven by engine at high speed (red area in this graph). Large surplus flow consumes large energy from engine.

By introducing 2-stage pump (compress oil twice in one revolution, 2 pressurize chambers are isolated to each other), a smart flow control is enabled.

- The ‘active flow control’: add one flow control valve (controlled by an extra solenoids), if the flow calculation shows half pump flow can meet the flow needs in CVT, this flow valve can be controlled to short-cut 1 half of pump, thus can save half of the driven power. See Fig. 11.

Fig. 11 Pump flow of 2-stage pump

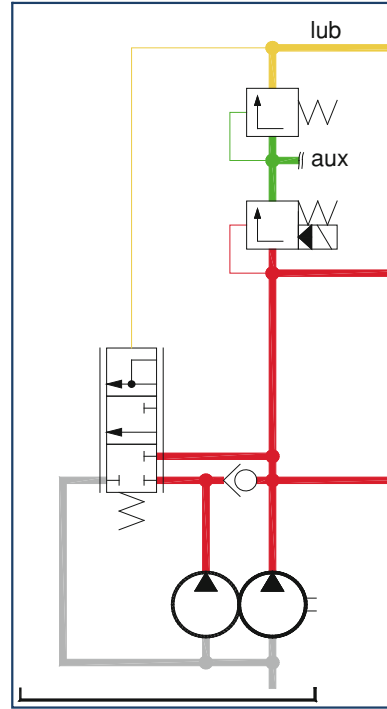


- The ‘passive flow control’: in active control, there’s one more solenoids needed, and more control resource in TCU is needed to control it. If we can make use of lubrication pressure as the control of flow valve instead of solenoids, we can save extra hardware and resources. Since the lubrication pressure is the function of lubrication flow and accumulated damp in lubrication circuit, it is possible to calibrate the flow valve spring to control flow passively. Instead, accumulated damp in lubrication circuit should be calibrated more accurate (including orifices of sprays, damp of oil cooler etc.). The hydraulic scheme in Fig. 12 shows how passive control valve linked to lubrication pressure.

In test bench, the flow saved by flow control can contribute approx. 1.5 % fuel saving to the vehicle level.

2.6 Direct Controlled Solenoids

In order to control high flow, high pressure circuit, main valves are driven by pilot circuits, which are controlled by solenoids. Thus addition spools and oil channels must be added. Nowadays, Bosch’s latest direct controlled solenoids (called DESC) can control higher pressure and flow, which make it possible to eliminate the pilot circuits. In the low torque CVT design at Bosch, DESC can replace all pilot circuits, thus result in a much lighter and simple hydraulic body. Compared to the conventional hydraulic body, the DESC design can be as big as 1/2 of original size and use less spools (3 spool valves V.S. 13 spool valves in old design) [2–3].

Fig. 12 Hydraulic scheme

2.7 Modularity

In new design, the connection to engine can be designed as module. Thus if there's needs to install T/C or upgrade to hybrid, this modularized interface can be easily adopted to T/C design or add e-motor between engine and CVT.

2.8 Improvements to Fuel Efficiency

When applying all innovations and solutions, the fuel efficiency of vehicle level can be improved a lot to state-of-art CVT (see Fig. 13). The internal loss of CVT can be reduce over 50 %, equivalent fuel saving in vehicle is 7 %. So compared to MT, future CVT can save up to 9 % fuel in a vehicle [4].

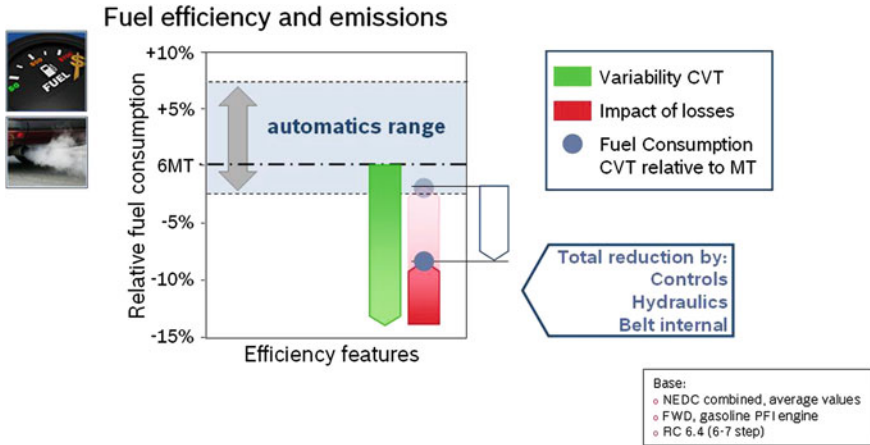


Fig. 13 CVT fuel efficiency improvement by new technologies

3 CVT in Future

According to above improvements, CVT can help conventional vehicle to dig out a potential in fuel economics. However, in future of electrification, CVT can contribute further:

- In HEV: CVT has proven its value in hybridized powertrain. More and more CVT hybrid vehicle launched on road (Honda Civic, Insight, Jazz etc.). The flexibility in ratio optimized the engine and motor, contribute a lot in fuel saving.
- In EV: according to latest study, with a high efficient CVT (transmission efficiency is as high as 95 %), applying CVT can offer up to 7 % energy saving in an EV.

4 Conclusion

With the new CVT technologies, the fuel consumption can be reduced by 7 % (vehicle level) compared to the state-of-art CVT's. Thus in near future, the new CVT technologies can help CVT vehicle realize up to 9 % less fuel consumption when compared with MT vehicle. New CVT technologies will bring us a green future.

References

1. Francis VDS, Tom VD, Gert-Jan VS (2007) Fuel consumption potential of the pushbelt CVT. In: SAE paper 2007-01-1457
2. Arno V (2010) Driving CVT into a new area. In: SAE transmission seminar 2010
3. Martin K (2011) Transmitting CVT into the Chinese market. In: SAE transmission symposium 2011
4. Gert-Jan VS (2012) CVT pushes to fulfil market needs. In: SAE transmission symposium 2012

Part IV
Transmission Control System

The Control Authority of Passive and Active Torque Vectoring Differentials for Motorsport Applications

Anthony Tremlett, Francis Assadian, David Purdy,
Nick Vaughan, Adrian Moore and Martin Halley

Abstract Limited Slip Differentials (LSD) have traditionally been shown to offer significant improvements in traction and vehicle stability [1, 2]. In the motorsport environment however, during high lateral accelerations, the grip level of the inner driving wheel can be compromised and force the LSD torque bias to switch directions. Thus initial corner entry understeer, snaps to mid-corner oversteer as the inner wheel saturates. Torque Vectoring Differentials (TVD) offer greater flexibility and provide a system which can both improve vehicle stability and agility [3, 4]. The result is a more predictable car, which is more linear in its response to steering inputs. To date, such systems have required costly hydraulic or electromechanical control systems and as a result, are banned in all but the highest echelons of motorsport [5]. This paper investigates the potential of a passive torque vectoring differential strategy which apportions torque depending on lateral acceleration levels. The resulting objective is to decouple the torque transfer direction from the driven wheel speed difference and redistribute torque to the driven wheel with most grip. Differential models for a passive LSD (PLSD), active and passive TVDs (ATVD, PTVD) are presented, then combined with a 8 Degree Of Freedom (DOF) vehicle model to evaluate their influence on handling behaviour. The models are constructed in the Matlab/Simulink environment and parameterised around a RWD saloon racing vehicle. The PLSD was shown to reduce the yaw rate response of a vehicle during turn in and was more uncontrollable at the limit due to driven wheel tyre saturation. The ATVD control

F2012-C04-002

A. Tremlett (✉) · F. Assadian · D. Purdy · N. Vaughan
Cranfield University, Cranfield, Bedfordshire, UK
e-mail: a.j.tremlett@cranfield.ac.uk

A. Tremlett · A. Moore · M. Halley
Xtrac Limited, Berkshire, Thatcham, UK

strategy was able to modify vehicle handling balance, both improving its linearity and extending the point at which control could be maintained. The PTVD was shown to increase vehicle agility by improving initial yaw rate response and extend the linear handling region. However, careful consideration must be given to the magnitude of the torque transfer at higher lateral accelerations, since lateral and longitudinal tyre forces are strongly coupled in this region. For performance applications, this paper brings to light the need to optimise passive differential torque transfer around tyre force characteristics.

Keywords Vehicle dynamics • Limited slip differential • Torque vectoring differential • Yaw moment control

Nomenclature

A_p	empirical differential friction factor
F_p	differential preload force (N)
$N_{l,r}$	left and right ATVD clutch speed ratios
R_r	mean contact radius between ramp and crosspin (m)
$R_{o,i}$	outer and inner radius of clutch disc (m)
r_{ref}, r	reference and actual yaw rate (rad/s)
r_e	Yaw rate error (rad/s)
T_d	differential input torque (Nm)
$T_{dd,dc}$	drive and coast critical input torque (Nm)
$T_{cl,cr}$	left and right ATVD clutch torques (Nm)
$T_{p,atvd,ptvd}$	plate, ATVD and PTVD differential locking torque (Nm)
T_{max}	normalisation locking torque (Nm)
V_{ref}, v	V reference and actual lateral velocity (m/s)
V_e	lateral velocity error (m/s)
Z_f	number of friction faces
Z_i	No. of teeth on ATVD gear train, where $i = 1-6$
$\alpha_{f,r}$	average front/rear slip angle (deg)
θ_r	drive/coast ramp angle (degrees)
$\lambda_{v,r}$	lateral velocity and yaw rate weighting factor
λ_T	torque transfer scaling factor
μ_p	clutch plate surface friction coefficient
μ_r	ramp to crosspin friction coefficient

1 Introduction

LSD have traditionally been shown to offer significant improvements in traction and vehicle stability [1, 2]. These benefits are achieved through the transfer of

torque from the faster to slower driving wheel. In the motorsport environment however, during high lateral accelerations, the grip level of the inner driving wheel can be compromised and force the LSD torque bias to switch directions. This typically means that initial corner entry understeer, snaps to mid-corner oversteer as the inner wheel saturates. TVD offer greater flexibility in this respect, by utilising an active control system to bias torque in either direction, as required. This provides a system which can both improve vehicle stability and agility [3, 4]. The result is a more predictable car, which is more linear in its response to steering inputs. To date, such systems have required costly hydraulic or electromechanical control systems and as a result, are banned in all but the highest echelons of motorsport and are only used in the high-end automotive sector. Racing regulations dictate that this torque bias is controlled passively and typically through purely mechanical means [5].

This paper aims to investigate the potential of a passive torque vectoring differential strategy which apportions torque depending on lateral acceleration levels. The resulting objective is to distribute torque to the driven wheel with most grip and to decouple the torque transfer direction from the driven wheel speed difference. Differential models for a passive LSD, active and passive TVDs are presented, then combined with an 8DOF vehicle model to evaluate their influence on handling behaviour, during several sub and on-limit manoeuvres.

2 Differential Simulation Models

2.1 Passive Limited Slip Differential

Figure 1a shows an exploded view of an Xtrac [6]. plate type, or ‘Salisbury’ differential [2]. in which a torque bias is generated through the thrust loads of a ramp pair acting against two wet clutch packs. The model has previously been described [7]. and allows the effect of ramp angle (θ_r) the number of friction faces (Z_f), preload force (F_p) and a speed dependant friction surface coefficient (μ_p) to be evaluated. The resulting locking torque (T_p) can be defined for both on-throttle (drive) and off-throttle (coast) conditions. Below critical drive and coast input torques (T_{dd} , T_{dc}), T_p is equal to a preload locking torque (T_{lp}). Above these critical input torques, T_p is governed by a more significant ramp locking torque (T_{lr}). These regions are defined in Eqs. 1 and 2 and typical locking characteristics are shown in Fig. 1b.

$$\text{Ramp Locking Torque } (T_{lr}) = \frac{2}{3} \left[\frac{T_d}{R_r} \left(\frac{\cos \theta_r - \mu_r \sin \theta_r}{\sin \theta_r + \mu_r \cos \theta_r} \right) \right] \mu_p Z_f \left(\frac{R_o^3 - R_i^3}{R_o^2 - R_i^2} \right) \quad (1)$$

$$\text{Preload Locking Torque } (T_{lp}) = \frac{2}{3} \left(\frac{R_o^3 - R_i^3}{R_o^2 - R_i^2} \right) \mu_p F_p Z_f + A_p T_d \quad (2)$$

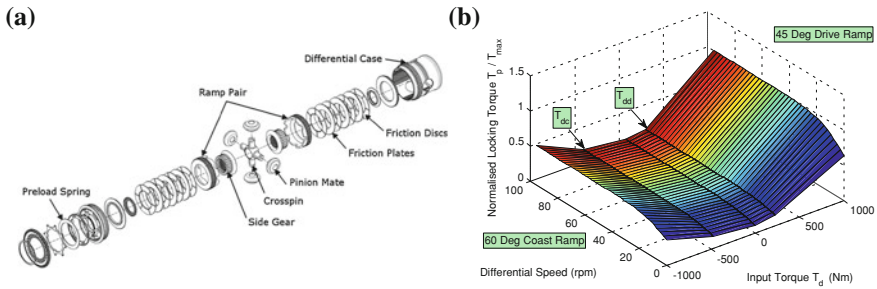


Fig. 1 a Exploded view of an Xtrac [6] plate differential and b typical normalised locking characteristics

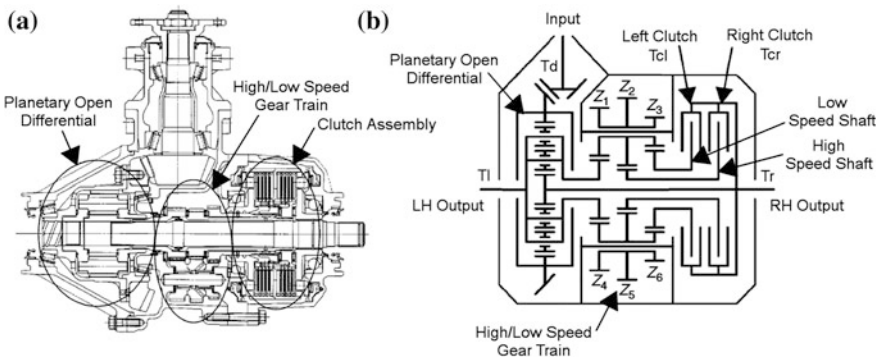


Fig. 2 a SAYC rear torque vectoring differential cross section and b schematic [9]

2.2 Active Torque Vectoring Differential

Although PLSDs offer significant improvements in overall traction and cornering ability, these devices can only ever be used for generating stabilising (understeer) vehicle moments, up to the limit of traction at one wheel. To increase the flexibility of the unit, active control can modulate the magnitude of the bias torque. Critically however, control over the direction of torque transfer allows both understeer and oversteer moments to be generated, improving vehicle stability and agility. Several methods have been used to establish this means of torque bias control [3, 4, 8]. Most rely on high speed gear trains and selective operation of clutches to provide a left or right hand torque bias. The model used in this paper is based on the ‘Super Active Yaw Control’ (SAYC) system described by Sawase [9] and is depicted in Fig. 2.

At its heart, a conventional spur (planetary) open differential provides a means of wheel speed independence. An additional gear train is then used to divert a

proportion of the input torque (T_d) to speed up and slow down a set of shafts relative to the main differential housing. Selective activation of two clutches then gives a torque transfer in the desired direction. When the left hand clutch is engaged, the torque transmitted to left (T_l) and right (T_r) wheels is defined by:

$$T_l = \frac{T_d}{2} + N_l T_{cl} \quad (3)$$

$$T_r = \frac{T_d}{2} - T_{cl} \quad (4)$$

$$T_l - T_r = T_{avd} = T_{cl}(N_l + 1) \quad (5)$$

And similarly when the right hand clutch is engaged:

$$T_l = \frac{T_d}{2} - N_r T_{cr} \quad (6)$$

$$T_r = \frac{T_d}{2} + T_{cr} \quad (7)$$

$$T_r - T_l = T_{avd} = T_{cr}(N_r + 1) \quad (8)$$

where $N_l = Z_1 Z_6 / 2 Z_3 Z_4$, $N_r = Z_1 Z_5 / 2 Z_2 Z_4$ and $Z_{1,6}$ represents the number of teeth on each of the gears in the high/low speed gear train shown in Fig. 2b. The magnitude and direction of the torque transfer is controlled by a yaw moment controller described in Sect. 3.1.

2.3 Passive Torque Vectoring Differential

In order to evaluate the potential of a new type of device that provides a means of passive torque vectoring, the differential bias torque is now assumed to be a function of lateral acceleration only, with no means of active control. It is thought that rather than relying on traditional passive torque sensing methods (as in the PLSD case), lateral acceleration will more accurately reflect the grip levels at each tyre. In this paper, only the predicted performance of such a system is investigated and as a result, the mechanical system required to achieve such characteristics is outside the scope of this paper. Two methods are proposed and depicted in Fig. 3. In the first (PTVD—linear), locking torque (T_{ptvd}) linearly increases up to a saturation value. This saturation value is critical, since at high lateral accelerations the coupling between longitudinal and lateral tyre forces is significant. Consequently, excessive transfer torque is likely to saturate the driving axle. The second method, (PTVD non-linear), attempts to account for this tyre force coupling by using a non-linear profile which saturates as lateral tyre forces would. It seems appropriate then, that this profile is based on the well-established Magic Formula curve fit described by Pacejka [10]. The differential transfer torque is delivered to

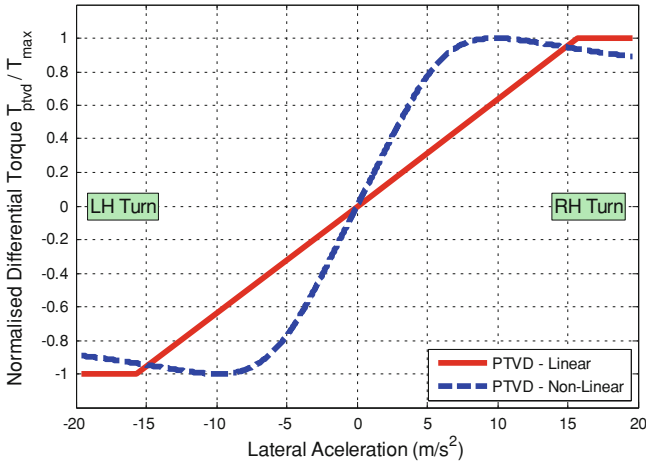


Fig. 3 Passive TVD locking torque characteristics based on lateral acceleration

the outside wheel during cornering, such that for a right hand corner, the torque transfer is positive.

3 Vehicle Model

To evaluate the influence of PLSD, Active Torque Vectoring Differential (ATVD) and PTVDs on vehicle handling, an 8 degree of freedom model constructed in the Matlab/Simulink environment was used. The equations of motion for the system describe longitudinal, lateral, yaw and roll vehicle motions in addition to four wheel rotations [11]. This is combined with a non-linear Pacejka tyre model [10] and vehicle parameters from a RWD saloon racing vehicle. Steering inputs are generated by open loop pre-defined manoeuvres (step or ramp steer) or closed loop, through the use of a preview steer driver model [12]. Longitudinal velocity is controlled with a Proportional Integral (PI) controlled throttle parameter, used in conjunction with saturation functions generated from each tyre. This effectively limits the control input under conditions in which the tyres have exceeded their optimum longitudinal slip ratio (i.e. slip at which peak longitudinal force is generated). As a result, the steer and throttle controls give a degree of driver realism when the vehicle limit has been reached. The model structure is shown in Fig. 4. The reader should note that the yaw moment controller shown is only used in the ATVD case. The differential models were included as look-up tables and considered perfect actuators, which did not account for any dynamic clutch engagement effects.

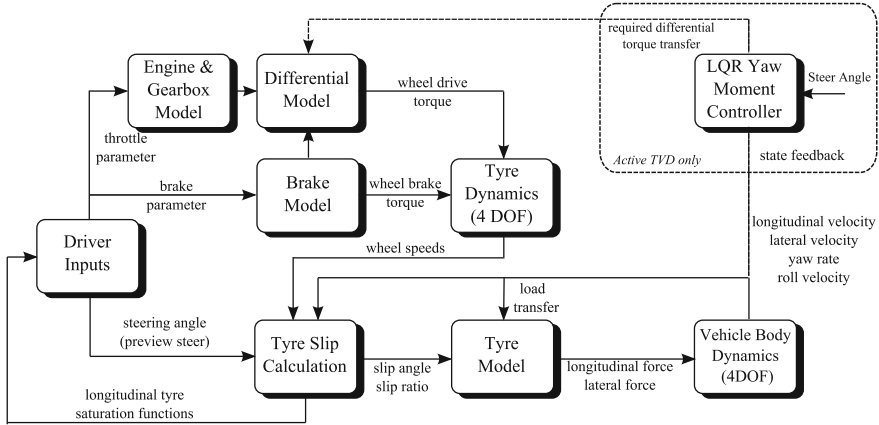


Fig. 4 8DOF vehicle model structure

3.1 ATVD Yaw Moment Control Design

Linear optimal control theory provided the basis for yaw moment controller design, the aim of which was to direct both the direction and magnitude of the ATVD torque transfer. This helped to establish the potential of a TVD device, in extending controllability and linearity up to the vehicle limit. The controller was based around a Linear Quadratic Regulator (LQR) [13, 14], used to minimise the error between side slip velocity (V) and yaw rate (r) of the 8DOF non-linear model and that of a 2DOF linear reference model (V_{ref}, r_{ref}). The resulting cost function (Eq. 9) seeks to minimise both the error in vehicle states (V_e, r_e) and the control input, which in this case, is the magnitude of differential torque bias required (T_{atvd}):

$$J = \lambda_v \int (V_{ref} - V)^2 dt + \lambda_r \int (r_{ref} - r)^2 dt + \int \frac{1}{\lambda_T^2} T_{atvd}^2 dt \quad (9)$$

λ_v and λ_r are the appropriate weightings of side slip and yaw rate error cost and λ_T is a scaling factor to limit the input to a suitable magnitude. A dynamic saturation is also applied to the control input and the 2DOF reference yaw rate. This is to ensure that the target yaw rate is realistic and that the torque supplied to each driving wheel will not saturate the tyre when their adhesion limit has been reached (Fig. 5).

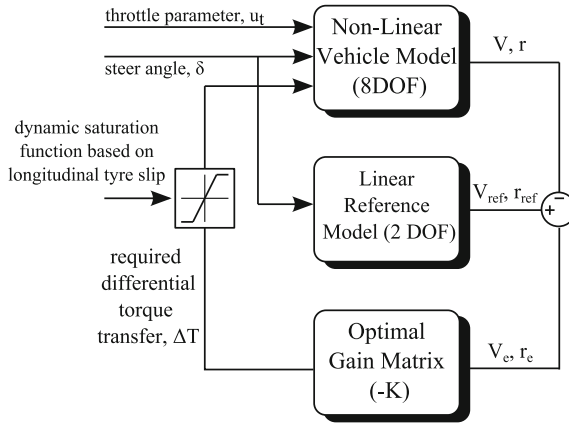


Fig. 5 LQR yaw moment control structure

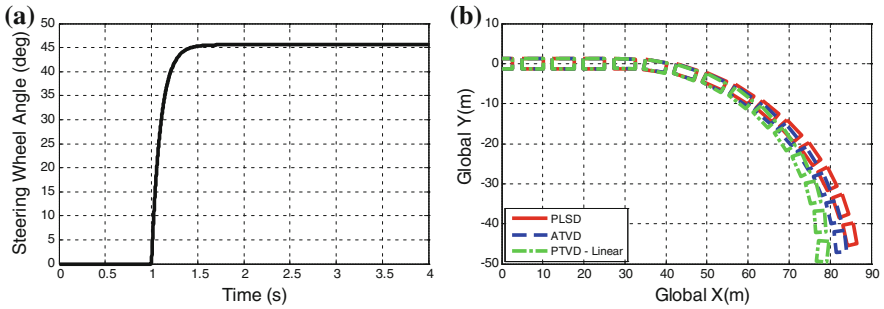


Fig. 6 a Step steering input with first order lag function b vehicle path for PLSD, ATVD and PTVD differentials

4 Simulation Results

4.1 Step Steer Response

To evaluate the influence of each differential during the initial turn in phase of a corner, a step steer test was conducted at a constant speed of 25 m/s. To avoid unrealistically high steering rates, a first order lag function with a time constant of 0.1 s was applied to a steering wheel input of 45° (see Fig. 6a). Figure 6b shows the resulting vehicle path for PLSD, ATVD and PTVD differentials.

As might be expected, the PLSD demonstrates the greatest path radius in relation to the TVD types. This is confirmed in Fig. 7a in which the PLSD generates the lowest yaw rate, whilst the ATVD is shown to follow the reference yaw rate set by the 2DOF reference model. The PTVD generates the highest yaw rate,

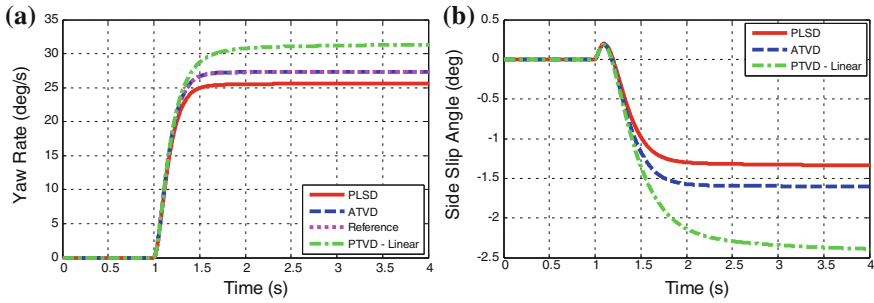


Fig. 7 a Yaw rate and b side slip angle (right) responses

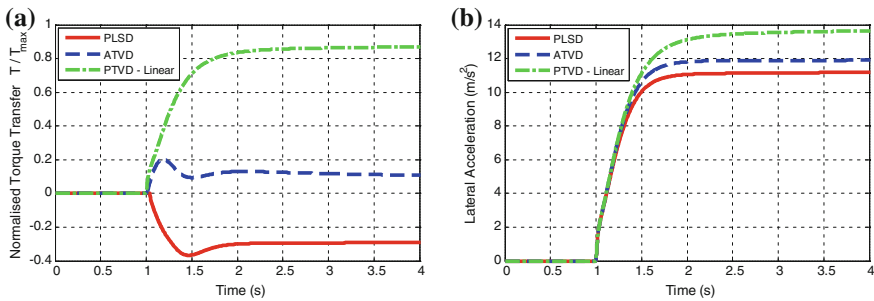


Fig. 8 a Normalised differential torque transfer and b lateral acceleration

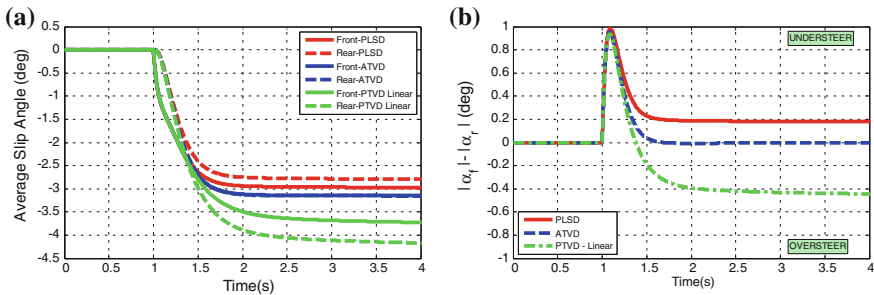


Fig. 9 a Average lateral axle slip angles and b absolute lateral slip angle difference

but also encourages the greatest side slip angles, approaching -2.5° by the end of the manoeuvre (see Fig. 7b). This behaviour can be explained by the torque transfer characteristics of each device. In the PLSD case, the cornering limit of the vehicle has not been reached which has avoided the onset of inside wheel saturation. The resulting torque transfer is therefore negative (see Fig. 8a) giving an under steering yaw moment throughout the manoeuvre. Since the base vehicle is

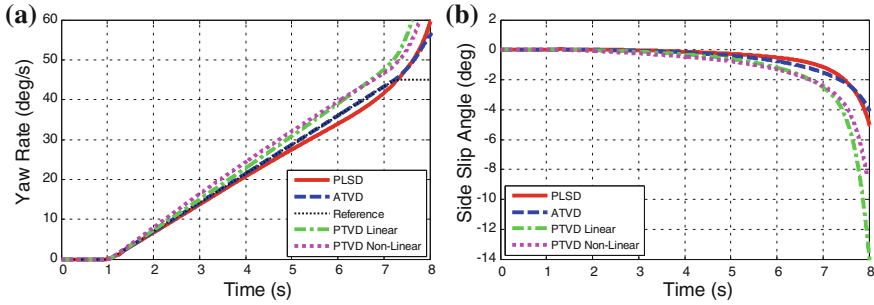


Fig. 10 a Yaw rate and b side slip angle (*right*) responses

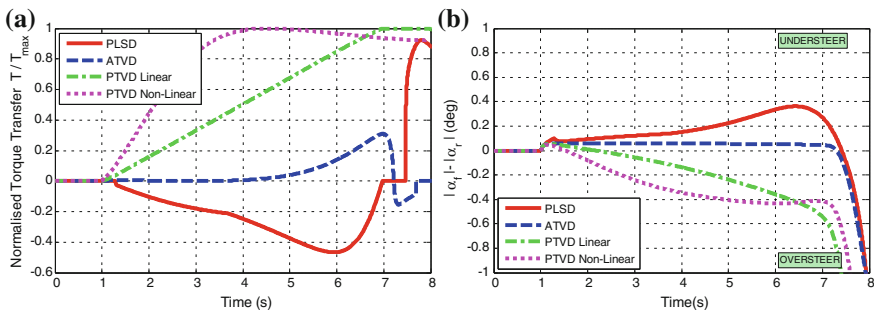


Fig. 11 a Normalised differential torque transfer and b absolute lateral slip angle difference

very close to neutral steer (at this lateral acceleration level), the ATVD only applies a small positive (oversteer) torque transfer to maintain handling neutrality. Conversely, since the torque transfer of the PTVD relies on lateral acceleration only, a much larger oversteering moment is applied. This is confirmed by evaluating the average front and rear slip angles of the vehicle (see Fig. 9a). The difference between the two gives a measure of overall handling balance and is shown in Fig. 9b. The PLSD is shown to understeer, whilst the ATVD is very close to remaining neutral, with the PTVD promoting oversteer behaviour.

4.2 Ramp Steer Response

To demonstrate the differential influence over a range of lateral accelerations, a constant speed ramp steer test was conducted. The vehicle velocity was held at 20 m/s whilst the steering wheel angle was increased at a rate of 15°/s, starting at 1 s. Fig. 10a shows the resulting yaw rates which behave in a similar manner to the step steer test (Sect. 4.1) until 7 s. At this point the reference yaw rate of the ATVD saturates, but the device is no longer able to apply a corrective understeer

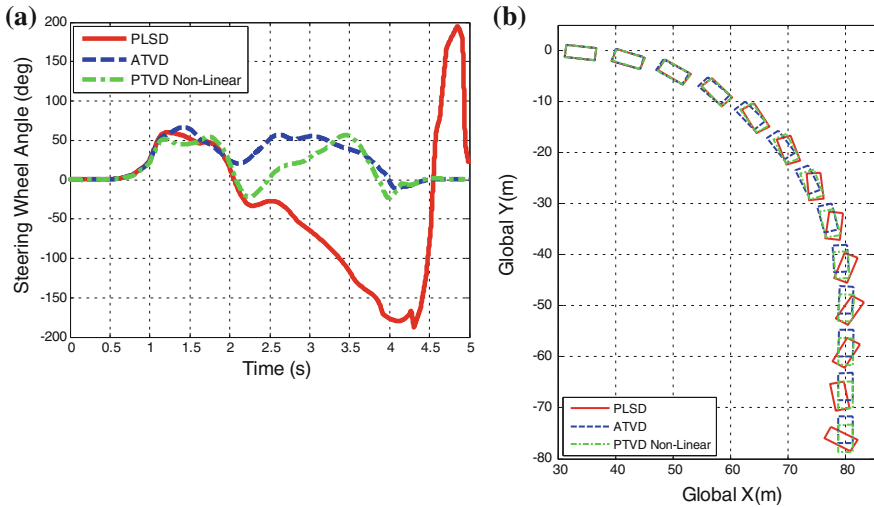


Fig. 12 a Steering wheel angle and b vehicle path through 50 m radius corner

moment to maintain handling neutrality. This is due to inner wheel saturation and reinforces the argument that TVD devices in general are better at generating oversteer moments than understeer [15]. At this point, all devices encourage side slip angles to increase dramatically (see Fig. 10b) which can be interpreted as a loss of control of the back end as the rear axle saturates.

The torque transfer of the PLSD is shown to be negative at low lateral accelerations (see Fig. 11a) and after a period of locking at approximately 7 s switches sign to positive on account of inner wheel tyre saturation. This is shown to saturate the rear axle sooner than the ATVD, which remains linear up to the limit (see Fig. 11b). The PTVD with linear locking characteristics is actually shown to make the car more unstable at higher lateral accelerations, as indicated by the higher negative gradient seen in Fig. 11b. The PTVD with non-linear locking characteristics (which more closely accounts for tyre saturation effects) is shown to remain much more linear up to the vehicle limit, which again delays the onset of rear axle saturation when compared to the PLSD.

4.3 Corner Simulation

To assess the practical implications of these changes in handling balance, a 50 m radius corner test is simulated at a constant velocity of 28.0 m/s. The steady state lateral acceleration at this speed is 15.6 m/s² (1.6 g) and is designed to test driver workload, right at the edge of the performance envelope. A more representative degree of driver control is introduced with a preview steer driver model, which uses a pre-defined path to generate steering corrections based on vehicle position

and yaw angle [12]. Figure 12 shows the resulting vehicle path and steering required to maintain the reference path. All the steering traces (see Fig. 12a) show that opposite steering lock is required after 2 s to correct the vehicle's excessive side slip. However, as the PLSD has started to saturate the rear axle sooner than either of the TVDs, the steering angle required is dramatically increased, and starts to become oscillatory after 4 s. An interpretation of this behaviour is that both the TVDs reduce driver workload and allow the vehicle to be more controllable up to its cornering limit.

5 Conclusions

This paper has described three types of differential model. The first PLSD model is only able to bias torque from the faster to slower driven wheel, and hence can only provide stabilising vehicle yaw moments up to the tyre saturation limit. A conventional active TVD model is then defined and shown to be more effective at altering vehicle dynamics. A novel passive TVD control strategy is then proposed as a potentially more cost effective solution for motorsport.

The simulation results of several sub and on-limit manoeuvres showed that:

- A conventional PLSD will typically reduce the yaw rate response of a vehicle. Under conditions which the differential is able to lock the axle, the vehicle may be more uncontrollable at the limit due to driven wheel tyre saturation.
- The ATVD control strategy was shown to be able to modify a vehicle's handling balance, both improving its linearity and extending the point at which control can be maintained.
- The PTVD with a non-linear torque bias regime was shown to increase vehicle agility by improving initial yaw rate response and extended the linear handling region. Moreover, this demonstrates that a differential which more accurately reflects tyre saturation characteristics will help provide a more predictable vehicle which is more controllable up to its cornering limit.

References

1. Kopf P, Escher M, Gazyakan U, Oberhauser M (1990) Optimization of traction and driving stability in 2-wheel drive cars by means of electro-hydraulic limited-slip differentials. SAE paper 905108
2. Milliken WF, Milliken DL (1995) Race car vehicle dynamics. SAE
3. Shibahata Y, Kuriki N, Kitamura K, Honda K, Wada K, Kajiwara H, Nori A, Kuwahara K, Okuma S (1997) Development of left-right torque distribution system. HONDA R&D Tech Rev 9:166–180

4. Mohan SK, Sharma A, Mizon R, Burns T (2005) Torque vectoring systems: architecture, stability performance and efficiency considerations. In: Proceedings of the 6th all-wheel drive congress, pp 166–180, Graz, Austria
5. FIA technical regulations. <http://www.fia.com/sport/regulations>. Accessed 9 July 2012
6. Xtrac, Xtrac Limited, Kennet Park, Gables Way, Thatcham, Berkshire, RG19 4ZA
7. Tremlett A, Purdy D, Vaughan N, Assadian F, Moore A, Halley M (2012) The influence of torque and speed sensitive differential characteristics in a FWD vehicle during on limit manoeuvres. FISITA world automotive congress
8. Piyabongkarn D, Lew JY, Rajamani R, Grogg JA (2010) Active driveline torque management systems. *IEEE Control Syst Mag* 30(4):86–102
9. Ushiroda Y, Sawase K, Takahashi N, Suzuki K, Manabe K (2003) Development of super AYC. *Mitsubishi Motors Tech Rev* 15:73–76
10. Pacejka HB, Besselink IJM (1997) Magic formula tyre model with transient properties. *Veh Syst Dyn Suppl* 27:234–249
11. Genta G (1997) Motor vehicle dynamics: modeling and simulation (series on advances in mathematics for applied sciences—vol 43), World Scientific Publishing Co. Pte. Ltd
12. Sharp RS, Casanova D, Symonds P (2000) Mathematical model for driver steering control, with design, tuning and performance results. *Veh Syst Dyn* 33(5):289–326
13. Komatsu A, Gordon TJ, Best MC (2000) 4WS Control of handling dynamics using a linear optimal reference model. In: Proceedings of AVEC
14. Friedland B (2005) Control system design. An introduction to state-space methods. McGraw-Hill, New York
15. Hancock M (2006) Vehicle handling control using active differentials. Doctoral thesis, University of Loughborough

Modeling and Simulation of a New Type Hydraulic System on CVT

Yanhui Lu, Mingshu Liu and Yang Liu

Abstract CVT (Continuously Variable Transmission) is the ideal transmission for vehicle, for it can provide better fuel economy than other transmissions by enabling the engine to run at its most efficient revolutions area for a range of vehicle speeds. And hydraulic system is the core of CVT. This chapter presents the new design hydraulic system of CVT which focus on its efficiency. According to the CVT test carried out by Bosch Group, the pump takes the largest part in CVT's fuel consumption. In hydraulic system of traditional CVT, pump is driven directly by engine. So its flow rate is proportional to the engine speed. We need to consider the extreme working conditions when we develop the requirement to its flow rate/power. And to satisfy the extreme conditions means to overflow on the other conditions and that costs much loss. Therefore, in traditional powertrain, the fuel consumption of CVT takes 8 % of the vehicle fuel consumption. The primary goal of this chapter is to improve the efficiency of CVT to further reduce its fuel consumption by developing the new hydraulic system. We designed a new hydraulic system for CVT, it separates the control oil and the lubricating oil. According to the vehicle performance requirement, we determined the parameters of hydraulic system. In order to verify the efficiency of this hydraulic system also to optimize its parameters, a simulation model for hydraulic system, CVT and vehicle was built up with MATLAB and SIMULINK environment. Simulations were performed under typical driving conditions such as start up, instant acceleration and vehicle run cycle, and the pressure, flux characteristics of the hydraulic system together with the whole vehicle fuel consumption were obtained. The results indicated that compared with the traditional

F2012-C04-009

Y. Lu (✉) · M. Liu · Y. Liu
State Key Laboratory of Automotive Simulation and Control, Jilin University, Changchun,
China
e-mail: lyh.jlu@gmail.com

hydraulic system, the new one has more efficiency and therefore can lower the fuel consumption of the vehicle. Through reducing the clamping force, the efficiency of CVT can also be improved. However, due to the limitation of time, the topic is not included in this research. Also, we didn't develop the real hydraulic module to verify the system we designed. And in the future, we will develop the hydraulic module and apply it on CVT to test its performance on CVT test rig. All in all, this chapter introduced a new hydraulic system which separates the control oil and the lubricating oil. And through simulation, the efficiency of the new hydraulic system was proved. This research has important value for improving the efficiency of CVT.

Keywords CVT · Hydraulic control system · Simulation · Fuel consumption · Efficiency

1 Introduction

Metal belt continuously variable transmissions (CVTs) have been applied in the vehicles for many years. As we all know, CVTs can offer the potential for an improvement in fuel economy. However, the efficiency of CVTs is lower than that of mechanical transmissions. This somehow tends to negate the fuel economy benefits of CVTs. So how to improve the efficiency of CVTs has always been the subject of the research. There are a number of authors have done the research on the loss theory of metal belt CVT, such as Micklem [1, 2], Fujiii [3, 4], Akehurst [5–7].

According to the research of Bosch Group, the main part of loss on CVT is hydraulic system. So in this chapter, we design a new type of hydraulic system for CVTs. In the following, we'll introduce the model of designed hydraulic system and the simulation result.

2 Design of Double Circuit Hydraulic System

In the currently used single-circuit hydraulic control system, generally based on the need for maximum clamping force, which is the highest pressure of the ratio change mechanism to determine the rated working pressure of the pump. Clearly, the pressure level compared to the clutch control and lubrication cooling pressure level is much higher. In determining the displacement of the pump, the started working conditions and low speed conditions need to be considered, the oil flow for the clutch control and lubricating and cooling is greater than the flow for ratio change mechanism. When vehicles are in the steady-state driving, the engines' speed is higher, and the hydraulic oil flow is sufficient to meet the requirements of the entire system. Thus, there is a shortcoming when the entire system using one pump to supply the oil: to meet the control requirements of the ratio change mechanism, the pump supplies the high pressure oil to the clutch control and lubrication, cooling circuit, resulting in the loss of energy.

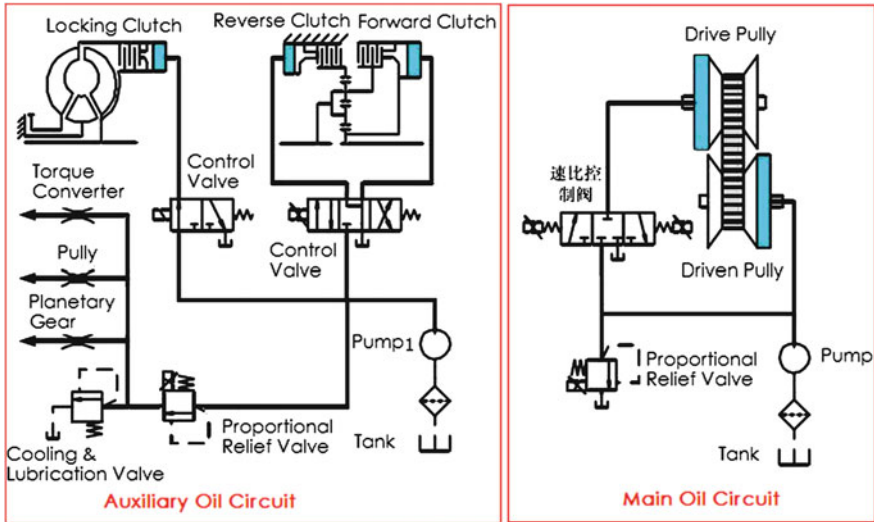


Fig. 1 Double circuit hydraulic system

Based on the above analysis, we design a double-circuit hydraulic system: the main loop to control the ratio change mechanism, the auxiliary circuit control lubrication and cooling system, different pumps are adopted for the two circuits according to their oil flow and pressure requirement. So what we have done is to improve the accordance of the need and supplement, to reduce system power consumption, and improve the efficiency of the transmission. The design of the hydraulic system is shown in Fig. 1.

2.1 Design of Main Oil Circuit

The speed change mechanism is the core component of the continuously variable transmission, hydraulic control system through the pressure relief valve and the speed ratio valve to control the clamping force and the speed ratio. The main parameters of this circuit, contain the maximum working pressure of the clamping force control valve, the speed ratio control valve flow as well as the main pump rated pressure and displacement.

2.1.1 Maximum Working Pressure of the Clamping Force Valve

The maximum working pressure of the clamping force valve determines the maximum clamping force on the metal band, and also determines the maximum torque of the ratio change mechanism can be transferred.

Analyze the forces on the metal belt and pulley of the ratio change mechanism, we can see that once the transferred torque is given, the driven wheel hydraulic cylinder control pressure can be calculated as follows:

$$P_s = \frac{\beta T_{in} \cos \alpha}{2\mu R_p A_s} \quad (1)$$

Where:

- T_{in} Input torque of transmission,
- β Reserve coefficient,
- α Pulley cone angle,
- μ Coefficient of friction,
- R_p Ideal radius of drive pulley,
- A_s Cross-sectional area of Driving pulley Hydraulic cylinder.

2.1.2 Maximum Flow of Ratio Control Valve

The speed ratio control is one of the main task of the hydraulic control system. When determine the maximum flow requirements of speed ratio control valve, we consider two cases: when the speed ratio increases, the active cylinder hydraulic oil is discharged through the speed ratio valve; when speed ratio is reduced, high-pressure pump pumps oil needs after speed ratio valve quickly to the driving cylinder.

The speed ratio increases, consider the steady-state vehicles travelling on hard acceleration and high speed vehicle deceleration. In order to obtain a large enough reserve power to improve the acceleration performance of the car, the need to improve the speed of the engine steady-state vehicles travelling on hard acceleration, so that the output power of the engine increases. This process, the hydraulic cylinder driving pulley speed ratio valve fast unloading, so that the transmission speed ratio increases rapidly. According to the axial displacement of the application of the formula (Eq. 2) to determine the flow:

$$Q_{p1} = \frac{A_p \cdot l_{p1}}{T_{p1}} \quad (2)$$

Condition of vehicle deceleration speed decreased rapidly, the speed of the driven pulley decrease rapidly. The statistics show that the vehicle in normal driving circumstances, the vehicle maximum braking strength from 100 km/h speed to stop time can be reduced to about 3 s. This process, the speed ratio from the minimum to the maximum, the outflow of driving pulley is:

$$Q_{p2} = \frac{A_p \cdot l_{p2}}{T_{p2}} \quad (3)$$

The speed ratio decreases, mainly considering the vehicle at full throttle start working condition. The vehicle is first started, in order to obtain optimum power,

the CVT speed ratio should be at the maximum. In order to make the engine speed always in ideal conditions, the ratio is reduced accordingly. For the modern vehicles, one hundred kilometers acceleration time is generally between 7–12 s, during this process, the requirements of speed ratio from the maximum to reduce to a minimum. The maximum flow rate flow into of the driving pulley hydraulic cylinder by the speed ratio control valve as follows:

$$Q_{p3} = \frac{A_p \cdot l_{p3}}{T_{p3}} \quad (4)$$

Based on the above analysis and calculation, select the formula (Eqs. 2, 3, and 4) determine the speed ratio control valve's maximum flow.

2.1.3 Design of Main Pump

There are three main performance parameters of the hydraulic pump, namely: the rated pressure, displacement, volumetric efficiency. Volumetric efficiency, the quality of the pump have a certain influence on the efficiency of the entire hydraulic system. The main contents of this chapter is the oil circuit design of the hydraulic system efficiency, this chapter does not consider the volumetric efficiency of the pump.

Among them, the rated pressure means the maximum pressure in the case of continuous use, can be achieved. This requires that the actual working pressure of the hydraulic pump can not exceed the rated pressure. In the main circuit, the pump speed change mechanism to achieve hydraulic control power source. Its mission is to, where necessary, to the driving and driven pulleys hydraulic cylinder oil, in order to achieve the purpose of changing the speed ratio. Furthermore, we need to provide enough pressure to adapt to the changing needs of the clamping force. Therefore, based on the maximum pressure of the hydraulic system needed to select the hydraulic pump rated pressure.

According to the system under various conditions, the pump provides a flow of demand, can determine the maximum flow of hydraulic pump. The engine speed should also be considered when determine the displacement of the pump in all operating conditions. During emergency braking process, the pump speed as the engine speed decreases rapidly. Obviously, emergency braking condition is higher on the requirements of the pump displacement. In order to ensure the pump to provide adequate flow, we choose the minimum speed of the engine as pump speed. According to the hydraulic pump should be provided emergency braking process flow to determine the displacement of the main pump.

2.2 Design of Auxiliary Oil Circuit

Auxiliary circuit using a separate pump for fuel supply, the main features include clutch control, as well as the major components of the cooling and lubrication. Series before cooling lubricating oil to a proportional relief valve, the relief

pressure is greater pressure for the clutch control system for cooling and lubrication systems. Cooling and lubricating valves as a back pressure valve to form a baseline hydraulic, to meet the demand for cooling and lubrication and torque converter.

2.2.1 Main Parameters of the Clutch Control Circuit

The relationship between the pressure of the clutch hydraulic cylinder and the torque is shown as follows:

$$P = \frac{12\beta TA_c}{\pi f D^3 (1 - c^3) A} \quad (5)$$

Where

- P Clutch hydraulic cylinder pressure,
- β Reserve coefficient of clutch,
- T Torque,
- A_c Force Area of clutch Friction plate,
- f Static friction coefficient,
- D The outer diameter of the friction plate,
- c inner and outer diameter ratio of Friction plate
- A Clutch piston area

The engage speed of clutch can influence the start performance of vehicles. Auxiliary oil pump need to provide a large enough flow to meet the needs of the clutch. The clutch flow can be calculated as follows:

$$Q_c = \frac{xA}{t} \quad (6)$$

Where,

- Q_c Clutch target flow,
- x Friction plate stroke,
- t Time

2.2.2 Design of Auxiliary Pump

The displacement of the auxiliary oil pump is mainly to consider the clutch flow requirements. The maximum pressure in the auxiliary circuit is based on reverse gear clutch goal of working pressure to determine.

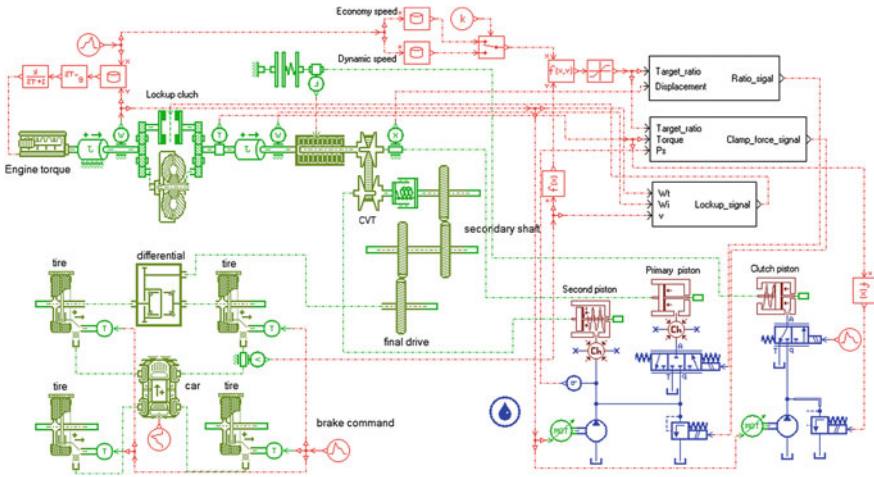
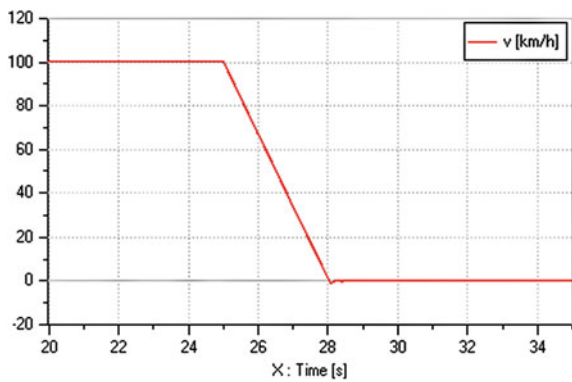


Fig. 2 CVT vehicle model

Table 1 Parameters of the vehicle

Vehicle mass (kg)	1540	Reduction ratio	5.247
Wheels radius (m)	0.29	Rolling resistance coefficient	0.018
Front area (m^2)	1.7	Moment of inertia ($km \cdot m^2$)	3.64

Fig. 3 Vehicle speed change



3 Modeling and Performance Verification of the Double Circuit Hydraulic System

To verify the designed Continuously Variable Transmission dual-circuit hydraulic system, a Matlab Simulink-AMESim model was established, as shown in Fig. 2. Main parameters used in the Model are shown in Table 1.

Fig. 4 Ratio change

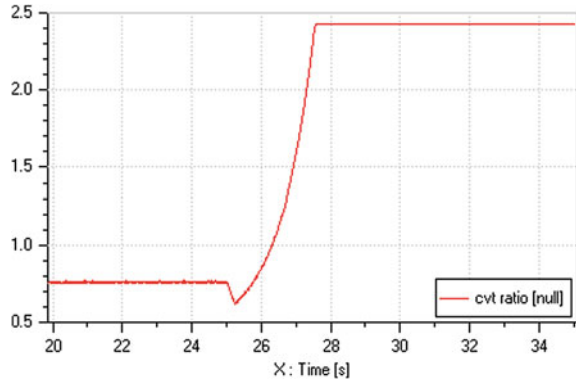


Fig. 5 Clutch engage pressure

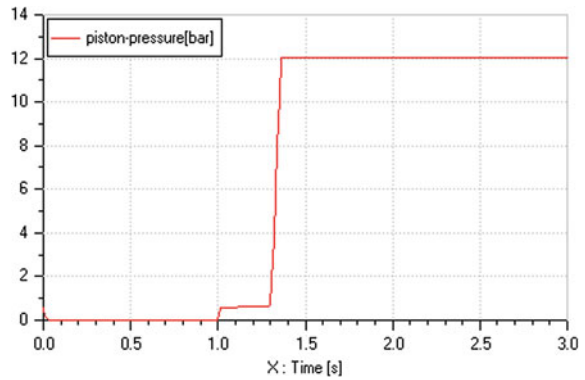
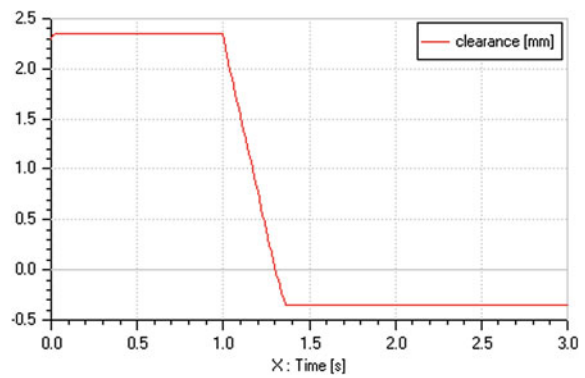


Fig. 6 Clutch clearance



3.1 System Performance Verification

Before the simulation and analysis of the efficiency of the system, first select the specific conditions to verify the control effect of the main parameters affecting the system in order to verify the correctness of the system.

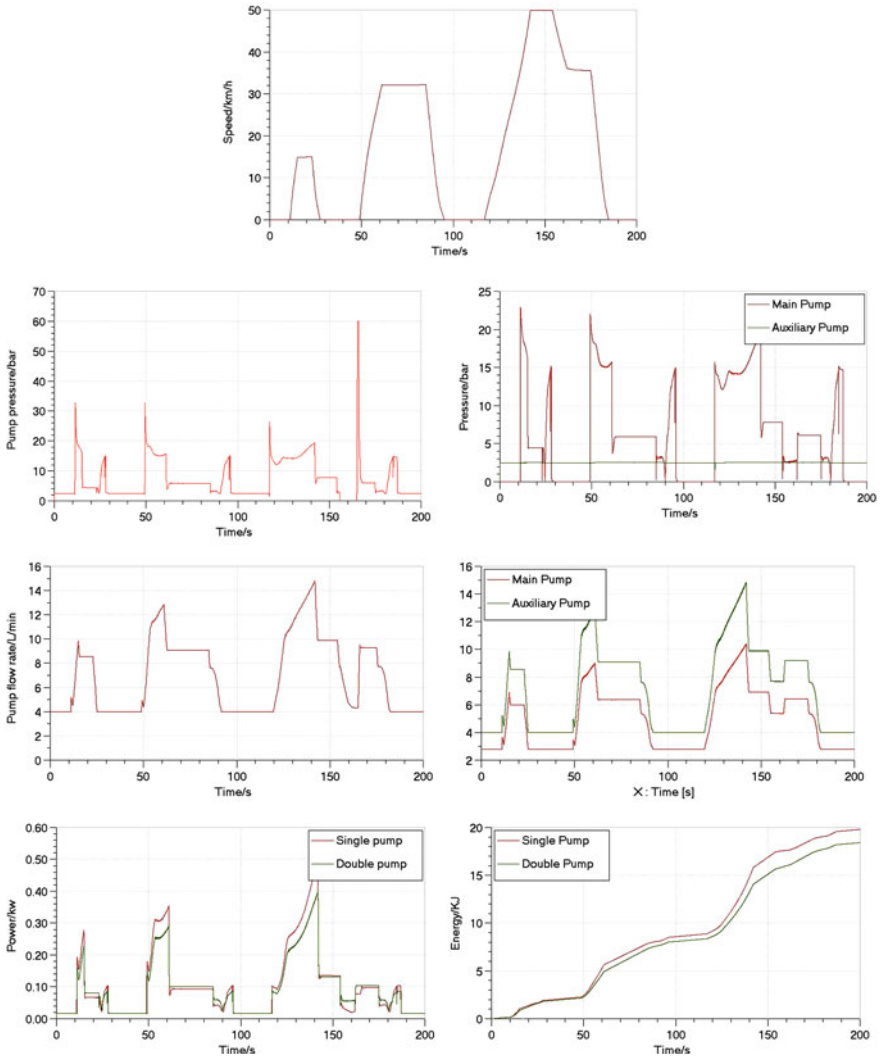


Fig. 7 Comparison between single circuit and double circuit hydraulic system

3.1.1 Displacement of the Main Pump

To determine the pump displacement, thinking about vehicle deceleration from 100 km/h to stop. The pump should provide sufficient flow during this process. It can be seen from Figs. 3 and 4. When the emergency brake happens, vehicle speed decreases rapidly from 100 km/h to 0 in 3 s. And the ratio increases to maximum in 3 s.

3.1.2 Displacement of the Auxiliary Pump

Selecting the idling condition, the pump speed is 800 r/min. The clutch control valve opens at 1 s, then the oil comes into the clutch cylinder through the valve. It can be seen from Figs. 5 and 6 that clutch free clearance begins to decrease at 1 s and becomes to zero at 1.3 s. This process shows that the displacement of the pump is in accordance with the design requirements.

3.2 ECE Driving Cycle Efficiency Analysis

ECE driving cycle simulation results are shown in Fig. 7.

Throughout the process, when the vehicle is travelling at low speed, less torque of the transmission delivery, the pump output pressure is low. When the vehicle is travelling at constant speed, compared to the double-circuit hydraulic system and the original system, the power loss is almost equal. When vehicle is accelerating, the ratio change mechanism requires high pressure. In the double circuit system, the advantage of small displacement of main oil pump is reflected. It can be seen from the above simulation results in the ECE driving cycle, the power loss of the double-circuit hydraulic system was significantly lower than the original hydraulic system, the relative reduction is 7.07 %.

4 Conclusion

In this chapter, first we analysis the shortcomings of the traditional hydraulic control system, then design a double circuit hydraulic control system. A vehicle model is constructed using Matlab Simulink and AMESim software. Simulation results shows that the designed hydraulic control system can save much more energy compared to the traditional hydraulic control system.

References

1. Micklem JD, Longmore DK, Burrows CR (1994) Modelling of the steel pushing V-belt continuously variable transmission, Proc. Instn Mech. Engrs, Part C: J Mech Eng Sci, 208, pp. 13–27
2. Micklem JD, Longmore DK, Burrows CR (1994) Belt torque losses in a steel V-belt continuously variable trans- mission, Proc. Instn Mech. Engrs, Part D: J Automobile Eng, 208, pp. 91–97
3. Fujii T, Kurokawa T, Kanehara S (1993) A study of a metal V-belt type CVT: Part 2 compression force between metal blocks and ring tension, SAE Trans., 930667
4. Fujii T, Kitagawa T, Kanehara S (1994) A study of a metal pushing V-belt type CVT: Part 3 what forces act on metal blocks?, SAE Trans., 940735

5. Akehurst S, Vaughan ND, Parker DA, Simner D: Modelling of loss mechanisms in a pushing metal V-belt CVT: Part 1 torque losses due to band friction, Proc. InstnMech. Engrs, Part D: J Automobile Eng
6. Akehurst, S., Vaughan, N. D., Parker, D. A. and Simner, D. Modelling of loss mechanisms in a pushing metal V-belt CVT: Part 2: pulley deflection losses and total torque loss validation, Proc. InstnMech. Engrs, Part D: J Automobile Eng
7. Akehurst S, Vaughan ND, Parker DA, Simner D: Modelling of loss mechanisms in a pushing metal V-belt CVT: Part 3: belt slip losses, Proc. InstnMech. Engrs, Part D: J Automobile Eng

Research and Control of Shift Without the Disengagement of the Clutch for Automatic Mechanical Transmission in Hybrid Vehicle

Shaohua Sun, Yulong Lei, Hongbo Liu, Yao Fu and Huabing Zeng

Abstract For the technical requirements of hybrid electric vehicle (HEV) equipped with automatic mechanical transmission (AMT), this chapter proposed an AMT control technology that shifts without the disengagement of the clutch. The technology' system components, working principle, engine and motor' control during shifting process and other key technologies were analyzed. Through dynamically modeling the various stages of shifting process, the shift characteristics and key factors affecting the quality of shifting were known. At the same time, a demo car without the disengagement of the clutch was tested. The results indicated: through controlling of engine, motor and AMT actuator, the HEV' AMT equipped without disengagement clutch can not only ensure smooth shifting, but also can effectively shorten the shift time, improve the shift quality significantly.

Keywords Hybrid vehicle · Automatic mechanical transmission · Shift without disengaging clutch · Shift quality · Coordinated control

F2012-C04-010

S. Sun · H. Liu · Y. Fu · H. Zeng
Jilin University, Changchun, China

Y. Lei (✉)
State Key Laboratory of Automotive Simulation and Control, Jilin University, No. 5988,
Renmin Street, 130022, Changchun, China
e-mail: leiyl@jlu.edu.cn

1 Introduction

Hybrid vehicle with automatic mechanical transmission (AMT) can achieve driving states such as pure electric, pure engine driving and hybrid driving etc. through the mode clutch separation and combination [1]. The shifting process under the engine and motor hybrid driving state is the most complex. So this chapter mainly studies the shift process coordinated control method under hybrid driving state.

In the shifting process of AMT, shifting impacts are mostly caused by the clutch separation and combination. The shift without the disengagement of the clutch technology can not only avoid the impacts of clutch separation and combination, reduce the controlling difficulty, but also shorten the shifting time effectively, improve the shifting quality [2].

For complexity of the hybrid vehicles power assembly, its control strategy for the shifting process has large differences with the traditional automobile [3]. Under hybrid driving state, to realize shift without the disengagement of the clutch needs controlling for the two power sources, the engine and the motor, at the same time, the controlling effects will directly affect the vehicle shift quality and driving performance. Therefore the coordinated control of engine and motor in the hybrid vehicle shift process is the key to achieve shifting without disengaging the clutch, to improve the shift quality and to enhance the driving performance [4].

2 System Composition and Working Principle

This chapter is based on a hybrid vehicle with 6-speed AMT as a development prototype, its forward gears with constant mesh gear transmission and it realizes shifting through the lock ring synchronizer, when reverse, it shifts with straight tooth sliding gear.

2.1 System Composition

Figure 1 is a hybrid vehicle AMT system composition diagram. Power provided by engine and motor, via a 6-speed gearbox, transmission shaft, final drive, eventually transmitted to wheels to drive the vehicle. AMT system consists of gear box, select and shift actuator, clutch, clutch actuator, Transmission Control Unit (TCU) and the corresponding position sensors and other components. TCU and Vehicle Control Unit (VCU), Engine Control Unit (ECU), Motor Control Unit (MCU) and Battery Management System (BMS) realized information interaction through the CAN bus and combined to control vehicle running.

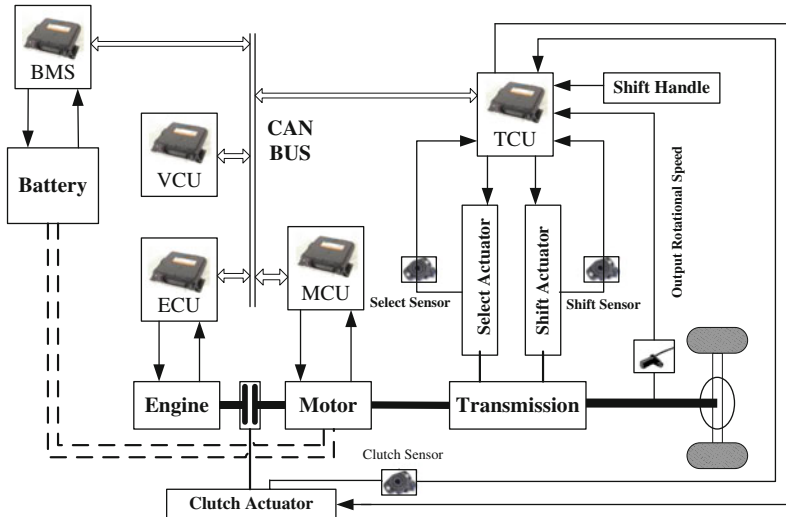


Fig. 1 AMT system composed of hybrid vehicle

Figure 1 shows that engine and motor transmit power through clutch, motor and input shaft of the gear box adopts mechanical connection. This design mainly considered to ensure the vehicle starting with pure electric mode and mode change between pure electric and hybrid.

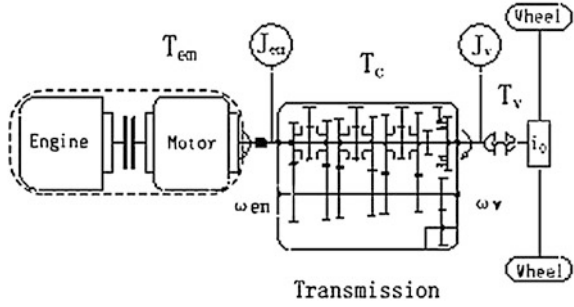
At the start, the clutch in separating condition, vehicle finishes starting through the low-speed torque and the speed regulation ability of motor. When the mode change from pure electric to hybrid, the speed difference between main part and driven part of clutch was eliminated by the closed-loop speed control function of engine, then through the combination of clutch, engine and motor hybrid driving was achieved.

2.2 Working Principle

The key to the shift without the disengagement of the clutch in AMT is to control the two power source include engine and motor co-ordinately in all stages of shifting process [5].

In the shifting process, the AMT control unit TCU communicate with engine control unit ECU and motor control unit MCU through the CAN bus. When shift to neutral, adjust the output torque of the engine and the motor, so that the output torque is close to zero, ensure the shift to neutral process easy and swift; When shift to a new gear, control of the rotational speed of engine and motor to approximate the target speed, at the same time control electric current and the

Fig. 2 Model of power train system for hybrid vehicle



position of the shift motor accurately, to achieve the shift without the disengagement of the clutch.

3 Dynamics Analysis of Shifting

The simplified model of transmission system of hybrid vehicles is as shown in Fig. 2.

Under hybrid drive mode, the relationship of power transmission including the kinematics and dynamics are as follows:

$$\frac{T_C}{i_g} = T_{em} - J_{em} \cdot \dot{\omega}_{em} \tag{1}$$

$$\frac{T_v}{i_o} = T_C - J_v \cdot \dot{\omega}_v \tag{2}$$

Where, T_c for synchronizer torque; T_{em} for engine and motor output torque; T_v for automobile driving resistance torque; J_{em} , J_v respectively for the moment of inertia converted to the transmission input shaft and output shaft ends; ω_{em} , ω_v respectively for transmission input shaft and output shaft speed; i_g , i_o respectively for the gearbox ratio and final drive ratio.

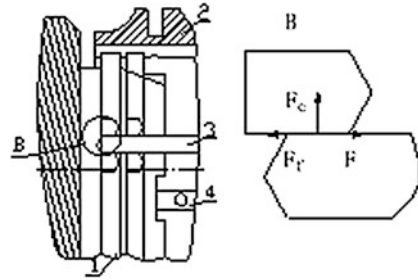
3.1 Picking Neutral Phase

Figure 3 is mesh force model when picking neutral, F for the force of picking neutral; F_c for synchronous transmission force; F_f for friction resistance force between mesh gears; f for friction coefficient between the mesh gears.

If the radius of mesh gear forcing point is for R :

$$F_f = F_C * f \tag{3}$$

Fig. 3 Force model on teeth in shift to neutral phase



$$F_C = T_C / \int dR \tag{4}$$

By formulas (3) and (4) is:

$$F_f = T_{Cf} / \int dR \tag{5}$$

Because resistance force mainly comes from mesh gear friction force when picking neutral, formula (5) shows that in order to achieve the least resistance force when picking neutral, one should try to reduce T_c as much as possible. By formulas (1) and (2) is:

$$T_C = \frac{J_{em} \cdot T_v \cdot \frac{i_g}{i_0} + J_v \cdot T_{em}}{J_{em} \cdot i_g + \frac{J_v}{i_g}} \tag{6}$$

The formula (6) shows, torque of synchronous transmission is the minimum when T_{em} is 0. So one should try to make engine and motor not to output torque.

3.2 Speed Adjustment Phase

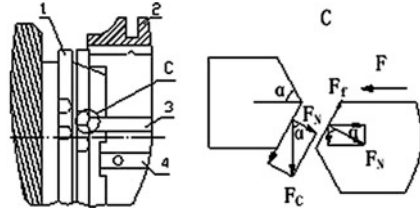
In the shifting process, the vehicle speed is constant, that is to say the transmission output shaft speed is constant. The target speed of the input shaft can be expressed as:

$$\omega_{em} = \omega_v * i_g \tag{7}$$

Where, ω_{em} for the input shaft target speed; ω_v for the output shaft speed when shifting; i_g for new gear ratio.

After calculation of the control unit of AMT (TCU), the input shaft target speed sent to the engine control unit ECU and motor control unit MCU through CAN bus in the process of shifting, then control the speed of engine and motor adjusting to approximate the target speed.

Fig. 4 Force model on teeth in shift gear phase



In order to make shifting smooth and reduce shifting impact, the difference value of engine and motor speed should be in a very small range after adjusting. As smaller the speed difference value is, the smaller impact and the higher the shifting comfort is [6]. Specific speed difference value should be depending on the engine and the motor control precision.

3.3 Engaging Gear Phase

According to position difference, synchronizer can be divided into two states as locking and unlocking in the process of shift gear [7].

Figure 4 is the meshing force model in the synchronization process. F for shift gear force; FN for positive pressure on contact surface; Fc for synchronous transmission force; Ff for friction force between mesh gears; f for the friction coefficient between mesh gears; α for friction cone angle on the contact surface.

$$F_N = F_C \cdot \cos \alpha \tag{8}$$

$$F_f = F_N \cdot f \tag{9}$$

The force analysis model shows that F must satisfy follows so that gear can be picked on successfully:

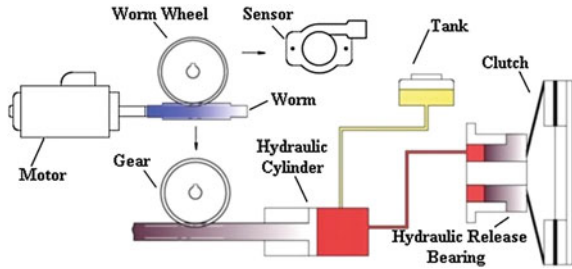
$$F > F_N \sin \alpha + F_f \cos \alpha \tag{10}$$

$$F > \frac{T_C}{\int dR} \cos \alpha \sin \alpha + \frac{T_C}{\int dR} \cos \alpha \cdot f \cdot \cos \alpha \tag{11}$$

At this time, the relations of vehicle power still satisfy formulas (1) and (2). The formula (11) shows that when the initial conditions of vehicle are constant, in order to make shifting light and smooth, torque of synchronous transmission Tc should be as small as possible, which requires the output torque of the engine and motor should be approximate to zero in the phase of engage gear.

After the speed difference becomes to zero, synchronizer changes into the unlocking state. The gear force is much greater than the resistance friction force, so it can easily drive and complete shifting process.

Fig. 5 Working principle of clutch actuator



4 Shift Control Strategy

4.1 Actuator Control

4.1.1 Clutch Control

Clutch actuator is electronically hydraulic control system. Its working principle is as shown in Fig. 5.

Clutch disengagement control: the motor rotating controlled by TCU, then it drives the worm screw rotating, the worm gear and gear coaxial rotating, gear drives the gear rack so that the piston moves to the right, build oil to the hydraulic isolation bearings, hydraulic isolation bearings facilitate separation refers to the small end, so that the clutch; the worm has a self-locking function, not to control the motor, the piston can still to maintain in the original state to maintain pressure, so that the clutch is in a separated state.

Combination process control: motor reverse rotating controlled by TCU, oil pressure removed, clutch combined under the diaphragm spring return force.

4.1.2 Select Shift Control

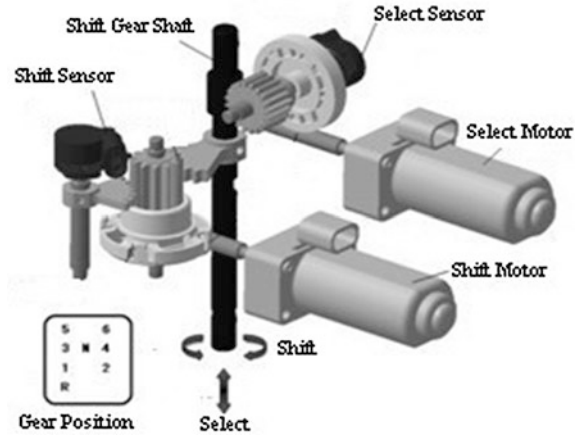
AMT selecting-shifting actuating mechanism adopts electric control electric way, its working principle as shown in Fig. 6.

Select process control: TCU controls select motor rotating; output torque drives the select axle to move up and down through worm gear to select different gears.

Shift process control: TCU control shift rotation of motor, output torque drives the shift axle clockwise or counters clockwise rotating through g worm gear to pick up gear.

After tests for many times, the clutch actuator and AMT selecting-shifting actuator can achieve the desired function very good.

Fig. 6 Working principle of select and shift gear actuator



4.2 Coordinate Control of Multi Controllers

The shift of hybrid electric vehicle is a coordinate control process between multi controllers. The controllers of the electric control system communicate with each other by CAN bus network, ECU, MCU, TCU communicate with VCU respectively. VCU is responsible for collecting vehicle state, forwarding CAN messages, arbitrating vehicle control right; ECU and MCU are responsible for collecting the information such as state, speed, torque and so on as well as responding the VCU torque request and control request; TCU is responsible for collecting the handle information and sending controlling message to the engine and the motor through as well as other actuator by the VCU, required for the vehicle; engine and motor information provided by VCU.

4.3 Shift Process Control

Due to the auxiliary of motor, HEV is more easier to achieve shift without disengaging clutch than the traditional engine vehicles. Its shift control process is as follows:

1. TCU communicates with ECU, MCU by VCU and controls the throttle opening degree of engine and the torque of motor coordinately so that the torque of transmission input axle is close to zero; then TCU controls shift actuator to pick off gear.
2. TCU sends the target speed to engine and motor, controls the speed of engine and the motor, and monitors the speed difference. At the same time, TCU control the actuator to complete gear selection operation.

3. when TCU detects speed difference in the allowable range, in order to prevent engine and motor to output torque after synchronizing which will cause shift jerk, the engine throttle opening degree and the motor torque should be controlled once again so that the transmission input axle torque is close to zero. At the same time the shift actuators complete gear engagement.
4. Coordinately control the throttle opening degree of engine and the motor torque, restore torque according to the power distribution between the engine and the motor to make vehicle running normally.

Compared to shift with disengaging clutch, shift coordinated control without disengaging clutch is simpler, and it can save the clutch open and close process as well as extend service life of the clutch [8].

5 Test Verification

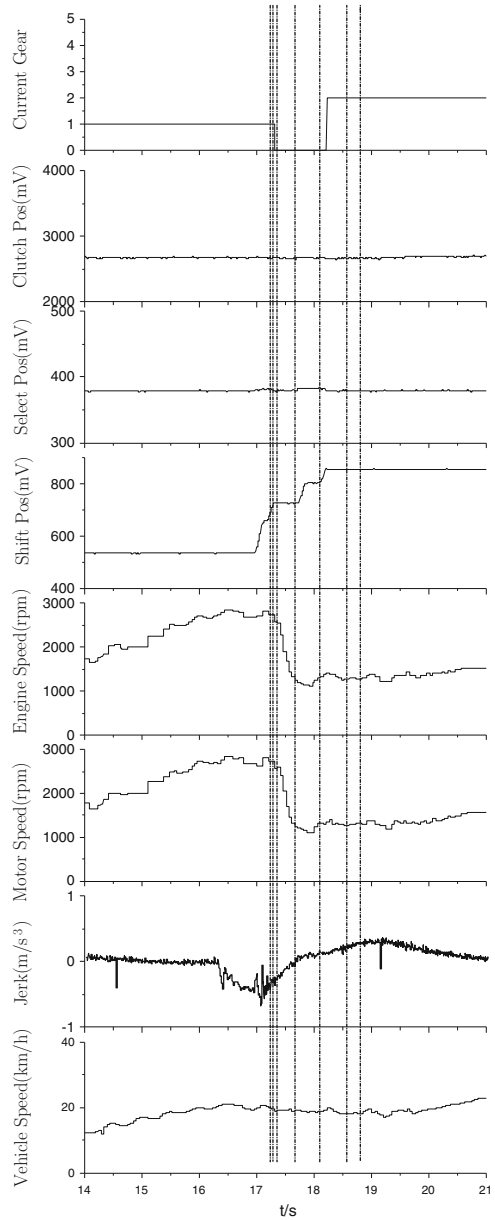
In order to verify the effect of control strategy of shift without disengaging clutch, modify the control parameter and debug the electronic control unit, a hybrid demo car with AMT undertook shift test.

Figure 7 is the shifting curve from first gear to second gear. One can see the variation of gear position, clutch position, select position, shift position, engine speed, motor speed and impact degree during shifting process without disengagement of the clutch from the figure. The shifting process can be divided into six stages as request shift, reduce torque, pick neutral, adjust speed, shift gear and recover torque.

Shift time is a comprehensive index for evaluating shift quality. The time of different stages in shift process is as shown in Table 1. Shift time can be defined as time from the power interruption (began to reduce torque) to the end of recovery of torque. From Table 1, the shift time from first gear to second gear is 0.962 s, which satisfies the technical requirements of less than 1 s. In the whole shift process, time of adjusting speed accounts for about 43.3 % of the total time. It shows that the control of engine speed and motor speed has great affect on the shift quality in the shift process; time of disengage and engage gear accounts for about 36.4 %, which mainly depends on factors such as how big the synchronous speed difference is, the efficiency of select and shift actuators as well as the response of select and shift motors; time of torque recovery is dependent on the driver request torque and the vehicle speed.

The degree of jerk is an important index to evaluate shift quality [9]. It expresses the longitudinal acceleration ratio of the vehicle. The curve of the degree of jerk shows that there is slight degrees of jerk during disengage gear and engage gear. Jerk is caused by torque mutations when disengaging gear; Jerk is caused by the big speed ratio of the first gear and the second gear make torque mutate when shift to a new gear. With the shift position rise, speed ratio difference decreases, the jerk of impact will become small [10]. In the whole shift process, jerk is very

Fig. 7 Curves of vehicle shift 1-2 process



small, and jerk is slight, which in the permitting the degree of jerk range, shift comfort.

In addition, speed difference directly affects the vehicle shift quality: the smaller the speed difference is, the shorter the shift time and the smaller the impact will [11]. The bigger the speed difference is, the longer the shift time and the

Table 1 Shift time

Number	Stage	Time (ms)
1	Request shift	32
2	Reduce torque	65
3	Picking neutral	226
4	Adjusting speed	497
5	Engaging gear	394
6	Restore torque	130

bigger the impact as well as the worse comfort will. Therefore, controlling speed difference effectively is very important to improve the shift quality.

6 Conclusion

For structural features and technical requirements of hybrid vehicle with AMT, this chapter proposes a control strategy that can realize the shift without disengagement of the clutch. Based on Matlab/Simulink to build the control strategy, a hybrid demo car equipped AMT with this shift strategy undertook the road test of 1,000 km in practice. The results showed that hybrid vehicles equipped AMT with this shift strategy effectively shortened the shifting time, reduced shifting impact, improved the ride performance and comfort. The development of AMT shifting without the disengagement of the clutch for hybrid vehicle has great importance for the progress of China's hybrid vehicle technology and industrialization.

References

1. Wang Y-c, Wang Q-n, XIE F (2010) Non-release-clutch Technology of AMT for Heavy Duty Truck. *Veh Technol* 4
2. Zhu H-t, Zhang J-z, Liao C-l (2005) Simulation of integrated gear shifting control for hybrid electric vehicle. *J Highw Transp Res Dev* 8
3. Yu Z-S (2006) *Automobile theory*. China Machine Press, Beijing 5
4. Lei Y-l, Ge A-l (1996) Testing study of improving shift quality of automated mechanical transmission. *Chin J Highw Transp* 4
5. Pei D (2007) Research on the Integrated control of no_separated_clutch AMT. College of automotive engineering, Jilin University, Changchun
6. Xi J-q, Wang L, Fu W, Liang W-W (2010) Shifting control technology on automated mechanical transmission of pure electric buses. *Trans Beijing Inst Technol* 30(1):42–45
7. Ryan A, Mc Gee (2003) Model based control system design and verification for a hybrid electric vehicle. Future transportation technology, conference Costa Mesa, California, June 23–25
8. Wishart JD (2001) Modelling, simulation, testing and optimization of advanced hybrid vehicle powertrains. University of Victoria

9. Zhang J-L (2007) Study on the shifting control without clutch operation of electrical controlled and electronic powered AMT. College of Automotive Engineering, Jilin University, Changchun
10. CHU M-Z (2007) Study on the electric shift of the amt of heavy-duty commercial vehicle without the disengagement of the clutch. College of Automotive Engineering, Jilin University, Changchun
11. Wang Y-C (2010) The Research on key technology of non-declutch amt for heavy commercial vehicle. College of Automotive Engineering, Jilin University, Changchun

Analysis of Desert Adaptation on Shifting Strategy for Heavy Off-Road AMT Vehicle

Yanghong Xue, Yuhui Hu and Huiyan Chen

Abstract According to the problem that the common power shift schedule can't fully meet the requirements of the heavy-duty vehicles with Automated Mechanical Transmission (AMT) in the desert, on the basis of introducing the off-road desert environment and traction characteristics, the impact of undulating road and power loss in the shift process on double parameter shifting schedule was analyzed. The feasibility of collecting and extracting the characteristics of the artificial shift points of the AMT manual mode in desert environment was discussed. And finally, combined with manual driving experience data, the review main points of double parameter shift schedule for off-road desert road conditions was proposed.

Keywords Desert off-road conditions · Automated mechanical transmission (AMT) · Shift schedule · Frequent shifting

1 Introduction

In addition to a few regions, there are no conditions to build roads in the desert area, which is wildly filled with loose sand. Heavy vehicles, often travelling on such unpaved roads, have not fixed path, and sometimes even have to drive off the

F2012-C04-011

Y. Xue (✉) · Yuhui. Hu · H. Chen
Beijing Institute of Technology, Beijing, China
e-mail: yh_xue@sina.com

Table 1 Gear ratio

Gear	R	1	2	3	4	5	6	7	8
Ratio	11.85	13.14	7.93	6	4.43	3.43	2.31	1.29	1

road, for the topographical constraints, sand dune movement and the other factors. The road condition and the change of the acceleration of the vehicles are complex and unpredictable at the same time. Because of the complex terrain, soft soil, heavy traffic, and continuous rolling surface, road characteristic, involving driving, is greatly different from ordinary cross-country ones, and have great influence on the mobility of the vehicles [1]. So if use AMT with ordinary double parameters schedule which is used on normal gravel road or hard soil road, due to the power loss and rough roads, the system will appear logical judgment error. And it can lead to the problems which go against the driver's intent such as frequent shifting and unexpected shifting. These problems not only affect the dynamics performance of the heavy off-road vehicles, but also reduce the using life, the reliability of AMT components [2].

According to double parameters shifting schedule, from the point of view of driving environment, the author examines influence mechanism of the power loss and rough road to shifting schedule, analyses the characteristic of manual shifting. And based on these, the author puts forward the amendment of double parameters shifting schedule adapt to desert off-road condition.

2 Vehicles Traveling in the Desert Roads

2.1 Characteristics of Vehicle

The test object is a 20-ton heavy off-road, with the rated power of 330 kW and maximum torque of 1950 Nm, With 8×8 drive type, it can also switch to the 8×6 or 8×4 . Its maximum speed can reach to 100 km/h on good road and 40 km/h on average on cross-country road. The largest climbing degree is 60 %. The gear ratio is shown in the Table 1.

The automatic mechanical transmission of this heavy vehicle is composed of gearbox with nine forward and one reverse gear, executing agency, electronic control unit (ECU), multi-functional shifting handle and other parts. The transmission is composed of the main box and the sub-box. The main box uses electronic-controlled hydraulic shifting structure, and the sub-box switches gear with the help of electronic-controlled pneumatic valve. The automatic clutch is controlled by the fuel tank connected to the clutch pedal to engage and disengage. AMT electronic control system has an independent ECU, and is able to achieve the CAN bus communication between the engine electronic control systems, vehicle integrated information systems, etc.

Fig. 1 Engine characteristic curves

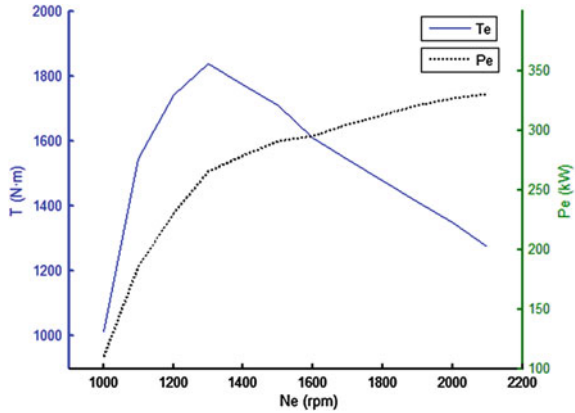
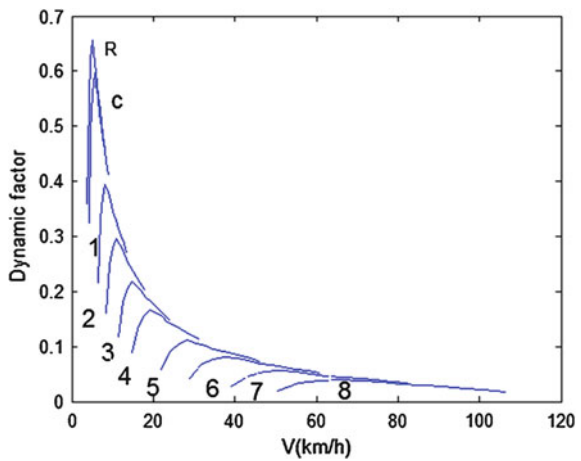


Fig. 2 Traction characteristics



The engine characteristic curves and traction characteristics of this vehicle is shown in Figs. 1 and 2.

2.2 The AMT Manual Mode

The AMT system uses multi-handle gear selector to drive in manual mode. When driving forward, no matter which gear it is in, and no matter how the speed and throttle change, once the handle is moved to “H”, it can stay in the gear till the next move of the handle. With the handle in the “H”, the driver can use “↑” “↓” to shifting on their own judgment, and the AMT system operates the following selecting and switching jobs on itself based on the signal from the handle.

Table 2 Conditions comparison of heavy-duty vehicles and common ones

Conditions	Desert off-road condition	Ordinary off-road condition
Soil	Soft, lots of ups and downs	Plain, less of ups and downs
Surface feature	Large rolling resistance, low adhesion coefficient	Low rolling resistance
Load	Rapid load change	Stable load
Shift	Frequent	Infrequent
Speed	Low and change	Stable

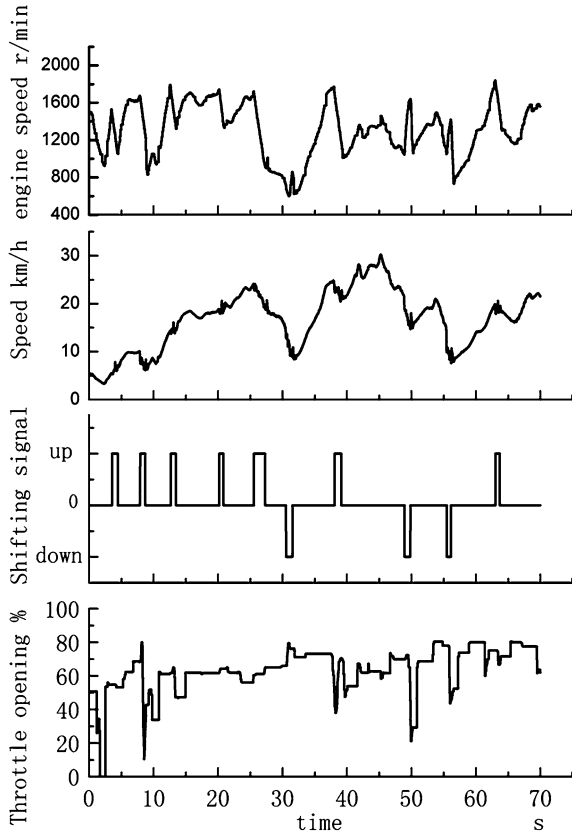
2.3 Desert Environment

Kubuqi Desert in Inner Mongolia is chosen the test environment, of which the annual average wind speed is 3.5 m/s, and maximum 7.0 m/s, and the soil can be regarded to be piled up with approximately spherical particles with very small difference. Analysis shows in the following table, that the desert off-road characteristics can be simplified to be with low adhesion coefficient large driving resistance, lots of ups and downs and rapid load change condition (Table 2).

Among the shifting schedules used today, whether the two-parameter shifting schedule based on stable driving conditions, or the multi-parameter shifting schedule based on the dynamic process are all established based on the vehicle power principles for a good straight road. This method can only reflect stable driving state, not considering the road conditions' impact on the shift schedule. When driving in desert, lots of ups and downs and bend conditions occur. The soil resistance also changes with various road conditions, the transmission carrying situation is complex and changing, besides, in pursuit of a higher speed on cross-country road, the driver will adjust the throttle frequently and severely, leading to the instability of the vehicle state and finally the frequent and unexpected shifting, as shown in Fig. 3.

In addition, the double parameters shifting schedule sometimes can not meet the drivers' intent very well. Such as driver's intent to maintain the gear location and speed up to the slope, but the actual speed increases to cause a upshift which is not expected. AMT is a non-dynamic shifting control and when it comes to the middle of the slope, the shortage of the power causes a downshift (as is shown in Fig. 1, 25–35 s). The unexpected shifting in this process will directly affect vehicle dynamics and ride comfort. Therefore, the shifting control strategy of heavy off-road vehicles need to be able to adapt to such characteristics of the desert condition, so that it ensures the dynamics, meanwhile reduces frequent and unexpected shifting.

Fig. 3 Test curve of auto mode for traveling in climbing desert off-road



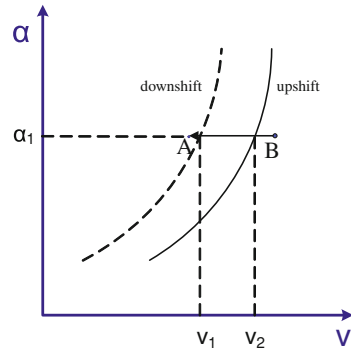
3 Frequent Shifting Reason Analysis

3.1 Power Loss During Shifting Process

The AMT system is a non-dynamic shifting process, so there will be power interruption. When the vehicle travels at a constant speed on a straight ordinary road, generally the road drag coefficient is small, the speed before and after the shifting process is approximately the same. But in the desert off-road, road drag coefficient is large, so the shifting impact cannot be ignored. The following is the analysis on shifting process when the vehicle goes uphill.

Take Fig. 2 for example, curve a and b represent upshift and downshift curves of two adjacent gears. With the throttle opening degree of α_1 , shift delay $v' = v_2 - v_1$, the vehicle state reaches point B, and the program judge to upshift operation, after the upshift, the speed loss $\Delta v > v'$, the vehicle state moves from point B to point A, before and after the process, the throttle opening degree is the same, then the judgment in accordance with the program logic to downshift, will do downshift operation, here comes the frequent shifting (Fig. 4).

Fig. 4 Analysis of frequent shifting for speed loss



Support surface type (asphalt, concrete and stone and other hard support surface as well as soil, sand, snow and wet dirt roads and other soft support surface), surface conditions (roughness and rain, snow and dust, etc.) and soil mechanical properties (grain, porosity, compressive strength and shear strength, etc.) are three major factors that affect the rolling resistance coefficient f . When a general vehicle travels at medium or low speed on different road, the f values are as given in Table 3 [3].

3.2 Power Loss During Shifting Process Analysis

Driving on hard road, the rolling resistance is the main movement resistance, and on unpaved road, the rolling resistance is the only main resistance. The aerodynamic resistance cannot catch up with the rolling resistance until the speed reaches 50 ~ 60 km/h.

The road resistance is affected by many factors in desert off-road condition, and the modeling is of much complex and requires simplification. The accurate calculation needs to use the dynamic weight of the vehicle, including acceleration, the vertical component of the trailer joint force and air resistance, etc. However, in the prediction of vehicle performance, changes in the dynamic weight value complex the calculating, but cannot improve the accuracy significantly. And the dynamic weight distribution between the front and rear axle has little effect on the total rolling resistance. Therefore, in analyzing of power loss in the shifting process, the static weight for calculating rolling resistance is already precise enough (only applied to linear motion) [4].

Rolling resistance is simplified as

$$F_f = Gf = mgf \tag{1}$$

Slope resistance is

$$F_i = G \sin \alpha = mg \sin \alpha \tag{2}$$

Table 3 Rolling resistance coefficients of different types of roads

Surface	f
Good asphalt or concrete	0.010–0.018
Medium asphalt or concrete	0.018 –0.020
Good pebble	0.025–0.030
Pit pebble	0.035–0.050
Gravel	0.020–0.025
Pressed dry stone	0.025–0.035
Ice road	0.015–0.03
Pressed snow	0.030–0.05
Pressed wet soil	0.050–0.15
Wet soil	0.1–0. 25
Wet sand	0.06–0.15
Dry sand	0.1–0.3

During the shifting process when the vehicle is going uphill, the clutch disengages, and the driving force F_t is 0. The vehicles decelerates relying on the inertia, and the resistance is negative, its value is

$$F_j = \delta m \frac{du}{dt} \tag{3}$$

$$\delta = 1 + \frac{1}{m} \frac{\sum I_w}{r^2} + \frac{1}{m} \frac{I_f i_g^2 i_0^2 \eta_T}{r^2} \tag{4}$$

Here, I_w represents the moment of inertia of the wheels, I_f is the moment of inertia of flywheel, i_0 is the main ratio, and i_g is the transmission drive gear ratio. The vehicle’s air resistance:

$$F_w = \frac{C_D A v^2}{21.145} \tag{5}$$

Here, C_D is the air drag coefficient, v is the relative air flow speed, A is the frontal area. $C_D = 0.75$, $A = 6 \text{ m}^2$ approximately. Equation of vehicle driving:

$$F_t = F_f + F_w + F_i + F_j \tag{6}$$

Substitute all equations,

$$-\frac{du}{dt} = \frac{mg(f \cos \alpha + \sin \alpha) + \frac{C_D A v^2}{21.145}}{\left(m + \frac{\sum I_w}{r^2} + \frac{I_f i_g^2 i_0^2 \eta_T}{r^2}\right)} \tag{7}$$

Since the clutch disengages, and the transmission is in neutral mode during the shifting process, while the equivalent mass of the moment of inertia of the wheels is very small compared to 20t heavy vehicles; In addition, the heavy vehicles does

not exceed 30 km/h in speed in the desert areas in general, so it can ignore the rotational inertia and air resistance, the equation can be simplified as

$$-\frac{du}{dt} = g(f \cos \alpha + \sin \alpha) \quad (8)$$

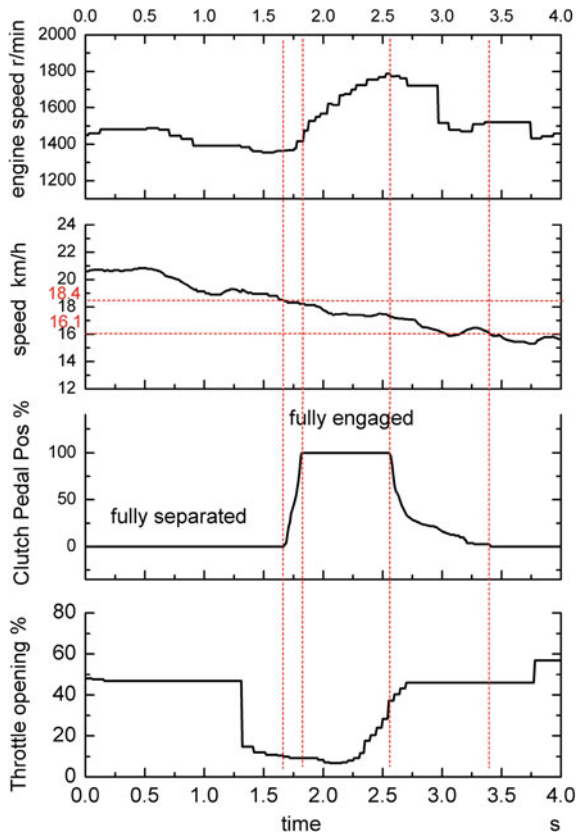
Shifting time of the vehicle can be divided into clutch disengaging time t_1 , the selecting and shifting operation time t_2 , and clutch engaging time t_3 . t_1 is the shortest in the three part so that can be ignored. The time of clutch engagement will vary with operating condition goes, and according to the data analysis, we know the shifting time is generally between 0.8 and 1.5 s, while t_2 is generally between 0.4 and 0.8, so that the power interruption time is about 0.6 s. Assuming the acceleration is constant in the shifting process, $g = 9.8 \text{ m/s}^2$, the vehicle traveling on different slopes, with different rolling resistance coefficient (RRC) of the roads, we get the vehicle speed loss in Table 3.

In Table 4, we can see that on general asphalt or concrete slope ($i \leq 5 \%$, $f \leq 0.03$) the shifting process contributes little to power interruption which indicates that it is reliable to regard the speed stable during the shifting process with general double parameters shifting schedule. While for heavy vehicles traveling in the desert environment, due to the combined effect of the sandy soil of the rolling resistance coefficient (0.1–0.3) and the dramatic changes of the unpaved road slope, there will be much speed loss when shifting in the uphill process. Figures 5 and 6 are the road test data of speed losses of heavy vehicles in the two different road during a shifting process.

4 AMT Manual Mode Process Analysis

From the paragraphs above, we can clearly see that in complex conditions, the ordinary double parameters shifting schedule can not correctly identify the environment and the driver's intent, and will cause frequent shifting, so when heavy vehicles traveling in the desert environment, in fact, manual mode is mostly applied. This is because the automated shifting schedule as well as double parameters shifting schedule has its inherent defects, and also because with human intervention, the vehicle can prejudge the condition ahead better and find appropriate time to shifting combined with the current vehicle status. The AMT core-idea of the shifting schedule is to take the best driver as the template and pursue the unity of the right drive intent and appropriate shifting timing. For heavy vehicles equipped with AMT system, if we can extract the information of the driver's intent and method in manual mode in desert environment, we get a big step forward in improving the adaptability of automatic shifting schedule in the desert environment.

Fig. 5 Speed loss in shifting process on dry soil



4.1 Gear Usage Statistics Analysis in Manual Mode

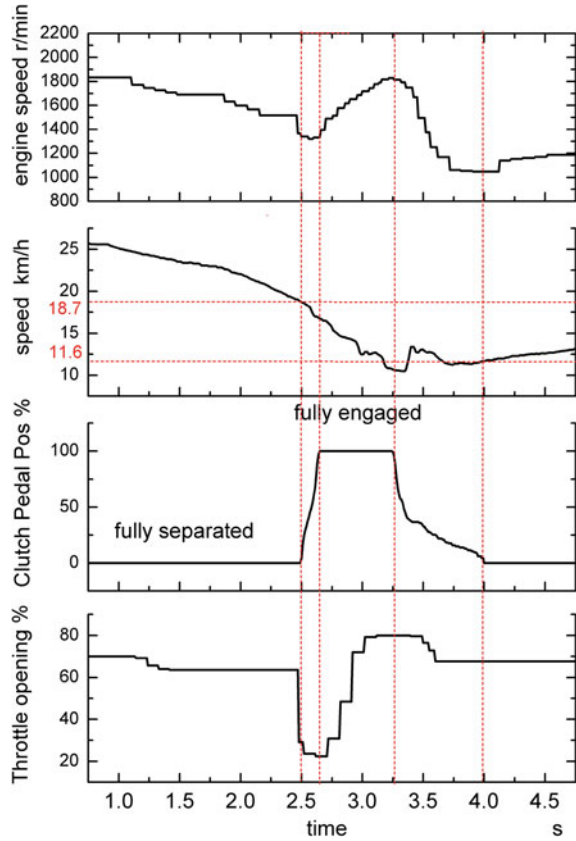
After study the data of 3,000 km road test, the frequency and times of the gear usage is shown in Table 4.

Table 5 shows that, in general, the heavy off-road vehicles in the desert travel mostly in middle and low gears, particularly in 3 or 4, and no higher than 6. The gear C and R is mainly used for special situation such as trapped car, or hill-start. This is consistent with the actual road conditions in the desert. And in fact 5th gear will normally be slightly lack of motivation and it is used mainly in the region where the sand is hard and flat.

4.2 Manual Shifting Schedule Statistics Analysis

The automatic shifting schedule is unable to adapt to the desert areas, and easy to cause frequent or unexpected shifting. While the shifting schedule based on the

Fig. 6 Speed loss in shifting process on desert off-road



driver’s experience, can serve as a good solution to the problem of frequent shifting, even though it cannot reach the best point in dynamic and the driver can not always accurately determine the parameters such as the vehicle speed, engine speed and throttle opening degree. So the excellent drivers’ experience is a great reference for the amendment of the shifting schedule.

The driver in this road test has rich experience on complex road conditions including desert, moreover, the 3000 km test mileage ensures the credibility of the sample. The data collected by the data acquisition system, you can extract the information of points when the driver judge and determine to shift in manual mode. Figures 7 and 8 show the data of the upshift and downshift points in manual mode.

It can be seen from the two graphs that the manual upshift points are distributed more regularly, while the downshift points are distributed in a mess, with few regularity.

The main characteristics of manual upshift regular patterns are:

1. In the desert, heavy off-road vehicles mostly shifting with large throttle opening in pursuit of the good power performance. Except the shifting from c to l, most

Table 4 Speed loss in shifting process

Slope i	0	2 %	5 %	10 %	15 %
RRC f					
0.02	0.12	1.27	0.41	0.70	0.99
0.05	0.29	1.44	0.59	0.88	1.16
0.15	0.88	2.02	1.18	1.46	1.75
0.30	1.76	2.88	2.06	2.34	2.62

Table 5 The usage of the gears with artificial shift in desert test

Gear	R	C	1	2	3	4	5	6	7/8
Number of times	70	562	497	652	1011	1297	572	17	0
Frequency	1.5	12.0	10.6	13.9	21.6	27.7	12.8	0.4	0

shifting operations are delivered with throttle opening more than 50 % and in low vehicle speed;

2. With gear order increasing, the degree of dispersion of the upshift points are also growing;
3. The vehicle speed will change, in a same shifting process and even with a same throttle opening degree;
4. Upshift points of all gears have some points with high the degree of dispersion;

The main characteristics of manual upshift regular patterns are:

1. The time of 2-1,1-c shifting process is obviously less than others;
2. In desert condition, there are no clear regional boundaries between the down-shift points of two gears, and there is some intersection region.

5 Amendment Points for AMT Desert Off-Road Shifting Shift Schedule

It can be found from the analysis above that, the large resistance of sand road and the ups and downs have great impact on shifting schedule. Since the prerequisite for smooth driving changes, the adoption of the shifting strategy established in the same way for ordinary roads has bad adaptability in the desert environment. The targeted amendment is needed. Based on the analysis discussed in previous chapters, the following points can be put forward:

1. Road test proved that, though this heavy vehicle has nine forward gears, only c-4 or 5 gears can well meet the requirement of desert condition, and except the needs of the accelerating process, c or 1 gears are rarely used, while 3rd and 4th gears are used more frequently. The average vehicle speed is between 20 and 25 km/h, so it is feasible to set 5th the top gear in desert condition.

Fig. 7 The upshift points

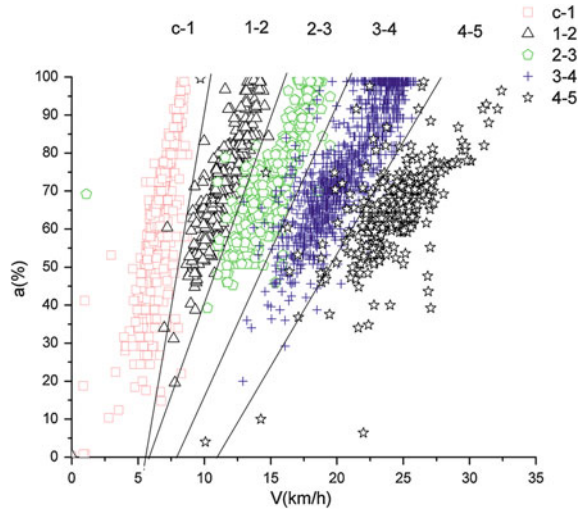
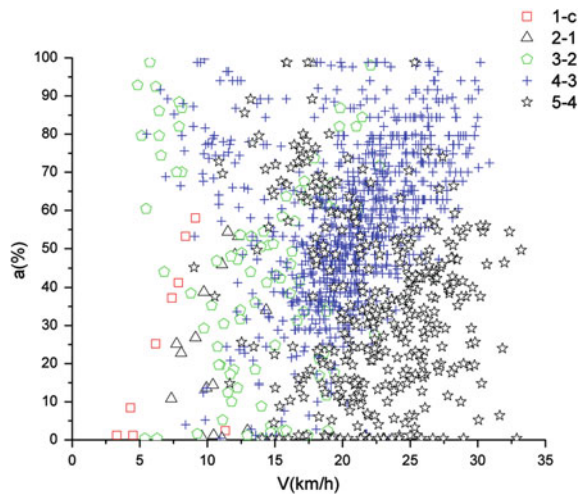


Fig. 8 The downshift points



2. Due to lack of long uphill or downhill but lots of ups and downs, the driver has quite strong will to sprint the slope, the judgment of upshift should be conservative and delay judgment can be adopted in upshift process in avoid of frequent shifting.
3. For resistance in the desert environment changes great and good power performance is required, the downshift logic can be “sensitive” to avoid the lack of motivation caused by the resistance change.
4. In response to the dramatic changes of the desert conditions and avoid flameout due to a sudden increase of resistance, the automatic shifting program should be set to downshift jumping operation, to ensure power performance in complex condition.

6 Conclusion

In this chapter, the author analyzed the factors of the impact on frequent shifting of speed loss and ups and downs in desert conditions for heavy off-road vehicles with AMT, introduced manual mode in desert conditions, and on the basis of the analysis on the statistics of manual shifting points, proved the regularity of manual upshift points (no regularity of downshift process). Finally, the author put forward the main amendment points for double parameters shifting schedule to adapt to desert conditions, and provides a theoretical basis and guidance for improvement of adaptability of AMT in the desert conditions for the future.

References

1. Zhuang JD (2001) Calculate Terramechanics. China Machine Press, Beijing
2. Wang HL, Liu HO, Zhang W, Chen HY (2009) A study on the elimination of unexpected and frequent shifting of off-road vehicle AMT. *Trans Beijing Inst Technol* 29:681–685
3. Peng M, Diao ZX (2009) Computing matching and evaluation of vehicle power system. Beijing Institute of Technology Press, Beijing
4. Ding HR (1993) Automatic transmission of vehicle. Beijing Institute of Technology Press, Beijing

Fuzzy Logic Controlled Electromagnetic Actuated Cvt System for Passenger Car

Rahman Ataur and Sharif Sazzad Bin

Abstract Modern cars are equipped with continuously variable transmission (CVT) to make the vehicle smooth operation and to reduce the transmission losses. Many researchers and car companies have developed several types of CVT to improve the transmission losses with maintaining the acceleration time. However, most of the studies reported that the developed CVT has some constrains in the actuation mechanism which leads this study to develop an innovative electromagnetic actuated continuously variable transmission (EMA-CVT) system. The mathematical models have been developed for the kinematics analysis of clamping and electromagnetic forces of EMA. The EMA of this study has been developed for $\frac{1}{4}$ scale car with two sets of solenoid. Each set of the solenoids has been equipped with primary and secondary pulleys for pushing and pulling the movable sheave. The operation of the solenoid is performed by controlling the supply current with a potentiometer. A simulation based Fuzzy Logic controller has also been introduced in this study to predict the EMA system dynamic behaviour for identifying the current control of the EMA actuation. The fuzzy simulation block embedded with a mathematical model assists to predict system responses. The EMA experiment has been conducted by controlling the currents that were identified from the fuzzy simulation. The EMA developed electromagnetic forces 108 N for current 1.21 amp and 301 N for current 3.37 amp which are good enough to overcome the clamping force for the $\frac{1}{4}$ scale car the maximum 278 N. It is observed that travelling time of the plunger is in the range of 1.8–3.1 s which could be considered as the acceleration time for the car. The correlations between

F2012-C04-013

R. Ataur (✉) · S. Sazzad Bin
Department of Mechanical Engineering, Kulliyah of Engineering International Islamic
University Malaysia, 50728, Kuala Lumpur, Malaysia
e-mail: arat@iium.edu.my

Fig. 1 EMA-CVT

the measured and predicted values of traction torque have been found 90.99 %. It indicates that the predicted data over the measured data have a closed agreement and thus, substantially verified the fuzzy simulation model.

Keywords Electromagnetic actuator • Fuzzy logic controller • Fuzzy-proportional-derivative-integrator • Acceleration time

1 Introduction

Electromagnetic actuators (EMA) are increasingly becoming the actuator of choice in industry, due to their ruggedness, low cost, reduced complexity, relative high force density and ease of control. One of the latest applications of solenoid based EMA's include electromagnetic continuously variable transmission (CVT) actuation systems as shown in Fig. 1. The ultimate goals of the CVTs design are to provide more torque and power than traditional transmissions, to have smooth speed change, wider-range speed ratio, and simple mechanism with low cost and less maintenance [1, 2]. The performance of a vehicle equipped with a 3,000 cc engine for the speed of 100 km/h in terms of acceleration time taken is reported as 7.85 s for conventional CVT system [3].

Magnetic force and torque actuated devices have been developed by researchers during their studies [4–8]. This study presents an Electromagnetic Actuated Continuously Variable Transmission (EMA-CVT) system which is mainly designed for a $\frac{1}{4}$ scale city car. The EMA configuration that is examined in this study is developed by two sets of solenoid with different number of turns. Each set of the solenoids has been equipped with individual pulley which one has been used for pushing and the other one for pulling along with a common plunger. The movable sheaves of the proposed EMA-CVT are controlled by developed

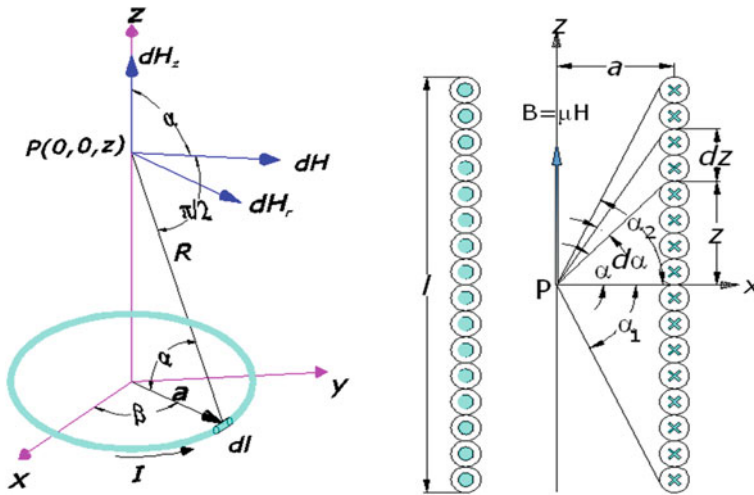


Fig. 2 Magnetic field of single and multiple coil winding

electromagnetic actuator (EMA) with a FLC and FPID. The proposed CVT is designed for ¼ scales Kencil Car weigh of 155.75 kg including current EMA-CVT system. To start the vehicle from rest, the primary (input) pulley radius will be smaller than the secondary one results higher torque multiplication. During speeding up of the car gradual synchronized manipulations of both pulleys give proper belt tension, less slip as well as exact gear ratio.

2 Methodology

The actuator solenoid has been designed to develop the maximum electromagnetic force to overcome the maximum clamping force. The mathematical representation is developed for the EMA by considering the dynamic behaviour of the magnetic flux, density, strength, electromagnetic force and energy. The total electromagnetic force at the magnetic field of current conducting solenoid is given by the general equation of Fleming’s (LH) rule [9],

$$F_{em} = BIl_{wire} \tag{1}$$

where, F_{em} is the electromagnetic force for the total solenoid coil length l_{wire} , B is the magnetic flux density for whole solenoid, I is the current passing through the conductor wire around which generates magnetic field. It is noted that the properties of EMA depends on the: geometry of the magnetic core (Fig. 2), amount of air gap in the magnetic circuit, core material and solenoid temperature.

So the magnetic flux density along the z direction for the segment of wire in a single winding can be estimated by using the equation of [9]:

$$\begin{aligned}
 B &= \hat{z} \sum_{a=h_1/2}^{h_2/2} \sum_{z=-L_{solenoid}/2}^{L_{solenoid}/2} \left(\frac{\mu \left(\iint_{S(r,l_{segment})} J dS_{wire} \right) a^2}{2 \cdot \sqrt{a^2 + z^2}} \right) \\
 &= \hat{z} N_{loop} \frac{\mu N_{wind \text{ per length}} I}{2 L_{solenoid}} (\sin \alpha_2 - \sin \alpha_1)
 \end{aligned} \tag{2}$$

where, μ is magnetic permeability (degree of magnetization of a material in response to magnetic field), $N_{wind \text{ per length}}$ is the number of turns in a single loop, N_{loop} is the number of loop in solenoid housing, $N = N_{wind \text{ per length}} \cdot N_{loop}$ is the total number of turns in the solenoid.

Therefore, the electromagnetic force:

$$F_{em} = N \frac{\mu I^2}{L_{solenoid}} (\sin \alpha_2 - \sin \alpha_1) l_{\sin \text{ glewinding}} \tag{3}$$

If the solenoid length is much larger than its radius, then $\alpha_2 \doteq 90^\circ$ and $\alpha_1 \doteq (-) 90^\circ$ in which Eq. 6 reduced to:

$$F_{em} = N \frac{\mu I^2}{L_{solenoid}} l_{\sin \text{ glewinding}} = N \frac{\mu I^2}{L_{solenoid}} 2\pi a \tag{4}$$

EMA for generation of electromagnetic force is designed in such a way that it can push and pull the pulley sheaves. The justification of the dimension of the solenoid is made by determining the space availability in the down scaled chassis so that it is not too long to fix and not too short to produce desired magnetic force. The number of windings, wire diameter and solenoid housing and length are considered to develop the EMA.

3 Control Staretyg: Fuzzy Logic Controller

Various types of modified PID controllers involving auto tuning and adaptive PID controllers have been proposed by [10–14]. However, fuzzy controller can also be applied for tuning PID parameters based on nonlinear mapping of system error and its derivative to PID parameters. The fuzzy logic controller (FLC) with FPID is preferred to control the EMA of the proposed study to control the EMA-CVT. The FLC is used in this study to control current flow to the EMA for maintaining the desired traction torque of the vehicle in different road conditions.

The control system of the EMA is structured with controlled variable and regulated variable. For this study controlled variable is considered as Torque Error (**TE**), Rate of change of Torque Error (**RTE**) and regulated variable as Power consumption (**P**) by EMA actuator. It is noted that the values of membership functions (**TE**, **RTE**) change their values with respect to time. For instance, the degree of **TE** changes in Nm from 5 to 90, **RTE** is fluctuates in Nm/s from -5 to 5 , and **P** is measured in watt from 50 to 200, respectively. It is noticed that different

Table 1 Coefficients of membership functions for FIS parameter of *TE*

Linguistic variables	Type	Coefficients (Nm)		
		<i>c</i> ₁	<i>c</i> ₂	<i>c</i> ₃
(VlowTE) Very low torque error	Z-shaped	5	26.25	–
(LowTE) Low torque error	Triangular	5	26.25	47.5
(AvgTE) Average torque error	Triangular	26.25	47.5	68.75
(HighTE) High torque error	Triangular	47.5	68.75	90
(XhighTE) Extreme high torque error	S-shaped	68.75	90	–

membership functions acquire on zero and nonzero values indicating the degree to which the linguistic value suitably illustrates the present value of *TE*. For example, at *TE* = 5; it is certain that the torque error is “very low (Vlow)”, and as the value of *TE* moves toward 26.25 it is become less certain that it is “Vlow” and more certain that it is “Low” shown in Table 1.

The notation *TE* indicates the system input and it has its membership function truth values that can be computed of membership function of the fuzzy inputs from fuzzy logic expert system where *i* stand for input from into Eq. (5), (6) and (7).

$$\mu_{Vlow}(TE(i_1)) = \left\{ \begin{array}{ll} 1; & (TE) \leq 5 \\ \frac{26.25 - (TE)}{21.25}; & 5 < (TE) < 26.25 \\ 0; & (TE) \geq 26.25 \end{array} \right\} \tag{5}$$

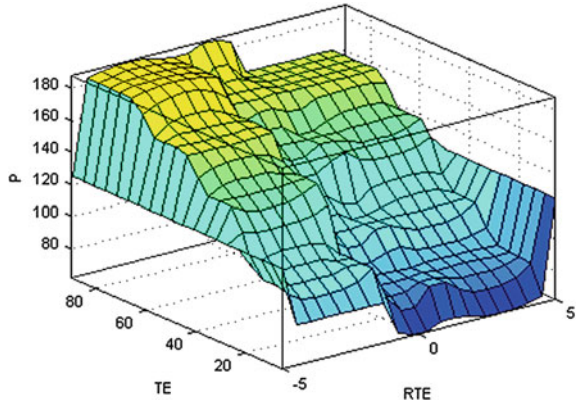
$$\mu_{Low}(TE(i_1)) = \left\{ \begin{array}{ll} 0; & (TE) \geq 5 \\ \frac{(TE) - 5}{21.25}; & 5 < (TE) \leq 26.25 \\ \frac{47.5 - (TE)}{21.25}; & 26.25 < (TE) < 47.5 \\ 0; & (TE) \geq 47.5 \end{array} \right\} \tag{6}$$

$$\mu_{Pos}(RTE(i_2)) = \left\{ \begin{array}{ll} 0; & (RTE) \leq 1 \\ \frac{(RTE) - 1}{2}; & 1 < (RTE) \leq 3 \\ \frac{5 - (RTE)}{2}; & 3 < (RTE) < 5 \\ 0; & (RTE) \geq 5 \end{array} \right\} \tag{7}$$

Rule view in fuzzy representing gives the corresponding output (power consumption) value for the inputs *TE* and *RTE* crisp value of which is 85.7 watt. The fuzzy inference system (FIS) seeks to determine which rules fire, to find out which rules are relevant to the current situation. The inference system combines the recommendations of all the rules, to come up with a final conclusion and take action.

Using MATLAB the fuzzy control surface is developed as shown in Fig. 3 which represents visual depiction of how fuzzy logic system operates dynamic

Fig. 3 Control surface of the fuzzy controller



behaviour of the system over time. The plot is used to check the rules and the membership functions predicted to improve the output. This surface view actually illustrates how dynamic and nonlinear the EMA-CVT system is to be controlled.

Fuzzy Simulink is advantageous to mimic the system characteristics without system fabrication in order to show system dynamic response over time. This virtual control of the EMA-CVT with fuzzy controller actually helps the dynamic system. System gain of the EMA-CVT can be represented directly into Simulink and test them out in a simulation environment with the help of transformed equation. A Simulink block diagram for this system is shown in the following Fig. 4. It contains a Simulink block called the Fuzzy Logic Controller block.

Graphical representation in Fig. 5 of the Simulink block diagram visualizes the response of the system with respect to time. Time required to reach the desired 85.19 Nm torque is close to 3.75 s. Initial current is high in order to overcome the stall torque which close to 4.5 amp and considerably plummeted to 1.75 amp for the next 3.75 s time period. As the stale torque is overcome; consumption of current decreases for the time being and after a while when the desired torque achieved current again jump and level off in 3.5 amp to hold the torque to its position for the secondary pulley sheave. Afterward, current response trend will be similar to the torque response trend. Torque response behaviour is same throughout the system running time. Here, desired torque is considered fluctuating with very small amplitude as car is running in an uneven terrain. However, further study is conducted only for primary pulley sheave as this study is concerned with the acceleration time of the car after overcoming the stale effect. So, naturally primary pulley shows the inverse characteristics in terms of graphical representation compared with secondary pulley.

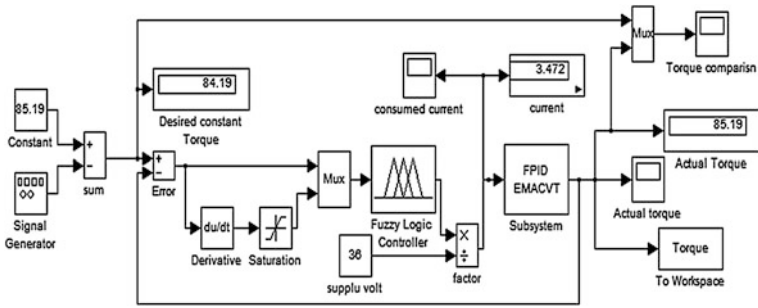


Fig. 4 Simulink block diagram for EMA-CVT system

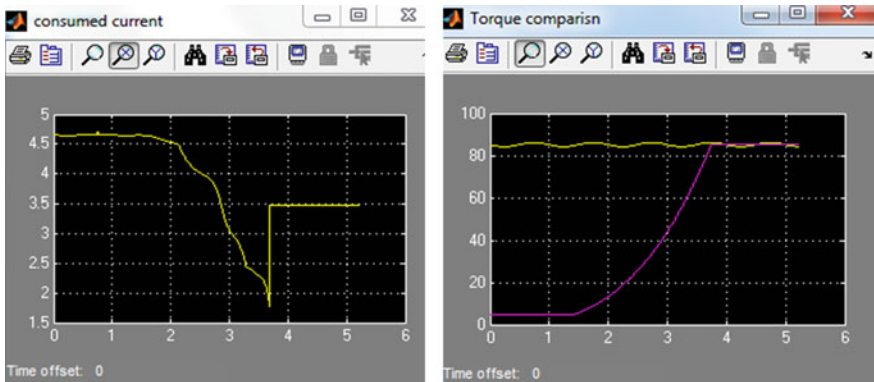


Fig. 5 Graphical representation of the Simulink block diagram

4 Result and Dicussion

Performance of the system is done from various points of view in accordance with controlled current flow followed by controlling voltage with a fuzzy controller to the EMA system. The performance of the EMA-CVT is measured keeping the system initially in high gear ratio. Different kinds of gear ratio mean different torque results various types electromagnetic force. In order to develop the electromagnetic forces only parameter that can be regulated is voltage as controlling current is not an easy task.

Electromagnetic force is the heart of this current EMA-CVT system which offers desired gear ratio by placing the pulley shave to its exact position. Figure 6 is showing the behaviour of electromagnetic force response of the primary pulley shave actuation system with varying the current supply. The gradual response of electromagnetic force from 108 N to about 300.82 is followed by a comparatively sharper increase of current which is in between 1.21 and 3.37 amp. The highest electromagnetic force is 300.82 N which is much higher than required maximum

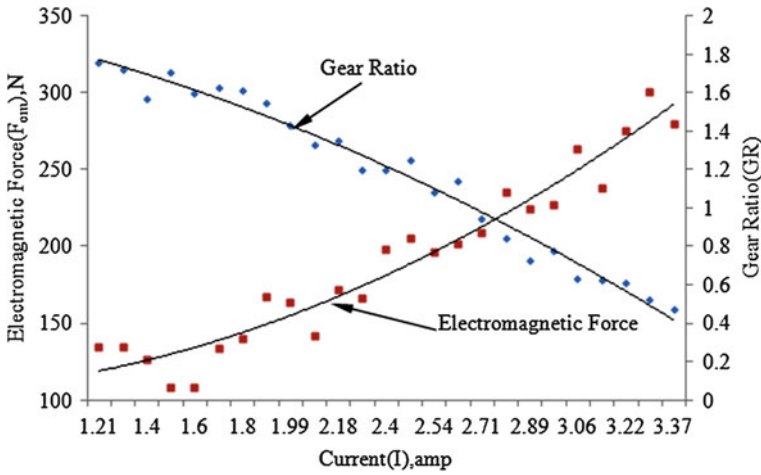


Fig. 6 Electromagnetic force in primary pulley, gear ratio VS supply current

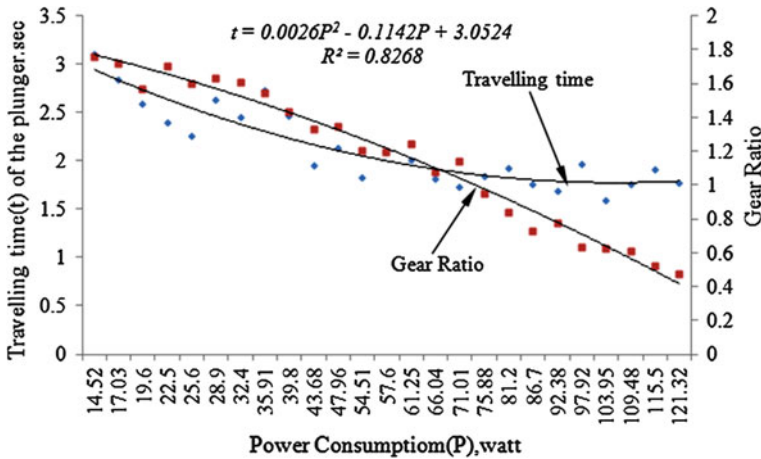


Fig. 7 Travelling time VS power supply

electromagnetic force 274.82 N. It supposed to be linear change with respect to power followed gear ratio.

Figure 7 illustrates the detail information regarding travelling speed of EMA with varying power supply. By referring to the current supplied to the coil, the variety of responding (travelling) time of the movable sheave is recorded from the experimental data. In the lowest power consumption region such 14.52 watt EMA system able accelerate the car within 3.1 s and there after travelling time declined almost steadily with the incremental power and appeared to be level off in 1.77 s until the power reaches to its maximum range 121.32 watt. This is an achievement

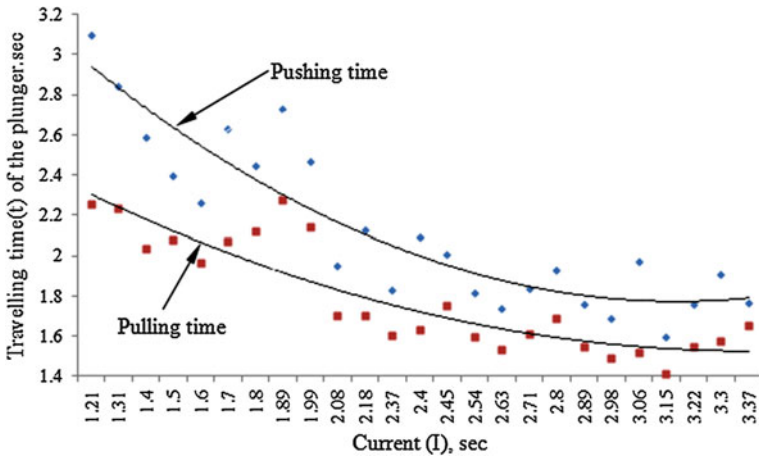


Fig. 8 Pushing and pulling time VS current

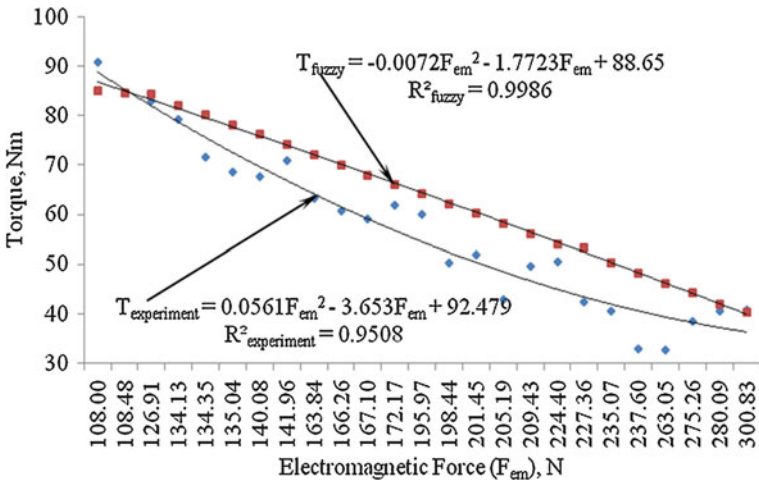


Fig. 9 Torque comparison with and without fuzzy controller

of this study; minimum time taken and power consumed by using FPID to accelerate the car during running time.

Travelling time (responding time) of the plunger of the EMA for pulling mechanism is found significantly lower than that of pushing counterpart as in Fig. 8. It is recorded that especially for lowest current 1.21 amp pushing time is 3.1 s whereas pulling time is 2.257 s. This variation (3.1–2.257 = 0.843 s) considerably decreased to 0.115 s and seems to be stabilized around this. It is noticed that the values of pulling time wildly fluctuating as they hovered around initial values of current. Subsequently it became marginally better as the current supply increase. The basic reason taking more time during pushing was the load on

matching area of the sheaves is higher and the pulling of the sheave was found easier than the pushing. Furthermore, clamping releasing force always tends to pull the movable sheave of the pulley towards the solenoid of the EMA while, clamping force push the movable sheave against the rotating belt.

Dynamic torque behaviour in between 30 and 90 Nm is observed in both without fuzzy (experimental) and with fuzzy controller as depicted in Fig. 9 during running condition. It reflects the reduced torque loss with using the fuzzy controller.

5 Conclusion

Fuzzy Logic Controller was developed to control the EMA-CVT for the vehicle different load conditions. The EMA-CVT performance has improved 4 % when the EMA is controlled by Fuzzy Logic Controller. The FLC with FPID is attractive to control the EMA because of its ability to maximize acceleration and deceleration regardless of road conditions.

This control of the EMA-CVT with fuzzy controller helps the system to operate smoothly to significantly reduce the delaying accelerating time of the vehicle and improve the transmission loss. It is observed that:

1. The EMA develops the electromagnetic force in the ranged of 108–301 N which has been maintained with supply current maximum 3.37 amp.
2. The traction torque has been estimated maximum 90 Nm by using the electromagnetic force 301 N which has been found with the corresponding supplied current 3.37 amp for the maximum gear of 1.8 with improved transmission.

6 Recommendation

Continuous duty solenoids must have adequate heat radiation due to magnetic flux leakage which is recorded 46 °C. The alignment of transmission is very crucial. Many work loss such as frictions can restrict the movement of the plunger resulting inaccurate gear ratio.

References

1. Burke M, Briffet G, Fuller J, Heuman H, Newall J (2003) Powertrain efficiency optimisation of the torotrak infinitely variable transmission (ivt). SAE 01:0971
2. Pesgens M, Vroemen B, Stouten B, Veldpaus F, Steinbuch M (2006) Control of a hydraulically actuated continuously variable transmission. Veh Syst Dyn 44(5):387–406

3. Ang KK, Quek A, Wahab A (2002) MCMAC-CVT: a novel on line associative memory based CVT transmission control system. *Neural Netw* 15:219–236
4. Toshie T et al (2004) Electromagnetic analysis coupled with motion for high speed circuit breakers of eddy current repulsion using the tableau approach. *IEE J Trans. PE* 124(6):859–865
5. Toshie T et al (2004) An electromagnetically actuated vacuum circuit breaker developed by electromagnetic analysis coupled with motion. *IEE J Trans. PE* 124(2):321–326
6. Ebine N, Ara K (1999) Magnetic measurement to evaluate material properties of ferromagnetic structural steels with planar coils. *IEEE Trans Magn* 35(5):3928–3930
7. Quandt E, Claeysen F (2000) Magnetostrictive materials and actuators. In: *Proceedings of actuator*. Bremen, Germany, pp 19–21
8. Rahman A, Mohiuddin AKM (2009) Electromagnetic actuated CVT system for passenger car. *International conference of industrial engineering and engineering management (IEEM)*. Paper no. IEEM09–960, Hong Kong, pp 8–11
9. Ulaby FT (2005) *Electromagnetics for engineers*. Pearson International Edition
10. Rahman A, Sharif S, Hossain A, Mohiuddin AKM, Zahirul Alam AHM (2012) Kinematics and nonlinear control of an electromagnetic actuated CVT system for passenger vehicle. *J Mech Sci Technol* 26(7):2189–2196
11. Carman BK (2008) Prediction of soil compaction under pneumatic tires a using fuzzy logic approach. *J Terramech* 45:103–108
12. Nascu L, De Keyser R, Folea S, Buzdugan T (2006) Development and evaluation of a PID auto-tuning controller. In: *IEEE international conference on automation, quality and testing, robotics*. pp 122–127, 25–28
13. Huang HP, Roan ML, Jeng JC (2002) On-line adaptive tuning for PID controllers. In: *IEE proceedings—control theory and applications*, vol 149, no 1. pp 60-67
14. Sazzad S, Rahman A, Hossain A, Mohiuddin AKM (2011) A study on the development of a fuzzy logic control electromagnetic actuated CVT system. *IJUM engineering congress (IEC 2011)*. ICMAAE'11, paper no. 183. pp 17–19

Modelling and Simulation of DCT Gearshifting for Real-Time and High-Fidelity Analysis

Lionel Belmon, Jun Yan and Andreas Abel

Abstract The gearshifting process of Dual Clutch Transmissions has an important impact on the customer felt-quality. It is necessary to balance gearshift timing, passenger comfort, clutch temperature etc. Dynamic simulation models are a great help to achieve satisfactory system behaviour. We illustrate in this paper how Modelica based models can be used from pre-design phases down to TCU calibration support.

Keywords Modelling · Transmission · Gearshifting · Comfort · Real-time

1 Context and Objectives

Developing a DCT system requires accurate predictions on the performance of driveline and gearshift actuators as well as appropriate implementation and calibration of the transmission controls. Due to closed-loop operation the overall system behaviour is always affected from the physical hardware as well as the software of the controls and their complex interactions. This strong linkage

F2012-C04-014

L. Belmon (✉)
Global Crown Technology, Beijing, China
e-mail: lyh.jlu@gmail.com

J. Yan
Dongfeng Motors, Wuhan, China

A. Abel
ITI GmbH, Dresden, Germany

requires, as early as possible, an examination of how these two sides interact with each other. It is not desirable to do this on prototypes only, since these are usually available only very late in the development process and should not be exposed to early deficient software prototypes. Simulation of the overall system provides an excellent solution to perform virtual testing and to solve issues as early as possible in the design process.

Following this scheme hardware/software development and evaluation/testing can run in parallel and in synergy with other modelling and simulation activities executed during development.

Requirements to the simulation models will change during the process. Whereas in earlier phases more and more detailed predictions and validations have to be made on simulation models and thus more and more high-fidelity models are required, there will be a shift to simpler but real-time capable models once the real TCU has to be tested and calibrated in real-time conditions.

In this paper we show, that it is possible and feasible to create a simulation and model framework, which is adaptable to the different development phases and allows supporting both, high dynamics as well as real-time simulation.

2 Vehicle and Powertrain Modeling

The models presented here have been developed under the platform SimulationX. Several of the available libraries for mechanical, transmission or hydraulic simulation, were applied. We introduce in the next parts the main subsystems. For confidentiality reasons, the specific structures of some subsystems are not provided.

2.1 Gearbox Model

The gearbox model accurately represents the internal dynamics of the shafts/gears assembly, including stiffness, inertia and frictions. We give the internal schematic of the gearbox model in the following Fig. 1, along with the packaged gearbox element.

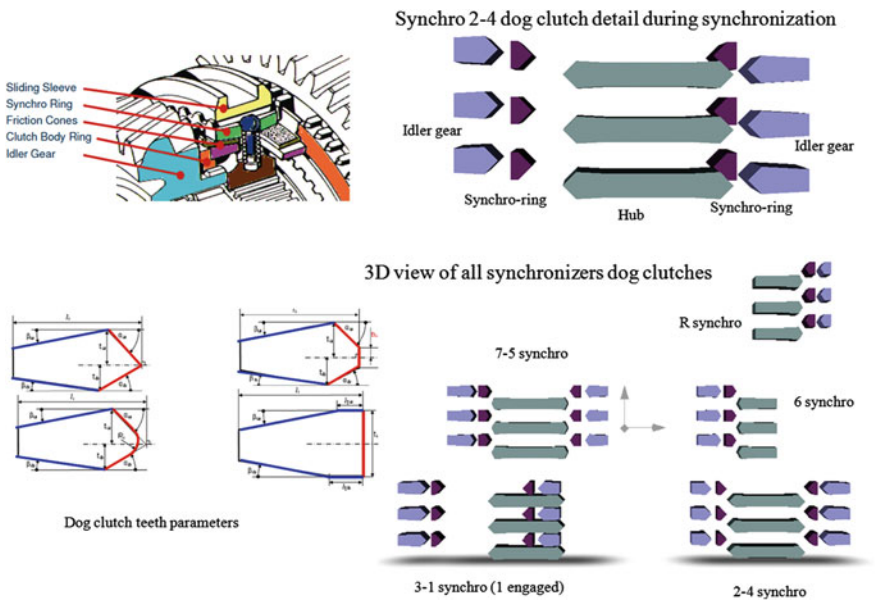
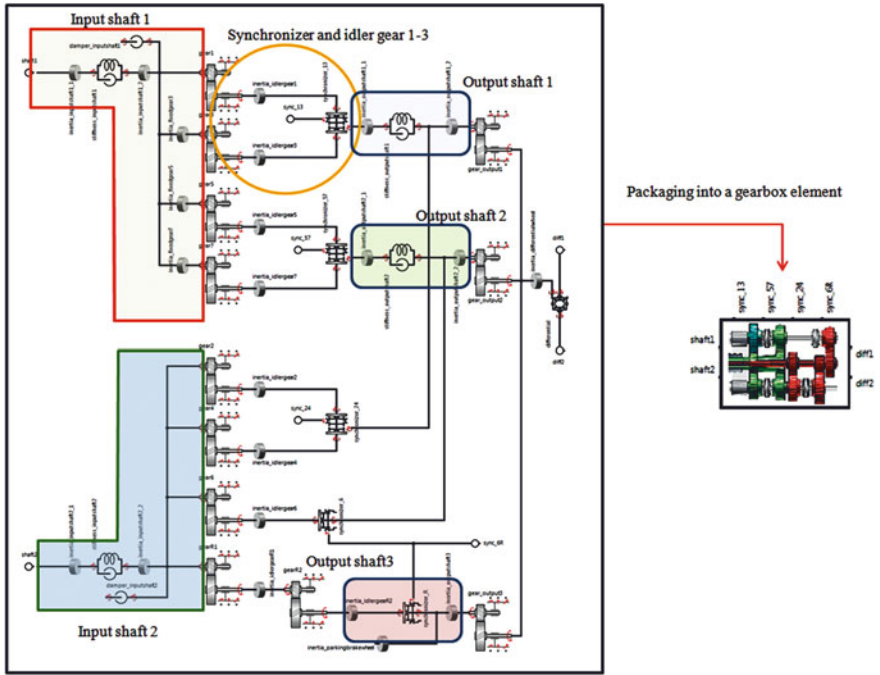


Fig. 1 Overview of synchronizer/dog clutch modelling

2.1.1 Shafts

According to the CAD drawings of the gearbox, the input and output shafts are discretized as 2 inertias and 1 stiffness. For the considered gearbox, such a model provides shafts eigenfrequencies above 500 Hz, which is high enough for the application.

2.1.2 Gears

Gear contacts are modelled based on the actual geometry of the gear teeth, including normal modulus, helix angle, common face width etc. The model automatically computes the resulting meshing stiffness from the provided geometry. Backlash and transmission error can also be included if we wish to perform a NVH (rattle/whine) analysis.

2.1.3 Synchronizers

The synchronizer models are based on the detailed geometry of the synchronizers, including friction cones and dog clutches. The synchronization process is simulated in a high fidelity manner and can reproduce effects such as engagement process with clashing. Details of synchronizer modelling can be found in [1, 2].

2.2 *Dual Clutch Model*

The clutch used in our application is a dry clutch. Dry clutches can be modelled with the following elements:

- On the actuator side, a non-linear spring with hysteresis for each clutch.
- On the friction element side, a table gives the normal press-on force as a function of actuator position.
- The friction element is a complex dry friction element with slipping/sticking coefficients that can have dependencies on speed and temperature.
- A clutch thermal model, based on a pseudo-1D thermal network.
- Non-linear rotary springs with friction and hysteresis (the “damper”).

Through simulation, it is usually not possible to obtain the characteristics for the actuator side non-linear spring, for the normal press-on force or for the friction coefficients. Supplier data and test data have to be provided as model parameters.

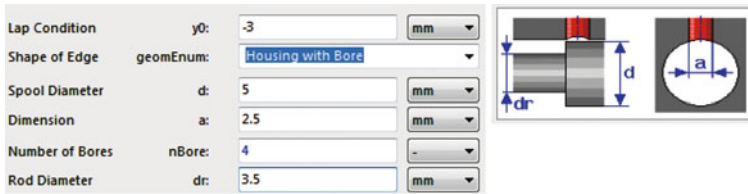


Fig. 2 Example of parameterization for a valve spool/housing geometry

2.3 Hydraulic Module Model

The hydraulic module is an independent module using its own hydraulic circuit and powered by an electrical pump. The gearbox actuators positions (synchronizers and clutches) are controlled by an arrangement of solenoid valves. The considered actuation system requires closed loop position controls for each synchronizer and each clutch. The hydraulic module performance is also well-known to be quite sensitive to oil temperature. A realistic and accurate model of the hydraulic module is very helpful for determining dynamic response of the actuators under different environmental conditions.

2.3.1 Detailed Solenoid Valve Models

The solenoid valves performance is a key factor in the overall dynamics of the actuation system. For this reason, a detailed model of each valve was created so that valves performances can be analyzed in depth. The detailed model takes into account the main relevant parameter for the design of such valves, as described in [3, 4]:

- Spool and housing geometry, as illustrated in the following Fig. 2
- Flow forces
- Laminar/turbulent regime, important to predict low temperature performance.
- Spring stiffness.
- Frictions.
- Solenoid iron geometry and coil properties as shown in the following Fig. 3.

Besides the detailed model, based on the geometry and internal characteristics of the valve, a functional model is also created with the objective of having simpler parameters sets and easier integration for Real-Time simulation with a fixed step solver. The functional model relies on characteristic curves defining each component's performance, such as outlet pressure/input current relationships. The details of Real-Time models are discussed in a further paragraph.

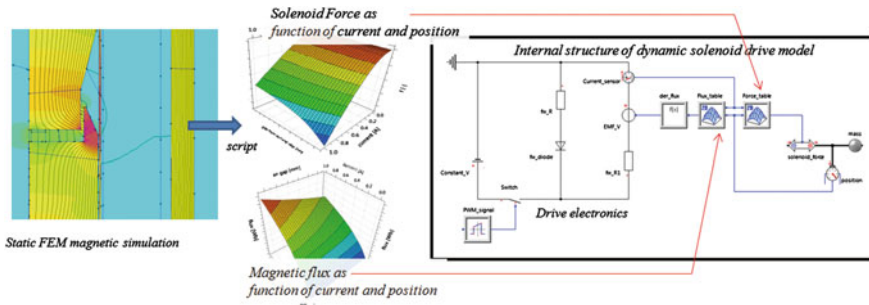


Fig. 3 Valve solenoid modelling from FEM to dynamic model

2.4 Engine, Vehicle and Driver Models

2.4.1 Engine and ECU

In this project, the focus is set on the gearbox simulation with the objective of providing an accurate plant model for supporting gearbox design and supporting Transmission Control Unit software development. In this frame, an engine model based on the engine torque map and engine inertia is assumed to be relevant. The torque is computed as a mean torque, even though it is possible to activate crank-angle torque excitations with a switch in the model. A fuel consumption map is also included in the model so that overall fuel efficiency on driving cycles such as NEDC can be evaluated.

The Engine Control provides important functions such as idle speed control, max speed control and, on request from the TCU, engine speed control mode or engine torque control mode. A starter motor is also added to simulate engine start situations. The Engine Control is implemented through a signal flow model and packaged into a SimulationX element.

2.4.2 Vehicle Model and Tyre Model

The vehicle modelling assumes a purely longitudinal motion, including rolling friction, aerodynamic drag and hill climbing resistances. A more sophisticated model is also possible by taking into account 2D or 3D dynamics and chassis/suspension parameters. The tyre model is based on the curve defining the slip ratio to the adherence coefficient and is fully parametric. This allows generating different road adherence conditions such as wet, snowy or dry road.

Vehicle inertias and tyres inertias are accounted for as rotary inertia or translational inertia.

A brake dry friction model is also added to the vehicle so that brake torque can be applied as a function of the driver brake pedal signal.

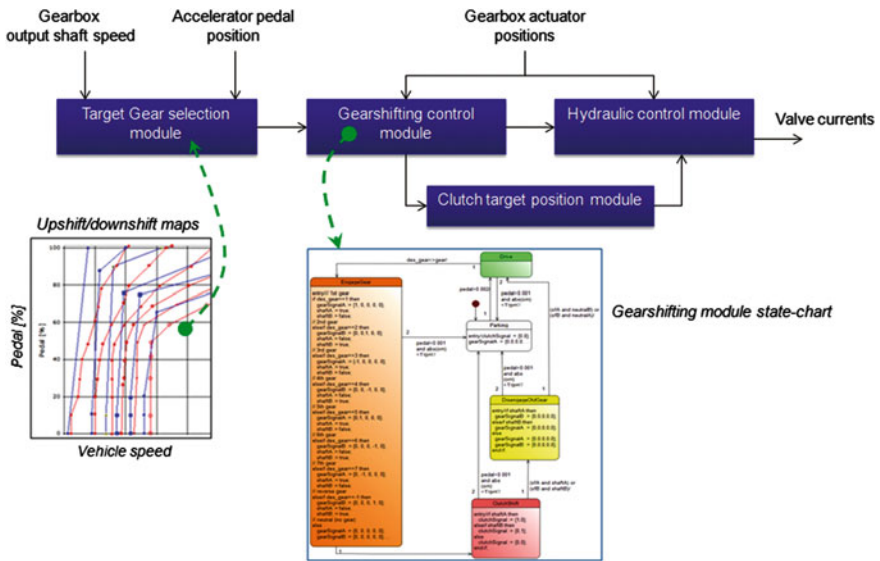


Fig. 4 Transmission control unit modules structures

2.4.3 Driver Model

The Driver model function is to follow a specified input speed profile (for instance NEDC). The driver model generates the necessary accelerator and brake pedal signals to follow this speed profile. The driver model can handle both, uphill or downhill road profiles. The driver model can also be bypassed so that accelerator or brake position can be provided as input.

3 Prototype Tcu and Controls

During the project, a prototype TCU model has been created for the considered gearbox. The main objectives of this work are:

- Pre-design and research on the high level control strategy of the DCT.
- Pre-design and research on low level closed loop position control for the hydraulic module.
- Overall powertrain model testing and validation.

The structure and main modules of this TCU logic are shown in the following Fig. 4.

The TCU model is based on a mix of signal flows and state-charts developed using the Statechart Designer of SimulationX.

4 Real-Time Models, Model Export

4.1 *Real-Time Constraints, Fixed Step Solvers and Model Simplification*

Real-time modelling requires using a fixed-step solver to provide quasi-deterministic CPU load in all conditions. However, using a fixed-step solver imposes constraints in the frequency content of the model. For instance a 1 ms time-step Euler solver could solve with a reasonable stability a model with a frequency content up to 50–100 Hz. The detailed model developed during the project contains high frequency dynamics (>5000 Hz). To solve such high-frequency dynamics, the time-step required is then so small that the solving process would be slower than real-time, even on a high performance CPU. It is then necessary to use models with smaller frequency content. To do so, the detailed model was simplified. The acausal modelling capability, along with the analysis tools of SimulationX are a great help in this process. For instance, it is possible to switch internal gearbox stiffness to “rigid” and remove thus high dynamics while keeping mostly the same model structure. Equations are automatically re-organized to gather the inertias into a larger lumped inertia. In a similar way, the hydraulic module is simplified by gathering volumes together and switching the detailed valves models to functional valve models.

Some components however require a drastic change in the model paradigm, such as the synchronizer, as explained below.

4.2 *Real-Time Synchronizers*

Even though ITI GmbH and Hoerbiger GmbH successfully created real-time applications based on complex detailed synchronizers models [2], we decided to adopt a simplified model for the current project. The real-time synchronizer model eliminates the high dynamics of the dog clutch contacts but can still reflect accurately a complete synchronization process, taking into account synchronization force, friction cones angles, friction cones diameters and drag torque influences from the gearbox. We give in the following Fig. 5 a comparison of synchronization process for identical conditions between the RT synchronizer model and the detailed synchronizer model.

An important feature of this synchronizer model is that the actuator force influence on the synchronization time is accurately represented. Since the considered gearbox uses closed-loop position control for the gearbox actuators, this link between actuator force and synchronization time must be taken into account if one wants to evaluate the quality of the actuator control.

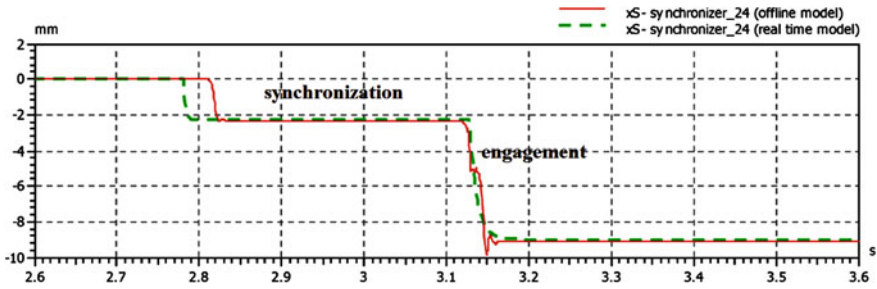


Fig. 5 Synchronization process, sleeve position: comparison of RT and detailed model results

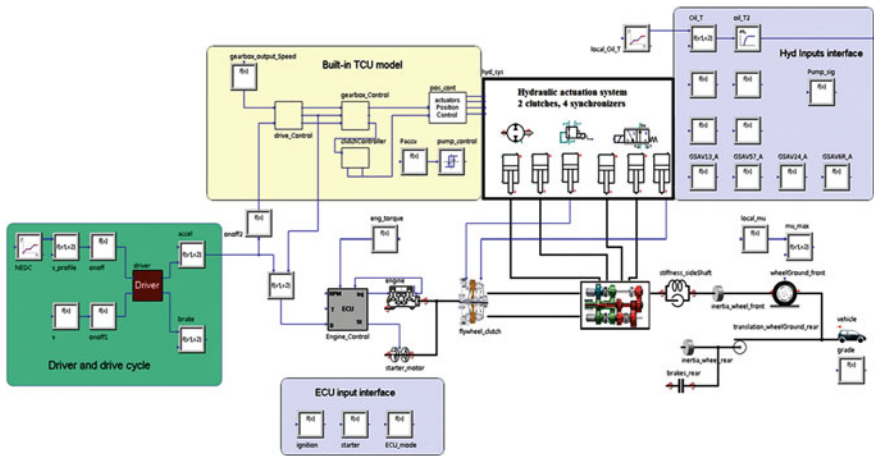


Fig. 6 Vehicle model with engine, gearbox, clutches, hydraulic actuators, TCU

4.3 I/O Interfaces and #Switch for Code Generation

In order to avoid multiple model versions, we implemented several switch features inside the SimulationX model. The concept of the switch is similar to `#ifdef` concept in C. For offline simulation, the SimulationX model will use the built-in TCU model. For code export/real-time simulation, the built-in TCU can be bypassed and signals provided from an external TCU can then be used instead. The advantage is that the plant model developer does not have to maintain multiple versions of his model; one model-source can be used for offline simulation and real-time simulation.

We provide the top-view of the overall model including I/O interfaces in the following Fig. 6

The results of RT model and detailed model are in excellent agreement. Only high frequency effects are neglected/smoothed, as shown in the following Fig. 7

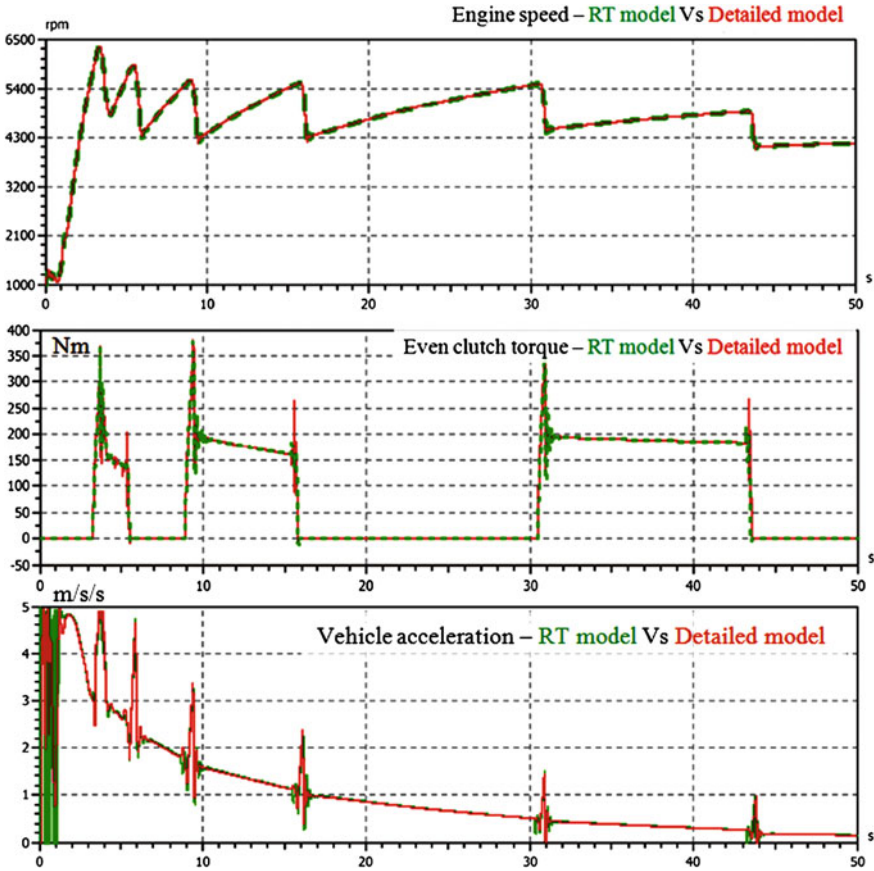


Fig. 7 Detailed model and real-time model results comparison on a 100 % throttle run

4.4 Real-Time Test in Ni Veristand, Real-Time Pxi With Pharlap Os

Finally, the model is compiled for a real-time target (NI Veristand) and real-time performance is validated. The model runs on 1 CPU core at around a 50 % load. This means that the plant model developed can be used for Hardware-in-the-loop tests (Fig. 8).

5 Applications, Gearshifting, Longitudinal Accelerations

Such model can be used for a large number of applications, including:



Fig. 8 PXI Real-time target, test system at global crown technology

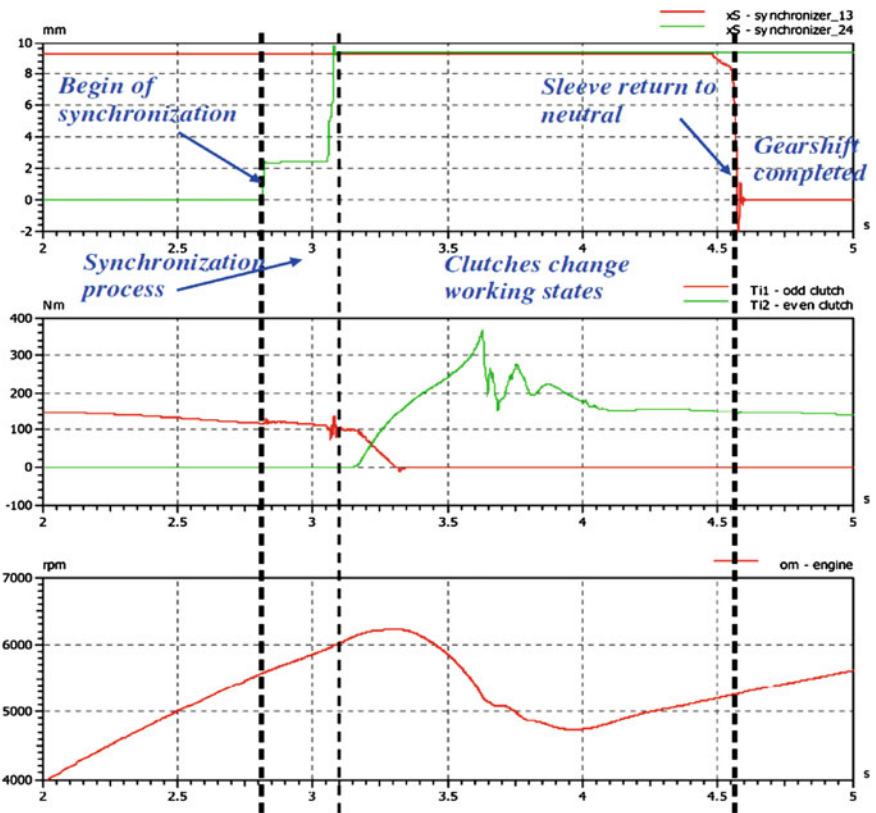


Fig. 9 Detail of a shift 1-2, full throttle. From top to bottom: synchronizers position, clutches torques, engine speed

- Gearshifting analysis, driveability and comfort [5].
- Clutch temperature management in traffic conditions, uphill launch.
- Hydraulic module design and selection.
- Fuel consumption analysis on driving cycles (NEDC).
- Control software testing and validation (MiL/virtual ECUs/HiL) [6, 7].
- Virtual pre-calibration [8].

In the following Fig. 9, we illustrate a simulated gearshifting process where the TCU, hydraulics, engine, driveline are coupled together into a complex system. The clutch control and the engine torque control must be calibrated in order to ensure different gearshift properties according to different driver request. For instance, at high accelerator pedal position, a fast gearshift is expected; at low accelerator pedal, a slower and smother gearshift can be accepted.

6 Conclusions

The modelling process for a DCT has been introduced, including prototype TCU, hydraulics, gearbox, synchronizers. This DCT model is coupled to a vehicle model with engine and EMS. The model can be used at different stages of the design process and for different purposes, from control strategy development to hydraulic module design. Based on this high frequency model, a real-time model has been derived that includes driveline modes up to 50 Hz. This model is suitable for Hardware-in-the-loop simulation, or for exporting as a s-function to Simulink (or other control development environments). Due to the preservation of fundamental dynamical effects in the real-time model it is able to reflect a physically correct transient behaviour and thus does not only permit pure functional testing on a HiL system (which is the typical scenario with standard models nowadays), but also the execution of pre-calibration tasks.

Using key features of the Modelica language (object-oriented, acausal/equation based, continuous-discrete models), it is possible to obtain high quality plant models that can be smoothly integrated into the development process of a new transmission.

References

1. Abel, Schreiber, Valsania, Fornelli (2005) Simulation based design of gearboxes for high-performance sports cars. Modena: 11th HTCES conference
2. Schreiber U, Todtermuschke K, Back O (2009) Experiencing and definition of the real shifting comfort at the virtual synchronizer in the virtual powertrain. CTI Innovative Automotive Transmissions symposium, Germany
3. Hudec (2010) Model-based virtual prototyping for early systems evaluation. Dresden: 13th ITI Symposium

4. Andersen (2003) Fluid power systems: Modeling and analysis. 2nd edn., Aalborg University
5. Schindler, Schreiber, Abel (2005) Improving shifting comfort quality by physical simulation of complete powertrains with non-stationary engine and transmission models. Berlin: 4th CTI Innovative automotive transmissions symposium
6. Chrisofakis Junghanns (2011) Simulation-based development of automotive control software with Modelica. Modelica international conference, Dresden
7. Tatar, Schaich, Breitingner (2010) Automated test of the AMG speedshift DCT control software, Berlin: 9th CTI Innovative automotive transmissions symposium
8. Bruckmann Strenkert (2009) Model-based development of a dual-clutch transmission using rapid prototyping and SiL. International VDI Congress Transmissions in Vehicles, Friedrichshafen

Optimized AMT Systems from ZF: A Choice for Comfort and Fuel Consumption Improvement in the Small Car Segment

Benedikt Schauder and Joerg Buhl

Abstract Automated manual transmissions show big advantages compared to other transmission types: They are the transmissions with the best efficiency (at least for lower and medium engine torques). And these transmissions are much more cost-effective than other automated transmission solutions like AT or DCT. However, the market penetration of these transmissions has stayed limited to small vehicles and light commercial vehicles due to comfort restrictions related to this transmission type: torque interruption and relatively long shifting times are criticized by many users of these vehicles. In the last years, ZF perceives a growing interest for AMT systems due to their low cost, low weight and small installation space. Therefore some optimizations have been done, in order to improve the comfort of the system without considerably increasing the costs. First step is to improve the electro-mechanic actuators in order to reduce shifting times and to increase robustness over lifetime. The next step is the optimization of the AMT software and functionality. New algorithms allow shorter shifting times, additional functions have been integrated. Out of the experience of former AMT and DCT projects, ZF has developed a new interface between engine and gearbox, leading to an improved shifting comfort. ZF is able to provide the whole AMT system including the TCU out of one hand, thus it is able to perfectly optimize the system to the customer's needs.

Keywords Automated manual transmission • Fuel economy • Small car segment • Improved driving comfort • Cost-effective solution

F2012-C04-015

B. Schauder (✉) · J. Buhl
ZF Friedrichshafen AG, Schweinfurt, Germany
e-mail: nong.zhang@zf.com

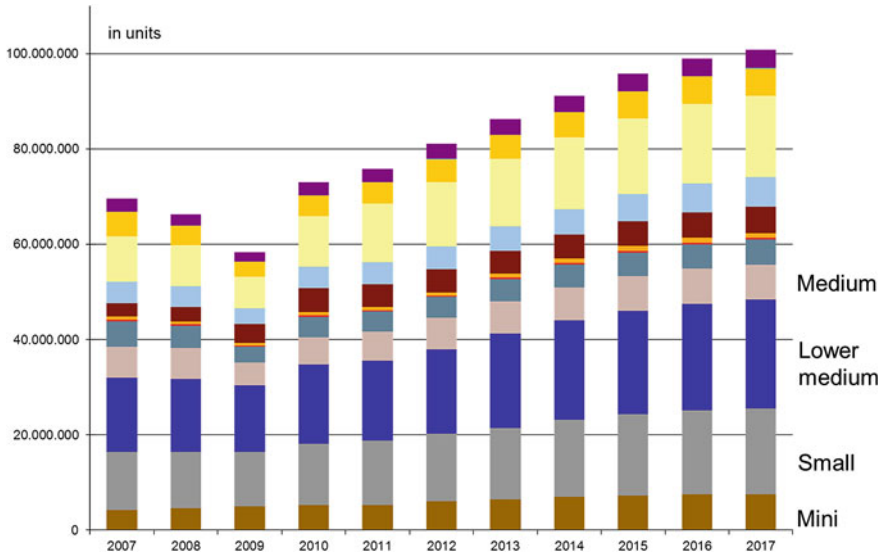


Fig. 1 World-wide vehicle production by segments [1]

1 Introduction

Today the world-wide automotive industry is facing some challenges in terms of reduction of fuel consumption and emissions. At the same time different markets require powertrains that can improve the driving comfort, especially when driving in huge megacities. Transmissions are an important part of these powertrains and can make a considerable contribution to fuel consumption and driving comfort. Many different transmission types like AT, CVT, DCT and AMT are available and compete in the various markets and vehicle segments. There is no ‘best’ solution for all markets and vehicle segments and the different transmission types will co-exist, but for the car manufacturers it is getting more and more important to make the right choice in order to reach their goals in terms of fuel efficiency, driving comfort, cost competitiveness and customer satisfaction.

In the following article we will deal with the small car vehicle segment, which is already very important and will have a sustainable world-wide growth in the next years as can be seen in Fig. 1.

This vehicle segment is underlying a strong cost competition since most of the potential buyers have only moderate incomes and often are first-time car owners. On the other hand these cars are often used in urban regions characterized by heavy city traffic.

The most cost-effective transmission solution would be the manual transmission (MT) which is a very common solution for the small car segment. The efficiency of MTs is excellent for the transmission itself. However, the driver has a strong influence on the real life consumption of the vehicle, since he selects the driving strategy. In city traffic MTs are often perceived as uncomfortable since the driver has to operate clutch and gearbox very often.

The classical automated transmission is the stepped automatic transmission (AT), typically using a torque converter as a launch element. This transmission type is largely used from lower medium up to luxury car segment and offers an excellent shift quality and driving performance. Modern AT transmissions reach excellent fuel efficiency ratings, but are too expensive and heavy for the small car segment.

The continuously variable transmission (CVT) is mainly used in Asia and also offers a very good driving quality. The efficiency of the transmission itself is worse than the MT's efficiency since the power transmission is operating with friction, which is the origin of some losses.

The newest type of transmission is the Dual Clutch Transmission (DCT) which also offers an excellent shift quality and driving comfort. But cost, weight and installation space are comparable to the AT transmission and therefore not suitable for the small vehicle segments.

We see, that all above mentioned automated transmissions have disadvantages that make them inappropriate for small vehicles, particularly due to high costs or lower efficiency.

The solution consists in preserving the advantages of the MT and in adding an automation that makes the driving strategy more independent of the driver and therefore helps to reduce the fuel consumption. The driver gets released from the clutch and gearbox operation and benefits from a much more comfortable driving under city conditions. This new transmission type is then called Automated Manual Transmission (AMT).

In the following, we would like to show how such a system looks like and what the technical advantages and challenges are.

2 System Overview

The base of the AMT is a manual transmission. In the small vehicle segment these transmissions generally exist and are produced in high volumes at low costs. ZF's philosophy is, to take advantage of these low costs and to use already existing MTs as a base for the AMT.

An actuator respectively for clutch and gearbox is added to the system (see Fig. 2). The control of the actuators is performed by the TCU (Transmission Control Unit). The clutch pedal is no longer needed and the gearshift lever is replaced by an electronic shifter. One additional sensor is needed for measuring the gearbox input shaft speed.

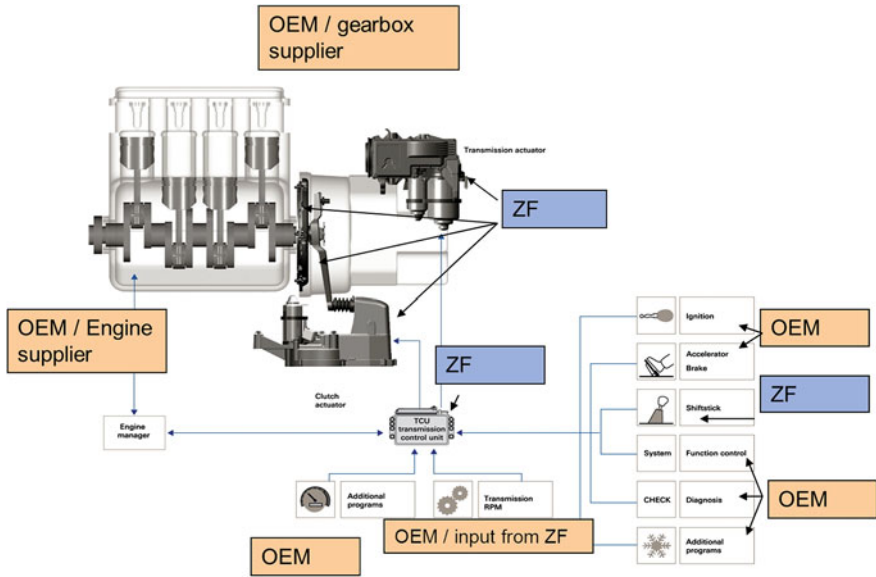


Fig. 2 AMT system overview

With these small changes it is possible to build-up an automated transmission system. Therefore ZF has designed the clutch and gear box actuator as an add-on solution.

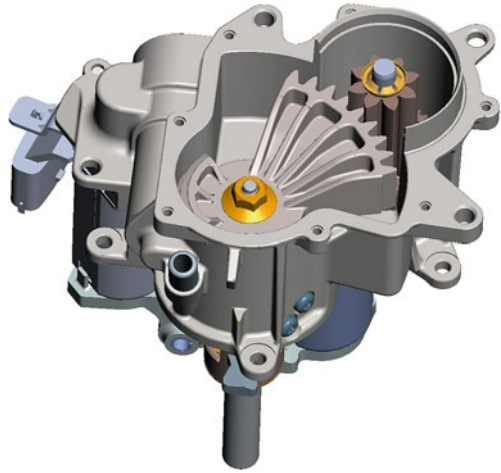
3 Disadvantages of an AMT System

In comparison with other automated systems like the DCT, CVT or AT there are some disadvantages on the AMT side.

These are

- Relatively long shifting time in combination with a torque interruption
- Shocks during shifting
- Insufficient spontaneity

However, with the new generation of AMT systems which were developed by ZF it was possible to improve the system performance in these points and to develop the best solution for small cars in the market.

Fig. 3 XY gear box actuator

4 Comparison Between Electro-Hydraulic and Electro-Mechanical Systems

There are two different AMT systems in the market. The electro-hydraulic solution is the first possibility to build-up an AMT system. This kind of system is mostly used for cars with a higher torque (>200 Nm), e.g. sports cars. The needed space for such a system is relatively big. Furthermore also its weight is relatively high, it is relatively complicated and expensive.

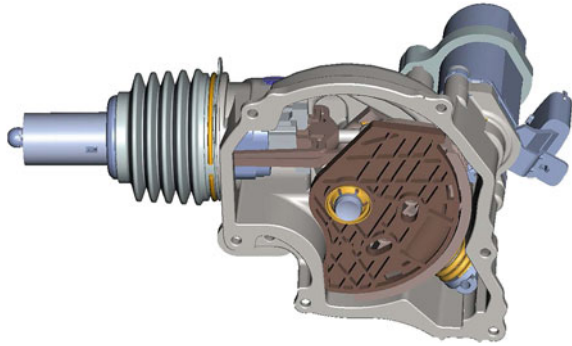
The second possibility is the electro-mechanical solution. This solution is used for cars with a torque up to 200 Nm. The electro-mechanical system works without any fluid and only with mechanical elements. It is not so complicated, more robust and more cost-effective.

ZF is developing electro-mechanical AMT components since the 1990s and has then started the first serial project. Therefore ZF has a lot of knowledge and experience about the mechanical parts and the software which is needed to build-up a well performing electro-mechanical AMT system.

5 Description of the Actuators

The new developed XY gear box actuator (see Fig. 3) is directly mounted on the gear box housing. The movement of the gear box actuator is transmitted from the actuator's shift shaft to the shift mechanism which is inside of the gear box housing. To shift and to select the gears with the actuator we need two DC motors. One engine is needed to generate the movement of the shift shaft for selection (longitudinal movement) and the other DC motor is needed to generate the movement for shifting (rotation of the shift shaft). The gear segments inside of the actuator are designed in

Fig. 4 Clutch actuator with compensation spring



plastic. With this new type of gear segments it was possible to reduce the inertia and to improve the shifting performance (e.g. 1 > 2 shifting in 100 ms without synchronisation). Furthermore it was possible to reduce the weight of such a gear box actuator by approximately 25 % compared to the first generation.

This new design and the new technology of gear segments make it possible to build-up an even more cost-effective gear box actuator.

The clutch actuator (see Fig. 4) is also directly mounted on the gear box housing. The actuator can work with a lever solution or with a fork. Both solutions are well known and in serial production. For actuation (opening/closing the clutch) only one DC motor is needed. Inside of the clutch actuator is located the so called compensation spring. This spring has two functions. The first one is to compensate the load which is given by the release load curve of the clutch (see Fig. 5). This means the compensation spring has to be designed especially for each clutch or family of clutches. The compensation of the clutch load is necessary to reduce the needed torque of the DC motor. By doing so, it is possible to use a smaller DC motor. This leads to a very cost-effective design. Furthermore the inertia of the DC motor will be also reduced which leads to an improved dynamic behaviour of the system. The time which is needed to open the clutch (closed position to touch point) is less than 100 ms. The accurate time depends on the clutch, the stroke from closed to touch point and the used compensation spring.

The second function of the compensation spring is to support the safety requirements. In case of a failure (e.g. broken wire in the cable harness) in the system, the clutch has to stay in the position where the failure occurs or has to open the system. This system is called normally stopped or normally opened. It is not permitted that the clutch gets closed, since this would be a security risk.

Three curves are shown in Fig. 5:

- The upper (red) curve shows the release load of the clutch during actuation
- The lower (orange) curve shows the force of the compensation
- The middle (blue) curve represents the resulting load which has to be actuated by the DC motor

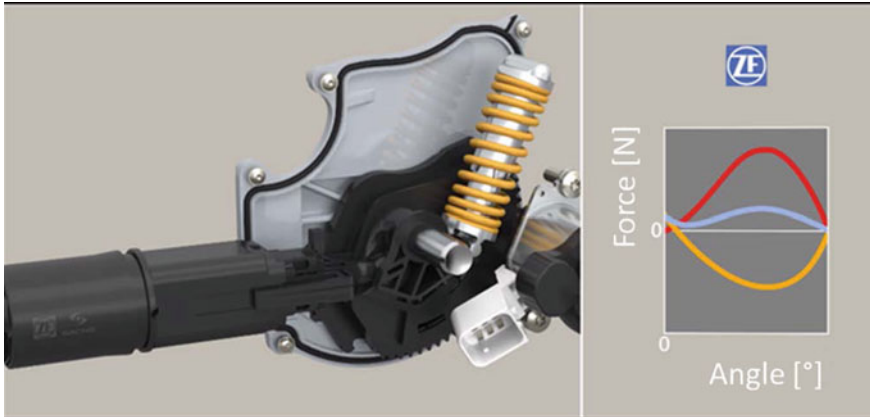
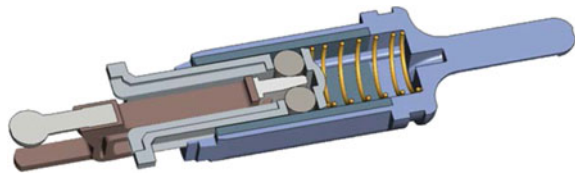


Fig. 5 Compensation spring and compensated release load

Fig. 6 Push rod with self adjustment



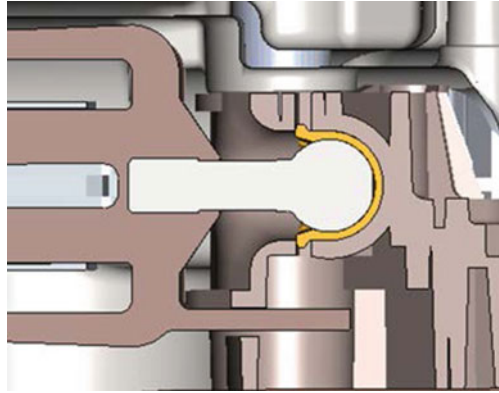
We see that the overcentre spring type characteristic of the compensation spring fits to the Belleville type characteristic of the clutch. The resulting forces are largely reduced compared to the original clutch characteristic.

In small cars the clutch cover assembly has no wear compensation device. Therefore it was necessary to develop a push rod for the clutch actuator which is able to compensate the wear of the clutch. Due to the clutch wear the position of the lever is moving continuously into the direction of the clutch actuator. As a result of this, the length of the push rod has to get shorter over life time. If the push rod was not able to compensate the clutch wear, the quality of shifting would get worse through the vehicle life and the transmittable torque of the clutch would get reduced. To guarantee a perfect shifting quality over life time and to work with the needed pre load, the so called “push rod with self adjustment” (see Fig. 6) was developed by ZF.

6 Performance Improvements

The requirements of the market for this kind of systems have increased continuously over the last years. The traffic in the cities is steadily growing, so is the number of actuations. This means it is necessary to open and to close the clutch frequently and creeping with the AMT system must be possible. Due to these heavy traffic

Fig. 7 Contact area push rod with steel pin



conditions in the cities, the higher numbers of actuations and the need for an improved shifting quality, the thermal stress for the DC motors has also increased.

In order to be more robust against thermal stresses and to guarantee a higher number of actuations, ZF has developed a new brush holder system for the DC motors. One step is the increased carbon volume inside of the DC motors. So it is possible to guarantee 1.5 Mio. load cycles for the clutch actuator compared to 1 Mio. load cycles for previous systems. The second step was to use a brush holder made out of metal instead of plastic. With this material change it was possible to improve the behaviour of the DC motors in high temperatures, which for example appear in traffic jam conditions.

To reach a higher number of actuations it was also necessary to rework some inner parts of the clutch actuator in order to reduce the wear of the system.

With the older systems, at end of life there could be considerable wear. This wear could lead to a loss of pre load or to a bad shifting performance. So the next big improvement is the reworked contact area of the push rod to the gear segment (see Fig. 7). In the newly developed clutch actuators ZF is using only metal parts in this area. By using the new design the wear could be reduced by more than 80 % after 1.5 Mio. load cycles.

Based on the positive experience from DCT applications which are also developed at ZF, it was possible to develop new algorithms for the AMT systems. With these new algorithms in combination with adaption/teach-in functions (e.g. clutch characteristic curve) the shifting comfort can be kept on a high level over the lifetime. Furthermore the shifting quality could be improved with the new algorithms, the new XY gear box actuator and the newly developed DC motors.

With this new system, the gear box actuator could operate faster than it is possible in the vehicle application due to gear box limits. These gear box constraints are noises during the shifting and the durability issues of the synchronizers.

As a last consequent step ZF has developed a platform TCU to optimize the AMT system. This new TCU can be used for different customers/projects. Because of the platform design the new TCU is very cost-effective, both in piece price and

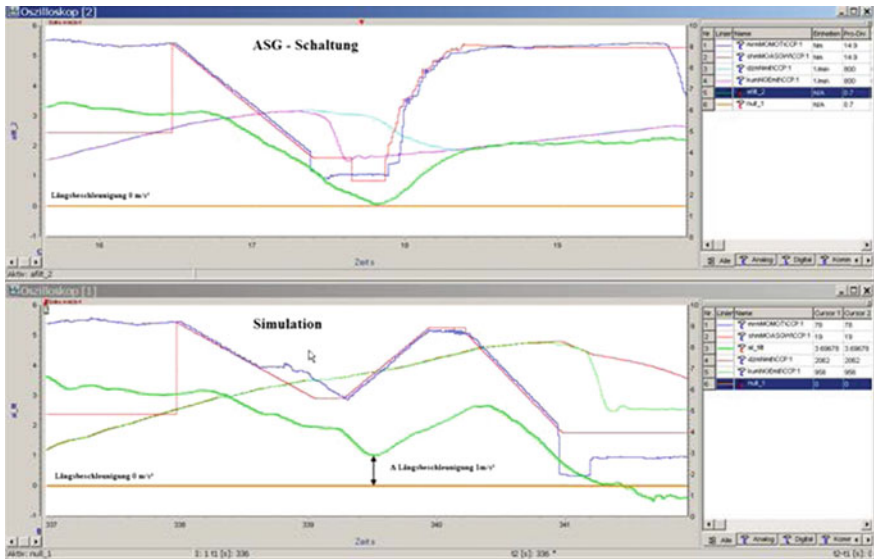


Fig. 8 1st and 2nd high load up shift sequence (comparison AMT shift with AMT support shift) [2]

development cost. The TCU works with high performance controllers (e.g. 2 MB Flash, 120 MHz frequency) to handle the new software algorithms.

7 Combination with Hybrid Systems

One big demand out of the market is the reduction of fuel consumption and CO2 emission. Current AMT applications are often equipped with start and stop systems to reach these targets. With such a system in combination with AMT it is possible to achieve a fuel consumption reduction by approx. 10 %, especially under city traffic conditions.

ZF is also studying full hybrid AMT powertrain solutions for the future. Such a technical concept offers the possibility to compensate or to minimize the torque interruption during shifting. The idea behind this concept is to fill-in the loss of torque during shifting with the torque from an electrical motor. The first results are looking promising in terms of improved shifting performance, cost and hybrid functionality. In particular for the small and middle class segment such a powertrain will be very attractive due to the reachable performance. The following curve (see Fig. 8) of the vehicle acceleration shows the potential of this technology. The above measurement shows the AMT system only. A torque interruption during shifting is noticeable.

The second measurement has been made with the same car (the mode of operation of the hybrid AMT system has been simulated) and shows the same up

shift under the same conditions. A sufficient longitudinal acceleration of the vehicle remains during the shifting operation. The driver's perception of the shift quality is much better.

8 Outlook

ZF is currently working on solutions for the next generation of AMT systems. Because of the increasing requirements of higher number of actuations, faster actuations and higher release loads of the clutches for small cars and the demand for AMT systems for light commercial vehicles there is a need for new electrical motors. Therefore ZF is working on BLDC motors with a reduced inertia to be faster while opening and closing the clutch. Furthermore the lifetime of a BLDC motor is much higher than the lifetime of a DC motor, because there is no carbon inside of a BLDC motor which is subject to wear. Another big advantage of a BLDC motor is the higher torque in combination with smaller dimensions compared to a DC motor with the same torque. But BLDC motors will considerably increase the system cost, therefore they will only be used in more expensive powertrains.

9 Conclusion

In the last years ZF has perceived a growing interest in AMT systems for small cars. Cost and fuel economy challenges make the system very attractive for this quickly growing- vehicle segment. Transforming an existing MT into an AMT by adding ZF's AMT components is the best and most cost-effective way to the automation of a small car. ZF can deliver all components and the software out of one hand—therefore the integration into the vehicle platform is very easy.

The second generation of AMT components has been developed and offers improved driving comfort and increased robustness in order to respond to the needs of customers in big cities.

In combination with a start/stop system or a hybrid drive further fuel savings and comfort improvements are possible.

References

1. ZF-Procast (2012) Production forecast automotive, ZF Friedrichshafen AG, Germany
2. Matthias H (2010) AMT today and for the future. VDI Wissensforum GmbH. internationaler VDI-Kongress Getriebe in Fahrzeugen. VDI-Berichte 2081. pp 343–354

Shifting Control Strategy Research in the Hard Accelerating Condition Based on the AMT Vehicle

Yang Gao, Yong Chen, Daguo Luo, Wenzhong Liu, Mingqi Gu
and Fuquan Zhao

Abstract This paper presents the gear optimization control strategy of the automated mechanical transmission (AMT) vehicles in the acceleration condition, analyzes the down shifting principle of the AMT vehicles in the acceleration condition, and establishes the in-loop simulation platform of the automatic transmission with Matlab/Simulink software. Further, the condition that the driver stepped on the accelerator pedal suddenly when the vehicle does not slow down the speed is simulated with the optimization control strategy and the traditional control strategy respectively. The results show that the proposed optimization control strategy can identify the driver's intention and reduce the shift times and the power break time, thereby improving comfort ability, and making the vehicle achieve the maximum speed faster.

Keywords AMT · Hard acceleration · Control strategy · Simulation platform

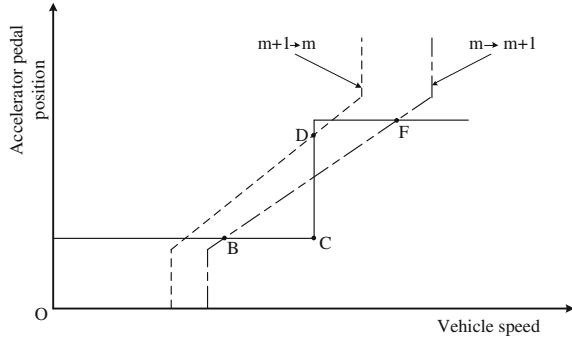
1 Introduction

The target gear of the tradition AMT shift schedule is determined according to the throttle and the speed, which can make the vehicle work in a better power and economy condition [1]. When the driver increases throttle opening suddenly, the transmission control unit will make the engine work in reasonable conditions according to the shift schedule curve. At this time, the transmission target gear will be lower. If it is not restricted the vehicle will take the state that it downshifts and

F2012-C04-016

Y. Gao (✉) · Y. Chen · D. Luo · W. Liu · M. Gu · F. Zhao
Zhejiang Geely Automobile Research Institute Co. Ltd, Hangzhou, China
e-mail: auto_gaoyang@163.com

Fig. 1 Downshift process of the hard accelerating condition



then rises to the original gear immediately. If it is shifted according to the target gear, the ground gained traction will be increased. But the AMT power interruption time will also be increased. The power interruption time is too long to satisfy the driver's intentions, which also reduces the power, the economy, and the transmission life. According to analysis of the transmission downshift principle in the accelerating conditions and estimation of whether the shift is reasonable, it presents the gear optimization control strategy of the automated mechanical transmission (AMT) vehicles in the accelerating condition. The software in-loop simulation platform of the automatic transmission was built with Matlab/Simulink software. The correctness of the proposed control strategy is verified by the simulation results.

2 Downshift Principle in the Accelerating Conditions

At present, a two-parameter shift schedule determined by the throttle opening and the vehicle speed is mainly used in automatic transmission. The shift process in the hard accelerating condition is shown in Fig. 1. When the vehicle speed rises to the point C and the driver steps on the accelerator pedal suddenly, the transmission will downshift because it goes across the current downshift curve. The driving force will increase after downshifting. But the power break time is too long during the shift process of the AMT vehicle. The transmission will also upshift when the vehicle speed arrives to the upshift point. So the shift in the hard acceleration condition will not always increase the power.

3 Optimization Control Strategy

It is an assumption that the wheel slip is neglect, the average wheel edge speed is equal to the vehicle speed, and the target vehicle includes six forward gears.

The outputting driving force of the engine can be calculated using the equation below:

$$F_{drive} = \frac{\eta * i_g * i_0 * (T_e - \frac{i_g * i_0}{R} \dot{v} * I_e)}{R}$$

In this equation:

- η Transmission gear efficiency;
- i_g Transmission speed ratio;
- i_0 Differential speed ratio;
- T_e Engine torque;
- R Average rolling radius of the wheel;
- \dot{v} Vehicle acceleration;
- I_e Engine inertia.

The resistance sum except the slope resistance can be calculated using the equation below:

$$F_{resistance} = \frac{1}{2} * \rho * C_D * A * v^2 + f_r * M * g + \frac{\dot{v} * I_{all_on_wheel} * i_0^2}{R^2}$$

In this equation:

- ρ Air density;
- C_D Coefficient of air resistance;
- A Effective frontal area of the vehicle;
- v Vehicle speed;
- f_r Coefficient of rolling resistance;
- M Fully loaded mass;
- g Acceleration due to gravity;
- $I_{all_on_wheel}$ Total vehicle wheel inertia.

The expected acceleration can be calculated using the equation below:

$$a_{exp} = \frac{F_{drive} - F_{resistance}}{M}$$

The broad-based slope resistance can be calculated using the equation below:

$$F_{slope} = M * (a_{exp} - \dot{v})$$

It is an assumption that the slope resistance is fixed during the modifying process. The acceleration can be calculated using the equation below:

$$\dot{v} = \frac{F_{drive} - F_{resistance} - F_{slope}}{M}$$

$$= \frac{\frac{\eta * i_g * i_0 * (T_e - \frac{i_g * i_0 * \dot{v} * I_e}{R})}{R} - \left(\frac{1}{2} * \rho * C_D * A * v^2 + f_r * M * g + \frac{\dot{v} * I_{all_on_wheel} * i_0^2}{R^2} \right) - F_{slope}}{M}$$

The acceleration function of the hard accelerating condition can be calculated using the equation below:

$$\dot{v} = f(\eta, i_g, T_e, I_{all_on_wheel})$$

The initial acceleration function keeping the current gear can be calculated using the equation below:

$$\dot{v}_{currentgear} = f(\eta_{currentgear}, i_{g_currentgear}, T_{e_currentgear}, I_{all_on_wheel_currentgear})$$

In this equation:

- $\eta_{currentgear}$ Transmission gear efficiency of the current gear;
- $i_{g_currentgear}$ Transmission speed ratio of the current gear;
- $T_{e_currentgear}$ Engine torque of the current gear;
- $I_{all_on_wheel_currentgear}$ Total vehicle wheel inertia of the current gear.

The initial acceleration function after changing to the target gear can be calculated using the equation below:

$$\dot{v}_{desiredgear} = f(\eta_{desiredgear}, i_{g_desiredgear}, T_{e_desiredgear}, I_{all_on_wheel_desiredgear})$$

In this equation:

- $\eta_{desiredgear}$ Transmission gear efficiency of the target gear;
- $i_{g_desiredgear}$ Transmission speed ratio of the target gear;
- $T_{e_desiredgear}$ Engine torque of the target gear;
- $I_{all_on_wheel_desiredgear}$ Total vehicle wheel inertia of the target gear.

When the target gear is current-1, the vehicle speed function keeping the current gear can be calculated using the equation below:

$$v_{currentgear} = v_0 + \int_0^{t_{currentgear}} \dot{v}_{currentgear} dt$$

In this equation:

- v_0 Initial vehicle speed;
- $t_{currentgear}$ Time during the current gear.

It is an assumption that the outputting average driving force of the engine is F_{shift} at shifting.

The action speed function of changing to the target gear can be calculated using the equation below:

$$v_{desiredgear} = v_0 + \int_0^{t_{downshift}} \frac{F_{shift} - F_{resistance} - F_{slope}}{M} dt + \int_{t_{downshift}}^{t_{upshift}} \dot{v}_{desiredgear} dt + \int_{t_{upshift}}^{t_{desiredgear}} \frac{F_{shift} - F_{resistance} - F_{slope}}{M} dt$$

In this equation:

- $t_{downshift}$ Downshift time;
- $t_{upshift}$ Upshift time;
- $t_{desiredgear}$ the time that it rises to the target gear.

The vehicle speed is v_f on the F point. If $v_{currentgear} = v_f$ then, $t_{currentgear} = t_{d1}$. If $v_{desiredgear} = v_f$ then, $t_{desiredgear} = t_{d11}$.

Using above method, the values can be calculated (Gdes is the desired gear; Gcur is the current gear; Gcom is the commanded gear.). If Gdes = Gcur - 2, the time that does not execute downshift is t_{d2} , the estimated time is t_{d21} executing Gcom = Gcur - 1, the estimated time is t_{d22} executing Gcom = Gcur - 2. If Gdes = Gcur - 3 the time that doesn't execute downshift is t_{d3} , the estimated time is t_{d31} executing Gcom = Gcur - 1, the estimated time is t_{d32} executing Gcom = Gcur - 2, the estimated time is t_{d33} executing Gcom = Gcur - 3. If Gdes = Gcur - 4 the time that doesn't execute downshift is t_{d4} , the estimated time is t_{d41} executing Gcom = Gcur - 1, the estimated time is t_{d42} executing Gcom = Gcur - 2, the estimated time is t_{d43} executing Gcom = Gcur - 3, the estimated time is t_{d44} executing Gcom = Gcur - 4. If Gdes = Gcur - 5 the time that doesn't execute downshift is t_{d5} , the estimated time is t_{d51} executing Gcom = Gcur - 1, the estimated time is t_{d52} executing Gcom = Gcur - 2, the estimated time is t_{d53} executing Gcom = Gcur - 3, the estimated time is t_{d54} executing Gcom = Gcur - 4, the estimated time is t_{d55} executing Gcom = Gcur - 5.

The method of the optimization project is shown in Table 1. The building process of the optimize shift control strategy [2-4] is shown in Fig. 2. Dkd is the accelerator pedal position gradient; HardAccPedGradient is the limit of the accelerator pedal position gradient; Kd is the accelerator pedal position; PedalHigh is the upper limit of the accelerator pedal position; PedalLow is the lower limit of the accelerator pedal position; and Review Timer is the waiting timer state. Gdes is the desired gear; Gcur is the current gear; and Gcom is the order gear.

4 Software-in-the-Loop Simulation Platform

A built vehicle transmission system software in- loop simulation platform with Matlab/Simulink software is shown in Fig. 3. The simulation platform mainly includes the vehicle model and the control strategy model. Kd_pad is the

Table 1 Method of the optimization project

	Preselect time (s)						Optimization project
	No shift	Drop 1 gear	Drop 2 gear	Drop 3 gear	Drop 4 gear	Drop 5 gear	
Gdes = Gcur - 1	t_{d1}	t_{d11}	-	-	-	-	$\text{Min}(t_{d1}, t_{d11})$
Gdes = Gcur - 2	t_{d2}	t_{d21}	t_{d22}	-	-	-	$\text{Min}(t_{d2}, t_{d21}, t_{d22})$
Gdes = Gcur - 3	t_{d3}	t_{d31}	t_{d32}	t_{d33}	-	-	$\text{Min}(t_{d3}, t_{d31}, t_{d32}, t_{d33})$
Gdes = Gcur - 4	t_{d4}	t_{d41}	t_{d42}	t_{d43}	t_{d44}	-	$\text{Min}(t_{d4}, t_{d41}, t_{d42}, t_{d43}, t_{d44})$
Gdes = Gcur - 5	t_{d5}	t_{d51}	t_{d52}	t_{d53}	t_{d54}	t_{d55}	$\text{Min}(t_{d5}, t_{d51}, t_{d52}, t_{d53}, t_{d54}, t_{d55})$

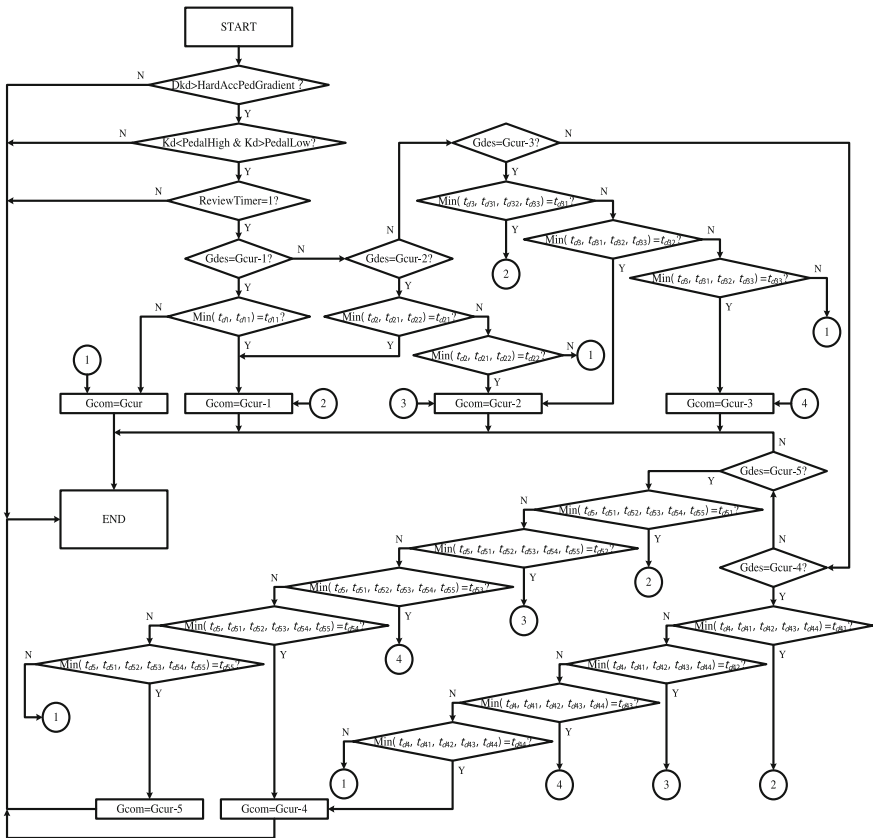


Fig. 2 Flow of the optimize shift control strategy

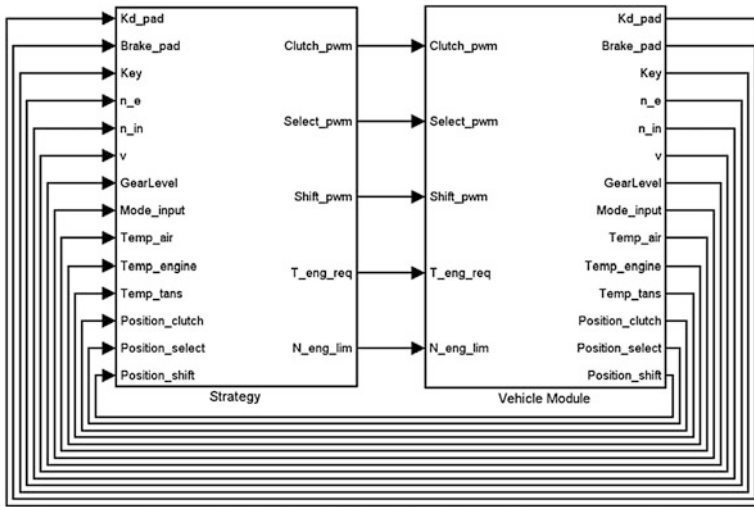


Fig. 3 Simulation platform interface

accelerator pedal position; Brake_pad is the brake pedal position; Key is the ignition switch; ne is the engine speed; n_in is the input shaft speed; v is the vehicle speed; GearLevel is the gear level position; Mode_input is the mode signal; Temp_air is the air temperature; Temp_engine is the engine temperature; Temp_tans is the transmission temperature; Position_clutch is the clutch position; Position_select is the select gear position; Position_shift is the shift gear position; Clutch_pwm is the control signal of the clutch actuator motor; Select_pwm is the control signals of the select gear motor; Shift_pwm is the control signals of the shift gear motor; T_eng_req is the engine requiring torque; and N_eng_lim is the engine speed limit.

5 Simulation Analysis

The vehicle equipped with automatic mechanical transmission and electronically controlled engines is taken as the study object. The conditions that the driver stepped on the accelerator pedal suddenly using the optimal control strategy and the traditional control strategy are simulated respectively on the built drive system software in- loop simulation platform [5, 6]. The Simulation conditions includes the initial speed 19.8 km/h, the first gear transmission ratio 6.194, the second gear transmission ratio 3.894, the third gear transmission ratio 2.260, the fourth gear transmission ratio 1.428, the fifth gear transmission ratio 1.000, the sixth gear transmission ratio 0.780, the transmission initial gear of the third gear, the rolling resistance coefficient 0.02, the road ramp angle 0 rad, and the head-on wind speed 0 km/h. The accelerator pedal position is defined in Fig. 4.

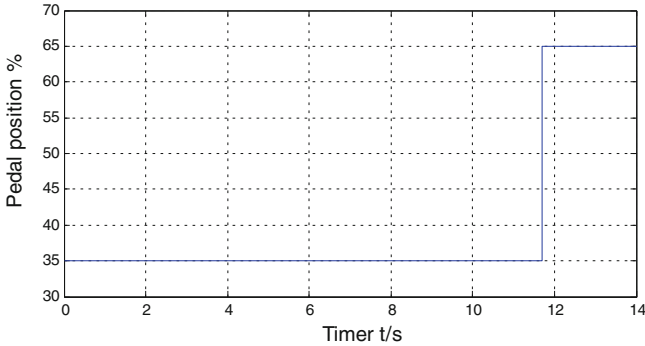


Fig. 4 Accelerator pedal position

Figure 5 shows the simulation curve that the vehicle speed, the current gear and the estimated time change with the acceleration time for the traditional shift schedule. t_{d1} is the estimating time when it does not downshift. t_{d11} is the estimating time when it reduces one gear. Figure 6 is the simulation curve that the vehicle speed, the current gear and the estimated time change with the acceleration time for the optimize shift schedule. From Fig. 5 it can be seen that the vehicle speed is 27.5 km/h when increasing the throttle suddenly and the transmission has been promoted to the fourth gear before the accelerator pedal position increases, the increased accelerator pedal position is 65 %, the transmission drops to the third gear from the fourth gear, the vehicle speed arrives at 29.2 km/h after 14 s accelerating. From Fig. 6 it can be seen that the vehicle speed is also 27.5 km/h when increasing the throttle suddenly and the transmission has been promoted to the fourth gear before the accelerator pedal position increases, the increased accelerator pedal position is 65 %, the transmission does not downshift, vehicle speed arrives at 29.6 km/h after fourteen seconds of acceleration.

The simulation results show that using the proposed optimal control strategy the driver intention can be identified, the shift times and the power break time will be reduced thereby, the comfort ability is improved, and the time that the vehicle achieves the maximum speed is reduced visibly after increasing the accelerator pedal position suddenly in the same condition.

6 Conclusion

The gear optimization control strategy of the AMT vehicles in the acceleration condition was presented according to analysis of AMT vehicles downshifting principle in this condition. The traditional control strategy is to compare with the optimal control strategy according to the simulation results from the software in-loop simulation platform of the vehicle transmission system. The results show that

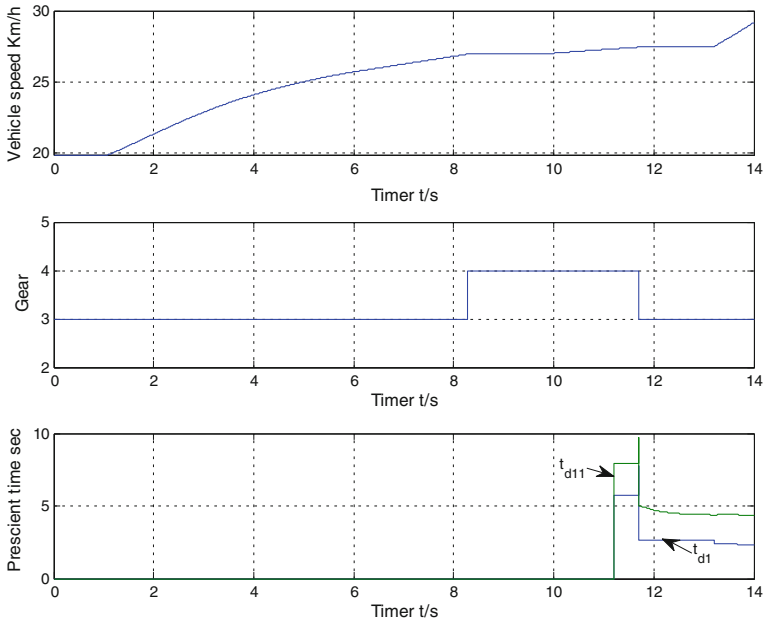


Fig. 5 Simulation curve of the traditional control strategy

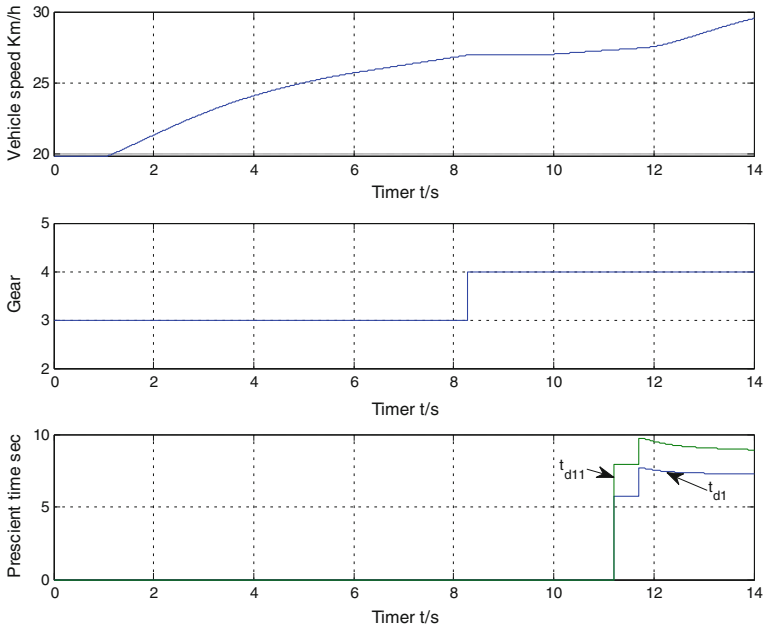


Fig. 6 Simulation curve of the optimize control strategy

the proposed optimization control strategy can identify the driver's intention, reduce the power break time and enhance comfort ability. The simulation results also verify the validation and the advantages of the proposed control strategy.

References

1. Yang Gao, Yong Chen, Daguo Luo et al. (2011) Optimization study of automatic transmission power shift schedule [C]. Mech Autom Control Eng MACE2011, pp. 5094–5097
2. Tai Zhang, Anlin Ge, Chunxue Tang et al (2007) A study on shift schedule of off-road vehicle with TC and AMT. Autom Eng 29(3):226–229,249 In Chinese
3. Guo Xiang en1, Li Yan (2009)Study on dynamic shift schedule of construction vehicle. J Wuhan University Technol (Transportation Science and Engineering), 33(5): 839-842(In Chinese)
4. Yue-hang DONG, Cheng-liang YIN, Li CHEN et al (2009) Optimal torque control strategy of electric transmission driver based on AMT during gear shift. J Shanghai Jiaotong University 43(2):217–221 In Chinese
5. Yuhai Wang, Jian Song and Xingkun Li Simulation of AMT autoshift process based on Matlab/Simulink/Stateflow[C]//SAE Paper 2004-01-2055
6. Xiaofeng Yin, Jingxing Tan, Yulong Lei et al. Combined control strategy for engine rotate speed in the shift process of automated mechanical transmission[C]//SAE paper 2004-01-0427

Robust Design Method for Automatic Calibration of Automatic Transmission Shift Control System

Ryoichi Hibino, Tomohiro Miyabe, Masataka Osawa
and Hideaki Otsubo

ABSTRACT Recently, automatic transmissions have a problem whereby the calibration of control signals for the shift control system demands an enormous amount of time due to the increase in gear ratio. This study proposes the hierarchical and inverse directional design method in order to avoid a lot of trial and error in calibration. This method has two model-based processes: the first is the design of the target driving torque and the second is the control signals design based on the target. Through on-vehicle tests our proposed method has the same performance as the conventional one.

Keywords Power transmission · Automatic transmission · Robust design · Hierarchy · Inverse directional design

1 Introduction

Recently, automatic transmissions in passenger cars have provided a large number of steps (eight-speed (1) and nine-speed) and a wide ratio to achieve better drivability performance and better fuel efficiency. There is, however, a problem whereby the calibration of control signals for the shift control system demands an enormous amount of time because the increase in the number of steps results in an

F2012-C04-020

R. Hibino (✉) · T. Miyabe · M. Osawa
Toyota Central R&D Labs Inc, Nagakute, Japan
e-mail: hibino@mosk.tytlabs.co.jp

H. Otsubo
Toyota Motor Corporation, Toyota, Japan

increase in the number of shift patterns [1, 2]. Formerly, simulation-based calibration was often recommended as a solution, but was not essential, because the empirical calibration process in bench and vehicle tests was only adopted in the computer. The objective of this study is the development of a systematic calibration process that avoids a lot of trial and error.

2 Concept Proposal

Figure 1 shows the problem of the empirical calibration process. When people adjust the control signals based on changes in driving force, acceleration, shift time and engine revolution speed, they encounter characteristic variations and nonlinearities which make calibrations difficult. For example, the hydraulic system has variations of response speed due to oil temperature changes, characteristic variations of control valves in the manufacturing, and clearance variations of the clutch pack, which cause shift shock in initial clutch engagement. An example of nonlinearities is a response speed change of oil pressure due to the difference between flow control mode and oil pressure control mode in the hydraulic system. Therefore the shift quality for the characteristic variations are guaranteed by the robustness of control signals which are made from past experiences.

In this study the above mentioned calibration process is replaced with the next design problem. If a time series pattern of driving force which satisfies all shift requirements exists and this pattern still satisfies the requirements in the conditions where characteristic variations of disturbances exist, this pattern is considered to be a robust target pattern. Also the control signal calculated inverse-directionally from the robust driving force pattern is considered to be a robust signal. That is, as shown in Fig. 2, the robust and systematic calibration (generation of control signals) can be achieved by the process, in which firstly the robust driving force patterns (which are the same as the output torque patterns) are calculated, and secondly control signals are generated from the patterns. Furthermore, in this process, nonlinearities can easily be treated with the models containing nonlinearities.

It is difficult to prove the above-mentioned idea. However, for example, target output torque pattern 2 shown in Fig. 3, which has a long shift time, tends to have low sensitivity for dead time Δt of oil pressure response in the hydraulic system. As a result, it can be considered that the control signal of oil pressure, which has small change over time, is the robust pattern for disturbances.

In the next chapter we discuss a hierarchical and inverse directional design method which consists of two model-based processes; the design of target driving torque and the control signals design of oil pressure and engine torque based on the target torque.

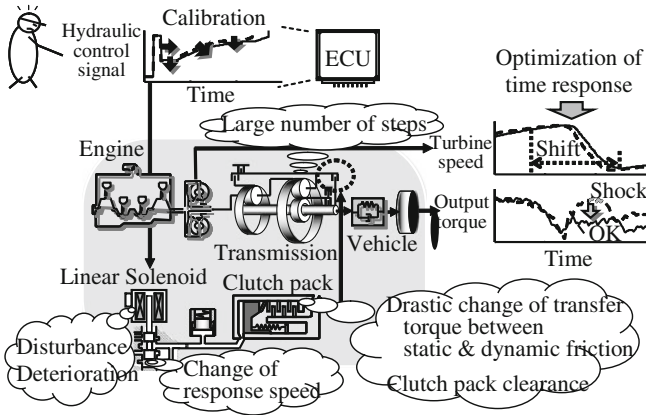
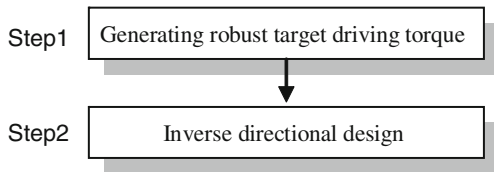


Fig. 1 Problem to be solved

Fig. 2 Concept of robust design



3 Generation of Target Patterns

3.1 Shift Action and Flow of Power

First, we pick up an example of 2–3 up shift, and explain the shift action. The 2nd clutch is released, and the 3rd clutch is engaged. Therefore the transmitted pass of engine power is changed and a pair of meshing gears is switched to another. The clutch release or engagement is controlled by each clutch hydraulic system. Figure 4 shows a time series of the oil pressure, torque and revolution speed of each part during the shift.

In the figure, lines of nominal and disturbed conditions are each shown by solid and dashed lines. The clutch transmitted torque is switched from 2nd clutch to 3rd following an increase of the oil pressure of the engaged clutch. Here the oil pressure of the released clutch is controlled to zero at the moment when all torque is switched to the 3rd clutch (end of torque phase). If the timing of the clutch release is too early the engine revolution speed increases quickly, and in the case of late timing a shock occurs. At this point the turbine revolution speed is still equal to 2nd synchronizing speed ω_{o2} (Fig. 4). Therefore the oil pressure of the engaged clutch is increased further so that the revolution is decreased to 3rd synchronizing speed ω_{o3} (inertia phase). The inertia phase (shift) is completed at the time when the turbine revolution speed is equal to the 3rd synchronizing speed.

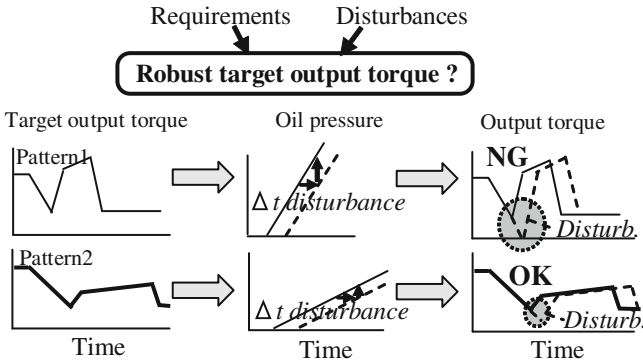
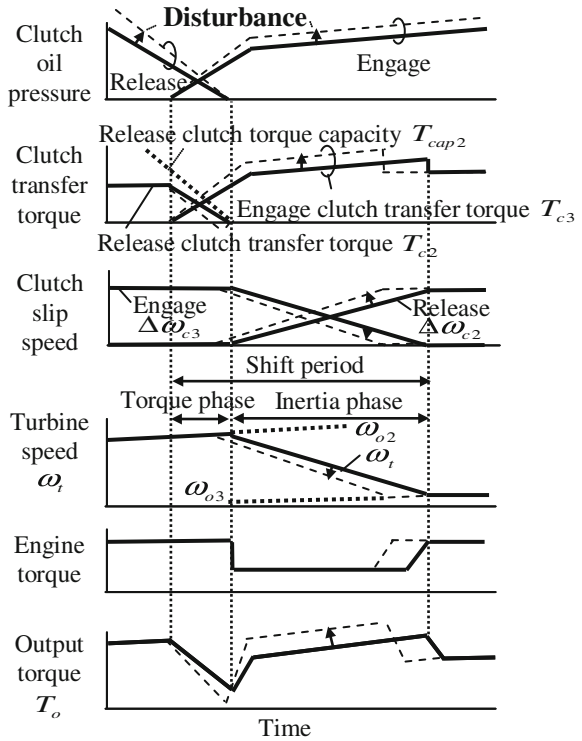


Fig. 3 Idea of robust design

Fig. 4 Time series of 2-3 up-shift



In the inertia phase the engine torque besides the oil pressure is controlled so as to be decreased so that a heat load along with the clutch slip can be temporarily reduced. Control of the engine ignition timing is applied since a quick response of engine torque is required. The delay of the timing enables torque reduction. The throttle is not applied because of the slow response.

3.2 Requirement Indexes and Characteristic Variations

First priorities in consideration of shift quality requirements are smoothness and quickness of output torque change. These are expressed by torque change indexes A , B and shift time indexes C , D which are typical characteristics of the output torque and turbine revolution speed patterns as shown in Fig. 5.

$$\text{Index I: Shift shock } J_s = A + B \quad (1)$$

$$\text{Index II: Shift time } J_t = C + D \quad (2)$$

The torque change index A is induced by the inertia torque transmitted to an output shaft, which is caused by engine revolution speed change from the end of the torque phase to the inertia phase. B is induced by a disappearance of the inertia torque at the end of the inertia phase. The smaller both indexes, the better for achieving good shift qualities. In the same way, the smaller the indexes C , D , the better, because the indexes are concerned with a feeling of long shift time. Furthermore we need to consider the heat load as a requirement for a hard limitation which is energy lost at the 3rd clutch in decreasing the engine revolution speed.

$$\text{Index III: Clutch heat load } J_q = Q = \int_0^{tc} T_{c3} \cdot \Delta\omega_{c3} dt \quad (3a)$$

$$tc = C + D \quad (3b)$$

$$\Delta\omega_{c3} = \omega_t - \omega_{o3} = (\omega_{o3} - \omega_{o2})/D \cdot t + \omega_{o2} - \omega_{o3} \quad (3c)$$

$$\Delta\omega_{c3} : \text{Slip speed of engaged clutch} \quad (3c)$$

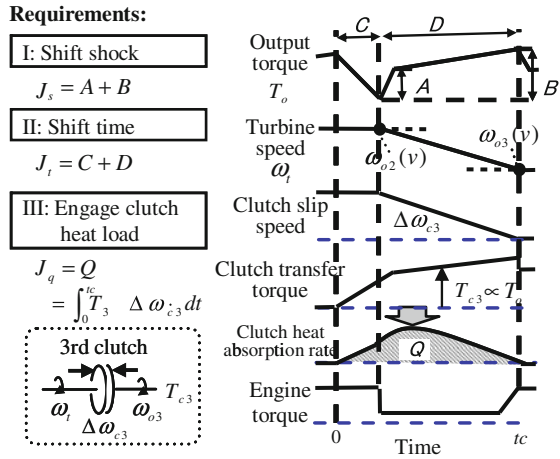
$$T_{c3} = \mu_3(\Delta\omega_{c3}) \cdot A_3 \cdot R_3 \cdot P_{c3} \quad (3d)$$

Here, the relation between the heat load Q and the indexes A – D , which are the characteristics of the output torque patterns, is discussed. In the torque phase, a multiplication of the 3rd clutch slip speed $\Delta\omega_{c3}$ and the clutch transmitted torque T_{c3} is equal to the heat load during the period when the torque transmitted passes are changed from the 2nd clutch to the 3rd. Therefore the heat load is determined depending on the index C , since C has a unique relation with the clutch torque T_{c3} . In the same way, the torque change index A , B and shift time index D in the inertia phase change according to the clutch torque T_{c3} . Conversely T_{c3} is determined when the values of indexes A , B , D are set. Therefore it is obvious that the clutch heat load can be expressed by the indexes A , B , D .

As mentioned above, the indexes A , B , C , D , which are the characteristics of the output torque patterns, are related to not only requirement indexes I, II, but also III.

The following can be given as factors of the characteristic variations; one is a change of pressure governor characteristic of an oil pressure control valve due to

Fig. 5 Requirements for AT shift control



a viscosity change along with oil temperature variation, another is a change of friction characteristic due to a temperature change of a clutch sliding plate. Moreover, we need to consider variations of the individual control valves and friction materials and variations of clutch pack clearance. It is considered the influences of these variations on the output torque are not sudden or stochastic, but mild ones over time, such as a change of a torque offset or torque slope. Therefore the variation ΔT of clutch transmitted torque, which affects the output torque, can be expressed by the variation $\Delta\mu$ of the friction coefficient or the variation ΔP of the oil pressure, as shown in Eq. (4). In the discussion below the variations of the oil pressure are applied as the representative ones, and the influences on the indexes of requirements are calculated with these variations.

$$T + \Delta T = (\mu + \Delta\mu)AR \cdot (P + \Delta P) \tag{4a}$$

$$\Delta T \approx AR(\Delta\mu \cdot P + \mu \cdot \Delta P) \equiv AR \cdot \mu \cdot \Delta P' \tag{4b}$$

$$\Delta P' = \Delta P + (P/\mu)\Delta\mu \tag{4c}$$

3.3 Research of Robust Target Output Torque

We apply the concept of the Taguchi Method (2) to select the most robust target pattern out of various possible patterns along with steps as shown in Fig. 6. The evaluation of robustness which is characteristic of this study is done by adding the hydraulic variations as the disturbances to the clutch oil pressures calculated from the possible targets. Next the steps are explained.

Fig. 6 Flow of robust target output torque search

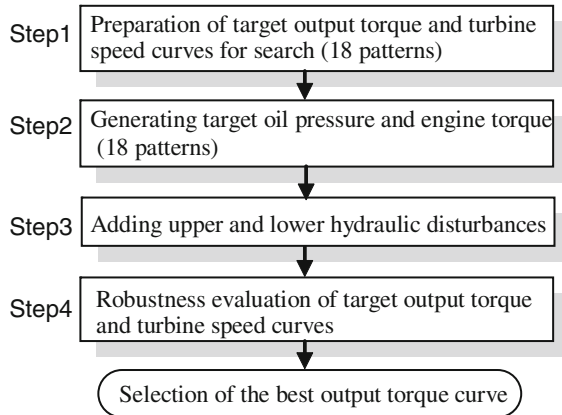
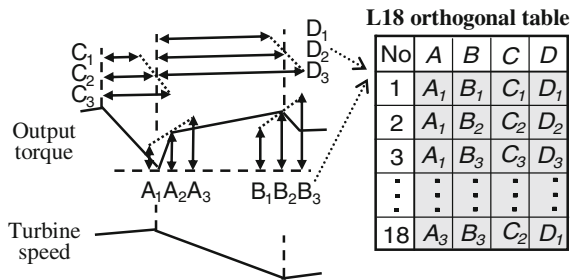


Fig. 7 Preparation of target patterns



Step 1: Set of possible target patterns

The output torque and turbine revolution speed patterns are set as possible target patterns. This is based on the fact that the characteristic indexes A, B, C, D of these target patterns are related to shift requirement indexes I, II and III as shown in previous section. Possible targets are made as follows; first, various levels of the output torque change indexes A, B values and the shift time indexes C, D values are set, next these values are combined as shown in Fig. 7. However, in this study target torque patterns T_{o_target} and target revolution speed patterns $\dot{\omega}_{t_target}$ are set with L18 orthogonal tables because of many possible combinations.

Step 2: Calculation of oil pressure and engine torque patterns with inverse directional design

We calculate the target oil pressure and engine torque patterns which are each related to the eighteen target output torque and turbine revolution speed patterns set in step 1 with the repeat simulation of the gear train system (in Fig. 8).

Concrete calculations of the target P_{c3} are repeatedly modified based on the deviation between the simulated output torque T_o and the target torque T_{o_target} with Eqs. (3d) and (5a) (in Fig. 8), because it is obvious from the above model equations that P_{c3} is related to the output torque. The reason for repeat modification is that there is a nonlinear characteristic of the clutch friction coefficient depending on the slip revolution speed.

Fig. 8 2–3 up-shift simulation model

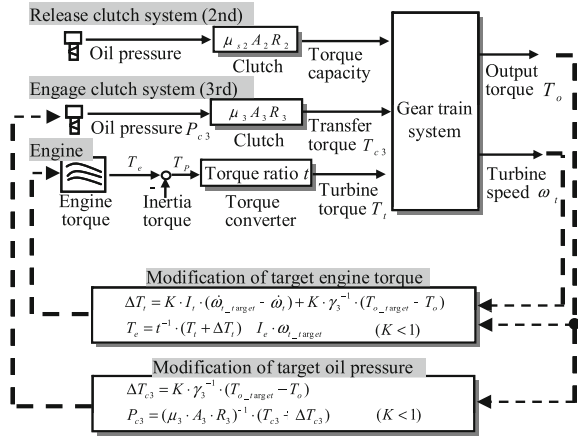
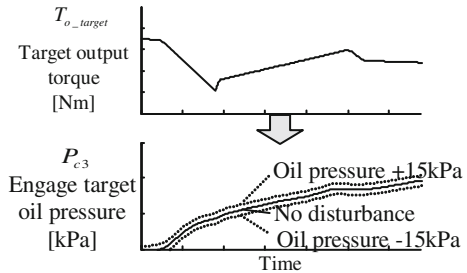


Fig. 9 Calculation of target oil pressure



The manner of the calculation of the target engine torque patterns T_e is the same. Calculations of the target T_e are repeatedly modified based on the deviation between the simulated turbine angular acceleration $\dot{\omega}_t$ and the target acceleration $\dot{\omega}_{t_target}$ with Eqs. (5b)–(5d), because T_e is related to the turbine angular acceleration $\dot{\omega}_t$ from the above model equations.

$$T_o = \gamma_3 \cdot T_{c3} \tag{5a}$$

$$I_t \dot{\omega}_t = T_t - T_{c3} \tag{5b}$$

$$T_t = t(\omega_t/\omega_e) \cdot T_p \tag{5c}$$

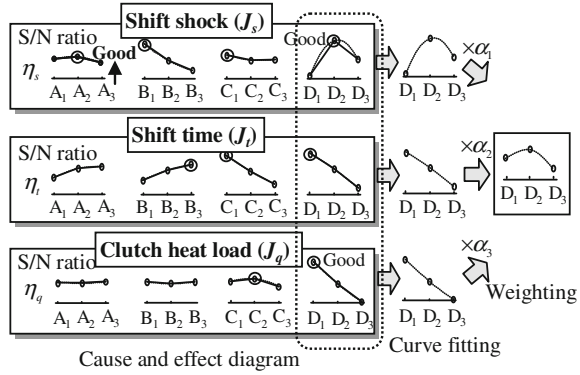
$$T_e = T_p + I_e \cdot \dot{\omega}_e \approx T_p + I_e \cdot \dot{\omega}_t \tag{5d}$$

Where γ_3 : 3rd gear ratio, I_t : inertia of turbine axis, t : torque ratio of torque converter.

Step 3: Addition of hydraulic variations (upper and lower values)

The upper and lower values of hydraulic variations are added to each target oil pressure pattern P_{c3} calculated in the previous step for the evaluation of robustness (allocation of error factor, Fig. 9).

Fig. 10 Determination of robust target output torque and disturbance



Step 4: Evaluation of robustness

The requirement indexes of shift shock, shift time and heat load shown in Sect. 3.2 are calculated from the forward simulation results which are made with the oil pressure pattern P_{c3} in step 3 and the patterns where the upper and lower variations are added. The total number of simulations is 54, because besides the eighteen combinations of the indexes A, B, C, D , the patterns with the upper and lower hydraulic variations are added. Each requirement index is evaluated by the S/N ratio (2) η in Eq. (6).

$$\text{Shift shock } \eta_s(i) = -10 \log(J(i)_{s0}^2 + J(i)_{s+}^2 + J(i)_{s-}^2) \tag{6a}$$

$$\text{Shift time } \eta_t(i) = -10 \log(J(i)_{t0}^2 + J(i)_{t+}^2 + J(i)_{t-}^2) \tag{6b}$$

$$\text{Heat load } \eta_q(i) = -10 \log(J(i)_{q0}^2 + J(i)_{q+}^2 + J(i)_{q-}^2) \tag{6c}$$

Where $i = 1, \dots, 18, J_0, J_+, J_-$: no variation, upper variation, lower variation.

Next, the relationship between the S/N ratios and the characteristic indexes A, B, C, D of the target patterns are represented as graphs of factorial effects (2) shown in Fig. 10. For example, as shown in Eq. (6d), the S/N ratio of the parameter A_1 is equal to an average of η for No.1, 2, 3, 10, 11, 12 that correspond to A_1 of the orthogonal table in Fig. 7.

$$\eta_s(A_1) = \frac{\eta_{s1} + \eta_{s2} + \eta_{s3} + \eta_{s10} + \eta_{s11} + \eta_{s12}}{6} \tag{6d}$$

The better the evaluation result is, and the smaller the magnitude of characteristic variation, the larger the calculated S/N ratio becomes. This graph of factorial effects enables us to find the characteristic index, which mostly affects each requirement index, and select the most robust level of each characteristic index. However, the two best levels of characteristic indexes may change due to the design weighting to shift shock and weighting to clutch heat load, as in the characteristic index D in the figure. Therefore weighting to each requirement index is performed and the level of the characteristic index is selected for each shift

Fig. 11 Robust target output torque patterns

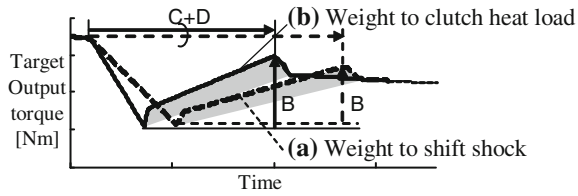
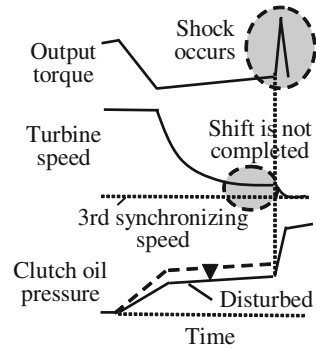


Fig. 12 Sensitivity for oil pressure disturbance



quality according to the weight. Concretely at first, the graphs of factorial effects are approximated with quadratic functions (as shown by the dashed lines in the figure), secondly each function is weighted ($\alpha_1, \alpha_2, \alpha_3$) so that one quadratic function can be made from each weighted function, and last, the levels are selected so that the value of the function can be a maximum. Examples of the target torque patterns are shown in Fig. 11 where the designs are (a) weight (0.7, 0.2, 0.1) to shift shock and (b) weight (0.1, 0.2, 0.7) to clutch heat load.

It is obvious from the index ($C+D, B$) of (a) weight to shift shock in the figure that the shift time is long and the index B of torque change is small. Ideally it is better that the output torque is made smaller and flatter in the inertia phase in Fig. 11 (a). However, the torque in the figure is not made smaller so that the robustness can be ensured. If the output torque is made flat and the oil pressure slightly falls by the hydraulic variations as shown in Fig. 12, the shift is not completed and finally a shock occurs when the oil pressure is raised for a complete engagement. On the other hand, it is obvious that (b) weight to heat load corresponds to shortening of the shift time index ($C+D$). This is because the shorter the shift time is, the shorter the time of heat generation is.

3.4 Verification of Robustness with Simulation

We took up 2–3 up shift of an 8 speed AT to verify the method mentioned in the previous section. The target oil pressure and the engine revolution speed could be calculated from the target output torque and turbine revolution speed, and the

Fig. 13 Robustness of shift shock

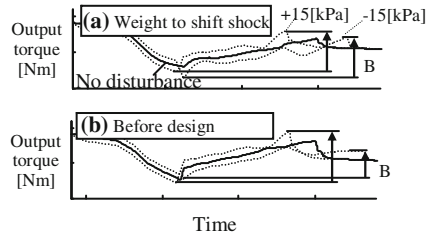


Fig. 14 Robustness of heat load

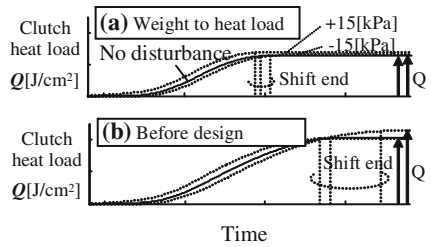
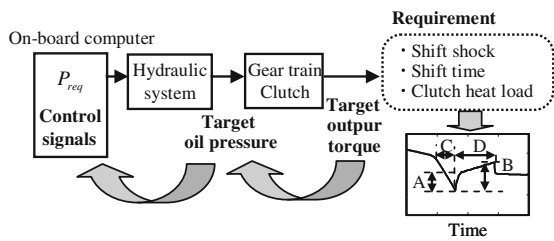


Fig. 15 Flow of the inverse directional design



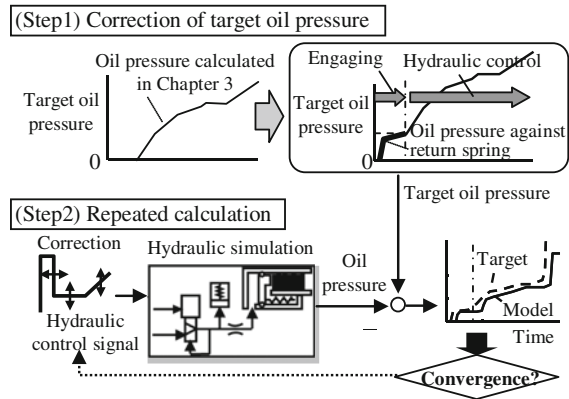
forward simulations were performed. Figure 13a shows the output torque patterns designed in the case of weight to shift shock and Fig. 14a shows the patterns in the case of weight to heat load. In both figures hydraulic variations of ± 15 [kPa] as characteristic variations are added and both are compared with the patterns before designs (Figs 13b and 14b).

It is obvious from Fig. 13 that in the proposed method (a) the shift is completed and the change of the index (torque change B) is smaller than that before design, even if a hydraulic variation of -15 [kPa] exists. Similarly, it is obvious from Fig. 14 that the heat load Q and its variation of the proposed method (a) is smaller than that before design (b) because of the short shift time of the proposed method. Thus the validity of the proposed method is verified.

4 Inverse Directional Design of Control Signal

The control signal of oil pressure is calculated from the target output torque patterns with the inverse directional design. This design flow is shown in Fig. 15. The process from the target output torque patterns to the target oil pressure

Fig. 16 Calculation of control signal



patterns in the flow of the figure has already been shown in the previous chapter. Therefore in this chapter the calculation process from the target oil pressure patterns to control signal patterns is explained in Fig. 16.

As an example of the difficulty in the clutch oil pressure control, the following is pointed out; that is the difference of the sensitiveness between the flow control mode where the clutch piston is moved and the pressure control mode where the clutch is engaged. In the flow control mode a dead time arises while the clutch is moved to the engaged position and furthermore the magnitude of the oil pressure response is smaller than that in the pressure control mode while the spring in the clutch pack is moved and squeezed. These characteristics are expressed by the model in Fig. 16 and applied to the calculation of the control signals from the target oil pressure patterns in this method. A convergent calculation is applied to the inverse directional design as mentioned in Chap. 3, that is, the control signal is repeatedly modified so that the deviation between the target oil pressure and the simulated pressure is kept small. Next, the inverse directional design of the engine torque control signals is explained. A delay element from the control signal to the target is the dead time which results from intermittent combustions of the engine. Therefore the engine torque control signals are made as the target pattern which is advanced by an amount equal to the dead time.

5 Verification of Validity with Simulations and Vehicle Tests

At first, simulation results of 8-3 down shift in the eight-speed automatic transmission are explained in Fig. 17 as an example showing the usefulness of the hierarchical and inverse directional design method proposed in this study. In this shift it is difficult to calibrate the control signals because it is necessary to control engagement of two clutches and release of other two clutches at the same time. Figure 18 shows the result before the calibration. The engine and turbine revolution

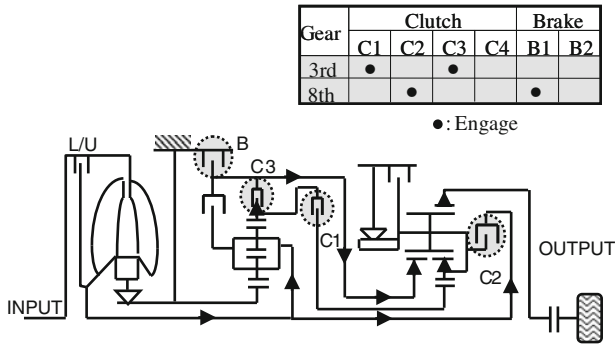
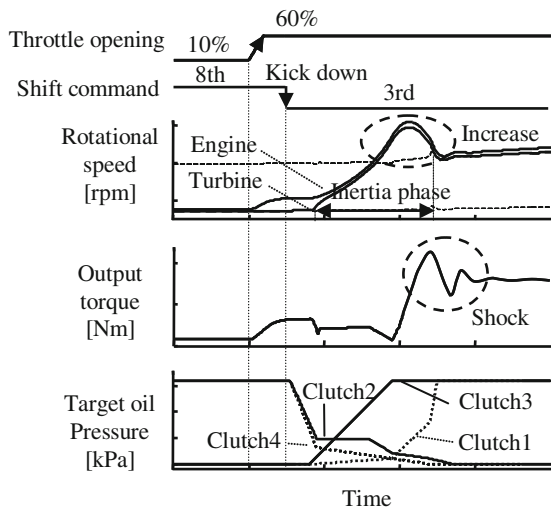


Fig. 17 8-speed automatic transmission

Fig. 18 Simulation results (8–3 down-shift): before design



speed increase quickly, and the shock occurs in the pattern of the output torque. On the other hand Fig. 19 shows the result where the proposed method is applied to the design. It is obvious that fine shift patterns can be achieved.

Next the designed control signal patterns of oil pressure were implemented on the on-board computer and tested for the verification of the proposed method in a vehicle. A limitation on this proposed model-based approach is that the accuracy of the control depends on the modelling errors. In this study, however, model identification tests were incorporated before the design process for model modification, which enabled the correction of the model parameters such as clutch friction coefficients. The results are shown in Fig. 20. The (a), (b) of the figure correspond to the case of no disturbance of oil pressure in Figs. 13 and 14. It is obvious that the shift patterns, which are the same as the ones of the simulation, have also been achieved in the vehicle tests.

Fig. 19 Simulation results (8–3 down-shift)

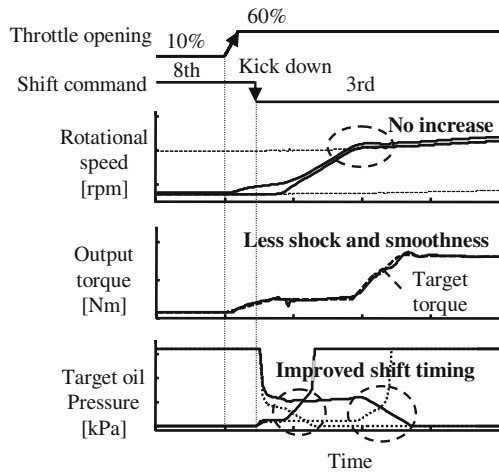
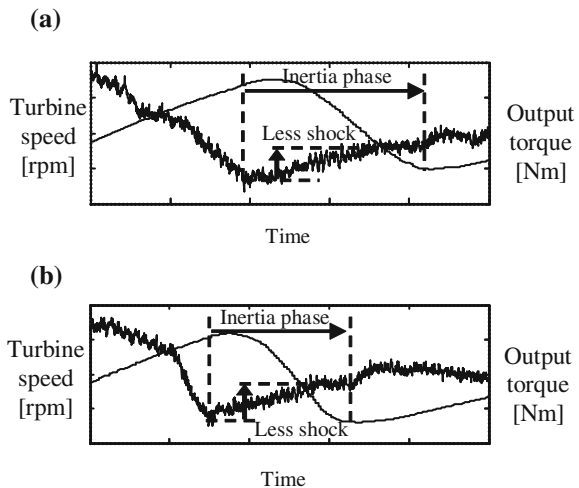


Fig. 20 Test results: 2–3 up-shift : after design



6 Conclusion

This study proposes the hierarchical and inverse directional design method in order to reduce the labour for the calibration of automatic transmission shift control system, and the validity of this method has been verified by the simulations and vehicle tests. In this method, first the shift requirement indexes are set, next the optimal values of the design parameters, namely, the indexes *A*, *B*, *C*, *D*, which are the characteristics of the target output torque patterns, are calculated, finally the control signal of oil pressure is calculated from those indexes. Therefore we think this method enables the verification of the validity and the prospect of the design during each process, and can be accepted by people who have a long history of calibration experience.

References

1. Ota H et al (2007) Toyota's world first 8-speed automatic transmission for passenger cars, SAE technical paper 2007-01-1101
2. Ross PJ (1996) Taguchi technique for engineering. McGraw-Hill, New York

Clutch Transmissible Torque Estimation for Dry Dual Clutch Transmission Control

Kihoon Han and Yongsoo Yoon

Abstract Driven by a strong pressure for fuel efficiency and dynamic performance, dual clutch transmission system is focused as next generation system. The online estimation of the characteristic curve of the clutch transmissible torque as a function of the actuator position is essential for precise clutch engagement control. For precise estimation of the clutch transmissible torque, nonlinear torque transfer model of dry clutch is defined and the sliding mode observer algorithm is implemented in the dual clutch transmission (DCT) control strategy to compensate the changes in clutch characteristic curve. Unknown input observer compensates modeling and estimation error. The dry clutch torque observers allow a better estimation of the actual transmitted clutch torque when activating the clutch engagement control. The stability and performance of estimation algorithm are verified by simulation result.

Keywords Dual clutch transmission · Dry clutch · Clutch torque · Torque curve adaptation · Sliding mode observer

1 Introduction

Recently, restrictions on emission of vehicle are getting strict and requests on improvement of fuel efficiency are increasing. New technology in order to improve fuel efficiency and increase effectiveness of transmission system is being studied

F2012-C04-021

K. Han (✉)

Continental Automotive Systems, Seoul, Korea
e-mail: kihoon.han@continental-corporation.com

Y. Yoon

Department of Mechanical Engineering, University of Minnesota, Minneapolis, USA

actively by many researchers, and dual clutch transmission (DCT) which is a combination of both auto transmission system's advantages and manual transmission's advantages is focused as a next generation transmission system [1–3].

DCT has advantages of both automatic and manual transmission, but it requires accurate and precise control to adjust complicated system. Especially the clutch control is a key element for the driving comfort during standing-start and gear shifting maneuvers in dual clutch transmission vehicles. Furthermore, online estimation of the characteristic curve of the clutch transmissible torque as a function of the actuator position is essential for precise clutch engagement control.

In previous studies, simplified linear estimation algorithm was applied without considering clutch speed effect. In this paper, for more precise estimation of the characteristic curve of the dry clutch, nonlinear model is defined and sliding mode torque observer is proposed. The sliding mode observer algorithm implemented in the low level of the DCT strategy has as its main purpose the compensation of the changes in clutch characteristic curve. The sliding mode observers allow a better estimation of the actual transmitted clutch torque when activating the clutch engagement control. The stability and performance of estimation algorithm are verified by numerical analysis and simulation result [4–9].

2 Torque Transfer Model of Dry Clutch

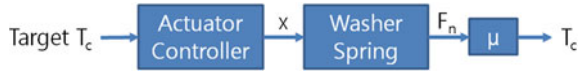
During the design of the optimal engagement control the online estimation of the characteristic curve $T_c(x)$ of the transmissible torque of the clutch as a function of the actuator position has been supposed perfect. This hypothesis allowed use of the clutch as a simple torque actuator thanks to the inversion of this characteristic curve done by the low levels of the TCU control strategy.

The $T_c(x)$ curve is the composition of two physically distinct components: the relation $F_n(x)$ between the normal force exerted on the friction pads and the actuator position and $T_c(F_n)$ linking the normal force to the effective torque transmitted by the clutch. The former, mainly set by the washer and cushion spring's stiffness, has quite a slow changing rate due to the friction pads wear and the aging of the springs. The second relation, on the other hand, is given by the friction-disk geometry and the friction coefficient that can have noticeable variations resulting from the heating of the friction surfaces.

The synchronization-assistance strategy is particularly sensible to an error of the friction coefficient since the chosen optimal trajectory with its final conditions must be well adapted to the driveline real state and particularly the actual torque transmitted by the clutch.

In order to compensate this limitation lower levels two observers, one estimating the friction coefficient and one directly the clutch torque, have been developed. These observers allow a better estimation of the actual transmitted clutch torque when activating the synchronized assistance.

Fig. 1 Schema of the clutch torque control



2.1 Dry Clutch Models

Figure 1 shows schema of the clutch torque control detailing the washer spring's characteristic and the friction coefficient:

Torque control of the clutch is made possible by the inversion of the relation between the maximal transmissible torque by the clutch for a given position of the actuator. This relation can be written as $T_c = \mu F_n$ is the coefficient linking the transmissible torque to the normal force F_n exerted by the washer spring.

The normal force F_n is function of actuator position as combination of washer spring and cushion spring of friction pad. According to clutch pad structure, when the clutch pad rotates the centrifugal force affects the normal force. Therefore clutch speed is also important factor.

$$T_c = \mu F_n = \mu(F(x) - I_{clutch}\omega_g^2) \quad (1)$$

where $F(x)$ is linear function of actuator position depending on mechanical lever structure.

2.2 Driveline Models

The driveline simplified model with the friction model is following equations having T_c and x as inputs.

$$\begin{aligned} I_e \dot{\omega}_e &= T_e - T_c \\ T_c &= \mu F_n = \mu(F(x) - I_{clutch}\omega_g^2) \\ \dot{\mu} &= 0 \end{aligned} \quad (2)$$

$$\begin{aligned} I_g \dot{\omega}_g &= T_c - k_g \theta_g - \beta_g (\omega_g - \omega_v) \\ I_v \dot{\omega}_v &= k_g \theta_g + \beta_g (\omega_g - \omega_v) \\ \dot{\theta}_g &= (\omega_g - \omega_v) \\ T_c &= \mu F_n = \mu(F(x) - I_{clutch}\omega_g^2) \\ \dot{\mu} &= 0 \end{aligned} \quad (3)$$

The friction coefficient μ figures as an additional constant state.

Since the clutch torque T_c given by simplified friction model is independent of the clutch sliding speed, the driveline dynamic model is actually composed by two

separate parts: Eq. (2) as engine model and others Eq. (3) as gearbox and vehicle model. Due to this separation the friction coefficient can be observed from the dynamics of only the section of the driveline upstream of the clutch.

3 Clutch Torque Observer

3.1 Sliding Mode Observer

For the robust estimation of given nonlinear system, Eq. (2) and (3), sliding mode observer is proposed. From nonlinear system dynamics of Eq. (2) and (3), the system output is $y = [\bar{\omega}_e \quad \bar{\omega}_g \quad \bar{\omega}_v]^T$ with signal error $\varepsilon = [\varepsilon_e \quad \varepsilon_g \quad \varepsilon_v]^T$.

The error vector is defined as following equation.

$$E = [\hat{\omega}_e - \bar{\omega}_e \quad \hat{\omega}_g - \bar{\omega}_g \quad \hat{\omega}_v - \bar{\omega}_v]^T \quad (3)$$

An observer may be constructed to estimate the friction coefficient μ in Eq. (2). Assuming a perfect estimation of $F(x)$ as clutch spring characteristics, consider a sliding mode observer of the form

$$\hat{\mu} = \frac{T_e - I_e \dot{\hat{\omega}}_e}{(F(x) - I_{clutch} \hat{\omega}_g^2)} + KE \quad (3)$$

where $K \in \mathfrak{R}^3$ is gain vector for stable estimation.

3.2 Unknown Input Observer

The friction coefficient observer is based on the hypothesis of a good reconstruction of the washer spring's characteristic F_n independently of the friction coefficient μ variation whose changes are mainly due to the heating of the friction surfaces. The heating of the friction disk also change the cushion spring stiffness and size, modifying the F_n curve especially around the contact point.

The friction coefficient observer is highly sensitive to a wrong estimation of the contact point since a positive transmitted torque with an estimated zero normal force or the opposite case induce very strong variations in the estimated friction coefficient.

Since the F_n value is not always trustworthy the possibility of estimating the transmitted clutch torque without resorting to this signal. Also, the engine control unit (ECU) gives an estimation of the mean output torque and engine speed based on several physical control parameters. These measures are broadcasted over the controller area network (CAN) to transmission control unit (TCU) every 10 ms. For simplicity this asynchronous setup error is considered as measurement noise.

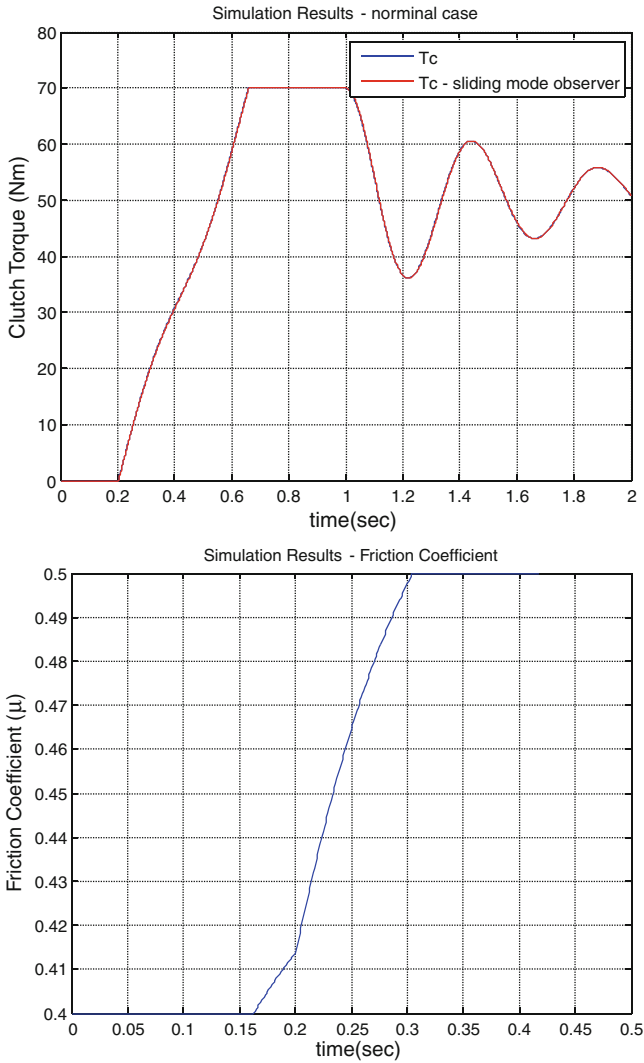


Fig. 2 Results of the clutch torque estimation—without dry clutch characteristic estimation error

The main perturbations affecting the observer are a variation in the clutch transmitted torque, either due to a change of the normal force exerted on the friction surfaces or a change in the friction coefficient due to the heating of the friction surface, the previously described measurement noise on the engine speed and engine output torque.

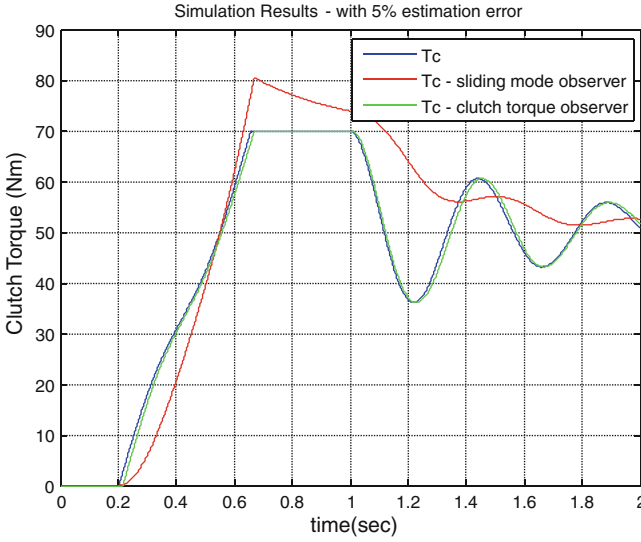


Fig. 3 Results of the clutch torque estimation—with dry clutch characteristic estimation error

Considering the perturbed system from Eq. (2),

$$\begin{aligned} I_e \dot{\omega}_e &= T_e - T_c \\ \dot{T}_c &= \varepsilon_1 \end{aligned} \tag{5}$$

having as outputs

$$\begin{aligned} \bar{\omega}_e &= \omega_e + \varepsilon_2 \\ \bar{T}_e &= T_e + \varepsilon_3 \end{aligned} \tag{6}$$

where ε_1 represents a variation on the torque transmitted by the clutch, ε_2 the engine speed measurement noise and ε_3 the engine torque estimation error.

The corresponding stable unknown-input linear observer can be designed by setting proper gain using pole-placement method.

$$\begin{aligned} \hat{\omega}_e &= \frac{1}{I_e} (T_e - \hat{T}_c) + k_1 (\bar{\omega}_e - \hat{\omega}_e) \\ \dot{\hat{T}}_c &= k_2 (\bar{\omega}_e - \hat{\omega}_e) \end{aligned} \tag{7}$$

4 Simulation Results

To verify stability and performance of dry clutch torque observer, simulation is performed.

Figures 2 and 3 allows a comparison of the performance of the sliding mode observer and unknown input observer on a simulated standing start on flat ground. Due to the validation domain of the $T_c = \mu F_n$ relation and the persistent excitation assumption the sliding mode observer is active only during the sliding phase (from 0.2 to 0.67 s). On the other hand, the unknown input observer is active during whole simulation.

In nominal case without dry clutch characteristic estimation error, sliding mode observer is well performing since it has no delay due to the input estimation. As shown in second graph of Fig. 2, sliding mode observer estimates clutch friction coefficient in very short time.

On the other hand, in the presence of a small error on the estimation of the washer spring characteristic, sliding mode observer only cannot estimate the transmitted torque. The unknown input observer guarantees a better estimation of the transmitted torque.

5 Conclusions

In the paper, the non-linear mathematical model of characteristic curve of the clutch transmissible torque is proposed. Based on non-linear mathematical model, the sliding mode observer is designed as the low level of the DCT strategy. The dry clutch torque observers allow a better estimation of the actual transmitted clutch torque when activating the clutch engagement control.

References

1. Bastin G, Gevers M (1988) Stable adaptive observers for nonlinear time varying systems. *IEEE Trans Auto Cont* 33:650–658
2. Besancon G (2000) Remarks on nonlinear adaptive observer design. *Syst Cont Lett* 41:271–280
3. Commault C, Dion JM, Sename O, Monteyian R (2001) Unknown input observer: a structural approach. *Proceedings ECC congress*
4. Kreisselmeier G (1977) Adaptive observer with exponential rate of convergence. *IEEE Trans Auto Cont* 22:2–8
5. Marino R, Tomei P (1995) Adaptive observer with arbitrary exponential rate of convergence for nonlinear systems. *IEEE Trans Auto Cont* 40:1300–1304
6. Zhang Q (2001) Adaptive observer for mimo linear time varying systems. INRIA research report: theme 4

7. Zhang Q Delyon B (2001) A new approach to adaptive observer design for mimo systems. Proceedings ACC congress
8. Dolcini P, Canudas C, Bechart H (2010) Dry clutch control for automotive applications. Springer, London
9. Spurgeon S (2008) Sliding mode observer: a survey. *Int J Syst Sci* 39:751–764

AMT Control for Parallel Hybrid Electric Vehicles

Gianluca Zito

Abstract This paper focuses on the gearshift control of hybrid transmissions with high primary shaft inertia. This relates to the case of the electrification of a conventional AMT in a pre-transmission HEV configuration. A strategy based on energy considerations, by combining the use of the electric motor torque and the mechanical synchronization torque (by means of a synchromesh), has been developed on a detailed AMESIM transmission model for obtaining a high quality gearshift performance in a hybrid driveline. The electric motor is used to compensate its own inertia by accelerating/decelerating the primary shaft during the first phases of the synchronization. The synchromesh is mainly used at the end of the synchronization as the mechanical energy to be dissipated is reduced to an acceptable level. Beside the primary speed control, an important aspect is to phase the electrical and mechanical synchronization actions in order to optimize the global gearshift time and to guarantee robustness. The gearshift control algorithms have been successfully validated on a plug-in parallel hybrid demo car developed at IFPEN, showing that the electrification of entry-level transmissions is a viable solution for developing affordable hybrid vehicles.

Keywords Parallel hybrid electric vehicle · AMT control · Driveline · Gearshift control · Transmission control

F2012-C04-022

G. Zito (✉)
IFP Energies Nouvelles, 1 et 4 avenue de Bois-Préau, 92852,
Rueil-Malmaison Cedex, France
e-mail: gianluca.zito@ifp.fr

1 Introduction

Parallel Hybrid Electric Vehicles (HEV) with an AMT are an effective solution for reducing pollutant emissions of low-medium size conventional vehicles by means of driveline electrification with reduced efforts in terms of transmission design. In post-transmission configurations a continuous torque can be applied to wheels even during driveline transients thanks to the electric motor position, enhancing drivability. On the other hand very high torque levels are required over a wide speed range to ensure the traction of the vehicle, making post-transmission configurations not suitable for implementing a pure electric mode at medium speed. Pre-transmission configurations take the benefit of using gear changes to extend the torque/speed range of the electric mode: compact high speed machines improve the performances and reduce the fuel consumption as they are able to cover the driver's low power demands with engine being off [1, 2]. A drawback of this configuration is that torque interruption can't be avoided during a gearshift. Moreover, when a high speed motor is sized to match the engine maximum torque/speed and permanently connected with a high gear ratio to the primary shaft, a dramatic increase of the equivalent inertia occurs. In this case conventional AMT control cannot be used as the synchromesh is not able to dissipate the energy required to synchronize the primary and secondary shaft speeds, and an appropriate synchronization strategy is necessary. An intuitive way to solve this problem is to use the electric motor to compensate its own inertia by accelerating/decelerating the primary shaft.

Previous works on electric assistance during a gearshift especially deal with clutch operation [3, 4]. The problem of the synchronization in hybrid transmissions with high primary shaft inertia is not investigated in details: with respect to previous works this paper presents a detailed strategy to manage electrical and mechanical synchronization phases in order to obtain a fast and safe gearshift. Therefore, we focus on the control of the effort applied to the synchromesh sleeve along all the gearshift phases.

The combined control of the electric/mechanical synchronization torque during the synchronization phase will be presented through simulation and experimental results. The strategy has been validated in real-time on a hybrid powertrain test bench to prepare its integration in the transmission control unit of the IFPEN hybrid demo car.

2 System Overview

2.1 IFPEN Plug-in Parallel Hybrid Vehicle Demo car

The AMT gearshift algorithms have been developed on a plug-in parallel hybrid demo car developed by IFPEN in order to test powertrain components and control algorithms. The base vehicle is a Renault Kangoo with a gasoline engine, and it

Table 1 Vehicle components and their characteristics

Electric motor	Speed range (rpm): 0–20000	Torque (Nm): 41	Power (KW): 37
ICE	Speed range (rpm): 0–6000	Torque (Nm): 127	Power (KW): 63
Battery	Output voltage range (V): 180–216		Capacity: 7.8 kW
DCDC	Output voltage range (V): 400–600		
Gearbox	AMT (5 gears)	Electric actuators	
Vehicle mass	1700 kg		

has been adapted to obtain a full hybrid vehicle by integrating available third party components. The characteristics of the main components of the vehicle are resumed in Table 1, views of the vehicle and of the hybrid powertrain architecture are presented in Fig. 1.

The original 1.6L gasoline engine has been replaced by a naturally aspirated one of 1.4L including a starter/generator for the Stop and Start function. An electric motor is permanently connected to the primary shaft by a series of gears with a global ratio of 3.307 (pre-transmission parallel configuration). With this ratio, the maximum torque and speed at primary shaft for the pure electric mode are comparable to those of the internal combustion engine. The electric energy is stored in a large capacity Lithium-Ion battery that is able to ensure the plug-in behavior of the vehicle.

3 AMT Gearshift Control Strategy with Electric Assistance

A schematic view of the IFPEN hybrid driveline is shown in Fig. 2. During a gearshift the inertia of the electric machine should be compensated in order to avoid an excessive load on the synchronizer. From the control point of view, the electric machine is an additional actuator available for performing the synchronization beside the mechanical action of the synchronizer. In what follows, only the synchronization problem will be considered, and it is assumed that the decoupling (coupling) of the engine is performed by using an appropriate strategy [5].

3.1 Gearshift Operation

The gearshift operation of a conventional (automated) manual transmission can be decomposed, as illustrated in Fig. 3 (right), in the following main steps:

- Idle State: the current gear is engaged;
- A gearshift is demanded: torque is no more transmitted to the final drive;
- Lever displacement: depending on the target gear, a different fork can be selected. Note that this step follows disengagement in manual transmission;
- Disengagement: the current gear is disengaged, neutral position is reached;

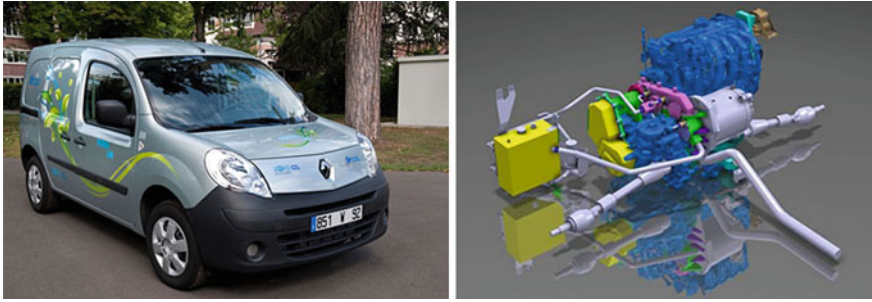


Fig. 1 IFPEN hybrid demo car: external view (left); detailed view of the hybrid powertrain (right)

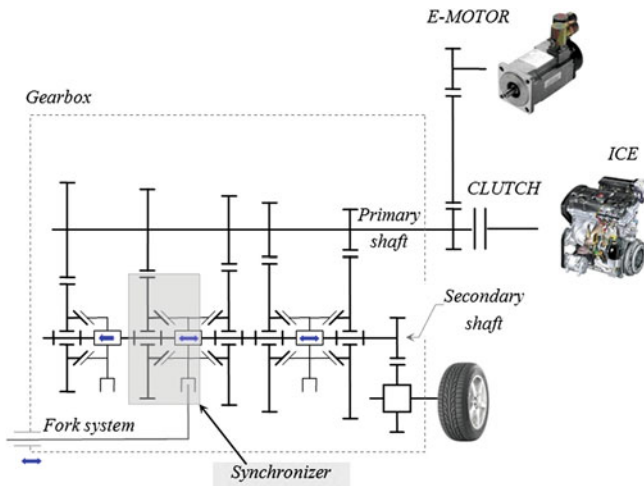


Fig. 2 IFPEN hybrid driveline

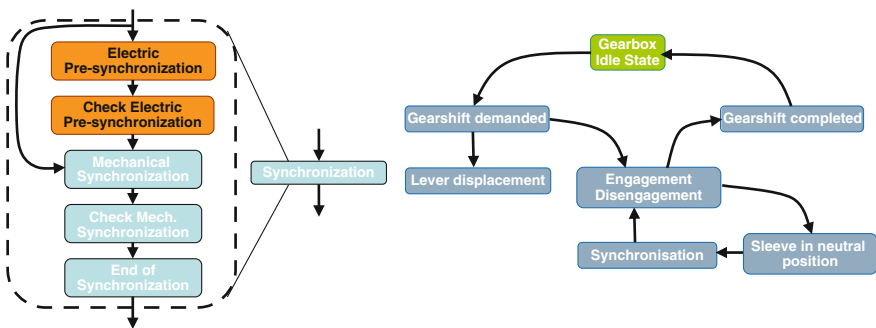
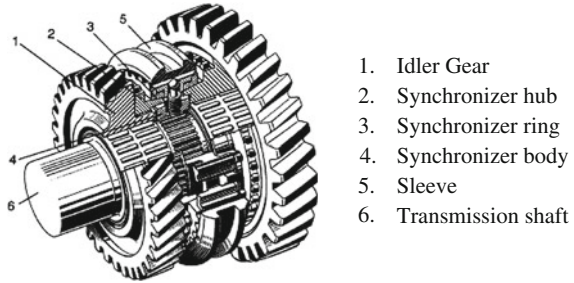


Fig. 3 Gearshift main steps: conventional case (right); details of the synchronization phase including electric assistance (left)

Fig. 4 Single cone synchronizer



1. Idler Gear
2. Synchronizer hub
3. Synchronizer ring
4. Synchronizer body
5. Sleeve
6. Transmission shaft

- Synchronization: input shaft speed is accelerated/decelerated to equalize the output shaft speed (taking into account the target gear ratio).
- Engagement: the target gear is engaged;
- Gearshift is completed: torque can be transmitted to the final drive.

The synchronization step is realized thanks to a synchronizer mechanism, a friction clutch that accelerates/decelerates the equivalent input shaft inertia by applying a friction torque in order to match the speeds of the input shaft and of the idler gear to be shifted.

3.2 Synchronizer Working

The synchronizer is a key element in the gearshift process. Different technologies exist to implement the synchronizer function. Figure 4 illustrates a single cone synchronizer and its inner components. Considering the gearshift process from the neutral position, the following phases are commonly identified to describe the synchronizer working [6]:

1. First free fly: the sleeve moves with a reduced axial effort, displacing the centering mechanism and thus pushing the synchronizer ring towards the cone of the idler gear;
2. Angular velocity synchronization: an increased force is applied to the sleeve that comes in contact with the ring, decreasing its speed to zero. The force applied to the sleeve is transmitted to the ring, and the friction torque reduces to zero the angular velocity difference between the ring and the idler gear;
3. Turning of the ring: when the angular velocity difference is close to zero, the friction torque disappears and the sleeve starts to move, turning the synchronizer ring and the idler gear;
4. Second free fly: the sleeves meshes with the synchronizer ring and approaches the idler gear chamfers. The sleeve can move at high speed with a reduced required effort. There is no velocity difference between the sleeve and the idler gear;

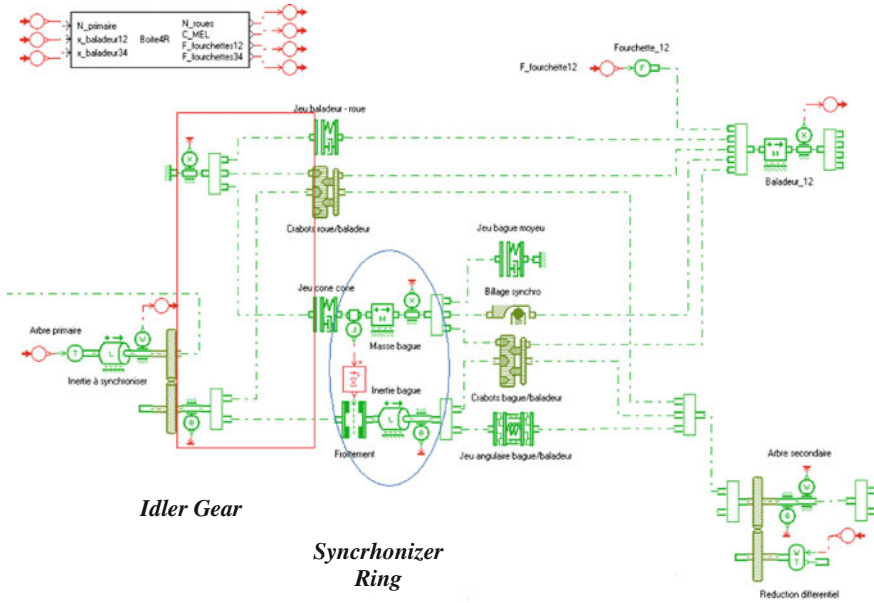


Fig. 5 Amesim driveline model including a half-synchronizer mechanism

5. Turning of the idler gear: the sleeve reduces its speed because of the film of oil formed between the chamfers surfaces. The force required to turn the gear depends on the relative position of the gear and sleeve splines.
6. Final free fly: the sleeve continues to move axially and meshes with the idler gear. The gearshift is completed.

In a conventional AMT the force applied to the sleeve is controlled (in open or closed loop) to operate the disengagement—synchronization—engagement sequence. During the synchronization step the synchronization torque is given by [6]:

$$C_{sync} = \frac{F \cdot \mu \cdot R}{\sin \alpha} \tag{1}$$

where α is the angle of the cone surface, F is the axial effort of the sleeve on the synchronizer ring, r is the synchronization cone radius, and μ is the friction coefficient. The instantaneous power transmitted to the synchronizer results as:

$$P_{sync} = C_{sync} \cdot \Delta\omega \tag{2}$$

where $\Delta\omega$ is the angular velocity difference between the secondary shaft and the idler gear to be synchronized. The resulting energy dissipated over the synchronization time t_{sync} is:

$$E_{sync} = \int_0^{t_{sync}} C_{sync} \cdot \Delta\omega dt \tag{3}$$

The energy required in order to synchronize the primary and secondary shaft is:

$$E_{diss} = \frac{J_{eq}}{2} abs(\omega_1^2 - \omega_2^2) \tag{4}$$

where J_{eq} is the equivalent inertia of all rotating masses reduced to the rotation axis of the idler gear, and ω_1 and ω_2 are the primary shaft speed at the beginning of and after the synchronization, respectively. In the conventional case the expression of the equivalent inertia is:

$$J_{eq} = J_p + J_f + \sum_{i=1}^n J_i R_i^2 \tag{5}$$

where J_p is the primary shaft inertia, J_f is the friction clutch inertia, J_i are the idler gears inertias at the secondary shaft, and R_i are the gear ratios. With respect to the conventional case, as the electric machine is connected to the primary shaft through a series of gears with a global ratio R_{red} of 3.308, an additional equivalent inertia should be added: the primary shaft equivalent inertia of the “electrified driveline” is then:

$$J_{eq}^* = J_p + J_f + J_{m_eq} + \sum_{i=1}^n J_i R_i^2 \quad \text{with} \quad J_{m_eq} = J_m R_{red}^2 + \sum_{i=1}^m J_{red_i} R_{red_i}^2 \tag{6}$$

where J_m is the electric machine inertia, J_{red_i} and R_{red_i} are the inertias and ratios of the gears composing the reducer.

The ratio between the J_{eq}^* and J_{eq} is approximately 14 : without any adaptation of the AMT gearshift control strategy, as an increase of the gearshift time with respect to the conventional case is not conceivable, the energy to be dissipated by the synchronizer during the synchronization phase will be unacceptable for the synchronizer mechanism.

3.3 Control Strategy Development

In the case of a pre-transmission parallel hybrid vehicle with high equivalent primary shaft inertia, the synchronization step can be decomposed, as illustrated by the diagram in Fig. 3 (left), in electric and mechanical synchronization:

3.3.1 Electric Pre-Synchronization

When the sleeve is in neutral position the electric machine torque is used to control the primary shaft speed in order to match the target primary shaft speed, derived from the current output shaft speed and the ratio corresponding to the gear to be engaged. During this phase the effort applied to the sleeve is able to move it into contact with the synchronizer ring, but not enough to generate a high friction torque level, as the angular velocity difference between the synchronizing elements (the ring and the idler gear) is too large.

3.3.2 Mechanical Synchronization

A friction torque can be applied by means of the synchronizer if the corresponding dissipated energy due to the existing angular velocity difference is lower than a calibrated threshold. The synchronization force can be computed from the synchronization torque by inversion of Eq. (1). The synchronization torque can be derived from energy considerations, as shown in the rest of this section.

The torque balance at primary shaft is:

$$J_{eq}^* \frac{d\omega_p}{dt} = C_{sync} + C_{loss} \quad (7)$$

where C_{loss} is the drag torque estimation that can be expressed as an affine function of the primary shaft speed:

$$C_{loss} = a \cdot \omega_p + b \quad (8)$$

By integrating the corresponding powers over the desired mechanical synchronization time t_{sync} , the corresponding energy equilibrium can be written as:

$$E_{diss} = E_{sync} + E_{loss} \quad (9)$$

Making the assumptions that the friction torque is constant during the mechanical synchronization and the primary shaft speed is varying linearly, the energy due to the synchronization is

$$E_{sync} = \int_0^{t_{sync}} C_{sync}(t) \cdot \omega(t) dt = \bar{C}_{sync} \cdot \frac{\omega_1 + \omega_2}{2} \cdot t_{sync} \quad (10)$$

Finally, from Eqs. (1), (2), (3), (4), (9) and (10) one can derive the expression of the required force:

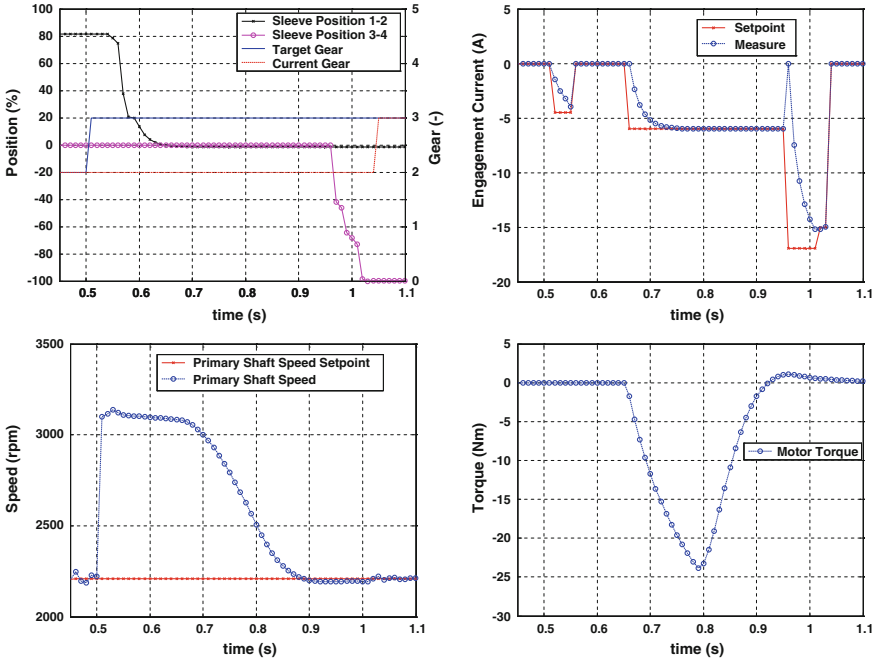


Fig. 6 Gearshift simulation results: upshift from 2nd to 3rd gear

$$\begin{cases} C_{sync} = 2 \cdot \frac{E_{diss} - E_{loss}}{I_{sync} \cdot (\omega_1 + \omega_2) \cdot R_i} \\ F = \frac{C_{sync} \cdot \sin \alpha}{\mu \cdot R} \\ I_{eng} = f(F_{sync}) \end{cases} \quad (11)$$

In the case of the AMT considered in this work, the force applied to the sleeve is generated by an electric actuator (DC motor) by means of a kinematic chain. A static relation between the force F and the current amplitude I_{eng} of the engagement DC motor has been obtained from experimental data.

3.3.3 Control Strategy Validation

In order to validate the gearshift control algorithms, the driveline of the hybrid vehicle has been modeled in the AMESIM environment. The model includes a precise description of the synchronizer mechanism to have a good representation of the different phases of the synchronizer working, from the neutral position to the engaged position. The initial primary shaft speed and the secondary shaft speed, that is supposed constant during the gearshift, are imposed. The control inputs are the electric machine torque and the force applied to the sleeve. Clutch operation is

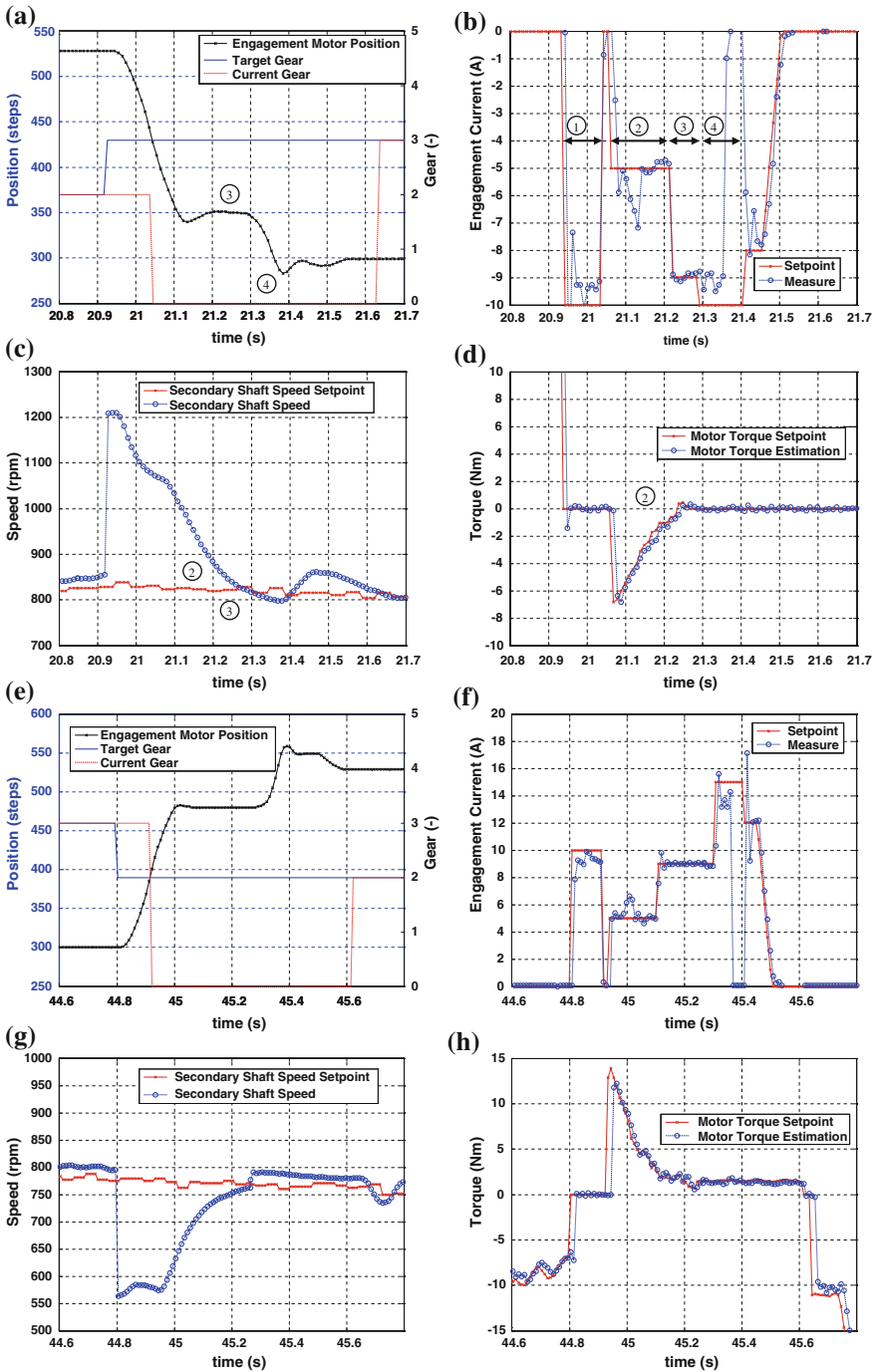


Fig. 7 Gearshift results of the IFPEN hybrid decemar: 2nd to 3rd gear (a–b–c–d); 3rd to 2nd gear (e–f–g–h)

not included. Simulation results of an upshift (2nd to 3rd gear) are presented in Fig. 6: sleeves position (top left), engagement motor current (top right), primary shaft speed (bottom left) and electric machine torque (bottom right). At the end of the electric synchronization, as the primary shaft speed is close to its setpoint, the friction torque due to the engagement motor is increased to dissipate the required energy as stated in (11) (Fig. 5).

4 Experimental Results

The AMT control algorithms have been implemented in the Transmission Control Unit (TCU) of the IFPEN hybrid demo car. The TCU controls three electric actuators (DC motors) for clutch operation and gear selection/engagement operation by means of PWM signals. The available measures are the positions and the currents of the DC motors: engagement motor position is used to estimate sleeve position and speed, while the engagement motor current intensity allows to estimate the force applied to the fork (and then to the sleeve). During the synchronization step of the gearshift the electric machine torque setpoint is computed and sent to the Motor Control Unit to control the primary shaft speed. The results obtained for an upshift (2nd to 3rd gear) and a downshift (3rd to 2nd gear) are illustrated in Fig. 7. As stated above, clutch operation is not considered. The force applied to the sleeve depends on the gearshift phase, as presented in the previous section. Figure 7b illustrates the engagement motor current profile imposed during an upshift. During the previous gear disengagement (zone 1) an open loop control is applied until the neutral position is reached. Then the primary shaft speed loop control is activated and the electric machine torque setpoint is sent to the MCU (electric pre-synchronization, zone 2, Fig. 7d). The motor current amplitude is reduced to avoid the synchronization friction torque. When the rotational speed difference is lower than a calibrated threshold (zone 3, Fig. 7c), mechanical synchronization is authorized and the engagement motor current amplitude is increased, and computed accordingly to Eq. (11). The position of the sleeve is constant (zone 3, Fig. 7a). After the synchronization of primary and secondary shaft speeds, the sleeve can move axially and complete the engagement (zone 4, Fig. 7a–b). The same remarks apply to the downshift (Fig. 7e–f–g–h). In this case one can observe that larger torque amplitude is required during the electric pre-synchronization as the drag torque of the gearbox acts against the primary shaft speed acceleration. A residual torque is applied during the engagement phase to help the turning of the ring and the engagement of the idler gear. Maximum shift time is about 0.8 s and comparable to that obtained with the AMT control in the conventional case, after having included the clutch opening/closing time.

5 Conclusion

A strategy for e-AMT control in pre-transmission parallel HEVs has been developed and validated on the IFPEN plug-in hybrid demo car. Fast gearshift times have been obtained by controlling the action of the electric motor and the conventional synchromesh. Simulation and experimental results prove the feasibility and robustness of the proposed method. Therefore, one of the drawbacks associated to the pre-transmission parallel architecture can be overcome by an appropriate adaptation of the conventional transmission control. This means that existing transmissions with entry level (“low cost”) AMT can be used to design hybrid drivelines without losing drivability, thus offering a promising solution for the production of affordable hybrid vehicles.

Acknowledgments The author wishes to thank Fabien Nicolas, Fabrice Deleau and François-Pierre Ninove for their relevant technical contribution.

References

1. Miller JM (2004) Propulsion systems for hybrid vehicles. Inst Eng Technol, London
2. Chris Mi, Abul Masrur M, David Wenzhong Gao (2011) Hybrid electric vehicles: principles and applications with practical perspectives. Wiley
3. Liao Chenglin, Zhang Junzhi, Zhu Haitao (2004) A study of shift control algorithm without clutch operation for automated manual transmission in the parallel hybrid electric vehicle, Fisita
4. Jonathan L Breen Glenn Bower, Clutchless Shifting of an Automated Manual Transmission in a Hybrid Powertrain. 2011-01-2194 SAE International
5. James McLaggan, Corin Wren (2007) The Development of a Diesel Full-Hybrid Vehicle for Very Low CO₂ Emissions. Aachener Kolloquium Fahrzeug- und Motorentechnik 2007 489
6. Lovas L, Play D, Marialigeti J, Rigal JF (2006) Mechanical behaviour simulation for synchromesh mechanism improvements. Proc Inst Mech Eng Part D J Automobile Eng 220:919

Part V
Other

Numerical Sensitivity Analysis of the Effect of Pump Outlet Radius on the Performance of Torque Converter

Qingdong Yan, Cheng Liu, Wei Wei and Boshen Liu

Abstract In order to study the influence of torque converter inlet and outlet radius, especially pump outlet radius, the traditional one-dimensional streamline theory and DOE were combined to analyze the parameter sensitivity. And the three-dimensional flow field simulation was adopted to validate the results of one-dimensional approach. The results showed that the pump outlet radius had a significant effect on stall torque ratio and pump torque coefficient. The pump torque coefficient increased and the stall torque ratio decreased with an increasing pump outlet radius. The sensitivity analysis results showed that the pump inlet radius had a great influence on the efficiency of torque converter. The results of both methods agreed well with each other and showed that the two methods were both effective. Decreasing pump outlet radius could reduce the pump load and increase stall torque ratio, and moreover, solve the problem of pump overload without much efficiency sacrifice.

Keywords Torque converter · One-dimensional flow theory · Three-dimensional flow simulation · DOE · Sensitivity analysis

F2012-C05-001

Q. Yan · C. Liu (✉) · W. Wei · B. Liu
School of Mechanical Engineering, Beijing Institute of Technology, Beijing, China
e-mail: liuchengbit@gmail.com

Q. Yan · W. Wei
Science and Technology on Vehicle Transmission Laboratory, Beijing, China

1 Introduction

Torque converter is a complex hydrodynamic machine which transforms power via liquid. As a flexible transmission device, torque converter is widely used in all kinds of transmissions such as cars, buses, wind turbines, engineering machinery and so on [1].

There are dozens of design parameters including torus parameters and cascade parameters, which makes it difficult to design and optimize torque converters [2, 3]. It is easier to modify torque converter parameters to achieve required performance than to design a brand new one. For example, pump blades were cut in some torque converters in order to improve stall working condition performance and change matching quality. But what is the relationship between design parameters and performance? And how to get required performance by modifying some specific parameters? For the sake of torque converter modification and series design, parameter sensitivity analysis should be taken to provide theoretical basis. Herein the traditional one-dimensional approach and design of experiment method were utilized as the analysis tool to investigate the influence of inlet and outlet radius on the torque converter performance, especially pump outlet radius. What's more, three-dimensional flow field simulation was performed to study how the pump outlet radius affect the flow in torque converter and validate the results of one-dimensional approach.

2 One-Dimensional Approach

Based on some strict assumptions, the complex three-dimensional flow in torque converters can be represented by mean streamline. And the hydrodynamic characters can be determined by conservation of energy and momentum [4]. According to Euler equation, the energy characteristic can be calculated by the following:

$$H_B = \frac{1}{g} \left(u_{B2}v_{uB2} - \frac{R_{D2}}{R_{B1}} u_{B1}v_{uD2} \right) = f(R_{B1}, R_{B2}, R_{D1}, Q) \quad (1)$$

$$H_T = \frac{1}{g} \left(u_{T2}v_{uT2} - \frac{R_{B2}}{R_{T1}} u_{T1}v_{uB2} \right) = f(R_{T1}, R_{T2}, R_{B2}, Q) \quad (2)$$

$$H_D = 0 \quad (3)$$

$$H_I = H_{IB} + H_{IT} + H_{ID} = f(R_{B1}, R_{B2}, R_{T1}, R_{T2}, R_{D1}, R_{D2}, Q) \quad (4)$$

where H , H_i represent for wheel energy and energy loss respectively. Subscript B, T, D means pump, turbine and stator. Subscript 1, 2 represent for inlet and outlet respectively. R is torus radius, which is taken as variable, and other torus and cascade parameters are set as constant. g is acceleration of gravity. u is the

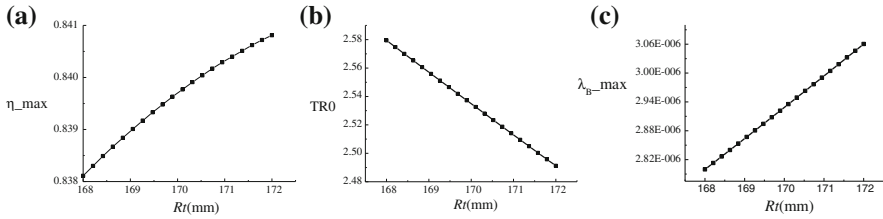


Fig. 1 Performance of torque converter with different pump outlet radius. **a** Maximum efficiency. **b** Torque ratio at stall condition. **c** Max pump capacity factor

convected velocity, v_u the component velocity in the circumferential direction. Q is the flow rate in torque converters.

According to conservation of energy, we can get $H_B + H_T + H_D + H_I = 0$. Then the torque characteristics can be determined as follows:

$$T_B = \rho Q (R_{B2} v_{uB2} - R_{B1} v_{uB1}) \quad (5)$$

$$T_T = \rho Q (R_{T2} v_{uT2} - R_{T1} v_{uT1}) \quad (6)$$

$$T_D = \rho Q (R_{D2} v_{uD2} - R_{D1} v_{uD1}) \quad (7)$$

Here T means torque, and flow rate Q can be determined by conservation of energy.

A Matlab program was developed based on the one-dimensional theory to predict the torque converter performance. Aiming at certain torque converter whose maximum diameter is 400 mm, the coefficients in the program were modified by experimental data, so the Matlab program could predict the performance of the torque converter precisely. The pump outlet radius (R_t) ranged from 168 to 172 mm was taken as variable. The performance of torque converter under different pump outlet radius was computed and shown in Fig. 1. The performance of torque converter was evaluated by efficiency (η), torque ratio (TR) and pump capacity factor (λ_B) given below:

$$SR = \frac{RS_{turbine}}{RS_{pump}} \quad (8)$$

$$TR = \frac{T_T}{T_B} \quad (9)$$

$$\eta = SR \times TR \quad (10)$$

$$\lambda_B = \frac{T_B}{\rho \times g \times RS_{pump}^2 \times D^5} \quad (11)$$

where RS represent for rotational speed, SR the speed ratio, ρ the density of hydraulic transmission oil, and D is the maximum diameter of the torus.

Table 1 The radius boundary of different wheel

	Upper	Lower
Pump inlet radius (RB1/mm)	124	128
Pump outlet radius (Rt/mm)	168	172
Turbine inlet radius (RT1/mm)	168	172
Turbine outlet radius (RT2/mm)	124	128
Stator inlet radius (RD1/mm)	116	120
Stator outlet radius (RD2/mm)	116	120

Figure 1 shows that the maximum efficiency and pump capacity factor increased as the pump outlet radius rose, but the torque ratio decreased slightly with an increasing pump outlet radius. The inlet and outlet radius of other wheels could also influence the performance of torque converter. Taking all radius parameters into consideration, an DOE method was performed to investigate the influence of the radius parameters. Latin cube approach was adopted to generate the variables matrix, two hundreds samples were used. The parameters were shown in Table 1.

After the calculation, the Pareto plot, which indicated the influence of variables, was acquired and shown in Fig. 2. In Pareto plots, the length of each bar indicated the influence level. Red bar meant negative correlation and blue bar meant positive correlation.

From Fig. 2 we could see that pump inlet radius was the most influential factor of maximum efficiency, and the turbine inlet radius came second. The most influential factor of torque ratio at stall condition was pump outlet radius, and turbine and stator inlet radius ranked second. For maximum pump capacity factor, pump outlet radius was the main influence factor and other variables had little influence. The performance plots versus pump outlet radius with other variables randomly defined were present in Fig. 3.

Figure 3 indicated that pump outlet radius had a main effect on stall torque ratio and maximum pump capacity factor, but it had no obvious influence on efficiency of torque converter, which well agreed with the Pareto results. After parameter sensitivity analyzing, such conclusions could be drawn: pump capacity factor increased with an increasing pump outlet radius, but stall torque ratio decreased as the pump outlet radius rose.

3 Three-Dimensional Flow Field Validation

A lot of research had been done to simulate torque convert internal flow field [5–8]. With the development of computational fluid dynamics and computer technology, it is now able to simulate the internal flow in the torque converter. Three-dimensional flow field simulation could determine the internal flow by solving Reynolds-Averaged-Navier–Stokes equations, by which the performance of torque converter

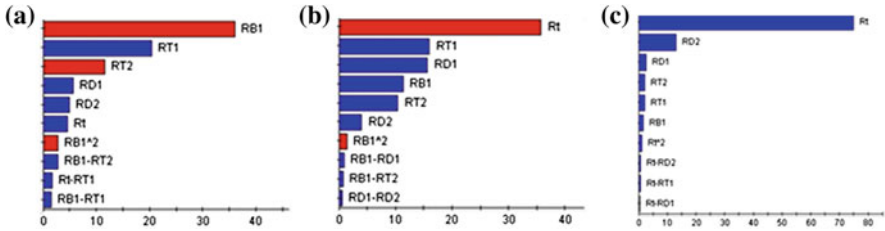


Fig. 2 The pareto diagram of torque converter performance. **a** Maximum efficiency. **b** Torque ratio at stall condition. **c** Max pump capacity factor

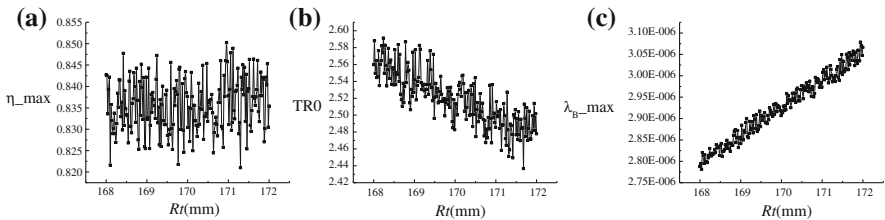


Fig. 3 Performance of torque converter with different pump outlet radius under multiple input. **a** Maximum efficiency. **b** Torque ratio at stall condition. **c** Max pump capacity factor

could be predicted precisely. Herein the three-dimensional flow field simulation method was performance to investigate how the pump outlet radius affect the internal flow and validate the results of one-dimensional approach.

Performances of different torque converters with pump outlet radius ranging from 168 to 171.5 mm were determined and shown in Figs. 4, 5 and 6. Figure 4 showed that when pump outlet radius increased, torque ratio in low speed ratio operating conditions decreased, but it increased in high speed ratio operating conditions. The maximum efficiency dropped and the high efficiency area shranked when the pump outlet radius decreased, which was shown in Fig. 5. We could see from Fig. 6 that the pump outlet radius had a tremendous effect on pump capacity factor, and pump capacity factor went up with an increasing pump outlet radius. A higher pump outlet radius meant more blade area, which increased the ability of absorbing power.

After simulation, the performances versus pump outlet radius were shown in Fig. 7. From Fig. 7 we could see that the trend of the three-dimensional simulation results agreed well with the one-dimensional approach. The maximum efficiency increased and the stall torque ratio decreased when pump outlet radius rose; and the maximum pump capacity factor rose with an increasing pump outlet radius. We could also see that the maximum efficiency fluctuated when the pump outlet radius increased, which meant that the pump outlet radius was not the main factor for maximum efficiency, but pump outlet radius had a significant influence on stall torque ratio and pump capacity factor, which also agreed with the Pareto results of one-dimensional approach.

Fig. 4 TR-SR figure with different pump outlet radius

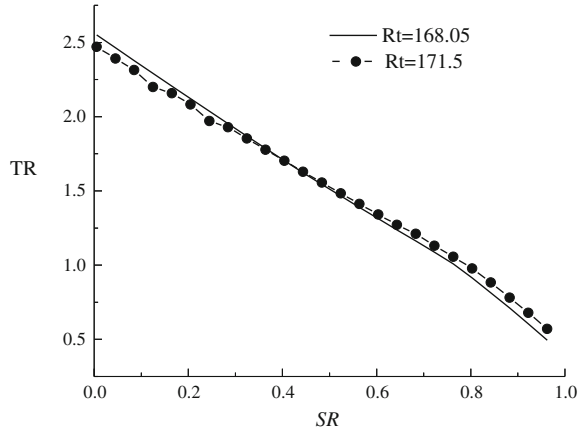


Fig. 5 η -SR figure with different pump outlet radius

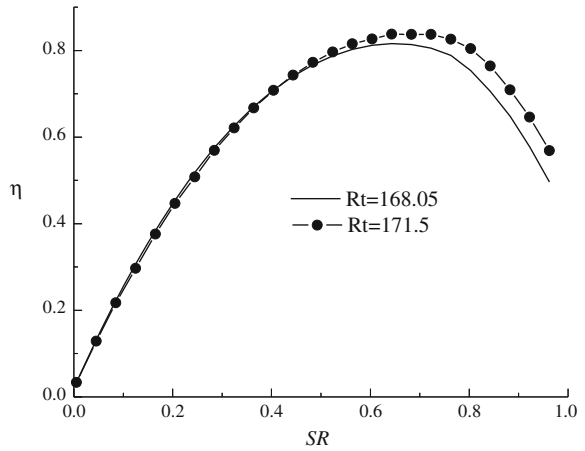
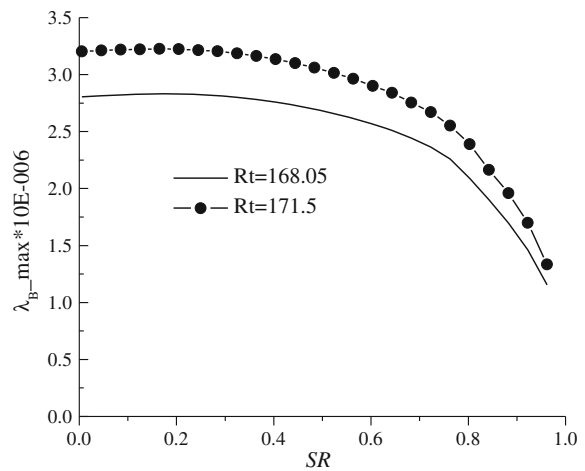


Fig. 6 λ_B -SR figure with different pump outlet radius



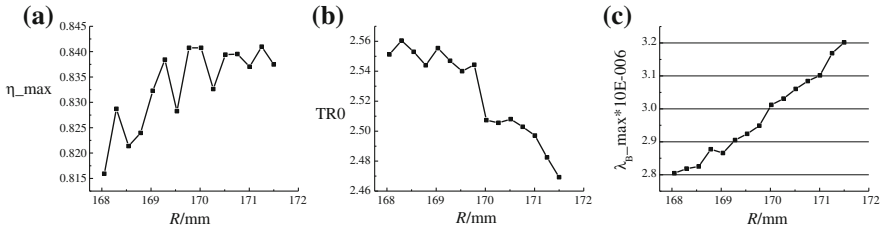


Fig. 7 Performances of torque converter with different pump outlet radius. **a** Maximum efficiency. **b** Torque ratio at stall condition. **c** Max pump capacity factor

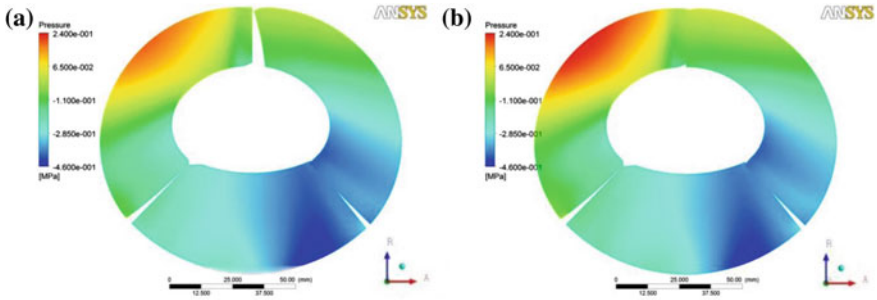


Fig. 8 The pressure distribution on the meridian plane under stall operating condition. **a** Low pump outlet radius. **b** High pump outlet radius

The pressure distribution under stall operating condition with different pump outlet radius were shown in Fig. 8. We could see that the distribution of different pump outlet radius were similar, but the pressure and high pressure area increased as the pump outlet radius rose, which resulted in high pump torque, i.e. high pump capacity factor. Meanwhile, when pump outlet radius rose, the pressure in turbine increased, too, which led to turbine torque increase. An increasing pump outlet radius not only raised the pressure in pump and turbine flow passages but also raised working surface of pump blade, so pump torque increased more than turbine torque, which meant that the stall torque ratio dropped when pump outlet radius increased.

4 Conclusion

The influence of pump outlet radius on the performance of torque converter was investigated by both one-dimensional approach and three-dimensional flow field simulation, the results of both methods were similar. The conclusions could be drawn:

1. Pump outlet radius was the main factor for pump capacity factor. When the pump outlet radius dropped, the pump blade surface decreased and the flow pressure dropped, too, which lowered the ability of absorbing power, i.e. lower the pump capacity factor.
2. Pump outlet radius had an negative effect on torque ratio. When pump outlet radius rose, the pump torque increased, and according to the definition, torque ratio dropped.
3. When pump outlet radius decreased, the non-blade area of pump expanded, and the secondary flow extended, so the efficiency dropped.

References

1. Wei W (2006) Parameters integrated optimization design system of hydrodynamic torque converter based on 3D flow field theory. Beijing Institute of Technology, Beijing
2. Dong Y, Korivi V, Attibele P (2002) Torque converter CFD engineering part I: torque ratio and K factor improvement through stator modifications. SAE technical paper 2002-01-0883
3. Asl HA, Azad NL, McPhee J (2011) Math-based modeling and parametric sensitivity analysis of torque converter performance characteristics. SAE technical paper 2011-01-0732
4. Zhu J (1991) Torque converter design and calculation. National Defense Industry Press, Beijing
5. Tian H (2005) Research on the modern design theory of torque converter. JinLin University, Chan Chun
6. Chu Y (2006) Theoretical and experimental research on design method of hydrodynamic torque converter based on CFD. JinLin University, ChangChun
7. Lim WS, Lee C, Jang W (2000) Three-dimensional flow field simulation to estimate performance of a torque converter. SAE 2000-01-1146
8. Schweitzer J, Gandham J (2003) Computational fluid dynamics in torque converters: validation and application. *Int J Rotating Mach* 9(6):411–418

Modelling of Oil Heating of Disengaged Lubricated Clutches in Hybrid Vehicles

Friedrich Brezger and Albert Albers

Abstract Due to increasing series development of hybrid vehicles many conventional components of the powertrain have to be replaced or changed. To avoid new technical failures, mostly well-known components are being used to create these new types of powertrains in series production. This chapter focuses on the drag torque of lubricated clutches which could be used in full parallel hybrids to disconnect the combustion engine from the powertrain instead of using a torque converter. There are some reasons to replace the torque converter with a clutch. Many cases and situations have to be calculated to forecast possible reduction of fuel consumption. Because of the complex interactions between NVH, comfort, wear and efficiency, there are a lot of boundary conditions to consider for these clutches. Therefore, special clutch types were developed for upper class cars with high torque engines. In aspects of high heat inputs there are newly developed designs of clutches. In the early state of product development the fuel consumption of different concepts is one important criterion for decision making. For a generic calculation of the drag torque, the heating of the oil in the clutch has to be paid attention to. The approach in this chapter is to firstly analyse the drag torque at a specific disengaged clutch. Therefore any other powertrain influences are cut off, by running tests on a test bench. Furthermore manoeuvres/test cases are defined in order to receive drag torques as objective as possible without temperature or bearing influences for example. By using analytical equations based on fluid dynamics, first hypotheses can be created. This chapter shows the previous works regarding the analytic modelling on lubricated clutches (e.g. Yuan et al. J Fluids

F2012-C05-002

F. Brezger (✉) · A. Albers
IPEK—Institute of Product Engineering, Karlsruhe Institute of Technology (KIT),
Karlsruhe, Germany
e-mail: friedrich.brezger@kit.edu

Eng Bd. 129:333) and their correlation to the specific clutch and secondly the important extension of the present models regarding the heating of oil in the clutch. In addition, the model results are validated by test bench measurements and the relative error is shown. Moreover, the methods for analysing and modelling lubricated clutches are described in this chapter using the example of one lubricated clutch.

Keywords Lubricated disengaged clutch · Drag torque · Modelling · Oil heating

Nomenclature

c_p	J/g/K (specific heat capacity)
E	J (energy)
h	mm (gap size between discs)
M	Nm (torque)
m	exponent in cinematic viscosity calculation
n	rpm (rotational speed)
r	m (radius)
T	°C (temperature)
V'	l/min (volumetric flow of oil)
ρ	kg/m ³ (density)
μ	Pa/s (viscosity)
ϑ	m ² /s (cinematic viscosity)
ω	rad/s (angular velocity)

1 Introduction

Due to increasing series development of hybrid vehicles, many conventional components of the powertrain have to be replaced or changed. To avoid new technical failures mostly well-known components are used to create these new types of powertrains in series production. This chapter focuses on the drag torque of lubricated clutches which could be used in full parallel hybrids to disconnect the combustion engine from the powertrain instead of using a torque converter.

There are some reasons to replace the torque converter with a clutch. The possible topology is a parallel hybrid, where the electric motor is situated behind the classical torque converter position in automatic transmission vehicles. Figure 1 shows a typical parallel hybrid topology, where this new type of clutch can be used.

Because of the functional principle of the converter, this element is not the optimal solution for separating the combustion engine from the drivetrain. The torque converter cannot disengage the power coming from the electric motor to the combustion engine completely, because of its pump and turbine. A typical schematic of a torque converter is shown in Fig. 2.

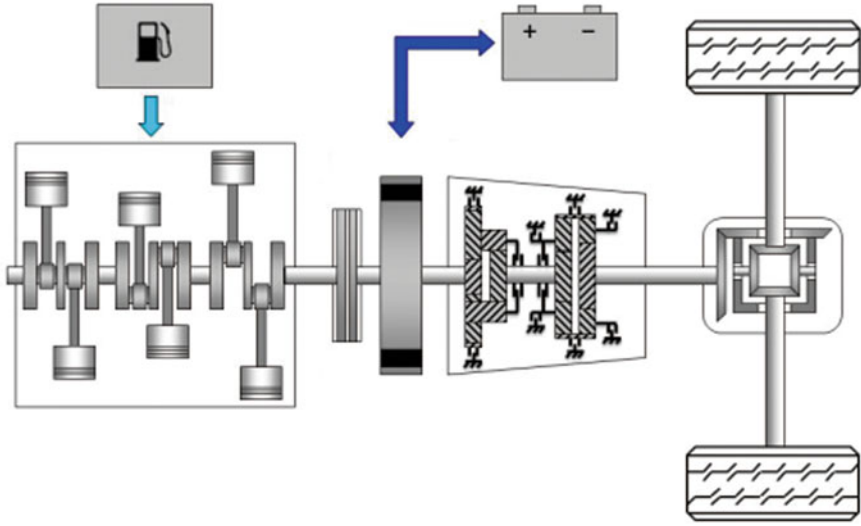


Fig. 1 Typical parallel hybrid topology with electric motor behind a clutch

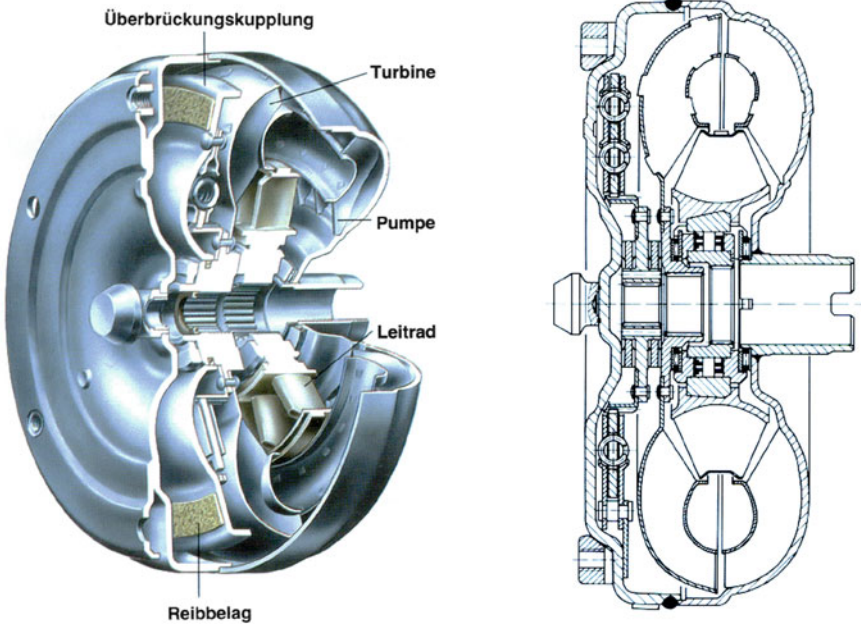


Fig. 2 Sketch of a typical torque converter with free-wheel clutch [11]

Utilizing a secondary clutch to avoid the losses of the torque converter would require more parts and components and therefore more design space. One possible solution is to replace the torque converter with a clutch. Doing so, very high conditions have to be met for this clutch due to the connection to an automatic transmission.

Many cases and situations have to be calculated in order to generate predictions of possible fuel consumption reductions. Because of the complex interactions between NVH, comfort, wear and efficiency, there are a lot of boundary conditions to consider for these clutches.

In the early state of product development the fuel consumption of different concepts is one important criterion for decision making. For a generic calculation of the drag torque, the heating of the oil in the clutch has to be paid attention to. The focus of this chapter lies on the disengaged state of fully filled lubricated clutches in contrast to many other publications like [1] which focus on heating models and heat transmission during actuations with e.g. KUPSIM.

2 State of the Art

2.1 Selected Working Principles of Lubricated Clutches

Typical lubricated clutches have an open case, where a mixture of oil and air can exist. During high loads while synchronizing the power carrying and load carrying side the oil flow is highly increased and the first contact of the clutch discs takes place by contacting the fluid in between. By increasing the normal forces on the clutch discs, different kinds of mixed friction are created. The rotational speeds and the given oil flow define the amount of oil in between the discs. If the oil flow is too low for example, the oil is transferred to the outside by the centrifugal force/pumping effects faster than the new oil is flowing between the contact surfaces. As a result, several areas of the contact surfaces have air in between. The regulation of the oil flow can be accomplished with mechanical valve controls or an electronic control unit. In both cases an external pump is supplying the oil flow. Typical drag torques of these disengaged clutches can look like the curves shown in Fig. 3.

There are three phases of the run shown in the diagram. In the first phase the drag torque is increasing almost linearly due to Newton's shear force in the fluid. Drag torque decreases abruptly to phase two, which is a result of air getting between the clutch discs. Afterwards, in phase 3, there can be a slight increase of the drag torque again, which can be induced by wobbling of the discs [2].

In contrast to the explained concept, Sasse [3] developed the so called "Euler Kupplung" further, to a kind of clutch which shows the behaviour of the torque converter. The experimental "Euler Kupplung" model is shown in Fig. 4, as well as a schematic principle of the oil stream between pump and turbine.

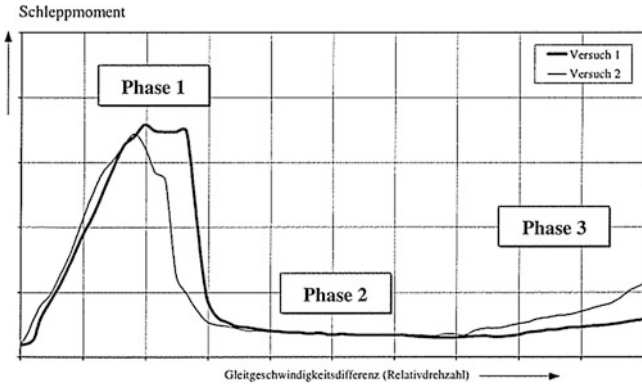


Fig. 3 Typical drag torque at increasing relative speeds of lubricated clutches [8]

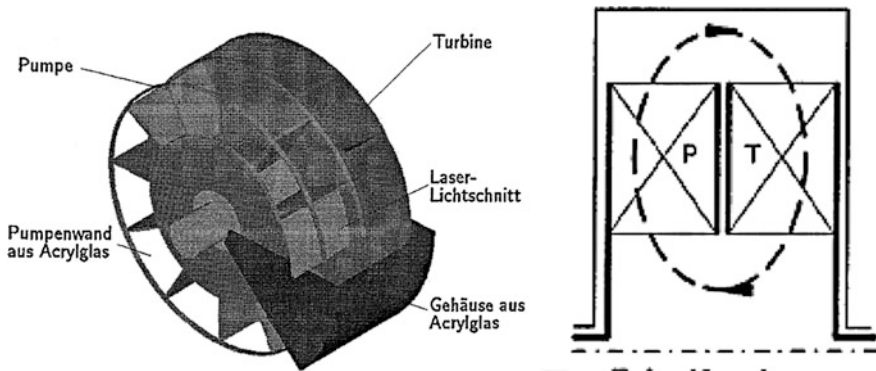


Fig. 4 Experimental clutch based on Euler principle for investigation (left), functional scheme of oil stream (right) [3]

The aim of the further development is given by the following citation: “The most important arguments are the thermal and mechanical robustness of the hydrodynamic power transmission with the controllability of the torque transfer and the radially-small, compact design of a wet clutch [3].”

The result is shown in Fig. 5. In this hydrodynamically cooled clutch (HCC) there are single sided discs with deep radial channels. Depending on the direction of power transmission the outer or inner discs act as the pump whereas the opposite discs act as the turbine.

This setup has the advantage of very high helical oil flows in the inside, which guarantees a very good heat transfer from the discs with frictional contact into the oil. Using this effect less oil is used to achieve the same cooling effect on the clutch discs. The clutch shown in Fig. 5 has oil stream velocities of up to 300 l/min [3].

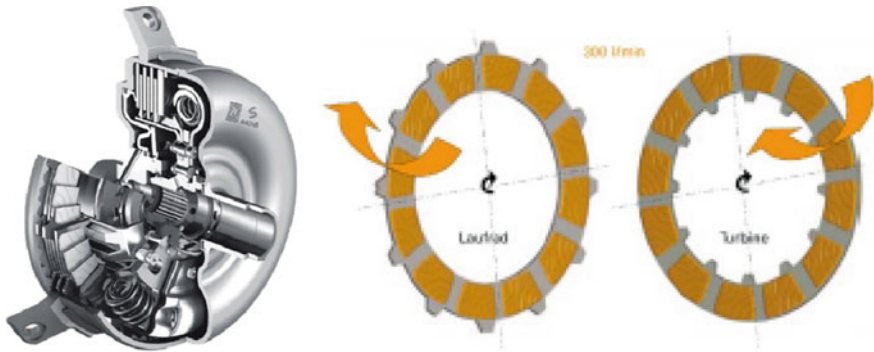


Fig. 5 A hydrodynamically cooled clutch by ZF [3]

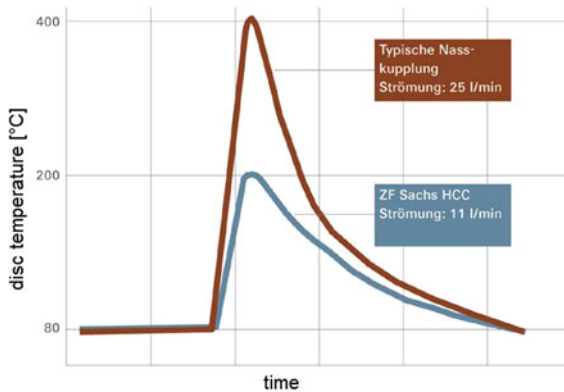


Fig. 6 Comparison of temperatures in a conventional lubricated clutch with HCC [3]

Because of that, the external peak oil flow created by a separate pump can be reduced drastically, which is explained by the measured temperatures at different oil flows in Fig. 6. That means that the power consumption of the external pump can be decreased greatly.

2.2 Analytical Models

In the early stages of product development a lot of data and parameters have to be defined, before exact calculations or CFD-simulations can be implemented. Nevertheless, choosing the working principles needs forecasts of many aspects, like energy efficiency.

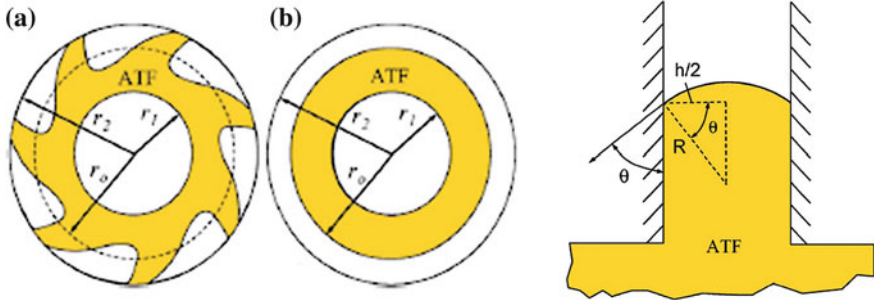


Fig. 7 Schematic of partial oil film within clutch (*left, a and b*); schematic of contact angle between the oil film and clutch plate (*right*) [6]

In this work the situation of the totally disengaged clutch shall be calculated regarding the drag torque. A short overview of the known analytical models will be given in the following.

Hashimoto et al. has combined the analytical formula of Newton’s shear stress of fluids with an empiric part for the turbulent stream, based on his research.

$$T = 2\pi N \int_{r_1}^{r_2} \frac{\mu\omega r^2}{h} (1 + 0.0012Re^{0.94}) dr \tag{1}$$

Equation 1: drag torque of oil between two rotating discs [4]

N_1 number of discs, r_1 inner radius, r_2 outer radius, μ_1 dynamic viscosity ω_1 rotational speed h_1 distance between discs, Re : reynolds number

In Eq. 1 the inner and outer radius is constant, the distances between the clutch discs is assumed to be constant and equal for each gap. Furthermore the discs do not have grooves.

Katos’ model takes the cavitation between the discs at higher rotational speeds into account. Therefore he calculated the pressure in addition to Hashimotos formula [5]. Kato assumed that the cavitation starts at the inner radius because of the pressure.

$$p(r) = p(r_2) + \frac{\mu \cdot Q_s}{2 \cdot \pi \cdot r_m \cdot h^3 \cdot N \cdot G_r} \cdot (r_2 - r) - \frac{\rho \cdot \omega^2}{2} \cdot (r_2^2 - r^2) \cdot (f + \frac{1}{4}) \tag{2}$$

Equation 2: pressure distribution between clutch discs [5].

Nevertheless Yuan [6] proves that the air included in the gap is not a result of cavitation at the typical clutch speeds, but a result of centrifugal forces in the oil stream which results in air taken in from the outer radius. He defines a resulting radius r_0 due to this effect shown in Fig. 7, left.

In addition Yuan criticizes that the surface tension is neglected. The geometrical sizes are shown in Fig. 7, right. He takes the Capillary Number, the Weber

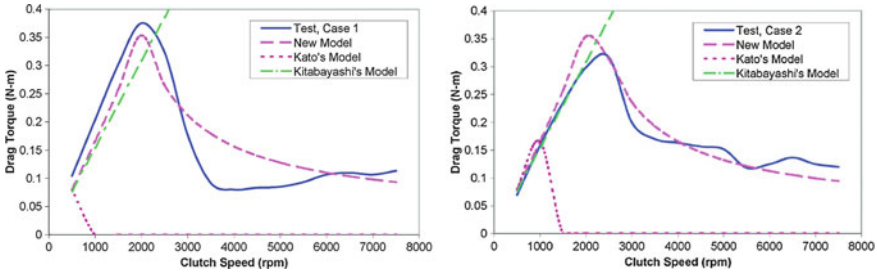


Fig. 8 Comparison of drag torques between model prediction and test case 1 and 2 [6]

Table 1 Parameters of test cases [6]

Case No	r_1 (mm)	r_2 (mm)	h (mm)	Q/facing (cm ³ /s)	T (°C)	ρ (kg/m ³)	μ (Pa s)	σ (N/m)
1	52.6	66.9	0.2	1.07	104	790.8	0.015	0.026
2	52.6	66.9	0.2	3.44	104	790.8	0.015	0.026

number and the Bond number additionally into account and finally defines following Eq. 3.

$$\frac{p \cdot \omega^2}{2} \left(f + \frac{1}{4} \right) r_0^2 - \frac{\mu \cdot Q}{2 \cdot \pi \cdot r_m \cdot h^3 \cdot G_r} r_0 + \frac{\mu \cdot Q}{2 \cdot \pi \cdot r_m \cdot h^3 \cdot G_r} r_1 - \frac{2 \cdot \sigma \cdot \cos(\theta)}{h} - \frac{p \cdot \omega^2}{2} \left(f + \frac{1}{4} \right) \cdot r_1^2 = 0 \tag{3}$$

Equation 3: difference of pressure at r_1 and r_0 equals zero [6].

Knowing the flow rate Q , Eq. 3 can be solved for r_0 . Now the drag torque between each disc is defined as:

$$T = 2\pi \int_{r_1}^{r_0} \frac{\mu \omega r^2}{h} (1 + 0.0012 \text{Re}^{0.94}) dr \tag{4}$$

Equation 4: drag torque between each disc [6] with r_0 derived from Eq. 3.

Yuan et al. validates the derived formula for different cases and shows the deviations of the former models; two results are shown in Fig. 8. The two test cases are different regarding the flow rate of oil (Table 1).

3 New Further Development of Analytical Models

For the special clutches mentioned in Chap. 2 there are other boundary conditions concerning the centrifugation of oil. The clutch is in a separate housing and filled with oil at all times. There are basically two important changes: Firstly, the oil

between the clutch discs is held longer than in open housings, because of the high turbulent tangential and radial estimated stream lines. Secondly, air is never taken in, so the housing is filled up with oil. Thirdly, there are deep grooves on each disc for the mentioned HCC-Effect.

It is assumed that the HCC-effect exists and works in the explained way. It is expected that the drag torque will permanently increase with the relative rotational speed, because no centrifugation is possible. That means that phase II of Fig. 3 will not take place. Furthermore, with increasing speed the oil temperature will increase as well as the turbulence. Higher temperatures mean lower viscosity and lower drag torque but the increasing turbulence means more friction and higher drag torque.

The following Sect. 3.1 presents measurements of a clutch with the HCC working principle in disengaged mode.

3.1 Measurements of a Hydrodynamically Cooled Clutch

In order to giving an impression of the measured characteristics, Fig. 9 shows the measured quantities. The test bench is speed driven. In this example the primary side of clutch is mechanically powered (combustion engine side) and the secondary side (gearbox) is locked. The second plot shows the drag torque which is increasing and never decreasing as seen with clutches with open housings (the little peaks are a result of accelerating the inertias). The third plot presents the temperatures of the test bench room (red), oil temperature in (blue) and oil temperature out (green). Finally the fourth plot shows the oil stream. The measurement took place during no oil stream. In order to get the temperatures in the clutch, oil was pumped through with 2 l/min for intervals of 5 s in between measurements. Because of that, there is a delay of ca. 25 s in the temperature curve, the time the oil from the input side needs to reach the sensor at the output side.

Newton's shear stress would predict a linear slope of drag torque over relative disc speed. However this is not true for discs with grooves as shown in Fig. 5. Taking this fact into account, a slightly increasing slope of drag torque is anticipated. Remember, the inside oil is accelerated by rotating discs and braked by standing discs. This causes a spherical oil stream inside the clutch which increases the oil viscous friction. Figure 10 shows the drag torque over relative speed and proofs this hypothesis.

3.2 Mathematical Modelling

In Sect. 3.1 it was shown that the drag torque is continuously rising with increasing relative speed. Additionally the slope of the curve is decreasing at higher speeds.

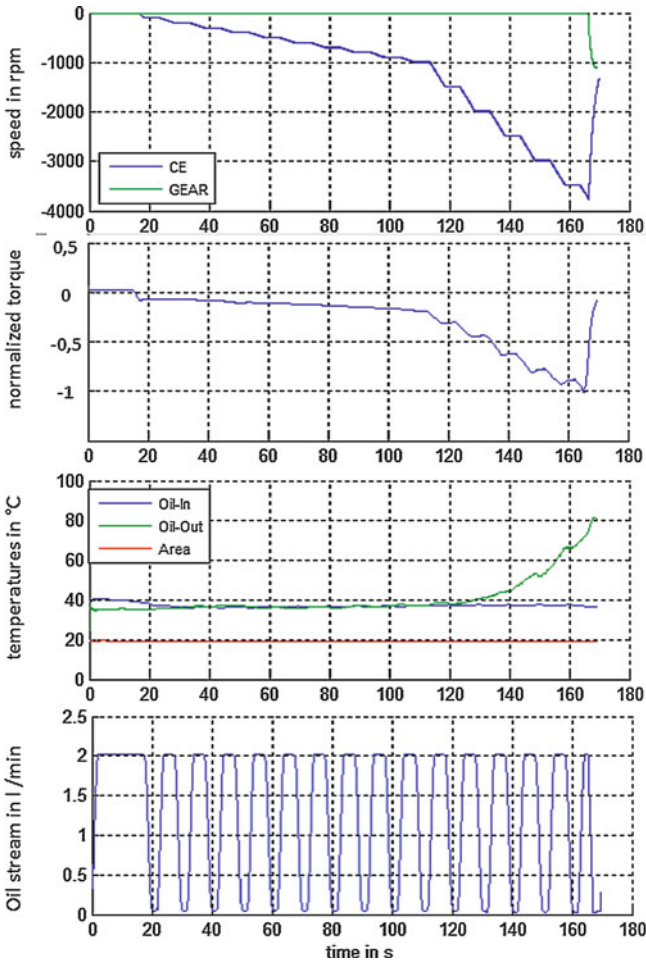


Fig. 9 Drag torque of a lubricated clutch with 6 discs

The hypothesis makes the increasing temperature responsible for this phenomenon, which will be modelled now. The approach uses the conservation of energy.

$$E_{kin} = \int_t \omega \cdot M dt = \int_t 2 \cdot \pi \cdot n \cdot M dt \tag{5}$$

Equation 5: kinetic energy

$$E_{term} = c_p \cdot m \cdot (T_{out} - T_{in}) \tag{6}$$

Equation 6: thermal energy

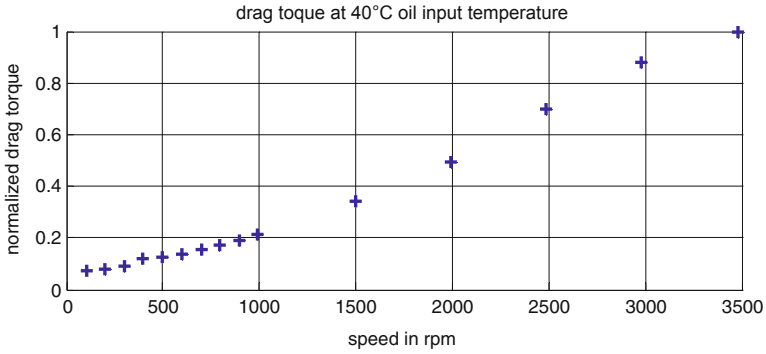


Fig. 10 Normalized drag torque over relative disc speed without inertias

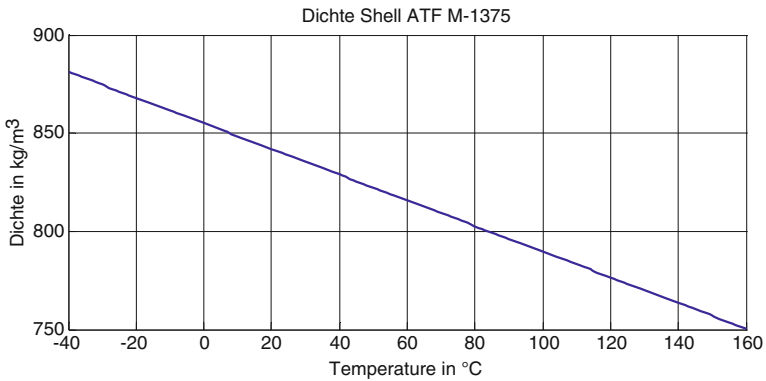


Fig. 11 Example of density-temperature-function of Shell ATF M-1375 ($\mu_{40\text{ °C}} = 85.2\text{ mPas}$) [12]

with:

$$m = \int_t \rho \cdot \dot{V} \cdot dt \tag{7}$$

Equation 7: mass of oil depending on the oil stream/second.

Equations 5 and 6 are equated and solved for ΔT . The thermal mass of the clutch and its pipes are neglected because of the very complex stream. Obviously there is a thermal transport between the oil and these components. For this simplification the measurements took place at operating point temperature.

Yuan’s model requires the dynamic viscosity which can be derived from $\mu = \vartheta \rho$.

The density is changing with the temperature. Function of the oil must be acquired (Fig. 11).

Fig. 12 Example of kinematic viscosity functions of ATF 134 (eta2, which is the more exact approach given by [7])

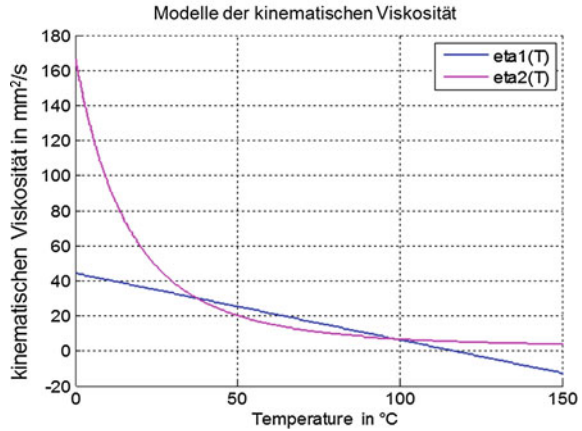
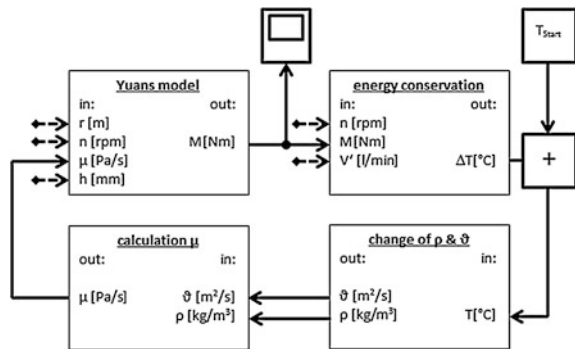


Fig. 13 Schematic model of the advanced drag torque model of lubricated clutches



The cinematic viscosity can be calculated with the given values in the specification sheet [7].

$$\vartheta(T) = e^{\frac{276,893 \cdot 10^6}{(T+273,15)^m}} \tag{8}$$

Equation 8: kinematic viscosity with:

$$m = \frac{\log(\log(\vartheta(T_1) + 0,8)) - (\log(\log \vartheta(T_2) + 0,8))}{\log(T_2 + 273,15) - \log(T_1 + 273,15)} \tag{9}$$

Equation 9: calculating exponent m (Fig. 12).

Finally the advanced model can be built. The schematic setup is shown in Fig. 13. This model calculates the drag torque of the oil between two non-grooved discs. In regard to the number of discs in the shown clutch (Fig. 5) the torque must be multiplied with 6.

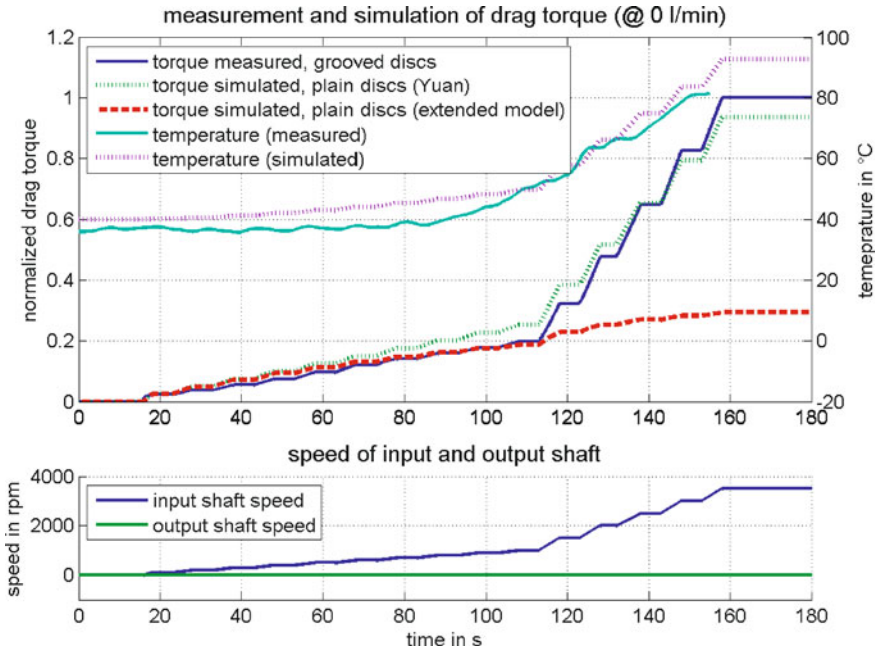


Fig. 14 upper measurement result of the grooved clutch discs (continuous blue) in comparison with plain simulated clutch discs with Yuan’s approach (dotted green) and the extended with a heat developing model (dotted red) further the simulated (dotted pink) and measured (turquoise) oil temperature is shown; below: the velocities of input and output shaft of the clutch

The outer radius r of a disc is constant due to the closed housing. The clearance h between the clutch discs must be assumed and will be discussed later. The model can also take varying distances between discs, so called “stochastically distributed” discs, into account. The rotational speed and the oil stream V' is defined by the operating control.

3.3 Comparison Between the Extended Oil Heating Model and Experiment

The approach of Yuan is modeled for plain, ideally distributed clutch discs. The goal of the extended model is to quantify the effect of the drag torque caused by the complex spherical oil stream (HCC) and the grooved clutch discs as well as a further influence caused by clutch discs with axial clearance. The real axial distribution is not known. Now, with help of the changing temperature, one unknown variable can be evaluated by the new extended model, which will now be verified in the following example setup:

The input shaft of the disengaged clutch is accelerated in certain steps and the output shaft is locked. After reaching each step the drag torque as well as the oil temperature is being measured. By proceeding this way, the inertias are not taken into account, as it can be seen in Fig. 14. The torque is normalized to the base of the highest measured drag torque.

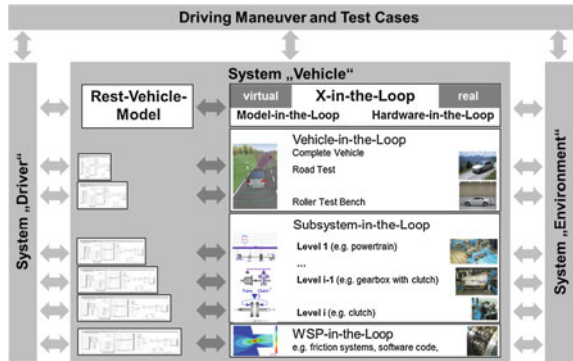
Figure 14 shows several things in the upper plot: firstly, the measured drag torque (continuous blue) of grooved discs and the simulated one of plain discs (dotted green) do not deviate significantly until reaching a relative velocity of 1000 rpm. That is not expected because of the different design and the free clutch discs resulting in an inhomogeneous axial distribution. So, a higher torque in the measurement is estimated. In between the drag torque measurements the oil is partly streaming out at 2 l/min (also see Fig. 9). Only a slight increase of the oil stream temperature is measured, which is a hint for a higher oil temperature between the discs. Secondly, the dotted red line is showing the drag torque result of the extended model, which takes oil heating into account. The model still uses plain, ideal distributed clutch discs. That's why a very big deviation to the measurement arises, when increasing the relative velocity above 1,000 rpm. The curve of the original model of Yuan is only similar by chance. Other measurements show a big deviation between Yuan's model and measurement, especially when the starting oil temperature is higher.

Additionally, the measured (continuous turquoise) and the simulated (dotted pink) oil temperature is plotted. The temperature curves are very similar. The small deviation can be explained by the neglected thermal masses in the oil heating model. The oil heating model based on energy conservation can be considered as verified for this specific clutch using the HCC-effect.

Several Hypotheses Can Be Made:

1. During small relative velocities ($\leq 1,000$ rpm) the difference in drag torque between grooved and non-grooved discs is very small, negligible. This discovery matches the results of Oerleke [8] before air is taken in (phase 1) in his setup. But furthermore, the oil heating is very similar and small, which is a result of the same small drag torques.
2. The grooved discs which are designed for the so called HCC-effect seem to work with relative velocities higher than 1,000 rpm in the used clutch system. This hypothesis is based on the following idea: If a spherical oil stream exists it is assumed that the drag torque has to rise because of the pumping losses.
3. The measurement is compared to ideally distributed clutch discs. Simulations based on Newton's shear stress predict a rising drag torque when shifting the clutch discs to an inhomogeneous distribution. Obviously the deviations are very little until reaching 1,000 rpm relative velocity, so it can be assumed that the real clutch discs are almost ideally distributed.
4. Raising the relative velocity above 1,000 rpm results in significant differences between the simulation of plain clutch discs with oil heating model and the measurement. There are two effects explaining the deviation: first, the inhomogeneous axial distribution of clutch discs. Secondly, the energy used for the

Fig. 15 The XiL-framework [9]



pump effects in the clutch. This phenomenon takes up to 70 % of the drag torque at a relative velocity of 3,500 rpm compared to plain, ideally distributed clutch discs.

3.4 Results in Aspects of the System "Vehicle"

These cognitions are based on investigations of the clutch system, which can be found in the real and virtual unit under test in the XiL-framework of IPEK in the level "Subsystem-in-the-loop" [9]. Figure 15 shows the different levels of investigation and the integration of driver, environment and rest-vehicle-model.

In aspects of using this clutch system in a full parallel hybrid vehicle (complete "Rest-Vehicle-Model" in interaction with driver, environment and maneuvers), these hypotheses lead to several possible steps. One important step is adapting the dimensioning of the electric motor for low speeds, if the clutch is used as introduced in order to receive low losses during electric driving. There are conflicts of aims regarding the degree of efficiency, packaging, high voltage system and driver behavior.

So, the other important thing on this specific clutch with its HCC-effect is that a development method has to be defined for developing the right clutch for the right drivetrain topology.

Therefore the XiL-framework delivers a method to take the remaining system at the beginning of a development project into account.

4 Summary and Outlook

First a specific clutch with HCC-effect for full parallel hybrids was introduced. The potentials of this clutch lie in the direct energy conversion from mechanical energy into kinetic energy of an oil stream for cooling itself as well as in the use of only one

clutch instead of two clutch systems. A development task is derived by improving the drag torque during disengaged state as it is in electric drive mode of the hybrid vehicle. Therefore an investigation on the clutch system was shown in two ways: the real clutch-system-in-the-loop as well as a virtual model-in-the-loop. By doing this the XiL-Approach was used. Now the ratio between the drag torque of plain clutch discs and grooved ones evoking the HCC-effect could be shown which amounts to 3:7 at 3,500 rpm relative velocity between the clutch discs. Therefore an extension of Yuan's existing approach was needed and introduced as well as implemented. Now it is possible to calculate the oil heating and furthermore the real drag torque because the changing viscosity of the oil is taken into account. The verification was shown exemplarily on an example setup.

In further investigations the axial positions of the clutch discs have to be measured. One approach would be to open the original housing and replacing a piece of metal housing with fused quartz. Using a rotational speed triggered camera it is possible to observe the axial position. Additionally a further validation platform investigating a single clutch disc can be used, as presented in: [10].

References

1. Frey D (2011) Wärmeübergang Lamellenkupplungen—Ermittlung von Wärmeübergangsverhalten und Schluckvermögen von Lamellenkupplungen und Verifizierung und Erweiterung der Modellierung des Wärmeübergangs in KUPSIM, FVA
2. Sachs Handel GmbH; Funktions- und Werkstatthinweise für Kraftfahrzeugteile; 2006 Schweinfurt
3. Sasse C, Sudau J (2009) HCC—Wet-Running clutch for automatic transmissions: with the best cooling concept, (almost) anything is possible. In: Augsburg: CTi, 2009, S. pp 161–173
4. Hashimoto H, Wada S, Murayama Y (1984) The performance of a turbulent-lubricated sliding bearing subject to centrifugal Effekt, 1984
5. Kato Y, Murasugi T, Hirano H, Shibayama T (1993) Fuel economy improvement through tribological analysis of the wet clutches and brakes of an automatic transmission. In: JSAE technical paper Nr. 9305436
6. Yuan Y, Liu EA, Hill J, Zou Q (2007) An improved hydrodynamic model for open wet transmission clutches. In: Journal of Fluids Engineering Bd. 129 (2007), Nr. 3, S. p 333
7. Gebhardt N (2008) Hydraulik: Grundlagen, Komponenten, Schaltungen. 4. Aufl. Berlin [u.a.]: Springer, 2008—ISBN 9783540795346
8. Oerleke C (1998) Leerlaufverhalten ölgekühlter Lamellenkupplung. FVA, Hamburg
9. Albers A, Schroeter J, Zingel CHR, Schwarz A, Behrendt M (2012) System-oriented validation aspects of a driver assistant system based on an accelerator-force-feedback-pedal. In: FISITA World Automotive Congress. Beijing, 2012
10. Albers A, Brezger F, Koch C (2012) Development of a new validation environment for CFD simulations on the example of a lubricated clutch; In VDI-Gesellschaft Entwicklung und Konstruktion Vertrieb(E.d.); Getriebe in Fahrzeugen 2012, Düsseldorf VDI Verlag GmbH
11. Sasse C (1995) Hydrodynamische Kupplung mit radialen Schaufelgittern: experimentelle Analyse der Strömung und Momentübertragung bei Variation der Gittergeometrie. Göttingen : Cuvillier, 1995—ISBN 9783895883521
12. Shell, ATF 134 specification sheet, Shell Deutschland Oil GmbH, 22284 Hamburg; 2007

AWD Coupling Modeling and Contribution to Vehicle Dynamics

Aris Maroonian, Tsutomu Tamura and Robert Fuchs

Abstract Controllable AWD coupling systems are applied for optimizing vehicle traction capability and dynamic performance by adequately distributing the torque between the front and the rear axle according to the driving conditions. With its linearity, compactness and low power consumption, JTEKT Intelligent Torque Controlled Coupling (ITCC) shows a high performance to power consumption ratio. A 5-dof model of an ITCC is proposed for satisfying the requirements on further insight on the internal dynamics and its interaction with the vehicle driveline. Difference in simulated vehicle performance is shown by comparing a generic 2-dof and the 5-dof model of the ITCC. The results obtained justify the development of evolved coupling modeling for a better understanding of the internal motion of the coupling and the interaction with the driveline.

Keywords AWD coupling · Torque distribution · Friction · Vehicle dynamics · Modeling

1 Introduction

FWD based AWD vehicles are known to offer a valuable compromise between dynamic performance and fuel consumption. The additional cost, weight and power consumption resulting from the implementation and operation of an AWD

F2012-C05-005

A. Maroonian (✉) · T. Tamura
JTEKT Corporation, R&D Center, Nara, Japan
e-mail: aris_maroonian@jtekt.co.jp

R. Fuchs
JTEKT Europe, EU Representative Office of JTEKT R&D Center, Paris, France

coupling are acceptable in comparison to the benefits gained from the enhanced capability of distributing the torque to the four wheels of the vehicle. The cost, weight and power penalties are regularly reconsidered with respect to changing market trends. Also, the quest of continuously improving vehicle performance along with the competition between the AWD couplings available on the market forces the engineers to deepen their understanding of the technology for delivering optimized solutions.

The main configurations of AWD coupling found are listed below

- Electro-mechanical configuration based on an electromagnetic actuation.
- Electro-mechanical configuration based on an electric motor actuation.
- Hydro-mechanical configuration based on an electric pump and valve actuation circuit.

The *Intelligent Torque Controlled Coupling* or *ITCC* of JTEKT is an electro-mechanical AWD coupling based on an electromagnetic actuation offering a high performance to power consumption ratio. It is characterized by a high power capacity, fast torque response and low level of NVH (Noise Vibration and Harshness).

While efforts in developing better material for the clutch plates, oil and actuation concepts have been published [1, 2, 3], little information is available on the dynamics of AWD couplings and its effect on the vehicle performance [4, 5]. One of the main reasons is the difficulty to accurately representing friction while ensuring fast computation in a simulation environment.

The objective of this paper is to present the development of a model of the dynamics of an ITCC. The model is composed of inertia, stiffness, damping, friction elements and drag torque. The computation of the actuator response should correlate with experimental measurements across the frequency range of operation. In actual driving conditions, the torque response of the coupling is defined within a bandwidth of about 10 Hz.

The remaining of this paper is organized as follows. The ITCC is described before presenting a 5 dof (degree-of-freedom) model. Then, the static and dynamic performances are illustrated with simulation and experimental data. The contribution of the ITCC dynamics to the vehicle performance is explored with simulation prediction. At last, conclusions are drawn and an outlook of this work is given.

2 Description of the ITCC

The conventional structure of an ITCC, represented in Fig. 1, is composed of two clutches (pilot and main) separated by a ball cam and an electromagnetic actuator. It has a coaxial configuration with the input shaft corresponding to the outside diameter or housing. The main clutch pack is composed of a 12×12 (inner vs. outer) paper-based wet type friction plates while the pilot clutch pack of a 1×2

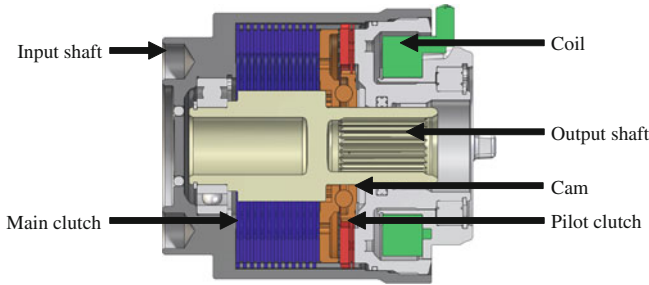


Fig. 1 Cut-view of an ITCC from JTEKT

iron-based ferromagnetic friction plates. Both clutches are connected to the input shaft. The inner plates of the pilot clutch are connected to the pilot cam, while those of the main clutch are connected to the output shaft. Six steel balls are located between the pilot and the main cam for generating an axial force to the main clutch depending on the torque equilibrium.

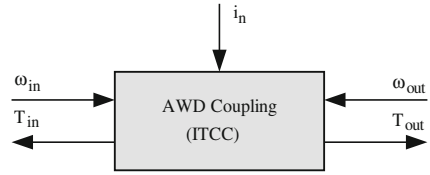
The axial or normal force of the pilot clutch is controlled with the current of the coil. Ideally, when no current is applied to the electromagnetic actuator, no torque is transmitted between the shafts regardless of the input and output speed. However, because of the lubrication fluid, a drag torque is observed even in the case of zero current. Applying a current to the electromagnetic actuator generates an axial force engaging the pilot clutch, thus coupling the pilot cam to the input shaft. Any torque imbalance between the pilot and the main cam causes the balls to travel along the cam profile generating an axial force to the main clutch. In summary, the ITCC enables the transmission of high torque from a small actuation power. The transmission of high torque is obtained with the pilot clutch and cam system that transform a small portion of the input torque into the adequate axial force of the main clutch.

3 Modeling

AWD couplings are nonlinear MIMO systems. The input and output shafts rotational speeds ω_{in} and ω_{out} together with the actuator command i_n represent the system inputs, while the shafts reaction torques T_{in} and T_{out} the system outputs (Fig. 2). As a convention, the input shaft is coupled to the transmission output side and the output shaft to the rear axle differential. The slip of the main clutch is defined as a function of the input and output rotational speeds.

Depending on the objective of the analysis, AWD couplings can be represented with different degrees-of-freedom (dof). The most common and simple modeling structure is composed of two inertias coupled with a friction torque. The dynamics of the actuator is included in this generic 2-dof model because of its significant contribution to the coupling response. The key in representing the coupling is the friction representation. The LuGre model offers an accurate and computationally

Fig. 2 AWD Coupling inputs and outputs



efficient representation of friction. This model has been developed with the intention of representing accurately friction with a continuous state formulation and which could be used in control applications. Moreover, it gives a representation of the friction effects such as the Stribeck effect, stiction and hysteresis [6].

The dynamics of a FWD powertrain equipped with an ITCC can be represented by using this generic model [7, 8]. Basic design investigation as well as fundamental dynamics of vehicle using high level controls, such as yaw moment control or torque vectoring, can be also addressed with that model. Nevertheless, accurate representation of the actual coupling and of its interaction in the driveline requires more detailed models to be developed. The proposed model has been developed with the objective of describing the internal mechanism of the ITCC. The interest is to describe the internal variables, such as the cam displacement, which are hardly measurable and to accurately represent the input–output performance. Applications of this model are intended for design optimization, interaction in the driveline and control development.

The motions of the components of the ITCC are defined in two directions: the x -direction representing the rotational motion (planar representation) and the y -direction representing the axial motion. It is assumed that the motion of the input shaft, the output shaft, the pilot clutch and the pilot cam are defined along the x -direction only, while that of the main clutch and the main cam in both the x and the y -directions. The friction of each clutch pack is lumped into a single friction coefficient parameter set. Effects caused by the variation of temperature, wear as well as the bearings friction are neglected.

Table 1 compares the two model structures introduced.

The developed ITCC model is composed of four inertias, the input shaft I_{in} , the pilot cam and pilot clutch inner plates I_p , the main clutch plates I_m and the output shaft I_{out} together with one mass m_m representing the main clutch inner plates and main cam. The five corresponding equations of motions write:

$$I_{in}\dot{\omega}_{in} = \vec{T}_{in} + \vec{T}_{m,s} + \vec{T}_{f,pc} + \vec{T}_d \tag{1}$$

$$I_p\dot{\omega}_p = \vec{T}_{f,pc} + \vec{T}_{Np} + \vec{T}_{Ff,p} \tag{2}$$

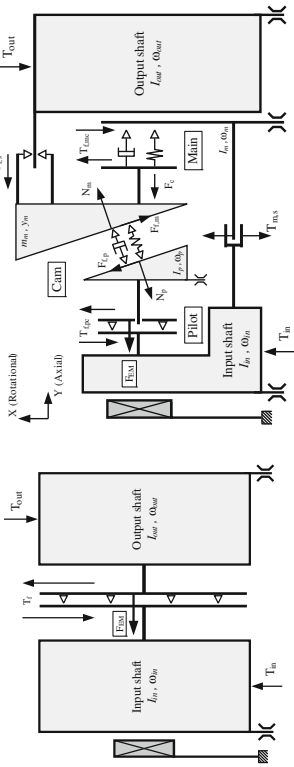
$$I_m\dot{\omega}_m = \vec{T}_{m,s} + \vec{T}_{f,mc} \tag{3}$$

$$I_{out}\dot{\omega}_{out} = \vec{T}_{out} + \vec{T}_{f,mc} + \vec{T}_{Nm} + \vec{T}_{Ff,m} + \vec{T}_d \tag{4}$$

$$m_m\ddot{y}_m = \vec{N}_m + \vec{F}_{f,m} + \vec{F}_c + \vec{F}_{f,s} \tag{5}$$

Table 1 Comparison of 2-dof and 5-dof model of AWD coupling

Model structure



2-dof model.

5-dof model.

Comparison of modeling representations

- Shafts inertia, stiffness and damping
- One clutch friction model
- Actuator normal force

- Shafts inertia, stiffness and damping
- Pilot and main clutches friction model
- Pilot actuator normal force
- Cam angle, ball stiffness and damping
- Main clutch nonlinear stiffness
- Axial clearance and friction
- Rotational backlash

Applications

- Basic design
- Vehicle dynamics
- Model-based control

- Detailed design (ITCC-like)
- Coupling parameter study
- Coupling response optimization
- Clutch friction improvements
- Vehicle dynamics interaction

where ω_{in} is the input shaft rotational speed, ω_{out} the output shaft rotational speed, ω_p the pilot cam and pilot clutch inner plates rotational speed, ω_m the main clutch plates rotational speed and y_m the main clutch inner plates and main cam axial position, T_{in} the input shaft torque, T_{out} the output shaft torque, $T_{f,pc}$ and $T_{f,mc}$ the pilot and main clutch friction torques, $T_{m,s}$ the main clutch spline torque, T_{Np} and T_{Nm} the pilot and main cam torques defined with the cam effective radius r_{cam} (radial distance between the shafts axis and the ball contact) and the cam internal forces N_p and N_m , $T_{Ff,p}$ and $T_{Ff,m}$ the load dependent friction torques in the cam defined by the cam effective radius and the cam internal friction forces $F_{f,p}$ and $F_{f,m}$, F_c the reaction force of the main clutch inner plates, T_d the oil drag torque defined by the input and output shafts rotational speeds difference and $F_{f,s}$ the spline load dependent friction force.

The clutch friction torques, $T_{f,mc}$ and $T_{f,pc}$, are defined with the friction coefficient, μ_p and μ_m , the number of plates, n_p and n_m , the clutch mean radius r_p and r_m , and the normal force $F_{n,m}$ and $F_{n,p}$:

$$\vec{T}_{f,pc} = \mu_p r_p n_p F_{n,p} \quad (6)$$

$$\vec{T}_{f,mc} = \mu_m r_m n_m F_{n,m} \quad (7)$$

The friction coefficients μ_p and μ_m are defined from the previously introduced LuGre model. The friction coefficient μ of the LuGre model is formulated as a function of the bristle deflection p and the slip v . The slip of the pilot and the main clutches are defined respectively as functions of the input and the output rotational speed, and the input and pilot cam rotational speed:

$$\mu = \sigma_0 p + \sigma_1 \dot{p} + \sigma_2 v \quad (8)$$

$$\dot{p} = v - \sigma_0 \frac{|v|}{g(v)} p \quad (9)$$

$$g(v) = \mu_c + (\mu_{ba} - \mu_c) e^{-(|v|/v_{sb})^2} \quad (10)$$

where μ_c is the Coulomb friction coefficient, μ_{ba} the peak friction coefficient, v_{sb} the Stribeck velocity, σ_0 and σ_1 the contact stiffness and damping coefficients in the tangential direction and σ_2 the viscous friction coefficient. Typically, these six parameters, related to the bristle state, are experimentally identified.

4 Static and Dynamic Performances

The static torque response against the current and the main clutch slip is illustrated in Fig. 3a. The transmitted torque is nonlinearly dependent on the current because of the nonlinear relation between the current and the normal force of the pilot cam. The

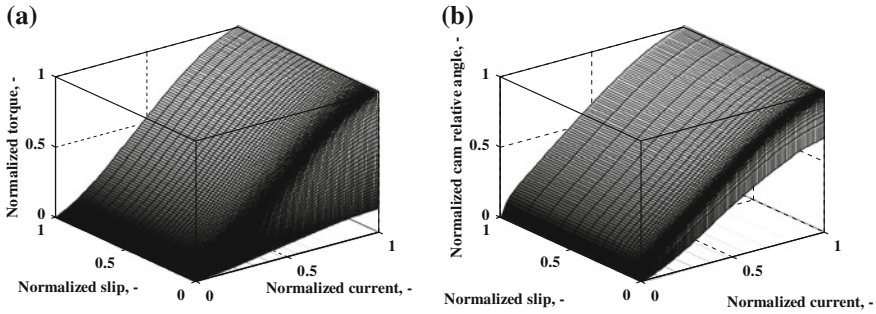
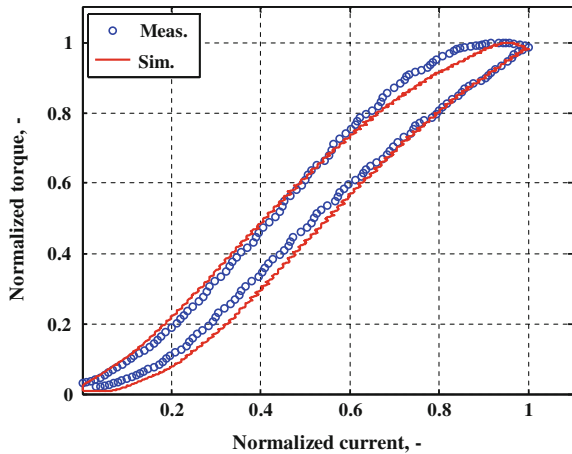


Fig. 3 Static characteristics

Fig. 4 Hysteresis of the current to torque response



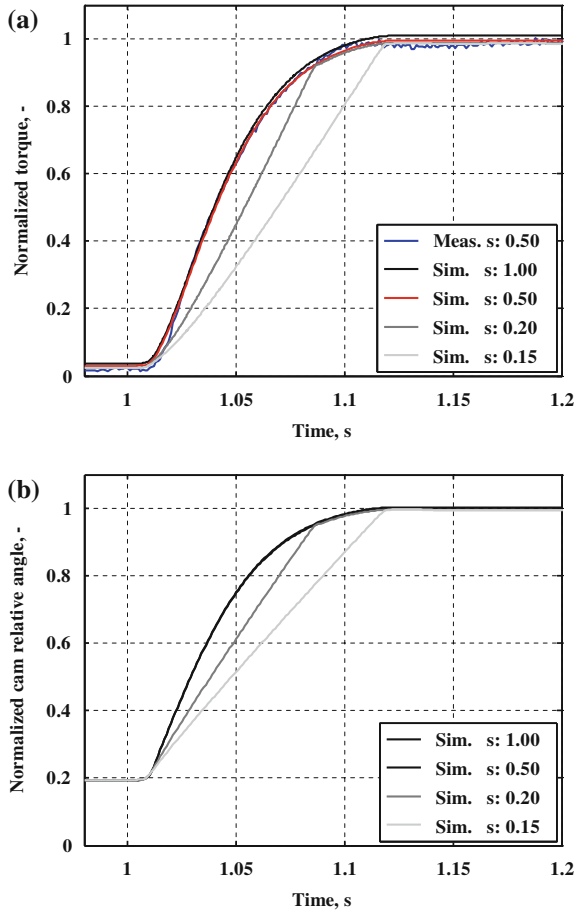
effect of slip is noticeable at low value with the stiff transition up to the Coulomb friction value. The torque is virtually independent of the slip at higher value.

The cam relative angle versus the current and the slip is illustrated in Fig. 3b. The tendency relative to the slip is similar to that observed for the torque response. The torque sensitivity decreases as the current increases. A quasi-linear relation is observed for typical operating values. The nonlinearities observed at low and high current are caused by the axial stiffness of the main clutch pack.

Because of the electromagnetic actuation and the internal friction, hysteresis in the static characteristic can be anticipated. This is illustrated in the current to torque static response shown in Fig. 4 where both measured and simulated data are in adequate correlation.

The dynamic input–output characteristic is illustrated with torque responses to current and speed steps. Figure 5 shows simulated torque and cam relative angle responses for current steps at different constant slip conditions. Experimental data are also given in the case of a slip of 0.5 showing good prediction accuracy from the simulation. The analysis of the torque response shows that, for high slip speeds

Fig. 5 Current step characteristics



conditions, the torque response is limited by the actuator dynamics, whereas for lower slip conditions, it is the dynamics of the internal mechanism that becomes dominant. This observation is valid for both torque and cam angular motion responses.

The torque responses to various slip ramp slopes and at constant current are presented in Fig. 6. This illustrates the effect of different acceleration conditions in the driveline. The rate of slip change delays the response of the torque transmitted. The response itself is virtually not affected by the slip rate.

5 Vehicle Performances

An in-house developed vehicle model, with its representations summarized in Table 2, is used to characterize the ITCC dynamics contribution to the vehicle

Fig. 6 Slip speed step characteristics

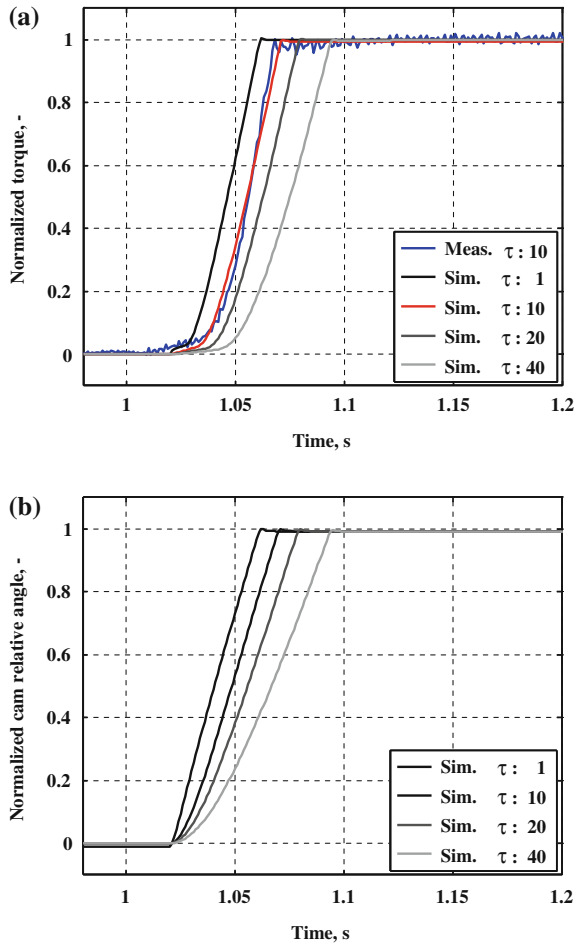
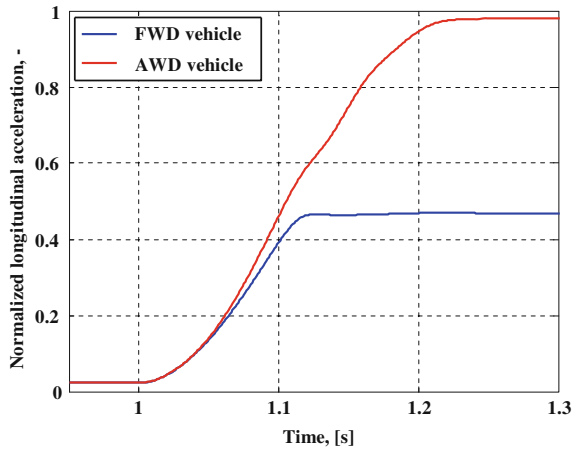


Table 2 Description of the vehicle model

System	Modeling	Description
Chassis-body	Suspension force/torque	Accurate location
	Aerodynamic force/torque	Lumped force, no torque
	Powertrain force/torque	Engine mapping, drivetrain
Wheel-tire	Weight/inertia distribution	Single mass, inertia
	Traction force	Simple nonlinear model
	Tire compliance force, contact normal force	Stiffness model, center of contact
Suspension	Brake torque	Direct input on wheel, friction
	Stiffness, damping, stopper	Linear or nonlinear coefficient
Steering	Linkage geometry, kinematic and compliance	Castor angle, basic constraints
	Compliance	Lumped to rack bar
	Rack force to steering force	Basic kinematic

Fig. 7 Longitudinal acceleration on low- μ



dynamics. The following vehicle dynamics simulations are accomplished without any feedback control of the ITCC.

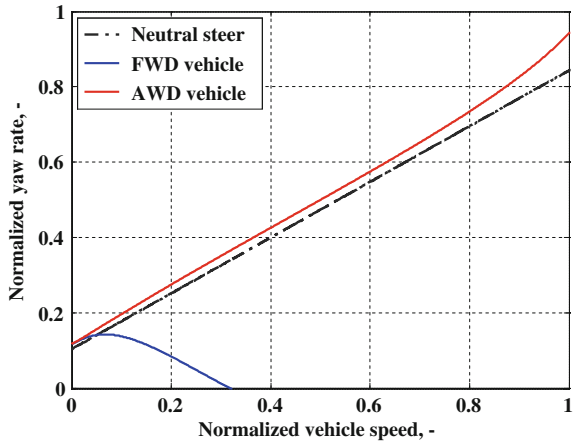
Comparisons of the dynamics of FWD and AWD vehicles are illustrated in Figs. 7 and 8 for longitudinal acceleration and constant radius cornering. The AWD-based vehicle model is composed of a FWD powertrain and an ITCC, which current command is maintained at high level resulting in a constant 50:50 torque distribution compared to the 100:0 distribution of the FWD vehicle. Both driving conditions are simulated on low- μ road surface conditions (ice).

The longitudinal acceleration simulation consists of a throttle command step applied at $t = 1$ [s]. The effect of the ITCC is best seen at the beginning of the acceleration where both vehicles have a similar acceleration until sufficient slip is generated across the ITCC for distributing the torque to the rear wheels. This results in a faster acceleration of the AWD vehicle after about 50 ms as seen in Fig. 6 (effect of slip on torque response). The basic improved traction performance of AWD vehicle is also observed with a significantly higher maximum longitudinal acceleration capability.

The constant radius cornering on low- μ road maneuvers, with a steering fixed at a certain angle and with the throttle command smoothly increasing, shows that AWD vehicles have a slight over-steer tendency along the neutral steer condition compared to the FWD under-steer characteristics. The tire longitudinal and side slip ratio along with the torque distribution are responsible of the trajectory deviations.

A study of the ITCC contribution in the vehicle dynamics is presented in Fig. 9. This simulation consists of a FWD based AWD vehicle initially stopped and with the ITCC coupling disengaged. At $t = 1$ [s], a ramp throttle command reaching 30 % at $t = 2.5$ [s] is applied. With initially dry road condition on the four wheels, the vehicle front axle drive torque increases implying a vehicle longitudinal acceleration and the rear axle to be driven.

Fig. 8 Constant cornering on low- μ



Throttle	0 %	Ramp (0 to 30%)	30 %
Road Condition	Front	Dry (High μ)	Snow (Low μ)
	Rear	Dry (High μ)	
ITCC	Disengaged		Engaged

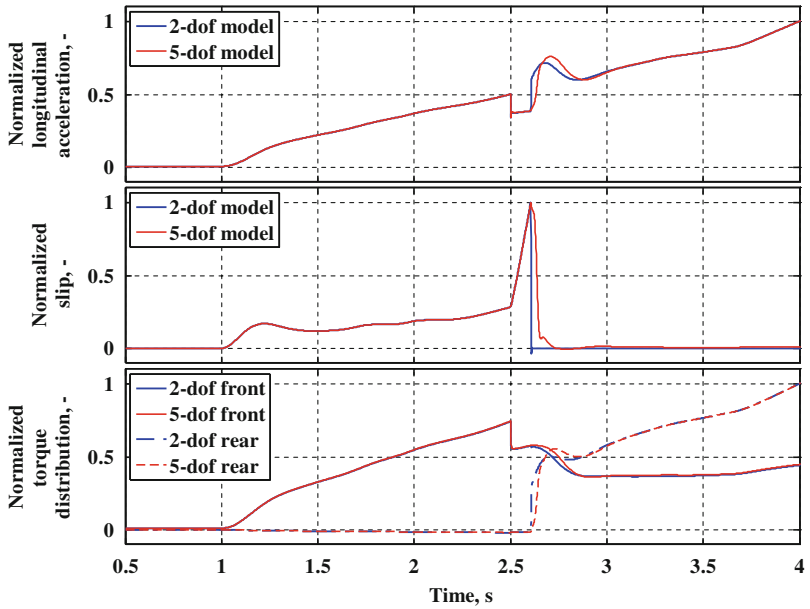


Fig. 9 ITCC dynamic contribution in the vehicle dynamics

At $t = 2.5$ [s], the front tires road condition changes to snow, resulting in a front axle drive torque drop and a sudden longitudinal deceleration. As the front axle wheels spin on the snow surface, the ITCC slip speed increases. At $t = 2.6$ [s], the ITCC is engaged distributing a part of the driving torque to the rear axle and reducing the slip speed.

As the ITCC is engaged, torque is transmitted to the rear axle with a certain dynamics defined by the coupling representation (2-dof or 5-dof). In the case of a 2-dof model, faster torque response implying drastic slip reduction and faster longitudinal acceleration dynamics, compared to the developed 5-dof, are observed. Because the generic representation has no internal dynamics, it shows ideal vehicle performance unfortunately not realistic as requiring too much energy for its actuation. This maneuver justifies the need of using evolved AWD coupling for an accurate representation of the vehicle performance.

6 Conclusion

A 5-dof model of an ITCC has been developed and validated in static and dynamic conditions against experimental data in actual operating conditions. The model enables the simulation of the motion of the internal mechanism, such as that of the cam relative angular displacement.

Contribution of the ITCC dynamics to the vehicle performance has been addressed so as to justify the development of such evolved model in opposition to generic 2-dof models. The results obtained demonstrate the requirement for such a detailed coupling model for design optimization and model-based control of AWD vehicles.

References

1. Ando J, Sakai N, Saito T, Kuwabara H, Kurosawa O (2007) Development of exclusive fluid for AWD coupling. In: JSAE 2007
2. Ginther BB, Kowalsky C (2007) Development of an AWD coupling and controls for a high performance sports car. In: SAE International 2007
3. Teraoka M (1993) Development of the electro-magnetic controlled limited slip differential unit. In: SAE International 1993
4. Ohba M, Suzuki H, Yamamoto T, Takuno H (1999) Development of a new electronically controlled 4WD system: Toyota active torque control 4WD. In: SAE International 1999
5. Ando H, Murakami T (2004) AWD vehicle simulation with the intelligent torque controlled coupling as a fully controllable AWD system. In: SAE International 2004
6. Canudas-de-Wit C, Olsson H, Alstrom KJ, Lischinsky P (1995) A new model for control of systems with friction. *IEEE Trans Autom Control* 40:419–425
7. Dolcini PJ, Bechart H, Canudas-deWit C (2005) Observer-based optimal control of dry clutch engagement. In: IEEE 2005
8. Cheli F, Pedrinelli M, Zorzutti A (2007) Integrated vehicle and driveline modeling. In: SAE International 2007